UNIVERSITY OF SOUTHAMPTON

FACULTY OF ENGINEERING AND THE ENVIRONMENT

Aeronautics, Astronautics and Computational Engineering and Design

Design and Control of Solar Radiation Pressure Assisted Missions in the Sun-Earth Restricted Three-Body Problem

by

Stefania Soldini

Thesis for the degree of Doctor of Philosophy

August 2016

Stefania Soldini: *Design and Control of Solar Radiation Pressure Assisted Missions in the Sun-Earth Restricted Three-Body Problem*, Doctor of Philosophy, Astronautics Research Group, Department of Aeronautics, Astronautics and Computational Engineering, Faculty of Engineering and the Environment, University of Southampton

ADVISORS:
Dr. Scott J. I. Walker
Dr. Camilla Colombo

EXAMINERS:
Prof. Colin McInnes, University of Glasgow
Dr. Dina Shona Lila, University of Southampton

LOCATION:
Southampton, England

DATE:
June 20, 2016

“For my part, I know nothing with any certainty, but the sight of the stars makes me dream” - Vincent Van Gogh.

Dedication

In memory of Robert W. Farquhar who passed away in October 2015. Farquhar gave a great contribution to spacecraft trajectory design in particular in the field of the restricted three-body problem. He is also credited with being the first to develop the use of halo orbits with NASA's ISEE-3 mission. The term "halo" was proposed by him in his Ph.D. thesis in 1968. It was simply by chance that, in October 2014, I met Farquhar and his wife, Irina Vostokova, at the 65^{th} International Astronautical Congress in Toronto. Farquhar was very inspiring to me. He was curious about my thesis, and he encouraged me to further my research in the restricted three-body problem. I was also honoured and delighted when I received a copy of his memoirs after we met at the conference.

Robert W. Farquhar (left) and Stefania Soldini (right) at the gala dinner of the 65^{th} International Astronautical Congress, Toronto, Canada, October 2014.

UNIVERSITY OF SOUTHAMPTON

ABSTRACT

FACULTY OF ENGINEERING AND THE ENVIRONMENT
Aeronautics, Astronautics and Computational Engineering and Design

Doctor of Philosophy

DESIGN AND CONTROL OF SOLAR RADIATION PRESSURE ASSISTED MISSIONS IN THE SUN-EARTH RESTRICTED THREE-BODY PROBLEM

by Stefania Soldini

The scientific interest in space exploration is driven by the desire to answer fundamental questions relating to the formation of our solar system and life on Earth. Space agencies are currently pushing the boundaries of space mission design to meet scientific goals. Thus, space missions require novel trajectories to further human space exploration. A modern approach that has arisen in space mission design is to use dynamical system tools that exploit the natural dynamics of the solar system. A spacecraft's natural dynamics are affected by environmental perturbations such as Solar Radiation Pressure (SRP). Traditionally, the design of space missions requires any perturbations to be counteracted through corrective manoeuvres. However, these corrective manoeuvres require propellant and therefore the pre-storing of fuel. This thesis investigates fuel-free propulsion for harnessing SRP in the design of space missions of the Sun-Earth restricted three-body problem. SRP propulsion is applied to the spacecraft's orbit control and furthermore to create the propulsion required for the design of transfers between quasi-periodic orbits and end-of-life disposal trajectories. The advantage of SRP manoeuvres is that the spacecraft can have access to an unlimited source of *propellant* (the Sun's radiation) consequently extending its *life* and reducing the overall mission costs; where the advancement in space technology makes harnessing SRP devices possible for future missions design. SRP manoeuvres are triggered by light and extended reflective deployable structures (i.e., mirror-like surfaces). The magnitude of the SRP acceleration is a function of the spacecraft's area-to-mass ratio, its reflectivity properties, mass and orientation of the reflective surface to the Sun-line direction. This thesis demonstrates that SRP manoeuvres are an effective and an efficient approach to stabilise the natural dynamics of the spacecraft in the Sun-Earth system. The size of the required reflective deployable area and spacecraft pointing accuracy are the ultimate outcomes of this research. Along with the design of the reflective area, the definition of a new control law, a method to perform transfers between quasi-periodic orbits and a strategy for the end-of-life disposal are the major important research findings.

Contents

List of Figures

List of Tables

Declaration of Authorship

I, Stefania Soldini , declare that the thesis entitled *Design and Control of Solar Radiation Pressure Assisted Missions in the Sun-Earth Restricted Three-Body Problem* and the work presented in the thesis are both my own, and have been generated by me as the result of my own original research. I confirm that:

- this work was done wholly or mainly while in candidature for a research degree at this University;
- where any part of this thesis has previously been submitted for a degree or any other qualification at this University or any other institution, this has been clearly stated;
- where I have consulted the published work of others, this is always clearly attributed;
- where I have quoted from the work of others, the source is always given. With the exception of such quotations, this thesis is entirely my own work;
- I have acknowledged all main sources of help;
- where the thesis is based on work done by myself jointly with others, I have made clear exactly what was done by others and what I have contributed myself;
- parts of this work have been published as: (Soldini et al., 2016a), (Soldini et al., 2015b), (Soldini et al., 2016b), (Soldini et al., 2016c) and (Colombo et al., 2015a)

Signed:.....

Date:.....

Acknowledgements

I would like to acknowledge all those people who have supported me over the last few years and who have helped me in the writing of the thesis with suggestions, criticisms and comments: to them goes my gratitude.

My deepest gratitude is to my first, Dr Scott J. I. Walker, and second, Dr Camilla Colombo, supervisors. Thank you for your supervision and allowing me the space and freedom I need to work. Without that freedom, I could not develop my self-confidence and creativity as a researcher. I would also like to thank my viva examiners, Prof. Colin McInnes, from the School of Engineering at the University of Glasgow and Dr Dina Shona Laila from the Electro-Mechanical Engineering Research Group at the University of Southampton, for their valuable insights and detailed comments on how this work in its original form could be improved.

I would like to give a special thank to Ms Emma Stephenson from the Graduate School office for being the first friendly face I have met at the commencement of my Ph.D. and for always having a prompt answer to my questions.

My gratitude is also extended to Prof. Gerard Gómez from the Department de Matemátiques i Informática at the Universitat de Barcelona and Prof. Josep J. Masdemont from the Department de Matemátiques at the Universitat Politécnica de Catalunya for being my mentors at the end of my Ph.D. Although the short internship, I am grateful for your personal and technical support. I could not have written Chapter 6 without you as mentors. I also would like to thank all the Ph.D. students of Astronet-II and Staff from the University of Barcelona for being very friendly with me. A special thank goes to my flatmate and officemate Dr. Ariadna Farrés Basiana and her family. Thank you for your friendship, and your inspiring conversations on Astrodynamics.

A special thanks goes to my dear friends Bahareh, Natalia, Ana and Coralie for your extraordinary friendship. I am grateful I moved to Southampton as I had the chance to meet you. Thank for your tireless support and friendship wherever I am in the world.

I would like to thank an “old” friend, Dr. Marta Ceccaroni. Although we have lived in different countries, I feel your friendship every day of my life. Thank you for being always present and supportive.

More than a thought goes to my family. I could not be the woman I am today without my granny, Marisa and my mum, Daniela. Thank you, granny for having taken a plane by yourself at the age of 81 for visiting me in Southampton. I could not have succeeded this journey without you in Southampton, the phone calls you made later on and all your prayers for me. You together with granddad have been a reference point since I was a child. I always carry my granddad Sergio in my heart; you have never been forgotten through the years!

A sweet thank you goes to my mum (my number one fan) that, despite what she thinks, she will always be for me the most successful woman I have ever met and an example to follow. My passion and the person I am are the results of your good heart and lovable personality.

My most profound love and care go to my brother, Riccardo. I cannot imagine a life without you. Thank you for having been strong when I left home. You were just a kid, and I know how much you have suffered since then. I want you to know that you can always count on my love and support no matter how far I am from home.

Last but certainly not least, I would like to thank my partner Gary. You have brought joy to my life. I feel blessed to have met you. You always found the right words to say in moments I fear I could not finish. You gave such beautiful and happy memories throughout this journey. I could not have completed this journey without you by my side. Thank you with all my heart.

List of Acronyms

2BP	**T**wo-**B**ody **P**roblem
3BP	**T**hree-**B**ody **P**roblem
ACE	**A**dvanced **C**omposition **E**xplorer
ARTEMIS	**A**cceleration **R**econnection **T**urbulence and **E**lectrodyna**MI**c**S**
AU	**A**stronomical **U**nit
CNES	**C**entre **N**ational d'**É**studes **S**patiales
CR3BP	**C**ircular **R**estricted **T**hree-**B**ody **P**roblem
CR3BP-SRP	**C**ircular **R**estricted **T**hree-**B**ody **P**roblem with **S**olar **R**adiation **P**ressure
CSA	**C**anadian **S**pace **A**gency
CRUISE	**C**ontrolled **R**outes by **U**sing **I**nnovative **S**olar-radiation **E**quipment
DESTINY	**D**emostration and **E**xperiment of **S**pace **T**echnology for **IN**terplanetary
DLR	**D**eutschen zentrums für **L**uft-und **R**aumfahrt (German Aerospace Centre)
DPO	**D**istant **P**rograde **O**rbit
DSCOVR	**D**scovr deep **S**pace **C**limate and **O**bser**V**ato**R**y
ECD	**E**lectro-**C**hromic **D**evices
ER3BP	**E**lliptic **R**estricted **T**hree-**B**ody **P**roblem
ER3BP-SRP	**E**lliptic **R**estricted **T**hree-**B**ody **P**roblem with **S**olar **R**adiation **P**ressure
ESA	**E**uropean **S**pace **A**gency
FM	**F**loquét **M**odes
FS	**F**orbidden **S**ubregions
GEO	**GE**ostationary **O**rbit
GOES	**G**eostationary **O**perational **E**nvironmental **S**atellite
GPS	**G**lobal **P**ositioning **S**ystem
GRAIL	**G**ravity **R**ecovery and **I**nterior **L**aboratory
HOI	**H**alo **O**rbit **I**nsertion
HSP	**H**amiltonian **S**tructure **P**reserving
IEEC	**I**nstitute D'**E**studis **E**spacials de **C**atalunia
INSAT	**I**ndian **N**ational **SAT**ellite

ISEE-3	**I**nternational **S**un-**E**arth **E**xplorer-**3**
ISC	**I**ntegrated **S**ymmetrical **C**oncentrator
JAXA	**J**apan **A**erospace e**X**ploration **A**gency
JPL	**J**et **P**ropulsion **L**aboratory
JWST	**J**ames **W**ebb **S**pace **T**elescope
LAGEOS	**LA**ser **GEO**detic **S**atellite
LEO	**L**ow **E**arth **O**rbit
LISA P.	**L**aser **I**nterferometer **S**pace **A**ntenna **P**athfinder
LPO	**L**ibration **P**oint **O**rbit
LVS	**L**ow-**V**elocity **S**ubregions
NASA	**N**ational **A**eronautics and **S**pace **A**dministration
OD	**O**rbit **D**etermination
OTS	**O**rbital **T**est **S**atellite
P-Lyapunov	**P**lanar Lyapunov
PO	**P**eriodic **O**rbit
PZVC	**P**ulsating **Z**ero-**V**elocity **S**urfaces
R3BP	**R**estricted **T**hree-**B**ody **P**roblem
R3BP-SRP	**R**estricted **T**hree-**B**ody **P**roblem with **S**olar **R**adiation **P**ressure
RCD	**R**eflective **C**ontrol **D**evice
SOHO	**SO**lar and **H**eliospheric **O**bservatory
SM	**S**ubregions of **M**otion
SMD	**S**pace **M**anifold **D**ynamic
SME	**S**urface of **M**inimum **E**nergy
SRP	**S**olar **R**adiation **P**ressure
SSPS	**S**pace **S**olar **P**ower **S**atellites
STM	**S**tate **T**ransition **M**atrix
V-Lyapunov	**V**ertical Lyapunov
WMAP	**W**ilkinson **M**icrowave **A**nisotropy **E**xplorer
ZVC	**Z**ero **V**elocity **C**urve

List of Symbols

$[\,]$	Non-dimensional units
$\square$	General variable
$\mathrm{L}_{1,2,3}$	Collinear lagrangian points
$\mathrm{L}_{3,4}$	Equilateral lagrangian points
W^{s}	Stable manifold
W^{u}	Unstable manifold
$\mathscr{F}_i$	Sidereal (inertial) reference frame
$\mathscr{F}_r$	Synodic (rotating) reference frame
$\mathscr{H}$	Hamiltonian
$\mathscr{L}$	Lagrangian
$\dot{\square}$	Derivative in time
$\square^T$	Transpose operator of a matrix or vector
$\square'$	Derivative in the pulsating coordinate
	Variables after the solar radiation pressure trajectory
	transfer manoeuvre
$\square^*$	Evaluation at the equilibrium point
$\square^c$	Variables with the effect of the control law
$\nabla\square$	Gradient
$\langle\square\cdot\square\rangle$	Scalar product
$\delta\square$	Small variations
$\odot$	Reference axis is perpendicular to the page and it is outward
$\oplus$	Reference axis is perpendicular to the page and it is inward
$\square_M$	Transfer manoeuvre
$\Delta\square$	Variations
$[\square]_\times$	Matrix form of the cross product operator
$s(\square)$	Sine function
$c(\square)$	Cosine function
$\Re(\square)$	Real part of a complex number
$\Im(\square)$	Imaginary part of a complex number

Nomenclature

a	Semi-major axis [km]
α	In-plane angle of the sail [°]
	Cone angle of the sail [°]
$\boldsymbol{A}$	Matrix of the linearised equations of motion [ ]
$\mathrm{A}_{1,2}$	Amplitudes of the stable and unstable invariant manifolds [km] or [ ]
$\mathrm{A}_{3,4}$	Amplitudes of the in-plane centre manifold [km] or [ ]
$\mathrm{A}_{5,6}$	Amplitudes of the out-of-plane centre manifold [km] or [ ]
$\mathrm{A}_{x,y,z}$	Amplitudes along the x, y and z axis [km] or [ ]
$\boldsymbol{a}_p$	Perturbing accelerations [N/kg]
$\boldsymbol{a}^s$	Solar radiation pressure acceleration [ ]
$\boldsymbol{a}^{\boldsymbol{s}}_{\boldsymbol{rr}}$	Double derivative of the solar radiation pressure acceleration [ ]
$\boldsymbol{a}^s_x$	Solar radiation pressure acceleration derivative in x [ ]
$\boldsymbol{a}^s_y$	Solar radiation pressure acceleration derivative in y [ ]
$\boldsymbol{a}^s_z$	Solar radiation pressure acceleration derivative in z [ ]
A	Reflective area [m^2]
A_{Sun}	Projected area exposed to the Sun [m^2]
A/m	Area-to-mass ratio [m^2/kg]
β	Lightness number [ ]
c	Speed of light [m/s]
c_R	Reflectivity coefficient [ ]
C	Jacobi integral [ ]
C^*	Critical Jacobi integral [ ]
C_a	Jacobi integral at the apocentre [ ]
C_p	Jacobi integral at the pericentre [ ]
$\boldsymbol{C}_1$	Direction cosine matrix between the sidereal and the perifocal reference frames [ ]
$\boldsymbol{C}_2$	Direction cosine matrix between the perifocal and the synodic reference frames [ ]
$\boldsymbol{C}_{ri}$	Direction cosine matrix between the synodic and the sidereal reference frames [ ]
δ	Out-of-plane angle of the sail [°]
	Clock angle of the sail [°]

e	Orbit eccentricity [ ]
E	Energy of the spacecraft [ ]
E_r	Total relative energy of the spacecraft [ ]
f	True anomaly angle [°]
Φ	In-plane angle between the spacecraft-Sun vector and x-z plane [°]
	In-plane phase of quasi-periodic orbits [°]
$\boldsymbol{\Phi}$	State transition matrix [ ]
$\gamma_{1,2}$	Earth-$SL_{1,2}$ distance [ ]
γ_3	Sun-SL_3 distance [ ]
$\Delta\gamma$	Distance between two libration points [ ]
G	Constant of gravitation [N m^2 kg^{-2}]
$G_{1,2,3}$	Control gains of the Hamiltonian structure preserving control [ ]
i	Inclination [°]
I	Integral [m]
$\boldsymbol{I}$	Identity matrix [ ]
λ_i	Eigenvalues of the equilibrium points [ ] with $i = 1, \ldots, 6$
	Eigenvalues of the monodromy matrix [ ] with $i = 1, \ldots, 6$
	Eigenvalues of the linearised equations of motion [ ] with $i = 1, \ldots, 6$
l	Earth-Sun distance [AU]
μ	Mass parameter [ ]
M_1	Mass of the first celestial body [kg]
$\boldsymbol{M}$	Monodromy matrix [ ]
	Matrix transformation between the orbit amplitudes and the state vector in the planar case [ ]
m_2	Mass of the second celestial body [kg]
n	Mean motion [rad s^{-1}]
$\hat{\boldsymbol{N}}$	Normal vector to the reflective area [ ]
Ψ	Out-of-plane angle between the spacecraft-Sun vector and the x-y plane [°]
	Out-of-plane phase of quasi-periodic orbits [°]
p_x	Momenta conjugate to x [ ]
p_y	Momenta conjugate to y [ ]
p_z	Momenta conjugate to z [ ]
P_{srp}	Solar pressure [N/m]
$P_{srp-1AU}$	Sun pressure at 1 AU [N/m]
ρ_a	Absorbed reflection [ ]
ρ_d	Diffusive reflection [ ]
ρ_s	Specular reflection [ ]
r	Position in the Kepler's problem [km]
$\hat{\boldsymbol{r}}$	Spacecraft-Sun direction [ ]

$\boldsymbol{r}$	Spacecraft state vector in the synodic frame [ ]
$\boldsymbol{r}_{Earth}$	Earth position in the synodic frame [ ]
$r_{Earth-Sun}$	Earth-Sun distance [ ]
$\boldsymbol{r}_{Sun}$	Sun position in the synodic frame [ ]
$\boldsymbol{R}_{Earth}$	Earth position in the sidereal frame [ ]
$\boldsymbol{R}_{Sun}$	Sun position in the sidereal frame [ ]
$\boldsymbol{S}$	Matrix transformation between the orbit amplitudes and state vector [ ]
σ	Sail load (mass-to-area) ratio [kg/m^2]
$\hat{\boldsymbol{s}}$	Sun-line direction [ ]
$\mathrm{SL}_{1,2,3}$	Artificial or pseudo libration points
SF	Solar flux [W/m^2]
t	Time [s] or [ ]
Dt	Time between two manoeuvres for the Floqét modes [ ]
τ	Inverse of the angular velocity of the Earth around the Sun [s/rad]
T	Orbital period [s] or [ ]
$\boldsymbol{T}$	Hamiltonian structure preserving control matrix [ ]
U	Potential energy [ ]
U^s	Potential energy of solar radiation forces for a Sun-pointing area [ ]
$\boldsymbol{u}_k$	Normalised controlled eigenvectors [ ]
$\boldsymbol{u}_k \cdot \boldsymbol{u}_k^T$	Projection tensor [ ]
ν	Out-of-plane frequency of quasi-periodic orbits [s^{-1}]
v	Earth's mean velocity of a circular orbit around the Sun [km s^{-1}]
$\boldsymbol{v}$	Spacecraft's velocity [km s^{-1}] or [ ]
Δv	Variation in the spacecraft velocity [km s^{-1}] or [ ]
V	Total potential [ ]
V_g	Gravitational potential [ ]
V_r	Rotating potential [ ]
$\boldsymbol{V_{rr}}$	Double derivatives of the total potential [ ]
$\bar{\boldsymbol{V}}_{\boldsymbol{rr}}$	Double derivatives of the total potential and the double derivatives of the solar radiation pressure acceleration [ ]
V_x	Total potential derivative in x [ ]
V_{x_i}	Total potential derivative in x_i [ ]
V_y	Total potential derivative in y [ ]
V_{y_i}	Total potential derivative in y_i [ ]
V_z	Total potential derivative in z [ ]
V_{z_i}	Total potential derivative in z_i [ ]
W	Argument of the integral I [ ]
ω	Angular velocity of the rotating system [rad s^{-1}]
	In-plane frequency of quasi-periodic orbits [s^{-1}]

	Argument of perigee [°]
Ω	Longitude of the ascending node [°]
	Total potential in the elliptic restricted-three body problem [ ]
Ω_C	Campagnola et al. (2008)'s total potential in
	the elliptic restricted-three body problem [ ]
Ω_S	Szebehely (1967)'s total potential in
	the elliptic restricted-three body problem [ ]
$\boldsymbol{\omega}_{ri}$	Angular velocity vector [rad s^{-1}]
$\boldsymbol{\xi}$	State vector of the spacecraft in a synodic system
	with origin of the system at the libration point [ ]
ξ, η and ζ	Coordinates of the spacecraft in the synodic system [ ]
	with origin of the system at the libration point [ ]
$\boldsymbol{x}$	Spacecraft state vector (positions and velocities)
	in the synodic reference frame [ ]
$\hat{\boldsymbol{x}}_k$	Eigenvectors of the linearised equations of motion [ ]
$\boldsymbol{X}$	Spacecraft state vector (positions [km] or [ ] and velocities [km s^{-1}] or [ ])
$\bar{\boldsymbol{X}}$	Spacecraft's trajectory (positions [km] or [ ] and velocities [km s^{-1}] or [ ])
$\boldsymbol{X}^s$	Initial state vector of the periodic orbit stable manifold
	(positions [km] or [ ] and velocities [km s^{-1}] or [ ])
$\boldsymbol{X}^u$	Initial state vector of the periodic orbit unstable manifold
	(positions [km] or [ ] and velocities [km s^{-1}] or [ ])
$\boldsymbol{x}_i$	Spacecraft state vector (positions [km] or [ ] and velocities [km s^{-1}] or [ ])
	in the sidereal reference frame
x_{Earth}	Earth x-coordinate in the synodic frame [km] or [ ]
x_{Sun}	Sun x-coordinate in the synodic frame [km] or [ ]
$x_{SL_{1,2,3}}$	Pseudo libration points x-coordinate in the
	synodic frame [km] or [ ]

Chapter 1

Introduction

In space mission design, the spacecraft motion is driven by the gravitational influence of the celestial bodies of the solar system (i.e., n-body problem). An approximate approach is to divide the solar system into various parts through the assumption that each celestial body has its gravitational sphere of influence. Thus, the spacecraft motion is affected by the effect of the proximal celestial body. This assumption reduces the n-body problem to one or multiple solutions to the two-body problem. The two-body problem describes the mutual gravitational interaction of two bodies. When the effect of perturbations is neglected, a particular solution of the two-body problem is the Kepler's problem. In most space applications, the Kepler's problem assumes that there is a large centre body (i.e. planet), where a Keplerian orbit describes the motion of the orbiting body (i.e. spacecraft) (i.e. ellipse, parabola or hyperbola shape orbit), also known as conic. Examples of the use of Kepler's problem are, in celestial mechanics, where the motion of the planets around the Sun can be approximated by Keplerian orbits; while, in space mission design, Kepler's problem is used to describe the motion of a spacecraft around a planet or the Sun. For example, the Apollo lunar mission used combined Keplerian orbits known as patched conics in its approach to the Moon; while numerical optimisation techniques (Patapoff, 1967) then refined the final approximated solution.

Space missions that require particular orbits to meet their goals cannot be achieved by the patched conic approximation alone. Indeed, the patched conic approach is a good approximation in the design of interplanetary transfer trajectories that make use of high-energy manoeuvres (i.e., gravity-assist[1] or swing-by manoeuvres). However, in some other applications, a more accurate model that exploits the solar system's natural dynamics for the design of low-energy trajectories is needed. Thus, a modern approach that has arisen in space mission design is to use Space Manifold Dynamics (SMDs) that

[1] A gravity assist around a planet changes the spacecraft's velocity by entering and leaving the gravitational field of the planet. The spacecraft's speed increases as it approaches the planet and decreases while escaping its gravitational pull.

exploits the natural dynamics of the solar system. SMD merges the knowledge of dynamical systems, celestial mechanics and astrodynamics, see e.g. the work of Celletti and Lhotka (2011); Perozzi and Ferraz-Mello (2010). SMD provides the *dynamical system tools* that can be applied to:

1) orbit control and maintenance (i.e., low-consumption station-keeping),

2) the design of interplanetary transfers (i.e., low-energy transit orbits), and

3) mission operations (i.e., eclipse avoidance),

fitting the required mission constraints (Gómez and Barrabés, 2011). SMD was proposed for the design of the SOHO mission (Gómez et al., 2001). SOHO was the European Space Agency (ESA)'s successor to the National Aeronautics and Space Administration (NASA)'s ISEE-3 mission (Dunhan and Farquhar, 2003).

The simplest dynamical model used for the SMD approach is the Restricted Three-Body Problem (R3BP). In the R3BP, the motion of the spacecraft is under the mutual gravitational influence of two main celestial bodies. In this work, the focus is in the design of space missions in the Sun-Earth system. Thus, the spacecraft motion is only influenced by the gravitational effect of the Sun and of the Earth+Moon barycentre[2].

Unlike the patched conic approximation, in the R3BP model, there exist five equilibrium points. These equilibrium points, known as libration points, are defined in a coordinate system rotating with the Sun-(Earth+Moon) (Szebehely, 1967; Gordon, 1993). Figure 1.1 shows the position of the libration points for the Sun-Earth system in a rotating reference frame. Currently, the libration points selected for space applications are the collinear points that are aligned with the Sun-(Earth+Moon) line. In particular, L_1, located between the line joining the Sun and the Earth+Moon barycentre and L_2, located in the anti-sunward direction along the Sun and the Earth+Moon barycentre line. A spacecraft placed in those points will keep a constant distance from the Sun and the Earth+Moon barycentre opening new opportunities in space mission design.

Spacecraft are usually placed in Libration Point Orbits (LPOs) that are in the *vicinity* of the equilibrium points $L_{1,2}$ rather than *at* the equilibrium points. Indeed, stopping a spacecraft at $L_{1,2}$ requires a high propellant consumption, increasing the overall mission costs. Moreover, the Earth-spacecraft communication link is complicated by the Sun-Earth and $L_{1,2}$ alignment (Canalias et al., 2003). Libration point orbits are periodic or quasi-periodic orbits that are relatively inexpensive to be reached via a direct launch from Earth. Orbits around L_1 are usually useful platforms when studying the Sun; while orbits near L_2 are selected for deep space observations (Perozzi and Ferraz-Mello, 2010).

[2]The barycentre point is the point in a system of bodies or an extended body at which the mass of the system may be considered to be concentrated and at which external forces may be deemed to be applied. It is also known as the centre of mass.

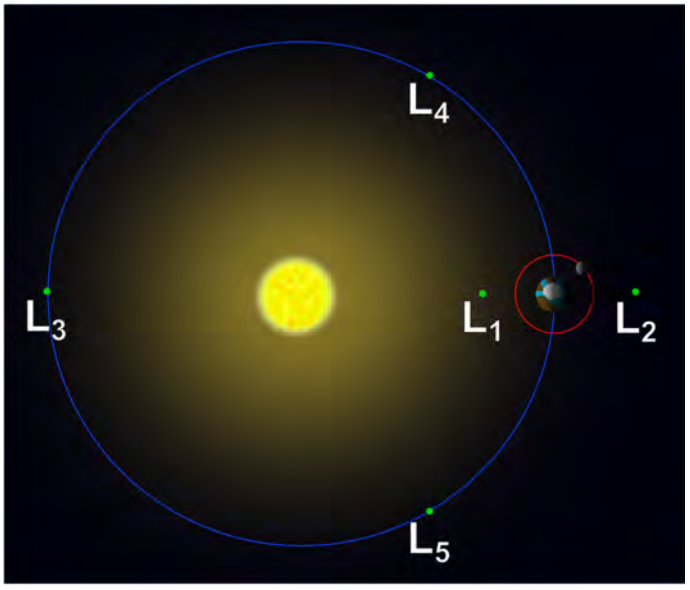

Figure 1.1: Position of the five Lagrangian points of the Sun-(Earth+Moon) system with respect to the synodic reference frame (not to scale).

In 1968, Farquhar (1991) was the first to propose a space mission to LPOs around the Lagrangian points of the Earth-Moon system as a communication relay for the far side of the Moon. The growing interest of the space agencies in LPOs started after the success of the ISEE-3 mission in 1978. Current examples of LPO missions include SOHO that studies the Sun's outer corona (Olive et al., 2013) and the Gaia space telescope to chart a three-dimensional map of our Galaxy (Hechler and Cobos, 2002). ESA and NASA have recently succeeded in launching LISA Pathfinder that will test key technologies for gravitational wave observations (ESA-website, 2015b). The NASA/ESA/CSA's James Webb Space Telescope will provide astronomical measurements to understand the formation of our Universe (NASA-website, 2016) and ESA's Euclid will map the geometry of the dark Universe (ESA-website, 2015a).

Due to the unstable nature of L_1 and L_2, a spacecraft placed around the equilibrium points will naturally diverge from them. Thus, trajectories designed in the R3BP require the spacecraft to be manoeuvred to maintain its nominal trajectory by counteracting the unwelcome environmental instabilities (Wertz, 1999). Among the environmental effects, the stronger perturbations are the motion of the Moon around the Earth, the eccentricity of the Earth+Moon barycentre's orbit around the Sun, the gravitational effect of passing planets and the Solar Radiation Pressure (SRP). After the gravitational effects, SRP is a significant factor in the Sun-(Earth+Moon) system, particularly when the spacecraft has extended high reflective areas, e.g. James Webb Space Telescope (Evans, 2003).

The aim of this research is to exploit SRP to perform the required correcting manoeuvres to keep the spacecraft on the nominal trajectory. The advantage of using SRP as the source of propulsion is in the design of innovative propellant-free devices that reduce the pre-stored fuel onboard the spacecraft (McInnes, 1999). Therefore, SRP is a natural

and unlimited source of "propellant". Due to this unlimited "propellant", space missions that use SRP could have longer mission lifetimes, potentially decreasing the number of spacecraft launched to LPO's. Reducing the number of launches will reduce the Space Agencies overall cost budget allocated for LPOs missions. Moreover, a reduced number of spacecraft at LPOs will also make the space market more sustainable by limiting the potential space debris in the vicinity of the libration points. Furthermore, the single space mission cost budget is highly related to the mass of the spacecraft, where the pre-storage of onboard propellant has a significant impact on the overall single mission costs. Thus, an SRP harnessing device mainly has the significant advantage of reducing the costs relating to the propulsion system. The first application of SRP stabilisation was proposed for attitude control in 1959 (Sohon, 1995), and it is successfully implemented for geosynchronous satellites such as OTS, TELECOM 1 and INMARSAT 2.

In this research, SRP enhancing devices are applied to future LPO missions designed in the Sun-Earth system; the idea is to exploit the effect of SRP from the beginning to the end of the mission. In the field of the R3BP, SRP stabilisation is applied to the:

1) development of orbital control methods for LPOs,

2) transfer trajectories within the Sun-Earth system, and

3) the end-of-life disposal.

As this research focuses on the design of future innovative missions through an SMD approach, concern is given to dispose safely of the spacecraft when it reaches the end of its operational life. The end-of-life disposal is a recent topic in the context of the R3BP as, currently, the space community has recognised the need for mitigation of LEO and GEO spacecraft. However, less concern is given for LPOs, as no guidelines for the mitigation of LPO satellites have been formulated by the Space Agencies (Colombo et al., 2014b, 2015a; ESA-website, 2013).

SRP trajectory stabilisation requires devices on board the spacecraft that can react to SRP acceleration (McInnes, 1999). The SRP stabilisation has been demonstrated by JAXA's Ikaros mission that utilises a 20-m span square solar power sail (Tsuda et al., 2013). The SRP acceleration forces are enhanced by the spacecraft's reflective area, its reflectivity properties, the reflective area orientation (to the Sun), and the reduction of the spacecraft's mass. Thus, SRP devices require a light and extended highly reflective area (i.e. reflective deployable structures such as solar sails, solar flaps, sunshields and space mirrors). The acceleration needed to manoeuvre the spacecraft is controlled by mechanical variations in the former parameters, e.g. controlling the surface reflectivity (Lücking et al., 2012b) or by changing the area through deployable mechanisms (McInnes, 1999).

1.1 Research questions

The present research aims to develop methodologies for the design and control of spacecraft trajectories enhanced by Solar Radiation Pressure (SRP) acceleration. This work expands the effort made by previous authors in the context of solar sail missions in the Sun-Earth system where the ultimate research questions of this thesis are:

Q.1 - *Can pre-existing spacecraft's reflective deployable structures enhance the design and control of solar radiation pressure assisted missions in the restricted three-body problem?*

Q.2 - *Which structural requirements are needed for the design of solar radiation pressure missions from the beginning to the end of the spacecraft's lifetime?*

To answer those final questions, we have to formulate and answer former research questions such as:

Q.3 - *What type of control law can be used for stabilising spacecraft at libration point orbits that make use of solar radiation pressure propulsion?*

Q.4 - *Which methodology can be used to perform transfers between quasi-periodic orbits enhanced by solar radiation pressure manoeuvres?*

Q.5 - *How can we design an end-of-life disposal strategy that makes use of solar radiation pressure enhancing devices to dispose of a spacecraft safely in a graveyard trajectory?*

The approach used to answer those questions focuses on the design of spacecraft trajectories through SRP manoeuvres that make use of the invariant manifold theory. The dynamical model used is the restricted three-body problem with solar radiation pressure. The natural dynamics of the Sun-Earth system are thereby investigated on SRP propulsion for different mission phases such as the control of periodic orbits around the libration points, the design of transfer trajectories within the Sun-Earth system and the design of spacecraft end-of-life disposal paths. The reflective area required for the trajectory design and the spacecraft pointing requirements are the final outcomes of this research. These requirements are highly dependent on the selected mission phases. Thus, differently designed trajectories require different deployable area configurations. Along with the design of the reflective area, the definition of a new control law, a method to perform transfers between quasi-periodic orbits and a strategy for the end-of-life disposal are the major outstanding research contributions to this research.

1.2 Research contribution

The major contributions of these research are presented in Chapter 5, Chapter 6 and Chapter 7. Chapter 5 focuses on the design of a Hamiltonian structure preserving control law extended to high amplitudes libration point orbits. Chapter 6 investigates a methodology to perform transfer trajectories between Lissajous orbit; while, Chapter 7 presents a strategy of spacecraft end-of-life disposal. The final outcome of this research is to identify the structural drivers and the spacecraft pointing-accuracy to perform control, transfer and end-of-life manoeuvres enhanced by solar radiation pressure. Each of these chapters corresponds to a journal publication either already published or submitted.

Chapter 3 and Chapter 4 present the theoretical model used to describe the motion of the spacecraft in the restricted three-body problem. Chapter 3 presents the circular restricted three-body problem that it is already available in the literature. A minor contribution to the state-of-art of the circular restricted three-body problem was given by the author in Section 3.5.2; where, the computation of libration points was performed through numerical continuation techniques. Conversely, Chapter 4 summarises the theory of the elliptic restricted three-body problem. Note that, the dynamics of the spacecraft in the elliptic problem are less known than the ones in the circular model and the references available in the literature are limited and often not clear. Thus, a significant effort was made in Chapter 4 to merge what is well known in the literature and the author understanding of the spacecraft behaviour in the elliptic model. Part of the finding in Chapter 4 are presented in an under review publication.

In this thesis, the dynamical system tools to compute objects (such as equations of motion, equilibrium points, numerical computation of libration point orbits, the computation of invariant manifolds, and the calculation of the regions of feasible motions) was entirely developed as no pre-existing tools were available to the author. Thus, a dynamical system algorithm named by the author as Controlled Routes by Using Innovative Solar-radiation Equipment (CRUISE) was developed as a final result of this research. CRUISE merges well known methods for the computation of objects in the restricted three-body problem as well as the newly developed methodologies for the design and control of LPOs missions assisted by SRP manoeuvres. The CRUISE code architecture is described in Appendix A

The research developed in this thesis has been published in some journals and conference papers.

JOURNAL PUBLICATIONS

- C. Colombo, E. A. Alessi, W. van der Weg, S. Soldini, F. Letizia, M. Vetrisano, M. Vasile, A. Rossi, M. Landgraf, 'End-of-life disposal concepts for Libration Point Orbit and Highly Elliptical Orbit Missions, *Acta Astronautica*, vol 110, pp 298-312, 2015, doi: 10.1016/j.actaastro.2014.11.002 (Colombo et al., 2015a);

- S. Soldini, C. Colombo, S. Walker, 'The end-of-life disposal of satellites in Libration-point orbits using solar radiation pressure', *Advances in Space Research Special issue: Asteroids & Space Debris*, vol 57, pp 1664-1679, 2016, doi:10.1016/j.asr.2015.06.033 (Soldini et al., 2016a). The content of this publication is presented in Chapter 7;

- S. Soldini, C. Colombo, S. Walker, 'Solar radiation pressure enhanced disposal in the elliptic restricted three-body problem: applications to the Gaia mission, *Celestial Mechanics and Dynamical Astronomy* (Under review), December 2015 (Soldini et al., 2015b). The content of this publication is presented in Chapter 7;

- S. Soldini, C. Colombo, S. Walker, 'Solar radiation pressure feedback control strategy for unstable periodic orbits in the restricted three-body problem, *Journal of Guidance, Control, and Dynamics* (Under review), March 2016 (Soldini et al., 2016b). The content of this publication is presented in Chapter 5;

- S. Soldini, G. Gómez, J. J. Masdemont, C. Colombo and S. Walker, 'Design of transfer trajectories: solar radiation pressure assisted missions near Libration points, *Journal of Guidance, Control, and Dynamics* (In preparation) (Soldini et al., 2016c). The content of this publication is presented in Chapter 6.

INTERNATIONAL CONFERENCE PROCEEDINGS

- S. Soldini, C. Colombo and S. Walker, 'Adaptive Structures for Spacecraft Orbit Control', *In Proceedings of the 64th International Astronautical Congress*, IAC-13.C1.9.10, Beijing, China, 23-27 September 2013. (Soldini et al., 2013);

- C. Colombo, H. Lewis, F. Letizia, S. Soldini, L. Gossnitzer, E. M. Alessi, A. Rossi, L. Dimare, M. Vasile, W. Van der Weg, C. McInnes, M. Macdonalds and M. Landgraf, 'End-of-Life Disposal Trajectories for Libration Point and Highly Elliptical Orbit Missions', *In Proceedings of the 64th International Astronautical Congress*, IAC-13.A6.P.24, Beijing, China, 23-27 September, 2013. (Colombo et al., 2013);

- S. Soldini, C. Colombo, S. Walker and M. Landgraf, 'Libration-Point Orbit missions disposal at the end-of-life through solar radiation pressure', *In Proceedings of*

the 2nd International Academy of Astronautics Conference on Dynamics and Control of Space Systems (DyCoSS), IAA-AAS-DyCoSS2, Rome, Italy, 24-26 March, 2014. (Soldini et al., 2014c);

- C. Colombo, F. Letizia, S. Soldini, H. Lewis, E. M. Alessi, A. Rossi, M. Vasile, M. Vetrisano, W. Van der Weg and M. Landgraf, 'End-of-life disposal concepts for libration point and highly elliptical orbit missions', *In Proceedings of the 2nd International Academy of Astronautics Conference on Dynamics and Control of Space Systems (DyCoSS), IAA-AAS-DyCoSS2*, Rome, Italy, 24-26 March, 2014.(Colombo et al., 2014d);

- S. Soldini, C. Colombo, and S. Walker, 'Comparison of Hamiltonian structure-preserving and Floquét mode station-keeping for Libration-point orbits', *In Proceedings of the AIAA/AAS Astrodynamics Specialist Conference*, AIAA-2014-4118, San Diego, California, 4-7 August 2014. (Soldini et al., 2014a);

- S. Soldini, C. Colombo and S. Walker, 'A feasibility study of solar radiation pressure feedback control strategy for unstable periodic orbits in the restricted three-body problem', *In Proceedings of the 65th International Astronautical Congress*, IAC-14.C1.6.13, Toronto, Canada, 29 September-3 October 2014. (Soldini et al., 2014b);

- S. Soldini, C. Colombo, and S. Walker, 'Solar radiation pressure end-of-life disposal for Libration-point orbits in the elliptic restricted three-body problem', *In Proceedings of the AAS/AIAA Astrodynamics Space Flight Mechanics Meeting*, AAS 15-286, Williamsburg, VA, 11-15 January 2015. (Soldini et al., 2015a);

- C. Colombo, F. Letizia, S. Soldini and F. Renk, 'Disposal of libration point orbits on a heliocentric graveyard orbit: the Gaia mission', *In Proceedings of the 25th International Symposium on Space Flight Dynamics*, ISSFD, Munich, Germany, October 2015. (Colombo et al., 2015b).

AWARDS AND GRANTS

- European Space Agency, Sponsorship (Holland), September 2013
  Sponsored student at the 64th International Astronautical Congress, September 2013, Beijing, China;

- European Embedded Control Institute, Travel Grant (France), January 2014 Awarded 500 € to attend a course on nonlinear control at EECI School in April 2014, Paris, France;

- Institution of Engineering and Technology, Travel Grant (England), February 2014 Awarded 500 £ to attend the 2nd IAA conference in March 2014, Rome, Italy;

- Japan Society for the Promotion of Science, Fellowship (Japan), October 2015 JSPS Postdoctoral Fellowship to conduct research in Japan at the Japan Aerospace Exploration Agency.

RESEARCH STUDY PROJECT

- The work presented in Chapter 7 was initiated in the framework of the study contract 'Disposal strategies for libration point orbit and highly elliptical orbit missions' funded by the European Space Agency (ESA, ESA/GSP-SOW-12-602 (February 2013-December 2014). This project, led by Dr Camilla Colombo at the University of Southampton was a project within the General Study Programme of ESA, performed by the University of Southampton, SpaceDyS and the University of Strathclyde. This project investigates the End-of-Life disposal concepts for Lagrange-Points Orbit and High Elliptical Orbit Missions. This strategy was applied to Herschel, SOHO and Gaia spacecraft. As part of the team at the University of Southampton, I was in charge the analysis of the disposal strategy for LPOs that exploits the effects of solar radiation pressure for a propellant-free disposal. The work performed within this study is presented in Chapter 7 and it is published in (Soldini et al., 2016a) and (Soldini et al., 2015b).

RESEARCH COLLABORATION

- Between August and December 2015, I was an Early Stage Researcher in Astronet-II at the Institute D'Estudis Espacials de Catalunya (IEEC), Barcelona, Spain. Astronet-II is a Marie-Currie research training network in Astrodynamics. I worked on a four month research collaboration between the University of Southampton and the Universidad de Barcelona/IEEC. The project title 'Design of transfer trajectories - solar radiation pressure assisted mission near Libration points' was conducted under the supervision of Prof. Gerard Gómez and Prof. Josep J. Masdemont. Chapter 6 was entirely developed during this collaboration. As an outcome of this collaboration, one publication is in preparation (Soldini et al., 2016c).

1.3 Organisation of the thesis

The thesis is organised as follows: after the literature review presented in Chapter 2, Chapter 3 shows the restricted three-body problem model with solar radiation pressure with a particular focus on the equations of motion and the tools developed for the design of the target orbit. The effect of the Earth's orbit eccentricity is then introduced in Chapter 4 with the elliptic restricted three-body problem. Chapter 5 focuses on the orbital control strategies for LPO missions. In particular the focus of Chapter 5 is on the SRP Hamiltonian structure-preserving feedback control and its comparison with the Floquét mode technique; while Chapter 6 investigates a semi-analytical approach for harnessing SRP in the design of transfer trajectories within quasi-periodic orbits of the Sun-Earth system. Chapter 7 describes the proposed end-of-life disposal strategy enhanced by SRP manoeuvres. Finally, the conclusions and future work are presented in Chapter 8 focusing on the main research findings, research impacts and limitations.

Chapter 2

Literature Review

2.1 Restricted three-body problem

Space mission design requires the knowledge of the space environment to predict the motion of a spacecraft. The motion of a spacecraft is influenced by the gravitational effect of the celestial bodies of the solar system (i.e. Sun, planets, moons and asteroids) and other environmental perturbations (i.e., planets' environment, solar wind and galactic cosmic rays (Evans, 2003)). Thus, dynamical models that approximate the motion of the celestial bodies are useful tools in spacecraft trajectory design. A first approach is to divide our solar system into different parts. Thus, the motion of a spacecraft is under the gravitational sphere of influence of one celestial body at a time. The general n-body problem is then simplified by composing multiple Two-Body Problem (2BP) solutions. The 2BP describes the mutual gravitational interaction between a central body (i.e. the Sun or planets) and the spacecraft. When the effect of environmental perturbations is neglected, a special solution of the 2BP is the Kepler's problem. In the Kepler's problem, the central body has a spherically symmetrically distributed mass and the well-known equations of motion are:

$$\ddot{\boldsymbol{r}} = -\frac{\mu}{r^3}\boldsymbol{r}, \tag{2.1}$$

where, $\boldsymbol{r}$ is the position vector of the spacecraft and μ is the constant of gravitation of the central body. The solutions of Eq. (2.1) are Keplerian orbits which are conic sections. In the Kepler problem, the motion of the spacecraft can be determined by its coordinates, $\boldsymbol{r}$, and its velocity components, $\dot{\boldsymbol{r}}$, which identify a unique set of six orbital elements, called Keplerian elements (see Appendix B.1). In celestial mechanics, the Kepler's problem is used to approximate the motion of the planets of the solar system around the Sun or the motion of Moons around their planets; while, in space mission design, it is used to approximate the motion of a spacecraft around a planet.

In real space applications, small deviations from the two-body dynamics exist. The spacecraft motion is non-Keplerian when considering these perturbing forces. The Eq.

(2.1) turns then into Eq. (2.2) where $\boldsymbol{a}_p$ is the acceleration of perturbing effects:

$$\ddot{\boldsymbol{r}} = -\frac{\mu}{r^3}\boldsymbol{r} + \boldsymbol{a}_p. \tag{2.2}$$

Examples of perturbations for Earth orbiting spacecraft are: Earth's gravity harmonics (deviation from a perfect sphere), luni-solar gravitational attractions, atmospheric drag, Earth tides, solar radiation pressure and other additional planetary gravitational effects. For example, the Apollo mission used combined two-body problem solutions known as the patched-conics approach to perform the transfer from the Earth to the Moon (Patapoff, 1967).

Space missions require specific design concept to meet their goals that cannot be achieved by a patched-conic approximation. In the case of interplanetary transfers, the patched conic approximation is a good solution when high-energy manoeuvres are involved (i.e., gravity-assist) and it requires a manual trial and error search trajectory design followed by an optimisation procedure (Canalias et al., 2004). However, for the development of low-energy trajectories, a more accurate model is needed. A modern approach is to use Space Manifold Dynamics (SMD). SMD uses dynamical system theory that exploits natural dynamics for the design of interplanetary transfers (i.e., low-energy transit orbits discovered by Conley, 1968), for orbit control and maintenance (i.e., station-keeping), and for mission operations (i.e., eclipse avoidance). The application of dynamics system theory to space mission design was used, for example, in the design of the SOHO mission by ESA and the Genesis mission by NASA. The benefit in using dynamical system tools has been proven for example by the Genesis mission, where a Δv [1] of 100 m/s was saved for stabilising the spacecraft; therefore, this approach directly reduced the overall fuel cost. Moreover, dynamical system tools have been demonstrated to be an efficient way to perform a trajectory design. This was proven when the nominal trajectory of Genesis had to be redesigned due to a delayed launch (Canalias et al., 2004).

The Three-Body Problem (3BP) is the simplest model of an SMD approach and it was formulated and studied by Newton in 1687. The 3BP models the gravitational interaction of three celestial bodies by predicting their motions. Examples of 3BPs are the Sun-planet-planet, the Sun-planet-Moon or the Sun-planet-asteroid gravitational mutual interaction. When the mass of one body is infinitesimal compared to the other two, the 3BP can be further simplified. This can be the case of a Sun-planet-asteroid system or when the third body is a spacecraft (i.e. Sun-planet-spacecraft). The main assumption is that the gravitational effect of an infinitesimal mass onto two massive bodies is negligible. Thus, the 3BP is *restricted* to study the motion of an infinitesimal body under the gravitational influence of two massive ones. This approximation is known as the Restricted Three-Body Problem (R3BP) that is a subset of the 3BP. In the R3BP,

[1] The Δv is the variation in the spacecraft's velocity when an impulsive manoeuvre is given to keep the spacecraft on its design trajectory. The Δv is associated with the propellant consumption through the Tsiolkovsky's rocket equation. The Δv budget is an important figure in space mission design to estimate the mass of propellant needed for the entire mission.

the motion of the barycentre of the two largest celestial bodies is approximated with Kepler's problem that is the solution of Eq. (2.1). The R3BP changes depending on the assumption made for the celestial bodies motion. If the celestial bodies barycentre's orbit is approximated as a circular or elliptic orbit, the R3BP turns into the Circular Restricted Three-Body Problem (CR3BP) or the Elliptic Restricted Three-Body Problem (ER3BP) respectively. The CR3BP was formulated in a rotating (synodic) reference frame by Euler in 1767. Euler considered the two celestial bodies (i.e. the Sun and the Earth+Moon) along a straight line that rotates with their barycentre. The formulation of the CR3BP in a synodic reference frame was a significant development in the study of the 3BP (Szebehely, 1967; Musielak and Quarles, 2015).

Unlike the patch-conic approximation, in the R3BP five equilibrium solutions exist at which the gravitational forces of the celestial bodies balance out. Lagrange proved the existence of the equilibrium points of the CR3BP in 1772 known as Lagrangian or libration points. In 1906, the existence of the equilibrium points was observed in the Sun-Jupiter system where the Trojan asteroids are located close to two of the Lagrangian points. For the Sun-Earth system, the equilibrium points have the advantage of having a fixed distance from the Sun and the Earth+Moon barycentre (Canalias et al., 2004; Bernelli-Zazzera et al., 2004). The Lagrangian points open up the possibility of designing new missions where a spacecraft in the vicinity of the Lagrangian points will maintain a fixed configuration with the Sun and the Earth+Moon barycentre. Figure 1.1 shows the position of the equilibrium points in the synodic reference frame for the Sun-Earth system. Three of the five equilibrium points lie on the line that joins the Sun and the Earth+Moon barycentre, named as L_1, L_2 and L_3 respectively. L_1 is located between the Sun and the Earth; while, L_2 is located beyond the Earth as viewed from the Sun. L_3 is beyond the Sun on the opposite side to the Earth. Objects in L_3 cannot be seen from Earth. The last two equilibrium points, L_4 and L_5 are instead located in the plane of motion of the Sun-(Earth+Moon) forming an equilateral triangle with them.

While the 3BP has the advantage of having equilibrium solutions, in the transition from the 2BP to the 3BP some knowledge of the spacecraft motion is lost. Indeed, the concept of orbital elements and integral of motion for Kepler orbits no longer exist in the 3BP (Bernelli-Zazzera et al., 2004). However, Jacobi in 1836 used the formulation of the CR3BP in the synodic frame, introduced by Euler, to prove the existence of a constant of motion, the well-known Jacobi integral. The Jacobi integral was used by Hill in 1877 to study the motion of an asteroid in the 3BP and he introduced the concept of Zero Velocity Curves (ZVCs). The ZVCs establish regions in space where a small body is capable of moving. As a closed-form solution of motion is not possible in the 3BP, the ZVCs have the advantage of giving a qualitative picture of the region of motion of a small body (i.e. asteroids or spacecraft) under the influence of two celestial bodies. Hill also considered a special case of the CR3BP when two bodies have masses much smaller that the first one, known as the Hill's problem. In the late 1800s, Poincaré concluded

that the R3BP is non-integrable (Musielak and Quarles, 2015). An important reference book in the R3BP was published in 1967 by Szebehely (1967): *Theory of Orbits*.

A natural extension of the CR3BP is the ER3BP, where the effect of the two celestial bodies barycentre's orbit eccentricity is taken into account. In the ER3BP, the definition and the existence of the five Lagrangian points still holds. However, due to the effect of orbit eccentricity, the synodic frame is now rotating with a non-uniform angular velocity and the system shows a non-autonomous nature. Thus, the definition of the Jacobi integral no longer exists for the ER3BP (Szebehely, 1967). Figure 2.1 shows a qualitative representation of the 2BP and the 3BP. Figure 2.1(a) shows two examples of Kepler's problems the Earth-Moon and the Earth-spacecraft system. If the effect of a third body like the Sun or other perturbations is added to Eq. (2.1) as an external acceleration, $\boldsymbol{a}_p$, as shown in Eq. (2.2), the Kepler's problem turns into the 2BP. Figure 2.1(b) shows two examples of the R3BP as the Earth-Moon-spacecraft and the Sun-Earth-spacecraft systems. In this case, the mass of the spacecraft is much smaller compared to the other two celestial bodies masses. An example of 3BP is the mutual gravitational interaction of the Sun, the Earth and the Moon as shown in Figure 2.1.

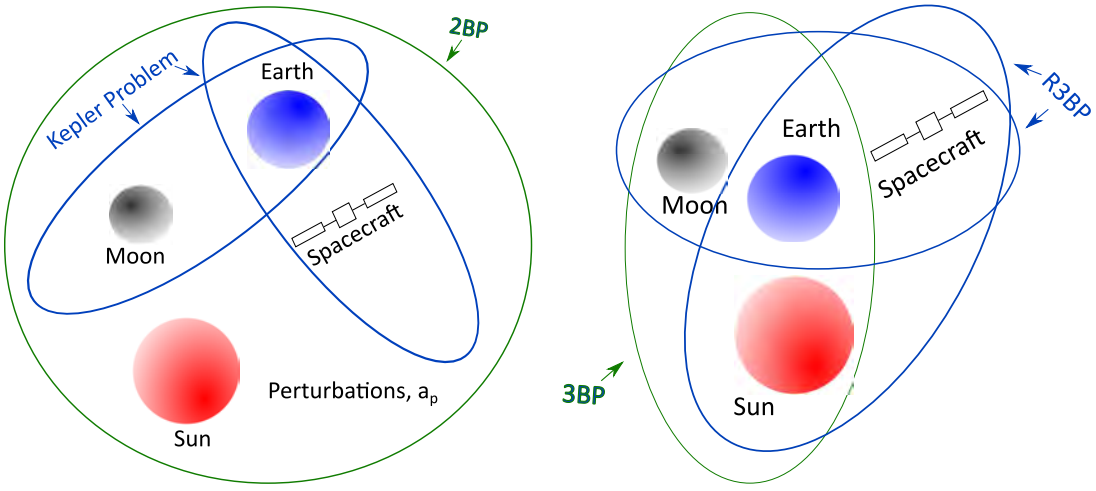

(a) Two-Body Problem (2BP) and Kepler's problem.

(b) Three-Body Problem (3BP) and Restricted Three-Body Problem (R3BP).

Figure 2.1: Qualitative representation of: the Two-Body Problem (2BP), the Kepler's problem, the Three-Body Problem (3BP) and the Restricted Three-Body Problem (R3BP).

In this thesis, the CR3BP and the ER3BP are the dynamical models used for spacecraft trajectory design in the Sun-Earth system. Thus, the satellite motion is influenced by the Sun and the Earth+Moon barycentre. In 1903, Poynting observed that the motion of particles, such as small meteors or cosmic dust are affected by gravitation and light radiation effects as they approach luminous celestial bodies (McInnes, 1999). Thus, stars (including the Sun) exert not only gravity but also radiation pressure on bodies moving nearby. When the effect of the Solar Radiation Pressure (SRP) is taken into account,

the R3BP becomes the photo gravitational R3BP (R3BP-SRP); where it can be either circular (CR3BP-SRP) or elliptic (ER3BP-SRP).

The scientific advantages of locating a spacecraft at the libration points explain the interest in the R3BP for space mission design. In particular, a spacecraft at the collinear points L_1 and L_2 has the advantage of being in a stable thermal environment, its field of vision is never obstructed by the Earth and Sun and the spacecraft-Earth distance is fixed which is beneficial for the communications subsystem design (Perozzi and Ferraz-Mello, 2010; Canalias et al., 2004).

Spacecraft are usually placed in Libration Point Orbits (LPOs) that are in the *vicinity* of the equilibrium points $L_{1,2}$ rather than *at* the equilibrium points. Stopping a spacecraft at $L_{1,2}$ requires a high propellant consumption, increasing the overall mission costs. Moreover, for a spacecraft placed at $L_{1,2}$, the Earth-spacecraft communication link is complicated by the Sun-Earth and $L_{1,2}$ alignment where a displacement from the $L_{1,2}$ points is required to enhance communications. Figure 3.10 gives a schematic picture of the position of the Sun, Earth, Moon, libration points and libration point orbits for the CR3BP in the synodic reference frame. The Sun-Earth distance is approximately of $1.5 \cdot 10^8$ km and the Moon orbit has a radius of circa $3.28 \cdot 10^5$ km. L_1 is located at 1.5 million km from Earth in the direction toward the Sun, Figure 3.10(a); while, L_2 is located approximately 1.5 million km in the anti-sunward direction along the line joining the Sun and the Earth+Moon barycentre, Figure 3.10(b). A physical explanation of L_1 and L_2 can be found in Appendix B.2.

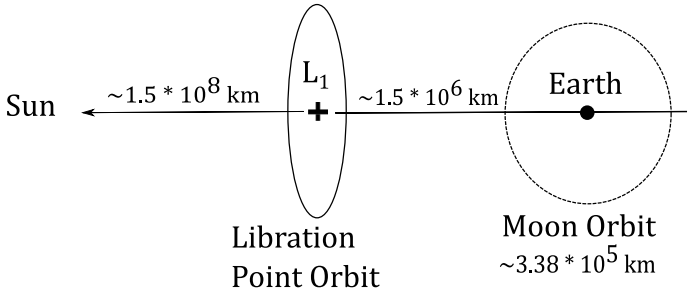

(a) Position of L_1 with respect to the Earth.

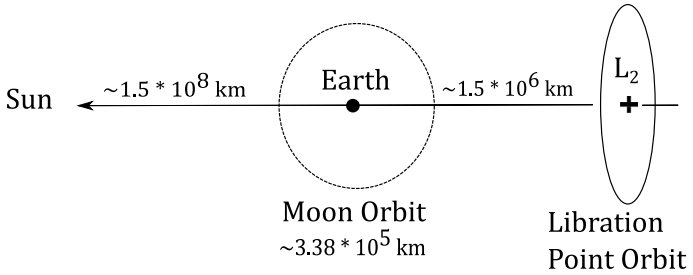

(b) Position of L_2 with respect to the Earth.

Figure 2.2: Schematic representation of: the position of the Sun with respect to the Earth, the position of the Libration points, $L_{1,2}$ with respect to the Earth, the libration point orbit and the Moon orbit.

2.1.1 Space missions at the collinear libration points, $L_{1,2}$

Orbits in the vicinity of L_1 and L_2 open up new possibilities for future space missions and planetary science. Libration points orbits are periodic or quasi-periodic orbits that are relatively inexpensive to be reached via a direct launch from Earth. Orbits around L_1 are usually good platforms when studying the Sun; while orbits near L_2 are selected for deep space observations, for example, see Perozzi and Ferraz-Mello (2010). The communication between a spacecraft in LPO and the Earth is relatively simple (and therefore has a low cost overhead) as L_1 and L_2 maintain a fixed distance of circa 1.5 million km from the Earth. In particular, LPOs around L_2 are good candidates for those missions that have heat sensitive instruments as a spacecraft in L_2 is never in shadow and is therefore not subjected to big temperature changes. Thus, L_2 has a favourable environment for non-cryogenic missions, suitable for space telescopes (Canalias et al., 2004). Recently, a formation of spacecraft in an LPO around L_2 was suggested to provide high-resolution observations (Hamilton et al., 2014).

LPOs in the Earth-Moon system can be used to establish a communication relay between the Earth and the far side of the Moon as suggested by A. C. Clark and proposed for the Apollo mission by Farquhar (1991). LPOs can also provide planetary ballistic captures as for the Hiten mission. The use of LPOs for transfer and Earth return trajectories was previously proven for example by the Genesis and Wind missions. They are considered gateway orbits as LPOs enhance low energy transfers which can be exploited to visit several moons in the Jovian-Saturn system (Koon et al., 2002; Gómez et al., 2004).

The interest of the space agencies in LPOs started after the success of the ISEE-3 mission. Current examples of LPO missions include SOHO that studies the Sun's outer corona (Olive et al., 2013), and the Gaia space telescope designed to chart a three-dimensional map of our Galaxy (Hechler and Cobos, 2002). ESA and NASA have also recently succeeded in launching LISA Pathfinder (ESA-website, 2015b) that will test key technologies for gravitational wave observations. The NASA/ESA/CSA's James Webb Space Telescope (JWST) will provide astronomical measurements to understand the formation of our Universe (NASA-website, 2016); while, ESA's Euclid will map the geometry of the dark Universe (ESA-website, 2015a). Table 2.1 shows the past, the current and the future space missions at the libration points. As one can see, most of the mission are designed for the Sun-Earth system with a growing scientific interest in missions at L_2 for space telescope applications.

The ESA Herschel, Soho and Gaia spacecraft are used in this thesis as case study mission scenarios. The Appendix B.3 shows the overall mission objectives and spacecraft characteristics.

2.2 Invariant manifold theory

Space manifold dynamics associated with the collinear equilibrium points of the restricted three-body problem provide a geometric understanding of the natural dynamics of the solar system. Dynamical system theory was founded by Poincaré at the end of the 1800s when he developed qualitative methods (dynamical system tools) to solve differential equations. Thus, he also described new phenomena, known as "chaos".

The study of the linear dynamics around the equilibrium (fixed) points provides a first step in understanding the non-linear behaviour of dynamical systems. Spacecraft trajectory design requires the knowledge of the spacecraft's behaviour around the collinear points L_1 and L_2. Thus, there is a need to study the stability of a body around L_1 and L_2, that are solutions of the linearised R3BP dynamics. The linear behaviour of L_1 and L_2 is of the type centre×centre×hyperbolic as shown in Figure 2.3. Essentially, the dynamics around $L_{1,2}$ is similar of the one of two oscillators combined with some hyperbolic behaviour. The study of linear stability around the equilibrium points prove the existence of at least one stable and one unstable eigenvalue with corresponding stable and unstable eigenvectors. Thus, if a spacecraft around $L_{1,2}$ is given a perturbation in the unstable direction, it will exponentially fall off from the nominal orbit. Conversely, if the spacecraft has the right initial condition, it will follow a trajectory that will exponentially approach the nominal orbit from the stable direction. The full set of

Name	**Space Agencies**	**Status**	**Launch**	**System**	**L-points**
ISEE-3	NASA	PAST	1978	Sun-Earth	L_1
Genesis	NASA	PAST	2001	Sun-Earth	$L_{1,2}$
ARTEMIS	NASA	PAST	2010	Earth-Moon	L_1
Chang'e 2	CNSA	PAST	2011	Sun-Earth	L_2
Herschel	ESA	PAST	2009	Sun-Earth	L_2
Planck	ESA	PAST	2009	Sun-Earth	L_2
Chang'e 5-T1	CNSA	PAST	2014	Earth-Moon	L_2
Wind	NASA	CURRENT	1994	Sun-Earth	$L_{1,2}$
SOHO	ESA, NASA	CURRENT	1995	Sun-Earth	L_1
ACE	NASA	CURRENT	1997	Sun-Earth	L_1
WMAP	NASA	CURRENT	2001	Sun-Earth	L_2
GRAIL	NASA	CURRENT	2011	Earth-Moon	L_2
Gaia	ESA	CURRENT	2013	Sun-Earth	L_2
DSCOVR	NASA	CURRENT	2015	Sun-Earth	L_1
LISA P.	ESA, NASA	CURRENT	2015	Sun-Earth	L_2
JWST	ESA, NASA, CSA	FUTURE	2018	Sun-Earth	L_2
Euclid	ESA	FUTURE	2020	Sun-Earth	L_2
DESTINY	JAXA	FUTURE	2020	Sun-Earth	L_2
ATHENA	ESA	FUTURE	2028	Sun-Earth	L_2

Table 2.1: Past, current and future space missions at the collinear libration points L_1 and L_2.

exponentially diverging and converging trajectories are the unstable and stable invariant manifolds. The term *invariant* means that through the propagation in time a spacecraft on the manifold will stay on the manifold (Davis et al., 2010).

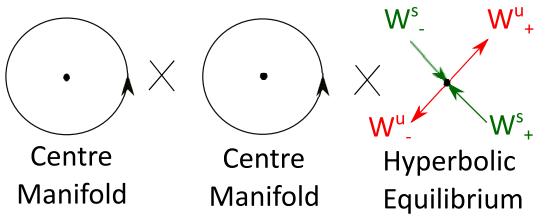

Figure 2.3: Centre×Centre×Hyperbolic equilibrium.

The invariant manifolds associated to $L_{1,2}$ give a geometrical structure of the natural spacecraft dynamics driven by the gravitational influence of the solar system's celestial bodies. The invariant manifolds can be seen as highways to travel within our solar system and they form a tube-like structure for periodic orbits. A spacecraft or a particle inside these tubes is carried by a *current* of the solar system's natural dynamics.

In particular, each orbit has two one-dimensional invariant manifolds associated to the hyperbolic solution: the stable, W^s, and the unstable, W^u, manifolds. Each manifold has two branches one corresponding to negative perturbation (W^s_-, green, and W^u_-, red, in Figure 2.3) and one corresponding to a positive perturbation (W^s_+, green, and W^u_+, red, in Figure 2.3). In the Sun-Earth system, the stable and unstable manifolds associated to L_1 and L_2 are the phase space structures that allow the transfer of a spacecraft to and from the Earth. Conversely, the centre×centre solutions of the collinear equilibrium points are linked to the centre manifold. The centre manifold is associated to the existence of families of periodic orbits (LPOs) as proved by the Lyapunov's Centre Theorem.

The stable and unstable manifold structures enhance transfer trajectories from Earth for ballistic capture to the Moon or to visit multiple Moons of the Jovian-Saturn system when combining multiple solutions of the R3BP (Koon et al., 2002; Gómez et al., 2004). For a space mission at LPOs, trajectories of the stable manifold are good candidates for transfer (Gómez et al., 1993). Gómez et al. (1993) proposed to take the approximation of the stable manifold of the nominal LPO; then propagate backwards in time to estimate the spacecraft velocity necessary to be inserted into the stable manifold of the selected LPO from a parking orbit around the Earth. Thus, one initial impulsive manoeuvre (Δv) to leave the parking orbit is needed to reach the LPO. In the Earth-Moon system, this dynamical system approach allows the design of ballistic capture to the Moon (Alessi et al., 2010). Note that a trajectory of this type uses less fuel than the standard Hohmann transfer [2]. Intersections between manifolds are called homoclinic and heteroclinic connections that allow transfer trajectories between LPOs around L_1

[2]In celestial mechanics, the optimum transfer within two coplanar Keplerian orbits around the same celestial body is called Hohmann transfer. The Hohmann transfer is considered an optimum transfer within the 2BP when no constraints on time are included as it requires the minimum Δv consumption associate to transfer manoeuvres.

and L_2 as for the Artemis and Wind missions, Table 2.1. Figure 2.4 shows a qualitative representation of the Artemis' transfer trajectory from L_1 to L_2. Dynamical system tools were also used to explain the origin of rings and spiral arms in barred galaxies. The rings and spirals are formed by chaotic orbits driven by the invariant manifolds associated to unstable orbits of the galaxy's equilibrium point (Romero-Gómez, 2006).

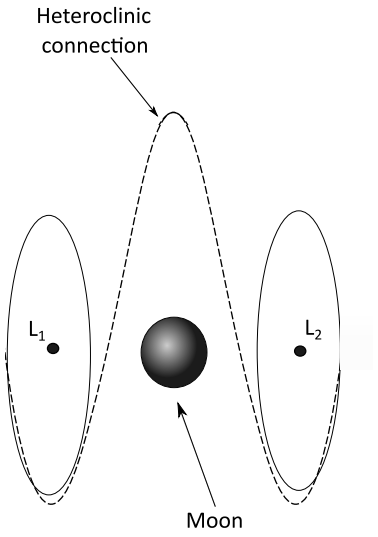

Figure 2.4: Qualitative representation of the Artemis' trajectory.

The centre manifold structure gives rise of two one-parameter families of periodic orbits known as planar and vertical Lyapunov. Together with periodic solutions, there exist quasi-periodic orbits (2D invariant tori). However, the hyperbolic components make orbits around L_1 and L_2 very unstable. Thus, station keeping to maintain the spacecraft on the LPOs is required. Simó et al. (1987) proposed to compensate the unstable manifold through impulsive (Δv) manoeuvres to insert the spacecraft onto the stable manifold of the nominal LPO. The SOHO mission uses this technique. The overall Δv required for SOHO's station-keeping was around 50 cm/s per year which is four times less than that of the ISEE-3 mission. This highlights once again the importance of dynamic system tools for spacecraft trajectory design.

The computation of periodic orbits around the collinear points is not an easy task due to the existence of the hyperbolic parts that make them highly unstable. Thus, the computation of LPOs requires the elimination of the instabilities. The computation of the central manifold can be done in three ways through the reduction of the central manifold, a semi-analytical approach (Linsted-Poincaré method) or numerical methods for an explicit computation of the orbits of the central manifold. The reduction of the central manifold was initially proposed by Deprit (1969) and then explored by Jorba and Masdemont (1999). The Lindsted-Poincaré method provides an explicit computation of the central orbits as a function of their amplitudes and phases (Richardson, 1980). This is a semi-analytical approach where the central orbits are solutions of the linear CR3BP equations around the equilibrium points. The numerical computation for the

determination of periodic and quasi-periodic orbits make use of the Newton's method. Multiple shooting methods (i.e. predictor-corrector algorithm) are used to overcome the effect of instability.

The computation of objects as fixed points, invariant manifolds and libration point orbits requires the use of dynamical system tools for the spacecraft trajectories design. The work of Poincaré led to a systematic search of periodic orbits. His idea was to study the full set of orbits rather than individual ones. Thus, the dynamical system approach looks at methods of solving the equations of motion from a global point of view by providing a qualitative and quantitative picture of the motion (Poincaré Map).

In this thesis, the dynamical system algorithms to compute objects was entire developed[3] as no pre-existing tools were available to the author. A few examples are: the computation of fixed points, the numerical computation of periodic orbits (required in Chapter 5 for the design of target orbits), the Lindsted-Poincaré method (required in Chapter 6 for the transfer trajectory design) and the computation of the invariant manifolds and the zero velocity curves (required in Chapter 7 for the end-of-life disposal).

2.2.1 Classification of orbits around the $L_{1,2}$ equilibrium points

As previously mentioned, the centre×centre part gives rise to two one-parameter families of periodic orbits known as Planar (P-) and Vertical (V-) Lyapunov orbits, shown in Figure 2.5. Moreover, there also exist a two-parameter family of 2D Tori, known as Lissajous orbits that connect the two Lyapunov families. A Lissajous orbit is a quasi-periodic orbital trajectory that winds around a torus but never closes in on itself.

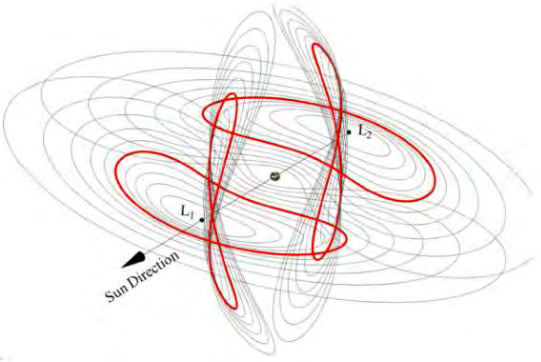

Figure 2.5: Families of Planar (P-) and Vertical (V-) Lyapunov orbits. Image credit Yárnoz et al. (2013).

A special solution of Lissajous orbits is halo orbits (Farquhar, 1968); where the in-plane and out-of-plane frequencies are equal. They are periodic three-dimensional orbits

[3] In CRUISE toolbox.

symmetric with the $y = 0$ plane of the synodic reference frame. The following paragraphs present a review of families of periodic orbits computed by several authors.

An accurate classification of families of periodic orbits in the Hill's problem and the R3BP was carried out by Hénon (1965a,b, 1966a,b, 1968). Hénon performed numerical studies on families of periodic orbits and compared his results with the hand-computed orbits by Kelvin (1892), Jackson (1913), Hill (1886) and Matukuma (1930, 1932, 1933). At the same time, a general study of CR3BP periodic orbits was developed by Strömgren (1922)'s group at Copenhagen and among others we should cite the work by Darwin (1911) and Moulton (1920). Deprit and Henrard (1967) developed a numerical continuation method for generating those families. A systematic numerical investigation into families of periodic orbits was performed by Broucke (1968) in which the work by Hénon's was extended to the CR3BP in Earth-Moon case. Schuerman (1980) was the first to add the effect of SRP to the CR3BP. Then, Elipe (1992) formulated the CR3BP with generalised forces, and found the periodic orbit solution in the R3BP-SRP (i.e., a binary star system which involves SRP). Finally, mission applications in the restricted three-body problem with SRP (CR3BP-SRP) were proposed by McInnes (1999).

There are many research studies currently being performed in the field of CR3BP-SRP dynamics that include: Barcelona's group (Farrés and Jorba, 2010; Villac et al., 2012; Farrés et al., 2013), Villac et al from University of California (Villac et al., 2012; Katherine and Villac, 2010), Howell (2001) from Purdue University, McInnes et al. from University of Glasgow and Verrier and Waters from University of Portsmouth, which are using a numerical continuation package (AUTO) to investigate the families of periodic orbits in CR3BP-SRP (Verrier and Waters, 2013). Recently, Yárnoz et al. (2014) studied the evolution of a- and g-families due to the effect of SRP in the Hill's problem of the Sun-Asteroid system, where, close to the asteroid, the SRP is around the same order of magnitude as the asteroid's gravitational effect.

Unfortunately, there is no unique classification of periodic families and some of them do not always exist in all planetary systems (changes in the mass parameter, μ). Therefore, it is useful to list them as in Tables 2.2-2.4. Table 2.2 lists the natural Periodic Orbit (PO) families in the Hill's problem, where the mass parameter, μ, of the system tends to zero, (i.e., Sun-Earth system). However, when extended to the PO solution for a general μ, as for the CR3BP, some of the families cease to exist as shown in Table 2.3 for the Earth-Moon system. Finally, Table 2.4 reports only a few examples of new PO families in the CR3BP-SRP, but a wider study on the families of POs was carried out by Verrier and Waters (2013) and Yárnoz et al. (2014).

Through this thesis, halo, Lissajous and planar g-family type orbits were selected for the design of SRP assisted missions in the Sun-Earth system.

Halo orbits are periodic three-dimensional orbits. These orbits are usually selected large enough so that the spacecraft is continuously in view of the Sun and the Earth. This,

therefore, aids the design of the communication link. However, the main disadvantages are with respect to the spacecraft's pointing requirements as those orbits are elongated with a big excursion in the ecliptic plane and a small excursion of the out-of-plane component. This fact affects the spacecraft communication link in a negative way as the spacecraft will need to be continuously controlled to maintain Earth pointing antennas. Herschel (Appendix B.3.1) and SOHO (Appendix B.3.2) are examples of spacecraft placed at halo orbits around L_2 and L_1 respectively. Alternatively, a spacecraft can be placed in a quasi-periodic orbit around the collinear libration points (Gordon, 1993).

Lissajous orbits are quasi-periodic orbits that allow mission flexibility as they can vary their size and shape. However, their main disadvantage is that the spacecraft field of vision can be obstructed by the Earth. This requires extra manoeuvres to avoid that the spacecraft enters in Earth's eclipse as for the case of Gaia spacecraft (Canalias et al., 2003). The Lissajous orbit of Gaia spacecraft is shown in Appendix B.3.3.

Future space missions could also take advantage of families of periodic orbits around the smaller celestial body (i.e. Earth of the Sun-Earth system and asteroid of the Sun-asteroid system) for planetary science or observations. These families are known as g-family or Distant Prograde Orbit (DPO). The DPO was chosen after an accurate classification and ranking of the most famous families existing in the CR3BP for new scientific mission applications. They are planar high amplitude stable or unstable orbits around the smaller celestial body. They seem to be advantageous for planetary science and mission observations. For example, icy planetary satellites like Europa suggested the use of a DPO to study the second primary in the CR3BP system (Lara and Russell, 2006). DPOs around an asteroid may be used for asteroids observation in the Sun-asteroid system. Moreover, DPOs can provide a good field of vision to detect Near Earth Objects in the Sun-Earth system as suggested by Stramacchia et al. (2016) for the stable orbits of the DPO type. High amplitude orbits are currently of interest to the Space Agencies for future LPOs and DPOs space missions since a lower insertion Δv is required to reach high amplitude orbits compared to low amplitude orbits, for example, the NASA's Wind mission performed multiple loops of DPO type as shown in Figure 2.6.

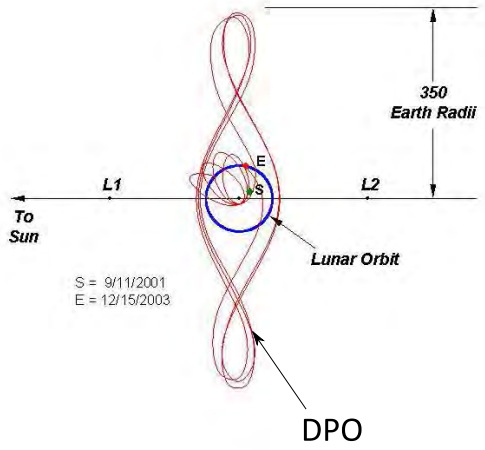

Figure 2.6: Wind spacecraft's DPO. Image credit NASA-website (2003).

Strömgren's Class	**Matukuma's Class**	**Characteristic**
a	F	Retrograde unstable simple PO around L_2.
b	-	Retrograde PO around L_3.
c	F	Retrograde unstable simple PO around L_1.
d	-	PO around L_4 (non-existing for $\mu = 0.5$).
e	-	PO around L_5 (non-existing for $\mu = 0.5$).
f	a	Retrograde stable PO around m_2.
g	A, B	Direct PO around m_2 (stable or unstable).
g'	H, E, I_2, G	Direct of second body, m_2 (stable or unstable).[a]
h	-	Retrograde circular PO of infinitesimal small radius about M_1 i.e. Sun. Small changes in the family structure happen when μ increases.
i	-	Direct PO of infinitesimal small radius about M_1: as μ increases, there are infinitely self-bifurcations. Then, subfamilies branches from it, and each of these exist only for certain μ.
k	-	PO around M_1 and m_2: direct motion in the rotating system.
l	-	PO around M_1 and m_2: retrograde motion in the rotating system and direct in the fixed one.
m	-	PO around M_1 and m_2: retrograde motion in the rotating system as well as in the fixed one.
n	-	Retrograde PO, asymmetric to y-axis. They are related to Class c, but are not generated from infinitesimal orbit around L_1.
o	-	Retrograde PO: asymmetric respect to y-axis.
r	-	Retrograde PO: asymmetric respect to y-axis.

Table 2.2: Families of planar Periodic Orbit (PO) in Hill's case. Comparison of Strömgren (1922)'s and Matukuma (1930, 1932, 1933)'s periodic orbits catalogue initiated by Hénon (1968), and updated in this table with the work of Bruno and Varin (2007). M_1 and m_2 stay for the first (i.e. Sun or Earth) and second (i.e. Earth or Moon) celestial body respectively. μ is the mass parameter of the two selected celestial bodies.

[a] family g' branches off family g at the critical orbit.

Broucke's Class	**Strömgren's Class**	**Characteristic**
G	c	Retrograde unstable elliptic PO around L_1 for μ of the Earth-Moon system.
J_1	a [a]	Stable and unstable PO around L_3. They are similar with G class around L_1, where class J_1 ends with a branching of family A_1. This family exist for $\mu = 0$ an has an evolution similar to the case $\mu \neq 0$. Probably this family exist for every μ.
A_1	f	Retrograde infinitesimal PO around M_1. The end of the family have not yet determined. Larger orbits close to m_2 with periodic collision orbits. Class A_1 contains 3 orbits that belong to three other families: G, J_1 and BD (3 branch points).
BD	g	Direct circular PO around M_1. This class contains 3 periodic collision orbit. Strömgren supposed that the end of class g was due to L_4 and L_5, where Bartlett stated to be correct. The initial orbits are stable; then, they became all unstable.
E_1	l	Direct PO around M_1 and m_2. A loop appears at one side of the orbits and later it evolves to a collision with M_1. Class l ends with two of the double asymptotic orbits at L_4 and L_5. This is not true for class E_1 in the Earth-Moon system.
F	l	Retrograde PO around M_1 and m_2. Correspond to family E_1. All the PO have positive energy. All the inside PO are unstable.
C	f	Retrograde PO around M_1. The beginning of the family is close to Keplerian circular orbit. Two periodic collisions. Not yet determined the natural end. All first circular orbits are stable; then, the last orbits are all unstable. Since they seem identical to class f, this would indicate that similar PO exist for every μ.

[a] When $M_1 = m_2$, L_1 and L_3 have similar properties.

H_1 and H_2	g	Direct PO around m_2. For H_1 is known the beginning of the family, but not the end. For H_2 is not known neither the beginning of the family, nor the end. Both families belong to the same class. Family H_2 contains some orbits that are circa symmetric image of certain orbits of H_1. H_1 and H_2 are close to Class g, but their evolution seem to be different.
I	-	Evolution of PO and quasi-PO around L_2. Initially, elliptical and gradually egg-shaped elongated toward M_1.
II	-	Evolution of PO and quasi-PO around L_2. Initially, egg-shaped elongated toward M_1, and gradually becomes elliptical.

Table 2.3: Families of planar Periodic Orbit (PO) in the R3BP: Broucke (1968) and Dutt and Sharma (2011). M_1 and m_2 stay for the first (i.e. Sun or Earth) and second (i.e. Earth or Moon) celestial body respectively. μ is the mass parameter of the two selected celestial bodies.

Farrés and Jorba's Class	**Sail's angles: α and δ [°]**	**Characteristic**
Halo 1	$\alpha = 0$ $\delta = 0$	Generating from the P-Lyapunov: 3D PO
Halo 2	$\alpha = 0$ $\delta = 0$	Generating from the P-Lyapunov: 3D PO.
Planar	$\alpha = 0$ $\delta = 0$	Generating from the P-Lyapunov: 2D PO.
A	$\alpha = 0$ $\delta \neq 0$	Generating from the P-Lyapunov: 3D PO.
B	$\alpha = 0$ $\delta \neq 0$	Generating from the P-Lyapunov: 3D PO.
Bow-tie shape	$\alpha = 0$ $\delta = 0$	Generating from the V-Lyapunov. The bow-tie shape is symmetric with the $z = 0$ plane.
Circular shape/ Bow-tie shape	$\alpha = 0$ $\delta \neq 0$	Generating from the V-Lyapunov. The PO close to the equilibrium are almost circular. Then, along the family the shape change in bow-tie without any symmetry of the two loops.

Table 2.4: Families of planar and out-of-plane Periodic Orbit (PO) in the R3BP-SRP: Farrés and Jorba (2010). P and V denote Planar and Vertical respectively.

2.3 Solar radiation pressure

Solar radiation pressure is the pressure acting on any surface exposed to electro-magnetic radiation. The electromagnetic radiation upon contact with a body can either be absorbed, transmitted or reflected. The force generated by radiation pressure onto objects is very small. Thus, makes it difficult to detect this effect on Earth. However, SRP becomes an important figure in space mission design where luminous bodies such as stars exert radiation pressure onto particles moving nearby (Poynting, 1904).

Table 2.5 lists a historical timeline associated with SRP discoveries (McInnes, 1999). The effect of SRP was firstly studied on tiny meteorites fragments or dust particles. The influence of the impinging photon radiation pressure on a space vehicle is called the solar radiation force. The solar radiation pressure is $9.12 \cdot 10^{-6}$ N/m^2 at 1 Astronomical Unit[4] (AU) (McInnes, 1999). As a result of solar activity, this value may fluctuate slightly ($< 1\%$). The first examples of SRP effects observed in space for geocentric orbits are associated with the Echo balloon (Shapiro and Harrison, 1960) and Vanguard I (Musen, 1960) satellites. The most common SRP effect on satellites in Keplerian orbits around the Earth is in the long-term oscillation in eccentricity and inclination [5], where the period depends on the area-to-mass of the satellite (Lücking et al., 2012b). SRP induces periodic variations in all orbital elements, and above altitudes of 800 km, it exceeds the effects of the atmospheric drag (Chobotov, 2002; Colombo and McInnes, 2011). The induced changes in perigee height can have significant consequences for the satellite's lifetime, suggesting a possible end-of-life strategy that uses SRP (Lücking et al., 2012a, 2013a).

Different SRP models were proposed for a variety of mission applications, but the simplest, therefore, the most popular, SRP model is known as the cannonball model. This model describes how SRP would affect a cannonball like spherical object which has equally distributed optical properties. Therefore, the spacecraft is modelled as a sphere, with the advantage that solar radiation pressure is expressed as a potential disturbance function. This model was first proposed for the LAGEOS mission (NASA-website, 1976) whose spacecraft looks like a cannonball, so this is the origin of its name. Alternatively, McMahon (2011) proposed to express the SRP force as a Fourier series, where the Fourier coefficients are functions of the body shape, its reflectivity properties and the Sun position. In spacecraft trajectory design, the classical approach is to use the cannonball model for preliminary studies. Thus, in this thesis, the cannonball model is used. Future works should consider using a more precise SRP model.

[4]The Astronomical Unit is a fundamental unit that corresponds to the Sun-Earth mean distance and it is equivalent to $1.496 \cdot 10^8$ km.

[5]For the definition of eccentricity and inclination refer to Appendix B.1.

In the cannonball model, the magnitude of the SRP accelerations depend on the size of the spacecraft's reflective area, the spacecraft's reflectivity properties and mass and the orientation of the spacecraft with respect to the Sun-line direction.

In libration point orbits of the Sun-Earth system, SRP is an important figure when the spacecraft has highly reflective and extended surfaces, such as for Herschel telescope's sunshield. Therefore, the radiation pressure acceleration will have a substantial effect in the case of the JWST (in Table 2.1) due to its large sunshield. This suggests that the spacecraft's control system should be designed to make use of these perturbing accelerations in performing the correction manoeuvres needed to keep the spacecraft on the target trajectory (Noam et al., 1998; Evans, 2003). SRP has the advantage of being an unlimited source of *propellant* as the propulsion system requires just a reflective area to enhance the radiation of the Sun. JAXA proved the effect of SRP with the Ikaros mission. The Ikaros spacecraft has a 20 m span squared solar sail and is propelled solely by SRP (Tsuda et al., 2013). In this thesis, the design of an SRP assisted mission in the Sun-Earth system is investigated for spacecraft control from the beginning of the mission (orbit control and transfer trajectories) until the end of its lifetime (i.e., for end-of-life disposal).

Year	***Study on SRP* (Author)**
1600	*Corpuscular theory of light*
1619	*Comet tails study* (J. Kepler)
1744	*Wave theory of light* (Euler)
1754	*Measurement of SRP* (de Marian and du Fay)
1785	*Electrostatics experiments* (Coulomb)
1812	*Demonstration that the Sun has an electrical charge* (Olbers)
1873	*Theory of electromagnetism radiation* (Maxwell)
1876	*Existence of SRP: second law of thermodynamics* (Baroli)
1900	*Experimentally demonstration of Maxwell's theory* (P. Lebedew)

Table 2.5: SRP Historical Background (McInnes, 1999).

2.4 Mission applications

Using SRP as a source of propulsion results in the design of innovative devices to control the spacecraft that require a limited fuel stored on-board with respect to a conventional propulsion system. Therefore, SRP is a natural and unlimited source of propellant. The design of SRP assisted missions in the Sun-Earth system is investigated here for spacecraft's orbit control and maintenance at LPOs, for enhancing transfer within the Sun-Earth system and for the design of graveyard trajectories when the mission reaches its end. For this reason the following sections will present past work in the subjects of:

1) orbit control and maintenance,

2) design of transfer trajectories, and

3) end-of-life disposal.

2.4.1 Orbit control and maintenance

A spacecraft placed around the equilibrium points will naturally diverge from them as they show an unstable nature (Section 2.2). Thus, trajectories designed in the R3BP require the spacecraft to perform manoeuvres to maintain its nominal trajectory by counteracting the unwanted environmental instabilities (Koon et al., 2008; Perozzi and Ferraz-Mello, 2010).

Previous applications of SRP control were aimed at controlling the attitude of the spacecraft. These applications were the first to demonstrate that the effect of SRP can be exploited to stabilise the spacecraft. Thus, even if this research does not include the attitude dynamics of the spacecraft, the experience of using SRP for attitude control is an important background step for this work.

Solar radiation pressure was successfully used for attitude stabilisation through cone shape (sail) reflective structures and solar array. The cone sail can passively control the spacecraft's angular momentum by changing its orientation with respect to the Sun-line to reach a stabilising condition. For example, Sohon (1995) proposed the attitude stabilisation of a spacecraft by using SRP. SRP attitude concepts are often used for geostationary satellites or some interplanetary spacecraft. INSAT[6] (Sathyanarayan et al., 1994) and GOES I-M (Hawkins, 1996) satellites have a conical-shaped solar-sail, mounted on a long boom, which is used to counteract the solar radiation disturbance torque caused by an asymmetrical solar-array configuration (Figure 2.7). SRP is also utilised for the attitude control of spacecraft placed in geosynchronous orbits such as OTS-2 (Renner,

[6]INSAT's cone sail has an high of 4.4 m and the radius of the base is 0.79 m; where, the cone sail is mounted on a 15 m boom.

1979), TELECOM 1 (Figure 2.8), and INMARSAT 2 (Wie, 2004). The SRP stabilisation can be achieved through an asymmetrical offsetting of the solar-array wings from the theoretical Sun-pointing orientation (by generating the "windmill" torque). Additional solar flaps mounted on the solar array can increase this torque control effect. Other attitude control methods for a Sun-pointing satellite, which exploits SRP are vane type tail surfaces, reflector-collector systems, corner mirror arrays, solar paddles, grated solar sails and mirror-like surfaces (Kumar and Behdinan, 2008). In the case of Mariner 10, asymmetrical twisting the solar panels was successfully applied during its flight to Mercury. Mariner 10 used solar panels and antennas for active solar pressure control (McInnes, 1999). This opens up the design of SRP manoeuvre enhanced by reflective deployable structures. Even though the beneficial effect of SRP in attitude control has been proven in space, the SRP is often considered to be an external disturbance for most satellites (Wie, 2004).

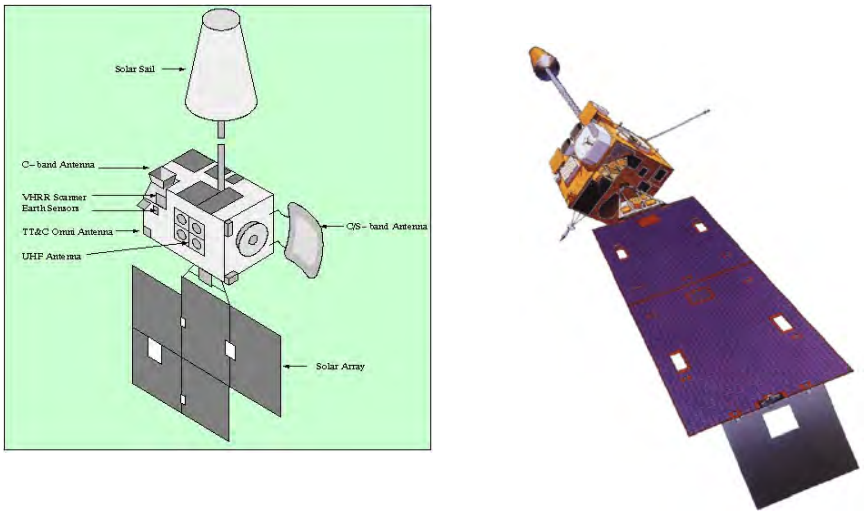

(a) INSAT-2 (b) GOES I-M

Figure 2.7: INSAT (image credit: ISRO) and GOES I-M (image credit: NASA).

In the framework of orbit feedback control, this literature review is focused on control strategies proposed for LPOs around L_1 or L_2 in the restricted three-body problem with SRP (RTBP-SRP). The magnitude of the SRP acceleration is controlled by the size of the spacecraft's reflective area, the spacecraft's reflectivity and mass and the spacecraft orientation with the Sun-line direction. Thus, in the design of a control law enhanced by SRP, these parameters are the required control variables.

The existing control strategies in LPOs are distinguished between linear and non-linear controllers, some of them also extended to SRP applications. Among the non-linear

Figure 2.8: Telecom 1 spacecraft (image credit: CNES)

controls, Xin and Pernicka (2008) developed a suboptimal control known as the θ-D technique, which established the control stability by using Lyapunov theory. Shahid and Kumar (2010) proposed a sliding-mode control for formation flight, enhanced by SRP; where, both the orientation angle and the area are control parameters. In the field of linear control, Simó et al. (1987) and Gómez et al. (2001) used the variational theory approach by exploiting the Floquét Modes (FM) to design the control law. Howell and Pernicka (1993) developed the target point technique, where, as for the FM approach, impulsive manoeuvres (Δv) are computed to keep the spacecraft near the nominal trajectory. Both the techniques were compared by Keeter (1994) and then extended to SRP applications by A. McInnes (McInnes, 2000) for the target point method and by Farrés and Jorba (2008, 2010, 2014) for the Floquét mode approach. In both cases, the only control parameter was the sail orientation angle, while the area was kept fixed. Scheeres et al. (2003a) proposed a Hamiltonian-Structure Preserving (HSP) control that stabilises the system in the sense of Lyapunov and it was intended for low thrust propulsion in formation flight applications. The HSP control law was then extended by Xu and Xu (2009) for SRP applications where both the area and the orientation angle were included as control parameters. Finally, the Linear Quadratic Regulator (LQR) technique in solar sail applications was first applied to LPO control with SRP by Bookless and McInnes (2008) and then used by Farrés and Ceriotti (2012); in both cases, the sail area and orientation angles were the control parameters.

In the design of trajectories, dynamical system tools that exploits the invariant manifold theory is of interest for this work. As discussed previously in Section 2.2, studying the linear behaviour of the spacecraft around the equilibrium points is important in

understanding the non-linear dynamics. Thus, a linear control that makes use of the invariant manifold theory was selected in this work for orbit maintenance. Among the linear controllers, LQR is the most popular. However, the FM and HSP have the advantage of exploiting the natural dynamics of the spacecraft. Thus, FM and HSP are also investigated as they both utilise the invariant manifolds.

The LQR is an optimal control where the control law is proportional to the state error. The objective of the control is to find the differential component of the control to be added to its target components. Then, the linear time-invariant approximation of the dynamical system is used to compute the differential control part. As an optimal control, it minimises the state error and the feedback control history. Since the control law is proportional to the state error, minimising the cost function leads to the need to solve the algebraic Riccati equation which gives the optimal gain values (Friedland, 2005). This control was proposed for solar sail station keeping of high-amplitude vertical Lyapunov orbits where the control vector is a function of the sail orientation and its area-to-mass ratio (Ceriotti and Farrés, 2012).

The FM verifies when the trajectory is moving onto the unstable manifold and to then determine a new sail orientation to return the trajectory back onto the target orbit. The principle of this control method is to let the solar sail follow its natural dynamics; which initially allows it to follow its unstable manifold. Then, the solar sail orientation is changed to bring the trajectory back to the stable manifold of the LPO target orbit. It is important to underline that this strategy uses information from the linear dynamics of the system to decide when the sail orientation has to be changed. However, the FM has the advantage to be able to control the system by using only the sail orientation as a control parameter (Farrés and Jorba, 2008, 2010, 2014).

The HSP feedback control aims to stabilise a periodic orbit in the sense of Lyapunov. This control is attractive since the fuel expenditure is small; resulting in it being proposed for low thrust application (Scheeres et al., 2003b). Scheeres et al. (2003b) control law was applied to LPO around the collinear equilibrium points L_1 and L_2. This control law preserves the Hamiltonian structure of the R3BP by projecting the relative position between the actual and target trajectories along both the stable and unstable manifolds. In that way, this control law simply creates an additional centre manifold which cancels out the hyperbolic equilibrium. As for the LQR and FM, the structure-preserving control uses the linearised dynamics for the design of the control law; moreover, since it uses the relative positions, it can be applied to spacecraft formation flight. The effectiveness of this control method was proven for the stabilisation of hyperbolic equilibria. As an example, Colombo et al. (2012) applied Hamiltonian structure-preserving control to Earth applications. When adding the Earth's oblateness (J_2) and SRP disturbances to the two-body dynamical system (Lücking et al., 2012b), the hyperbolic equilibrium

of the system corresponds to an anti-heliotropic[7] orbit that was proposed for studying the Earth's magnetotail. Finally, Xu and Xu (2009) proposed a modified structure-preserving control law for solar sail applications. The aim of this modified HSP control is still to remove the hyperbolic equilibrium, but in this case, the differential position is also projected along the centre manifold. As results, this control aims to modify the Coriolis accelerations. This control was tested on a solar sail stable Lissajous orbit, where the controller was generated by orienting the sail and by changing the lightness parameter.

As mentioned in Section 2.2.1, Space Agencies have a growing interest in future LPOs and DPOs space missions, in particular, in high amplitude orbits. In the case of high amplitude LPOs and DPOs, the HSP control laws proposed by Scheeres et al. (2003b) and Xu and Xu (2009) fail in keeping the spacecraft onto the nominal high amplitude orbit. Indeed, Scheeres et al. (2003b)'s and Xu and Xu (2009)' control laws are designed for a centre×hyperbolic equilibrium. However, high amplitude planar LPOs and DPOs show the appearance of a focus equilibrium along the orbit in replacement of the hyperbolic one. Thus, a new HSP control law is required to control spacecraft in high amplitude orbits (Chapter 5). Moreover, the HSP and the FM controllers share similarities as they both make use of the invariant manifold theory. Therefore, it would be interesting to compare both approaches to identify the pro and cons of both controllers (as shown in Chapter 5).

2.4.2 Design of transfer trajectories

Spacecraft in LPOs lie in a highly perturbed environment due to the hyperbolic nature of the collinear equilibrium points (Section 2.2). Thus, the stable and the unstable invariant manifolds associated to LPOs enhance transfer trajectories within the solar system.

The unstable manifold includes all the set of possible trajectories that a spacecraft could take to leave a nominal orbit (W^u). Conversely, the stable manifold involves the set of all possible trajectories that a spacecraft could take to reach a nominal orbit (W^s). The existence of low energy transfer orbits was proven by Conley (1968). The use of invariant manifolds for low energy transfer within the solar system was proposed for example for the Jupiter-Jovian Moon system (Anderson and Lo, 2004; Lo et al., 2006) and then for multiple visits of the moons of the Jovian-Saturn system (Koon et al., 2002; Gómez et al., 2004).

Transfers between unstable orbits of the solar system are possible due to the intersection of the invariant manifolds. These interactions are called homoclinic and heteroclinic

[7]The anti-heliotropic orbit is an orbit with the apses line in the direction of the Sun-Earth line and the apogee in the anti-Sun direction.

connections and are shown in Figure 2.9. The homoclinic point or orbits are the result of the interaction of the stable and unstable manifolds of the same fixed point or periodic orbit (Conley, 1968). Thus, a spacecraft can follow an homoclinic orbit departing from the unstable manifold and arrive at the same LPO through its stable manifold. The heteroclinic tangency instead involves the intersection of the stable and unstable manifold belonging to two distinct fixed points or LPOs. For example, a spacecraft leaving an LPO around L_1 from its unstable manifold can reach an LPO around L_2 through the stable manifold of L_2 (i.e., Artemis and Wind missions in Table 2.1). Heteroclinic connections were numerical proven by Koon et al. (2000) and Gómez et al. (2004).

The homoclinic orbits and heteroclinic connections allow transfers between unstable orbits in the CR3BP. These natural transfer trajectories exist within orbits with the same energy or Jacobi integral. If the transfer is required between orbits with different energies; then a manoeuvre to enhance the transfer is necessary (Davis et al., 2010).

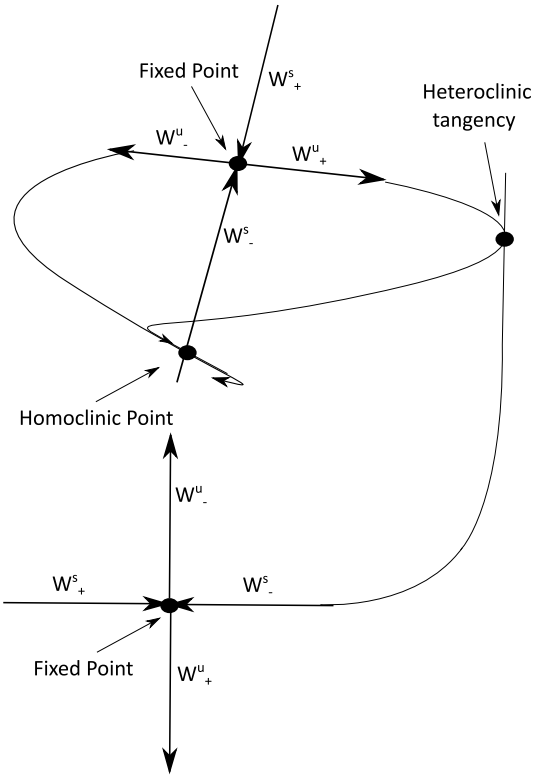

Figure 2.9: Schematic example of the homoclinic point and heteroclinic tangency.

Gómez et al. (1998) proposed transfers between a family of halo orbits around the same equilibrium point. These orbits have different energies; thus, one manoeuvre is required to inject the spacecraft onto the stable manifold of the desired halo. This transfer technique makes use of the Floquét theory for the design of the manoeuvre. The main idea is to exploit the invariant manifold through an impulsive manoeuvre. The impulsive manoeuvre aims to cancel out the tangential eigenvector of the Floquét modes (Tangent to the Family Manoeuvre, TFM). The TFM is then given to leave the initial halo orbit;

while, a second manoeuvre is required to insert the spacecraft into the target halo. Figure 2.10 shows a qualitative picture of the TFM. The transfer within the halo orbits that belongs to the same "cone" is performed by giving a manoeuvre tangential to the family direction.

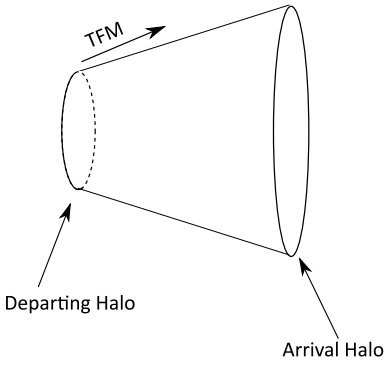

Figure 2.10: Qualitative representation of the tangent to the family manoeuvre.

While Gómez et al. (1998) proposed transfers within orbits around the same equilibrium point, Davis et al. (2010) proposed a method of using invariant manifolds to perform transfers between orbits around two distinct equilibrium points that have different energies. In this case, two deterministic manoeuvres are used to connect the unstable manifold of the departing orbit with the stable manifold of the target orbit. A genetic algorithm is used to vary the parameters that define the transfer.

Invariant manifolds were also proposed for the design of ballistic trajectories at the Moon. However, in the Earth-Moon system the stable and unstable manifolds associated to L_1 and L_2 pass quite far from the Earth. Alessi et al. (2010) proposed a two manoeuvre transfer to overcome this problem. A spacecraft is initially placed in a LEO orbit around the Earth. Two manoeuvres are required to perform the transfer to the Moon: the first manoeuvre is necessary to leave the LEO and the second to place the spacecraft directly into a Lissajous orbit or into its stable correspondent manifold as shown qualitatively in Figure 2.11.

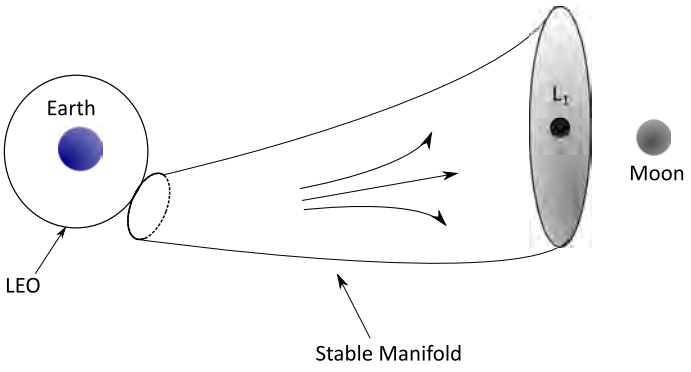

Figure 2.11: Moon ballistic capture.

Canalias et al. (2003) designed transfer trajectories between Lissajous orbits to perform eclipse avoidance manoeuvres for spacecraft around L_2. A semi-analytical approach was used to design impulsive manoeuvres that allow a change in phase or amplitudes of a Lissajous orbit. This transfer strategy is developed by looking at the semi-analytical solution of the linearised equations around L_2. The designed impulsive manoeuvre aims to cancel out the unstable manifold of the target orbit by using a phase space approach. A similar phase space approach was used for applications around the Earth when SRP and J_2 are considered by Lucking et al. and Colombo et al. The manoeuvre in the phase space is achieved by changing the reflectivity coefficient of the spacecraft through electro-chromic coating (Lücking et al., 2012c, 2013b).

In the field of transfer enhanced by SRP, Farrés and Jorba (2015) proposed to exploit the invariant manifold to transfer from $L_{1,2}$ to $L_{4,5}$. In this case, the effect of SRP is observed in moving the equilibrium points. Thus, a spacecraft injected into the unstable manifold of L_1 reaches the stable manifold of L_4 when an SRP manoeuvre is performed.

Limited work was carried out in harnessing SRP to enhance transfer trajectories within the Sun-Earth system. In particular, transfer trajectories between Lissajous orbits are solely proposed for the traditional impulsive propulsion. The effect of SRP can open up new design methodologies to perform transfer within Lissajous orbits. It would also be interesting to investigate if the spacecraft's sunshield or solar panels can be used to carry out the required SRP transfer manoeuvre (as shown in Chapter 6).

2.4.3 End-of-life disposal

Nowadays, spacecraft are a fundamental asset to the world's infrastructure, playing a significant role in telecoms, Earth observation and space explorations. The steady increase in the use of space in modern society and the lack of an international agreement to preserve the space environment have resulted in an ever rising number of debris objects. Satellites that have reached their end-of-life subsequently become categorised as debris objects and further add to the collision hazards for future space missions [8]. Currently, both ESA and NASA are working on setting guidelines and assessment procedures to limit the risk posed by orbital debris. For example, before the introduction of NASA Safety Standard 1740.14 NASA-website (1995), satellite end-of-life and disposal options were not considered during the design and operational phases of most satellites. This was due to the following extra design costs and the adverse effect on the available Δv budget. However, due to the increasing risk posed by orbital debris, especially in critical Earth orbital regions, satellite disposal has become increasingly important (Colombo et al., 2015a).

[8] Note that space debris can be categorised as natural debris and man-made objects at their end-of-life.

In 2008, ESA defined a set of requirements for tackling the threat posed by space debris and they are currently applicable to all future space systems such as launchers, satellites and inoperative objects (ESA, 2015). The international debris mitigation standards were also defined by the International Organisation for Standardization (ISO), such as the ISO-24113. Currently, the space community has recognised the need for mitigation of LEO and GEO. However, less concern is given for libration point orbits and no guidelines for the reduction of LPO satellites have been yet formulated (Colombo et al., 2014b).

Some research has been done for Earth applications through the exploitation of environmental perturbations such as drag force for low altitude orbits followed by a controlled re-entry (Alessi et al., 2014) and SRP for high amplitude orbits (Lücking et al., 2013a) or luni-solar for high elliptical orbits (Colombo et al., 2014a) and medium Earth orbits. However, limited work was done for LPO applications.

Van der Weg and Vasile (2014) suggest an end-of-life disposal for LPO spacecraft that is initially disposed of onto the unstable manifold and is then targeted such that the spacecraft impacts or are weakly captured by, the Moon. Colombo et al. (2015b) assessed the benefit of disposing of LPO spacecraft in heliocentric graveyard orbits, while Olikara et al. (2015) first proposed a disposal option, which injects the spacecraft towards the inner or the outer solar system and closes the zero velocity curves though a Δv manoeuvre.

Currently, the design of disposal options for LPO missions has been investigated for traditional propulsion. However, present research lacks investigation into the use of SRP as a propulsion source for the design of disposal manoeuvres. Thus, more research must be done in the field of end-of-life disposal trajectories design enhanced by SRP (see Chapter 7).

2.5 Solar radiation pressure enhancing devices

In the framework of reflective deployable structures as the main propulsion source, it is possible to distinguish them in two categories: solar sail technology and all the other reflective deployable structures. This is done as solar sails are designed to enhance SRP while the other reflective deployable structures (i.e. mirrors, antennas, solar panels and sunshield) are not intended to exploit SRP. In this Section, the discussion is focused on reflective structures and in reflective control devices that aim to modify the reflectivity property of the deployed area (i.e. solar sail or deployable structures). The advantage of adding flaps to enhance the effect of SRP was already introduced in Section 2.4.1.

2.5.1 Solar sail technology

Tsiolkovsky and Tsander first proposed solar sailing as a form of propulsion in the 1920s. The first vision of solar sailing was suggested by C. Wiley (1951) in his science fiction article. In 1958, R. Garwin (1958) published the first journal on solar sailing. The term "solar sailing" was coined by him in his journal publication. The first intuition of the use of solar sailing propulsion for future utilisation was given by A. C. Clark (1972). He published a story of a manned solar sail race in an Earth orbit. In 1977, the Jet Propulsion Laboratory (JPL) proposed a rendezvous mission to Halley's comet which employed a large solar sail (Friedman et al., 1978). The project was dropped at that time due to the high risk associated with the deployment. However, this was the first technical study into the use of a solar sail (McInnes, 1999). An important reference book in solar sailing was published by McInnes (1999): *Solar Sailing: Technology; Dynamics and Mission Applications.*

There exist different variations in the design of solar sailing devices. Among them, there are solar sails (McInnes, 1999; Wie and Roithmayer, 2001), Electric sails (E-sails[9]), also known as heliogyro (Janhunen, 2013; Quarta and Janhunen, 2008). The E-sail is a different variants of the solar sail principle; therefore, in this section, the discussion is limited to solar sails only like JAXA Ikaros mission(Tsuda et al., 2013), Figure 2.12.

Solar sails are large and light deployable reflectors that are propelled by the sunlight. Solar sails must be extremely light with a large area to generate a high acceleration from the momentum transported by photons. Thus, a key factor of this technology is the high value of the area-to-mass ratio; which, is related to the area exposed to the Sun and its reflectivity coefficient. An ideal solar sail must be near perfect reflector (i.e. mirrors-like surface) and must have a little loading which makes this technology challenging and difficult to develop (McInnes, 2003).

However, solar sail technology has ongoing relevance due to the recent advancement in payload miniaturisation which has led to lighter systems, and the interest in more novel mission applications. Examples of missions applications are (Howell, 2009):

1) exploration of the inner solar system,

2) maintenance of special artificial orbits (i.e. to overcome the problem of over-crowded GEO orbits or to achieve a large orbit inclination change),

3) solar power collectors,

4) delivery of large cargo, and

[9]Electrical sails are innovative propulsion concepts. The Satellite is spun around its symmetry axis and the rotational motion is used to deploy the tethers. The electric field generates by tethered shields the spacecraft from the solar wind ions. This generated a thrust that decays such as $(1/r)^{(7/6)}$, where, r is the Sun-sailcraft distance.

5) planetary protection.

Solar sail deployments have already been proven through ground test demonstrations such as NASA's and ATK Space System's successful deployment of a 20 m span sail in a 30 m vacuum chamber (April 2005). L'Garde also successfully deployed a 20 m span sail in July 2005. Moreover, space flight experiments have also been attempted such as the Cosmo 1 mission in June 2005, which was a 30 m span solar sail. However, due to a boost rocket failure, the mission did not achieve its goal. After the Cosmo 1 mission, the Nanosail-D spacecraft was launched in 2008 as a feasibility demonstration of deploying sails in orbit using a 3 m span sail. Unfortunately, due to a launch vehicle malfunction during stage separation, the Nanosail-D mission ended two minutes after launch (Wie, 2004). After these two unsuccessful in space sail demonstrations and thanks to recent advances in solar sail technology, JAXA is, with the success of Ikaros mission, the only agency that successfully tested a solar sail in space (Tsuda et al., 2013). This satellite has a 20 m span solar power sail that provides the propulsion and the on-board power requirements.

Solar sail technology still presents some engineering challenges in manufacturing a thin reflector film with a miniaturised bus, in realising and testing the deployable mechanisms and in the great mission costs. SRP, as a propellant-free form of propulsion, requires a high area-to-mass ratio which means having an extended area of minimum mass. These technological requirements make solar sails difficult to be developed and, as a result, it is a significant challenge to generate a commercial revenue from the use of these devices. For example, Sunjammer mission was a NASA's solar sail demonstrator constructed by L'Garde intended to demonstrate solar sail technology but was cancelled before launch. Indeed, NASA claims that a commercial revenue of this technology should be found to invest in the future of this technology[10]. Many projects are currently supported also in Europe by ESA/DLR based around the solar sail and inflatable boom technologies[11].

In the design and control of trajectories that makes use of SRP propulsion (Section 2.4), the order of magnitude of the required SRP manoeuvre is a function of the spacecraft's reflective area and its orientation with the Sun-line direction. Solar sails require a fixed large deployed area that constrained the magnitude in the SRP acceleration. They also have a very large moment of inertia that adds further mission constraints when re-orienting the spacecraft. Due to the need of variable geometry reflective areas for some mission applications and the high costs associated with solar sail technology, further technological solutions should be investigated for spacecraft trajectory design. Currently, no future missions are proposing to use an SRP enhancing device for the development and control of spacecraft in LPOs. This has created a void where reflective deployable structures can potentially pave the way for new mission design concepts and applications.

[10] 3^{rd} International symposium on solar sailing (ISSS, 2013).

[11] Inflatable booms are used as structural sail support and deployment method.

2.5.2 Reflective deployable structures and reflectivity control devices

As said, in the design of spacecraft trajectories enhanced by SRP, the area-to-mass ratio and the reflectivity coefficient are the key control parameters for stabilising the spacecraft. The area-to-mass ratio can be changed by reducing the spacecraft mass, which is a function of the fuel consumption or by changing its area exposed to the Sun. Nonetheless, the mass cannot be feasibly decreased; as a result, it is not a fully controllable parameter for orbit control applications. Thus, SRP assisted missions require an active control device that allows the projected area to be changed. The structural design is driven by the requirement in the size of the reflective area. The change in the reflective area's shape can be achieved through mechanisms or changes in its reflectivity properties (e.g., with electro-chromic materials). Besides the structural design, SRP enhancing devices are effective if the spacecraft is pointing in a favourable direction with the Sun. Thus, when designing missions that use SRP for propulsion and control, the required size of reflective deployable structures and the spacecraft pointing requirements need to be defined.

Large inflatable structures are surfaces that can be stowed and then deployed as lightweight extended area; these have a significant impact on a satellite's overall area-to-mass ratio (Cook, 2012). Applications of inflatable systems are:

1) solar power satellites,
2) membrane mirrors/reflectors,
3) sunshields,
4) solar arrays, and
5) communications antennae.

These deployable reflective structures are investigated here as possible candidates for harnessing SRP. Table 2.6 shows the area-to-mass ratio of past and current ESA missions to LPOs. The reflective area considered computing the area-to-mass ratio is mainly given by the contribution of the sunshield and solar array. Spacecraft with high area-to-mass ratios are sensitive to SRP perturbations requiring extra manoeuvres to keep the spacecraft onto the nominal LPO.

The first example of the major inflatable structures is solar power collectors. A Space Solar Power Satellite (SSPS) is a concept that has emerged over several decades; solar power is collected in space and used for terrestrial applications. Current advanced concepts considered by NASA are the symmetrically integrated concentrator and the Abacus/Reflector concept. In the case of a SSPS such as Abacus, the area-to-mass ratio is around 0.4 m^2/kg, which is large when compared to 0.02 m^2/kg for a typical

geosynchronous communication satellite. This requires considerable control torques[12] to counteract various environmental disturbances, i.e. SRP. Abacus requires 85, 000 kg of propellant per year for station-keeping, and attitude control achieved using 500 1 N electric propulsion thrusters with a specific impulse of 5, 000 s (Wie and Roithmayer, 2001). As a result, this leads to a heavy and consequently expensive system. This confirms that an alternative cheaper solution should be studied and an SRP assisted mission is strongly justified in SSPS applications.

Another application of the major inflatable structures is for space reflectors (membrane mirrors) which were proposed as an anti-global warming measure for climate change mitigation by deflecting the sunlight (Bewick et al., 2012). Deployable membrane structure technologies are rapidly advancing, making lightweight reflectors a potentially feasible technology. This technology requires a well-defined surface accuracy and consequently a precise surface control method (Hill et al., 2010). Hill et al. (2010) studied the profile of a reflector to determine the optimal grouping of actuators that assure a precise surface control.

A sunshield is another example of a large reflective deployable structure and is one of the core components for space telescopes to protect the optics from the Sun. The main perturbation at the Sun-Earth Lagrange points L_1 and L_2 comes from SRP, the Moon and the planets. The approach used so far is to correct this perturbation that affects the trajectory design at LPOs, for example for halo orbits this corresponds to correcting manoeuvres of 30-100 m/s per year. The gravitational effects of the other bodies are small and periodic, but they can not be neglected because perturbations in the direction of the unstable manifolds are enough to cause exponential growth of the trajectory within a few months. The main effect of the constant SRP is to shift the centre of the orbit by a small distance, but for spacecraft with large sunshields such JWST spacecraft, the SRP effect is greater than the other perturbations and depends mostly on the spacecraft attitude. Limited variations in the spacecraft attitude are enough to avoid the exponential growth of the trajectory at L_2, by using a closed-loop linear controller based on variations in SRP (Tene et al., 1998). In the case of the Wilkinson Microwave Anisotropy Probe (WMAP[13]), the tolerance allowed by the sunshade pointing requirement (0.2°) can be used to produce variations in the SRP. In that way, the resulting control force is of the same order of magnitude as the perturbations. Thus, this pointing requirement should be potentially be used for station-keeping without requiring any additional propulsion manoeuvres (Tene et al., 1998).

Solar arrays and large antennas could also potentially be used for the spacecraft trajectory stabilisation. In the case of orbit control, a modified design of the solar array and large deployable antennas should be investigated to equip them with a control device,

[12] An active three-axis attitude control is needed to maintain Sun pointing.

[13] WMAP mission was proposed to NASA in 1995, and launched in 2001. The scientific mission ended in August 2010. `http://map.gsfc.nasa.gov/mission/`

i.e., flaps (shown in Figure 2.8), that allows changes in their overall reflective areas. Conversely, they can be used for attitude control by changing their surface orientation towards the Sun-line direction. This technique of using the surface orientation of solar arrays for attitude control is already in use (Wie, 2004), but it could potentially be used for large antennas in specific mission operational modes i.e. cruise mode.

Another method of controlling the spacecraft's trajectory could be by changing its surface reflectivity properties through the so-called Reflective Control Device (RCD) or electro-chromic coating. The RCD are currently used by Ikaros for attitude control. Ikaros' orientation is controlled by using both diffusion and specular reflections, (see Figure 2.12). In the Ikaros configuration, these devices were placed at the sail corners to generate solar pressure torques. The force due to specular reflection (power off) is less of magnitude compared to the diffusion reflection (power on), so thanks to the alternative RCD power on/off strategy it is possible to generate the torques needed (Tsuda et al., 2013), (see Figure 2.12). Alternatively, the effective area can be reduced by temporary making some portions of the sail non-reflective, using electro-chromic materials with a reduction in the SRP thrust force for trajectory stabilisation (Ceriotti and Farrés, 2012).

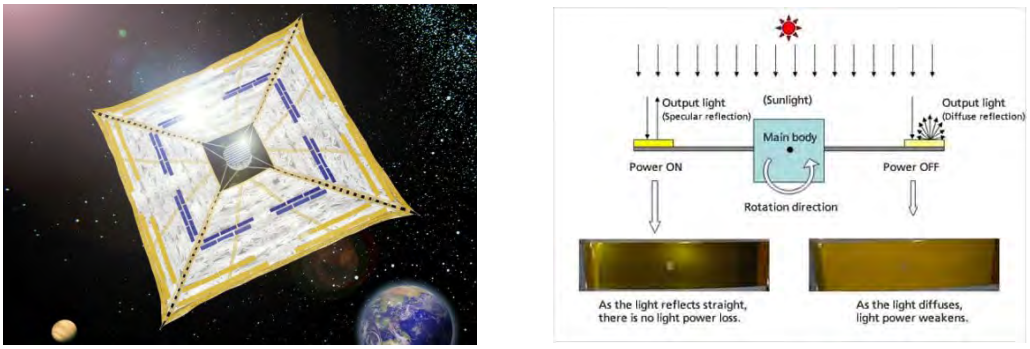

(a) Ikaros s/c (b) RCD

Figure 2.12: Ikaros and reflective control device, image credit: JAXA.

Electro-Chromic Devices (ECD) work in the infrared region of the electromagnetic spectrum (with mid to long wavelengths), where their emissivity is actively controllable. This technology was originally designed for spacecraft thermal control, but ECD variable emissivity from the long-wave infrared part of the spectrum and a passive cold mirror for solar rejection make them applicable also for trajectory control (Demiryont and Moorehead, 2009). For future microsatellites (i.e., SpaceChips swarm applications), ECD

coatings have also been demonstrated for future microsatellite applications (Lücking et al., 2012c, 2013b) as a feasible technology for orbit control since SpaceChips have a high area-to-mass ratio that makes them sensitive to SRP. ECD was also proposed for variable-shape multi-purpose platform sail applications; where distributed masses with variable reflectivity allow a change of the sail shape from a flat configuration, i.e. active trajectory control, and a parabolic shape for use a remote sensing device or communication antenna (Borggräfe et al., 2013). Recently, Ceriotti et al. (2013) proposed a variable geometry cone sail.

Name	**Mass (@ Launch) [kg]**	**Area [m^2]**	**A/m (@ Launch) [m^2/kg]**
Herschel	3400	16	0.004705882
Planck	1900	13.85	0.007291802
SOHO	1853	33.51	0.018084188
Gaia	2029	81.71	0.040272462
LISA P.	1900	2.8	0.001473684
JWST	6500	264	0.040615385
Euclid	2100	13.95	0.006642857

Table 2.6: Area-to-mass ratio of the ESA's missions at LPOs.

2.6 Summary

This section has presented the current state of the art of trajectory design and control for solar radiation pressure assisted missions. This began with the introduction of the restricted three-body problem along with the invariant manifold theory and the solar radiation pressure model. A background in the mission applications was carried out for:

1) the orbit control and maintenance,

2) the design of transfer trajectories, and

3) the end-of-life disposal.

The modern approaches used for the design of missions in the restricted three-body problem was investigated. Thus, it was possible to highlight the void in the literature between spacecraft's trajectories design and harnessing SRP for manoeuvres design.

Analysis onto the solar radiation pressure enhancing devices available in literature was performed to address the research questions stated in Section 1.1. This literature review shows a gap in the research where on-board deployable structures are currently not designed to control the spacecraft's trajectory. Consequently, finding a viable solution to harnessing SRP still presents a technological challenge. This demonstrates the difficulties in the broad spreading of SRP propulsion for the design and control of trajectories in the restricted three-body problem. To address the gap in the literature in the field of assisted missions through SRP, the circular restricted three-body problem needs to be initially presented in more details.

Chapter 3

Circular Restricted Three-Body Problem

As introduced in Chapter 2, the circular restricted three-body problem is a dynamical model that approximates the motion of the spacecraft under the gravitational influence of a primary body (e.g. the Sun) and a secondary body (e.g. the Earth) and describes the gravitational interaction of three masses (i.e., *three-body*) in which the third mass is smaller or infinitesimal (i.e., *restricted*) compared with the other two. The primary masses are called first and second primaries, and they are considered spherically symmetric so that they can be modelled as point masses. In this study, the primaries are the Sun and the Earth+Moon barycentre. The gravitational effect of the Moon is thus taken into account by adding the Moon's mass to the one of the Earth and considering that the Earth+Moon barycentre moves on a circular orbit around the system barycentre. Thus, in this model, the effect of the Moon contributes solely to the Earth's mass. The primaries' motion is assumed to be on the ecliptic plane, and their motion is approximated to be around their centre of mass (i.e. centre of mass of the Sun-(Earth+Moon)) with a circular orbit (i.e., *circular*). Since the third mass does not influence the primaries motion, the CR3BP describes the motion of this third mass, i.e. spacecraft's motion. When the solar radiation pressure is taken into account, this additional repulsive acceleration is added to the classical CR3BP equation and it turns into the CR3BP with SRP, (Szebehely, 1967; Koon et al., 2008; McInnes, 1999).

3.1 Sidereal and synodic reference frames

The definition of at least two fundamental reference frames is necessary when describing the motion of the spacecraft under the mutual gravitational effect of the Sun and the Earth+Moon barycentre. In this thesis, the motion of the spacecraft is outlined in the reference frame centred on the Sun and the Earth+Moon's centre of mass. The sidereal frame describes the motion of the spacecraft from the viewpoint of an inertial observer; where the axis of the reference system is fixed. We refer to the sidereal system with the symbol $\mathscr{F}_i$ and its correspondent inertial coordinates are $\{x_i, y_i, z_i\}$ as shown in Figure 3.1(a).

The importance of describing the motion of the spacecraft from the viewpoint of rotating coordinates was instead shown by Euler in 1767 (see Chapter 2). Thus, a synodic or rotating frame needs to be introduced, $\mathscr{F}_r$, where the correspondent rotating coordinates are $\{x, y, z\}$ as shown in Figure 3.1(a). As already mentioned, the main CR3BP assumption is that the two primaries' motion is assumed to be on the ecliptic plane, $\{\boldsymbol{x}_i, \boldsymbol{y}_i\}$, and the two masses lie on the x-axis of $\mathscr{F}_r$ frame. The position of the primaries is fixed in the synodic frame. The x-axis convention adopted here is such that the x-axis is pointing in the Sun-to-(Earth+Moon) direction as in Figure 3.1(a). Thus, the position of the Sun is always in the negative x-axis coordinates; while, the Earth+Moon position is always in the positive x-axis coordinate of the synodic system as shown in Figure 3.1(b). Note that, the out-of-plane directions of both frames are coincident ($\boldsymbol{z} = \boldsymbol{z}_i$). Thus, $\boldsymbol{z}$ is the axis of rotation: the $\{\boldsymbol{x}, \boldsymbol{y}\}$ frame rotates with respect to the $\{\boldsymbol{x}_i, \boldsymbol{y}_i\}$ frame with an angular velocity equal to the primaries mean motions, n [1]. The two frames are coincident when $t = 0$.

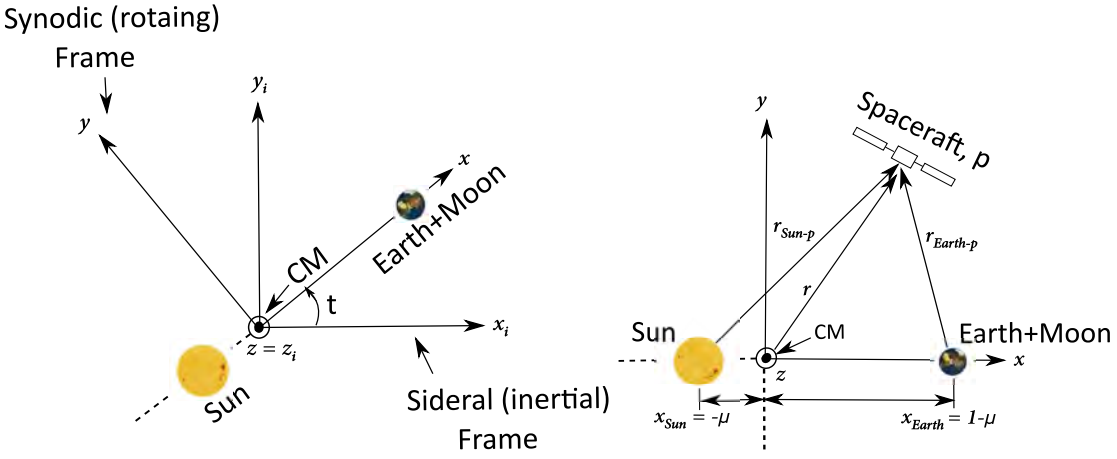

(a) Sidereal and synodic reference frames.

(b) Synodic reference frame.

Figure 3.1: Sidereal (inertial, $\mathscr{F}_i$) and synodic (rotating, $\mathscr{F}_r$) reference frames with origin in the Sun+(Earth+Moon)'s Centre of Mass (CM).

[1] The mean motion is the angular speed for a body to complete one orbit, assuming a constant speed on an equivalent circular orbit.

3.1.1 Conversion of the dimensionless coordinates from a synodic to a sidereal reference system

Under the hypothesis that the Earth+Moon barycentre describes a mean motion (circular orbit) around the Sun, it is possible to normalise the dimensional coordinates through the following parameters: l, τ and v. l is the distance of the Earth+Moon barycentre from the Sun. This distance corresponds to 1 Astronomical Unit (AU). τ is defined as $T/2\pi$, where T is the orbital period[2], and v is the Earth+Moon barycentre's mean velocity of a circular orbit around the Sun. Since l, τ and v are constants, it is possible to normalise the dimensional coordinates ($\boldsymbol{r}_d$ [km] and $\dot{\boldsymbol{r}}_d$ [km s^{-1}]) and write them as dimensionless coordinates ($\boldsymbol{r}$ [ ] and $\dot{\boldsymbol{r}}$ [ ]). The normalisation parameters are reported in Table 3.1.

$\boldsymbol{l}$ **[km]**	$\boldsymbol{\tau}$ **[s]**	$\boldsymbol{v}$ **[km s^{-1}]**
1 AU	$\sqrt{\frac{l^3}{(\mu_{Sun}+\mu_{Earth})}}$	$\frac{l}{\tau} = \sqrt{\frac{(\mu_{Sun}+\mu_{Earth})}{l}}$

Table 3.1: Normalisation parameters. Note that μ_{Earth} includes the mass of the Moon.

The normalised coordinates are written as follow:

$$\begin{cases} \boldsymbol{r} = \boldsymbol{r}_d/l \\ \dot{\boldsymbol{r}} = \dot{\boldsymbol{r}}_d/v \end{cases} . \tag{3.1}$$

The transformation of the state vector from the synodic system in dimensionless coordinates ($\boldsymbol{x} = \{\boldsymbol{r}, \dot{\boldsymbol{r}}\}^T$) to the sidereal system in dimensionless coordinate ($\boldsymbol{x}_i = \{\boldsymbol{r}_i, \dot{\boldsymbol{r}}_i\}^T$) requires the definition of the direction cosine matrix between the two systems. $\mathbf{C}_{ri}(t)$ is the direction cosine matrix between the rotating frame, $\mathscr{F}_r$, and the inertial frame, $\mathscr{F}_i$, which are related as:

$$\mathscr{F}_r = \mathbf{C}_{ri}(t)\mathscr{F}_i. \tag{3.2}$$

In Eq. (3.2), the direction cosine matrix is defined as follow:

$$\boldsymbol{C}_{ri}(t) = \begin{bmatrix} \cos\omega t & \sin\omega t & 0 \\ -\sin\omega t & \cos\omega t & 0 \\ 0 & 0 & 1 \end{bmatrix}, \tag{3.3}$$

where, ω is the angular velocity of the rotating system. Therefore, the transformation of position components between the $\mathscr{F}_r$ and the $\mathscr{F}_i$ is:

$$\boldsymbol{r}_i = \mathbf{C}_{ri}^T \boldsymbol{r}; \tag{3.4}$$

[2]The orbital period T is defined as $2\pi \cdot \sqrt{\frac{l^3}{(\mu_{Sun}+\mu_{Earth})}}$.

while, the transformation of velocity components between the $\mathscr{F}_r$ and the $\mathscr{F}_i$ is given by deriving Eq. (3.4) as follow:

$$\dot{\boldsymbol{r}}_i = \dot{\mathbf{C}}_{ri}^T \boldsymbol{r} + \mathbf{C}_{ri}^T \dot{\boldsymbol{r}}. \tag{3.5}$$

In Eq. (3.5), $\dot{\mathbf{C}}_{ri}^T(t)$ is given by:

$$\dot{\mathbf{C}}_{ri}^T = -\mathbf{C}_{ri}^T [\boldsymbol{\omega}_{ri}]_\times^T, \tag{3.6}$$

and, $\dot{\mathbf{C}}_{ri}^T(t)$ is function of the matrix $[\boldsymbol{\omega}_{ri}]_\times$. Considering the definition of the angular velocity vector, $\boldsymbol{\omega}_{ri}$:

$$\boldsymbol{\omega}_{ri} = \left\{ \begin{array}{c} 0 \\ 0 \\ \omega_z \end{array} \right\} = \left\{ \begin{array}{c} 0 \\ 0 \\ n \end{array} \right\}, \tag{3.7}$$

the matrix associated to the $\boldsymbol{\omega}_{ri}$ cross product operator, $[\boldsymbol{\omega}_{ri}]_\times$, is derived such as:

$$[\boldsymbol{\omega}_{ri}]_\times = \left[\begin{array}{ccc} 0 & -\omega & 0 \\ \omega & 0 & 0 \\ 0 & 0 & 0 \end{array} \right], \tag{3.8}$$

where, n is the mean motion angular velocity of the Sun and Earth+Moon around their barycenter[3]. The velocity transformation from the synodic to the sidereal reference frames assumes the form of:

$$\dot{\boldsymbol{r}}_i = -\left[\begin{array}{ccc} \cos nt & -\sin nt & 0 \\ \sin nt & \cos nt & 0 \\ 0 & 0 & 1 \end{array} \right] \left[\begin{array}{ccc} 0 & n & 0 \\ -n & 0 & 0 \\ 0 & 0 & 0 \end{array} \right] \boldsymbol{r} + \left[\begin{array}{ccc} \cos nt & -\sin nt & 0 \\ \sin nt & \cos nt & 0 \\ 0 & 0 & 1 \end{array} \right] \dot{\boldsymbol{r}}. \tag{3.9}$$

The derivation of Eq. (3.9) can be found in Appendix C.1, (Peter, 2004). In case of dimensionless coordinates, the equations above still hold by simply imposing that the mean motion n is equal to 1.

3.1.2 Conversion of dimensionless coordinates from a sidereal to a synodic reference system

In this section, the inverse conversion is shown in both spacecraft's position

$$\boldsymbol{r} = \mathbf{C}_{ri} \boldsymbol{r}_i, \tag{3.10}$$

and velocity

$$\dot{\boldsymbol{r}} = \dot{\mathbf{C}}_{ri} \boldsymbol{r}_i + \mathbf{C}_{ri} \dot{\boldsymbol{r}}_i. \tag{3.11}$$

[3]The mean motion n is defined as $\frac{2\pi}{T}$.

The derivative of the direction cosine matrix ($\dot{\mathbf{C}}_{ri}$) is written as:

$$\dot{\mathbf{C}}_{ri} = -[\boldsymbol{\omega}_{ri}]_{\times}\mathbf{C}_{ri}; \tag{3.12}$$

thus, the spacecraft's velocity full expression turns into:

$$\dot{\boldsymbol{r}} = -\begin{bmatrix} 0 & -n & 0 \\ n & 0 & 0 \\ 0 & 0 & 0 \end{bmatrix}\begin{bmatrix} \cos nt & \sin nt & 0 \\ -\sin nt & \cos nt & 0 \\ 0 & 0 & 1 \end{bmatrix}\boldsymbol{r}_i + \begin{bmatrix} \cos nt & \sin nt & 0 \\ -\sin nt & \cos nt & 0 \\ 0 & 0 & 1 \end{bmatrix}\dot{\boldsymbol{r}}_i. \tag{3.13}$$

3.2 Definition of the normal vector, $\hat{\boldsymbol{N}}$

The normal vector, $\hat{\boldsymbol{N}}$, to the reflective surface is a function of the spacecraft's orientation with the Sun-line direction. In the literature, two choices of the angles exist and they are both used in this thesis as they have advantages depending on the application.

3.2.1 In-plane and out-of-plane angles

In Figure 3.2, the in-plane and out-of-plane angles of the normal vector, $\hat{\boldsymbol{N}}$, are shown and $\hat{\boldsymbol{N}}$ is defined as:

$$\hat{\boldsymbol{N}} = \begin{Bmatrix} \cos(\Phi+\alpha)\cdot\cos(\Psi+\delta) \\ \sin(\Phi+\alpha)\cdot\cos(\Psi+\delta) \\ \sin(\Psi+\delta) \end{Bmatrix}, \tag{3.14}$$

where, the angles Φ in Figure 3.2(a) and Ψ in Figure 3.2(b) describe the spacecraft-Sun vector with respect to the rotating system $\{x,\ y,\ z\}$. Figure 3.2 shows a 3D view of the reference frame where α (in-plane angle in Figure 3.2(a)) and δ (out-of-plane angle in Figure 3.2(b)) are the angles between the spacecraft-Sun vector and $\hat{\boldsymbol{N}}$ projections to the x-y plane and y-z plane, respectively. They can assume values between $-\pi/2$ and $\pi/2$ (Farrés and Jorba, 2008; Biggs et al., 2008). This formulation has the advantage of being relatively simple to understand from a geometrical point of view. However, the scalar product between the spacecraft-Sun vector, $\hat{\boldsymbol{r}}$, and the normal vector, $\hat{\boldsymbol{N}}$, to the reflective surface has a complicated expression which is:

$$\left\langle \hat{\boldsymbol{N}}\cdot\hat{\boldsymbol{r}} \right\rangle = \frac{(z^2+(y^2+(x+\mu)^2)\cos(\alpha))\cos(\delta) - z\cdot\boldsymbol{r}_{xy,Sun-p}(\cos(\alpha)-1)\sin(\alpha)}{(x+\mu)^2+y^2+z^2}. \tag{3.15}$$

The condition of Sun-pointing is reached when the scalar product in Eq. (3.15) is equal to zero. For a spacecraft motion constrained in the x-y plane (when Ψ and δ are zero), the Sun-pointing condition is reached for α equal to zero, as in this particular case, α is the angle between the Sun-line direction and the normal vector.

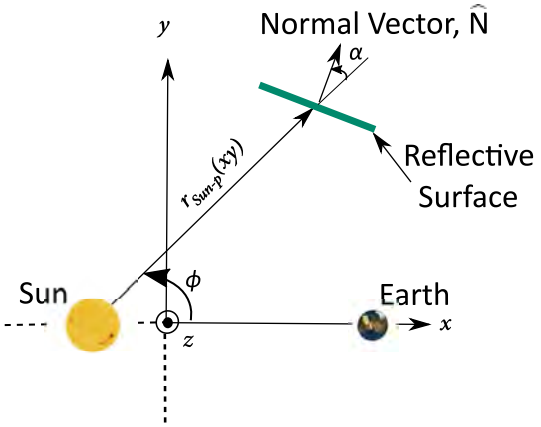

(a) In-plane angle, α.

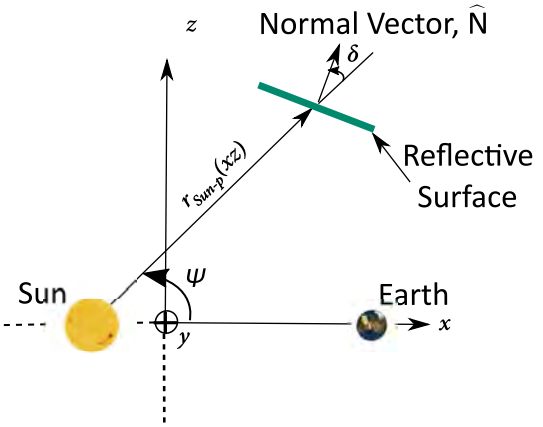

(b) Out-of-plane, δ.

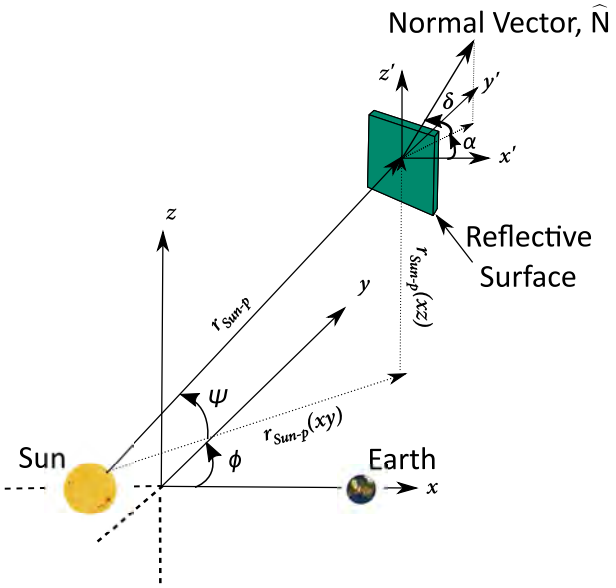

(c) 3D view of the in-plane angle, α and the out-of-plane angle, δ.

Figure 3.2: Definition of α, Ψ, δ and Φ angles.

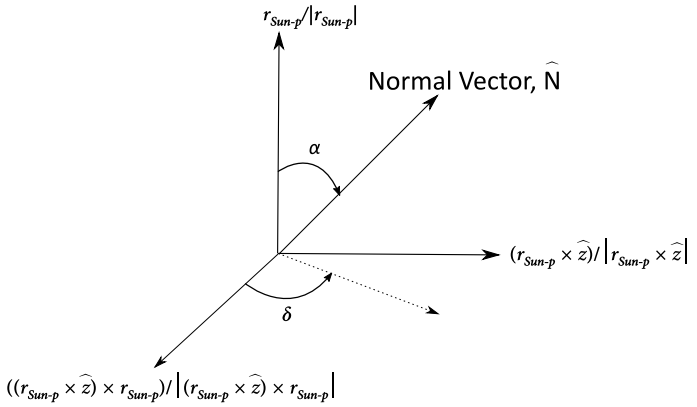

Figure 3.3: Definition of the cone angle, α, and the clock angle, δ.

3.2.2 Cone and clock angles

In Figure 3.3, the reference frame selected for the definition of the cone and the clock angles is defined as follow:

1) The third axis corresponds to the unitary vector of the spacecraft-Sun line, $\frac{\boldsymbol{r}_{Sun-p}}{|\boldsymbol{r}_{Sun-p}|}$,
2) The second axis is chosen perpendicular to the plane defined by the unitary vector of the spacecraft-Sun line, $\frac{\boldsymbol{r}_{Sun-p}}{|\boldsymbol{r}_{Sun-p}|}$, and the unitary vector of the synodic reference frame's z-axis, $\hat{z}$. Thus, the second axis is given by $\frac{\boldsymbol{r}_{Sun-p}\times\hat{z}}{|\boldsymbol{r}_{Sun-p}\times\hat{z}|}$, and
3) The first axis is derived from the former axes flowing a right-handed coordinate system definition such as $\frac{(\boldsymbol{r}_{Sun-p}\times\hat{z})\times\boldsymbol{r}_{Sun-p}}{|(\boldsymbol{r}_{Sun-p}\times\hat{z})\times\boldsymbol{r}_{Sun-p}|}$.

The cone and clock angles are defined with respect to the Sun-line direction, so they have an advantage when describing the attitude of the sail with respect to the Sun. The cone angle, α, is the angle between the Sun-line direction, $\hat{\boldsymbol{r}}$, and the normal vector to the reflective surface, $\hat{\boldsymbol{N}}$, Figure 3.3. The clock angle, δ, is defined as in Figure 3.3 (McInnes, 1999, 2000). The SRP acceleration in the synodic system is given by Eq. (3.25).

In case of the cone and the clock angles, $\left\langle \hat{\boldsymbol{r}} \cdot \hat{\boldsymbol{N}} \right\rangle$ is equal to $\cos\alpha$, where $\hat{\boldsymbol{r}}$ is defined as:

$$\hat{\boldsymbol{r}} = \frac{\boldsymbol{r}_{Sun-p}}{|\boldsymbol{r}_{Sun-p}|}. \tag{3.16}$$

Thus, the full expression of $\hat{\boldsymbol{N}}$ is:

$$\hat{\boldsymbol{N}} = \cos\alpha\frac{\boldsymbol{r}_{Sun-p}}{|\boldsymbol{r}_{Sun-p}|} + \sin\alpha\cos\delta\frac{(\boldsymbol{r}_{Sun-p}\times\hat{z})\times\boldsymbol{r}_{Sun-p}}{|(\boldsymbol{r}_{Sun-p}\times\hat{z})\times\boldsymbol{r}_{Sun-p}|} + \sin\alpha\sin\delta\frac{\boldsymbol{r}_{Sun-p}\times\hat{z}}{|\boldsymbol{r}_{Sun-p}\times\hat{z}|}. \tag{3.17}$$

Further details of Eq. (3.17) are given in Appendix C.4. The definition of the normal vector as in Eq. (3.17) is more complicated than the one shown in Eq. (3.14). However, this formulation has a simpler definition of the scalar product $\left\langle \hat{\boldsymbol{r}} \cdot \hat{\boldsymbol{N}} \right\rangle$. Thus, the Sun-pointing condition is achieved when $\alpha = 0°$.

3.3 Modelling the solar radiation effect

In libration point orbit applications, solar radiation pressure is an important figure and it is one of the largest non-gravitational environmental perturbation that affects the orbital dynamics of LPO's satellite as for space telescopes like Herschel. When those

telescopes are close to their end-of-life, a precise SRP model is needed for predicting their uncontrolled attitude and orbit evolution. In this thesis, as the SRP is enhanced to achieve low energy manoeuvres, the effect of the SRP on the spacecraft motion needs to be defined. The cannonball model is adopted as mentioned in Section 2.3.

In the general case, the SRP is a non-conservative perturbation. The most difficult aspect when modelling SRP is in the prediction of the solar cycles. The solar pressure at 1 AU, $P_{srp-1AU}$, is derived from the Einstein's law that relates energy with mass, and it is measured at Earth's distance from the Sun (1 AU) as:

$$P_{srp-1AU} = \frac{SF}{c} = \frac{1367\ W/m^2}{3 \cdot 10^8\ m/s} = 4.57 \cdot 10^{-6}\ \frac{N}{m^2}. \tag{3.18}$$

In Eq. (3.18), SF is the solar flux and c is the speed of light. Note that a more precise model on the SF (Wertz, 1999) exists, where instead of a constant value, the SF is modelled as a function of the time and it takes into account of yearly variations (Vallado, 2004). To determine the solar radiation pressure at any distance, the solar radiation pressure at 1 AU, $P_{srp-1AU}$, can be rescaled to the inverse square of the spacecraft-Sun distance, r_{Sun-p}, as:

$$P_{srp} = P_{srp-1AU} \left(\frac{r_{Earth-Sun}}{r_{Sun-p}} \right)^2. \tag{3.19}$$

Clearly, the magnitude of SRP drastically decreases for space missions to the outer planets, which limits the use of SRP for those applications. The SRP acceleration, a^s, is a function of the reflectivity coefficient, c_R, the radiation pressure, P_{srp}, the projected area exposed to the Sun, A_{Sun} and the spacecraft's mass, m:

$$a^s = P_{srp} \frac{A_{Sun}}{m} c_R. \tag{3.20}$$

In Eq. (3.20), the reflectivity coefficient, c_R, can vary between 0 and 2, and indicates how the satellite reflects the Sun's radiation. A value of 0 indicates that the surface is translucent, hence there is no SRP force produced, but maybe some refraction. A value of 1 means that the radiation is completely absorbed (i.e., a black body). A c_R equal to 2 means that the spacecraft surface is reflective (i.e., a flat mirror perpendicular to the Sun-line direction) (McInnes, 1999). c_R is a function of the reflective surface orientation, and for the cannonball model is:

$$c_R = \left\{ \left(2\rho_s \left\langle \hat{\boldsymbol{N}} \cdot \hat{\boldsymbol{s}} \right\rangle + \frac{2}{3}\rho_d \right) \hat{\boldsymbol{N}} + (\rho_a + \rho_d)\, \hat{\boldsymbol{s}} \right\}. \tag{3.21}$$

In Eq. (3.21), ρ_s is the specular reflection, ρ_a is the absorbed reflection, ρ_d is the diffusive reflection, $\hat{\boldsymbol{s}}$ is the Sun-line direction, where $\rho_s + \rho_a + \rho_d = 1$ and $\hat{\boldsymbol{N}}$ is the normal to the reflective surface. The relationship between $\hat{\boldsymbol{N}}$ and the spacecraft's orientation angles was shown in Section 3.2.

In Figure 3.4, the value of the reflectivity coefficient is shown for a reflectance, abortion and diffusion surfaces as a function of the orientation angle; below 40°, a reflective surface provides higher SRP acceleration than a near perfect diffusion surface. Conversely, if the orientation angle is above 40°, a diffusive surface is desirable rather than a near perfect reflective surface. This might suggest the exploitation of different reflective properties when designing a re-orientable deployable reflective device for enhancing the effects of SRP. Moreover, the projected area, A_{Sun}, illuminated by the Sun is a function of the actual area, and the surface orientation so that $A_{Sun} = A\left\langle \hat{\boldsymbol{N}} \cdot \hat{\boldsymbol{s}} \right\rangle$. However, for applications at LPOs, the Sun-line corresponds to the spacecraft-Sun distance, $\hat{\boldsymbol{s}} = \hat{\boldsymbol{r}}$, therefore, Eq. (3.20) turns into:

$$\boldsymbol{a}^s = P_{srp}\frac{A}{m}\left\langle \hat{\boldsymbol{N}} \cdot \hat{\boldsymbol{r}} \right\rangle \left\{ \left(2\rho_s \left\langle \hat{\boldsymbol{N}} \cdot \hat{\boldsymbol{r}} \right\rangle + \frac{2}{3}\rho_d \right) \hat{\boldsymbol{N}} + \left(\rho_a + \rho_d\right) \hat{\boldsymbol{r}} \right\}. \tag{3.22}$$

When using SRP for spacecraft trajectory design, it is convenient to introduce a structural parameter that is function of the area-to-mass ratio (A/m in Eq. (3.22)) and the Sun's luminosity, $\sigma^* = \frac{L_{Sun}}{2\pi c \mu_{Sun}}$. This parameter is known as the lightness parameter, β, and is defined as:

$$\beta = \frac{\sigma^*}{\sigma}, \tag{3.23}$$

where, σ is the sail load i.e. the mass-to-area ratio (m/A). The lightness number is the ratio between the solar radiation pressure acceleration and the solar gravitational acceleration. It describes the performance of reflective deployable structures. β can vary between 0 and 1. When β increases, the SRP counteracts the gravitational force of the Sun, so the dynamical system resemble an equivalent R3BP with a smaller attractor (i.e. a "lighter" Sun). For $\beta = 0$, the CR3BP-SRP turns into the case without the effect of SRP (CR3BP). The case of $\beta = 1$ is an ideal case when the acceleration of SRP compensates the Sun's gravity acceleration. Thus, the CR3BP-SRP turns into the case of the Kepler problem, where only the gravitation of the Earth+Moon barycentre is taken into account.

It is convenient to express Eq. (3.22) as a function of β. Thus, the first step is to write P_{srp} as a function of the SF by substituting Eq. (3.18) into Eq. (3.19) such as:

$$P_{srp} = \frac{SF}{c}\left(\frac{r_{Earth-Sun}}{r_{Sun-p}}\right)^2. \tag{3.24}$$

By expressing, SF as function of the Sun luminosity, L_{Sun}, Eq. (3.22) turns into:

$$\boldsymbol{a}^s = \beta\frac{\mu_{Sun}}{r_{Sun-p}^2}\left\langle \hat{\boldsymbol{N}} \cdot \hat{\boldsymbol{r}} \right\rangle^2 \hat{\boldsymbol{N}}. \tag{3.25}$$

For further details in the derivations see Appendix C.3.

For a Sun-pointing reflective surface (when $\hat{\boldsymbol{r}} = \hat{\boldsymbol{N}}$), the acceleration of SRP can be expressed as the potential energy of the SRP forces as:

$$U^s = \beta \frac{\mu_{Sun}}{r_{Sun-p}}. \tag{3.26}$$

From Eq. (3.26) the acceleration due to SRP can be derived as:

$$\boldsymbol{a}^s = \nabla U^s \hat{\boldsymbol{r}} = \beta \frac{\mu_{Sun}}{r^2_{Sun-p}} \hat{\boldsymbol{r}}. \tag{3.27}$$

This is a special case where the system is conservative since the SRP acceleration acts as a radial force (even if it is a non-gravitational force); therefore, it can be included in the potential expression of the generalised system of forces. When $\hat{\boldsymbol{r}} \neq \hat{\boldsymbol{N}}$, instead the SRP cannot be written as a potential.

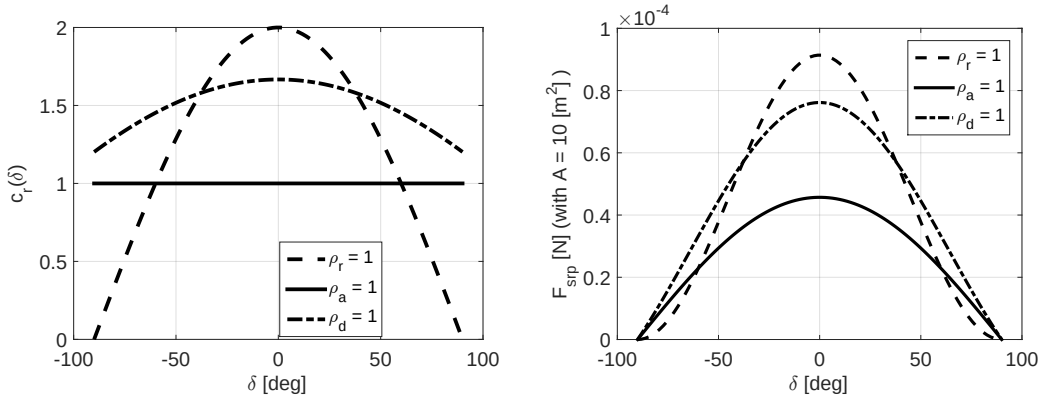

(a) Reflectivity coefficient.

(b) SRP force for a 10 m^2 reflective area.

Figure 3.4: Surface reflectance ρ_r, absorption ρ_a and diffusion ρ_d as a function of the orientation angle (McInnes, 1999).

For a non near-perfect reflective structure, it is convenient to write β as a function of c_R. In this case, the acceleration of solar radiation pressure is Eq. (3.22) and it is simplified into:

$$\boldsymbol{a}^s = P_{srp} \frac{A}{m} \left\langle \hat{\boldsymbol{N}} \cdot \hat{\boldsymbol{r}} \right\rangle \; c_R \hat{\boldsymbol{N}}, \tag{3.28}$$

where for the Sun-pointing case $\hat{\boldsymbol{r}} = \hat{\boldsymbol{N}}$. Eq. (3.28) turns into:

$$\boldsymbol{a}^s = P_{srp-1AU} \left(\frac{r_{Earth-Sun}}{r_{Sun-p}} \right)^2 \frac{A}{m} c_R \hat{\boldsymbol{r}}. \tag{3.29}$$

Eq. (3.25) represents the SRP acceleration to be included in the equations of motion of Eq. (3.39). To express β as a function of c_R, Eq. (3.29) is derived similarly to Eq. (3.27), and the lightness parameter is then defined such as:

$$\beta = P_{srp-1AU} \frac{r^2_{Earth-Sun}}{\mu_{Sun}} \frac{A}{m} c_R. \tag{3.30}$$

3.4 Equations of motion of the circular restricted three-body problem with solar radiation pressure

In the CR3BP the non-linear equations of motion are derived in the inertial (sidereal) and rotating (synodic) frames; then, a change of coordinate is performed from dimensional to dimensionless variables through the transformation presented in Section 3.1.1 in Eq. (3.1) (Szebehely, 1967; Koon et al., 2008). The equations of motion in the synodic reference frame are derived through the Lagrangian and the Hamiltonian approach that is dealt with in Section 3.4.2 and Section 3.4.3 respectively (Koon et al., 2008).

3.4.1 Equations of motion in the sidereal system

The equations of motion of the CR3BP in the sidereal frame, $\mathscr{F}_i$, are given by the Newton's Law of Gravity as:

$$\begin{cases} m\ddot{x}_i = V_{x_i} \\ m\ddot{y}_i = V_{y_i} \\ m\ddot{z}_i = V_{z_i} \end{cases}, \tag{3.31}$$

where V_{x_i}, V_{y_i} and V_{z_i} are the partial derivatives in the x, y and z of the gravity potential, V, in the inertial frame and m is the spacecraft's mass. In Eq. (3.31), V is the mutual gravitational potential function and it is defined as:

$$V = \frac{\mu_{Sun}}{R_{Sun-p}} m + \frac{\mu_{Earth}}{R_{Earth-p}} m, \tag{3.32}$$

where, μ_{Sun} and μ_{Earth} are the Sun and the Earth+Moon barycentre gravitational parameters[4]. R_{Sun-p} and $R_{Earth-p}$ are the distances of the Sun and the Earth from the spacecraft in the $\mathscr{F}_i$ frame and are given by:

$$R_{Sun-p} = \sqrt{(x_i - x_{i_{Sun}})^2 + (y_i - y_{i_{Sun}})^2 + (z_i - z_{i_{Sun}})^2} \tag{3.33}$$

and

$$R_{Earth-p} = \sqrt{(x_i - x_{i_{Earth}})^2 + (y_i - y_{i_{Earth}})^2 + (z_i - z_{i_{Earth}})^2}. \tag{3.34}$$

Since the position of the Sun and the Earth are well known in the rotating frame as $\boldsymbol{r}_{Sun} = \{-d_{Sun}, 0, 0\}$ and $\boldsymbol{r}_{Earth} = \{d_{Earth}, 0, 0\}$, it is possible to find their expression by using the rotational direction cosine matrix $\boldsymbol{C}_{ir}(t)$ as shown in Section 3.1.1. The Sun's

[4] $\mu_{Sun} = G \cdot m_{Sun}$ and $\mu_{Earth} = G \cdot (m_{Earth} + m_{Moon})$, where G is the universal gravitational constant and m_{Sun} and m_{Earth} are the masses of the Sun and the Earth+Moon barycentre, respectively.

and the Earth+Moon barycentre's positions are then:

$$\boldsymbol{R}_{Sun} = \left\{ \begin{array}{c} -d_{Sun}\cos(nt) \\ -d_{Sun}\sin(nt) \\ 0 \end{array} \right\}; \qquad \boldsymbol{R}_{Earth} = \left\{ \begin{array}{c} d_{Earth}\cos(nt) \\ d_{Earth}\sin(nt) \\ 0 \end{array} \right\}. \tag{3.35}$$

The equations of motion in the sidereal frame for the dimensional coordinates are then:

$$\left\{ \begin{array}{l} \ddot{x}_i = -\frac{\mu_{Sun}(x_i - x_{i_{Sun}})}{R^3_{Sun-p}} - \frac{\mu_{Earth}(x_i - x_{i_{Earth}})}{R^3_{Earth-p}} \\ \ddot{y}_i = -\frac{\mu_{Sun}(y_i - y_{i_{Sun}})}{R^3_{Sun-p}} - \frac{\mu_{Earth}(y_i - y_{i_{Earth}})}{R^3_{Earth-p}} \\ \ddot{z}_i = -\frac{\mu_{Sun}(z - i - z_{i_{Sun}})}{R^3_{Sun-p}} - \frac{\mu_{Earth}(z_i - z_{i_{Earth}})}{R^3_{Earth-p}} \end{array} \right. . \tag{3.36}$$

Substituting Eq. (3.35) into Eq. (3.36), becomes:

$$\left\{ \begin{array}{l} \ddot{x}_i = -\frac{\mu_{Sun}(x_i + d_{Sun}\cos(nt))}{R^3_{Sun-p}} - \frac{\mu_{Earth}(x_i - d_{Earth}\cos(nt))}{R^3_{Earth-p}} \\ \ddot{y}_i = -\frac{\mu_{Sun}(y_i + d_{Sun}\sin(nt))}{R^3_{Sun-p}} - \frac{\mu_{Earth}(y_i - d_{Earth}\sin(nt))}{R^3_{Earth-p}} \\ \ddot{z}_i = -\frac{\mu_{Sun} z_i}{R^3_{Sun-p}} - \frac{\mu_{Earth} z_i}{R^3_{Earth-p}} \end{array} \right. . \tag{3.37}$$

Finally, $l = d_{Sun} + d_{Earth}$ is the Sun-Earth distance which corresponds to 1 AU for the Sun-(Earth+Moon) system. $M = m_{Sun} + m_{Earth}$ is the total mass of the Sun and the Earth+Moon barycentre and $t^* = nt$ is the dimensionless time. Note that the mean motion n is defined as $2\pi/T$ which correspond to τ^{-1} and $t^* = \tau^{-1}t$. The author will hereafter refer to dimensionless time as t instead of t^* to have a simpler notation. $\mu_{Sun} = m_{Sun}/M = d_{Earth}/l$ and $\mu_{Earth} = m_{Earth}/M = d_{Sun}/l$ are the only remaining constants of the system. Moreover, the relation between μ_{Sun} and μ_{Earth} is $\mu_{Sun} + \mu_{Earth} = 1$, if dimensionless coordinates are used. This means that it is possible to define $\mu_{Sun} = 1 - \mu_{Earth}$; indeed, the system is a function of one constant only. By defining, $\mu_{Earth} = \mu$ and $\mu_{Sun} = 1 - \mu$ it is possible to determine one mass as a function of the other. Finally, the dimensionless distances of the spacecraft, m, from the Sun and the Earth are defined as $r_{Sun-p} = R_{Sun-p}/l$ and $r_{Earth-p} = R_{Earth-p}/l$ respectively. The dimensional rectangular coordinates in an inertial frame are, instead, defined as $x = x_i/l$, $y = y_i/l$ and $z = z_i/l$. The equations of motion in the dimensionless coordinates are then:

$$\left\{ \begin{array}{l} \ddot{x} = -\frac{\mu_{Sun}(x + \mu_{Sun}\cos t)}{r^3_{Sun-p}} - \frac{\mu_{Earth}(x - \mu_{Earth}\cos t)}{r^3_{Earth-p}} \\ \ddot{y} = -\frac{\mu_{Sun}(y + \mu_{Sun}\sin t)}{r^3_{Sun-p}} - \frac{\mu_{Earth}(y - \mu_{Earth}\sin t)}{r^3_{Earth-p}} \\ \ddot{z} = -\frac{\mu_{Sun} z}{r^3_{Sun-p}} - \frac{\mu_{Earth} z}{r^3_{Earth-p}} \end{array} \right. . \tag{3.38}$$

System	**Reference**	$\boldsymbol{\mu}$	$\boldsymbol{e}$
Earth+Moon	Campagnola et al. (2008)	0.0123	0.054
Double Stars	Luk'yanov (2005)	0.3	$0.2 - 0.9$
Sun-(Earth+Moon)	Stramacchia et al. (2016)	$3.04042 \cdot 10^{-6}$	0.01674
Sun-Jupiter	Stramacchia et al. (2016)	$9.53 \cdot 10^{-4}$	0.0489
Sun-Mars	Stramacchia et al. (2016)	$3.2268 \cdot 10^{-7}$	0.0935
Jupiter-Io	Stramacchia et al. (2016)	$4.704 \cdot 10^{-5}$	0.0041

Table 3.2: Mass parameter, μ, and eccentricity, e, for different systems.

3.4.2 Synodic equations of motion: Lagrangian approach

In this section, the equations of motion are written with respect to a synodic (rotating) reference frame in dimensionless coordinates as presented in Eq. (3.1). The advantage of having a rotating system is to loose the dependence on time, t, in the equations of motion. Having considered the dimensionless coordinates, the equations of motion are now depending only on one parameter: the mass parameter, μ. The selected applications refer to the Sun-(Earth+Moon) system, where the primaries distance, l, is $1.496 \cdot 10^8$ km (1 AU), their velocity, v, corresponds to 29.784 km/s, and the orbital period, T, is $3.147 \cdot 10^7$ s. The mass parameter, μ, is $3.04042 \cdot 10^{-6}$ in dimensionless units. The phase space of the system is highly dependent on μ, which can vary between 0 and 0.5, depending on the selected celestial bodies (Koon et al., 2008). Table 3.2 shows different examples of mass parameters, μ, and orbit eccentricity [5], e, for different systems.

The equations of motion of the CR3BP-SRP in Lagrangian dimensionless coordinates are shown in Eq. (3.39), and derived in Appendix C.2 (Koon et al., 2008):

$$\begin{cases} \ddot{x} - 2\omega\dot{y} = V_x + a_x^s \\ \ddot{y} + 2\omega\dot{x} = V_y + a_y^s \\ \ddot{z} = V_z + a_z^s \end{cases} \tag{3.39}$$

where, x, y, z and $\dot{x}$, $\dot{y}$, $\dot{z}$ are the spacecraft positions and velocities in the synodic (rotating) frame and, a_x^s, a_y^s and a_z^s are the components along x-, y- and z-axis of the solar radiation pressure acceleration, $\boldsymbol{a}^s$. V is the total potential,

$$V = V_r + V_g, \tag{3.40}$$

which includes the contribution of the rotating system potential, V_r, and the gravitational potential, V_g. The rotating potential is:

$$V_r = \frac{1}{2}(x^2 + y^2) \tag{3.41}$$

[5]For the CR3BP, the approximation made is that the two primaries are in a circular orbit thus with eccentricity equal to zero. However, Table 3.2 shows the real values in eccentricity for different systems.

and the gravitational potential is:

$$V_g = \frac{\mu_{Sun}}{r_{Sun-p}} + \frac{\mu_{Earth}}{r_{Earth-p}}. \tag{3.42}$$

In Eq. (3.42), r_{Sun-p} and $r_{Earth-p}$ are the spacecraft's distance from the Sun and the Earth respectively as shown in Figure 3.1(b) and defined as:

$$r_{Sun-p} = \sqrt{(x - x_{Sun})^2 + y^2 + z^2} \tag{3.43}$$

and

$$r_{Earth-p} = \sqrt{(x - x_{Earth})^2 + y^2 + z^2}. \tag{3.44}$$

In non-dimensional coordinates, $x_{Sun} = -\mu$ is the position of the Sun and $x_{Earth} = 1-\mu$ is the position of the Earth. Thus, Eq. (3.39) turns into:

$$\begin{cases} \ddot{x} = 2\dot{y} + x - \frac{(1-\mu)(x-x_{Sun})}{r^3_{Sun-p}} - \frac{\mu(x-x_{earth})}{r^3_{Earth-p}} + a^s_x \\ \ddot{y} = -2\dot{x} + y - \frac{(1-\mu)}{r^3_{Sun-p}} y - \frac{\mu}{r^3_{Earth-p}} y + a^s_y \\ \ddot{z} = z - \frac{(1-\mu)}{r^3_{Sun-p}} z - \frac{\mu}{r^3_{Earth-p}} z + a^s_z \end{cases} . \tag{3.45}$$

In the synodic frame the Lagrangian, $\mathscr{L}$, is given by the relative kinetic energy minus the potential energy as:

$$\mathscr{L} = \frac{1}{2}\left((\dot{x} - y)^2 + (\dot{y} + x)^2 + \dot{z}^2\right) - U, \tag{3.46}$$

where, in the Lagrangian, $\mathscr{L}$, U is the potential energy of the conservative forces (i.e., solar radiation pressure)[6] and it can be derived from the potential function V through a change of its sign such that $U = -V$. The potential energy, V, is defined as in Eq. (3.42). Eq. (3.39), can be alternatively derived by using the Lagrangian approach as follow (Biscari et al., 2005):

$$\frac{d}{dt}\frac{\partial \mathscr{L}}{\partial \dot{q}_k} - \frac{\partial \mathscr{L}}{\partial q_k} = Q^{n.c}_k. \tag{3.47}$$

In Eq. (3.47), $Q^{n.c}_k$ indicates the Lagrangian components of the non conservative force. $Q^{n.c}_k$ is zero for $a^s_x = a^s_y = a^s_z = 0$ or when SRP acts as a conservative force and is included in the Lagrangian, $\mathscr{L}$ (i.e., spacecraft's Sun-pointing). Note that the same nomenclatures in the spacecraft's state vector for both the dimensionless coordinates in the inertial system, Eq. (3.38), and rotating system, Eq. (3.39), is used to avoid a complex definition of the variables.

[6] The forces are conservative when the SRP acceleration is zero or for a deployable reflective structure is at 90° with respect to the Sun, i.e. SRP potential depends only on the position not on the velocity.

3.4.3 Synodic equations of motion: Hamiltonian approach

For $a_x^s = a_y^s = a_z^s = 0$, the Hamiltonian form of the equations of motion can be derived from the Lagrangian, $\mathscr{L}$, through the Legendre transformation (Koon et al., 2008). In the Lagrangian approach the state vector is $\{x, y, z, \dot{x}, \dot{y}, \dot{z}\}$; where as in the Hamiltonian approach the state vector is $\{x, y, z, p_x, p_y, p_z\}$. p_x, p_y and p_z are the momenta conjugate to x, y and z, defined as:

$$\begin{aligned} p_x &= \frac{\partial \mathscr{L}}{\partial \dot{x}} = \dot{x} - y \\ p_y &= \frac{\partial \mathscr{L}}{\partial \dot{y}} = \dot{y} + x \\ p_z &= \frac{\partial \mathscr{L}}{\partial \dot{z}} = \dot{z} \end{aligned} . \tag{3.48}$$

In the rotating frame, the Hamiltonian, $\mathscr{H}$, can be expressed as:

$$\mathscr{H} = p_x\dot{x} + p_y\dot{y} + p_z\dot{z} - \mathscr{L}. \tag{3.49}$$

From Eq. (3.49), the Hamiltonian equations can be derived as:

$$\begin{aligned} \dot{x} &= \frac{\partial \mathscr{H}}{\partial p_x} = p_x + y \\ \dot{y} &= \frac{\partial \mathscr{H}}{\partial p_y} = p_y - x \\ \dot{z} &= \frac{\partial \mathscr{H}}{\partial p_z} = p_z \\ \dot{p}_x &= -\frac{\partial \mathscr{H}}{\partial x} = p_y - x + V_x \\ \dot{p}_y &= -\frac{\partial \mathscr{H}}{\partial y} = -p_x - y + V_y \\ \dot{p}_z &= -\frac{\partial \mathscr{H}}{\partial z} = V_z \end{aligned} . \tag{3.50}$$

By substituting the Lagrangian, $\mathscr{L}$, in Eq. (3.46) to the Hamiltonian, $\mathscr{H}$, in Eq. (3.49), the Hamiltonian turns into:

$$\mathscr{H} = p_x\dot{x} + p_y\dot{y} + p_z\dot{z} - \frac{1}{2}((\dot{x} - y)^2 + (\dot{y} + x)^2 + \dot{z}^2) - V_g. \tag{3.51}$$

From the first three equations in Eq. (3.50), $\dot{x} - y = p_x$, $\dot{y} + x = p_y$ and $\dot{z} = p_z$ can be substituted in the Hamiltonian in Eq. (3.51) to be rewritten as:

$$\mathscr{H} = p_x(p_x + y) + p_y(p_y - x) + p_z^2 - \frac{1}{2}(p_x^2 + p_y^2 + p_z^2) - V_g. \tag{3.52}$$

By collecting the conjugate momenta, Eq. (3.52) turns into:

$$\mathscr{H} = \frac{1}{2}((p_x + y)^2 + (p_y - x)^2 + p_z^2) - \frac{1}{2}(x^2 + y^2) - V_g, \tag{3.53}$$

where the conservative forces are collected in the total potential, V, as in Eq. (3.40):

$$\mathscr{H} = \frac{1}{2}((p_x + y)^2 + (p_y - x)^2 + p_z^2) - V. \tag{3.54}$$

By using the matrix notation, Eq. (3.50) becomes:

$$\begin{Bmatrix} \dot{x} \\ \dot{y} \\ \dot{z} \\ \dot{p}_x \\ \dot{p}_y \\ \dot{p}_z \end{Bmatrix} = \begin{bmatrix} 0 & 0 & 0 & 1 & 0 & 0 \\ 0 & 0 & 0 & 0 & 1 & 0 \\ 0 & 0 & 0 & 0 & 0 & 1 \\ -1 & 0 & 0 & 0 & 0 & 0 \\ 0 & -1 & 0 & 0 & 0 & 0 \\ 0 & 0 & -1 & 0 & 0 & 0 \end{bmatrix} \cdot \begin{Bmatrix} \frac{\partial \mathscr{H}}{\partial x} \\ \frac{\partial \mathscr{H}}{\partial y} \\ \frac{\partial \mathscr{H}}{\partial z} \\ \frac{\partial \mathscr{H}}{\partial p_x} \\ \frac{\partial \mathscr{H}}{\partial p_y} \\ \frac{\partial \mathscr{H}}{\partial p_z} \end{Bmatrix}, \tag{3.55}$$

that can be written in a compact way as:

$$\dot{\boldsymbol{X}} = \boldsymbol{Z} \nabla \mathscr{H}, \tag{3.56}$$

where, $\boldsymbol{Z}$ is the matrix of Eq. (3.55) and $\nabla \mathscr{H}$ is the gradient of the Hamiltonian, $\mathscr{H}$.

3.5 Libration points

In the CR3BP five equilibrium points exist as shown for the Sun-Earth system in Figure 1.1 of Chapter 2. The existence of the equilibrium points was proved by Lagrange in 1772 where the first evidence of their existence was observed in 1906 for the Trojan asteroids in the Sun-Jupiter system (Chapter 2). The equilibrium points are the zero velocity points in the rotating frame which correspond to stationary solutions on the equipotential surface. These points correspond to the positions in the rotating frame in which the gravitational forces and the centrifugal forces are all cancelled out.

When the effect of SRP is taken into account, the equilibrium points are shifted from their original position in the CR3BP. The equilibrium points now correspond to the position in the rotating system where the gravitational, the centrifugal and SRP forces are balanced. In this case, the libration points are called "artificial" or "pseudo" libration points (SL_i). The work in this thesis is focused on the design of space missions around the SL/L_1 and SL/L_2 collinear points. The points are located close to the Earth and are placed along the Sun-Earth line. L_1 is located between the Sun and the Earth; while, L_2 is beyond the Earth and cannot be seen from the Sun (as shown in Figure 3.5).

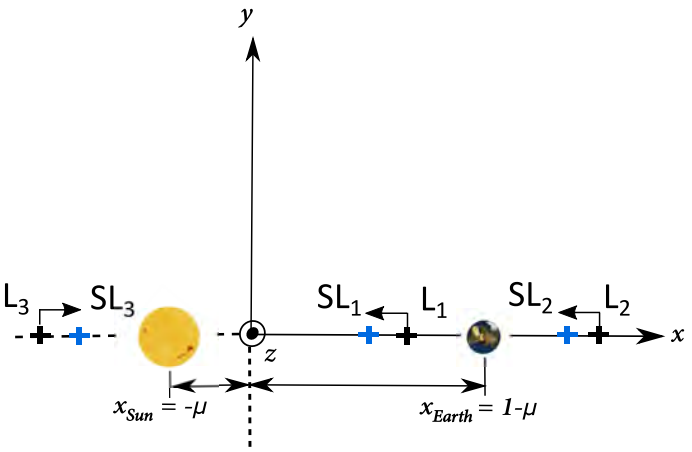

Figure 3.5: Position of the pseudo libration points, SL_i, for a Sun-pointing surface and position of the libration point, L_i, without the effect of SRP.

3.5.1 Collinear Lagrangian points for a Sun-pointing reflective structure

In the case of a Sun-pointing reflective deployable structure ($\hat{\boldsymbol{r}} = \hat{\boldsymbol{N}}$), the collinear librations points, $L_{1,2,3}$, are shifted along the $x-$axis of the rotating system as shown in Figure 3.5. Under this assumption, the SRP acceleration behaves as a potential force, Eq. (3.26); thus, it counteracts the effect of the Sun's gravitation. The larger the magnitude of the SRP acceleration, the closer the pseudo libration points get to the Sun. Given the equations of motion in Eq. (3.39), the equilibrium points for a Sun-pointing reflective structure are found by setting the velocities and the accelerations of Eq. (3.39) to zero. Moreover, by using Eq. (3.25) for the SRP acceleration, the equations of equilibrium are:

$$\begin{cases} V_x + U_x^s = x - \frac{(1-\beta)(1-\mu)(x-x_1)}{r_{Sun-p}^3} - \frac{\mu(x-x_2)}{r_{Earth-p}^3} = 0 \\ V_y + U_y^s = y - \frac{(1-\beta)(1-\mu)}{r_{Sun-p}^3} y - \frac{\mu}{r_{Earth-p}^3} y = 0 \\ V_z + U_z^s = -\frac{(1-\beta)(1-\mu)}{r_{Sun-p}^3} z - \frac{\mu}{r_{Earth-p}^3} z = 0 \end{cases} . \tag{3.57}$$

The position along the x-axis can be computed by solving:

$$x_{SL_i} - \frac{(1-\beta)(1-\mu)(x_{SL_i} - x_{Sun})}{r_{Sun-p}^3} - \frac{\mu(x_{SL_i} - x_{Earth})}{r_{Earth-p}^3} = 0. \tag{3.58}$$

The fifth-order polynomial coefficients depend on the space region in which the equilibrium points coordinate, x_{SL_i}, is defined. The range of validity for the collinear Lagrangian points is:

$$\begin{cases} -\mu \leq x_{SL_1} \leq 1-\mu \\ -\mu \leq 1-\mu \leq x_{SL_2} \\ x_{SL_3} \leq -\mu \leq 1-\mu \end{cases} . \tag{3.59}$$

In Eq. (3.59), $-\mu$ is the position of the first celestial body (i.e. Sun) and $1-\mu$ is the position of the second celestial body (i.e. Earth). The fifth-order polynomials in Table 3.3 have five roots in which one is real and the other four are complex. The positions of the collinear points on the x-axis correspond to the real root. Even if the computation of the collinear Lagrangian points is not new (McInnes et al., 1994; McInnes, 1999; Elipe, 1992; McInnes, 2000). More details on the derivation of the fifth-order polynomial derivation are reported in the Appendix C.5.

$\mathbf{SL_i}$	$\boldsymbol{x^5}$	$\boldsymbol{x^4}$	$\boldsymbol{x^3}$	$\boldsymbol{x^2}$	$\boldsymbol{x}$	$\boldsymbol{Const}$
SL_1	1	$-(3-\mu)$	$(3-2\mu)$	$-(\mu+\beta\mu_{Sun})$	2μ	$-\mu$
SL_2	1	$(3-\mu)$	$(3-2\mu)$	$-(\mu-\beta\mu_{Sun})$	-2μ	$-\mu$
SL_3	1	$(2+\mu)$	$(1+2\mu)$	$-(1-\beta)\mu_{Sun}$	$-2(1-\beta)\mu_{Sun}$	$-(1-\beta)\mu_{Sun}$

Table 3.3: Fifth-order polynomials coefficients.

In the CR3BP, the phase space of the system is highly dependent on the mass parameter, μ, which can vary from 0 to 0.5. When the effect of SRP is taken into account for a Sun-pointing area, the phase space of the CR3BP-SRP depends on μ and the lightness number, β. Figure 3.6 shows the coordinate, x_{SL_i}, of the collinear libration points as a function of μ and β.

The trend of L_1, L_2 and L_3 as a function of μ are shown in Figure 3.6(a), where L_1 is located between the two celestial bodies ($x_{Body-1} < x_{L_1} < x_{Body-2}$), L_2 is behind the second primary ($x_{L_2} > x_{Body-2}$) and L_3 is behind the first primary ($x_{L_3} < x_{Body-1}$). When μ tends to zero, the CR3BP can be approximated to the Hill's problem (as stated in Section 2.1). This is the case for the Sun-Earth system, where, μ is close to zero. However, when μ tends to 0.5, the two celestial bodies have the same masses, and L_1 collapses into Centre of Mass (CM) of the system. Meanwhile, L_2 and L_3 move to an equivalent distance from their closer primary respectively.

Figure 3.6(b) shows the position of the collinear points as a function of β for a Sun-pointing surface, $\hat{\boldsymbol{r}} = \hat{\boldsymbol{N}}$, where μ is set for the Sun-(Earth+Moon) system. In this case, the lightness parameter, β, was changed within its range of validity between 0 and 1. When $\beta = 0$ in Figure 3.6(b), the points represents the libration points solutions for the CR3BP without solar radiation pressure. The CR3BP condition for the Sun-Earth system shown in Figure 3.6(b) for $\beta = 0$ also corresponds to the solution shown in Figure 3.6(a) for $\mu = 3.036 \cdot 10^{-6}$. Conversely, when β tends to 1, the CR3BP dynamics degenerates into the two body problem dynamics in a rotating frame. Thus, the SRP force counteracts completely the Sun's gravity force and SL_1 and SL_3 converge to the origin of the system. This means that by increasing β, the positions of SL_1 and SL_3 move closer to the Sun, and the position of SL_2 gets closer to the Earth. This is due to the balancing of the gravitational, the Coriolis, and the SRP acceleration. Although this graph is generated with a value of μ based on the Sun-Earth system, the result is, in general, sensitive to the value of μ (McInnes, 1999, 2000).

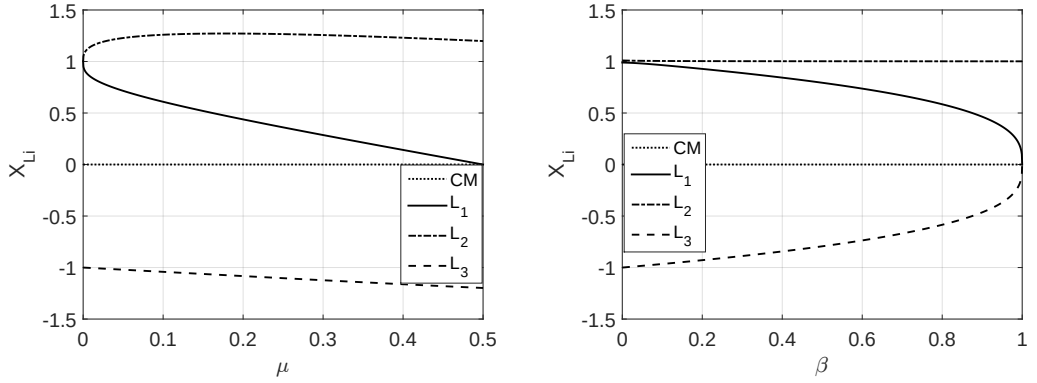

(a) Collinear Lagrangian points: $\mu \neq 0$ and $\beta = 0$.

(b) Collinear Lagrangian points: $\beta \neq 0$ and $\mu = 3.036 \cdot 10^{-6}$.

Figure 3.6: Collinear libration points with a function of β and μ (McInnes, 1999, 2000).

3.5.2 Equilibrium points with the effect of solar radiation pressure

For a general orientation of the reflective structure, the collinear equilibrium points of the CR3BP-SRP results in surfaces of "artificial" libration points (SL_i) as a function of the sail orientation angles. Thus, the system now has two-dimensional families of equilibrium points (McInnes et al., 1994; McInnes, 1999, 2000; Farrés and Jorba, 2010). The equations of equilibrium are given by Eq. (3.39) when the accelerations ($\ddot{x}$, $\ddot{y}$ and $\ddot{z}$) and velocities ($\dot{x}$, $\dot{y}$ and $\dot{z}$) of the spacecraft are equal to zero. In Eq. (3.39), the SRP acceleration is modelled using the definition of the normal vector, $\hat{\boldsymbol{N}}$, defined by the cone and the clock angles as shown in Eq. (3.17). The system of equations to solve for a general orientation of a reflective deployable structure is:

$$\begin{cases} V_x + a_x^s = 0 \\ V_y + a_y^s = 0 \\ V_z + a_z^s = 0 \end{cases} . \tag{3.60}$$

Eq. (3.60) together with Eq. (3.25) can be written in a compact way as (McInnes, 2000):

$$-\nabla V = \beta \frac{\mu_{Sun}}{r_{Sun-p}^2} \cos^2 \alpha \hat{\boldsymbol{N}}. \tag{3.61}$$

The existence of the artificial equilibrium points is limited by the reflective structure orientation; where, the normal vector, $\hat{\boldsymbol{N}}$, must be parallel to ∇V; thus, $-\nabla V \times \hat{\boldsymbol{N}} = 0$ (McInnes, 2000) which implies:

$$\hat{\boldsymbol{N}} = \frac{-\nabla V}{|-\nabla V|}. \tag{3.62}$$

By considering the cone and clock angles definition of $\hat{\boldsymbol{N}}$, the scalar product between the Sun-line direction and the normal vector is $\cos\alpha$ such that:

$$\cos\alpha = \left\langle \hat{\boldsymbol{r}} \cdot \hat{\boldsymbol{N}} \right\rangle = \left\langle \hat{\boldsymbol{r}} \cdot \frac{-\nabla V}{|-\nabla V|} \right\rangle. \tag{3.63}$$

By substituting Eq. (3.63) into Eq. (3.61), the artificial libration points satisfy the flowing equation (McInnes et al., 1994; McInnes, 1999, 2000):

$$\beta = \frac{r_{Sun-p}^2}{\mu_{Sun}} \frac{|-\nabla V|^3}{\langle \hat{\boldsymbol{r}}_{Sun-p} \cdot -\nabla V \rangle^2}. \tag{3.64}$$

Note that not all the solutions of Eq. (3.64) are feasible due to the constraint in the direction of the SRP acceleration; indeed, it is not physically possible to produce acceleration in the direction toward the Sun (McInnes, 1999, 2000). Thus, a constraint inequality equation is here introduced:

$$\langle \hat{\boldsymbol{r}} \cdot (-\nabla V) \rangle \geq 0. \tag{3.65}$$

Note that the limit condition for the existence of motion under the effect of SRP is when $\langle \hat{\boldsymbol{r}} \cdot (-\nabla V) \rangle = 0$. Figures 3.7, 3.8 and 3.9 show the position of the libration points for the planar case for the x-y and x-z planes. The solutions shown in these figures are well-know in the literature (McInnes et al., 1994; McInnes, 2000; Farrés and Jorba, 2010); however, they were reconstructed in this work as they are a useful tool in the design of transfer trajectories (Chapter 6). In Figures 3.7, 3.8 and 3.9, each point along the coloured curves corresponds to an equilibrium point for a fixed area orientation and β. The curves are obtained by fixing the value of β and by letting values in x, y and z in Eq. (3.64) to vary from 0.985 to 1.01 in x and between $\pm$ 0.015 in y and z. The position of the libration point is a function of α for a fixed value of δ. Thus, δ fixes the plane of motion of the spacecraft. The x-y plane is given by fixing $\delta = 90°$; while, the x-z plane is given for a value of δ equal to $0°$. Each coloured scale line represents the positions of the libration point for values of α between $-90°$ and $90°$ with a fixed β. The shaded area represents solutions that are not feasible due to the constraint in Eq. (3.65).

Figure 3.7 shows the position of the libration points in the vicinity of the Earth for four different ranges of β, when the motion is restricted to the x-y plane. The value of β is normally within a range of 0 (No SRP effect) and 1 (two body problem). However, higher values of β are shown here since it is possible to find graphically the boundary of the shaded area for an infinitely growing value of β, as shown in Eq. (3.65) when the inequality is equal to zero.

Figure 3.8 and Figure 3.9 show the positions of the equilibrium points when the motion is restricted to the x-z plane. Note that Figure 3.8 shows solutions close to the Earth, while Figure 3.9 shows the same solutions for a wider region that includes the Sun and Earth+Moon system.

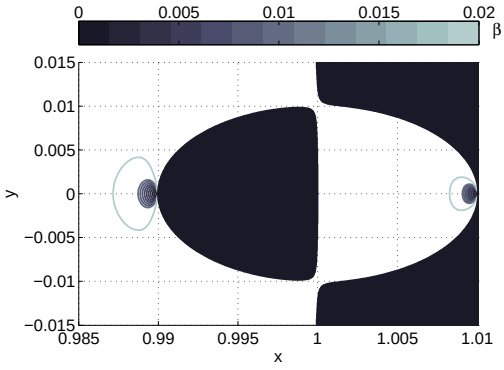

(a) $\beta = 0$ up to 0.02.

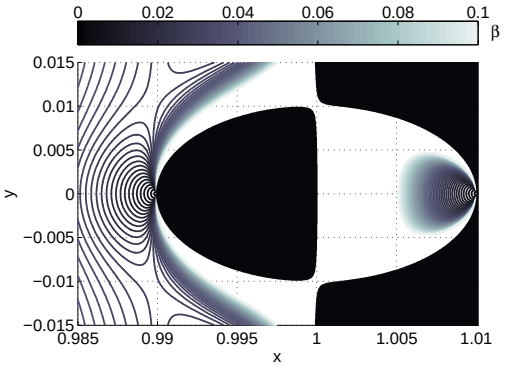

(b) $\beta = 0$ up to 0.1.

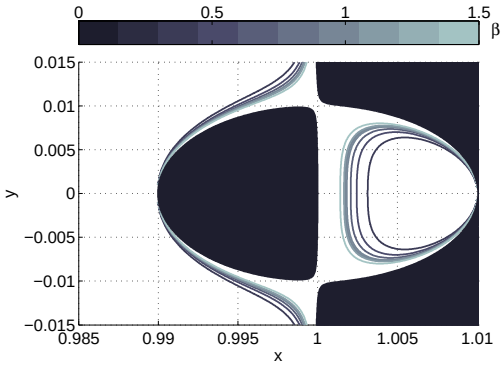

(c) $\beta = 0$, 0.3, 0.5, 0.7, 0.9, 0.99, 1, 1.1, 1.5.

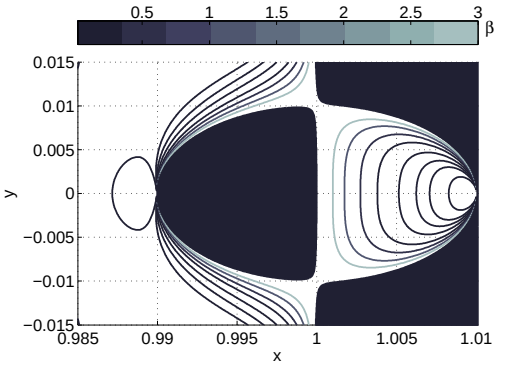

(d) $\beta = 0.02$, 0.04, 0.06, 0.1, 0.2, 0.4, 1, 3.

Figure 3.7: Position of the artificial libration points as a function of β, x-y plane in the vicinity of the Earth (McInnes et al., 1994; McInnes, 2000; Farrés and Jorba, 2010).

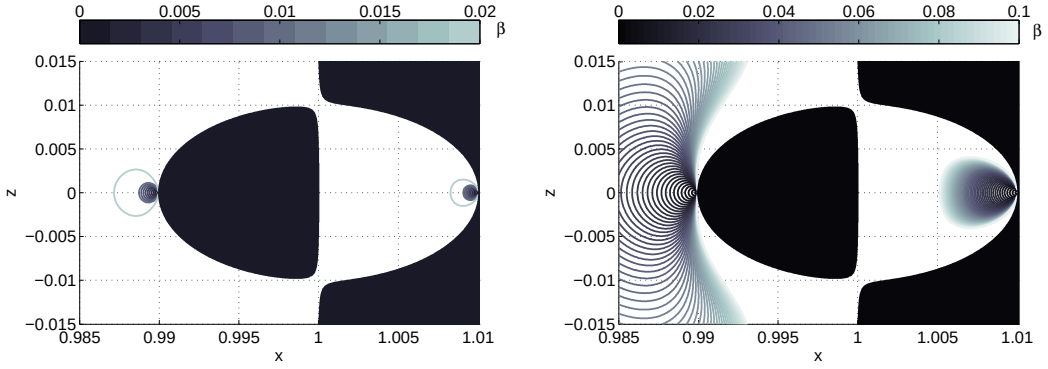

(a) $\beta = 0$ up to 0.02.

(b) $\beta = 0$ up to 0.1.

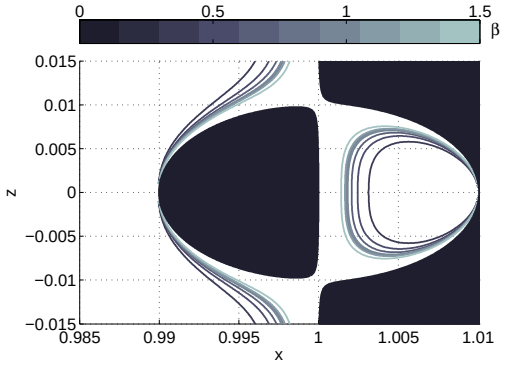

(c) $x - z$ plane with $\beta = 0$, 0.3, 0.5, 0.7, 0.9, 0.99, 1, 1.1, 1.5.

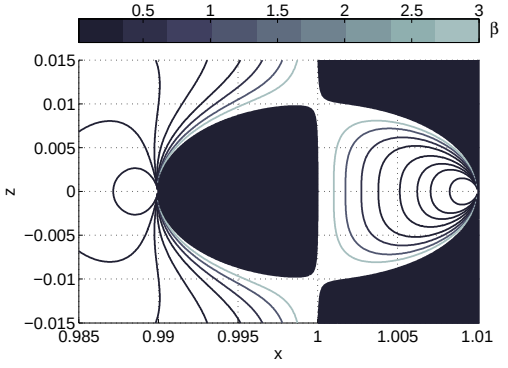

(d) $\beta = 0.02$, 0.04, 0.06, 0.1, 0.2, 0.4, 1, 3.

Figure 3.8: Position of the artificial libration points as a function of β, x-z plane in the vicinity of the Earth (McInnes et al., 1994; McInnes, 2000; Farrés and Jorba, 2010).

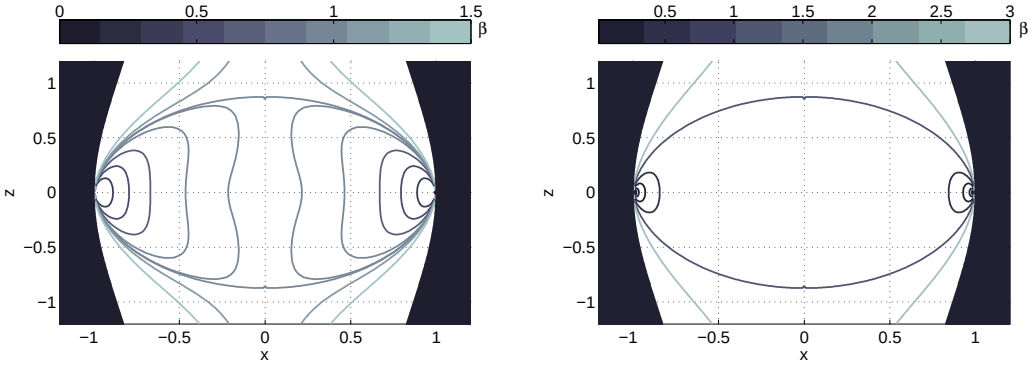

(a) $\beta = 0, 0.3, 0.5, 0.7, 0.9, 0.99, 1, 1.1, 1.5$.

(b) $\beta = 0.02, 0.04, 0.06, 0.1, 0.2, 0.4, 1, 3$.

Figure 3.9: Position of the artificial libration points as a function of β, x-z plane in the Sun-(Earth+Moon) system (McInnes et al., 1994; McInnes, 2000; Farrés and Jorba, 2010).

Although Eq. (3.64) gives a quick tool to represent the positions of the libration points, a database of the equilibrium points' positions as a function of the orientation angles is needed for the study in Chapter 6. For this reason, a numerical continuation method was developed to obtain the coordinates of the libration point in the x-y plane for fixed values of β and variable α was developed. Details of the numerical continuation algorithm used are shown in next Section.

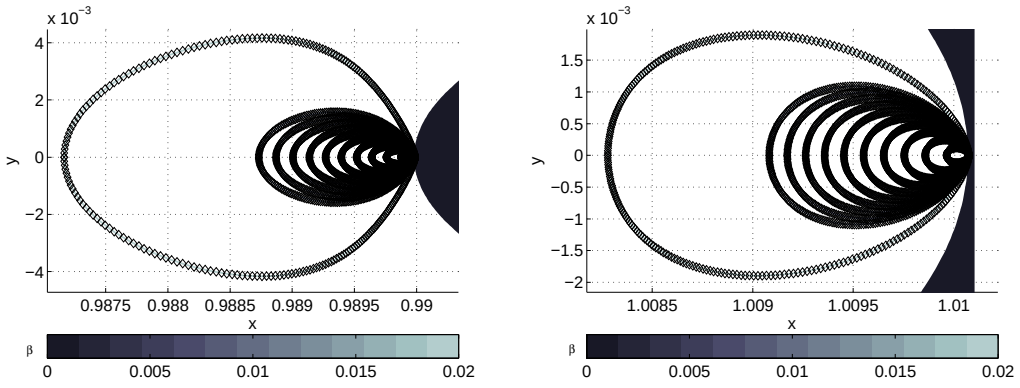

(a) L_1.

(b) L_2.

Figure 3.10: Position of the artificial libration points for $\beta = 0$ up to 0.02.

3.5.3 Numerical continuation for the computation of equilibrium points

In this section, the coordinates of the libration points as a function of the spacecraft-pointing accuracy are obtained through numerical continuation techniques. The algorithm presented here is limited to the planar case where the position of the equilibrium points is constrained in the x-y plane and it is function of the in-plane angle, α. For the

planar dynamics, $z = 0$, Eq. (3.39) turns into:

$$\begin{cases} \ddot{x} - 2\dot{y} = -V_x + a_x^s \\ \ddot{y} + 2\dot{x} = -V_y + a_y^s \end{cases}, \tag{3.66}$$

where the SRP acceleration is:

$$\boldsymbol{a}^s = \beta \frac{\mu_{Sun}}{r_{Sun-p}^2} \cos^2 \alpha \hat{\boldsymbol{N}}, \tag{3.67}$$

and, the normal vector is given by:

$$\hat{\boldsymbol{N}} = \frac{\cos\alpha}{r_{Sun-p}} \begin{Bmatrix} x - x_1 \\ y \end{Bmatrix} + \frac{\sin\alpha}{r_{Sun-p}} \begin{Bmatrix} y \\ -(x - x_{Sun}) \end{Bmatrix}. \tag{3.68}$$

Thus, the SRP acceleration for the x-y plane motion are:

$$\begin{cases} a_x^s = & \beta \frac{\mu_{Sun}}{r_{Sun-p}^3} \left[\cos^3\alpha (x - x_{Sun}) + \cos^2\alpha \sin\alpha y\right] \\ a_y^s = & \beta \frac{\mu_{Sun}}{r_{Sun-p}^3} \left[-\cos^2\alpha \sin\alpha (x - x_1) + \cos^3\alpha y\right] \end{cases} \tag{3.69}$$

Finally, the equations of motion for the equilibrium points ($\ddot{x} = \ddot{y} = \dot{x} = \dot{y} = 0$) become:

$$\begin{cases} x + \frac{\mu_{Sun}}{r_{Sun-p}^3}(1 - \beta\cos^3\alpha)(x - x_{Sun}) - \beta\frac{\mu_{Sun}}{r_{Sun-p}^3}\cos^2\alpha\sin\alpha y + \frac{\mu_{Earth}}{r_{Earth-p}^3}(x - x_{Earth}) & = 0 \\ y + \frac{\mu_{Sun}}{r_{Sun-p}^3}(1 - \beta\cos^3\alpha) y + \beta\frac{\mu_{Sun}}{r_{Sun-p}^3}\cos^2\alpha\sin\alpha(x - x_{Sun}) + \frac{\mu_{Earth}}{r_{Earth-p}^3} y & = 0 \end{cases} \tag{3.70}$$

By having fixed β, the angle α was added as an additional variable to the system and varied between 0 and $\pi/2$. Thus, it is possible to write:

$$\begin{cases} F_1 = & x + \frac{\mu_{Sun}}{r_{Sun-p}^3}(1 - \beta\cos^3\alpha)(x - x_{Sun}) - \beta\frac{\mu_{Sun}}{r_{Sun-p}^3}\cos^2\alpha\sin\alpha y + \frac{\mu_{Earth}}{r_{Earth-p}^3}(x - x_{Earth}) \\ F_2 = & y + \frac{\mu_{Sun}}{r_{Sun-p}^3}(1 - \beta\cos^3\alpha) y + \beta\frac{\mu_{Sun}}{r_{Sun-p}^3}\cos^2\alpha\sin\alpha(x - x_{Sun}) + \frac{\mu_{Earth}}{r_{Earth-p}^3} y \end{cases}; \tag{3.71}$$

where, DF is given by:

$$DF = \begin{bmatrix} F_{1x} & F_{1y} & F_{1\alpha} \\ F_{2x} & F_{2y} & F_{2\alpha} \end{bmatrix}. \tag{3.72}$$

The prediction of the solution requires:

$$\bar{Z} = Z_0 - dsH; \tag{3.73}$$

where, Z is given by $\{x, y, \alpha\}$. H is the kernel of the map $DF(\bar{Z})$ and ds is the tolerance and it is set to be 10^{-4} in this case. If we now impose $H_\alpha = 1$, it is possible to write:

$$H_{x,y} = -\begin{bmatrix} F_{1x} & F_{1y} \\ F_{2x} & F_{2y} \end{bmatrix}^{-1} \begin{Bmatrix} F_{1\alpha} \\ F_{2\alpha} \end{Bmatrix} \tag{3.74}$$

The correction of the solution requires that:

$$F(Z^{k+1}) = F(Z^k) + DF(Z^k)\Delta Z + O(2) \simeq 0, \tag{3.75}$$

and now ΔZ is:

$$\Delta Z = Z^{k+1} - Z^k = \begin{Bmatrix} \Delta x \\ \Delta y \\ \Delta \alpha \end{Bmatrix}. \tag{3.76}$$

The aim of the predictor-correction algorithm is to have $\Delta\alpha = 0$ thus $\Delta Z_\alpha = 0$ such as:

$$\Delta Z_{x,y} = -\begin{bmatrix} \bar{F}_{1x} & \bar{F}_{1y} \\ \bar{F}_{2x} & \bar{F}_{2y} \end{bmatrix}^{-1} \begin{Bmatrix} \bar{F}_1 \\ \bar{F}_2 \end{Bmatrix}; \tag{3.77}$$

where, finally the corrected state is:

$$Z^{k+1} = Z^k + \Delta Z. \tag{3.78}$$

Eq. (3.78) is used to numerically compute the curves shown in Figure 3.7(a) and compared with the one obtained from Eq. (3.64). Figure 3.10 shows the comparison for β varying from 0 up to 0.02 for L_1, in Figure 3.10(a), and L_2, in Figure 3.10(b). The advantage of using a numerical continuation method is in the precision of determining the contour curves. An equilibrium points database is required as a quintic polynomial equation does not exist for a general reflective surface's orientation. Note that, the position of the collinear points are simply displaced in the x-axis when the normal to the reflective surface and the Sun-line direction are aligned as shown in Figure 3.5 (Sun-pointing case).

3.6 Energy, zero-velocity curves and forbidden regions for a Sun-pointing reflective surface

The equations of motion of the CR3BP (Eq. (3.39) when the SRP acceleration is zero) are Hamiltonian and independent of time; thus, they have an energy integral of motion. When the effect of SRP is taken into account, Eq. (3.39), the equations of motion of the CR3BP-SRP are Hamiltonian under the hypothesis of a Sun-pointing deployable reflective structure ($\hat{\boldsymbol{N}} = \hat{\boldsymbol{r}}$). Thus, an energy integral of motion also exists for a Sun-pointing reflective structure. The energy integral for a Sun-pointing reflective structure is derived by multiplying the equations of motion in Eq. (3.39) by $\dot{x}$ (first equation), by $\dot{y}$ (second equation) and by $\dot{z}$ (third equation). Finally, by summing the three equations, the energy derivative is:

$$\dot{E} = \ddot{x}\dot{x} + 2\dot{y}\dot{x} - V_x\dot{x} + a_x^s\dot{x} + \ddot{y}\dot{y} - 2\dot{x}\dot{y} - V_y\dot{y} + a_y^s\dot{y} + \ddot{z}\dot{z} - V_z\dot{z} + a_z^s\dot{z}. \tag{3.79}$$

For a non-conservative system (general orientation of the reflective structure), the energy is defined as:

$$E = \frac{1}{2}(\dot{x}^2 + \dot{y}^2 + \dot{z}^2) - V + \int_t \boldsymbol{a}^s \cdot \boldsymbol{v}\ d\tau. \tag{3.80}$$

In Eq. (3.80), the integral term is the work of the non-conservative SRP acceleration, where $\boldsymbol{v}$ is the satellite velocity along its orbit. When, the reflective structure is Sun-pointing, $\hat{\boldsymbol{N}} = \hat{\boldsymbol{r}}$, its possible to write the potential of the SRP force as in Eq. (3.26). Thus, the energy in Eq. (3.80) assumes its simplified form as:

$$E = \frac{1}{2}(\dot{x}^2 + \dot{y}^2 + \dot{z}^2) - V + U^s. \tag{3.81}$$

The full expression of the energy integral for a Sun-pointing near perfect reflective structure is:

$$E = \frac{1}{2}(\dot{x}^2 + \dot{y}^2 + \dot{z}^2) - \frac{1}{2}(x^2 + y^2) - (1-\beta)\frac{\mu_{Sun}}{r_{Sun-p}} - \frac{\mu_{Earth}}{r_{Earth-p}}. \tag{3.82}$$

The energy integral of the CR3BP can be found from Eq. (7.3) for β equal to zero. In celestial mechanics "$-2E$" is often used, which is called the Jacobi integral[7], C, given by:

$$C = -(\dot{x}^2 + \dot{y}^2 + \dot{z}^2) + 2V - 2U^s, \tag{3.83}$$

for a Sun-pointing reflective deployable structure.

As mentioned in Chapter 2, the Jacobi integral was used by Hill to study the motion of asteroids in the 3BP and he also introduced the concept of Zero Velocity Curves (ZVCs). The ZVCs define regions in space where the spacecraft is allowed to move. They have the advantage of giving a qualitative picture of the motion of the spacecraft under the influence of the Sun's and the Earth+Moon barycentre's gravitational effects. The

[7]Note that the Jacobi constant is referred in the literature using either the symbol C or J.

ZVCs for a Sun-pointing deployable reflective structure are given by the intersection of the energy of the spacecraft with the total potential in Eq. (3.40) plus the contribution of SRP given by Eq. (3.26). Figure 3.11 shows the potential energy (in pink) as a function of the x and y coordinates. The Sun and the Earth represent the singularities in the potential energy; while, the libration points, $L_{1,2,3,4,5}$, are the stationary points of the potential energy.

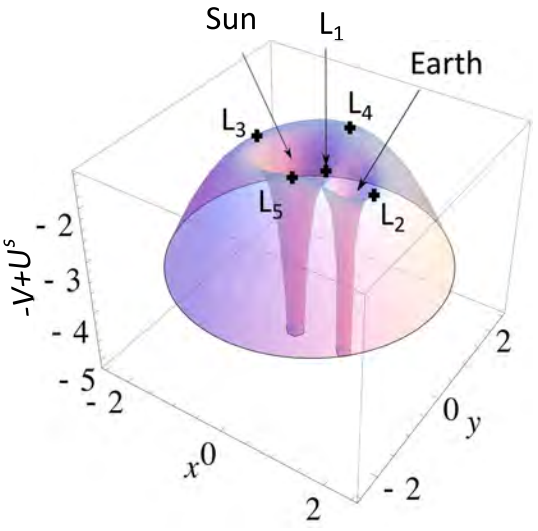

Figure 3.11: Rotating and gravitational potential in the CR3BP-SRP for a Sun-pointing reflective area.

Figure 3.12 gives qualitative information about the spacecraft motion. Indeed, by fixing the initial state of the spacecraft, the energy of the spacecraft remain constant as there are no dissipative effects in the CR3BP-SRP dynamical model for the Sun-pointing case. The ZVC (dashed black line in the Figure 3.12) is obtained from the intersection of the energy of the spacecraft with the potential function in Figure 3.11. The grey regions in Figure 3.12 represents the forbidden area where the motion of the spacecraft is not physically possible; while, the white area represents regions of possible motion. Figure 3.12 shows the LPO (black line) where the spacecraft is placed. The regions close to $SL_{1,2}$ are called "bottle neck" regions.

Figure 3.13 shows a particular case of the ZVCs when the spacecraft has the same energy as L_1 and L_2. In the case of L_1, the spacecraft can be trapped inside the L_1-L_2 region as the bottle neck regions are closed at both L_1 and L_2. When the bottle neck is closed at L_2, a spacecraft placed in an orbit around the Sun with a Sun-spacecraft distance bigger than the Sun-L_2 distance will never return to the Earth.

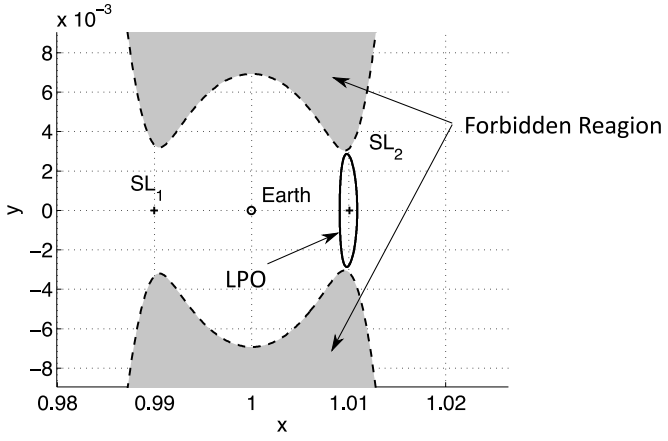

Figure 3.12: Zero velocity curves for a spacecraft in LPO.

The boundaries of the forbidden regions are shown by the black dashed line in Figure 3.12-3.13 and they correspond to a condition where the velocity of the spacecraft is zero. The condition of forbidden region is defined to be:

$$C < C^* \tag{3.84}$$

where, C and C^* are, respectively, the Jacobi and the critical Jacobi integrals. In particular, C^* is given when the velocity of the spacecraft is set to zero as:

$$C^* = 2V - 2U^s. \tag{3.85}$$

Figure 3.14 shows the potential energy for a Sun-pointing reflective area for different values in the lightness parameter, β. In this figure, it is possible to detect the same behaviour of Figure 3.6(b) where for $\beta = 0$ the CR3BP-SRP becomes the CR3BP with no SRP effect; while $\beta = 1$ is the case of the Kepler problem in a rotating frame. For $\beta = 1$, the SL_1 and SL_3 points collapse into the centre of mass of the Sun-Earth system. By observing Figure 3.14, the effect of β changes the shape of the ZVCs for a fixed value of the energy ($-V + U^s$ in the figure). This intuition is the starting point of the design of the end-of-life disposal in Chapter 7.

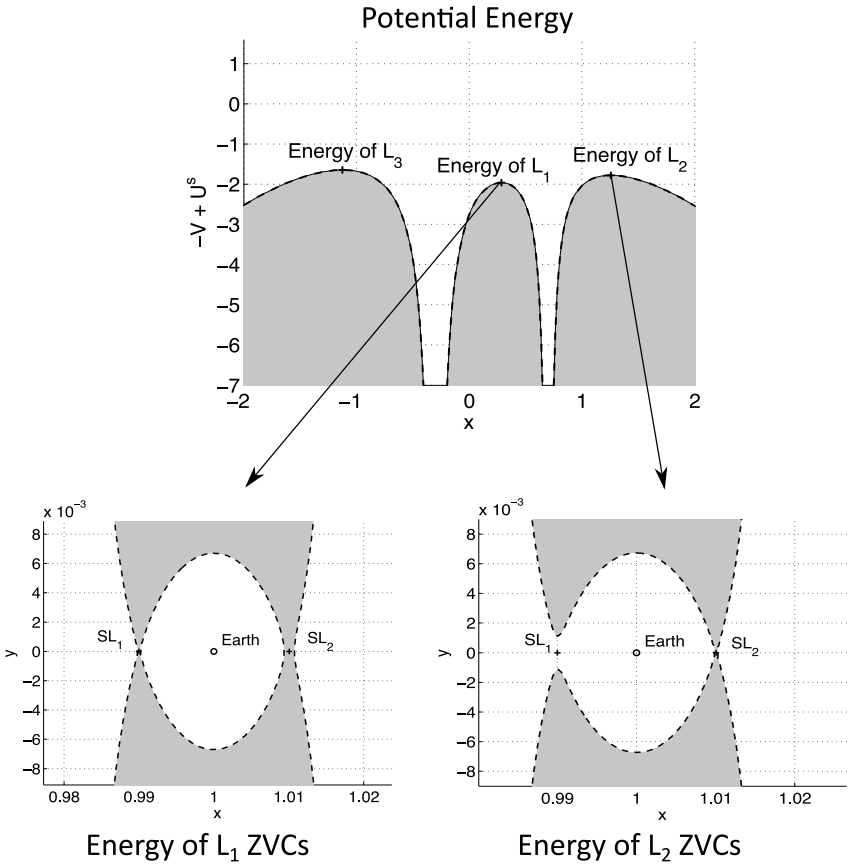

Figure 3.13: Potential energy and zero velocity curves for L_1 and L_2.

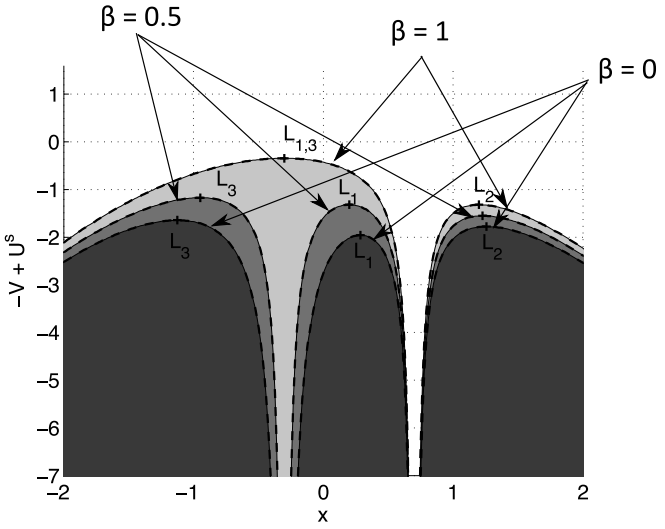

Figure 3.14: Potential energy as a function of the lightness parameter, β, for a Sun-pointing reflective area.

3.7 Linearised equations of motion around the libration points

The scientific advantages of locating a spacecraft in the vicinity of the libration points were already pointed out in Section 2.1. To investigate the motion of the spacecraft around the libration points, it is important to study the stability of the equilibrium points of the non-linear system. The information about the non-linear stability of the equilibrium points for the non-linear system can be obtained by linearising the equations of motion, in Eq. (3.39), around the equilibrium points. In this way, it is possible to provide the variational equations about the equilibrium solutions. These linear variational equations associated to the libration, L_i, or pseudo libration, SL_i, points describe to the position of the libration point about the barycentre. This linear equation can be determined through a Taylor expansion around L_i or SL_i.

In order to study the stability of the equilibrium points, Eq. (3.39) is linearised around the equilibrium points. First, a change of coordinates is made to centre the system in the equilibrium point, SL_i, as follows:

$$\begin{cases} \xi &= x - x_{SL_i} \\ \eta &= y - y_{SL_i} \\ \zeta &= z - z_{SL_i} \\ \dot{\xi} &= \dot{x} \\ \dot{\eta} &= \dot{y} \\ \dot{\zeta} &= \dot{z} \end{cases} \tag{3.86}$$

In Eq. (3.86), ξ, η and ζ are the coordinates of the spacecraft in the synodic reference system with dimensionless coordinates; where, the origin of the system is centred at the equilibrium point, SL_i. Figure 3.15 shows the position of the pseudo libration points under the influence of SRP acceleration in the synodic reference frame. The Sun-SL_3 distance is indicated with γ_3; while, the Earth-$SL_{1,2}$ distances are $\gamma_{1,2}$. Moreover, the system $\{\xi, \eta, \zeta\}$ centred at the libration points is shown in Figure 3.15 .

By expanding V and a^s around SL_i and adding the change of coordinates of Eq. (3.86) to Eq. (3.39), the linearised equations become:

$$\begin{cases} \ddot{\xi} - 2\dot{\eta} = (V^*_{xx} + a^{s*}_{xx})\xi + (V^*_{xy} + a^{s*}_{xy})\eta + (V^*_{xz} + a^{s*}_{xz})\zeta \\ \ddot{\eta} + 2\dot{\xi} = (V^*_{yx} + a^{s*}_{yx})\xi + (V^*_{yy} + a^{s*}_{yy})\eta + (V^*_{yz} + a^{s*}_{yz})\zeta \\ \ddot{\zeta} = (V^*_{zx} + a^{s*}_{zx})\xi + (V^*_{zy} + a^{s*}_{zy})\eta + (V^*_{zz} + a^{s*}_{zz})\zeta \end{cases} , \tag{3.87}$$

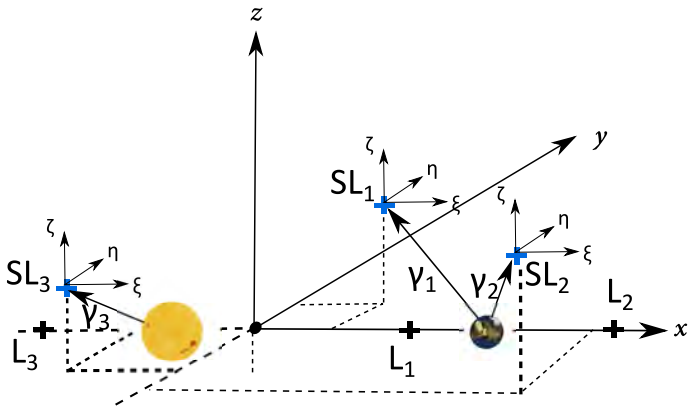

Figure 3.15: Position of the equilibrium points in the rotating system. Definition of a reference system centred at the libration points; where, γ_1, γ_2 and γ_3 are the relative distances between the libration points and the closest primary.

where, the symbol * means that the variables are evaluated at the equilibrium point SL_i. Eq. (3.87) can be rewritten in a vectorial way as:

$$\frac{d}{dt}\begin{bmatrix}\xi\\ \eta\\ \zeta\\ \dot{\xi}\\ \dot{\eta}\\ \dot{\zeta}\end{bmatrix} = \begin{bmatrix} 0 & 0 & 0 & 1 & 0 & 0\\ 0 & 0 & 0 & 0 & 1 & 0\\ 0 & 0 & 0 & 0 & 0 & 1\\ \bar{V}^*_{xx} & \bar{V}^*_{xy} & \bar{V}^*_{xz} & 0 & 2 & 0\\ \bar{V}^*_{yx} & \bar{V}^*_{yy} & \bar{V}^*_{yz} & -2 & 0 & 0\\ \bar{V}^*_{zx} & \bar{V}^*_{zy} & \bar{V}^*_{zz} & 0 & 0 & 0\end{bmatrix}\begin{bmatrix}\xi\\ \eta\\ \zeta\\ \dot{\xi}\\ \dot{\eta}\\ \dot{\zeta}\end{bmatrix}. \tag{3.88}$$

In Eq. (3.88), $\bar{\boldsymbol{V}}^*_{\boldsymbol{rr}}$ includes the effect of the total potential, $\boldsymbol{V}^*_{\boldsymbol{rr}}$, and of the SRP acceleration, $\boldsymbol{a}^*_{\boldsymbol{rr}}$, evaluated at the equilibrium point. When the effect of SRP corresponds to a Sun-pointing reflective area, the collinear equilibrium points are aligned along the x-axis; thus, $y_{SL_i} = z_{SL_i} = 0$ as shown in Figure 3.5. In some cases, the effect of SRP affects the stability of the collinear equilibrium points as a consequence of the effect of the orientation angles.

In Eq. (3.88), the double derivatives of the total potential, V, and the SRP acceleration, $\boldsymbol{a}^s$, are shown in Appendix C.6 and Appendix C.7 respectively. Eq. (3.88) can be written in a more compact way as:

$$\dot{\boldsymbol{X}} = \boldsymbol{A}^* \cdot \boldsymbol{X}, \tag{3.89}$$

where, the matrix $\boldsymbol{A}^*$ is written as:

$$\boldsymbol{A}^* = \begin{bmatrix}\boldsymbol{0} & \boldsymbol{I}\\ \bar{\boldsymbol{V}}^*_{\boldsymbol{rr}} & 2\boldsymbol{J}\end{bmatrix} \qquad \boldsymbol{J} = \begin{bmatrix} 0 & 1 & 0\\ -1 & 0 & 0\\ 0 & 0 & 0\end{bmatrix} \qquad \bar{\boldsymbol{V}}^*_{\boldsymbol{rr}} = \boldsymbol{V}^*_{\boldsymbol{rr}} + \boldsymbol{a}^*_{\boldsymbol{rr}}. \tag{3.90}$$

The stability of the equilibrium points can then be studied by solving the eigenvalues problem of matrix $\boldsymbol{A}^*$.

3.7.1 Stability of the equilibrium points

In Section 2.2, it was mentioned that the collinear equilibrium points of the CR3BP are unstable. This can be easily verified by setting the SRP acceleration to zero in Eq. (3.88) moreover, by computing the eigenvalues of the matrix $\boldsymbol{A}^*$. In this case, six eigenvalues exist two real and opposite sign roots that correspond to the hyperbolic equilibrium and two couples of imaginary roots with opposite signs that identify the in-plane and the out-of-plane centre respectively. When the effect of SRP is taken into account, it is important to verify how the stability of the equilibrium points changes. It was verified that the solutions of the pseudo collinear points are still of the saddle×centre×centre type for a Sun-pointing sail as the effect of β does not affect the stability of a Sun-pointing reflective structure.

For a Sun-pointing structure, the eigenvalues of the matrix $\boldsymbol{A}^*$ can be found through its characteristic polynomial. As the in-plane and the out-of-plane dynamics of the CR3BP-SRP are decoupled, it is possible to study the eigenvalues for the planar equations of motion in x and y and then extend the study to the third dimension. Thus, the characteristic equation of matrix $\boldsymbol{A}^*$ for the x-y plane is given by:

$$\Lambda^2 + (4 - \bar{V}^*_{xx} - \bar{V}^*_{yy})\Lambda + \bar{V}^*_{xx}\bar{V}^*_{yy} - \bar{V}^{*^2}_{xy} = 0, \tag{3.91}$$

where $\Lambda = \lambda^2$. Through the definition of:

$$\beta_1 = 4 - \bar{V}^*_{xx} - \bar{V}^*_{yy} \qquad \beta_2 = \bar{V}^*_{xx}\bar{V}^*_{yy} - \bar{V}^{*^2}_{xy}, \tag{3.92}$$

the solutions are:

$$\Lambda_1 = \frac{-\beta_1 + \sqrt{\beta_1^2 - 4\beta_2}}{2} > 0, \tag{3.93}$$

and

$$\Lambda_2 = \frac{-\beta_1 - \sqrt{\beta_1^2 - 4\beta_2}}{2} < 0. \tag{3.94}$$

Finally, the four eigenvalues are of the type:

$$\lambda_1 = \pm\sqrt{\Lambda_1} = \pm\lambda \qquad \lambda_2 = \pm\sqrt{\Lambda_2} = \pm\omega \cdot i, \tag{3.95}$$

where, i is the complex unit and λ and ω are:

$$\lambda = \sqrt{\frac{-\beta_1 + \sqrt{\beta_1^2 - 4\beta_2}}{2}} \qquad \omega = \sqrt{\frac{\beta_1 + \sqrt{\beta_1^2 - 4\beta_2}}{2}}. \tag{3.96}$$

This means that λ_1 and λ_2 are real and λ_3 and λ_4 are imaginary. Finally, the equation along the third dimension ζ is:

$$\ddot{\zeta} - \bar{V}^*_{zz}\zeta = 0, \tag{3.97}$$

and the characteristic equation is:

$$\zeta^2 - \bar{V}^*_{zz} = 0 \qquad \zeta = \pm\sqrt{|\bar{V}^*_{zz}|}i \qquad \nu = \sqrt{|\bar{V}^*_{zz}|}, \tag{3.98}$$

thus, λ_5 and λ_6 are imaginary roots.

When β is fixed ($\delta = 0°$ and $\alpha = \pm 90°$) and the equilibrium points belong to the x-z plane (as shown in Figure 3.8), they are all saddle×centre×centre equilibrium. The equilibrium points that lie in the x-y plane are obtained if we hold on δ equal to 90° allow α to vary between ±90° (as shown in Figure 3.10). In this case, the equilibrium points show variations in the stability, Figure 3.16-3.17; where, the in-plane centre equilibrium degenerates in a stable or unstable focus at a specific value of α.

Figure 3.16 and Figure 3.17 show the eigenvalues of the matrix $\boldsymbol{A}^*$ for the pseudo equilibrium points close to L_1, in Figure 3.10(a), and L_2, in Figure 3.10(b), respectively. The equilibrium solutions correspond to the hyperbolic×focus×centre equilibrium due to displacements of the equilibrium points along the y-axis (Figure 3.10) (Farrés, 2009).

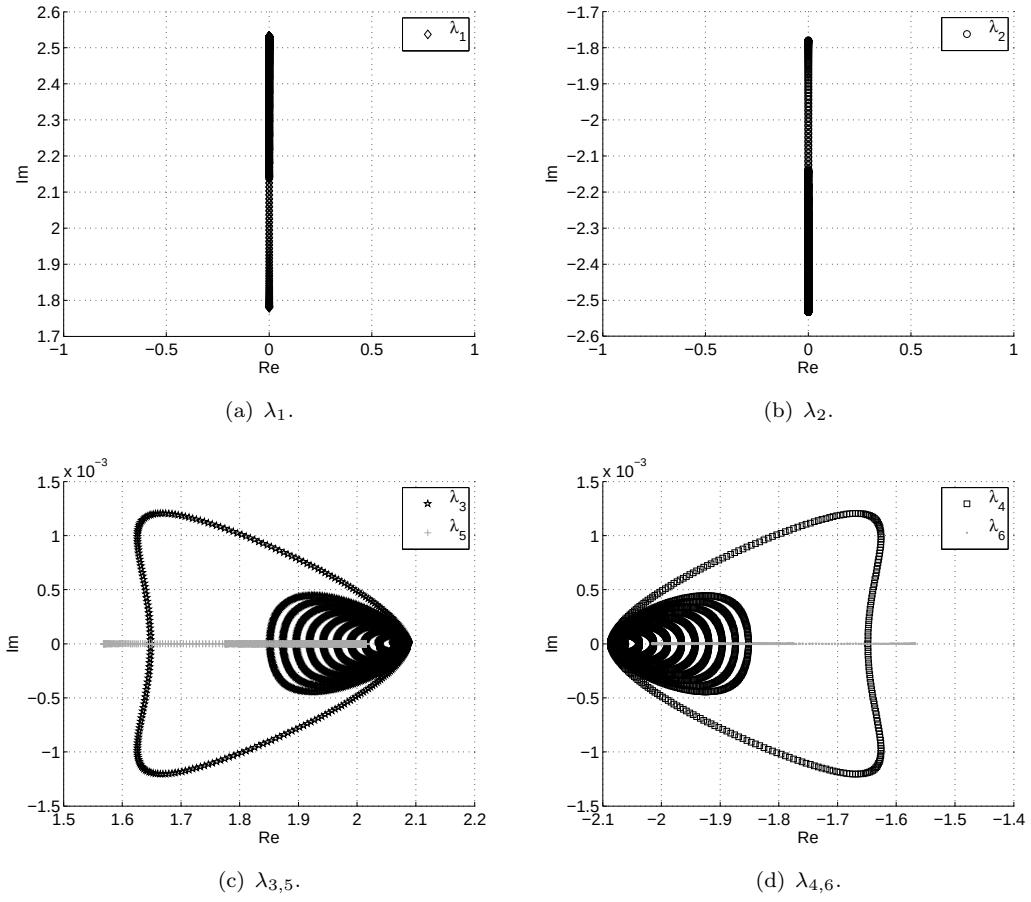

(a) λ_1. (b) λ_2.

(c) $\lambda_{3,5}$. (d) $\lambda_{4,6}$.

Figure 3.16: Eigenvalues of SL_1.

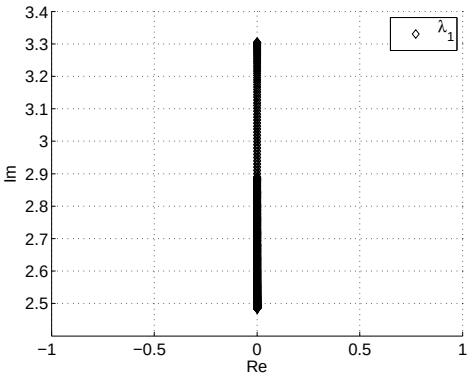

(a) λ_1.

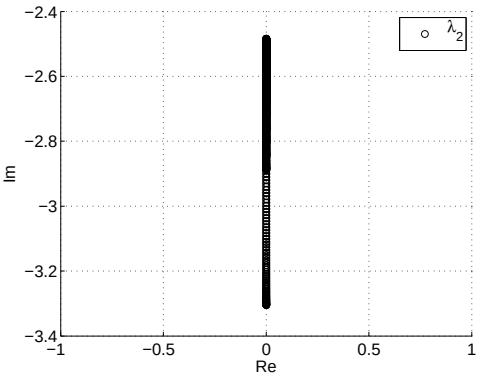

(b) λ_2.

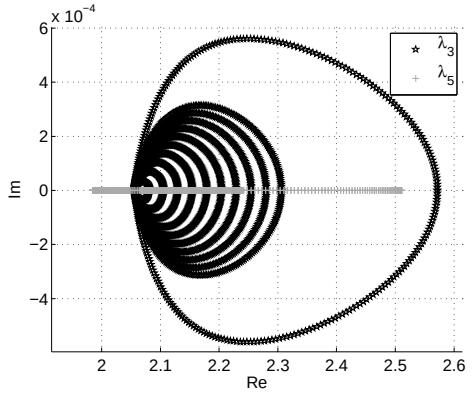

(c) $\lambda_{3,5}$.

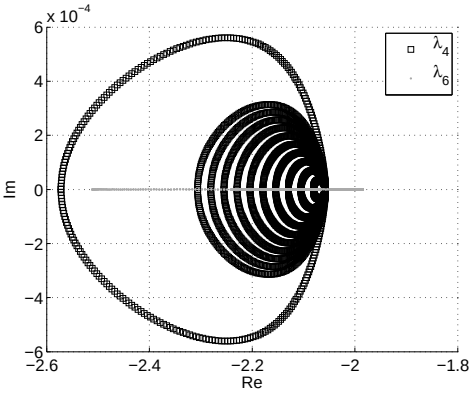

(d) $\lambda_{4,6}$.

Figure 3.17: Eigenvalues of SL_2.

Figure 3.18 shows a schematic representation of the eigenvalues of the matrix $\boldsymbol{A}^*$ under different SRP conditions. In the case of the CR3BP and the CR3BP-SRP for a Sun-pointing or for equilibrium points in the x-z plane, the equilibrium points are all hyperbolic×centre×centre equilibrium. In the case of the CR3BP-SRP for equilibrium points that belong to the x-y plane, the equilibrium points are hyperbolic×stable or unstable focus×centre. The stable focus corresponds to equilibrium points with $\alpha > 0°$; while, the unstable focus corresponds to equilibrium points with $\alpha < 0°$.

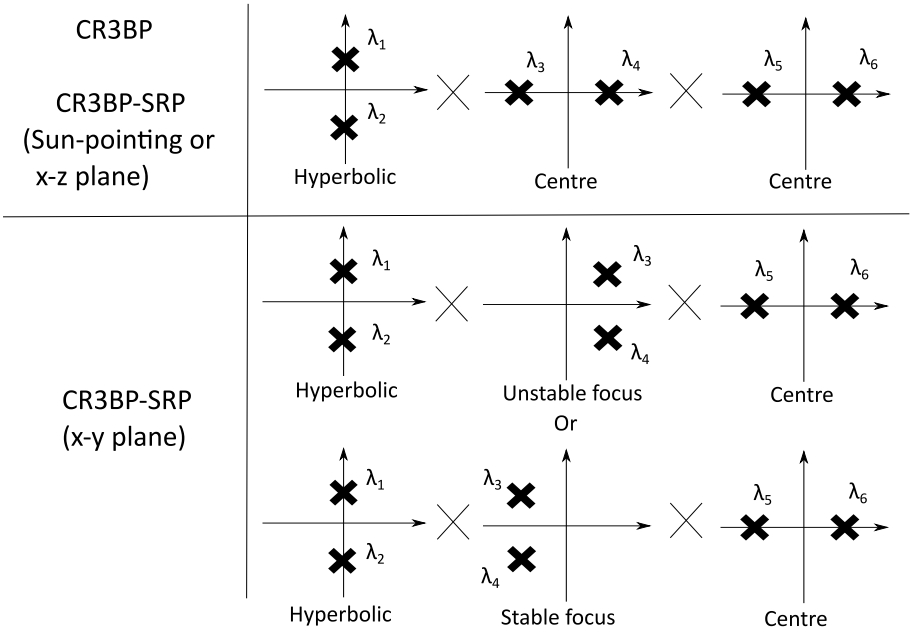

Figure 3.18: Eigenvalues of matrix $\boldsymbol{A}^*$ for the CR3BP and the CR3BP-SRP. In the case of the CR3BP-SRP, the stability is studied for a Sun-pointing surface, for equilibrium points in the x-z plane and for equilibrium points in the x-y plane.

3.8 Design of periodic orbits around the libration points

As mentioned in Chapter 2, the design of periodic orbits around the collinear points is not an easy task due to the existence of the hyperbolic equilibrium that makes them highly unstable. The computation of LPOs requires to the instabilities (hyperbolic manifold) to be removed. In this thesis, the computation of the central manifold, introduced in Section 2.2, was done in two ways: through a semi-analytical approach and numerical methods.

3.8.1 Semi-analytical approach

The computation of LPOs can be done through a semi-analytical approach (Richardson, 1980; Canalias et al., 2003). With respect to Richardson (1980); Canalias et al. (2003), the effect of SRP is added. For a Sun-pointing reflective structure, the linearised equations of motion are:

$$\frac{d}{dt}\begin{bmatrix}\xi\\ \eta\\ \zeta\\ \dot{\xi}\\ \dot{\eta}\\ \dot{\zeta}\end{bmatrix} = \begin{bmatrix}0 & 0 & 0 & 1 & 0 & 0\\ 0 & 0 & 0 & 0 & 1 & 0\\ 0 & 0 & 0 & 0 & 0 & 1\\ 1+2c_{2,\beta} & 0 & 0 & 0 & 2 & 0\\ 0 & 1-c_{2,\beta} & 0 & -2 & 0 & 0\\ 0 & 0 & -c_{2,\beta} & 0 & 0 & 0\end{bmatrix}\begin{bmatrix}\xi\\ \eta\\ \zeta\\ \dot{\xi}\\ \dot{\eta}\\ \dot{\zeta}\end{bmatrix}, \tag{3.99}$$

where, $c_{2,\beta}$ is a constant that depends on the position of the pseudo libration points $\mathrm{SL}_{1,2,3}$ and on the lightness parameter, β. The full derivation of Eq. (3.99) is given in Appendix C.8. Thus, the analytical solution of Eq. (3.99) for a saddle×centre×centre equilibrium is:

$$\begin{cases}\xi &= A_1 e^{\lambda t} + A_2 e^{-\lambda t} + A_3\cos(\omega t) + A_4\sin(\omega t)\\ \eta &= c\cdot A_1 e^{\lambda t} - c\cdot A_2 e^{-\lambda t} + k\cdot A_3\cos(\omega t) - k\cdot A_4\sin(\omega t)\\ \zeta &= A_5\cos(\nu t) + A_6\sin(\nu t)\\ \dot{\xi} &= \lambda\cdot A_1 e^{\lambda t} - \lambda\cdot A_2 e^{-\lambda t} - \omega A_3\sin\omega t + \omega A_4\cos\omega t\\ \dot{\eta} &= \lambda c\cdot A_1 e^{\lambda t} + \lambda c\cdot A_2 e^{-\lambda t} + \omega k\cdot A_3\cos\omega t + \omega k\cdot A_4\sin\omega t\\ \dot{\zeta} &= -\nu\cdot A_5\sin\nu t + \nu\cdot A_6\cos\nu t.\end{cases} \tag{3.100}$$

By using the definition of $\bar{V}^*_{xx}$, $\bar{V}^*_{yy}$ and $\bar{V}^*_{xy}$ as shown in Appendix C.8, β_1 and β_2 in Eq. (3.92) can be rearranged as $\beta_1 = 2 - c_{2,\beta}$ and $\beta_2 = 1 + c_{2,\beta} - 2c^2_{2,\beta}$ respectively, λ, ω and ν are expressed as:

$$\lambda = \sqrt{\frac{c_{2,\beta} - 2 + \sqrt{9c^2_{2,\beta} - 8c_{2,\beta}}}{2}}, \quad \omega = \sqrt{\frac{2 - c_{2,\beta} + \sqrt{9c^2_{2,\beta} - 8c_{2,\beta}}}{2}}, \quad \nu = \sqrt{c_{2,\beta}}; \tag{3.101}$$

while, the constants k and c are defined as:

$$c = \frac{\lambda^2 - 1 - 2c_{2,\beta}}{2\lambda} \qquad k = \frac{-\omega^2 - 1 - 2c_{2,\beta}}{2\omega}. \tag{3.102}$$

In Eq. (3.100), the A_1 and A_2 amplitudes are associated to the unstable and stable invariant manifolds respectively; while, $\mathrm{A}_{3,4}$ are the amplitudes associated to the in-plane centre and $\mathrm{A}_{5,6}$ are associated to the out-of-plane centre. The centre solution can be thus found analytically by imposing $\mathrm{A}_1 = \mathrm{A}_2 = 0$. Moreover, it is convenient to define the remaining amplitudes as: $A_3 = A_x\cos\Phi$, $A_4 = -A_x\sin\Phi$, $A_5 = A_z\cos\Psi$ and

$A_6 = -A_z \sin\Psi$ such that Eq. (3.100) turns into:

$$\begin{cases} \xi &= A_x \cos(\omega t + \Phi) \\ \eta &= kA_x \sin(\omega t + \Phi) \\ \zeta &= A_z \cos(\nu t + \Psi) \\ \dot{\xi} &= -\omega A_x \sin(\omega t + \Phi) \\ \dot{\eta} &= k\omega A_x \cos(\omega t + \Phi) \\ \dot{\zeta} &= -\nu A_z \sin(\nu t + \Psi). \end{cases} \tag{3.103}$$

In Eq. (3.103), the LPOs are expressed by the amplitudes along the x-, y- and z-axis, their frequencies, ω and ν, and phases, Φ and Ψ. When $\omega \neq \nu$, the LPO is a Lissajous type orbit; while, when $\omega = \nu$, the LPO is a halo orbit. This analytical formulation has the advantage of computing the state of the spacecraft in the libration point reference frame from the amplitudes and vice versa through the following transformations:

$$\begin{Bmatrix} \xi \\ \eta \\ \dot{\xi} \\ \dot{\eta} \end{Bmatrix} = \begin{bmatrix} e^{\lambda t} & e^{-\lambda t} & \cos\omega t & \sin\omega t \\ ce^{\lambda t} & -ce^{-\lambda t} & k\sin\omega t & -k\cos\omega t \\ \lambda e^{\lambda t} & -\lambda e^{-\lambda t} & -\omega\sin\omega t & \omega\cos\omega t \\ c\lambda e^{\lambda t} & c\lambda e^{-\lambda t} & k\omega\cos\omega t & k\omega\sin\omega t \end{bmatrix} \cdot \begin{Bmatrix} A_1 \\ A_2 \\ A_3 \\ A_4 \end{Bmatrix} \tag{3.104}$$

$$\begin{Bmatrix} \zeta \\ \dot{\zeta} \end{Bmatrix} = \begin{bmatrix} \cos\nu t & \sin\nu t \\ -\nu\sin\nu t & \nu\cos\nu t \end{bmatrix} \cdot \begin{Bmatrix} A_5 \\ A_6 \end{Bmatrix}, \tag{3.105}$$

where, the inverse transformations are:

$$\begin{Bmatrix} A_1 \\ A_2 \\ A_3 \\ A_4 \end{Bmatrix} = \begin{bmatrix} -\frac{k\omega}{2d_1}e^{-\lambda t} & \frac{\omega}{2d_2}e^{-\lambda t} & \frac{k}{2d_2}e^{-\lambda t} & \frac{1}{2d_1}e^{-\lambda t} \\ -\frac{k\omega}{2d_1}e^{\lambda t} & -\frac{\omega}{2d_2}e^{\lambda t} & -\frac{k}{2d_2}e^{\lambda t} & \frac{1}{2d_1}e^{\lambda t} \\ \frac{c\lambda}{d_1}\cos\omega t & \frac{\lambda}{d_2}\sin\omega t & -\frac{c}{d_2}\sin\omega t & -\frac{1}{d_1}\cos\omega t \\ \frac{c\lambda}{d_1}\sin\omega t & -\frac{\lambda}{d_2}\cos\omega t & \frac{c}{d_2}\cos\omega t & -\frac{1}{d_1}\sin\omega t \end{bmatrix} \cdot \begin{Bmatrix} \xi \\ \eta \\ \dot{\xi} \\ \dot{\eta} \end{Bmatrix} \tag{3.106}$$

and

$$\begin{Bmatrix} A_5 \\ A_6 \end{Bmatrix} = \begin{bmatrix} \cos\nu t & -\frac{1}{\nu}\sin\nu t \\ \sin\nu t & \frac{1}{\nu}\cos\nu t \end{bmatrix} \cdot \begin{Bmatrix} \zeta \\ \dot{\zeta} \end{Bmatrix}, \tag{3.107}$$

where, $d_1 = c\lambda - k\omega$ and $d_2 = c\omega + k\lambda$. This analytical formulation has the advantage of studying the motion of the spacecraft in the phase space.

3.8.2 Differential correction

Besides the semi-analytical methods, the computation of periodic or quasi-periodic orbits can be achieved using a numerical method. This numerical method is known as *Differential Correction*. This method uses an analytical approximation as a first guess and it produces the initial conditions that belongs to the LPOs through an iterative numerical computation. The differential correction, also known as shooting method,

uses a process of targeting to find the LPO. The LPO trajectory is indicated as $\bar{\boldsymbol{X}}(t)$, which is the reference trajectory. Thus, starting from an initial state $\bar{\boldsymbol{X}}(t_0)$ the aim is to reach the final state $\bar{\boldsymbol{X}}(t_1)$ under the effect of the natural dynamics in Eq. (3.39). This can be done by adjusting the initial state, $\bar{\boldsymbol{X}}(t_0)$, through small variations, $\delta\bar{\boldsymbol{X}}(t_0)$, such that the corrected trajectory will reach the desired state, $\bar{\boldsymbol{X}}(t_d)$, close to $\bar{\boldsymbol{X}}(t_1)$. The differential correction is essentially a modified version of the Newton method, that aims to find the zero of a function by changing the initial conditions (Koon et al., 2008). The Eq. (3.39) can be written in a compact way such as:

$$\dot{\boldsymbol{X}} = f(\boldsymbol{X}). \tag{3.108}$$

In Eq. (3.108), the trajectories with $\boldsymbol{X}(t_0) = \boldsymbol{X}_0$ can be indicated as $\Phi(t, t_0)$; where, $\Phi(t, t_0) : \boldsymbol{X}_0 \rightarrow \boldsymbol{X}(t_1)$ is the *flow map* of the dynamical system in Eq. (3.108) and is indicated as $\Phi(t; \boldsymbol{X}_0)$. The flow map tracks the evolution of a small set of initial conditions at time, t_0, to their location at time, t and it satisfies the equations of motion such as:

$$\dot{\Phi}(t; \boldsymbol{X}_0) = f(\Phi(t; \boldsymbol{X}_0)) \qquad \text{with} \qquad \Phi(t_0; \boldsymbol{X}_0) = \boldsymbol{X}_0. \tag{3.109}$$

A trajectory $\bar{\boldsymbol{X}}(t)$ that starts from a perturbed initial condition such as $\bar{\boldsymbol{X}}_0 + \delta\bar{\boldsymbol{X}}_0$ at time t_0 will evolve as:

$$\delta\bar{\boldsymbol{X}}(t) = \Phi(t; \bar{\boldsymbol{X}}_0 + \delta\bar{\boldsymbol{X}}_0) - \Phi(t; \bar{\boldsymbol{X}}_0). \tag{3.110}$$

By measuring Eq. (3.110) at time t_1 and by expanding the right hand side in a Taylor series, we have:

$$\delta\bar{\boldsymbol{X}}(t_1) = \frac{\partial\Phi(t_1, \bar{\boldsymbol{X}}_0)}{\partial\boldsymbol{X}_0}\delta\bar{\boldsymbol{X}}_0 + O(2). \tag{3.111}$$

In Eq. (3.111) the matrix $\frac{\partial\Phi(t_1, \bar{\boldsymbol{X}}_0)}{\partial\boldsymbol{X}_0} = \boldsymbol{\Phi}(\boldsymbol{X}_0, t_1)$ is named the *State Transition Matrix* (STM) and it is indicated with the symbol $\boldsymbol{\Phi}(\boldsymbol{X}_0, t_1)$. This matrix plays an important role in the differential correction and it gives the linear relationship between initial and final variations. The STM computation is shown in Appendix C.9.

The computation of PO through a differential correction method is presented here. PO in the x-y plane shows a symmetry along the x-axis. Having a symmetry along the x-axis for a PO, means that the spacecraft crosses the x-axis twice with its velocity being parallel to the y-axis (or perpendicular to the x-axis). It is possible to solve half of the problem of generating the entire orbit, by adjusting the initial condition ($\boldsymbol{X}_0$) for reaching the final condition ($\boldsymbol{X}_1$) state after half a period, $t_1 = T/2$. The state vector for a planar orbit is defined such that $\boldsymbol{X}(t) = \{x(t), y(t), \dot{x}(t), \dot{y}(t)\}$. For the condition of a planar periodic x-axis symmetric solution, the position in y and the velocity in x should be zero at $t_0 = 0$. Then, the state vectors are respectively defined

as $\boldsymbol{X}(t_0) = \{x(t_0), 0, 0, \dot{y}(t_0)\}$ and $\boldsymbol{X}(t_1) = \{x(t_1), 0, 0, \dot{y}(t_1)\}$. The system of Eq. (3.39) turn into:

$$\begin{cases} \ddot{x} - 2\bar{\omega}\dot{y} = V_x + a_x^s \\ \ddot{y} + 2\bar{\omega}\dot{x} = V_y + a_y^s \end{cases} . \tag{3.112}$$

For numerical reasons, the system needs to be written as four first-order equations by redefining the state vector as $\boldsymbol{X} = \{x_1, x_2, x_3, x_4\} = \{x, y, \dot{x}, \dot{y}\}$ or more simply $\boldsymbol{X} = \{x_1, x_2, x_3, x_4\} = \{x, y, v_x, v_y\}$; thus, Eq. (3.112) turns into:

$$\begin{cases} \dot{x}_1 = x_3 \\ \dot{x}_2 = x_4 \\ \dot{x}_3 = 2x_4 + \frac{\partial V}{\partial x_1} + \frac{\partial \boldsymbol{a}^s}{\partial x_1} \\ \dot{x}_4 = -2x_3 + \frac{\partial V}{\partial x_2} + \frac{\partial \boldsymbol{a}^s}{\partial x_2} \end{cases} . \tag{3.113}$$

The system in Eq. (3.113) can be represented in the compact form as in Eq. (3.112). The STM is the solution of the differential equation as shown in Appendix C.9. For a planar, symmetric and periodic orbit, the initial value of $\boldsymbol{X}$ is set to $\{x, 0, 0, v_y\}$. After half a period, $\Phi(\boldsymbol{X}, T_{1/2}) = \{\tilde{x}, 0, \tilde{v}_x, \tilde{v}_y\}$; the correction procedure should ensure that $\tilde{v}_x = 0$. The differential correction changes the initial value of $\boldsymbol{X}$ in terms of velocity v_{y_0}, with fixed initial position x_0, until the algorithm converges to a final null velocity ($v_{x_1} = 0$) at $T/2$. This is done through:

$$\Phi(\boldsymbol{X} + \Delta\boldsymbol{X}, T_{1/2} + \Delta T) = \Phi(\boldsymbol{X}, T_{1/2}) + \left[\frac{\partial \boldsymbol{\Phi}(\boldsymbol{X}, T_{1/2})}{\partial \boldsymbol{X}}\right] \Delta\boldsymbol{X} + \frac{\partial \Phi(\boldsymbol{X}, T_{1/2})}{\partial t}\Delta t. \tag{3.114}$$

Since the choice is restricted to the initial condition, where $\Delta\boldsymbol{X} = \{\Delta x, 0, 0, \Delta v_y\}$, and, having fixed the initial condition in x, $\Delta x = 0$ was imposed. Then, this provides the velocity along y-axis,

$$\Delta v_y = -(\phi_{34} - \frac{f_3\phi_{24}}{f_2})^{-1}\tilde{v}_x, \tag{3.115}$$

and the $T/2$ value. Finally, the initial value of $\boldsymbol{X}$ is modified as follow at every new iteration:

$$\boldsymbol{X}^{i+1} = \boldsymbol{X}^i + \Delta\boldsymbol{X} = \begin{Bmatrix} x^i \\ 0 \\ 0 \\ v_y^i \end{Bmatrix} + \begin{Bmatrix} 0 \\ 0 \\ 0 \\ \Delta v_y \end{Bmatrix}. \tag{3.116}$$

A complete derivation of this algorithm is reported in the Appendix C.10, and can be found in: Koon et al. (2008); Stramacchia et al. (2016); Thurman and Worfolk (1996). This algorithm is useful when generating POs within the same family; however, when studying the interaction within different families, it seems more convenient to write a differential correction algorithm by fixing the energy (E_0) instead of the position (x_0). The derivation of this modified differential correction algorithm can be found in Appendix C.11; only the final results are shown here. In this new differential correction algorithm, the derivative of the energy formulation, Eq. (3.79) is added to Eq. (3.113).

As before, the choice of the initial condition is restricted to $\Delta \boldsymbol{X} = \{\Delta x, 0, 0, \Delta v_y\}$ by fixing the initial energy E ($\Delta E = 0$), so, at the end, this will provide the initial position Δx and velocity Δv_y. Then, at every new iteration the initial guess is modified as follow:

$$\boldsymbol{X}^{i+1} = \boldsymbol{X}^i + \Delta \boldsymbol{X} = \begin{Bmatrix} x^i \\ 0 \\ 0 \\ v_y^i \\ E^i \end{Bmatrix} + \begin{Bmatrix} 0 \\ 0 \\ 0 \\ \Delta v_y \\ \Delta E \end{Bmatrix}. \tag{3.117}$$

3.9 Numerical continuation

The numerical continuation is needed when generating families of periodic orbits. Usually, the families of periodic orbits are designed by progressively increasing their amplitude, by perturbing the previous PO initial conditions (Koon et al., 2008). Therefore, a small variation in the initial conditions are allowed since not any set of initial solutions converge when corrected with the differential correction method. However, the main subject of this work is not to generate families of POs, but to design and control unstable trajectories among and from them.

For the design of POs such as family-g and -a (introduced in Section 2.2.1), the initial guess solution of one PO of family-g given by Hénon (1968) was used. Then it was adjusted with the differential correction by imposing $\beta = 0$ and the in-plane angle equal to 0°. At this point, β was increased, keeping the spacecraft Sun-pointing and the previously corrected solution was used to generate the new orbit. This numerical continuation is based on slightly increasing β and using the previous PO's corrected solution as the initial guess. In this way, it was possible to compute the PO by introducing the SRP acceleration. The same principle was used for halo orbits under the effect of SRP.

3.10 Orbit stability

In this section, the stability of POs was analysed. Therefore, a stability criteria should be defined. The two tools commonly used for testing the stability of LPOs are the stability index, k, which is an analytical approach (Broucke, 1968), and the Poincaré section which is a numerical method (Koon et al., 2008).

The stability index is defined from the eigenvalues of the *Monodromy Matrix*, $\boldsymbol{M}$, that is the STM evaluated after one orbital period, T, as shown in Appendix C.9. The study of the stability of the eigenvalues of $\boldsymbol{M}$ gives information about the overall orbit's stability. For a planar PO, four eigenvalues of $\boldsymbol{M}$ exists; while, for halo obits there are six eigenvalues. The stability index is only an approximation of the stability condition,

which is less accurate when the eigenvalues of the monodromy matrix are large. The state transitional matrix, $\boldsymbol{\Phi}(\boldsymbol{X}_0, t)$, for a PO can be computed numerically by integrating the linearised equations (Appendix C.9) along one orbital period, T. The monodromy matrix of an autonomous Hamiltonian system has the characteristic of being symplectic; therefore, if λ and $\bar{\lambda}$ are eigenvalues of M, also their inverse λ^{-1} and $\bar{\lambda}^{-1}$ are eigenvalues of $\boldsymbol{M}$. Moreover, for a planar orbit in the CR3BP-SRP, one pair of eigenvalues are equal to unity ($\lambda_1 = \lambda_2 = \bar{\lambda} = 1$), and the other pair are real ($\lambda_3 = \lambda > 1$ and $\lambda_4 = 1/\lambda_3 = 1/\lambda$). The stability index, k, can now be computed numerically as (Broucke, 1968):

$$k = tr(\boldsymbol{M}) - 2 \simeq \lambda + \frac{1}{\lambda}.^{8} \tag{3.118}$$

The PO is stable if k is within the range of ± 2. When studying the eigenvalues and eigenvectors of the monodromy matrix, we are looking at the stability of an orbit perturbed in its initial conditions (Deprit and Henrard, 1967). This is the reason why the stability index is only an approximation of the stability for large eigenvalues.

A numerical method to study the PO stability is through the Poincaré section. The equations of motion are numerically integrated for several orbital periods (from $t_0 = 0$ to $t_1 = q \cdot T$, with q real). Then, the intersection of the trajectory with the $y = 0$ plane is recorded at the chosen, Poincaré section as shown in Figure 3.19. For every orbital period, if the spacecraft passes through the neighbourhood of the initial condition, then the orbit remains stable. If instead the solution diverges from the original condition the PO is unstable. In this thesis, both the stability index and the numerical method have been used when verifying the PO stability.

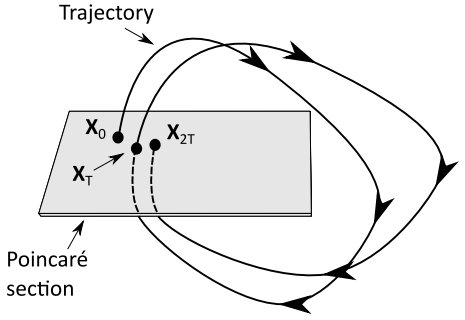

Figure 3.19: Qualitative picture of the Poincaré section. X_0, X_T and X_{2T} are the intersections of the trajectory with the Poincaré section at the initial condition, after one period, T, and after two periods, $2T$.

[8] tr($\boldsymbol{M}$) is the trace of the monodromy matrix, and it is defined as: $tr(\boldsymbol{M}) = \lambda_1 + \lambda_2 + \lambda_3 + \lambda_4 = 1 + 1 + \lambda + \frac{1}{\lambda}$, where $\lambda > 1$

3.11 Computation of the invariant manifolds associated to periodic orbits

The direction of the stable and unstable manifolds are given by the eigenvalues and the eigenvectors of the monodromy matrix (Koon et al., 2008). Having previously discussed the structure of the eigenvalues in Section 3.10, now the focus is on the computation of the eigenvectors of the stable, $Y^s(\lambda_4)$ and unstable, $Y^u(\lambda_3)$ directions. Thus, it is possible to compute the stable, Eq. (3.119), and unstable, Eq. (3.120), manifolds as follow:

$$X^s(X_0) = X_0 + \epsilon Y^s(X_0) \tag{3.119}$$

and,

$$X^u(X_0) = X_0 + \epsilon Y^u(X_0), \tag{3.120}$$

where, X_0 is the initial condition of the integration, i.e., the state vector along the PO. Then, the state vectors X^s and X^u are used as the initial condition for the integration of the non-linear dynamics which gives the manifold trajectories. Moreover, ϵ is a small perturbation from X_0. Gómez et al. (2001) suggests a value of ϵ around 10^{-6}, which corresponds to a displacement error in the spacecraft's position of 200 km. For a generic starting point along the orbit, the stable and unstable manifolds can be computed as:

$$X^s(X_{orbit}(t)) = X_{orbit}(t) \pm \epsilon \frac{Y^s(X(t))}{||Y^s(X(t))||} \tag{3.121}$$

and,

$$X^u(X_{orbit}(t)) = X_{orbit}(t) \pm \epsilon \frac{Y^u(X(t))}{||Y^s(X(t))||}. \tag{3.122}$$

In Eq. (3.121) and Eq. (3.122), $Y^s(X(t))$ and $Y^u(X(t))$ should be normalised since the state transition matrix does not preserve the norm. In this case, $Y^s(X_0)$ and $Y^u(X_0)$ are the stable and unstable eigenvectors of the monodromy matrix at $t_0 + T$, thus:

$$X^s(X(t)) = X_{orbit}(t) \pm \epsilon \frac{\Phi(\boldsymbol{X}_0, t) Y^s(X_0)}{||\Phi(\boldsymbol{X}_0, t) Y^s(X_0)||} \tag{3.123}$$

and,

$$X^u(X(t)) = X_{orbit}(t) \pm \epsilon \frac{\Phi(\boldsymbol{X}_0, t) Y^u(X_0)}{||\Phi(\boldsymbol{X}_0, t) Y^u(X_0)||}. \tag{3.124}$$

For the numerical computation of the unstable vector in Eq. (3.124), a forward integration in time for both $+\epsilon$ and $-\epsilon$ is required. Whereas, in the case of the stable vector in Eq. (3.123), a backwards integration in time for both $\pm\epsilon$ is needed. Therefore, the manifolds are found by integrating forward and backward $X^u(X(t_i))$ and $X^s(X(t_i))$; where $X(t_i)$ is the state vector along the periodic orbit.

The manifolds are an essential tool for the feedback Hamiltonian structure preserving control (see Chapter 5), the design of transfers (see Chapter 6) and for the end-of-life disposal (see Chapter 7). These techniques are enhanced by SRP acceleration and exploit the natural dynamics of the libration points.

3.12 Summary

This chapter has been devoted to presenting the dynamical model in the circular restricted three-body problem, with particular attention to the solar radiation pressure modelling and the conversions adopted. This chapter has also presented numerical dynamical system tools that are used throughout the thesis:

- Two methods to design the spacecraft's target orbit were presented: a semi-analytical approach and a numerical method. The semi-analytical approach is adopted to design transfer trajectories within the Sun-Earth system (Chapter 6); while a numerical method is chosen to design the target LPO for orbit control (Chapter 5), and for the end-of-life disposal (Chapter 7);
- The semi-analytical approach for the design of quasi-periodic orbits was presented here for a special case where the spacecraft is Sun-pointing. A good understanding of the Sun-pointing solution is necessary to comprehend the derivation of a spacecraft with a general orientation. The general solution for complex roots that corresponds to equilibrium points displaced in the y-axis will be presented in Chapter 6;
- The computation of the invariant manifolds associated to the periodic orbit is a fundamental tool for the design of low-energy manoeuvres (Chapter 5-7);
- The study of the stability of libration points under the influence of solar radiation pressure affects the motion of the spacecraft and it is exploited for the spacecraft's trajectories control and design. For example, Chapter 5 makes use of the monodromy matrix and its stability properties for the design of the Hamiltonian-structure preserving control;
- The stability of periodic orbit is widely used as an indicator of the control law performance, Chapter 5;
- The zero-velocity curves are a useful dynamical system tool that is used in this thesis for the design of the spacecraft's end-of-life disposal, 7.

An understanding of these tools is, therefore, an essential foundation for detailed work presented in the following chapters.

A natural extension of the CR3BP is the elliptic restricted three-body problem. The ER3BP includes the effect of the Earth's orbit eccentricity onto the spacecraft's dynamics. This represents a further more accurate model compared with the CR3BP. The ER3BP shares the same principles of the CR3BP where the major differences between the two approximations need to be further explored in next chapter.

Chapter 4

Elliptic Restricted Three-Body Problem

The elliptic restricted three-body problem is a natural extension of the circular restricted three-body problem, where the effect of the Earth's orbit eccentricity is taken into account. In this model, the motion of the Sun and Earth+Moon has an elliptic orbit in the two-body problem; thus, the angular velocity is no longer a constant (Szebehely, 1967). When the effect of solar radiation pressure is taken into account, the ER3BP becomes the ER3BP-SRP.

In this chapter, particular attention is given to the definition of the reference frames, the conversion from dimensional inertial coordinates (sidereal reference frame) to rotating dimensionless coordinates (synodic reference frame) and in the approximation of the zero velocity curves.

The major research contributions of this chapter are section listed:

- Section 4.3.1 shows the analytical expression of the energy associated to the libration points for a Sun-pointing spacecraft,
- Section 4.4.2 presents the definition of surface of minimum energy extended for a Sun-pointing spacecraft,
- Section 4.4.3 demonstrates that the approximation made with the surface of minimum energy is different from minimising the integral of the extra energy effect associated to the Earth orbit eccentricity, and
- Section 4.4.4 compares different approximations of the zero-velocities curves for the elliptic dynamics available in literature by giving and insight of the zero velocity curves behaviour with the spacecraft's dynamics.

Section 4.3.1, Section 4.4.2, Section 4.4.3 and Section 4.4.4 are part of an under review publication (Soldini et al., 2015b).

4.1 Reference frames

In the case of the elliptic problem, it is necessary to define three reference frames to describe the motion of the spacecraft: the sidereal (inertial) frame, the synodic (rotating) frame, where now the angular velocity is not uniform, and a perifocal (orbit) reference frame. Both the sidereal and the synodic reference frames were already introduced in Figure 3.1 in Section 3.1; while, the perifocal reference frame was presented in Chapter 2 and in Appendix B.1.

4.1.1 Conversion from the dimensional sidereal to the dimensionless synodic coordinates

The rotation matrix between the sidereal and perifocal reference frames is necessary when starting from a set of initial conditions expressed in the sidereal reference frame (i.e. spacecraft's ephemeris). Starting from the spacecraft's ephemeris available from Horizon (the NASA on-line spacecraft trajectory catalogue) expressed in the sidereal reference frame, a conversion is needed to describe the spacecraft's position and velocity in the synodic reference frame. A rotation is first required to change the coordinates from the sidereal to the perifocal reference frame as shown in Figure B.1 of Appendix B.1. The second rotation is then needed to move from the perifocal to the synodic reference frame, where the synodic reference frame rotates around the $\boldsymbol{h}$-axis with a rotation angle equal to the true anomaly angle, f (defined in Appendix B.1).

The two rotations involved are derived here, where the rotation matrix from a perifocal reference frame to a rotating reference frame is:

$$\boldsymbol{C}_2 = \begin{bmatrix} \cos(f) & \sin(f) & 0 \\ -\sin(f) & \cos(f) & 0 \\ 0 & 0 & 1 \end{bmatrix}, \tag{4.1}$$

and the rotation matrix from an inertial reference frame to a perifocal reference frame is:

$$\boldsymbol{C}_1 = \begin{bmatrix} c(\Omega)c(\omega) - s(\Omega)s(\omega)c(i) & s(\Omega)c(\omega) + c(\Omega)s(\omega)c(i) & s(\omega)s(i) \\ -c(\Omega)s(\omega) - s(\Omega)c(\omega)c(i) & -s(\Omega)s(\omega) + c(\Omega)c(\omega)c(i) & c(\omega)s(i) \\ s(\Omega)s(i) & -c(\Omega)s(i) & c(i) \end{bmatrix};^{1} \tag{4.2}$$

[1] $s(\square)$ and $c(\square)$ denotes $\sin(\square)$ and $\cos(\square)$, respectively.

thus, the overall rotation from inertial to rotating reference frame is:

$$\mathbf{C}_{ri} = \boldsymbol{C}_2\boldsymbol{C}_1, \tag{4.3}$$

which is function of the true anomaly angle, f, of the Earth+Moon barycentre around the Sun, the longitude of the ascending node, Ω, and the argument of pericenter ω. These parameters are introduced in Appendix B.1. The derivative of the rotation matrix is then constructed as:

$$\dot{\mathbf{C}}_{ri} = \dot{\boldsymbol{C}}_2\boldsymbol{C}_1 + \boldsymbol{C}_2\dot{\boldsymbol{C}}_1, \tag{4.4}$$

where $\dot{\boldsymbol{C}}_2$ is defined to be:

$$\dot{\boldsymbol{C}}_2 = \begin{bmatrix} -\sin(f) & \cos(f) & 0 \\ -\cos(f) & -\sin(f) & 0 \\ 0 & 0 & 1 \end{bmatrix} \cdot \dot{f}, \tag{4.5}$$

and $\dot{\boldsymbol{C}}_1$ is defined as:

$$\dot{\boldsymbol{C}}_1 = \begin{bmatrix} c_{11} & c_{12} & c_{13} \\ c_{21} & c_{22} & c_{23} \\ c_{31} & c_{32} & c_{33} \end{bmatrix}. \tag{4.6}$$

The components of Eq. (4.6) are specified as follows:

$$\begin{aligned}
c_{11} = \;& -s(\Omega)c(\omega)\dot{\Omega} - c(\Omega)s(\omega)\dot{\omega} - c(\Omega)s(\omega)c(i)\dot{\Omega} - s(\Omega)c(\omega)c(i)\dot{\omega} + s(\Omega)s(\omega)s(i)\dot{i}, \\
c_{12} = \;& c(\Omega)c(\omega)\dot{\Omega} - s(\Omega)s(\omega)\dot{\omega} - s(\Omega)s(\omega)c(i)\dot{\Omega} + c(\Omega)c(\omega)c(i)\dot{\omega} - c(\Omega)s(\omega)s(i)\dot{i}, \\
c_{13} = \;& c(\omega)s(i)\dot{\omega} + s(\omega)c(i)\dot{i}, \\
c_{21} = \;& s(\Omega)s(\omega)\dot{\Omega} - c(\Omega)c(\omega)\dot{\omega} - c(\Omega)c(\omega)c(i)\dot{\Omega} + s(\Omega)s(\omega)c(i)\dot{\omega} + s(\Omega)c(\omega)s(i)\dot{i}, \\
c_{22} = \;& -c(\Omega)s(\omega)\dot{\Omega} - s(\Omega)c(\omega)\dot{\omega} - s(\Omega)c(\omega)c(i)\dot{\Omega} - c(\Omega)s(\omega)c(i)\dot{\omega} - c(\Omega)c(\omega)s(i)\dot{i}, \\
c_{23} = \;& -s(\omega)s(i)\dot{\omega} + c(\omega)c(i)\dot{i}, \\
c_{31} = \;& c(\Omega)s(i)\dot{\Omega} + s(\Omega)c(i)\dot{i}, \\
c_{32} = \;& s(\Omega)s(i)\dot{\Omega} - c(\Omega)c(i)\dot{i}, \\
c_{33} = \;& -s(i)\dot{i},
\end{aligned} \tag{4.7}$$

where, $\dot{\omega}$, $\dot{i}$ and $\dot{\Omega}$ are the angular velocities of the argument of pericenter, ω, the inclination, i, and the ascending node, Ω, respectively. ω, i and Ω are angles measured in radians and are defined in Appendix B.1.

Starting from an orbit described in the sidereal reference frame in dimensional coordinates ($\boldsymbol{r}_i$) it is possible to find the correspondent non-dimensional coordinates in the ER3BP-SRP synodic reference frame ($\boldsymbol{r}$) as follows. The pulsating and dimensionless positions in the rotating reference frame are:

$$\boldsymbol{r} = \mathbf{C}_{ri}\frac{\boldsymbol{r}_i}{r}, \tag{4.8}$$

where, $\boldsymbol{r}_i$ are the dimensional sidereal coordinates and r is defined in Eq. (B.1) of Appendix B.1. For small inclinations of the ecliptic on the order of 10^{-6} radians, the rotational matrix is defined as:

$$\boldsymbol{C}_{ri} = \begin{bmatrix} \cos(f+\Omega+\omega) & \sin(f+\Omega+\omega) & 0 \\ -\sin(f+\Omega+\omega) & \cos(f+\Omega+\omega) & 0 \\ 0 & 0 & 1 \end{bmatrix}. \tag{4.9}$$

The velocity expressed in the synodic reference frame is given by deriving Eq. (4.8) as (Goméz et al., 1991):

$$\dot{\boldsymbol{r}} = \mathbf{C}_{ri}\frac{\dot{\boldsymbol{r}}_i}{r} + \dot{\mathbf{C}}_{ri}\frac{\boldsymbol{r}_i}{r} + \mathbf{C}_{ri}\boldsymbol{r}_i\frac{d}{dt}\frac{1}{r}, \tag{4.10}$$

where, the derivative of the rotating matrix, $\dot{\mathbf{C}}_{ri}$, is:

$$\dot{\boldsymbol{C}}_{ri}(t) = \begin{bmatrix} -\sin(f+\Omega+\omega) & \cos(f+\Omega+\omega) & 0 \\ -\cos(f+\Omega+\omega) & -\sin(f+\Omega+\omega) & 0 \\ 0 & 0 & 0 \end{bmatrix} \cdot \left(\dot{f}+\dot{\Omega}+\dot{\omega}\right). \tag{4.11}$$

In the case analysed, the variation of Ω and ω due to perturbations are very small so their derivatives can be ignored. The derivative in f must be considered and $\dot{f}$ can be defined starting from the actual angular velocity of the Sun-(Earth+Moon) system and is described in the ephemeris model as:

$$\boldsymbol{\omega} = \frac{\boldsymbol{r}_{EM-Sun} \times \boldsymbol{v}_{EM-Sun}}{\| \boldsymbol{r}_{EM-Sun} \|^2} \tag{4.12}$$

where, $\boldsymbol{r}_{EM-Sun}$ and $\boldsymbol{v}_{EM-Sun}$ are the Earth+Moon's distance and velocity with respect to the Sun viewed from an inertial reference frame.

$\dot{f}$ is approximated with the third component of $\boldsymbol{\omega}$ in Eq. (4.12) as:

$$\dot{f} = \omega_z. \tag{4.13}$$

In the ER3BP approximation, the Sun and the Earth+Moon belongs to the x_i-y_i sidereal and x-y synodic reference planes where the z_i-axis is parallel to the z-axis. Thus, the two frames rotates with angular velocity, $\boldsymbol{\omega} = \left\{0, 0, \dot{f}\right\}$, along the z_i-axis, defined as in

Eq. (4.13). In general, the Sun and the Earth+Moon orbit plane shows an inclination, i, with respect to the inertial reference plane (Appendix B.1) where Eq. (4.12) gives the angular velocity as viewed from the inertial frame of the NASA's ephemeris model. The ER3BP approximation uses Eq. (4.13) to propagate the spacecraft's dynamics where ω_z is computed from the third component of Eq. (4.12).

Given the initial conditions in the pulsating coordinates, the dynamics are then propagated using the angular velocity given by Kepler's third law which is (Battin, 1978):

$$\dot{f} = \frac{h}{r^2} = \frac{\mu^{\frac{1}{2}}(1 + e\cos f)^{\frac{1}{2}}}{a^{\frac{3}{2}}(1-e^2)^{\frac{3}{2}}}, \tag{4.14}$$

where, h is the angular momentum, μ is $G \cdot (M_{Sun} + m_{Earth+Moon})$ and G is the constant of gravitation. In Eq. (4.14), a is the semi-major axis and e is the orbit eccentricity (see Appendix B.1). The derivative of the dimensionless coordinate in Eq. (4.10) is:

$$\frac{d}{dt}\frac{1}{r} = -\frac{a(1-e^2)e\sin f\dot{f}}{(1+e\cos f)^2 r^2}. \tag{4.15}$$

Thus, the velocity transformation in Eq. (4.10) can be written as:

$$\dot{\boldsymbol{r}} = \mathbf{C}_{ri}\frac{\dot{\boldsymbol{r}}_i}{r} + \dot{\mathbf{C}}_{ri}\frac{\boldsymbol{r}_i}{r} - \mathbf{C}_{ri}\boldsymbol{r}_i\frac{a(1-e^2)e\sin f\dot{f}}{(1+e\cos f)^2 r^2}. \tag{4.16}$$

The equations of motion in the ER3BP are written in a non-dimensional, non-uniformly rotating (synodic reference frame) and pulsating frame in which the equations of motion have the simplest form. The pulsating coordinates have the advantage of keeping fixed the positions of the Sun and the Earth+Moon as viewed from a synodic reference frame. Thus, the spacecraft's position and velocity are now functions of f. When using a pulsating reference frame, the derivative of the position with respect to f is required. In order to have derivatives with respect to f, it is necessary to define $\dot{f}$ as shown in Eq. (4.14) and derive them through the *inverse function rule*. By using the Leibniz's notation, the derivatives are:

$$\frac{d\boldsymbol{r}}{df} = \boldsymbol{r'} = \frac{d\boldsymbol{r}}{dt}\frac{1}{df/dt}. \tag{4.17}$$

The symbol $\square'$ denotes the derivation with respect to the true anomaly while $\dot{\square}$ denotes the derivation with respect to the time. The velocity in pulsating coordinates is then:

$$\boldsymbol{r'} = \mathbf{C}_{ri}\frac{\dot{\boldsymbol{r}}_i}{r\dot{f}} + \dot{\mathbf{C}}_{ri}\frac{\boldsymbol{r}_i}{r\dot{f}} - \mathbf{C}_{ri}\boldsymbol{r}_i\frac{a(1-e^2)e\sin f}{(1+e\cos f)^2 r^2}. \tag{4.18}$$

As a test case, the ephemeris of the Gaia spacecraft in a sidereal reference frame in dimensional coordinates (Alessi et al., 2014) was transformed to synodic non-dimensional

coordinates in the osculating R3BP (Goméz et al., 1991; Colombo et al., 2014c). This full body transformation is compared to the one in the ER3BP explained above in Figure 4.1. The two solutions were compared when the spacecraft performs one year of its orbit from 1/4/2019 to 1/4/2020. It is important to note that the ER3BP-SRP is a good approximation of the high fidelity model as shown for Gaia's positions and velocities, displayed in Figures 4.2(a) and 4.2(b) respectively.

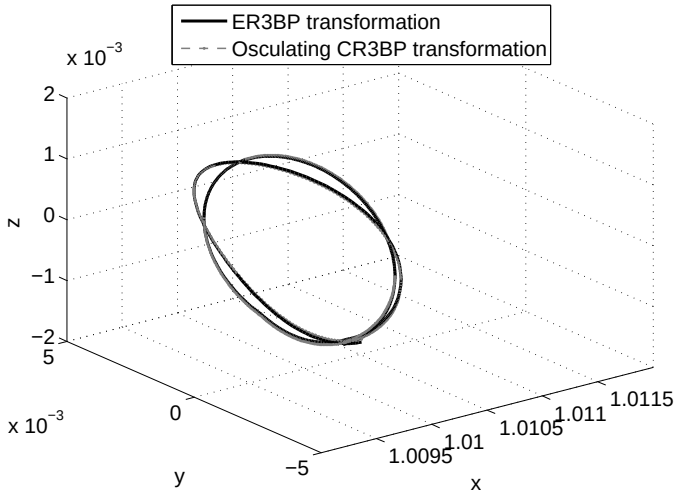

Figure 4.1: Gaia orbit in a synodic reference frame from 1/4/2019 to 1/4/2020: Sun-(Earth+Moon) barycentre. The black continuous line is the trajectory after the transformation to the ER3BP, while the dashed gray line is the one in the osculating CR3BP.

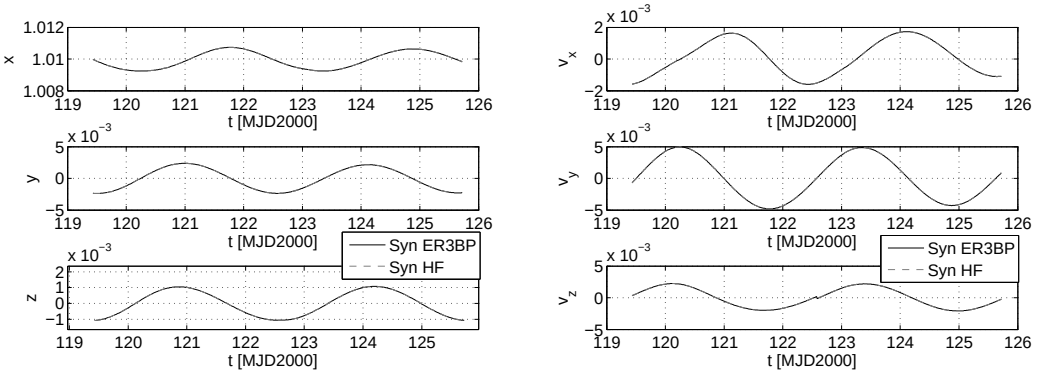

(a) Gaia's positions along the nominal LPO.

(b) Gaia's velocities along the nominal LPO.

Figure 4.2: Comparison of the ephemeris and ER3BP models of Gaia's state vectors in a synodic reference frame from 1/4/2019 to 1/4/2020: Sun-(Earth+Moon) barycentre.

4.2 Equations of motion for a Sun-pointing reflective structure

The dynamics of the ER3BP, with the effect of solar radiation pressure for a Sun-pointing reflective surface are written in a non-dimensional, non-uniformly rotating and pulsating reference frame (Szebehely and Giacaglia, 1964; Baoyin and McInnes, 2006), where as said the motion of the Earth+Moon around the Sun is described by an ellipse under the two-body problem approximation in Eq. (B.1).

The equations of motion for the non-dimensional synodic frame are (Luk'yanov, 2005):

$$\begin{cases} x'' - 2y' = \Omega_x \\ y'' + 2x' = \Omega_y \\ z'' = \Omega_z \end{cases} \tag{4.19}$$

where, x, y and z are the spacecraft's coordinates (non-dimensional) in the synodic frame centred at the Sun-(Earth+Moon) barycentre. Ω is the total potential function of the reference frame defined as:

$$\Omega = \frac{1}{(1 + e\cos f)} \left[\frac{1}{2}(x^2 + y^2 - ez^2 \cos f) + V \right], \tag{4.20}$$

where, V is the potential of the gravitational effect and of SRP and it is defined as in Eq. (3.40). As shown in Eq. (3.40), for a Sun-pointing deployable structure, V is defined as:

$$V = (1 - \beta)\frac{\mu_{Sun}}{r_{Sun-p}} + \frac{\mu_{Earth}}{r_{Earth-p}}. \tag{4.21}$$

In Eq. (4.21), r_{Sun-p} and $r_{Earth-p}$ are defined in Eq. (3.43) and Eq. (3.44), respectively. μ_{Sun}, μ_{Earth} and β were previously defined for the CR3BP in Section 3.4.2. The full derivation of the equations of motion in Eq. (4.19) is given in Appendix D.

Moreover, the transformation that converts dimensional coordinates ($\boldsymbol{r}_d$ [km] and $\dot{\boldsymbol{r}}_d$ [km s^{-1}]) in the synodic frame from the non-dimensional pulsating coordinates ($\boldsymbol{r}$ [ ] and $\boldsymbol{r}'$ [ ]) in the synodic frame is given by

$$\begin{cases} \boldsymbol{r}_d = \boldsymbol{r} \cdot r \\ \dot{\boldsymbol{r}}_d = \boldsymbol{r}' \cdot r\dot{f} + \boldsymbol{r} \cdot \dot{r} \end{cases} . \tag{4.22}$$

In Eq. (4.22) the dot represents the derivative with respect to time.

The position of the pseudo libration points for a Sun-pointing reflective area in the ER3BP-SRP is given from Eq. (4.19) by setting the velocities and accelerations equal to zero. The five equilibrium points in the ER3BP-SRP expressed in pulsating coordinates have the same coordinates of the one in the CR3BP-SRP (Szebehely and Giacaglia, 1964); thus, the equations found in the CR3BP-SRP still holds for the ER3BP-SRP. The reason for the invariance of the position of the libration points in the synodic reference frame is that in Eq. (4.19), when the velocities and accelerations are zero, it is possible to separate the variables as a function of the true anomaly from the other variables (Szebehely and Giacaglia, 1964).

Figure 4.3 shows a trajectory for the Gaia spacecraft associated to the unstable invariant manifold that leaves the operational LPO when the Earth+Moon is at the pericenter with the Sun and integrating Eq. (4.19) for 15.7 years. From this figure, it can be seen that there is a periodicity in the trajectory as the spacecraft returns close to the Earth every 15.7 years (for this particular trajectory leg). The spacecraft's position in correspondence of when the Earth+Moon barycentre is at their pericenter (circle) or apocenter (star) is also shown along the trajectory.

4.3 Orbital energy with the effect of the Earth's orbit eccentricity

In Chapter 2, it was mentioned that the dynamics of the ER3BP-SRP does not allow the use of the Jacobi integral due to the non-autonomous nature of the equations of motion (Szenkovits et al., 2004; Luk'yanov, 2005; Campagnola et al., 2008). Thus, the total energy, E, in the ER3BP-SRP is a function of the initial true anomaly angle of the Earth+Moon around the Sun, f_0:

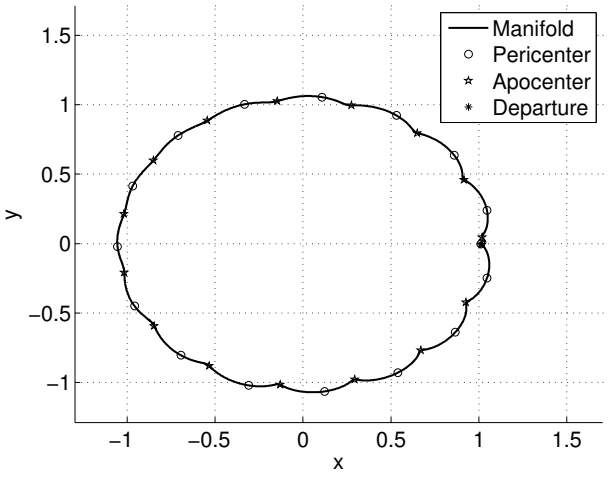

Figure 4.3: Gaia's trajectory evolution when leaving the orbit in correspondence of when the Earth+Moon are at their pericenter around the Sun and propagating for 15.7 years.

$$E(f_0, \boldsymbol{x}(f_0), f, \beta_0) = \frac{1}{2}v^2 - \Omega + I \tag{4.23}$$

where, $v^2 = x'^2 + y'^2 + z'^2$ and W is:

$$W = (x^2 + y^2 + z^2)/2 + V. \tag{4.24}$$

The total energy is function of the integral, I:

$$I = \int_{f_0}^{f} \frac{e \sin f}{(1 + e\cos f)^2} W df, \tag{4.25}$$

and of the relative energy $E_r = \frac{1}{2}v^2 - \Omega$. Thus, the total energy can be rewritten as:

$$E(f_0, \boldsymbol{x}(f_0), f, \beta_0) = E_r + I. \tag{4.26}$$

As demonstrated by Luk'yanov (2005), the total energy is conserved along a selected trajectory. Indeed, having fixed f_0 that is the true anomaly of Earth+Moon around the Sun where the spacecraft is injected into an unstable leaving trajectory associated to the LPO, the energy stays constant along the trajectory since the state vector of the spacecraft in Eq. (4.23) is a function of the true anomaly and it is the solution of Eq. (4.19). Both the relative mechanical energy, E_r, and the integral, I, oscillate along the trajectory as shown in Figure 4.4(a) and Figure 4.4(b), respectively. However, the total relative energy, E, in Eq. (4.26) remains constant.

As for the CR3BP-SRP, the zero-velocity curves for a Sun-pointing spacecraft are given by the intersection of the energy of the spacecraft with the total potential $-\Omega + I$, when in Eq. (4.23) the spacecraft's velocity, v, is set to zero. However, a unique

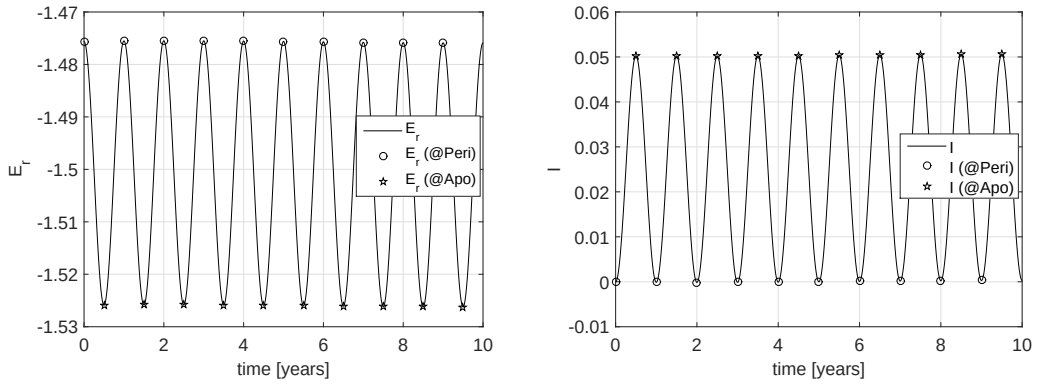

(a) Relative energy.

(b) Integral.

Figure 4.4: Variation of the relative energy and the integral along a selected trajectory.

representation of the zero-velocity curves does not exist for the ER3BP-SRP since the integral, I, cannot be solved. Instead, different approximations of I are available; which, unfortunately, do not respect the ER3BP-SRP dynamics as they show an oscillating behaviour that depends on the approximation used. This phenomenon was already pointed out by Campagnola et al. (2008); thus, it seems troubling to use approximated zero-velocity curves for the ER3BP-SRP. However, even if the zero-velocity curves cannot be represented, the energy of the spacecraft and the pseudo libration points stay constant for a fixed f_0 and it can be numerically computed. For the case of the pseudo collinear libration points, i.e. SL_2, an analytical expression of the energy at SL_i is derived in this chapter.

Figure 4.5 shows the energy of the spacecraft when injected to a leaving trajectory from the LPO (after an impulsive manoeuvre was given) as a function of the initial true anomaly of the Earth+Moon barycentre, f_0 that are the initial conditions given to generate the unstable manifold associated to the LPO. To aid the visualisation of Figure 4.5, the delta energy between the energy of L_2 and the spacecraft is shown in Figure 4.6. Note that, in Figure 4.5, the interest is in the sign of the delta energy. A negative value in the delta energy indicates that the energy of the spacecraft is greater than the energy in L_2; thus, the spacecraft is free to cross the Earth-L_2 region. The reason why the delta energy is not constant is justified as the trajectory of Gaia spacecraft was given in the ephemeris model after a Δv manoeuvre was computed to inject the spacecraft in the unstable manifold (Colombo et al., 2015b); while, the energy of L_2 is found analytically. Thus, the variation in the delta energy is due to numerical errors. However, this small error does not affect the results of this study in Chapter 7 since the spacecraft positions and velocities along the trajectory are used as initial conditions to place the spacecraft in the unstable invariant manifold.

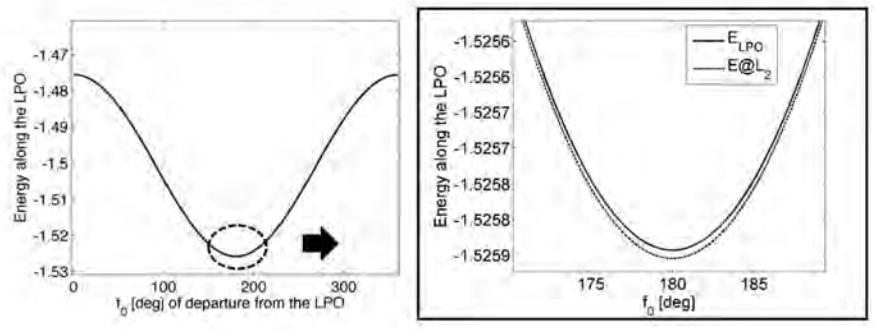

Figure 4.5: Energy of the spacecraft and of L_2 when leaving the LPO as a function of the initial true anomaly, f_0 (Earth+Moon barycentre position around the Sun).

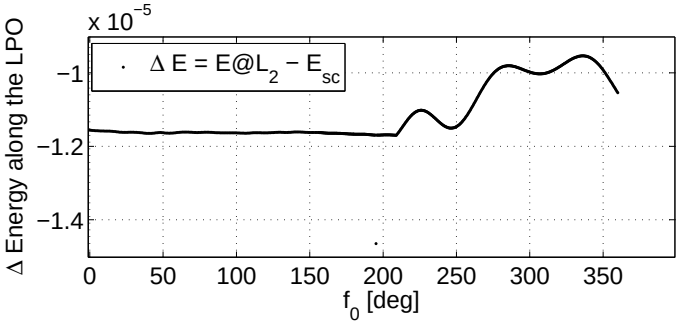

Figure 4.6: Δ energy between L_2 and the spacecraft when leaving the LPO as a function of the initial true anomaly, f_0 (Earth+Moon barycentre position).

4.3.1 Analytical expression of the collinear libration points' energy

The analytical formulation of the libration points' energy is derived in this section. The energy equation in the ER3BP-SRP for the libration points comes from Eq. (4.23) in correspondence of $\boldsymbol{x} = \boldsymbol{x}_{SL_i}$:

$$E_{SL_i}(f_0, \boldsymbol{x}_{L_i}(f_0), f, \beta_0) = -\Omega(\boldsymbol{x}_{SL_i}) + \int_{f_0}^{f} \frac{e \sin f}{(1 + e\cos f)^2} W(\boldsymbol{x}_{SL_i}) df; \tag{4.27}$$

where,

$$W(\boldsymbol{x}_{SL_i}) = \frac{1}{2} x_{SLi}^2 + V(\boldsymbol{x}_{SL_i}) \quad \text{and} \quad V(\boldsymbol{x}_{SL_i}) = (1-\beta)\frac{\mu_{Sun}}{r_{Sun-SL_i}} + \frac{\mu_{Earth}}{r_{Earth-SL_i}} \tag{4.28}$$

are constants. Thus, Eq. (4.27) turns into:

$$E_{SL_i}(f_0, \boldsymbol{x}_{SL_i}(f_0), f, \beta_0) = -\Omega(\boldsymbol{x}_{SL_i}) + W(\boldsymbol{x}_{SL_i}) \left[\frac{1}{(1 + e\cos f)} - \frac{1}{(1 + e\cos f_0)} \right]; \tag{4.29}$$

where,

$$\Omega(\boldsymbol{x}_{SL_i}) = \frac{1}{1 + ecosf} \left[\frac{1}{2} x_{SLi}^2 + V(\boldsymbol{x}_{SL_i}) \right]. \tag{4.30}$$

Thus, finally, the analytical expression of the energy of the pseudo collinear libration points is:

$$E_{SL_i}(f_0, \boldsymbol{x}_{SL_i}(f_0), f, \beta_0) = -\frac{W(\boldsymbol{x}_{SL_i})}{1 + e\cos f_0}; \tag{4.31}$$

which, is a function of f_0 and constant during the integration time.

4.4 Representation of the zero-velocity curves in the elliptic restricted three-body problem with the solar radiation pressure effect

As mentioned in Chapters 2 and 3, a closed form solution for either the circular or the elliptic restricted three-body problem dynamics does not exist, so the zero velocity curves have the remarkable advantage of giving a qualitative picture of where the spacecraft's motion can evolve. For the CR3BP, the energy is an integral of motion, known as the Jacobi constant. Therefore, the ZVCs can be easily computed as in Eq. (3.83). However, the computation of the ZVCs in the ER3BP is not straightforward due to the non-autonomous nature of the dynamics and the non-existence of an integral of motion. Szebehely (1967) showed that the difficulties of finding the ZVCs in the ER3BP are related to the integral, I, in Eq. (4.25). As can be seen from the equations of motion, Eq. (4.19), the state vector of the spacecraft is a function of the true anomaly angle. However, an explicit expression of the state vector as a function of the true anomaly

ZVCs	**Szebehely (1967)**	**Campagnola et al. (2008)**	**Luk'yanov (2005)**
PZVC	$2\Omega_S = C(1 + e\cos f)$	NA	NA
FS	NA	$\{2\Omega_C - A - C_p < 0\}$	NA
SM	NA	$\{2\Omega_C - A - C_a > 0\}$	NA
LVS	NA	$\{\ 2\Omega_C - A - C_p > 0$ and	NA
		$2\Omega_C - A - C_a < 0\}$	NA
SME	NA	NA	$C_p'(1 + e\cos f) =$
			$2\Omega(1 + e\cos f) - 2W_{min}$

Table 4.1: ZVCs approximation, where $\Omega = \Omega_C - A/2 = \Omega_S/(1 + e\cos f)$.

cannot be found. Thus, the integral, I, cannot be analytically solved but it requires an approximate solution.

In general, the definition of the ZVCs in the ER3BP is given by setting $v = 0$ in Eq. (4.23):

$$E_0 = -\Omega(\beta_0) + I(\beta_0), \tag{4.32}$$

where, $E_0 = E(f_0, \boldsymbol{x}(f_0))$ is a constant for a selected trajectory computed as a solution of the equations of motion, Eq. (4.19), for a fixed value of the initial true anomaly, f_0.

4.4.1 Approximation of the zero-velocity curves

A review was carried out to evaluate which approximation of the ZVC is the best option for studying the end-of-life of satellite in the ER3BP, Chapter 7. In the literature, important contributions were given by Szebehely (1967), Campagnola et al. (2008) and Luk'yanov (2005). These authors used different notations; thus, a comparison among different definitions is made summarised in Table 4.1. In order to make this study comparable to previous authors' work, it is important to slightly modify the definition in Eq. (4.23) by setting $E = -C/2$. The constant C recalls the Jacobi integral for the CR3BP. In this case, the effect of SRP is neglected; thus, $\beta_0 = 0$ and the ZVCs are defined as:

$$C = 2\Omega - 2I. \tag{4.33}$$

For a planar motion ($z = 0$), Szebehely (1967) proposed an approximation of the ZVCs in the ER3BP by discarding the integral, i.e., $I = 0$ in Eq. (4.33). Note that Szebehely (1967) defined a potential energy Ω_S equal to $\Omega(z = 0) \cdot (1 + e\cos f)$. Where, Ω is defined here as in Eq. (4.20) moreover, to be compared with the definition of Szebehely (1967), Ω_S, the component z in Eq. (4.20) was set to zero. Thus, the author expressed the ZVCs such as:

$$(1 + e\cos f) \cdot C = 2\Omega_S. \tag{4.34}$$

In this way, Szebehely (1967) separates the dependence of the true anomaly angle on the left hand-side of Eq. (4.34) moreover, the dependence of just the position components of the state vector at the right hand-side of Eq. (4.34). Campagnola et al. (2008) showed that the definition of the ZVCs of Szebehely (1967) can be extended for out-of-plane solutions and that, by neglecting the integral I, the ZVCs defined by Szebehely (1967) do not correctly bound the dynamics due to their high pulsating oscillatory behaviour because of the spacecraft's crossing the forbidden regions. The ZVCs of Szebehely (1967) are also known as *Pulsating Zero-Velocity Surfaces* (PZVC) due to their highly pulsating behaviour.

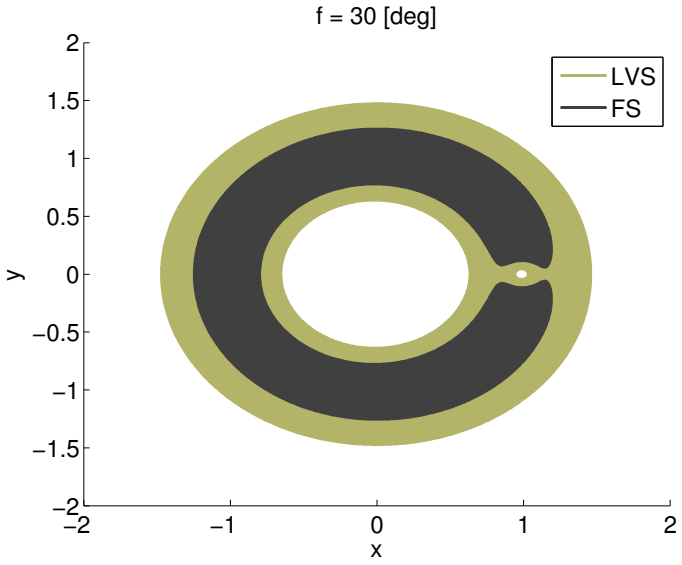

Figure 4.7: Definition of the Forbidden Subregions (FS), black area, the Low-Velocity Subregions (LVS), gray area, and the Subregions of Motion (SM), white area, for $f = 30°$. (Campagnola et al., 2008).

Campagnola et al. (2008) defined instead the *Forbidden Subregions* (FS), the *Subregions of Motion* (SM) and the *Low-Velocity Subregions* (LVS). In Figure 4.7, the FS, the SM and the LVS are given for $f = 30°$ and correspond to the black, the white and the gray area respectively. The boundaries of the ZVCs are approximated for initial conditions of the spacecraft when the Earth+Moon is at the pericenter and apocenter in correspondence of when the integral, I, is minimum and maximum respectively, as shown in Figure 4.4(b). Thus, two energy levels are set when the spacecraft has an initial condition at the Earth+Moon pericenter, $f_0 = 0$ with constant of Jacobi C_p and at the apocenter, $f_0 = \pi$ with constant C_a. The boundaries in the ZVCs are obtained from Eq. (4.33), by knowing that the integral, I, is equal to zero in correspondence of the initial condition. In this case, Campagnola et al. (2008) used a different definition of the potential energy such that Ω defined in Eq. (4.20) corresponds to this thesis author's

Definition	**Approximation**
FS	$\{2\Omega_C - \Omega_A - C_p < 0\}$
SM	$\{2\Omega_C - \Omega_A - C_a > 0\}$
LVS	$\{2\Omega_C - \Omega_A - C_p > 0 \text{ and } 2\Omega_C - \Omega_A - C_a < 0\}$

Table 4.2: Subregions of motions by Campagnola et al. (2008).

definition of $\Omega_C - \Omega_A/2$. Ω_C has the same definition as the one of the CR3BP in Eq. (3.83) of Chapter 3, thus, Ω_C is equal to $\Omega(e = 0)$ in Eq. (4.20). Ω_C corresponds also to Ω_S for $z = 0$. While, Ω_A is defined as:

$$\Omega_A = 2\frac{e\cos f}{1 + e\cos f} \cdot \left[\Omega_C + \frac{z^2}{2}\right]. \tag{4.35}$$

Using the definition by Campagnola et al. (2008), the ZVCs at the pericenter and apocenter are respectively:

$$C_p = 2\Omega_C - \Omega_A \qquad\qquad C_a = 2\Omega_C - \Omega_A. \tag{4.36}$$

The definition of FS, SM and LVS are listed in Table 4.2; where the FS represent the curve associtaed to the energy of the spaceraft when the Earth+Moon are at the pericenter while SM is the curve associated to the energy of the spacecraft when the Earth+Moon are at the apocenter. Finilly, the LVS represents the intersections of the previous two reagions. Also, the LVS curves are oscillating (as a function of the true anomaly the spacecraft covers) but less compared to the PZVC. Note that the LVS are defined similarly to the PZVC by imposing $I = 0$ in Eq. (4.33). The main difference is that the constant C of the LVS is not multiplied by the pulsating term $(1 + e\cos f)$ as for the PZVC. Multiplying the Jacobi constant by the pulsating term is incorrect due to the conservation of the spacecraft's energy along a selected trajectory (for a chosen f_0). Thus, the pulsating term has to be included in the potential energy to represent the bounding motion of the spacecraft correctly. A more precise approximation of the integral, I, was proposed by Luk'yanov (2005) in the so called *Surface of Minimum Energy* (SME).

4.4.2 Surface of minimum energy

The surface of minimum energy purpose is to approximate the integral, I, by noticing that the minimum of its integrand function, W, can be found analytically. Thus, the integrand function, W, can be seen as the sum of the minimum of W, W_{min}, and of an unknown function $\tilde{W} = W - W_{min}$ that does not posses an analytical expression.

In this thesis, the same notation as Luk'yanov (2005) is used for the energy definition in Eq. (4.23). We start from the idea that the integral, I, reaches its maximum and

minimum at the apocenter and pericenter of the Earth+Moon orbit respectively. The amplitude of I is a small quantity if the eccentricity is small and it is equal to zero for $e = 0$. Thus, the integral, I, can be considered as an additional energy or a perturbed energy to the one of the CR3BP. Luk'yanov (2005) noticed that a certain part of this additional energy, I, in Eq. (4.25) is known and can be analytically integrated in correspondence to the minimum assumed by the function W in Eq. (4.24). This can be done since W is continuous and bounded from below ($W > 0$). The minimum of W can be determined by solving the following system:

$$\begin{cases} \frac{\partial W}{\partial x} = x - (1-\beta)\frac{1-\mu}{r^3_{Sun-p}}(x+\mu) - \frac{\mu}{r^3_{Earth-p}}(x+\mu-1) = 0 \\ \frac{\partial W}{\partial y} = y\left(1 - (1-\beta)\frac{1-\mu}{r^3_{Sun-p}} - \frac{\mu}{r^3_{Earth-p}}\right) = 0 \\ \frac{\partial W}{\partial z} = z\left(1 - (1-\beta)\frac{1-\mu}{r^3_{Sun-p}} - \frac{\mu}{r^3_{Earth-p}}\right) = 0 \end{cases} . \tag{4.37}$$

Eq. (4.37) is similar to the equations for the computation of the libration points in Eq. (3.57). As one can see, the computation of the co-linear libration points ($L_{1,2,3}$) requires to set $y = z = 0$ and thus both Eq. (4.37) and Eq. (3.57) share the same five-order polynomial in x. Moreover, the two equilateral solution $L_{4,5}$ hold also for Eq. (4.37) when $z = 0$. Luk'yanov (2005) already showed that W has five equilibrium solutions, and he also demonstrated the existence of the libration ring for W. The libration ring exists for W due to the term z^2 in Eq. (4.24). This is evident by looking at the function W as function of the y and the z coordinates for $x = 0$ in Figure 4.8 with the symbol W_{yz} where a minimum ring solution exists (red circle). The $L_{4,5}$ equilateral points belong to the libration ring for $z = 0$. This means that for $z \neq 0$, the Sun and the Earth's gravitational potential cancel out in correspondence of the third vertex of any out-of-plane equilateral triangles that has other two vertexes the Sun and the Earth+Moon. All these equilateral vertexes have the analytical expression of a circle as shown in Figure 4.9.

The minimum of W occurs at the libration ring as shown in Figure 4.8, while the collinear points are saddle solutions of W. In this work, the solution of Luk'yanov (2005) was extended for the case of a Sun-pointing deployable structure; in this case the coordinates of the libration ring are:

$$x = \frac{(1-\beta)^{\frac{2}{3}}}{2} - \mu \qquad y^2 + z^2 = (1-\beta)^{\frac{2}{3}}\left[1 - \frac{(1-\beta)^{\frac{2}{3}}}{4}\right]. \tag{4.38}$$

The minimum of W in correspondence of the libration ring for a Sun-pointing deployable structure [2] is:

$$W_{min} = \frac{1}{2}\left[3(1-\beta)^{\frac{2}{3}} + \mu\left(2 - 3(1-\beta)^{\frac{2}{3}} + \mu\right)\right]. \tag{4.39}$$

[2] Note that for $\beta = 0$, $W_{min} = \frac{1}{2}\left[3 - \mu(1-\mu)\right]$, which is the case studied by Luk'yanov (2005).

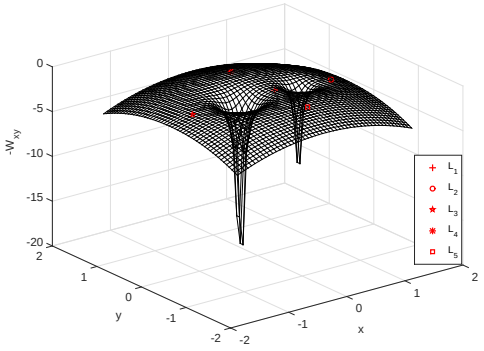

(a) $-W$ for $z = 0$.

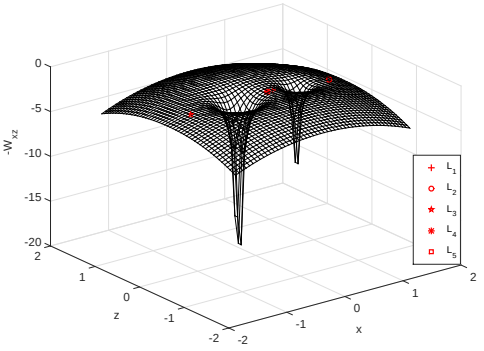

(b) $-W$ for $y = 0$.

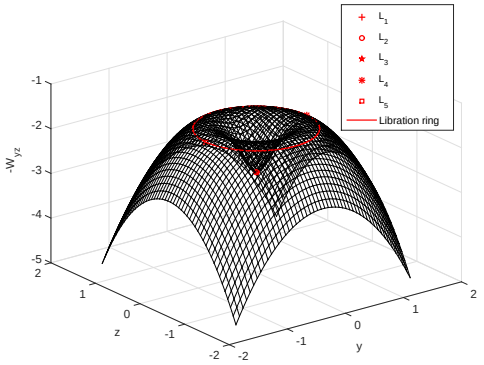

(c) $-W$ for $x = 0$.

Figure 4.8: $-W$: the five libration points and the libration ring in different views.

As previously said, the function W can be now split into two parts as $W = \tilde{W} + W_{min}$ where W_{min} collects the integrable part of the integral, I. Thus, the integral, I, turns into (Luk'yanov, 2005):

$$I = \int_{f_0}^{f} \frac{e \sin f}{(1 + e \cos f)^2} \tilde{W} df + \frac{W_{min}}{1 + e \cos f} - \frac{W_{min}}{1 + e \cos f_0} = \tilde{u}(f) + \frac{W_{min}}{1 + e \cos f} - \frac{W_{min}}{1 + e \cos f_0}. \tag{4.40}$$

In Eq. (4.40), $\tilde{u}(f)$ is an unknown function of f. According to the approach of Luk'yanov (2005) the integral, I, can be approximated with its minima:

$$I = W_{min} \left[\frac{1}{1 + e \cos f} - \frac{1}{1 + e \cos f_0} \right]. \tag{4.41}$$

By using the approximation proposed by Luk'yanov (2005), the energy in Eq. (4.23) and the ZVC in Eq. (4.33) turns into:

$$E_{tr}(f_0, \boldsymbol{x}(f_0), f) = \frac{1}{2} V^2 - \Omega + \frac{W_{min}}{1 + e \cos f} - \frac{W_{min}}{1 + e \cos f_0} \tag{4.42}$$

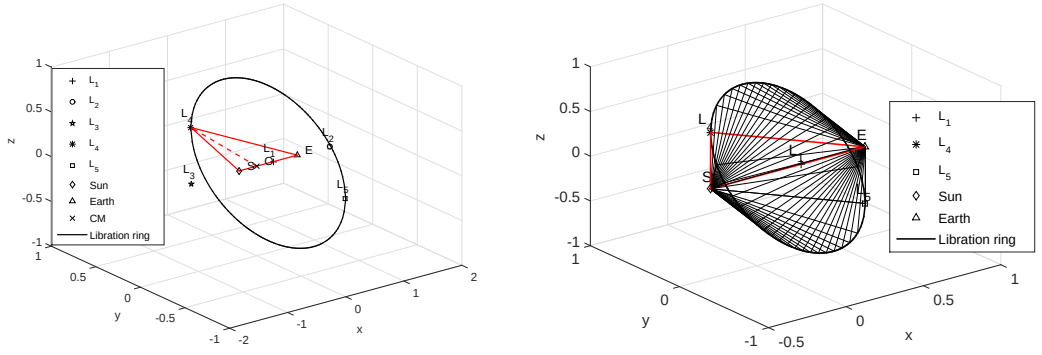

(a) Representation of the libration ring that intersect the L_4 and L_5 points for $z = 0$.

(b) All the points that belongs to the libration ring represent stable conditions for $z \neq 0$.

Figure 4.9: The libration ring is the minimum of W.

and,

$$C = 2\Omega - 2\left[\frac{W_{min}}{1 + e\cos f} - \frac{W_{min}}{1 + e\cos f_0}\right] \tag{4.43}$$

respectively. In Eq. (4.43), the ZVCs are defined by setting the constant of Jacobi, C, to a constant value. Luk'yanov (2005) considered a condition starting from the pericenter, $f_0 = 0$, since I is minimum at the pericenter and thus he set the constant C in Eq. (4.43) at the pericenter as $C_p = -V_p^2 + 2\Omega_p$ where the subscript "$_p$" indicated the condition at the pericenter. Luk'yanov (2005) also further simplified Eq. (4.43) by introducing the constant C_p' defined as:

$$C_p' = C_p - 2\frac{W_{min}}{1 + e\cos f_0}, \tag{4.44}$$

and by giving the definition of surface of minimum energy as follows:

$$C_p' \cdot (1 + e\cos f) = 2\Omega(1 + e\cos f) - 2W_{min}. \tag{4.45}$$

In Eq. (4.45), the left-hand side is not a constant as for the case of Szebehely.

Furthermore, the SME defined in Eq. (4.45) shows that the true anomaly (left-hand side of Eq. (4.45)) is separated from the variables that depend on the state position vector (right-hand side of Eq. (4.45)). However, as said before, it is inconsistent to have a pulsating Jacobi constant as the energy of the spacecraft is conserved along its trajectory. In the CR3BP, the ZVCs are used as a tool to have a qualitative representation of the bounded motion of the spacecraft. This definition holds in the ER3BP if the Jacobi constant corresponds to the spacecraft's energy. Thus, the Jacobi constant can not be pulsating. In this thesis, the Jacobi constant, C, is equal to the energy of the spacecraft along its trajectory as presented in Eq. (4.43). Eq. (4.43), together with the additional contribution of the SRP effect, represents the main differences of this study compared to the one by Luk'yanov (2005).

4.4.3 Why W_{min} does not correspond to I_{min}

The aim of this section is to demonstrate that the stationary points of the integral are not coincident with the one of the function W. This means that the integral of the function containing W_{min} does not correspond to I_{min}. As already shown, W has a minimum in correspondence of the libration ring, while the integral has a minimum and a maximum in correspondence of the pericenter and apocenter conditions. Starting from the definition of the integral, I, as in Eq. (4.25), the stationary point can be found by setting the derivative of the integral to zero:

$$\frac{dI}{df} = \frac{d}{df}\left[\int_{f_0}^{f} W(\tilde{f}) \cdot g(\tilde{f}) d\tilde{f}\right] = W(f) \cdot g(f), \tag{4.46}$$

where, $g(\tilde{f})$ is:

$$g(\tilde{f}) = \frac{e \sin \tilde{f}}{1 + e \cos \tilde{f}}. \tag{4.47}$$

For the fundamental theorem of the integral calculus, the derivative of the integral is defined as:

$$\int_{f_0}^{f} \left[\frac{d(W(\tilde{f}) \cdot g(\tilde{f}))}{d\tilde{f}}\right] d\tilde{f} = W(f) \cdot g(f) - W(f_0) \cdot g(f_0), \tag{4.48}$$

then, the derivative of the integral in Eq. (4.46) can be also written as:

$$\frac{dI}{df} = \int_{f_0}^{f} \frac{dW(\tilde{f})}{d\tilde{f}} \cdot g(\tilde{f}) d\tilde{f} + \int_{f_0}^{f} W(\tilde{f}) \cdot \frac{dg(\tilde{f})}{d\tilde{f}} d\tilde{f} + W(f_0) \cdot g(f_0). \tag{4.49}$$

In the case of the minimum of W, the gradient of W is zero thus $W_x = W_y = W_z = 0$, which implies that:

$$\frac{dW(\tilde{f})}{d\tilde{f}} = \frac{\partial W}{\partial x}\frac{dx}{d\tilde{f}} + \frac{\partial W}{\partial y}\frac{dy}{d\tilde{f}} + \frac{\partial W}{\partial z}\frac{dz}{d\tilde{f}} = W_x x' + W_y y' + W_z z' = 0. \tag{4.50}$$

This evidence shows that the condition of minimum W does not correspond to the condition of the minimum of I, indeed the derivative of I does not depend solely on the derivative of W. Thus, the condition of $dW/d\tilde{f} = 0$ is not sufficient for having $dI/df = 0$ and the approximation of Luk'yanov (2005) can be either conservative or an underestimation of I depending on the sign of "$\sin \tilde{f}$" in Eq. (4.25) since $W > 0$ and $W = \tilde{W} + W_{min}$ as shown in Eq. (4.40).

4.4.4 Comparison and interpretation of the zero velocity curves approximations

In the previous section the approximations of the ZVCs introduced by Szebehely (1967), Campagnola et al. (2008) and Luk'yanov (2005) were described. Table 4.1 summarises the definition of the ZVCs for these authors. The definitions given in Table 4.1 shows that both Szebehely (1967) and Luk'yanov (2005) include the effect of the true anomaly in the constant, C, thus, in these two cases, the oscillating effect of the ZVCs is given by a different point of intersection of the selected energy constant with the fixed part of the potential. Having a Jacobi constant value that fluctuates with the true anomaly makes hard to interpret the oscillation of the ZVCs with respect to the energy of the spacecraft that instead is kept constant along a selected trajectory.

Figure 4.10 compares the trend in the Jacobi constant defined by Luk'yanov (2005) (surface of minimum energy) and by Campagnola et al. (2008) (low-velocity subregions), as listed in Table 4.1, with respect to the Jacobi constant of the spacecraft leaving the LPO when the Earth+Moon is at the pericenter. The spacecraft has a constant energy (dashed gray line, in Figure 4.10(a)), while the approximated ZVCs of Luk'yanov (2005) (SME) are obtained with different energy levels (oscillating dashed black curve, in Figure 4.10(a)). Conversely, in Campagnola et al. (2008) the LVS are achieved by maintaining the ZVCs constant, C, fixed with the true anomaly as shown in Figure 4.10(b) for the apocenter (gray line) and pericenter (black line). The pericenter constant, C_p, corresponds to the energy of the spacecraft when leaving the LPO (dashed gray line).

Figure 4.11 shows the comparison of the approximated ZVCs of Szebehely (1967) (PZVC), Campagnola et al. (2008) (LVS) and Luk'yanov (2005) (SME) with respect to the motion of the spacecraft (black circle). From Figure 4.11(b) to Figure 4.11(f), the position of the spacecraft (black circle) is shown at specific epoch f with respect to the approximated velocity curves. As a general rule, a good approximation of the ZVCs have to minimise the effect of the oscillations of the ZVCs in time f associated to the error introduced during the approximation. The revised definition of the ZVCs is used for the case of the PZVC and the SME in order to have a consistent ZVCs approximation with respect to the energy of the spacecraft. The pulsating term was thus included in the potential energy rather than in the Jacobi constant. The problem of having a pulsating Jacobi constant can be solved by using the definition of the PZVC and the SME as presented in Eq. (4.33) for I equal to zero and in Eq. (4.43) respectively, rather than using the final expression summarised in Table 4.1. In this way, it is possible to compare the PZVC and the SME approximations of the ZVCs with respect to the spacecraft dynamics by conserving the energy of the spacecraft. In the case of Campagnola et al. (2008), the equations of the LVS in Table 4.1 still hold.

In Figure 4.11, the low-velocity subregions (black and gray lines) are compared with the surface of minimum energy (red line). The same case treated by Campagnola et al.

(2008), where μ and e are for the Earth+Moon system as shown in Table 3.2 is analysed. In this case, a trajectory leaving an LPO in correspondence of L_1 is selected. As an initial condition we select $x_0 = 1.3 \cdot 10^8$ km, $y_0 = z_0 = 0$ km and the modulus of the velocity $V_0 = 1.8$ km/s. The velocity direction is set with an azimuth of $\alpha = -110°$ and an elevation of $\delta = 0°$. The orientation angles are expressed with respect to the synodic reference frame where α is the azimuth defined within - $\pi/2$ and $\pi/2$ and δ is the elevation defined within $-\pi$ and π as shown in Figure 4.12.

The forbidden subregions and the surface of minimum energy in black and red respectively are obtained starting from a pericenter condition; however, the gray line is representative of a condition starting from the apocenter; thus, the LVS is the region within the black and the gray lines. From Figure 4.10(b), it is clear that the condition starting at the apocenter (gray line) is not representative of the energy of the spacecraft making it difficult to link the spacecraft dynamics with the boundaries of the LVS. Note that; the FS are defined as the PZVC except the fact that the pulsating term $(1 + e\cos f)$ does not multiply the energy constant C; thus, they are not represented here.

From Figure 4.11, it is possible to note that by neglecting the integral, I in Eq. (4.33), the oscillations in the ZVCs are wider (black line) than in the case when at least a part of the integral is approximated as for the SME in Eq. (4.43), (red line). For this reason, the approximation selected is the one proposed by Luk'yanov (2005), the SME, but in our proposed version shown in Eq. (4.43) where the Jacobi constant is kept constant with the spacecraft's energy.

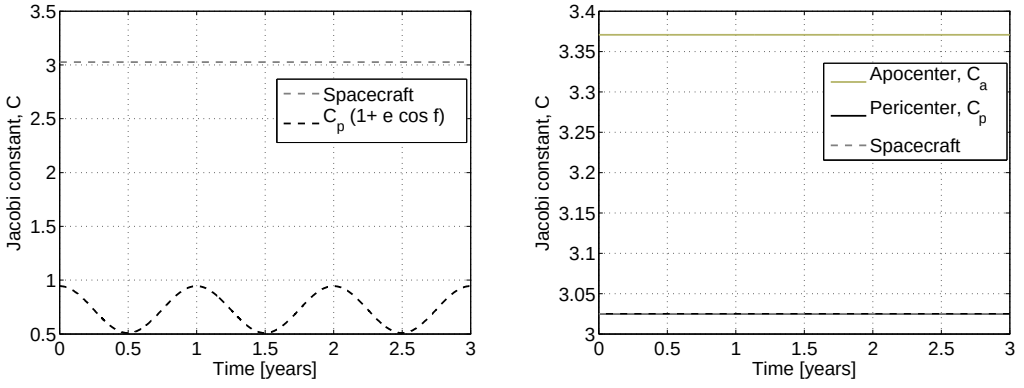

(a) Constant of Jacobi for the spacecraft, C_{sc}, and for the SME, $C'_p(1 + e\cos f)$. Note that $C'_p = C_{sc} - 2W_{min}/(1 + e\cos f_0)$. For aid of visualisation it was used $e = 0.3$.

(b) Constant of Jacobi for the spacecraft, at the apocenter C_a and at the pericenter C_p. In this case, it was used the eccentricity of the Earth+Moon system, shown in Table 3.2.

Figure 4.10: Interpretation of the approximated zero velocity curves for different definitions of the Jacobi constant.

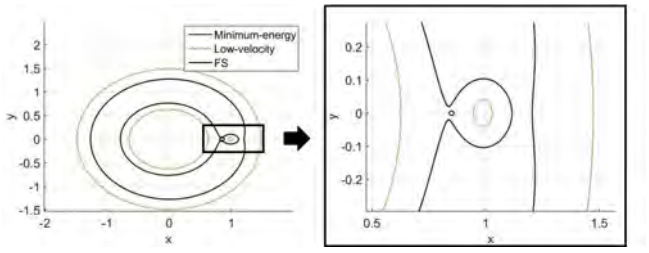

(a) Leaving the LPO at the pericenter, $f_0 = 0°$.

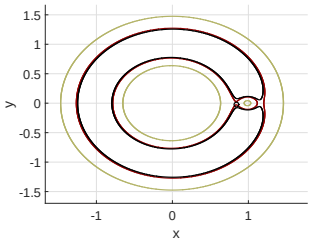

(b) $f = 30°$.

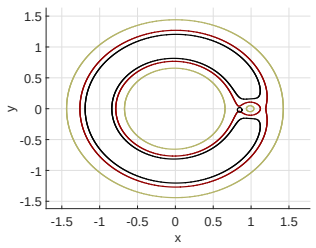

(c) $f = 60°$.

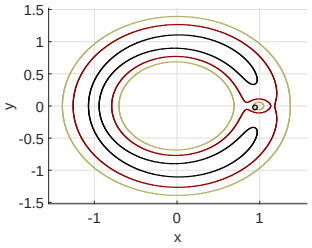

(d) $f = 90°$.

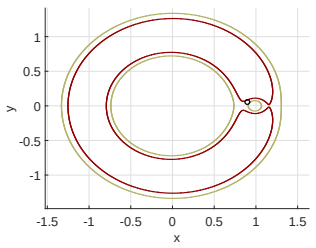

(e) $f = 120°$.

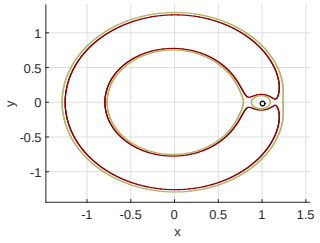

(f) $f = 150°$.

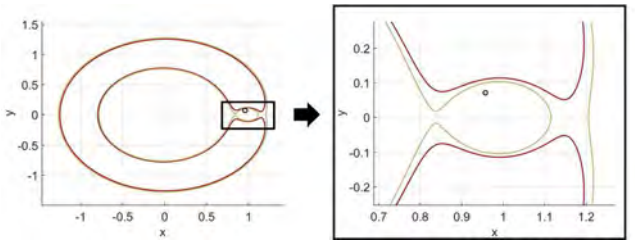

(g) Reaching the apocenter, $f_{end} = 180°$.

Figure 4.11: Comparison of the Forbidden subregions (FS) in black, Low-Velocity region (gray and black) and the Surface of Minimum Energy (red) with the dynamics of the spacecraft (circle) in the Earth+Moon ER3BP dynamics, Table 3.2. The initial condition is set at the pericenter, $f_0 = 0$.

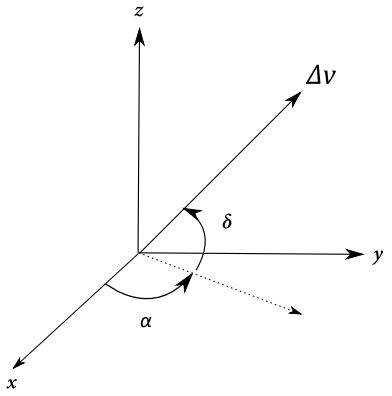

Figure 4.12: Δv orientation angles: azimuth, α, and elevation, δ, with respect to the synodic reference frame, $\{x, y, z\}$.

4.5 Summary

This chapter has attempted to provide some insight into the elliptic restricted-three body problem. The ER3BP is an even more accurate dynamical model with respect to the circular restricted-three body problem presented in Chapter 3. The ER3BP takes into account the effect of the Earth's orbit eccentricity that is an important figure for the design of the spacecraft's end-of-life disposal (Chapter 7). The important achievements of this chapter are:

- The transformation from the sidereal dimensional coordinates to the synodic dimensionless coordinates is necessary when the real spacecraft's dynamics are approximated in the ER3BP dynamics. For example, in Chapter 7, the robustness of the proposed end-of-life strategy will investigated for Gaia mission where the dynamics are provided by the NASA's spacecraft ephemeris;
- By defining the transformation from the sidereal to the synodic coordinates, the ER3BP shows to be a good approximation of the full-body dynamics when other perturbations are taken into account;
- The most serious attempt of this chapter is to provide a comprehensive understanding of the approximated zero-velocity curves in the ER3BP. The surface of minimum energy has been demonstrated to be the most precise approximation of the ZVCs;
- A modified version of the SME was extended here for a Sun-pointing spacecraft. This modified SME for a Sun-pointing spacecraft is a fundamental element for a good understanding of the effect of the Earth's orbit eccentricity onto the end-of-life disposal option (Chapter 7).

The key topics presented in this section are a fundamental theory for the end-of-life disposal and it is one of the major research areas of this thesis.

As the ultimate focus of this work is to harness solar radiation pressure for trajectories control and design from the beginning to the end of the space mission, the mission phases under this research interest are:

1) the nominal mission phase (i.e. orbit control and maintenance),
2) the operational or extended mission phase (i.e. to transfer from the nominal orbit to a new one), and
3) the end-of-life mission phase (i.e. for the spacecraft's disposal).

A definition of a new control law is first investigated in next chapter for harnessing solar radiation pressure during the spacecraft's nominal mission phase.

Chapter 5

Hamiltonian Structure-Preserving Control

A spacecraft placed in libration point orbits about L_1 and L_2 will naturally diverge from them due to the hyperbolic nature of the libration points (Section 2.2). Thus, trajectories designed in the R3BP require the spacecraft to perform control manoeuvres to maintain its nominal orbit by counteracting the unwanted environmental instabilities (Koon et al., 2008; Perozzi and Ferraz-Mello, 2010).

The aim of this chapter is to investigate the design of a control law that stabilises the spacecraft's dynamics through solar radiation pressure manoeuvres and to answer one of the research questions:

Q.3 - *What type of control law can be used for stabilising spacecraft at libration point orbits that make use of solar radiation pressure propulsion?*

In Section 2.2, a review of different periodic orbits was performed. Based on the scientific interest in using those orbits, two kinds of target orbits were selected, namely libration point orbits around either L_1 or L_2 (i.e. Halo type and family-a), and distant prograde orbits around the Earth (i.e. family-g).

As mentioned in Section 2.2.1, the scientific advantage of placing a spacecraft in LPOs and DPOs is justified for the Sun or deep space observations and for studying the composition of the smaller celestial body. No restriction was given on the size of the selected unstable periodic orbits; thus, the control law should work for either low or high amplitude orbits. This was done to have a generalised control law that adds mission design flexibility.

As mentioned in Chapter 2, preference is given to control laws that make use of the invariant manifold theory for achieving the stability of the spacecraft. In Section 2.4.1,

linear control laws were investigated as the linear behaviour of the spacecraft around the equilibrium points is important to understand the non-linear dynamics. Two control laws that make use of the invariant manifold theory were selected to be further investigated in this chapter: the Hamiltonian Structure Preserving (HSP) control (Scheeres et al., 2003b) and the Floquét Mode (FM) control (Gómez and Barrabés, 2011).

The HSP control law is preferred on the FM method as it stabilises periodic orbits in the sense of Lyapunov. This control is attractive since the fuel expenditure is small; resulting in being proposed for low thrust applications (Scheeres et al., 2003b). The HSP control is applied here considering the effect of solar radiation pressure. The HSP controller is designed in the circular restricted three-body problem with the effect of SRP. It aims to replace the libration points' hyperbolic equilibrium with an artificial centre manifold by preserving the Hamiltonian nature of the equations of motion. Thus, the equilibrium will change from saddle×centre×centre to an artificial centre×centre×centre equilibrium due to the effect of the control law. As previously mentioned, the HSP control proposed by Scheeres et al. (2003b) and the FM controller share similarities; thus, a sensitivity analysis is carried out to investigate the features of both controllers and their robustness.

Once the HSP control performances are compared with the FM, the required acceleration magnitudes can then be compared to investigate whether this can be provided by actuators onboard the spacecraft that controls the effect of SRP. Such actuators could control the reflectivity of the spacecraft, the reflective area illuminated by the Sun or the spacecraft's orientation with respect to the Sun.

The major research contributions of this chapter are section listed:

- Section 5.1.3 presents the Hamiltonian-structure preserving control extended to high amplitude orbits where complex eigenvalues appear,
- Section 5.2 shows how to select the gain to guarantee the stability for the extended control law presented in Section 5.1.3,
- Section 5.4 compares the well known Floquét mode technique with the Hamiltonian-structure preserving control,
- Section 5.5 studies the robustness of the Floquét mode and Hamiltonian-structure preserving control laws under contingencies analysis,
- Section 5.7 demonstrates that the Target point technique extended to solar radiation pressure applications cannot ensure the simple Lyapunov stability,
- Section 5.8 presents the control requirements in term of variable reflective actuators and pointing accuracy of the spacecraft for solar radiation pressure orbit control of Halo and high amplitude orbits, and

- Section 5.9 investigates the possible structural design for an actuator system that enhance solar radiation pressure.

The results of this chapter were presented in Soldini et al. (2016b) and are under review.

5.1 Design of the control law that preserves the Hamiltonian structure of the system

The Hamiltonian structure-preserving control uses the eigenstructure of the linearised equations of motion to create a control law that ensures Lyapunov stability (Khalil, 2002). As shown by Scheeres et al. (2003a), this controller aims to remove both the stable and unstable manifolds (red and green arrows in Figure 5.1) by projecting the state position error (between the current and the target orbit) along the manifold direction. This creates an artificial centre manifold, as shown in Figure 5.1 that keeps the trajectory close to the target orbit, as the eigenvalues of the linearised dynamics, are placed along the imaginary axis. In this chapter, the target orbit is numerically computed as shown in Section 3.8.2.

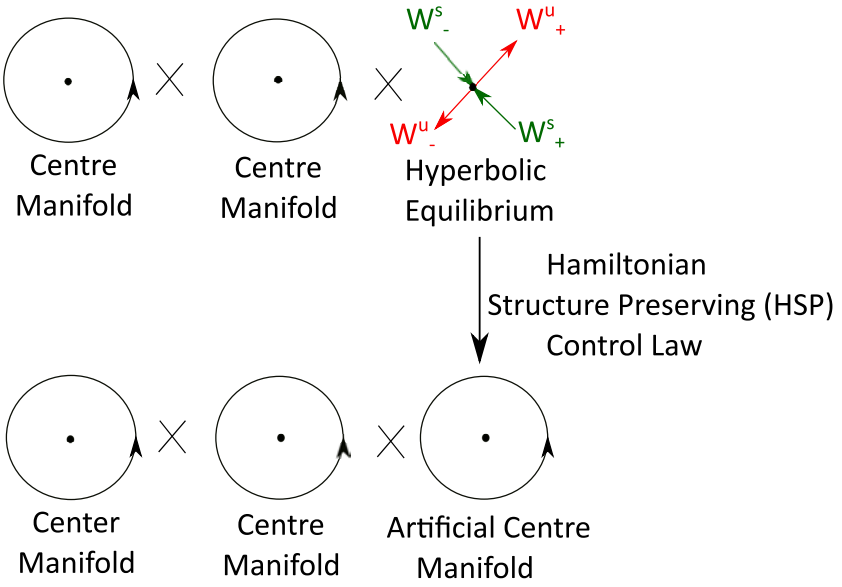

Figure 5.1: The effect of the Hamiltonian structure preserving control law is to replace the hyperbolic equilibrium with an artificial centre manifold.

The local stability impacts onto the periodic orbit stability (introduced in Section 3.10) by affecting the eigenvalues of the monodromy matrix, $\boldsymbol{M}$. The monodromy matrix is the state transitional matrix, $\boldsymbol{\Phi}(t_0 + T, t_0)$, of the system evaluated after one orbital period, T, where t_0 is the initial time (see Appendix C.9). For Lyapunov stability, the controller should place the eigenvalues of the matrix $\boldsymbol{M}$ on the unitary circle of the complex plane (Ginoux, 2009), see Figure 5.2.

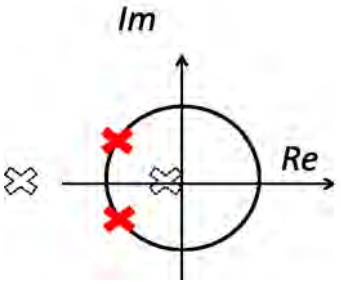

Figure 5.2: Eigenvalues of the monodromy matrix with (red crosses) and without (white crosses) the effect of the HSP controller.

Remark 5.1. An important remark is that the positioning of eigenvalues relative to the unitary circle in Figure 5.2, is compared to the positioning of eigenvalues on the right/left side of the complex plane as those plotted in the figures in Section 3.7.1, as well as in Figure 5.4. This eigenvalues plot in Figure 5.2 is on a z-plane, which is used in discrete-time framework, whereas the plot in Section 3.7.1 and in Figure 5.4, are on a s-plane, which is used in continuous-time framework. More discussion on this is presented in Section 5.1.1, and more information can be found in Astrom and Wittenmark (1996).

Thanks to the effect of the control, the matrix $\boldsymbol{M}$ is still sympletic, since the two pairs of eigenvectors are one the inverse of each other, but the existence of a Jacobi integral is no longer guaranteed since the central two real solutions equal to one are removed. Moreover, the fact that the monodromy matrix is symplectic ensures also that the system is still autonomous and Hamiltonian (Scheeres et al., 2003a). Scheeres et al. (2003a) demonstrated that the study of local stability is connected to the periodic orbit stability. This will be summarised in the following as it is useful to introduce the extension of the controller proposed in this work. As seen in Section 3.4.2, the natural dynamics in Eq. (3.39) can be written in a compact form as:

$$\dot{\boldsymbol{X}} = f(\boldsymbol{X}). \tag{5.1}$$

In Eq. (5.1), f is the flow field and, $\boldsymbol{X} = \{x,\ y,\ z,\ \dot{x},\ \dot{y},\ \dot{z}\}$ is the state vector. The variational equations are:

$$\delta\dot{\bar{\boldsymbol{X}}}(t) = \boldsymbol{A}(\bar{\boldsymbol{X}}(t))\delta\bar{\boldsymbol{X}}(t) \tag{5.2}$$

which are the linearised equations for the evaluation of the variations $\delta\bar{\boldsymbol{X}}(t)$. In Eq. (5.2), $\boldsymbol{A}(\bar{\boldsymbol{X}}(t))$ is the Jacobian matrix of the flow field, f, evaluated along the reference trajectory.

For the linearised equations, solving the eigenvalues of the variational equations matrix, $\boldsymbol{A}(\bar{\boldsymbol{X}}(t))$, is an approximation of solving the eigenvalue problem of the STM, $\boldsymbol{\Phi}(t, t_0)$.

The variational equations of Eq. (5.2) are (Koon et al., 2008):

$$\frac{d}{dt}\begin{bmatrix}\delta\boldsymbol{r}\\ \delta\dot{\boldsymbol{r}}\end{bmatrix}=\begin{bmatrix}\boldsymbol{0} & \boldsymbol{I}\\ \boldsymbol{V_{rr}} & 2\omega_0\boldsymbol{J}\end{bmatrix}\begin{bmatrix}\delta\boldsymbol{r}\\ \delta\dot{\boldsymbol{r}}\end{bmatrix},\qquad \text{where,}\qquad \boldsymbol{J}=\begin{bmatrix}0 & 1\\ -1 & 0\end{bmatrix},\tag{5.3}$$

$\boldsymbol{V_{rr}}$ is the Jacobian matrix of the potential acceleration in Eq. (3.40) and $2\omega_0\boldsymbol{J}$ is the term associated to the Coriolis acceleration. In Eq. (5.3), $\delta\boldsymbol{r}$ and $\delta\dot{\boldsymbol{r}}$ are the state position and velocity errors, respectively. The eigenvalues of the linearised dynamics are the solutions of the characteristic equation $D(\lambda)=|\boldsymbol{A}-\lambda\boldsymbol{I}|=0$, where the characteristic polynomial is:

$$\Lambda^2+b\Lambda+c=0\qquad\text{where,}\qquad\begin{cases}b=4\omega_0^2-V_{xx}-V_{yy}\\ c=V_{xx}V_{yy}-V_{xy}^2\\ \Delta=b^2-4c\end{cases}.\tag{5.4}$$

As exploited by Scheeres et al. (2003a), the solutions of Eq. (5.4) are affected by the sign of Δ. When, $\Delta>0$ the system produces two real and unequal roots; while, when $\Delta<0$ there are two complex and conjugate solutions. The change in the stability of the eigenvalues is evident for high amplitude orbits where it is possible to identify two cases along the trajectory where the eigenvalues are couples of real and pure imaginary numbers (saddle×centre equilibrium, i.e., the black line in Figures 5.3(a)-5.3(b), when $b<0$, $\Delta>0$ and $c<0$), or where the eigenvalues are couples of complex numbers and conjugate pairs (stable×unstable foci, i.e., the red line in Figures 5.3(a)-5.3(b), when $b<0$, $\Delta<0$ and $c<0$).

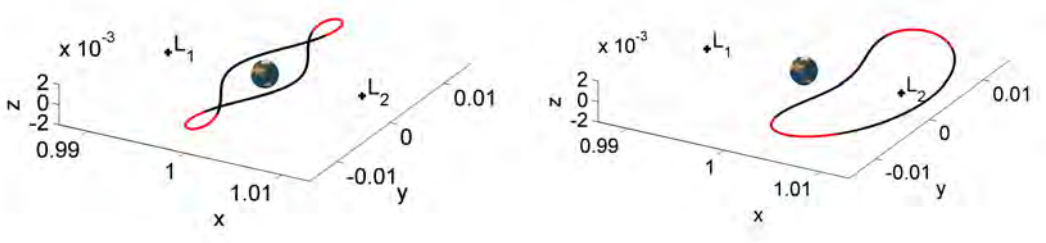

(a) Distant Prograde Orbit (DPO). (b) Planar-Lyapunov.

Figure 5.3: Eigenvalues along the LPO. The black arc denotes the hyperbolic×centre solutions and the red arc represents couples of complex and conjugate solutions (Note the Earth is not to scale).

The general solution of Eq. (5.4) is given by:

$$\Lambda_1 = \lambda_{1,2}^2 = \frac{-b + \sqrt{\Delta}}{2} \qquad \Lambda_2 = \lambda_{3,4}^2 = \frac{-b - \sqrt{\Delta}}{2} \qquad \widehat{\boldsymbol{x}}_k = \left\{ \begin{array}{c} 1 \\ u_k \\ \lambda_k \\ \lambda_k \cdot u_k \end{array} \right\}; \tag{5.5}$$

where, λ_k are the eigenvalues and $\widehat{\boldsymbol{x}}_k$ their corresponding eigenvectors for k varying from 1 to 4. The HSP control proposed by Scheeres et al. (2003a) aims to project the state position error along the eigenvectors direction. From a vectorial point of view, it is like defining a projection tensor given by $\boldsymbol{u}_k \boldsymbol{u}_k^T$ (Scheeres et al., 2003a). The first two normalised components of $\widehat{\boldsymbol{x}}_k$ in Eq. (5.5) represent the unitary vector $\boldsymbol{u}_k$, and the expression of $\boldsymbol{u}_k$ is:

$$\boldsymbol{u}_k = \frac{1}{\sqrt{1 + u_k \bar{u}_k}} \left[\begin{array}{c} 1 \\ u_k \end{array} \right] \qquad\qquad u_k = \frac{\lambda_k^2 - V_{xx}}{V_{xy} + 2\omega_0 \lambda_k} \tag{5.6}$$

where, $u_k \bar{u}_k$ is the product of u_k and its conjugate. Since the HSP control aims to stabilise the system in the sense of Lyapunov, the control law is designed such as to affect the sign of b, c and Δ of Eq. (5.4). Indeed, the simple Lyapunov stability can be achieved by placing the eigenvalues of the linearised dynamics on the imaginary axis, as shown in Figure 5.4, by adding to the matrix $\boldsymbol{V_{rr}}$ an artificial potential, the centre manifold (matrix $\boldsymbol{T}$).

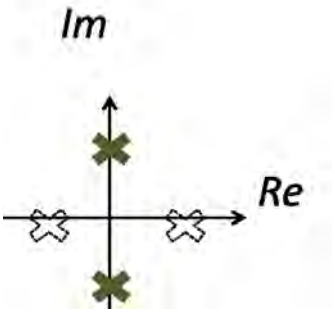

Figure 5.4: Eigenvalues of the linearised dynamics with (green crosses) and without (white crosses) the effect of the HSP controller.

The artificial centre manifold, the matrix $\boldsymbol{T}$, is constructed from the linear combination of the projection tensors $\boldsymbol{u}_k \boldsymbol{u}_k^T$ and the gains. This linear combination is selected such as b^c, c^c and Δ^c, which are the indexes of stability affected by the control law, are all greater than zero (Scheeres et al., 2003a). $\{b^c > 0 \;\&\; c^c > 0 \;\&\; \Delta^c > 0\}$ is the condition of simple Lyapunov stability; where, the HSP control is added to the dynamics in Eq. (3.39) as an additional control acceleration, $\boldsymbol{a}^c$, that will be modelled as SRP acceleration. Thus, $\boldsymbol{a}^c$ is given by the actuators model, $\boldsymbol{a}^s$. $\boldsymbol{a}^c$ is obtained by multiplying the matrix $\boldsymbol{T}$ by

the state position error between the target orbit and the actual spacecraft trajectory $\delta \boldsymbol{r}$,

$$\boldsymbol{a}^c = \boldsymbol{T}\delta\boldsymbol{r}. \tag{5.7}$$

The acceleration, $\boldsymbol{a}^c$, affects the linearised dynamics and the matrix $\boldsymbol{A}(\bar{\boldsymbol{X}}(t))$, in Eq. (5.3) which turns into the matrix $\boldsymbol{A}^c(\bar{\boldsymbol{X}}(t))$:

$$\boldsymbol{A}^c(\bar{\boldsymbol{X}}(t)) = \begin{bmatrix} \boldsymbol{0} & \boldsymbol{I} \\ \boldsymbol{V_{rr}^c} & 2\omega_0 \boldsymbol{J} \end{bmatrix}. \tag{5.8}$$

The effect of the controller modifies $\boldsymbol{V_{rr}}$ into $\boldsymbol{V_{rr}^c}$ such as:

$$\boldsymbol{V_{rr}^c} = \boldsymbol{V_{rr}} + \boldsymbol{T}. \tag{5.9}$$

In this work, the full formulation of the proposed extended HSP controller is derived for high amplitude orbits. The control law designed by Scheeres et al. (2003a) is used when there is a hyperbolic×centre equilibrium ($\Delta > 0$); Scheeres et al. (2003a) control law is summarised in Section 5.1.2. However, in the case of couples of complex and conjugate solutions ($\Delta < 0$), the dynamics requires a modified control law proposed by the author in Section 5.1.3.

5.1.1 Short-term and long-term stability

Scheeres et al. (2003a) demonstrate that the short-term stability is an approximation of the long-term stability for a periodic linearised dynamical system:

$$\dot{\boldsymbol{x}} = \boldsymbol{A}(t)\boldsymbol{x} \qquad\qquad \boldsymbol{A}(t+T) = \boldsymbol{A}(t), T > 0. \tag{5.10}$$

In this section, details are given to show the relationship between the short-term stability (shown in Figure 5.4) and the long-term stability (shown in Figure 5.2) (Scheeres et al., 2003a). The stability of periodic orbit solutions (long-term stability shown in Figure 5.2) can be studied in term of the Floquét multipliers and can be linked to the Poincaré map method presented in Section 3.7.1. For linear periodic system, the Floquét theorem states the follow:

Theorem 5.2 (Floquét theorem (Kuchment, 1993))**.** *If $\boldsymbol{\Phi}(t)$ is a fundamental matrix solution of the periodic system in Eq.(5.10), thus so is $\boldsymbol{\Phi}(t+T)$. Moreover, there exists an invertible periodic matrix $\boldsymbol{P}(t)$ with T-period such that:*

$$\boldsymbol{\Phi}(t) = \boldsymbol{P}(t)e^{\boldsymbol{B}t}, \tag{5.11}$$

and $\boldsymbol{B}$ is a constant matrix.

Remark 5.3. Since $\boldsymbol{\Phi}(t+T) = \boldsymbol{\Phi}(t)\boldsymbol{C}$ with $\det\boldsymbol{C} \neq 0$, $e^{\boldsymbol{B}} = \boldsymbol{C}$, the eigenvalues ρ of $\boldsymbol{C}$ are called the *characteristic multipliers* of the periodic linear system. The eigenvalues λ of $\boldsymbol{B}$ are called the *characteristic exponents* of the periodic linear system where $\rho = e^{\lambda T}$.

In the R3BP, halo orbit has one pair of hyperbolic characteristic exponents and two circulation frequencies, one equal to the orbital period, T, and one slightly longer. Because of the presence of the unstable manifold, uncontrolled relative motion to the target orbit will diverge in few orbital periods.

To maintain long-term trajectory close to the target orbit, the spacecraft must be placed in the center manifold of the periodic orbit. However, the use of natural center manifolds is restrictive due to the unstable nature of the periodic orbit. Thus, the effect of the HSP control given along the trajectory aims to remove the instability by adding an artificial center manifold.

If we now focus on the short-term motion over a time much lower than the orbital period, although the description of the relative motion in Eq. (5.11) holds true, it does not give a direct indication of the relative motion over short time period. The state transition matrix, $\boldsymbol{\Phi}$, can be represented over one period as the product of mappings over much shorter time as (Scheeres et al., 2003a):

$$\boldsymbol{\Phi}(t_0 + T, t_0) = \prod_{i=1}^{N} \boldsymbol{\Phi}\left[t_0 + \frac{T}{N}i, t_0 + \frac{T}{N}(i-1)\right], \tag{5.12}$$

where the mapping over a time interval $\Delta t = T/N$ is represented as $\boldsymbol{\Phi}(t_i + \Delta t, t_i)$ and satisfies the equation:

$$\dot{\boldsymbol{\Phi}}(t_i + \delta t, t_i) = A(t_i + \delta t)\boldsymbol{\Phi}(t_i + \delta t, t_i) \qquad 0 \leq \delta t \leq \Delta t << T. \tag{5.13}$$

For small Δt, the matrix $\boldsymbol{A}$(t) can be expanded in a Taylor series:

$$\boldsymbol{A}(t_i + \delta t) = \boldsymbol{A}(t_i) + \dot{\boldsymbol{A}}(t_i)\delta t + \ldots \tag{5.14}$$

Scheeres et al. (2003a) found that for periodic orbits around the libration point $\dot{\boldsymbol{A}}(t_i)$ does not vary strongly over the time. This means that Δt can be chosen small enough to ensure that $||\boldsymbol{A}(t_i)|| >> ||\dot{\boldsymbol{A}}(t_i)\Delta t||$. Under this restriction, Scheeres et al. (2003a) found that the state transition matrix differential equation can be approximated over short-time intervals as:

$$\boldsymbol{\Phi}(t_i + \delta t, t_i) \sim e^{\boldsymbol{A}(t_i)\delta t} + \ldots \tag{5.15}$$

or

$$\boldsymbol{\Phi}(t_i + \delta t, t_i) \sim \boldsymbol{I} + \boldsymbol{A}(t_i)\delta t + \ldots \tag{5.16}$$

Note that series expansion of the higher order terms were neglected because the time interval is chosen to be sufficiently small. Eq. (5.16) is commonly used in discrete-time model, the Euler model, which is a first order numerical approximation of the continuous-time dynamics. The relative motion can be finally characterised over a short period of time by the eigenvalues and eigenvectors of the exponential map defined from equation:

$$(\lambda \boldsymbol{I} - \boldsymbol{\Phi})\boldsymbol{u} = 0, \tag{5.17}$$

where λ is the eigenvalue and $\boldsymbol{u}$ is the eigenvector. By substituting Eq. (5.16) to Eq. (5.17) this can be written as:

$$\left(\frac{(\lambda - 1)}{\delta t}\boldsymbol{I} - \boldsymbol{A}(t_i)\right)\boldsymbol{u} = 0. \tag{5.18}$$

For a time-invariant system, the eigenvalue of the state transition matrix λ in Eq. (5.17) is equal to $e^{\gamma \cdot \delta t}$, where γ is the characteristic exponent of the system. The eigenvalues of Eq. (5.18) can be approximated as:

$$\gamma \sim \lim_{\delta t \to 0} \frac{\lambda - 1}{\delta t}. \tag{5.19}$$

Under these approximations, the relative motion over a short-time can be understood by analysing the eigenstructure of the matrix $\boldsymbol{A}(t_i)$. The error induced by this approximation was investigated by Scheeres et al. (2003a) and is shown to be reasonable. Scheeres et al. (2003a) derive the HSP control law by using the short-term dynamics to guide the understanding of the stability. The relative motion along the instantaneous unstable manifold is seen as a precursor to the motion along the unstable manifold of the full orbit, as defined by Floquét Theory. Note that the full orbit may still be unstable even if the instantaneous map is stable at each time step.

Eq. (5.7) generalises the relative motion along the longer time span as well because the eigenstructure of the dynamical system are well defined as a function of time and the local eigenstructure does not change in the region around the halo orbit as demonstrated by Scheeres et al. (2003a). In this sense, the stability of the controlled orbit can be analysed using classical techniques developed for periodic orbits as presented in Section 3.7.1. As previously said, the stabilisation of the relative motion over short-time is a necessary but not sufficient condition to ensure that the motion of the spacecraft will be stable over long-time span. The condition to reach the stability are presented in Scheeres et al. (2003a). The stability of the system can however be evaluated by application of Floquét Theory and numerical integration.

The stability is evaluated as follows. The periodic orbit and its associated state transition matrix modified by adding the effect of the control is numerically integrated over one period of motion. At each time step, the spectrum of the open-loop system (specified

by the linear equations) is computed and added in:

$$\delta\dot{\bar{\boldsymbol{X}}}(t) = \boldsymbol{A}^c(\bar{\boldsymbol{X}}(t))\delta\bar{\boldsymbol{X}}(t), \tag{5.20}$$

where $\boldsymbol{A}^c(\bar{\boldsymbol{X}}(t))$ is defined as in Eq. (5.8) and is the time-varying matrix used in the state transition matrix computation. The resulting state transition matrix, computed using Eq. (3.109), is denoted as $\boldsymbol{\Phi}^c(t_0 + t, t_0)$, and the monodromy matrix evaluated over one period of motion is $\boldsymbol{\Phi}^c(t_0 + T, t_0)$. The stability of the closed-loop system can be evaluated by computing the eigenvalues μ of this map (the monodromy matrix):

$$|\mu\boldsymbol{I} - \boldsymbol{\Phi}^c(t_0 + T, t_0)| = 0. \tag{5.21}$$

As it is well know, these eigenvalues must occur in complex and conjugate pairs and in inverse pairs. Stability of this system occurs when all eigenvalues have unit magnitude that corresponds to the unit circle in the complex plane and have the form $\mu = e^{\pm i\theta}$ as shown in Figure 5.2.

An important remark is that the HSP control is a linear control for periodic dynamical system and is designed in the time domain where the link between short-term stability (along the trajectory) and long-term stability (at every one orbital period T) is guaranteed by the Floquét theory and the Lyapunov transformation. This is related to the discrete-time systems theory, where the continuous-time dynamics either in time (t) or frequency/Laplace (s) domains are transformed into their discrete-time equivalence in time (k) or frequency (z) domains, where $z = e^{sT}$ with T being the sampling time (z-plane). Based on this, Figure 5.2 is the plot of discrete-time eigenvalues in z-plane, while Figure 5.4 is the plot of continuous-time eigenvalues in s-plane (see also Remark 5.1 in Section 5.1).

5.1.2 Control law for local hyperbolic×centre equilibrium

In this section the control law proposed by Scheeres et al. (2003a) is summarised since this control law is used in the case of local hyperbolic×centre equilibrium (i.e., low amplitude orbits), see Figure 5.5.

The hyperbolic characteristic exponents for the stable (λ_1) and unstable (λ_2) directions are the solutions of the linearised dynamics in Eq. (5.5); where, now the real roots $\lambda_{1,2}$ are denoted as $\pm\sigma$. The corresponding eigenvector for σ is:

$$\boldsymbol{u}_1 = \frac{1}{\sqrt{1+u_1^2}}\begin{bmatrix} 1 \\ u_1 \end{bmatrix} \qquad u_1 = \frac{\sigma^2 - V_{xx}}{V_{xy} + 2\omega_0\sigma} \qquad \boldsymbol{u}_1\boldsymbol{u}_1^T = \frac{1}{1+u_1^2}\begin{bmatrix} 1 & u_1 \\ u_1 & u_1^2 \end{bmatrix}; \tag{5.22}$$

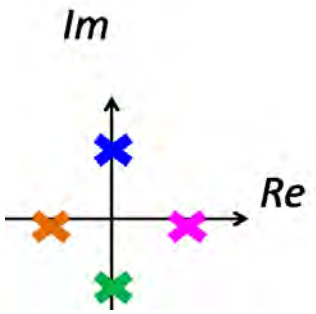

Figure 5.5: Couples of real and pure imaginary eigenvalues of the linearised equations: λ_1 (magenta cross), λ_2 (orange cross), λ_3 (blue cross) and λ_4 (green cross).

where u_1 is real and the projection tensor $\boldsymbol{u}_1\boldsymbol{u}_1^T$ is real. The corresponding eigenvector for $-\sigma$ is, instead:

$$\boldsymbol{u}_2 = \frac{1}{\sqrt{1+u_2^2}}\begin{bmatrix} 1 \\ u_2 \end{bmatrix} \qquad u_2 = \frac{\sigma^2 - V_{xx}}{V_{xy} - 2\omega_0\sigma} \qquad \boldsymbol{u}_2\boldsymbol{u}_2^T = \frac{1}{1+u_2^2}\begin{bmatrix} 1 & u_2 \\ u_2 & u_2^2 \end{bmatrix}; \tag{5.23}$$

where u_2 is real and the projection tensor $\boldsymbol{u}_2\boldsymbol{u}_2^T$ is real. The control law proposed by Scheeres et al. (2003a) is then:

$$\boldsymbol{a}^c = -\sigma^2 G_1 \left[\boldsymbol{u}_1\boldsymbol{u}_1^T + \boldsymbol{u}_2\boldsymbol{u}_2^T\right]\delta\boldsymbol{r}. \tag{5.24}$$

As said, the validity of the control law in Eq. (5.24) is for solutions where the instantaneous stability map has two couples of real and pure imaginary eigenvalues. This is the case for low amplitude LPOs.

5.1.3 Control law for complex and conjugate pairs

When couples of complex and conjugate numbers occur, as in the case of high amplitude orbits, the eigenvalues are the solution of the linear system in Eq. (5.5), where $\lambda_{1,2,3,4}$ are complex and conjugate pairs; thus now $\lambda_{1,2}$ and $\lambda_{3,4}$ are $\pm(\sigma+\gamma i)$ and $\pm(\sigma-\gamma i)$ respectively, as shown in Figure 5.6. The idea proposed here for the design of the extended control law is to get rid of the imaginary components in order to have a real control acceleration where the control law proposed in Eq. (5.24) fails to stabilise high amplitude orbits. Thus, the eigenvector components are separately analysed, in this thesis, in order to highlight possible conjugate terms for the design of the eigenvectors normalisation and the control acceleration. Starting from $\lambda_1 = \sigma + \gamma i$, its correspondent eigenvector component u_1 is:

$$u_1 = \frac{\sigma^2 - V_{xx} - \gamma^2 + 2\sigma\gamma i}{V_{xy} + 2\omega_0\sigma + 2\omega_0\gamma i} = \frac{A_1 + B_1 i}{C_1 + D_1 i}, \tag{5.25}$$

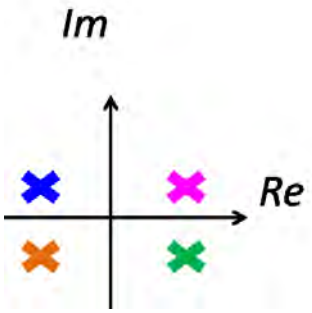

Figure 5.6: Couples of complex an conjugate eigenvalues of the linearised equations: λ_1 (magenta cross), λ_2 (orange cross), λ_3 (green cross) and λ_4 (blue cross).

that, after mathematical manipulation, it can be written as:

$$u_1 = \frac{(A_1C_1 + B_1D_1) - (A_1D_1 - B_1C_1)i}{C_1^2 + D_1^2} \qquad \begin{cases} A_1 = \sigma^2 - V_{xx} - \gamma^2 \\ B_1 = 2\sigma\gamma \\ C_1 = V_{xy} + 2\omega_0\sigma \\ D_1 = 2\omega_0\gamma \end{cases} . \tag{5.26}$$

The same approach can be used for $\lambda_2 = -\sigma - \gamma i$; where, the correspondent eigenvector component is defined as

$$u_2 = \frac{\sigma^2 - V_{xx} - \gamma^2 + 2\sigma\gamma i}{V_{xy} - 2\omega_0\sigma - 2\omega_0\gamma i} = \frac{A_2 + B_2 i}{C_2 - D_2 i}. \tag{5.27}$$

Thus, it is possible to highlight the real and imaginary part of u_2 as

$$u_2 = \frac{(A_2C_2 - B_2D_2) + (A_2D_2 + B_2C_2)i}{C_2^2 + D_2^2} \qquad \begin{cases} A_2 = \sigma^2 - V_{xx} - \gamma^2 \\ B_2 = 2\sigma\gamma \\ C_2 = V_{xy} - 2\omega_0\sigma \\ D_2 = 2\omega_0\gamma \end{cases} . \tag{5.28}$$

As before, the correspondent eigenvector component u_3 to $\lambda_3 = \sigma - \gamma i$ is:

$$u_3 = \frac{\sigma^2 - V_{xx} - \gamma^2 - 2\sigma\gamma i}{V_{xy} + 2\omega_0\sigma - 2\omega_0\gamma i} = \frac{A_3 - B_3 i}{C_3 - D_3 i} \tag{5.29}$$

and, by manipulating the previous expression, it is possible to write:

$$u_3 = \frac{(A_3C_3 + B_3D_3) + (A_3D_3 - B_3C_3)i}{C_2^2 + D_2^2} \qquad \begin{cases} A_3 = \sigma^2 - V_{xx} - \gamma^2 \\ B_3 = 2\sigma\gamma \\ C_3 = V_{xy} + 2\omega_0\sigma \\ D_3 = 2\omega_0\gamma \end{cases} . \tag{5.30}$$

Finally, in the case of $\lambda_4 = -\sigma + \gamma i$, the correspondent eigenvector component is u_4,

$$u_4 = \frac{\sigma^2 - V_{xx} - \gamma^2 - 2\sigma\gamma i}{V_{xy} - 2\omega_0\sigma + 2\omega_0\gamma i} = \frac{A_4 - B_4 i}{C_4 + D_4 i} \tag{5.31}$$

and it can be defined also as:

$$u_4 = \frac{(A_4C_4 - B_4D_4) - (A_4D_4 + B_4C_4)i}{C_4^2 + D_4^2} \qquad \begin{cases} A_4 = \sigma^2 - V_{xx} - \gamma^2 \\ B_4 = 2\sigma\gamma \\ C_4 = V_{xy} - 2\omega_0\sigma \\ D_4 = 2\omega_0\gamma \end{cases} . \tag{5.32}$$

By noticing that

$$\begin{cases} A_1 = A_2 = A_3 = A_4 = A = \sigma^2 - V_{xx} - \gamma^2 \\ B_1 = B_2 = B_3 = B_4 = B = 2\sigma\gamma \\ C_1 = C_3 = C = V_{xy} + 2\omega_0\sigma \\ C_2 = C_4 = \bar{C} = V_{xy} - 2\omega_0\sigma \\ D_1 = D_2 = D_3 = D_4 = D = 2\omega_0\gamma \end{cases} , \tag{5.33}$$

it is possible to rewrite the expression of u_k, with k defined from 1 to 4, as:

$$u_1 = \frac{(AC + BD) - (AD - BC)i}{C^2 + D^2} \qquad u_2 = \frac{(A\bar{C} - BD) + (AD + B\bar{C})i}{\bar{C}^2 + D^2} \tag{5.34}$$

$$u_3 = \frac{(AC + BD) + (AD - BC)i}{C^2 + D^2} \qquad u_4 = \frac{(A\bar{C} - BD) - (AD + B\bar{C})i}{\bar{C}^2 + D^2}. \tag{5.35}$$

So u_1 and u_3 are complex and conjugate and u_2 and u_4 are complex and conjugate too. Moreover, if a change of variables is applied,

$$\begin{cases} a_* = AC + BD \\ b_* = AD - BC \\ c_* = C^2 + D^2 \\ d_* = A\bar{C} - BD \\ e_* = AD + B\bar{C} \\ f_* = \bar{C}^2 + D^2 \end{cases} , \tag{5.36}$$

it is possible to define the eigenvectors and their normalisations by knowing that u_3 is the conjugate of u_1 and u_4 is the conjugate of u_2:

$$\boldsymbol{u_1} = \frac{1}{\sqrt{1 + u_1 u_3}} \begin{bmatrix} 1 \\ u_1 \end{bmatrix} \qquad u_1 = \frac{a_* - b_* i}{c_*} \tag{5.37}$$

$$\boldsymbol{u_3} = \frac{1}{\sqrt{1+u_1u_3}} \begin{bmatrix} 1 \\ u_3 \end{bmatrix} \qquad u_3 = \frac{a_* + b_* i}{c_*} \tag{5.38}$$

$$\boldsymbol{u_2} = \frac{1}{\sqrt{1+u_2u_4}} \begin{bmatrix} 1 \\ u_2 \end{bmatrix} \qquad u_2 = \frac{d_* + e_* i}{f_*} \tag{5.39}$$

$$\boldsymbol{u_4} = \frac{1}{\sqrt{1+u_2u_4}} \begin{bmatrix} 1 \\ u_4 \end{bmatrix} \qquad u_4 = \frac{d_* - e_* i}{f_*} \tag{5.40}$$

where, a_*, b_*, c_*, d_*, e_* and f_* are functions of the eigenvalues and $\boldsymbol{V_{rr}}$:

$$\begin{cases} a_* = (\sigma^2 - V_{xx} - \gamma^2)(V_{xy} + 2\omega_0\sigma) + (2\sigma\gamma)(2\omega_0\gamma) \\ b_* = (\sigma^2 - V_{xx} - \gamma^2)(2\omega_0\gamma) - (2\sigma\gamma)(V_{xy} + 2\omega_0\sigma) \\ c_* = (V_{xy} + 2\omega_0\sigma)^2 + (2\omega_0\gamma)^2 \\ d_* = (\sigma^2 - V_{xx} - \gamma^2)(V_{xy} - 2\omega_0\sigma) - (2\sigma\gamma)(2\omega_0\gamma) \\ e_* = (\sigma^2 - V_{xx} - \gamma^2)(2\omega_0\gamma) + (2\sigma\gamma)(V_{xy} - 2\omega_0\sigma) \\ f_* = (V_{xy} - 2\omega_0\sigma)^2 + (2\omega_0\gamma)^2 \end{cases} . \tag{5.41}$$

Since u_1 and u_3 are complex and conjugate and u_2 and u_4 are complex and conjugate, it is possible to write a new control law for high amplitude orbits as follows. From the normalisation, it is know that:

$$u_1u_3 = (a_* - b_* i) \cdot (a_* + b_* i) = a_*^2 + b_*^2, \tag{5.42}$$

and

$$u_2u_4 = (d_* + e_* i) \cdot (d_* - e_* i) = d_*^2 + e_*^2. \tag{5.43}$$

The four projection tensors are now defined as:

$$\boldsymbol{u_1u_1}^T = \frac{1}{1+u_1u_3} \begin{bmatrix} 1 & u_1 \\ u_1 & u_1^2 \end{bmatrix}, \qquad \boldsymbol{u_3u_3}^T = \frac{1}{1+u_1u_3} \begin{bmatrix} 1 & u_3 \\ u_3 & u_3^2 \end{bmatrix}, \tag{5.44}$$

$$\boldsymbol{u_2u_2}^T = \frac{1}{1+u_2u_4} \begin{bmatrix} 1 & u_2 \\ u_2 & u_2^2 \end{bmatrix}, \quad \text{and} \qquad \boldsymbol{u_4u_4}^T = \frac{1}{1+u_2u_4} \begin{bmatrix} 1 & u_4 \\ u_4 & u_4^2 \end{bmatrix}. \tag{5.45}$$

It is interesting to note that the only linear combination among the projection tensors, that guarantees a real control law, requires the couples of projection tensors to be weighted with the same gain. This can be demonstrated by looking at $\boldsymbol{u}_k$ and u_k in Eq. (5.37)-(5.40). For removing the imaginary numbers, the only solution is to keep the tensors associated to $\boldsymbol{u_1}$ and its conjugate $\boldsymbol{u_3}$ in proportion with the same gain

magnitude so that:

$$\boldsymbol{u_1}\boldsymbol{u_1}^T + \boldsymbol{u_3}\boldsymbol{u_3}^T = \frac{1}{1+u_1u_3}\begin{bmatrix} 1 & u_1+u_3 \\ u_1+u_3 & u_1^2+u_3^2 \end{bmatrix}, \tag{5.46}$$

$$u_1 + u_3 = a_* - b_*i + a_* + b_*i = 2a_* \tag{5.47}$$

and

$$u_1^2 + u_3^2 = (a_* - b_*i)^2 + (a_* + b_*i)^2 = 2(a_*^2 - b_*^2) \tag{5.48}$$

are all real. For the same reason, the tensors associated to $\boldsymbol{u_2}$ and $\boldsymbol{u_4}$ should be weighted with the same gain to achieve a real control acceleration. So,

$$\boldsymbol{u_2}\boldsymbol{u_2}^T + \boldsymbol{u_4}\boldsymbol{u_4}^T = \frac{1}{1+u_2u_4}\begin{bmatrix} 1 & u_2+u_4 \\ u_2+u_4 & u_2^2+u_4^2 \end{bmatrix}, \tag{5.49}$$

$$u_2 + u_4 = d_* + e_*i + d_* - e_*i = 2d_* \tag{5.50}$$

and

$$u_2^2 + u_4^2 = (d_* + e_*i)^2 + (d_* - e_*i)^2 = 2(d_*^2 - e_*^2) \tag{5.51}$$

are real terms too. The proposed control law for high amplitude orbits needs to be weighted with the same gain couples of complex and conjugate eigenvectors, in order to have a real control acceleration and to cancel the imaginary parts out. So:

$$\boldsymbol{a}^c = \left\{-\lambda_1\lambda_3 G_1\left[\boldsymbol{u_1}\boldsymbol{u_1}^T + \boldsymbol{u_3}\boldsymbol{u_3}^T\right] - \lambda_2\lambda_4 G_2\left[\boldsymbol{u_2}\boldsymbol{u_2}^T + \boldsymbol{u_4}\boldsymbol{u_4}^T\right]\right\}\delta\boldsymbol{r} \tag{5.52}$$

where,

$$\lambda_1\lambda_3 = (\sigma+\gamma i)(\sigma-\gamma i) = \sigma^2+\gamma^2 \qquad \lambda_2\lambda_4 = (-\sigma-\gamma i)(-\sigma+\gamma i) = \sigma^2+\gamma^2 \tag{5.53}$$

are all real and positive numbers. Thus, $\boldsymbol{a}^c$ can be further simplified to:

$$\boldsymbol{a}^c = -\left(\sigma^2+\gamma^2\right)\left\{G_2\left[\boldsymbol{u_1}\boldsymbol{u_1}^T + \boldsymbol{u_3}\boldsymbol{u_3}^T\right] + G_3\left[\boldsymbol{u_2}\boldsymbol{u_2}^T + \boldsymbol{u_4}\boldsymbol{u_4}^T\right]\right\}\delta\boldsymbol{r}. \tag{5.54}$$

In conclusion, the HSP control algorithm is designed such that:

$$\boldsymbol{a}^c = \begin{cases} \text{Equation [5.24]} & \text{if } \Delta > 0 \quad \text{Scheers et al. (2003a)} \\ \text{Equation [5.54]} & \text{if } \Delta < 0 \quad \text{Soldini et al. (2016b).} \end{cases} \tag{5.55}$$

The proposed control in Eq. (5.55) was implemented in the CRUISE (Controlled Routes by Using Innovative Solar-radiation Equipment) algorithm in Matlab. A description of CRUISE architecture is shown in Appendix A. An important remark is that not all the gain sets (G_1, G_2 and G_3) can stabilise the orbit, since the local stability is not a necessary condition of the periodic orbit stability due to resonance effects (Scheeres et al., 2003a). It is useful to compare this formulation with the proposed control law

for complex and conjugate roots (in Section 5.1.3) in order to understand the main differences.

5.2 Gain definition to achieve simple Lyapunov stability

The simple stability is guaranteed for:

$$\begin{cases} b^c = 4\omega^2 - V^c_{xx} - V^c_{yy} > 0 \\ c^c = V^c_{xx}V^c_{yy} - (V^c_{xy})^2 > 0 \\ \Delta^c = (b^c)^2 - 4c^c > 0 \end{cases} . \tag{5.56}$$

The linear stability was already proven by Scheeres et al. (2003a) for the hyperbolic×centre equilibrium; in this case, G_1 in Eq. (5.24) should be selected to be large enough to guarantee linear stability. In this section, a similar approach is used to study the stability as a function of G_2 and G_3 associated to the extended control in Eq. (5.54); where, complex and conjugate eigenvalues occur. For the definition of the control law in Eq. (5.54), V^c_{xx}, V^c_{yy} and V^c_{xy} are defined as:

$$V^c_{xx} = V_{xx} - G_2\frac{(\sigma^2+\gamma^2)}{1+u_1u_3} - G_3\frac{(\sigma^2+\gamma^2)}{1+u_2u_4} \tag{5.57}$$

$$V^c_{yy} = V_{yy} - G_2\frac{(\sigma^2+\gamma^2)(u_1^2+u_3^2)}{1+u_1u_3} - G_3\frac{(\sigma^2+\gamma^2)(u_2^2+u_4^2)}{1+u_2u_4} \tag{5.58}$$

$$V^c_{xy} = V_{xy} - G_2\frac{(\sigma^2+\gamma^2)(u_1+u_3)}{1+u_1u_3} - G_3\frac{(\sigma^2+\gamma^2)(u_2+u_4)}{1+u_2u_4}. \tag{5.59}$$

The definition of b^c is:

$$b^c = b + (\sigma^2+\gamma^2)\left[G_2\frac{1+u_1^2+u_3^2}{1+u_1u_3} + G_3\frac{1+u_2^2+u_4^2}{1+u_4u_4}\right]. \tag{5.60}$$

Since $b < 0$ and b^c must be greater than zero, it is important to study the sign of the terms associated to the controller. In Eq. (5.60), $u_1u_3 = a_*^2 + b_*^2$ and $u_2u_4 = d_*^2 + e_*^2$ are positive terms, thus all the fractions are positive (> 0). This means that, for the first condition in Eq. (5.56), G_2 and G_3 should be positive and big enough to keep $b^c > 0$. As a consequence of Eq. (5.56), $(b^c)^2$ must be greater than $4c^c$ such as $\Delta^c > 0$. The definition of Δ^c is

$$\Delta^c = (4\omega^2 - V^c_{xx} - V^c_{yy})^2 - 4(V^c_{xx}V^c_{yy} - (V^c_{xy})^2) \tag{5.61}$$

where, Eq. (5.61) can be rewritten as:

$$\Delta^c = 8\omega^2 b^c + (V^c_{xx} - V^c_{yy})^2 + 4(V^c_{xy})^2. \tag{5.62}$$

Since $(V^c_{xx} - V^c_{yy})^2$ and $(V^c_{xy})^2$ are positive terms, the condition $\Delta^c > 0$ is satisfied by $b^c > 0$. The definition of c^c is:

$$c^c = c + (\sigma^2+\gamma^2)^2 \left[G_2^2 \frac{u_1^2+u_3^2}{(1+u_1u_3)^2} + G_3^2 \frac{u_2^2+u_4^2}{(1+u_2u_4)^2} + \frac{G_2G_3(u_2^2+u_4^2+u_1^2+u_3^2)}{(1+u_2u_4)(1+u_1u_3)} \right] + K_n; \tag{5.63}$$

where, K_n collects all the negative terms:

$$\begin{aligned} K_n = \; & -(\sigma^2+\gamma^2) \Big\{ G_2 \left[\tfrac{V_{xx}(u_1^2+u_3^2)+V_{yy}}{1+u_1u_3} - \tfrac{2V_{xy}(u_1+u_3)}{1+u_1u_3} + G_2(\sigma^2+\gamma^2) \tfrac{(u_1+u_3)^2}{(1+u_1u_3)^2} \right] \\ & + G_3 \left[\tfrac{V_{xx}(u_2^2+u_4^2)+V_{yy}}{1+u_2u_4} - \tfrac{2V_{xy}(u_2+u_4)}{1+u_2u_4} + G_3(\sigma^2+\gamma^2) \tfrac{(u_2+u_4)^2}{(1+u_2u_4)^2} \right] \\ & + 2G_2G_3(\sigma^2+\gamma^2) \tfrac{(u_1+u_3)(u_2+u_4)}{(1+u_2u_4)(1+u_1u_3)} \Big\}. \end{aligned} \tag{5.64}$$

Since $c < 0$, K_n collects all the negative terms and c^c must be > 0, G_2 and G_3 must be positive and big enough to guarantee the stability. Note that, as a result of both the conditions $b^c > 0$ and $c^c > 0$, either G_2 or G_3 must be non zero.

5.3 Floquét modes control

In this section, the Floquét Mode (FM) control is shortly presented since it will be compared with the HSP control. The Floquét mode based control approach was originally developed by Simó et al. (1987) and Gómez et al. (2001). The principle of this control method was presented in Section 2.4.1. When extended to SRP missions, the FM method let the solar sail follow its natural dynamics; which initially allows it to follow its unstable manifold. Then, the solar sail orientation is changed to bring the trajectory back to the stable manifold of the LPO target orbit.

The FM approach exploits the invariant manifold theory and the Floquét modes to compute the required Δv manoeuvres. The Floquét modes are used to compute the unstable components of the error state vector, by exploiting the eigenstructure of the monodromy matrix, $\boldsymbol{M}$. Then, the manoeuvre is computed to compensate for the instability (i.e., unstable manifold). In this investigation, the FM algorithm used is the one formulated by Keeter (1994). In Keeter's (1994) work, the FM was compared to the target points station-keeping approach (Howell and Pernicka, 1993). For periodic orbits, the monodromy matrix is symplectic and its eigenvalues have the following characteristics:

- two real eigenvalues m_1 and $m_2 = \frac{1}{m_1}$ that identify the stable and unstable manifolds of the hyperbolic equilibrium;
- two real eigenvalues equal to one $m_3 = m_4 = 1$ for the in-plane centre manifold;
- two complex eigenvalues m_5 and m_6 for the out-of-plane centre manifold.

Since the eigenvalues of the STM are not periodic functions of time, the elements of the STM change as the time increases and the dominant eigenvalues (unstable direction) show an exponential growth. Therefore, it becomes challenging and inaccurate to obtain the eigenvectors from the STM as the time increases (Gómez et al., 2001; Keeter, 1994). It is convenient to express the eigenstructure of the STM with an alternative representation by using the Floquét theory to avoid numerical problems in the computation of the STM, (Wiesel and Pohlen, 1994). The FMs are a particular modal approach applied for time-invariant Hamiltonian systems with periodic solutions. Note that, the advantage of using a modal analysis is well known in structural engineering when studying the dynamical properties of a system. Thus, the computation of the Floquét modes in the CR3BP is (Keeter, 1994):

$$\tilde{\boldsymbol{E}}(t, t_0) = \boldsymbol{\Phi}(t, t_0) \cdot \boldsymbol{S} e^{-\tilde{\boldsymbol{J}} t} \tag{5.65}$$

where, $\boldsymbol{S}$ is a real matrix and collects all the eigenvectors of the monodromy matrix $\boldsymbol{M} = \boldsymbol{\Phi}(T, t_0)$ by separating their real and imaginary parts, and $\tilde{\boldsymbol{J}}$ is the Jordan matrix which is a function of the eigenvalues of the monodromy matrix. The columns of the matrix $\tilde{\boldsymbol{E}}$ correspond to the Floquét mode that are periodic eigenvectors associated to the monodromy matrix.

A summary of the FM control approach is presented by following the notation of Keeter (1994) as it is useful for the following comparison of the FM and HSP control algorithms. As previously stated, the FM controller aims to cancel the projection of the state error onto the unstable direction. The controller uses the information from all the components of the state error vector in position $\delta \boldsymbol{r}$ and in velocity $\delta \dot{\boldsymbol{r}}$. Since the state error should be projected onto the FM ($\tilde{\boldsymbol{E}}$ with column component vectors $\bar{e}_i$), once the FM are determined, it is possible to compute the correction manoeuvres by first computing the projection tensor as:

$$\Pi_i = \frac{\bar{e}_i \cdot \bar{e}_i^T}{\bar{e}_i^T \cdot \bar{e}_i} \qquad\qquad i = 1, \ldots, 4 \tag{5.66}$$

then, by considering that $\delta \boldsymbol{x} = \{\delta \boldsymbol{r},\ \delta \dot{\boldsymbol{r}}\}$ is the difference between the actual trajectory and the target orbit, each components $\delta \boldsymbol{x}_i$ can be determined as:

$$\delta \boldsymbol{x}_i = \Pi_i \cdot \delta \boldsymbol{x} \qquad\qquad i = 1, \ldots, 4 \tag{5.67}$$

where, $\delta \boldsymbol{x}_1$ is the unstable direction to be counteracted; while, $\delta \boldsymbol{x}_2$, $\delta \boldsymbol{x}_3$ and $\delta \boldsymbol{x}_4$ are associated to the stable, centre and centre direction respectively. The controller is designed so that a Δv is given to compensate $\delta \boldsymbol{x}_1$ (Gómez et al., 2001; Keeter, 1994) as follows:

$$\Delta v = \left(\sum_{i=2}^{n} \alpha_i \cdot \delta \boldsymbol{x}_i \right) - \delta \boldsymbol{x}_1 \tag{5.68}$$

where, the unknowns are α_i and Δv. Note that the index n is equal to 4 for planar motion and 6 for three dimensional dynamics. The velocity components are also required to cancel out the unstable part; however, there are more unknowns than equations. For this reason, there is an infinite number of solutions and for 3-axis control an optimisation is required to minimise a cost function. However, for our purposes, a x-axis control was considered where a closed-form solution exists (see Appendix E.2 for more details).

5.4 Comparison of the Hamiltonian structure preserving and the Floquét modes approaches

Both the HSP and the FM control methods aim to project the error state vector along the eigenvectors of the STM. The main difference between these two approaches is that the HSP control law uses the information of the local eigenvectors of the linearised equations in Eq. (5.3) as an approximation of the STM instantaneous stability map, whereas the FM uses the information of the global eigenvectors in Eq. (5.65) (i.e. the eigenvectors that belong to the monodromy matrix) of the linearised equations.

For time-invariant systems with small time variations (Scheeres et al., 2003a), a good approximation of the STM is computed as shown in Appendix C.9, is:

$$\boldsymbol{\Phi}(t) = e^{\boldsymbol{A}(\bar{\boldsymbol{X}}(t))\cdot t}; \tag{5.69}$$

where, $\boldsymbol{A}(\bar{\boldsymbol{X}}(t))$ is the matrix of the linearised equations of motion. The HSP controller uses the eigenstructure of $\boldsymbol{A}(\bar{\boldsymbol{X}}(t))$; while, the FM uses the eigenstructure of $\boldsymbol{\Phi}$. Eq. (5.69) is the link between the HSP and the FM approaches since both controllers are linear.

Another important aspect is that the effect of the HSP controller is to remove both the stable and unstable directions of the instantaneous map in Eq. (5.55); while, the FM controller compensates only the unstable directions of the target orbit (mapped at each orbital period) in Eq. (5.68). As already mentioned, the reasoning behind the control law proposed by Scheeres is that both the stable and unstable directions need to be compensated to guarantee simple Lyapunov stability, Eq. (5.4). Indeed, the Lyapunov stability cannot be achieved by only compensating for the unstable direction. Thus, a main difference between the HSP and FM control strategies is related to the Lyapunov stability. By adding the effect of the HSP or FM control to the dynamics, Eq. (3.39) changes into:

$$HSP: \begin{cases} \ddot{x} - 2\omega_0 \dot{y} = V_x + a_x^c \\ \ddot{y} + 2\omega_0 \dot{x} = V_y + a_y^c \\ \ddot{z} = V_z + a_z^c \end{cases} \qquad FM: \begin{cases} \ddot{x} - 2\omega_0 \dot{y} = V_x \\ \ddot{y} + 2\omega_0 \dot{x} = V_y \\ \ddot{z} = V_z \end{cases} \tag{5.70}$$

where a_x^c, a_y^c, a_x^c are the components acceleration of $\boldsymbol{a}^c$. In the case of the FM, the effect of the $\Delta v = \{\Delta\dot{x}, \Delta\dot{y}, \Delta\dot{z}\}$ is added to the spacecraft velocity as $v = \{\dot{x} + \Delta\dot{x}, \dot{y} + \Delta\dot{y}, \dot{z} + \Delta\dot{z}\}$, at the time of the given impulsive manoeuvre. The HSP controller is designed for low thrust applications as the control law is given as a continuous acceleration. Whereas, the FM controller is usually used for impulsive manoeuvres where a discrete Δv is required; however, it can also be extended to low thrust applications.

From a physical point of view, the HSP controller creates an artificial centre manifold that eliminates the stable and unstable directions; thus, the controller changes the shape of the potential function. However, the spacecraft will not stay indefinitely on the target orbit since the HSP controller can only guarantee simple Lyapunov stability. This means that the decay of the spacecraft is now slower, from an exponential decay (i.e. no control) to a polynomial decay (i.e. HSP control). In comparison, the FM controller gives an instantaneous Δv that changes the energy of the system; therefore, the potential function is unchanged. However, between two manoeuvres, the spacecraft will start drifting and the decay can be compensated for by a new Δv. This is since the HSP controller uses the eigenvalues and eigenvectors of the actual trajectory, whereas the FM uses the modes of the target orbit.

From Orbit Determination (OD), a complete and exact knowledge of the state of the spacecraft is not possible (Gordon, 1993); thus, an important aspect in selecting a control law from the OD point of view is the knowledge of the state vector of the spacecraft. The HSP controller requires the knowledge of the spacecraft position, whereas the FM requires the knowledge of both the position and velocity. Moreover, uncertainty in determining the spacecraft state vector is often related to an inadequate representation of the dynamical model. For example, a further approximation is to use the linearised system of equations to model the nonlinear system (Gordon, 1993). However, Scheeres demonstrated the robustness of the HSP control with nonlinearities. Therefore, in the following, a sensitivity analysis is performed for both the HSP and FM controllers to identify the characteristics and the robustness of these approaches.

Finally, when it is of interest to find the optimal solution, both the controllers require the definition of a weight matrix that describes the propellant cost. Thus, it is necessary to select the optimum gains of the HSP control or to choose the minimum Δv for a 3-axis FM control.

In this study, the sensitivity analysis of the two controllers is performed by changing the most important design parameter (the gains for the HSP control and the time of

Control	**Hamiltonian Structure Preserving (HSP)**	**Floquét Modes (FM)**
Controller compensates	Stable and unstable directions	Unstable direction
Lyapunov stability	Yes	No
Propulsion system	Low thrust	Impulsive manoeuvres
Controlled trajectory	Polynomial decay	Follow the nominal path
Weight matrix (optimum control)	Only for optimum gains	Only 3-axis control
Disadvantages	Polynomial decay of the s/c	Specific Jordan matrix for different orbits
Controller uses info on	Actual trajectory	Target trajectory
State vector error in	Position	Position and velocity

Table 5.1: Summary of HSP and FM main features.

manoeuvre for the FM control), rather than finding an optimal solution. In this way, the results will depend on the time of the manoeuvre along the orbit for the x-axis FM control and the gain for the HSP control. Table 5.1 lists a summary of the main features of the HSP and the FM approaches.

Thruster	Type	$\mathbf{I_{sp}}$ [s]	Thrust
RIT-10	Ion	2500-3700	0.3-41 [mN]
FEEP	Cesium	7000-11000	0.1-1200 [μ N]
FEEP	Indium	10000	1-100 [μ N]
Colloid	-	500-1500	0.5-25 [μ N]

Table 5.2: Thrusters data sheet (Leach and Neal, 2002).

5.5 Robustness to failure in the orbit insertion manoeuvre

In the previous section, a qualitative comparison of the HSP and the FM was given and their main features and differences were presented in Table 5.1. Conversely, in this section, a sensitivity analysis of the control parameters is carried out to verify the robustness of the two control laws. An injection error due to the launch vehicle uncertainties or due to failures in the Halo Orbit Insertion (HOI) manoeuvre is taken into account.

The ESA/NASA's SOHO spacecraft is selected as a mission scenario as it has a nominal orbit similar to the ISEE-3 mission. Other authors such as Keeter (1994) used similar orbits as a reference for a comparison between FM and the target point controllers. Therefore, this allows a comparison of this work with other control laws. The SOHO spacecraft is in a halo orbit at L_1 with a period of 177.86 days.

The sensitivity analysis is performed as a function of the gains for the HSP control law and of the Δt between two manoeuvres for the FM control. The performance of the HSP and FM controllers are presented regarding the total Δv required, computed as

$$\Delta v = \int_{t_0}^{t} |\boldsymbol{a}^c| d\tau \tag{5.71}$$

for the HSP control and as

$$\Delta v = \sum_{k=1}^{m} \Delta v_k, \tag{5.72}$$

for the FM control, where m is the number of manoeuvres; while, t_0 and t are the initial and final times respectively. The HSP gives a continuous acceleration (small thrusters) and it is possible to compute the approximate thrust profile by multiplying the acceleration by the wet spacecraft mass (which in the case of SOHO is 1853 kg). However, the fuel consumption is not taken into account; thus, the requirements of the thrust are more conservative as the time increases. Note that, a threshold concerning the minimum and maximum thrust provided by the propulsion system should be taken into account. However, the acceleration is not bounded in our simulations but the level of thrust provided by the thrusters, shown in Table 5.2, will be compared with the required controlled acceleration (Leach and Neal, 2002).

In the case of the FM control, there is a minimum Δt between two manoeuvres due to OD and telecommunication constraints, which is around 30 days. Furthermore, in real applications, the minimum Δv should not be lower than 2 cm/s. Otherwise, the Δv would be of the same order of magnitude as the tracking errors (Keeter, 1994). Also in this study, the Δv and the tracking error constraints are not considered to make the FM performance comparable to the HSP, without being influenced by any thresholds.

This investigation uses the equations of motion shown in Eq. (3.39) without the effect of SRP, $\boldsymbol{a}^s = 0$. Thus, the two control laws are compared independently from the SRP effect. SOHO's orbit has eigenvalues that are real pairs and pure imaginary ($\Delta > 0$). The control law was extended to the z direction in Appendix E.1 here instead is presented for planar dynamics. For the case of the FM control, the control law given by Eq. (5.72) of Appendix E.2 is used. The results are obtained by increasing the injection error in both position and velocity to emulate an error in the HOI manoeuvres caused by the launcher. Thus, the spacecraft is displaced from its target orbit. The range in the injection error is selected to include representative errors conditions and possible failures in the manoeuvre. Different test cases were analysed where, the injection error is, firstly, given in position along the x-, y- and z- axis respectively by progressively increasing the injection error in the range of $\{0, 10, 100, 1000, 10^4, 10^5\}$ km. Then, an injection error given in velocity along each single axis is also explored, where the range is selected as $\{0, 2, 4, 6, 8, 10\}$ m/s. The values in the selected injection error are chosen to push the performance of the two controllers into a non-linear dynamical regime.

Each test is performed for the HSP and the FM controllers, but in the first case a sensitivity analysis in the gain parameter is carried out where set of twenty gains is selected such that:

- fifteen gains, G, are equally distributed within 1 and 10,
- $G = 15$,
- $G = 30$,
- $G = 60$,
- $G = 90$, and
- $G = 100$.

Also for the FM control, twenty different Δt values between two consecutive manoeuvres are selected by defining the number of intervals N along the period, T, where the manoeuvre occurs. Thus, $\Delta t = T/N$ and values of N are selected such as:

- N is between 2 and 14 with step 1,

- N is between 17 and 40 with step 5,
- $N = 50$, and
- $N = 177$.

These values in N correspond to values in Δt within 1 day and 89 days.

Under the contingency, test the threshold of orbit stability is defined in this study as an orbit that stays within a maximum distance of 10^5 km from the target orbit for at least nine orbital periods (which corresponds to 4.4 years of the mission lifetime).

Figure 5.7 shows SOHO's orbits (coloured scale curves) after an initial displacement along the z-axis from the target orbit (black curve) is given. The color scale in Figure 5.7 indicates the selected gain for the HSP control (Figure 5.7(a)) or the Δt between two manoeuvres for the FM control (Figure 5.7(b)). As shown in Figure 5.7(a), a higher gain stabilises the orbit for the HSP control; while, lower Δt between two manoeuvres stabilise the orbit for the FM control as in Figure 5.7(b). For both the HSP and the FM strategies, it is evident that both controllers are robust to errors along the z-axis in both position and velocity since the required Δv is relatively low and few solutions lead to an uncontrolled orbit. This advantage is due to the fact that the controlled orbits have a smaller amplitude along z compared with the target orbit as shown in Figure 5.7.

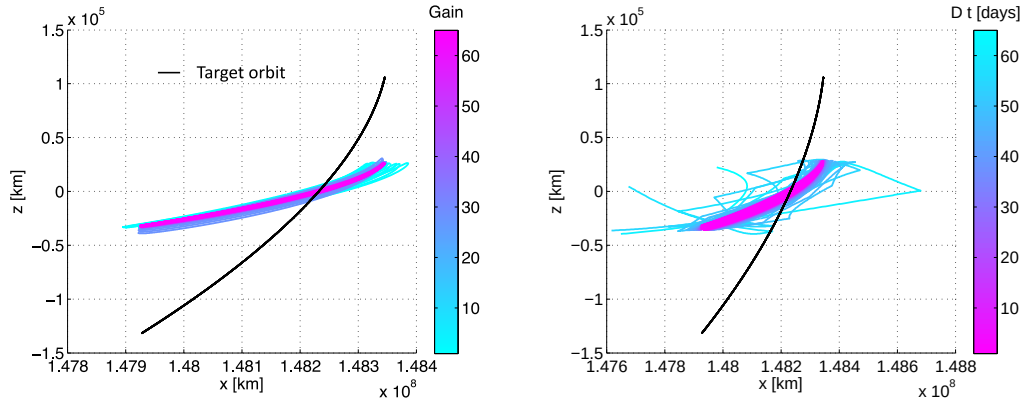

(a) HSP control.

(b) FM control.

Figure 5.7: Controlled trajectories for 10^5 km of z-axis injection error.

The next step is to analyse the case of positional injection errors along either the x or y axis. The two controllers can not be pushed to high errors in velocity due to failures in stabilising the orbit. Figure 5.8 shows as before the controlled orbit after a given offset along the y-axis. The HSP shown in Figure 5.8(a) is more robust to contingency cases when compared to the FM data in Figure 5.8(b) since high offsets in positions requires relatively small gains. For the HSP controller, the effect of an initial injection error in position excites the frequency of the artificial centre manifold such that the spacecraft oscillates along the target orbit. Although the satellites orbit oscillates around the

target orbit, the control approach manages to stabilise the orbit to a sufficient degree of accuracy.

Figure 5.9 shows the required Δv for both controllers as a function of the errors along the y-axis which is calculated from the gains for the HSP control (Figure 5.9(a)) and from the Δt between two manoeuvre for the FM control (Figure 5.9(b)). The Δv is computed using Eq. (5.71) for the HSP control and using Eq. (5.72) for the FM control and it is presented using a logarithmic scale. As can be seen in Figure 5.9(a) the HSP control requires a very low total Δv, in the range of $3.53 \cdot 10^{-7}$ m/s to 7 m/s. Instead, the FM requires Δv between $4.19 \cdot 10^{-3}$ m/s and 7210 m/s as shown in Figure 5.9(b). Note that the performance of the FM could be further improved with a 3-axis control and the Δv could approximately be reduced to a third of these values. Therefore, the requirements for the FM with 3-axis control would be expected to be between $1.39 \cdot 10^{-3}$ m/s and 2400 m/s. This is a conservative approach since the Δv obtained with 3-axis control is higher than shown by Keeter (Keeter, 1994). In any case, the HSP control requires a lower fuel consumption when compared to the FM control.

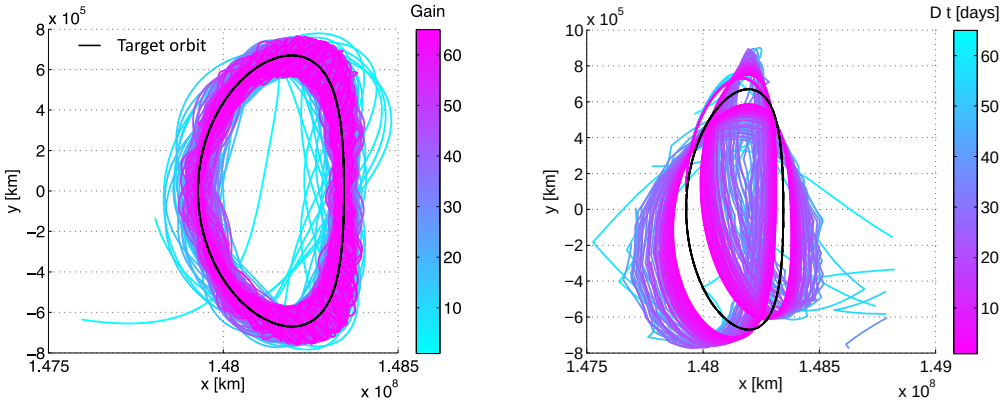

(a) HSP control. (b) FM control.

Figure 5.8: Controlled trajectories for 10^5 km of y-axis injection error.

Figure 5.10 and Figure 5.11 show a sensitivity analysis as a function of the gain for the HSP, Figure 5.10, and Δt between two manoeuvres for the FM, Figure 5.11; the maximum position error between the SOHO spacecraft and the target orbit is shown. This has been calculated for different injection errors along the y-axis from 10 to 10^5 km. Note that, the FM often requires manoeuvres to be performed more frequently than the OD limit of 30 days and, for this reason, several solutions should be discarded as shown in Figure 5.9(b).

Figure 5.10 shows how to select the gain to achieve the minimum error, $|dr|$, after a certain number of orbital periods n, for a specific initial injection error. $|dr|$ is the error between the spacecraft's distance from the origin of the synodic reference frame and a threshold of 10^5 km. This threshold was selected to identify all the unstable trajectories that may occur. This might be useful information for OD. Note that, with a small gain;

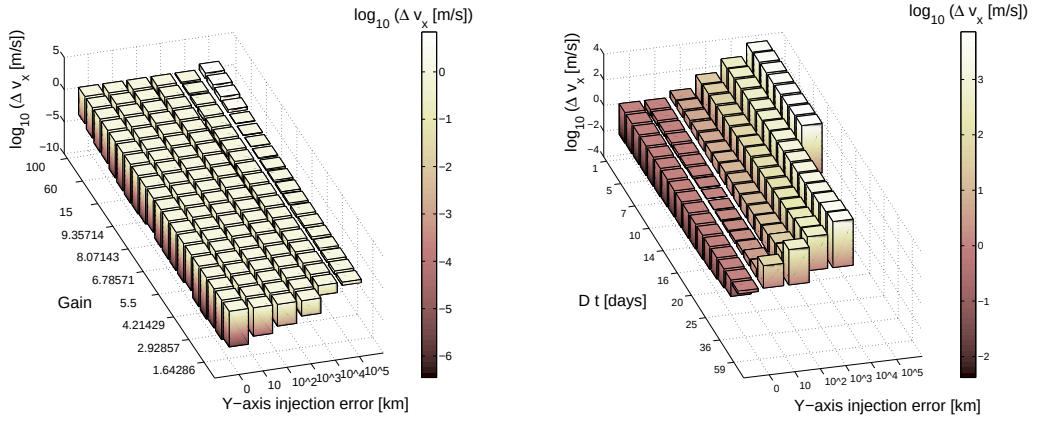

(a) HSP control.

(b) FM control.

Figure 5.9: error in logarithmic scale.

a tiny white area indicates unstable solutions for the HSP control as the gain is not high enough to stabilise the orbit. Instead, for the FM the white area in Figure 5.11 denotes uncontrolled orbit solutions. The white area increases with the injection error when the time between manoeuvres (Δt) is constrained, decreasing the stabilisation of the orbit. Thus, these maps can be used in trade-off studies for OD and to determine the overall time mission duration as a function of the initial injection error for both controllers.

The previous tests verified the robustness of the two control laws under contingency analysis due to failure in the insertion launcher manoeuvre. Now a nominal injection error due to uncertainty in the spacecraft's position and velocity will be considered. A standard order of magnitude of the injection error in the position and velocity is around 10 km and 1 m/s respectively (Keeter, 1994), by taking into account that launcher vehicle errors are typically on the same order of magnitude in velocity of 1 m/s Serban et al. (2002). Thus, this analysis will study a realistic nominal injection error. The injection error is given in a random direction: in position, in velocity and position and velocity together. In these tests, the modulus of the error in the position is selected to be around 15 km and the one in velocity is chosen to be around 3 m/s. A typical injection error in position is $\boldsymbol{r} = \{6.49,\ 11.25,\ 7.5\}$ km and in velocity is $\dot{\boldsymbol{r}} = \{0.0013,\ 0.00225,\ 0.0015\}$ km/s. A Δt of 30 days and a gain of 10 is selected for the FM control systems respectively. In order to cancel the error in position, the total Δv is 0.98 m/s for the FM and $1.4 \cdot 10^{-4}$ m/s for the HSP. For the case of an error in velocity, the total Δv is 440 m/s for the FM and $2.14 \cdot 10^{-2}$ m/s for the HSP. Finally, when an error both in position and in velocity is given, the total Δv is 2250 m/s for the FM and $2.96 \cdot 10^{-2}$ m/s for the HSP.

Figure 5.12 shows the scenario when the injection error is given in both position and velocity. The controlled orbits are shown respectively in Figure 5.12(a) for the HSP and Figure 5.12(c) for the FM. Figure 5.12(b) shows the control thrust required for the HSP control reported that can be compared to values to the typical thruster values; this

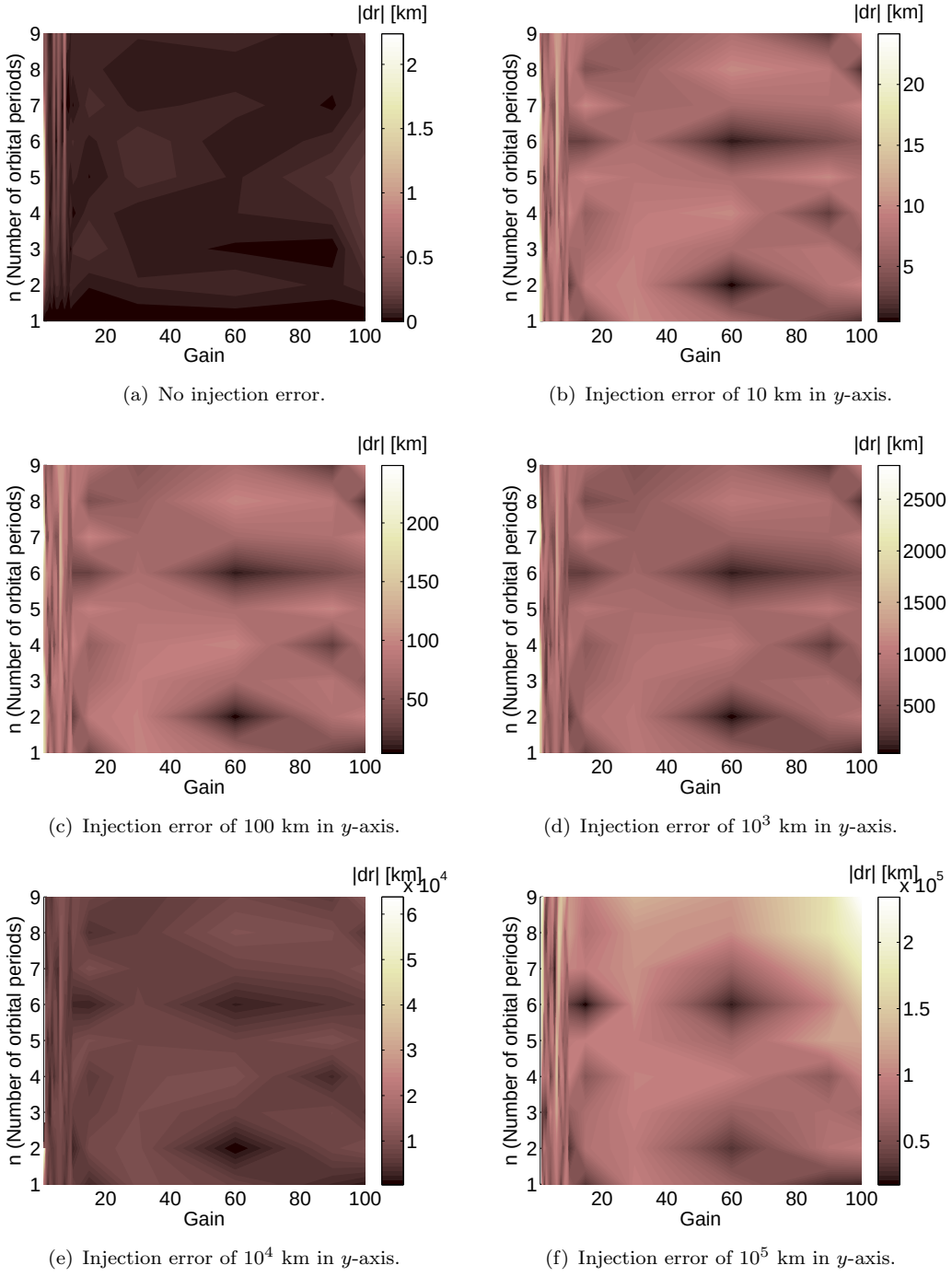

(a) No injection error.

(b) Injection error of 10 km in y-axis.

(c) Injection error of 100 km in y-axis.

(d) Injection error of 10^3 km in y-axis.

(e) Injection error of 10^4 km in y-axis.

(f) Injection error of 10^5 km in y-axis.

Figure 5.10: HSP control: sensitivity analysis of |dr| at each orbital period n as a function of the selected control gains.

can be compared in Table 5.2; while, Figure 5.12(d) shows the Δv required for the FM control. Once again, the requirements in the HSP control in term of total Δv are lower than with the FM approach.

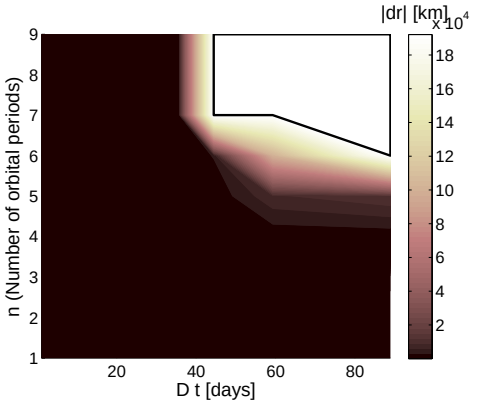

(a) No injection error.

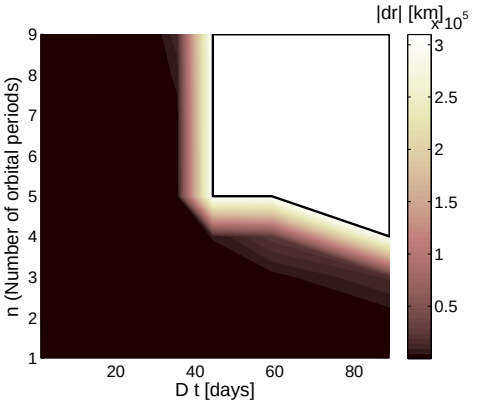

(b) Injection error of 10 km in y-axis.

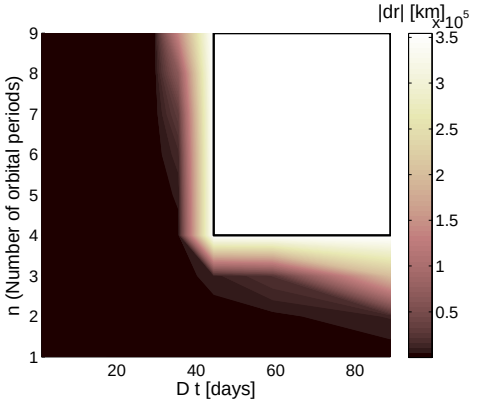

(c) Injection error of 100 km in y-axis.

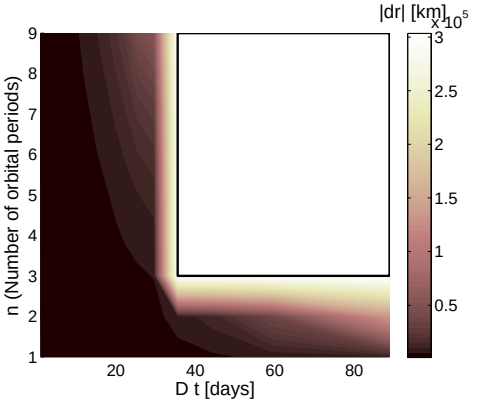

(d) Injection error of 10^3 km in y-axis.

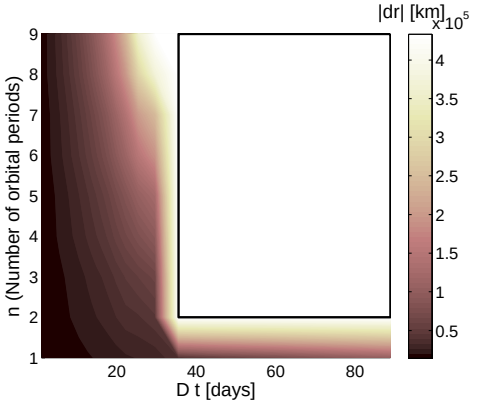

(e) Injection error of 10^4 km in y-axis.

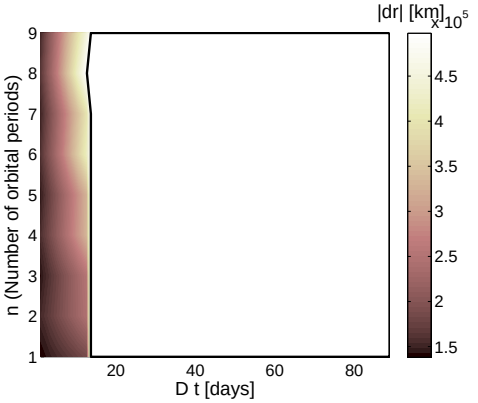

(f) Injection error of 10^5 km in y-axis.

Figure 5.11: FM control: sensitivity analysis of |dr| at each orbital period n as a function of the time between two consecutive manoeuvres Δt.

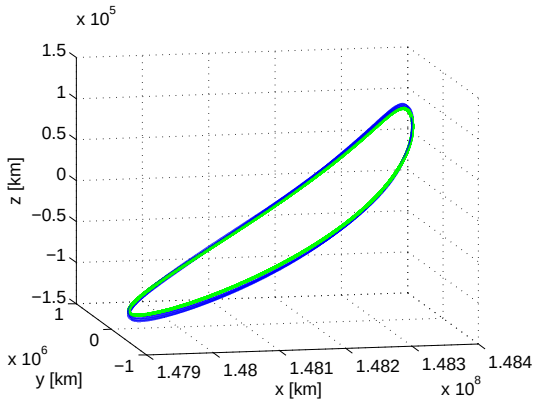

(a) Orbit controlled with HSP.

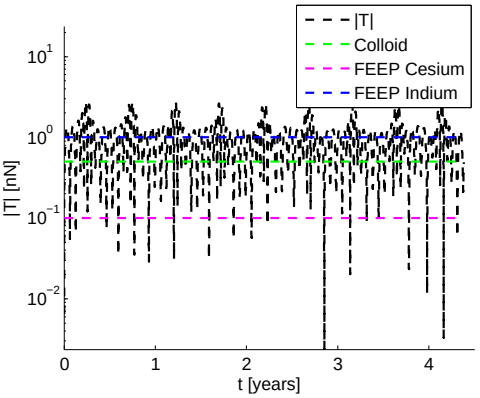

(b) Thrust evolution as a function of time.

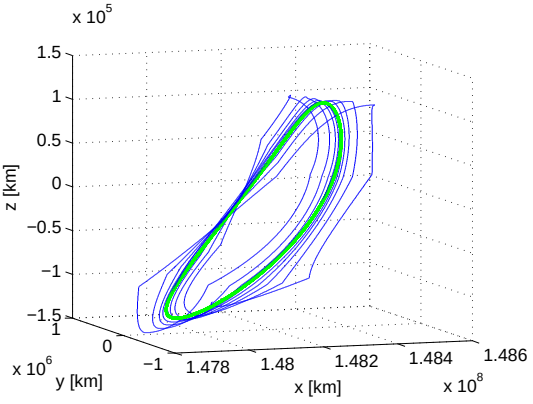

(c) Orbit controlled with FM.

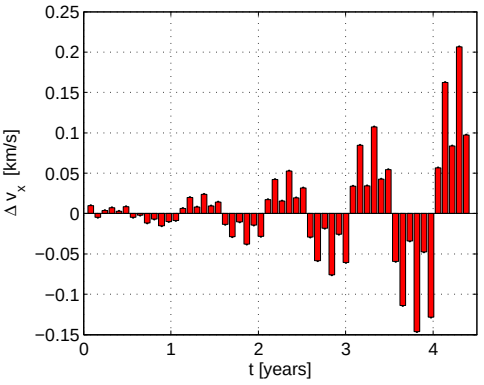

(d) ΔV_x evolution as a function of time.

Figure 5.12: Controlled orbit and control requirements in case of an injection error in position and velocity with a modulus of 15 km and 3 m/s.

5.5.1 Remarks

The Hamiltonian-Structure Preserving control was compared with the Floquét mode approach. By giving a high initial injection error due to failure in the halo insertion manoeuvre, it was possible to verify the robustness of the two methods by comparing their performances:

- the HSP control has shown to be robust when a failure in the halo insertion manoeuvre occurs, whereas the FM control does not always converge to a stable solution;
- the HSP control also works in a regime of non-linearities as already proven by Scheeres et al. (2003a);
- the advantage of the HSP control is that only an estimation of the state position error is needed;
- the HSP control does not depend on the selected orbit as for the FM control;
- the continuous acceleration required by the HSP control is tiny (the overall Δv is less when compared to the FM control requirements).

These results suggest that the HSP control is preferable for low-thrust applications or, when possible, for propellant-free systems that exploit SRP. The advantage of the HSP control is in exploiting the natural dynamics of the restricted three-body problem to stabilise the motion of the spacecraft and it has been shown to be a promising approach.

5.6 Actuators model: deployable reflective structures

As shown by Farrés and Jorba (2008) and Xu and Xu (2009), the control accelerations can be expressed with the linear approximation in the orientations angles and area, so $\boldsymbol{a^s}$ is defined as:

$$\begin{aligned}\boldsymbol{a^s}(\alpha,\delta,\beta) = \quad & \boldsymbol{a^s}(\alpha_0,\delta_0,\beta_0) + \left.\frac{\partial \boldsymbol{a^s}}{\partial \alpha}\right|_{(\alpha_0,\delta_0,\beta_0)} (\alpha-\alpha_0) + \left.\frac{\partial \boldsymbol{a^s}}{\partial \delta}\right|_{(\alpha_0,\delta_0,\beta_0)} (\delta-\delta_0) \\ & + \left.\frac{\partial \boldsymbol{a^s}}{\partial \beta}\right|_{(\alpha_0,\delta_0,\beta_0)} (\beta-\beta_0) + O(2).\end{aligned} \tag{5.73}$$

It is possible to write $\Delta\alpha = (\alpha-\alpha_0)$, $\Delta\delta = (\delta-\delta_0)$ and $\Delta\beta = (\beta-\beta_0)$ and by imposing that the SRP acceleration is given by the HSP control as $\boldsymbol{a^s}(\alpha,\delta,\beta) = \boldsymbol{a}^c$, Eq. (5.73)

can be rewritten as:

$$\boldsymbol{a}^c = \boldsymbol{a}^{\boldsymbol{s}}(\alpha_0, \delta_0, \beta_0) + \left[\frac{\partial \boldsymbol{a}^{\boldsymbol{s}}}{\partial \boldsymbol{\Theta}}\right]\Bigg|_{(\alpha_0,\delta_0,\beta_0)} \Delta\boldsymbol{\Theta} + O(2), \tag{5.74}$$

where, $\Delta\boldsymbol{\Theta}$ is defined such as $\{\Delta\alpha, \Delta\delta, \Delta\beta\}^T$, and the Jacobian matrix is defined as:

$$\left[\frac{\partial \boldsymbol{a}^{\boldsymbol{s}}}{\partial \boldsymbol{\Theta}}\right]\Bigg|_{(\alpha_0,\delta_0,\beta_0)} = \left[\begin{array}{ccc} \frac{\partial \boldsymbol{a}^{\boldsymbol{s}}}{\partial \alpha}\Big|_{(\alpha_0,\delta_0,\beta_0)}, & \frac{\partial \boldsymbol{a}^{\boldsymbol{s}}}{\partial \delta}\Big|_{(\alpha_0,\delta_0,\beta_0)}, & \frac{\partial \boldsymbol{a}^{\boldsymbol{s}}}{\partial \beta}\Big|_{(\alpha_0,\delta_0,\beta_0)} \end{array}\right]. \tag{5.75}$$

The derivatives of the SRP acceleration in Eq. (5.75) is given in Appendix E.3 and by inverting Eq. (5.74), the variation in the control parameters is given by:

$$\Delta\boldsymbol{\Theta} = \left[\frac{\partial \boldsymbol{a}^{\boldsymbol{s}}}{\partial \boldsymbol{\Theta}}\right]^{-1}\Bigg|_{(\alpha_0,\delta_0,\beta_0)} \left(\boldsymbol{a}^c - \boldsymbol{a}^{\boldsymbol{s}}(\alpha_0, \delta_0, \beta_0)\right). \tag{5.76}$$

5.7 Study of stability with the effect of the solar radiation pressure acceleration

The performance of the HSP control when used with SRP acceleration can now be investigated; the control acceleration is given by the actuators model described in Section 5.6, and the control law proposed by A. McInnes (2000). A. McInnes (2000)' work is based on a trajectory station-keeping technique proposed by Howell and Pernicka (1993), the target point approach, and modified by A. McInnes (2000) such that the manoeuvres are given by the effect of SRP acceleration when changing the sail orientation angles. The work of A. McInnes has been extended to include variations in the lightness parameter, β, to allow the comparison. Note that A. McInnes assumed that the variation of the control parameters (α, δ and in this extended case β) are constants along the trajectory arc of interest (Target point approach). Thus, the variational equations can be written as:

$$\frac{d}{dt}\left[\begin{array}{c} \delta\boldsymbol{r} \\ \delta\dot{\boldsymbol{r}} \\ \delta\boldsymbol{s} \end{array}\right] = \left[\begin{array}{ccc} \boldsymbol{0} & \boldsymbol{I} & \boldsymbol{0} \\ \boldsymbol{V_{rr}} & 2\omega_0\boldsymbol{J} & \boldsymbol{a^s_{rs}} \\ \boldsymbol{0} & \boldsymbol{0} & \boldsymbol{0} \end{array}\right]\left[\begin{array}{c} \delta\boldsymbol{r} \\ \delta\dot{\boldsymbol{r}} \\ \delta\boldsymbol{s} \end{array}\right]; \tag{5.77}$$

where, as for Eq. (5.3), $\delta\boldsymbol{r}$ is the position error with respect to the target orbit, $\delta\dot{\boldsymbol{r}}$ is the velocity error with respect to the target, $\boldsymbol{J}$ is defined as in Eq. (5.3) and $\delta\boldsymbol{s} = \{\alpha,\ \delta,\ \beta\}$ is the vector of the control parameters in term of SRP angles and the lightness parameter. Note that Eq. (5.3) and Eq. (5.77) differ for the selected state variables where here the SRP control parameters, $\delta\boldsymbol{s}$, are included in the state. The target point algorithm is written in term of a cost function that contains the deviation of the actual trajectory, given by:

$$\delta\bar{x}(t) = \boldsymbol{\Phi}(t, t_0) \cdot \delta\bar{x}(t_0), \tag{5.78}$$

where $\boldsymbol{\Phi}$ is the STM shown in Appendix C.9, which is now affected by the SRP acceleration. The deviation from the actual trajectory is then used to design the target point cost function (for further details refer to Howell and Pernicka (1993) and A. McInnes (2000)). The aim here is not to derive the target point algorithm but to study the Lyapunov stability of Eq. (5.77). The target point algorithm is compared to the HSP control where $\boldsymbol{A}^c(\bar{\boldsymbol{X}}(t))$ is defined as in Eq. (5.8) to demonstrate that the effect of the SRP acceleration in the target point algorithm in Eq. (5.77) does not affect the local stability. However, the orbit stability is affected by SRP acceleration since this control modifies the STM in Eq. (3.111) as for the Floquét Mode approach. Howell and Pernicka (1993) compared the target points and the Floquét Mode approaches. The idea is to study the stability of this new linearised equations; where, the characteristic polynomial is given by computing the determinant of $D(\lambda) = |\boldsymbol{Df}^c - \lambda \boldsymbol{I}| = 0$, where here $\boldsymbol{Df}^c$ is defined as the matrix in Eq. (5.77). For the planar dynamics, the characteristic polynomial is found to be:

$$\Lambda^2 + (4 - V_{xx} - V_{yy})\Lambda + (V_{xx}V_{yy} - V_{xy}^2) = 0. \tag{5.79}$$

From Eq. (5.79), it becomes clear that these modified linearised equations do not affect the local behaviour of the system since it was found the same characteristic polynomial as the planar case without the effect of SRP acceleration in Eq. (5.4). Thus, changing the angles or β will not stabilise the system and the system will still have hyperbolic×centre eigenvalues or couples of complex and conjugate values. The simple Lyapunov stability cannot be reached; thus, an artificial potential that affects the sign of b, c and Δ is needed as for the HSP control. However, note that the eigenvalues of the monodromy matrix are affected by the SRP acceleration in Eq. (3.111) through Eq. (5.77). Thus, the target point approach cannot guarantee Lyapunov stability.

5.8 Hamiltonian structure preserving control through solar radiation pressure actuactors

The purpose of this study is to investigate the use of SRP for station-keeping of spacecraft in high amplitude DPOs. The selected orbits are high-amplitude DPOs (in Figure 5.3(a)) and planar-Lyapunov orbits shown in Figure 5.3(b). When SRP is incorporated, to have a feasible acceleration, the values of the unstable manifold should never be negative (i.e. the spacecraft should be escaping outwards from the Sun). Gómez et al. (2001) named this peculiarity as the "always towards the Sun rule". This effect causes saturation in the actuator system when the lightness parameter, β, is constrained between zero and one and the orientation angles should be limited between $-\pi/2$ and $+\pi/2$ in both α and δ. Gómez et al. (2001) explained that this effect cannot be overcome unless a very high area-to-mass ratio is used. A previous extension of HSP with SRP proposed

by Xu and Xu (2009) fulfilled the "always towards the Sun" rule by selecting a very high area-to-mass ratio to avoid saturation in the control parameters. Xu and Xu (2009) selected a Lissajous orbit to apply their control law and they used an initial lightness parameter β_0 of 0.5059 which for a spacecraft with the same mass as SOHO (order of 10^3 kg) corresponds to an initial area of $6.1270{\cdot}10^5$ m^2 (which is equivalent to a 782.75 m span of a square sail area). Currently, JAXA's IKAROS mission demonstrated the capability to deploy a 20 m span sail (Tsuda et al., 2013); thus, this size of area required, as an example, for SOHO is infeasible with current technology. As our study aims to understand which parameters affect the pointing requirements and the size of the actuator area for high amplitude orbits, the structural requirements were first analysed for the simple case of halo orbits (relevant to the SOHO mission) where the SRP acceleration is provided by the HSP control law designed by Scheeres et al. (2003b).

5.8.1 SOHO mission scenario

In this section, SOHO is used as a mission scenario to verify when SRP is a feasible option to control a spacecraft in a Halo orbit using the HSP controller. In this case, the control works in the regime of the hyperbolic equilibrium and a gain of $G_1 = 10$ is required to stabilise the orbit. The mass of SOHO is set to 1000 kg and the necessary control parameters are regarding reflective area, A, in-plane angle, α, and out-of-plane angle, δ. These are computed as a function of the injection error and the primary reflective area of the spacecraft. The spacecraft is originally Sun-pointing before the action of the HSP controller. The controller is tested for a maximum of nine orbital periods that corresponds to 4.4 years.

In this analysis, the spacecraft has an initial reflective area of A_0 when the control action is off. Due to the effect of the control law, the primary area A_0 can be reduced or increased to meet the control requirements and the range in the controlled area is denoted here by A. The results are shown in Table 5.3 where it can be seen that high injection errors require a higher initial area, A_0, to guarantee a feasible solution. For example, Figure 5.13 shows the case of $A_0 = 20$ m^2 and an offset of -40 km. The solution is not feasible because of the requirements of a negative area; thus, for this specific initial injection error a minimum initial area of 35 m^2 in A_0 is required to have a feasible deployable area as shown in Table 5.3. In the case of no error in the HOI manoeuvre, the pointing requirements and the area needed to control the spacecraft are very tiny as shown in Table 5.3 for the case of $A_0 = 70$ m^2. This shows that the HSP control requires very little acceleration to stabilise the orbit. This is confirmed by Figure 5.14 that compares the same case scenario with (Figures 5.14(a), 5.14(c) and 5.14(e)) and without (Figures 5.14(b), 5.14(d) and 5.14(f)) an initial injection error. Note that, when the injection error is not considered, the controller acceleration is zero at the first orbital period because the spacecraft is precisely placed on the target orbit. Table 5.3

$x-$**axis offset [km]**	$\mathbf{A}_0$ [$\mathbf{m}^2$]	β_0	$\mathbf{A}$ [$\mathbf{m}^2$]	β	α [°]	δ [°]
-40	10	$1.53 \cdot 10^{-5}$	–	–	–	–
-40	20	$3.06 \cdot 10^{-5}$	–	–	–	–
-5	20	$3.06 \cdot 10^{-5}$	15.5−21.5	$2.4 \cdot 10^{-5} - 3.29 \cdot 10^{-5}$	± 2.5	$\pm\ 7 \cdot 10^{-3}$
-40	30	$4.59 \cdot 10^{-5}$	–	–	–	–
-40	35	$5.355 \cdot 10^{-5}$	0.5−47	$1.306 \cdot 10^{-6} - 7.24 \cdot 10^{-5}$	± 10.5	± 3
-40	40	$6.12 \cdot 10^{-5}$	5.5−52.32	$8.331 \cdot 10^{-6} - 8.004 \cdot 10^{-5}$	± 9.5	± 2.5
-40	70	$1.071 \cdot 10^{-4}$	35−83.3	$5.436 \cdot 10^{-5} - 1.259 \cdot 10^{-4}$	± 5.5	± 1.5
0	70	$1.071 \cdot 10^{-4}$	69.99−70.0001	$1.071 \cdot 10^{-4}$	$\pm\ 2.635 \cdot 10^{-5}$	$\pm\ 7.5 \cdot 10^{-8}$
-40	100	$1.53 \cdot 10^{-4}$	65.66−112	$1.004 \cdot 10^{-4} - 1.718 \cdot 10^{-4}$	± 3.8	± 1.02

Table 5.3: Area and orientations angles required for different initial reflective area and injection errors.

shows that for $A_0 = 20$ m^2 and an injection error of -5 km the solution exist and it requires reasonable variations in the area required and in the orientation angles. It also shows that, in this case, the controller should be limited to changes in just the area and the in-plane angle, α, since the variations in the out-of-plane angle, δ, are very tiny; thus are not feasible.

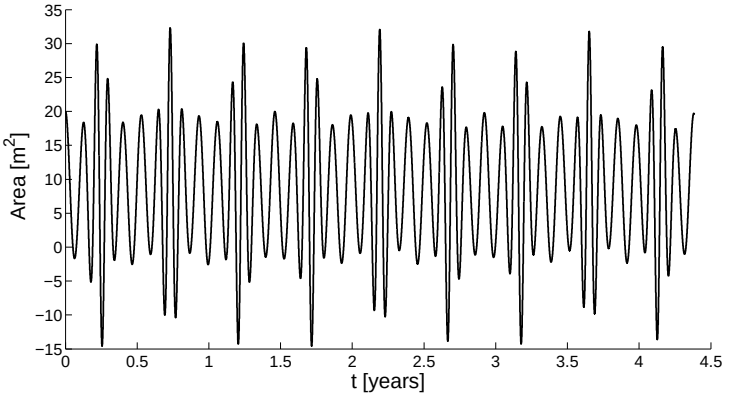

Figure 5.13: Required area when the initial area is 20 m^2 and an initial offset in x of -40 km is taken into account.

These results suggest that the HSP controller is a good candidate to perform propellant-free control using SRP acceleration. The primary area required depends on the initial injection error; however, an initial offset is required to avoid tiny control requirements that cannot be physically achieved. For example, an offset of -5 km from the target orbit requires an initial area of 20 m^2 with variations of the area of 15.5-21.5 m^2 as shown in Table 5.3. The pointing requirements are feasible in the angle α required by the controller. α shows to be on the same order of magnitude of the telescopes' sunshade Sun-tracking angle for LPOs; while, in this case in δ a control action is not necessary.

In case of the design of variable geometry actuators, the control acceleration should be limited in the variations of the control area required. Thus, the Hamiltonian structure preserving control acceleration should be a discrete time control to avoid a continuous change in time of the reflective area.

5.8.2 High amplitude planar distant prograde orbits and libration point orbits

In this section, the performance of the HSP controller enhanced by SRP is tested for high amplitude orbits where couples of complex and conjugate eigenvalues occur. The controller devised in Section 5.1 is used. The mass of the spacecraft is still 1000 kg and the gains required to stabilise the orbit are $G_1 = G_2 = G_3 = 31$. The controller was tested for the planar LPOs in Figure 5.3(a) and for the DPOs orbit shown in Figure 5.3(b). A primary reflective area of 70 m^2 is selected and an initial offset along the $x-$axis is included to avoid tiny control requirements. Figure 5.15 shows the required area and in-plane angle for the selected high amplitude orbits. In this case, the controller cannot be subjected to high injection errors due to infeasible solutions; thus, a minimum offset of -1 km and -0.5 km are selected for the LPO (Figure 5.15(a) and 5.15(c)) and for the DPO (Figure 5.15(b) and 5.15(d)) respectively. In both cases, a small offset

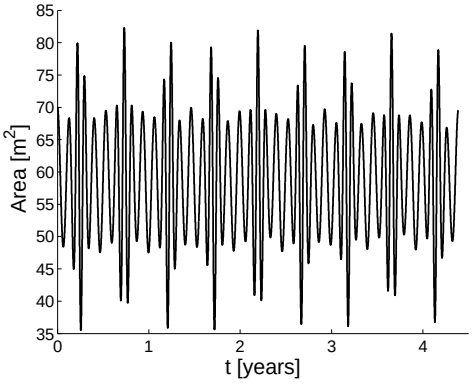

(a) Area required: offset of -40 km in $x-$ axis.

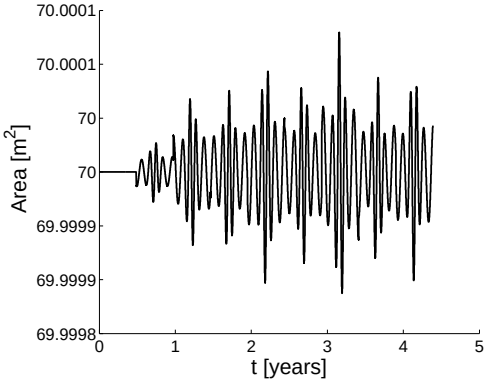

(b) Area required: no offset in $x-$ axis.

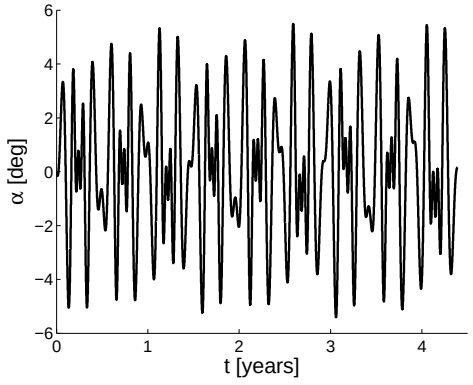

(c) In-plane angle, α: offset of -40 km in $x-$ axis.

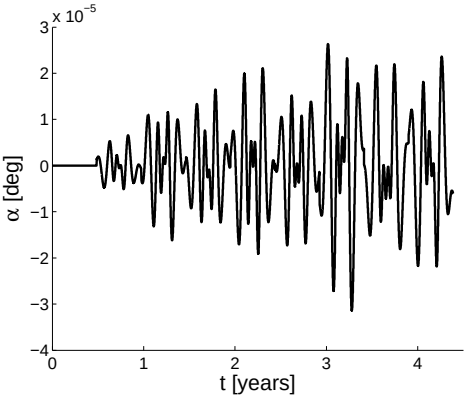

(d) In-plane angle, α: no offset in $x-$ axis.

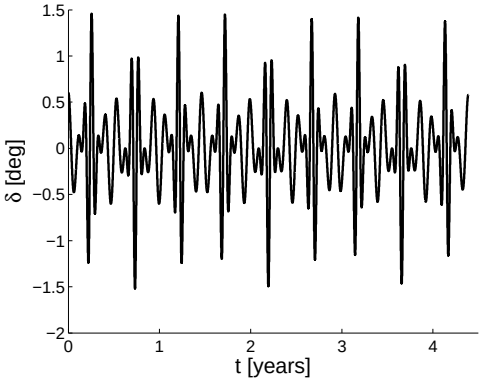

(e) Out-of-plane angle, δ: offset of -40 km in $x-$ axis.

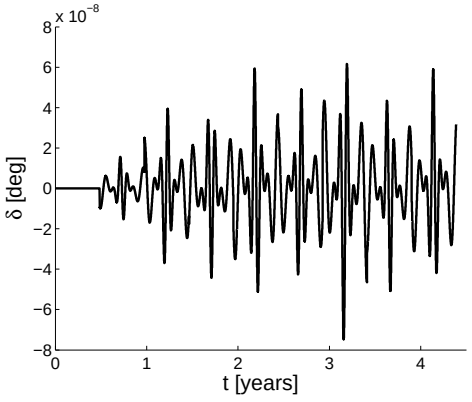

(f) Out-of-plane angle, δ: no offset in $x-$ axis.

Figure 5.14: Comparison of the effect of the initial injection error along the x-axis on to reflective area and orientations angle required for stabilising the orbit when an initial area of 70 m^2 is selected.

required relatively high variations in area and α when compared to the SOHO case study. This is because these orbits have an index of stability that are much smaller than Halo orbits; thus, a small deviation from the target shows higher values in the control requirements. Therefore, high amplitude orbits require a precise insertion manoeuvre with a tiny deviation from the target if the control is to be performed using SRP.

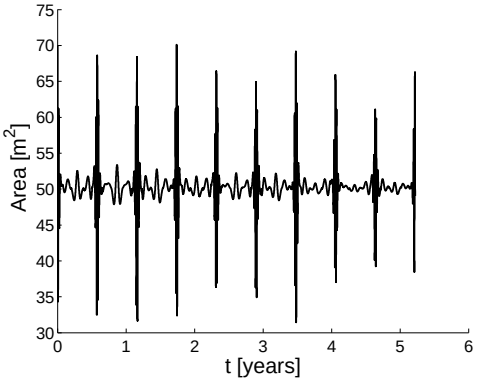

(a) Area required for the planar-LPO: offset of -1 km in $x-$axis.

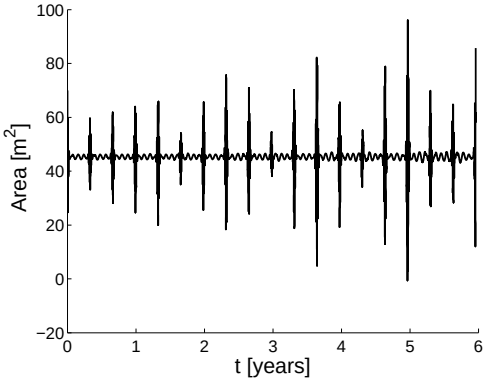

(b) Area required for the DPO: offset of -0.5 km in $x-$axis.

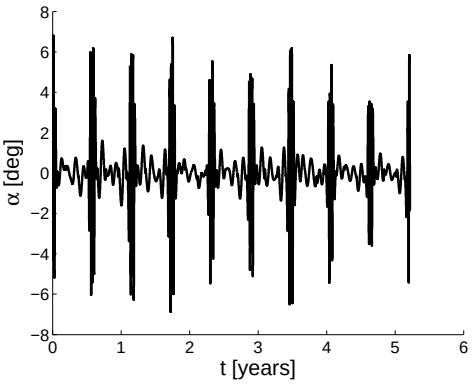

(c) In-plane angle for the planar-LPO, α: offset of -1 km in $x-$axis.

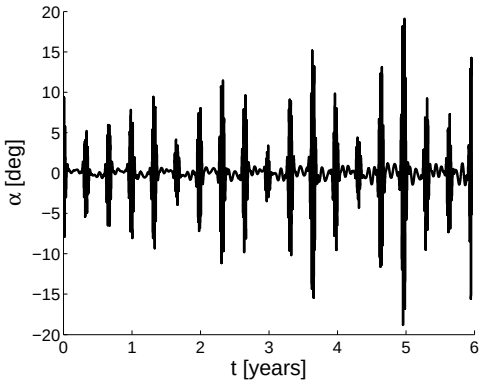

(d) In-plane angle for the DPO, α: offset of -0.5 km in $x-$axis.

Figure 5.15: Area and in-plane angle required for the planar-LPO in Figure 5.3(b) and the DPO in Figure 5.3(a).

5.9 Deployable structure solutions

As shown in Section 5.8, the HSP control requires small variations in the reflective area and in the in-plane angle, α. It was also found that the variation in the out-of plane angle, δ is very small, on the order of 10^{-5}-10^{-8} degrees. Thus, in this case, the controller is effective in the variation of area and α. The variation in the angle α is achievable with the LPO's spacecraft pointing requirements. For example, SOHO and Herschel spacecraft require a 3-axis attitude stabilisation with pointing accuracy of 1 arcsec, while Gaia spacecraft is spin-axis stabilised, where the angle between the spin axis and the Sun-line direction (shown in Figure 5.16) is of 45°. The area variation of the reflective control actuators depend on the effect of the disturbances, where initial offset of the spacecraft from the target orbit due to failure in the orbit insertion manoeuvre was evaluated.

In this section, the required additional flaps to achieve a variable geometry actuator system is presented for a class of LPOs spacecraft similar to SOHO mission shown in Appendix B.3.2. Figure 5.16 shows an example of nominal configuration[1] for a spacecraft that has a near perfect reflective deployable area of 20 m^2 and a mass of 1000 kg. The case studied is shown in Table 5.3 for $A_0 = 20$ m^2 when an initial offset in position of -5 km is considered. It is supposed that the square area of the spacecraft bus is not reflective (white prism in Figure 5.16). The bus area is 11.61 m^2 (3.4073 m $\times$ 3.4073 m). It is also assumed that one side of the solar array and of the reflective actuator flap match the side of the spacecraft bus with a width of 3.4073 m as shown in Figure 5.16. The SOHO spacecraft solar array are designed to have an area of 21.9 m^2. Each of the four solar paddle (blue area in Figure 5.16) has thus an area of 5.475 m^2. By knowing that the width of the solar paddle is 3.4073 m (as the solar bus size), the length of each of the four solar paddle is 1.6068 m.

From Table 5.3, the initial β_0 required for a near perfect area is of $3.06 \cdot 10^{-5}$. The reflectivity coefficient of the solar array, C_r^{sa}, is 1.08 at the beginning of life. The lightness parameter for the solar array, β_{sa}, can thus be calculated through Eq. (3.30). The solar array lightness parameter, β_{sa}, for a 1000 kg spacecraft corresponds to 1.8227 $\cdot 10^{-5}$. An initial near perfect reflective flap, $C_r^f = 2$, has to be added to reach the β_0 condition[2]. The lightness number associated to the nominal reflective flap, β_0^f, is given by:

$$\beta_0^f = \beta_0 - \beta_{sa}. \tag{5.80}$$

The initial total area of the reflective flaps is 8.0867 m^2 ($\beta_0^f = 1.2373 \cdot 10^{-5}$). Two flaps of area $A_0^f = 4.0434$ m^2 (1.1867 m $\times$ 3.4073 m) are required (yellow area in Figure 5.16).

[1] The nominal configuration of the control area was previously denoted with A_0. It is the initial area before activating the control law.

[2] Note that $C_r^f = 2$ is a theoretical value and it is true at the beginning of life; however, some concern should be given on the degradation of reflectivity due to the space environment.

Note that it is possible to sum lightness numbers of different area with different reflectivity since the definition of equivalent reflectivity coefficient is given by:

$$C_r^* = \frac{2 \cdot C_r^f \cdot A_0^f + 4 \cdot C_r^{sa} \cdot A_{sa}}{2 \cdot A_0^f + 4 \cdot A_{sa}}, \tag{5.81}$$

where C_r^* is an equivalent reflectivity coefficient. The total lightness number β_0 is given by Eq. (3.30) and it turns into:

$$\beta_0 = \frac{P^*}{m_{sc}} \left(2 \cdot A_0^f + 4 \cdot A_{sa}\right) \cdot C_r^* = \frac{P^*}{m_{sc}} \cdot \left(2 \cdot C_r^f \cdot A_0^f + 4 \cdot C_r^{sa} \cdot A_{sa}\right) = \beta_0^f + \beta_{sa}, \tag{5.82}$$

where m_{sc} is the total mass of the spacecraft and $P^* = P_{srp-1AU} \frac{r_{Earth-Sun}^2}{\mu_{Sun}}$. From Eq. (5.82), it is clear that operations within lightness numbers of different reflective surfaces are possible.

The total length of the spacecraft in its nominal configuration is therefore 13.5525 m. The length of SOHO spacecraft without the reflective actuator flaps was originally of 9.8 m.

As shown in Table 5.3 for a near perfect reflective area[3] of $A_0 = 20$ m^2, the total area variation needed to meet the control requirements is between 15.5-21.5 m^2, thus the variation in the total reflective area $2 \cdot \Delta A_0^f$ as to be between -4.5 m^2 and 1.5 m^2. For each reflective flap, the initial A_0^f has to be reduced by 2.25 m^2 (0.6603 m $\times$ 3.4073 m) or increased by 0.75 m^2 (0.2201$\times$3.4073 m). In summary, the minimum flap area is of $A_{min}^f = 1.7934$ m^2, the maximum flap area is of $A_{max}^f = 4.7934$ m^2, while the nominal flap area is $A_0^f = 4.0434$ m^2.

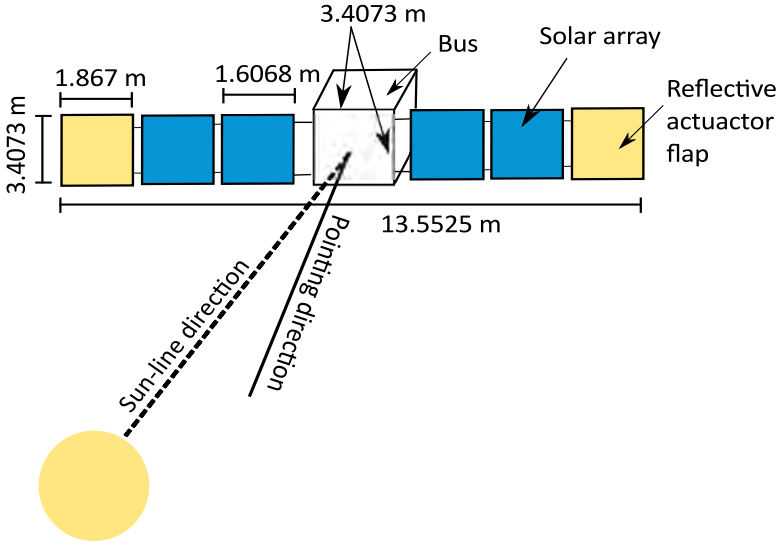

Figure 5.16: Actuators configuration for a class of spacecraft like SOHO mission.

[3]Note that here A_0 is the contribution of the solar array and the additional flaps area at the nominal condition, thus $A_0 = 4 \cdot A_{sa} + 2 \cdot A_0^f$.

The material proposed to design highly reflective and light actuator flap is solar sail technology. The best sail substrate is kapton and has a surface density of 7.1 g/m^2. The best choice of the surface coating is aluminium with a surface density of 1.35 g/m^2 (McInnes, 1999). The maximum area of one flap is of 4.7934 m^2 and the mass of the flap material is 40.5 g (0.0405 kg). To support the flap material, a 7.9914 m of mast structure, as shown in Figure 5.17, is required that has a linear mass of 70 g/m (Murphy and Macy, 2004), which totals 560 g (0.56 kg). The total mass of one flap is therefore 600.5 g, and the total mass of the two flaps is 1.201 kg. Allowing a 20% mass margin (McInnes, 1999), the total mass of the reflective actuator system is 1.4412 kg. Figure 5.17 shows the front and the back view of the reflective actuator flap with a maximum area of $A^f_{max} = 4.7934$ m^2.

Shahid and Kumar (2010) proposed a sliding-mode control for LPO spacecraft enhanced by solar radiation pressure. In Shahid and Kumar (2010) case, the initial area required for the control is around 40 m^2. For a 1000 kg spacecraft, it was proposed by Shahid and Kumar (2010) the use of a solar sail with a final mass of 6 kg. In this thesis, two additional flaps to the spacecraft solar array is proposed with a total area of 8.0867 m^2 and an additional mass of 1.4412 kg.

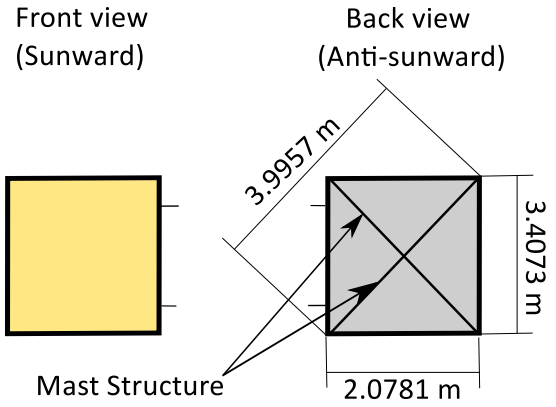

Figure 5.17: Front and back views of the reflective actuator flap for $A^f_{max} = 4.7934$ m^2.

Table 5.4 summarises the overall size of the spacecraft and the size in the reflective actuator flaps. Note that the nominal area is 20 m^2 for a near perfect reflective area. However, the contribution of 21.9 m^2 of solar array was taken into account thus A_0 now include the area of the near perfect flaps and of the solar array with reflectivity coefficient 1.08. Due to the non perfect reflective property of the solar array, a nominal area of 31.4868 m^2 is therefore required.

An example of variable shape areas were proposed by Borggräfe et al. (2013) who also suggested the use of electro-chromic devices for the control of multi-purpose variable-shape sails. Borggräfe et al. (2013) consider distributed masses with variable reflectivity allowing a change of the sail shape from a flat configuration, i.e. active trajectory control, to a parabolic shape for use as a remote sensing device or communication antenna. A

Area	**m^2**	**Number**
Spacecraft bus	11.61	1
Solar paddle, A_{sa}	5.475	4
Reflective actuator flap, A^f_{max}	4.7934	2
Nominal area from Table 5.3, A_0	20	-
Control area required from Table 5.3, A_{min}-A_{max}	15.5-21.5	-
Nominal area needed, $A_0 = 4 \cdot A_{sa} + 2 \cdot A^f_0$	31.4868	-
Variation of the reflective actuator, A^f_{min}-A^f_{max}	1.7934-4.7934	2

Table 5.4: Spacecraft areas datasheet.

similar approach can be adopt here by having a reflective actuator flap covered by pixel of reflective control device. The control law can thus be transformed in electric impulse to switch on (highly reflective pixel, in yellow in Figure 5.18) and off (absorption pixel, in gray in Figure 5.18) the reflective control devices. In this case, the shape of the flap is kept fixed and the effect of variable geometry is obtained by changing the surface luminosity of the flaps. Figure 5.18 shows how to modify the reflective area of the flap through reflective control device. The advantage of this method is in allowing the change of the reflective area without mechanical moving parts. This method could also add flexibility in the control law mission design. It would be possible to adjust the requirements of the control law by reshaping the on/off switching configuration. The main disadvantage is related to the effect of degradation of the material in the space environment, thus a margin in the area should be included to compensate effect of degradations during the all duration of the mission.

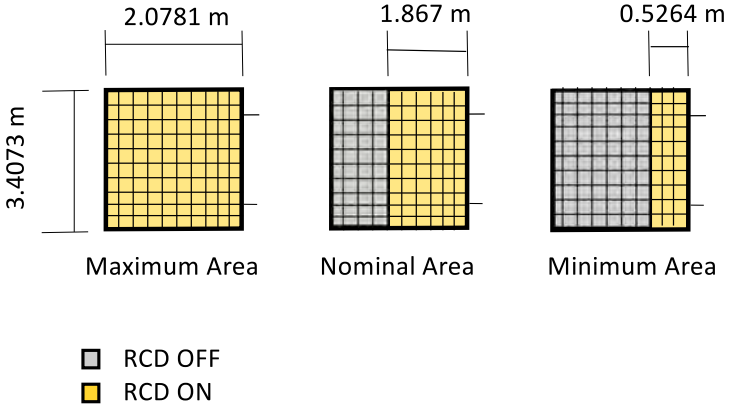

Figure 5.18: Concept of pixel Reflective Control Device (RCD).

Other options investigate the use of mechanism to change the geometry of the controlled area. Recently, Ceriotti et al. (2013) proposed a variable geometry cone sail achieved using controlled mechanisms. Current, mechanical solutions do not allow a continuous

variation of the area thus the proposed controlled acceleration has to limit the fluctuation in the required area when using the current space mechanism.

The continuous variable area requires the design of deployable mechanisms that enhance the variable shape of the SRP actuators. As previously stated, current space technology does not provide solutions for a continuously varying geometry actuator system. This suggests that further study should be done in the design of future space missions to find innovative solutions. Future deployment concepts could explore new design approaches based on bio-inspired robotic engineering. This approach is a promising solution which draws on concepts in nature and applies these concepts to engineering systems, developing features such as variable skin shape and muscle-like filaments.

An example of bio-inspired design is a soft materials developed by the Massachusetts Institute of Technology team that mimic the octopus ability to change its shape (Guttag and Boyce, 2015). The material is composed from two different polymers with different degree of stiffness where more rigid particles (in black in Figure 5.19) are embedded within a matrix of a more flexible polymer (in gray in Figure 5.19). This material was produced by a 3-D printer and when squeezed (black arrows in Figure 5.19), the material's surface changes from smooth to a pattern of flat apexes and valleys. The material design depends primary on the geometry of the particles. The texture control was reach through physical pressure, however it is suggested that can be achieved through electric charge (Guttag and Boyce, 2015). This is a very interesting concept that it has been proposed to change for example the area of the aircraft wings to reduce the drag forces. A similar concept could be investigated for space applications to have a variable geometry flap to enhance the solar radiation pressure effect. In this case the polymer surface should be reflective by adding a coating material. There are also some requirements that polymeric materials must meet for space applications (Willis and Hsieh, 1999) as:

- the capability to function in hard vacuum,
- a very low outgassing,
- resistance to ultraviolet light,
- endurance over wide temperature, and
- the ability to survive the life mission.

Although the proposed controllable surface is not tested to meet the space requirements listed above, the ploymeric materials are the basis for many spacecraft components such as adhesives, circuit boards, blankets, coatings, electrical insulation, paints and high stiffness components (Willis and Hsieh, 1999). It seems thus interesting to consider this approach as possible candidate for electro-mechanical variable geometry reflective area.

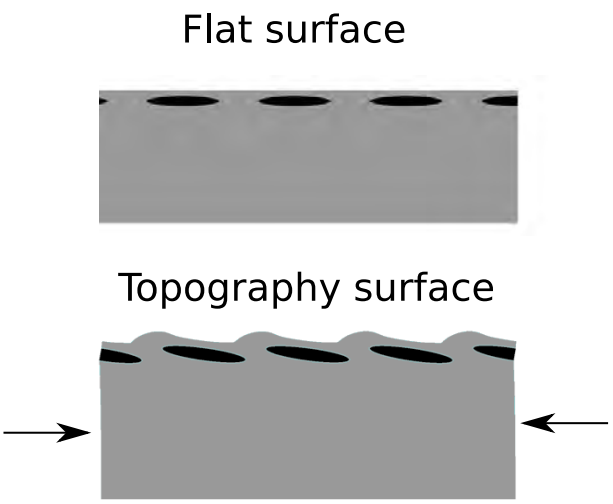

Figure 5.19: Controllable geometry surface (image credit Guttag and Boyce (2015)).

Other examples of variable geometry mechanism is a flower robot with six 3-D printed muscles that can open and close as shown in Figure 5.20. The concept behind this design is to make use of a standard ninjaflex filament 3-D printer controlled through air pressure. This, therefore, utilises air-powered actuators systems. Although this innovative technology is not designed for space applications, it represents an example of a future deployment approach which could utilised for satellite control.

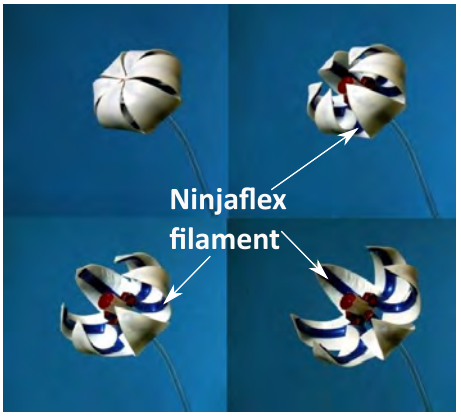

Figure 5.20: Flower robot with six 3D printed muscles that can open and close (image credit www.3ders.org).

The optical model used in this thesis for orbit control and design do not take into account of the optical degradation of the thin metallised polymer film due to the erosive effect of the space environment. Dachwald et al. (2005) proposed a parametric model for optical solar sail degradation and its effect onto trajectory and attitude control. One of the major problem related to degradation of the material is not only a lower intensity in the solar radiation pressure forces but also it reduces the controllability of the sail as the magnitude of solar radiation pressure is reduced in its perpendicular component (Dachwald et al., 2005). In Dachwald et al. (2005) model, the solar photons and particles are the solely source of degradation. Dachwald et al. (2005) show that the effect of degradation affect the spacecraft trajectory for example an increase of degradation factor has a remarkable consequences on the time of flight for Mars and Mercury randevouz missions and fast Neptune flyby missions. Future analysis has to take into account the effect of optical degradation when using reflective actuator flaps for LPO orbit control.

5.10 Summary

The Hamiltonian structure-preserving control aims to stabilise the unstable periodic orbit as a result of removing the hyperbolic equilibrium with an artificial centre solution. The local stability of the linearised equation is important to understand the impact of the control to the PO stability. A comparison between the HSP and the Floquét mode control was performed to assess their robustness to error in the initial injection. An HSP control law was derived here for high amplitude orbits where couples of complex and conjugate solutions occur. The HSP was then applied for fuel-free solar radiation pressure propulsion.

This chapter has demonstrated that the HSP control has better performance than the FM method and by comparing their features, it has been shown that the HSP control:

- is robust to failures in the halo insertion manoeuvre;
- works in a regime of non-linearities;
- requires solely the estimation of the spacecraft position error;
- is independent of the selected orbit;
- requires a little continuous acceleration.

The key research findings of this chapter are:

- a new HSP control law for high amplitude orbits was fully derived by opening up the use of the HSP control for a general case where the solution is independent of the target orbit size (i.e., space missions to distant prograde orbits),
- the control acceleration is feasible with a solar radiation pressure actuators system,
- to enhance a feasible control acceleration the spacecraft has to be offset in position from the target orbit,
- a variable geometry actuators system is required where the reflective area varies with time,
- the control area pointing requirements shows to match the LPO spacecraft pointing-requirements where the major action of control is given in the in-plane angle rather than in the out-of-plane angle.

In the case of orbit control manoeuvres, this study shows that variable geometry deployable actuators should be further investigated.

Besides the spacecraft's nominal mission phase, additional operational manoeuvres may be required for example to prevent the spacecraft from entering in the Earth's shadow by compromising its vital functionality. In other cases, when the nominal mission reaches its end, the space agencies can approve an extension of the mission that requires new trajectory design planning. The design of transfer trajectories between LPOs through SRP manoeuvres are explored in the following chapter to meet these additional mission requirements.

Chapter 6

Design of Transfer Trajectories enhanced by Solar Radiation Pressure

Space missions often require additional spacecraft manoeuvres from the nominal orbit design, for example to prevent the spacecraft from crossing the Earth's shadow as this would compromise its functionality. Space agencies can also approve an extension of the mission when the primary mission goals are achieved. To meet these additional mission requirements, the design of transfer trajectories between LPOs through SRP manoeuvres is explored here.

This chapter investigates the design of transfer trajectories within the Sun-Earth system. This chapter is the result of a four month collaboration between the University of Southampton (Southampton, UK) and the Institut d'Estudis Espacials de Catalunya and the Universitat de Barcelona (Barcelona, Spain) within the Astronet-II programe and it aims to answer the following research question:

Q.4 - *Which methodology can be used to perform transfers between quasi-periodic orbits enhanced by solar radiation pressure manoeuvres?*

The invariant manifold theory, presented in Chapter 2, is used here to answer the above research question. The motion of the spacecraft is described in the circular restricted three-body problem with the effect of SRP. The equations of motion and the SRP acceleration were presented in Chapter 3.

In this chapter, the geometry of the equilibrium points of the Sun-Earth system is exploited to perform transfer within Lissajous orbits. In this case, the approximated analytical solution presented in Section 3.8.1 is extended to the case of saddle×focus×center

equilibrium. The normal vector, $\hat{\boldsymbol{N}}$, to the reflective area for the SRP acceleration is defined through the cone and the clock angles presented in Section 3.2.2.

This strategy enhances transfer within Lissajous orbits assisted by the SRP acceleration and it makes use of the linearised equations of motion to evaluate wherever it is possible to perform a transfer. The main idea is to give a manoeuvre that counteracts the unstable manifold of the target Lissajous orbit so that the spacecraft will follow a stable trajectory to reach the target Lissajous orbit. Canalias et al. (2003) was the first to investigate a similar strategy through impulsive, Δv, manoeuvres to avoid the spacecraft being eclipsed with the Earth. The approach proposed by Canalias et al. (2003) was used by Colombo et al. (2015b) to compute the eclipse avoidance manoeuvre for the Gaia mission.

A preliminary study is presented in this chapter; where, two main cases are analysed. In the first case, a Sun-pointing area was selected; where, the SRP transfer manoeuvre is given through changes in the reflective area. A second option is explored; where, the manoeuvre is provided in the x-y plane through changes in the cone angle, α, for a fixed area.

The results of this chapter are part of a publication in preparation (Soldini et al., 2015b).

6.1 Design of the transfer strategy through solar radiation pressure manoeuvres

The design of the investigated transfer technique makes use of the geometry of the equilibrium points of the Sun-Earth system. A semi-analytical approach is utilised for the computation of the Lissajous orbits and their correspondent invariant stable and unstable manifolds following the procedure presented in Section 3.8.1. The idea is to give a manoeuvre assisted through the SRP acceleration that aims to cancel out the unstable manifold of the target Lissajous orbit.

As said in Section 3.8.1, the linearised equations of motion are written in a reference system centred at the libration point as in Eq. (3.88). The effect of SRP acceleration displaces the position of the collinear equilibrium points of the CR3BP along the x, y and z axis of the synodic reference frame centred on the Sun-Earth's center of mass, Figure 3.15. The positions of the pseudo libartion points, SL_i, as a function of the cone and clock angles and the lightness parameter, β, are shown in Section 3.5.2. Depending on the location of the equilibrium points after the SRP manoeuvre, the stability of the equilibrium points can change from saddle×center×center to saddle×focus×center as it can be seen in Figure 3.18. Thus, the analytical solution of the linearised equations of motion will depend on the stability of the equilibrium points.

As the effect of the SRP manoeuvre changes the location and the stability of the equilibrium points, the proposed transfer strategy makes use of the geometry of two equilibrium points: one for the departure Lissajous orbit (before the SRP manoeuvre) and the second for the target Lissajous orbit (after the SRP manoeuvre). Thus, the solution of the linearised equations of motion is initially referred to a system centred at its correspondent libration point; however, after the manoeuvre, the solution is centred at the new equilibrium point of the target Lissajous orbit.

This transfer strategy requires the definitions of three reference systems: the synodic (rotating) reference frame centred on the Sun-Earth's center of mass, the synodic reference system centred at the departure libration point (SL_i) with coordinates ξ, η and ζ, and a synodic reference system centred at the libration point of the target Lissajous orbits (SL_i') with coordinates ξ', η' and ζ'. Figure 6.1 shows the position of the equilibrium point before (SL_1) and after (SL_1') the SRP manoeuvre and their respectively reference frames. Thus, transformations within these reference frames are needed to perform the transfer strategy. In Figure 6.1, γ_1 and γ_1' are the distances from the Earth to the libration points before (SL_i) and after (SL_i') the SRP manoeuvre respectively; while, $\Delta\gamma$ is the distance between the two libration points.

The SRP manoeuvre is given such as the effect of the unstable manifold of the target Lissajous orbit is cancelled out. When using the semi-analytical approach presented in Section 3.8.1, this condition corresponds to have the unstable manifold's amplitude, A_1, of the target Lissajous orbit equal to zero.

In the work of Canalias et al. (2003), transfer within Lissajous orbits is proposed through Δv manoeuvres. In the case of Δv manoeuvres, the motion of the spacecraft is described in the CR3BP; where the positions of the five libration points remain invariant after the manoeuvre. Thus, in this case, the target Lissajous orbit shares the same libration point with the departure Lissajous orbit. The transfer strategy through a Δv manoeuvre makes use of the geometry of one libration point as the Δv does not affect the position of the libration points. When harnessing SRP, the SRP manoeuvre can be seen as an instantaneous change in position with the reference frame centered in the libration point; conversely, the Δv manoeuvre results in an instantaneous change in velocity. This is the main difference between this thesis work, and the one of Canalias et al. (2003).

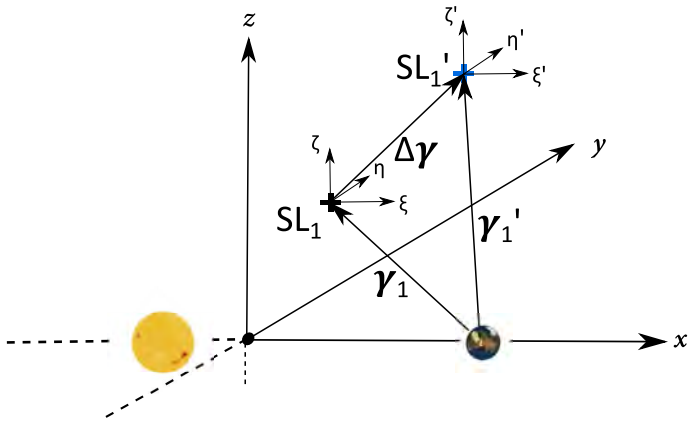

Figure 6.1: Position of the equilibrium points before (SL_1) and after (SL_1') the SRP manoeuvre.

6.1.1 Transformations for changes in coordinates

The coordinate transformation from a synodic reference frame, centered at the Sun-Earth's center of mass, to a reference frame, centred at the libration point, is shown in Eq. (3.86). Thus, by using Eq. (3.86) before (SL_i) and after (SL_i') the SRP manoeuvre, it is possible to write the following transformation:

$$\begin{cases} \xi' &= \xi + x_{SL_i} - x_{SL_i'} \\ \eta' &= \eta + y_{SL_i} - y_{SL_i'} \\ \zeta' &= \zeta + z_{SL_i} - z_{SL_i'} \\ \dot{\xi}' &= \dot{\xi} \\ \dot{\eta}' &= \dot{\eta} \\ \dot{\zeta}' &= \dot{\zeta} \end{cases} . \tag{6.1}$$

Eq. (6.1) represents the composition of reference systems centered at the libration points when a SRP manoeuvre is given. The variable with the symbol [′] are the one after the SRP manoeuvre. From the point of view of a reference frame centered at the Sun-Earth's center of mass, the state vector of the spacecraft ($\{x,y,z,\dot{x},\dot{y},\dot{z}\}$ in Eq. (3.86)) does not change at the instant of time when the SRP manoeuvre is given. Indeed, a SRP manoeuvre can be seen as a low-thrust propulsion; where, the spacecraft's acceleration is changed in a continuous way.

From Eq. (6.1), it is also clear that the transfer strategy with SRP manoeuvre makes use of the geometry of the libration point before (SL_i) and after (SL_i') the manoeuvre. In the case of Canalias et al. (2003)'s work, the impulsive manoeuvre causes an instantaneous change in the spacecraft's velocity of the synodic reference frame centered at the center of mass; while the libration point coordinate does not change (SL_i).

6.1.2 Design of the transfer trajectory

The procedure used to design a transfer trajectory assisted by a SRP manoeuvre that uses the geometry of two libration points is described in the following steps:

1) Design of the departure Lissajous orbit:

For the design of the departure Lissajous orbit, a semi-analytical solution is used to approximate the center manifold. The departure Lissajous orbit can be defined as in Eq. (3.103) for the case of a Sun-pointing reflective area. Eq. (3.103) is shown here as:

$$\begin{cases} \xi &= A_x \cos(\omega t + \Phi_0) \\ \eta &= kA_x \sin(\omega t + \Phi_0) \\ \zeta &= A_z \cos(\nu t + \Psi_0) \\ \dot{\xi} &= -\omega A_x \sin(\omega t + \Phi_0) \\ \dot{\eta} &= k\omega A_x \cos(\omega t + \Phi_0) \\ \dot{\zeta} &= -\nu A_z \sin(\nu t + \Psi_0). \end{cases} \tag{6.2}$$

As already mentioned in Section 3.8.1, ω and ν are the in-plane and out-of-plane frequencies of their respectively center manifolds; while, Φ_0 and Ψ_0 are the in-plane and the out-of-plane phases. The effective phases Φ and Ψ are defined as $\Phi = \omega t + \Phi_0$ and $\Psi = \nu t + \Psi_0$, respectively. Thus, the departure Lissajous orbit requires the definition of the amplitudes in A_x or A_y[1] and A_z. On the other hand, the frequencies in Eq. (6.2) depends on the stability of the eigenvalues of the linearised matrix of the selected libration point as shown in Section 3.8.1. Eq. (6.2) holds for a Sun-pointing reflective area; where, the frequencies change because the position of the pseudo libration point is influenced by the selected lightness parameter, β.

There are two ways to represent Lissajous orbits: in the Cartesian reference frame centered at the center of mass (or centered at the libration point) and in the phase space. Figure 6.2 shows the departure Lissajous orbit in the synodic reference system centered at the center of mass of the Sun-Earth system and the phase space. In this case, it was selected a square Lissajous orbit such as $A_y = A_z$ with an amplitude of 250,000 km. In the Cartesian system, Figure 6.2(a), the Lissajous orbit is represented by its coordinates; while, in the phase space, Figure 6.2(b), is represented through its effective phases, Φ and Ψ.

Once the amplitude and the equilibrium point, for instance β, are selected, it is possible to define the Lissajous orbit through the time, t, by fixing the initial Φ_0 and Ψ_0 as shown in Figure 6.2 in black curve for the Cartesian frame (Figure 6.2(a)) and black stars for the phase space (Figure 6.2(b)). Conversely, it can be

[1] It is possible to choose the amplitude in x or y since their relationship is $A_y = kA_x$.

convenient to fix the time, t, equal to zero and vary Φ_0 and Ψ_0 between 0 and 2π as shown in gray in the Cartesian frame (Figure 6.2(a)) and gray squares for the phase space (Figure 6.2(b)). The advantage of representing the Lissajous orbit through the phases (when t is fixed and Φ_0 and Ψ_0 are free to vary) is that the points along the Lissajous orbit (grey cylinder in Figure 6.2) are equally distributed in the phase space where the points that belong to the Lissajous orbit are the grey squares in Figure 6.2(b). By observing Figure 6.2(b), it is clear that the design of the Lissajous orbit through the phases gives uniform solutions in the phases where the grey squares cover an entire rectangles in the phase space. When the Lissajous orbit is defined through the time for a fix Φ_0 and Ψ_0, the initial conditions along the orbit are not uniformly distributed in the phase space as the black stars in Figure 6.2(b) do not covers the grey squares. Thus, if the phase space is used to design the manoeuvre a better representation of the Lissajous orbit is given through its phases rather than with the time.

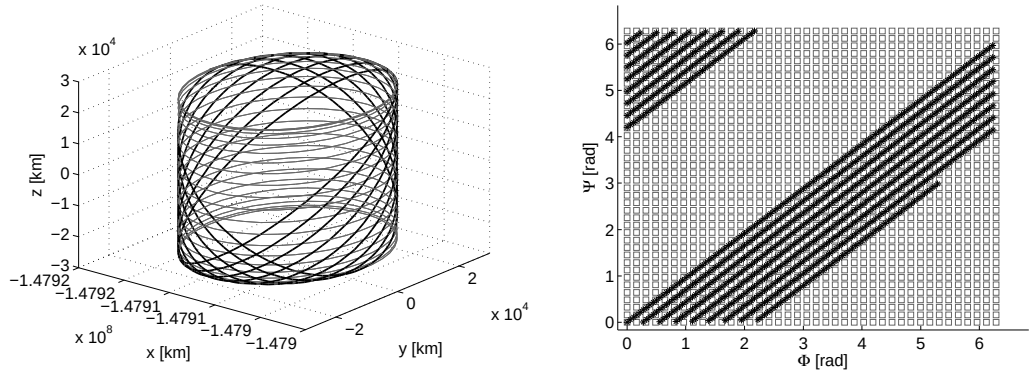

(a) Lissajous orbit in the synodic refernce frame.

(b) Liassajous orbit in the phase space.

Figure 6.2: Departure Lissajous orbit in the synodic reference frame and in the phase space.

Current and future space missions that make use of Lissajous orbits have amplitudes in A_y varying between 81,000 km to 750,000 km; while, 90,000 km and 450,000 km in A_z. In this chapter, the focus is on square Lissajous orbits around SL_1 where $A_y = A_z$. Three amplitudes where selected 25,000 km, 250,000 km and 750,000 km for the design of the departure Lissajous orbits. In Appendix F, a solution is shown for a Lissajous orbit like Gaia mission that has $A_y = 340{,}000$ km and $A_z = 90{,}000$ km. Note that an overview of Gaia mission can be found in Appendix B.3.3.

Once the departure Lissajous orbit is selected, an SRP manoeuvre given along the departure Lissajous orbit was investigated to compute the values in the amplitudes of the unstable, A_1, and stable, A_2, manifolds of the target Lissajous orbit. The aim is to follow a stable trajectory of the target Lissajous orbit; where due to the SRP manoeuvre the unstable effect is cancelled out ($A_1 = 0$).

2) Composition of the reference systems centered at the libration points due to the SRP manoeuvre:

A spacecraft placed at a departure Lissajous orbit associated to the libration point for a selected initial lightness parameter, β_0, will follow the geometry of $\mathrm{SL}_i(\beta_0)$. When a SRP manoeuvre is given, the lightness parameter is now β_M and the motion of the spacecraft is now driven by the geometry of the new equilibrium point, $\mathrm{SL}_i(\beta_M)$. This effect is given by the transformation in Eq. (6.1) that for a Sun-pointing reflective area can be written as:

$$\begin{cases} \xi' &= \xi + x_{SL_i}(\beta_0) - x_{SL_i}(\beta_M) \\ \eta' &= \eta \\ \zeta' &= \zeta \\ \dot{\xi}' &= \dot{\xi} \\ \dot{\eta}' &= \dot{\eta} \\ \dot{\zeta}' &= \dot{\zeta} \end{cases} . \tag{6.3}$$

Once the state vector of the spacecraft expressed in the synodic reference frame centered at the new equilibrium point, $\mathrm{SL}_i(\beta_M)$, is given after the SRP manoeuvre, it is possible to find the amplitudes associated to the target Lissajous orbit. This can be done through the transformation in Eq. (3.106) and Eq. (3.107). Eq. (3.104) and Eq. (3.105) give the state vector of the spacecraft in the synodic system centered at the libration point as a function of the amplitudes. Eq. (3.104) and Eq. (3.105) can be written in a compact way as:

$$\boldsymbol{\xi} = \boldsymbol{S}(\beta, t) \cdot \boldsymbol{A}. \tag{6.4}$$

In Eq. (6.4) the matrix $\boldsymbol{S}$ is function of the time, t, and the lightness parameter, β, for a Sun-pointing reflective area. $\boldsymbol{\xi}$ is the state vector of the spacecraft for a synodic reference frame centered at the libration point; while, $\boldsymbol{A}$ is the vector of the amplitudes ($\{A_1, A_2, A_3, A_4, A_5, A_6\}$). The inverse transformation shown in Eq. (3.106) and Eq. (3.107) is defined in a compact way such as:

$$\boldsymbol{A} = \boldsymbol{S}^{-1}(\beta, t) \cdot \boldsymbol{\xi}. \tag{6.5}$$

3) Computation of the amplitudes of the target Lissajous orbit when the SRP manoeuvre is given:

By using Eq. (6.5) for the spacecraft's state vector at the time of the given SRP manoeuvre, $\boldsymbol{\xi}'$, in Eq. (6.3), it is possible to find the amplitudes of the target

Lissajous orbit, $\boldsymbol{A}'$ such as:

$$\boldsymbol{A}' = \boldsymbol{S}^{-1}(\beta_M, t_M) \cdot \boldsymbol{\xi}'. \tag{6.6}$$

In Eq. (6.6), t_M is the time when the SRP manoeuvre is given. Now it is possible to check if the amplitude A'_1 is zero. In case the unstable manifold of the target Lissajous orbit is zero ($A'_1 = 0$), it is possible to follow the stable manifold of the target orbit, A'_2. The amplitudes, the frequencies and the phases of the target Lissajous orbit can be thus computed. The amplitudes of the target Lissajous are given by:

$$A'_x = \sqrt{A'^2_3 + A'^2_4} \qquad\qquad A'_z = \sqrt{A'^2_5 + A'^2_6}; \tag{6.7}$$

while, the phases are given by:

$$\Phi'_0 = \arctan\left(-\frac{A'_4}{A'_3}\right) \qquad\qquad \Psi'_0 = \arctan\left(-\frac{A'_6}{A'_5}\right). \tag{6.8}$$

The in-plane, ω', and out-of-plane, ν', frequencies are function of β_M; thus, the target Lissajous orbit is defined as follow:

$$\begin{cases} \xi' &= A'_x \cos(\omega' t + \Phi'_0) \\ \eta' &= k' A'_x \sin(\omega' t + \Phi'_0) \\ \zeta' &= A'_z \cos(\nu' t + \Psi'_0) \\ \dot{\xi}' &= -\omega' A'_x \sin(\omega' t + \Phi'_0) \\ \dot{\eta}' &= k'\omega' A'_x \cos(\omega' t + \Phi'_0) \\ \dot{\zeta}' &= -\nu' A'_z \sin(\nu' t + \Psi'_0). \end{cases} \tag{6.9}$$

Eq. (6.9) expressed in the synodic reference frame centered at the departure libration point, $\mathrm{SL}_i(\beta_0)$, can be found by applying the inverse transformation of Eq. (6.3) such as:

$$\begin{cases} \xi &= A'_x \cos(\omega' t + \Phi'_0) - x_{SL_i}(\beta_0) + x_{SL_i}(\beta_M) \\ \eta &= k' A'_x \sin(\omega' t + \Phi'_0) \\ \zeta &= A'_z \cos(\nu' t + \Psi'_0) \\ \dot{\xi} &= -\omega' A'_x \sin(\omega' t + \Phi'_0) \\ \dot{\eta} &= k'\omega' A'_x \cos(\omega' t + \Phi'_0) \\ \dot{\zeta} &= -\nu' A'_z \sin(\nu' t + \Psi'_0). \end{cases} \tag{6.10}$$

In Eq. (6.10), the effective phases are $\Phi' = \omega' t + \Phi'_0$ and $\Psi' = \nu' t + \Psi'_0$. Thus, the departure and the target Lissajous orbits will show in the phase space an instantaneous change in the effective phases (from Φ and Ψ to Φ' and Ψ') as a consequence of the SRP manoeuvre.

4) Computation of the spacecraft's trajectory after the SRP manoeuvre:

   The trajectory followed by the spacecraft after the SRP manoeuvre is given by Eq. (6.4) and it turns into:

$$\boldsymbol{\xi}_2' = \boldsymbol{S}(\beta_M, t_2) \cdot \boldsymbol{A}'. \tag{6.11}$$

   In Eq. (6.11), t_2 is the time along the trajectory after the time of manoeuvre, t_M.

5) Trajectory of the spacecraft in the synodic system centered at the Sun-Earth's center of mass:

   It is now possible to express the trajectory in the synodic reference frame centered at the center of mass of the Sun-Earth system through the transformation in Eq. (3.86) that for a Sun-pointing spacecraft becomes:

$$\begin{cases} x &= \xi_2' + x_{SL_i}(\beta_M) \\ y &= \eta_2' \\ z &= \zeta_2' \\ \dot{x} &= \dot{\xi}_2' \\ \dot{y} &= \dot{\eta}_2' \\ \dot{z} &= \dot{\zeta}_2' \end{cases} . \tag{6.12}$$

6.2 Phase space for a Sun-pointing spacecraft

In this section, the SRP manoeuvre to perform transfers between Lissajous orbits is investigated for a Sun-pointing reflective area; where, the manoeuvre is achieved through changes in the lightness number, β.

First, it was verified if a direct transfer from the departure Lissajous orbit towards the target Lissajous orbit is possible. Then, an intermediate manoeuvre was included to inject the spacecraft in the unstable manifold of the departure Lissajous orbit; where the SRP moreover is finally given to reach the target orbit.

6.2.1 Solar radiation pressure manoeuvre given at the departure Lissajous orbit

Initial conditions uniformly distributed in phases were considered along the departure Lissajous orbit to perform a direct transfer towards the target Lissajous orbit. A square Lissajous of amplitudes $A_y = A_z$ of 250,000 km was selected; thus, in the phase space the departure Lissajous orbit is a rectangle as shown in Figure 6.2(b) for the grey

squares. For each grey squares of Figure 6.2(b) that represent a point along the departure Lissajous orbit, the transfer procedure shown in Section 6.1.2 was applied. Thus, the amplitudes of the target Lissajous orbit, $\boldsymbol{A'}$, are computed through Eq. (6.6). Therefore, it was possible to check the values in the amplitudes associated to the unstable, A'_1, and stable, A'_2, manifolds of the target Lissajous orbit.

Figure 6.3 shows the values in the amplitudes associated to the unstable, A'_1, and stable, A'_2, manifolds of the target Lissajous orbit when the manoeuvre is given along the departure Lissajous orbit. Three values in β_M are selected to perform the manoeuvre from an initial value in the lightness parameter of $\beta_0 = 0$ to a final value of β_M of 0.001 in Figure 6.3(a)-6.3(b), of 0.01 in Figure 6.3(c)-6.3(d) and of 0.02 in Figure 6.3(e)-6.3(f). From Figure 6.3, it is possible to note that a direct transfer from the departure Lissajous orbit is not possible as $A'_1 \neq 0$. Indeed, a direct transfer from the departure Lissajous orbit to the target Lissajous orbit is possible if the manoeuvre could cancel the effect of the instability of the target Lissajous orbit, A_1. Moreover, the amplitudes A'_1 and A'_2 assume the same value when the manoeuvre is given. The effect of SRP manoeuvre affect the effective phase Φ, while Ψ remain constant, and by increasing the effect of β_M, the amplitudes increase in magnitude.

Figure 6.4 shows an example of the manoeuvre where the initial β_0 is decreased rather than increased like in Figure 6.3. An initial β_0 of 0.01 is considered where, after the manoeuvre, β_M is set to zero. Also in this case, A'_1 is equal to A'_2 with $A'_1 \neq 0$ showing the same behaviour of Figure 6.3 with a difference in the sign of the amplitudes.

As a direct transfer from the departure Lissajous orbit is not possible with a Sun-pointing area, the next step is to investigate if it is possible to perform an orbital transfer by first leaving the departure Lissajous orbit along its unstable manifold and then by giving the SRP manoeuvre. Note that the condition $A'_1 \neq 0$ does not exclude the possibility to perform transfers within transit orbits; however, in this preliminary study, the focus was on transfers within Lissajous orbits (bottleneck region) [2].

[2] In the Sun-Earth's R3BP, a spacecraft can move from the region around the Sun to the region close to the Earth and vice versa following transit orbits; while it remains in the same region if it follows a non-transit orbit (Koon et al., 2008).

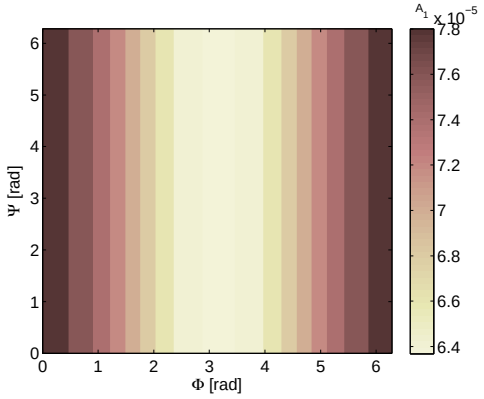

(a) Amplitude of the unstable manifold, A_1', of the target Lissajous orbit: $\beta_M = 0.001$.

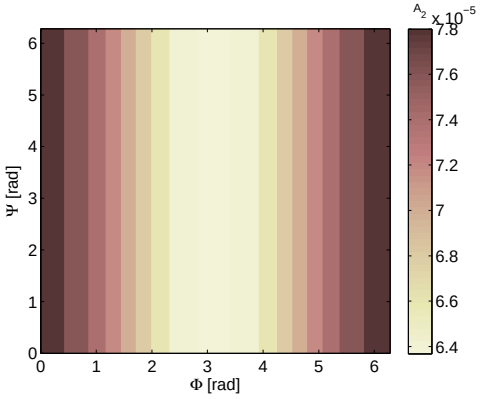

(b) Amplitude of the stable manifold, A_2', of the target Lissajous orbit: $\beta_M = 0.001$.

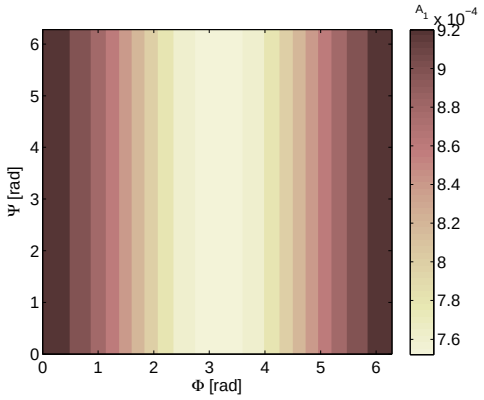

(c) Amplitude of the unstable manifold, A_1', of the target Lissajous orbit: $\beta_M = 0.01$.

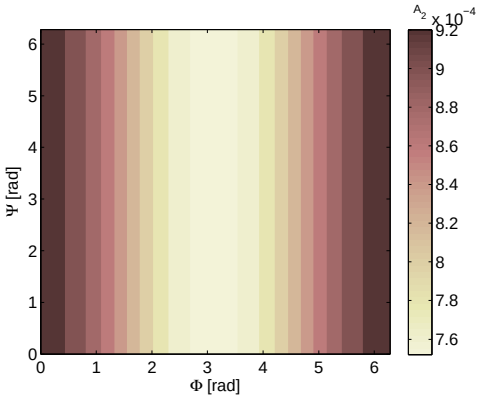

(d) Amplitude of the stable manifold, A_2', of the target Lissajous orbit: $\beta_M = 0.01$.

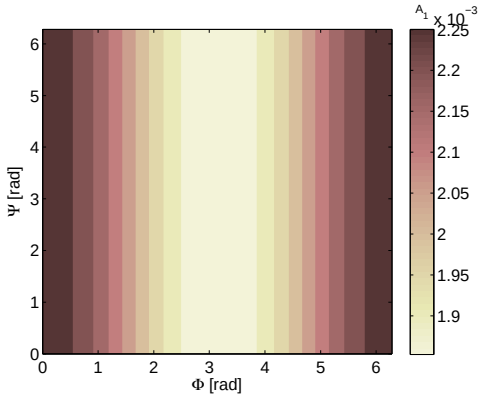

(e) Amplitude of the unstable manifold, A_1', of the target Lissajous orbit: $\beta_M = 0.02$.

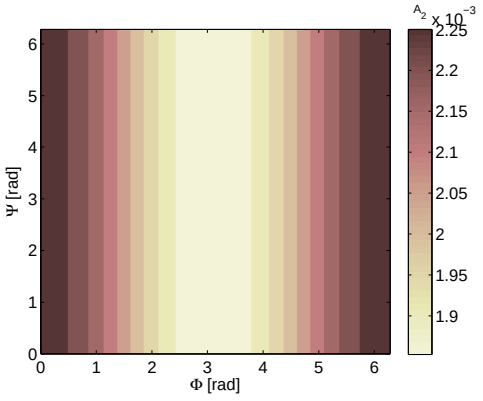

(f) Amplitude of the stable manifold, A_2', of the target Lissajous orbit: $\beta_M = 0.02$.

Figure 6.3: Amplitude of the unstable, A_1', and stable, A_2', manifolds of the target Lissajous orbit with $\beta_0 = 0$ when the SRP manoeuvre is given along the departure Lissajous orbit.

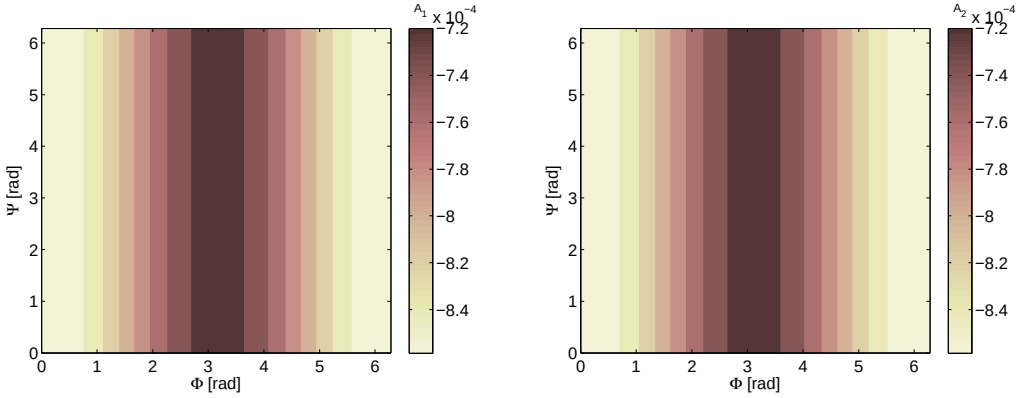

(a) Amplitude of the unstable manifold, A_1', of the target Lissajous orbit: $\beta_M = 0$.

(b) Amplitude of the stable manifold, A_2', of the target Lissajous orbit: $\beta_M = 0$.

Figure 6.4: Amplitude of the unstable, A_1', and stable, A_2', manifolds of the target Lissajous orbit with $\beta_0 = 0.01$ when the SRP manoeuvre is given along the departure Lissajous orbit.

6.2.2 Solar radiation pressure manoeuvre given along the unstable manifold

In this section, an SRP manoeuvre for a Sun-pointing area is investigated to transfer from a departure to a target Lissajous orbit. The spacecraft is initially injected into the unstable manifold of the departure Lissajous orbit and then an SRP manoeuvre is given to reach the target orbit. An arc of the departure square Lissajous orbit was selected as shown in Figure 6.5 with $A_y = A_z = 250{,}000$ km. Figure 6.5 shows the selected arc of the departure Lissajous orbit in the synodic reference frame centered on the Sun-Earth's center of mass (black curve in Figure 6.5(a)) and in the phase space (black stars in Figure 6.5(b)).

In this case, the design of the transfer trajectories described in Section 6.1.2 requires an intermediate step between point 1) and 2). After the selection of an arc of the departure Lissajous orbit, the spacecraft has to be injected into its unstable manifold. Thus, a impulsive manoeuvre[3] is given such that $A_1 = 10^{-6}$ and $A_2 = 0$. For the design of the unstable manifold, the value in A_1 was selected to minimise the error between the spacecraft's state vector at the departure Lissajous orbit and the state vector at the time of injection onto the unstable manifold.

Figure 6.6 shows the transfer strategy for one trajectory that belongs to the unstable manifold of the departure Lissajous orbit. The spacecraft is first injected in the unstable trajectory (black curve in Figure 6.6) when the initial β_0 of the spacecraft is equal to

[3]In order to fall off from the Lissajous orbit it is assumed an impulsive Δv provided by the attitude thrusters. Future analysis will consider to perform this manoeuvre with solar radiation pressure. However, SRP is constrained in direction, thus it is expected that only manurers in the anti-sunward manifold can be given.

0.03. Thus, the spacecraft will initially follow the geometry of SL_1. When the SRP manoeuvre is given (red point in Figure 6.6), the spacecraft has a final value in β_M equal to zero. At this point, A_1' of the target Lissajous orbit is close to zero on the order of 10^{-8} in non-dimensional unit and the spacecraft follows the stable manifold of the target Lissajous orbit around SL_1' (blue curve in Figure 6.6).

Figure 6.7 shows the same transfer sequence shown in Figure 6.6 but in the phase space. The black circles are representative of points along the departure Lissajous orbit where the spacecraft can be injected onto the unstable manifold. One point was selected to inject the spacecraft in an unstable trajectory as shown in green. After that green point, the spacecraft will follow the unstable trajectory (black line). The red star represents the point in which the SRP manoeuvre is given that causes an instantaneous change in the phases. Finally, the spacecraft will follow the stable manifold of the target Lissajous orbit (blue line). It is quite convenient to make use of the phase space as the trajectories are simply represented as straight lines and it clearly shows the effect of the manoeuvre in the phases.

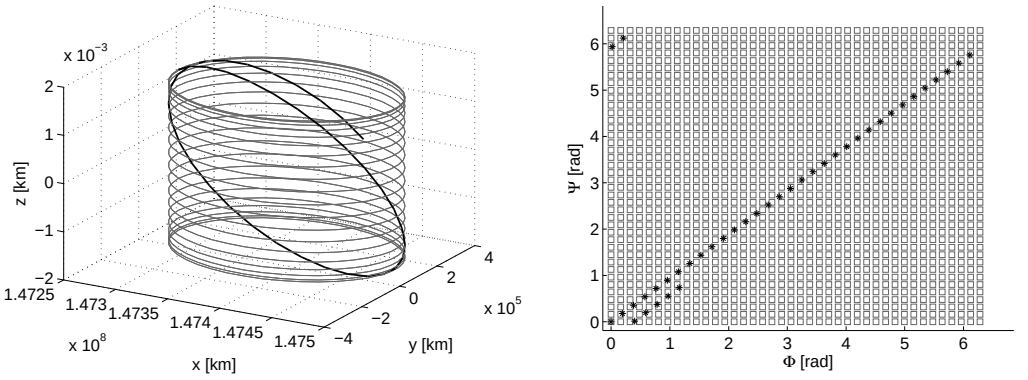

(a) Arc of Lissajous orbit in the synodic reference frame.

(b) Arc of Liassajous orbit in the phase space.

Figure 6.5: Selected arc of the departure Lissajous orbit to perform the SRP manoeuvre shown in the synodic reference frame and in the phase space.

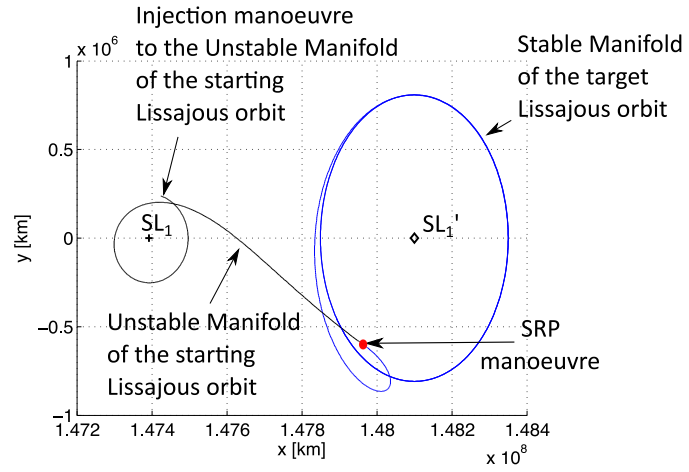

Figure 6.6: Transfer strategy in the synodic reference frame centered at the Sun-Earth's center of mass.

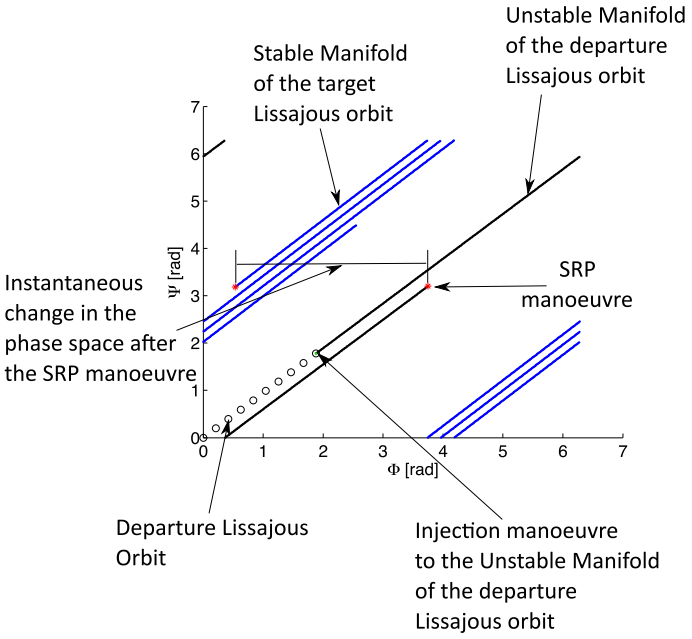

Figure 6.7: Transfer strategy in the phase space.

When the manoeuvre aims to decrease the lightness parameter of the spacecraft (from a big to a smaller reflective area), the spacecraft reaches a final orbit with a higher amplitude with respect to the departure one as shown in Figure 6.8. In Figure 6.8, the black Lissajous orbit is the departure one; while, the red orbit is the target Lissajous orbit. The reason why, due to the decreasing of β, the spacecraft can reach higher amplitudes can be explained by checking the energy of the spacecraft and the shape of the potential function with a particular attention to the zero-velocity curves. The equation of the spacecraft's energy for a Sun-pointing reflective area was shown in Eq. (3.82). By observing Eq. (3.82), the energy of the spacecraft decreases with a smaller value of β. Moreover, the effect of a decrease in β affects the shape of the potential as shown in Figure 3.14. Thus, a decrease in β will cause the ZVCs to be more open at the

bottleneck of the Lagrangian point after the SRP manoeuvre. In this way, the target orbit reaches higher amplitudes.

Figure 6.9 shows the energy of the spacecraft along the departure (black) and the target (red) Lissajous orbits. The intersection of the spacecraft's energy with the potential gives the shape of the ZVC before and after the SRP manoeuvre.

The point along the unstable manifold where the SRP manoeuvre is given such as A_1' of the target Lissajous orbit is equal to zero can be analytically found by using the first equation of Eq. (6.6) such that:

$$A_1'(\beta) = \frac{k(\beta)}{d_2(\beta)}\dot{\xi} + \frac{1}{d_1(\beta)}\dot{\eta} - \frac{k(\beta)\omega(\beta)}{d_1(\beta)}\left[\xi + \Delta x_{L_1}(\beta)\right] + \frac{\omega(\beta)}{d_2(\beta)}\eta; \tag{6.13}$$

where, $\Delta x_{L_1}(\beta)$ is:

$$\Delta x_{L_1}(\beta) = x_{L_1}(t_{M^-}) - x_{L_1}(t_M). \tag{6.14}$$

In Eq. (6.14), t_{M^-} is the time before the SRP manoeuvre while t_M is the instant in which the manoeuvre is given. Thus, it is possible to find β and t_M to minimise A_1':

$$\min_{\beta} A_1'(\beta) \simeq 0. \tag{6.15}$$

It was verified that a good approximation in the transfer strategy for the linearised equations of motion can be achieved when A_1' is on the order of 10^{-8}-10^{-9} or lower values.

The natural effect of the Sun-light deflected by the spacecraft's reflective area causes an acceleration in the Sun opposite direction. Figure 6.10 shows that is not possible to return to the departure Lissajous orbit due to the constraints in direction of the solar radiation pressure acceleration. Thus, a spacecraft cannot return to the departure Lissajous orbit if a second manoeuvre is performed along the target orbit such that β is increased to the initial value of β_0 (Figure 6.10). In conclusion, it is not possible to perform the inverse manoeuvre from the final to the departure Lissajous orbit through SRP manoeuvre as this strategy shows to be unidirectional, and the spacecraft can transfer just in the opposite direction of the Sun (McInnes, 1999). The SRP manoeuvre for a Sun-pointing area can be only designed by decreasing the effect of β. Figure 6.10 shows that by increasing β, the spacecraft will follow a trajectory (red curve) in opposite direction with the Sun.

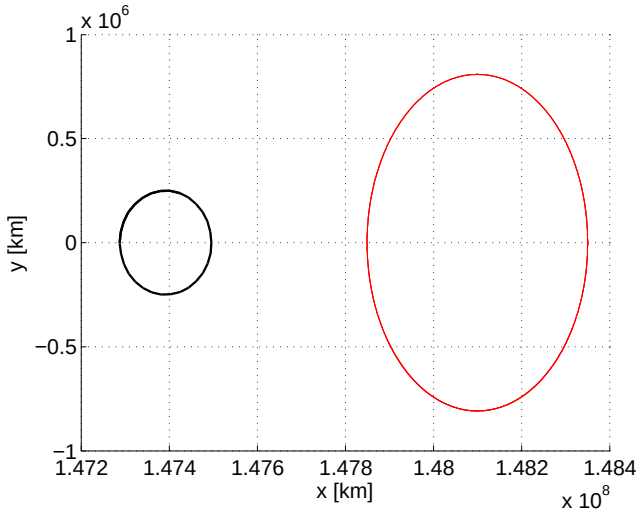

Figure 6.8: Lissajous of the departure (black) and target (red) orbit.

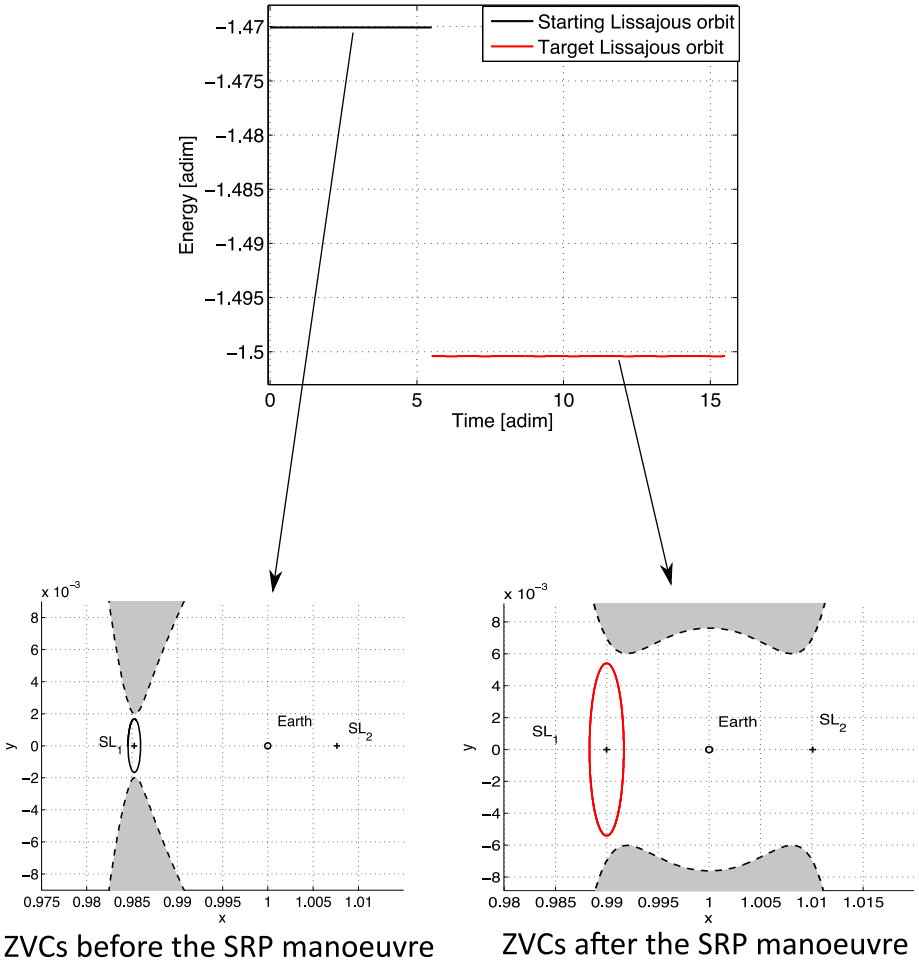

Figure 6.9: Energy and Zero Veocity curves associated to the departure (black) and target (red) Lissajous orbit.

Figure 6.11 shows a schematic representation of the transfer strategy for a Sun-pointing reflective area. The main properties of an SRP manoeuvre for a Sun-pointing area are:

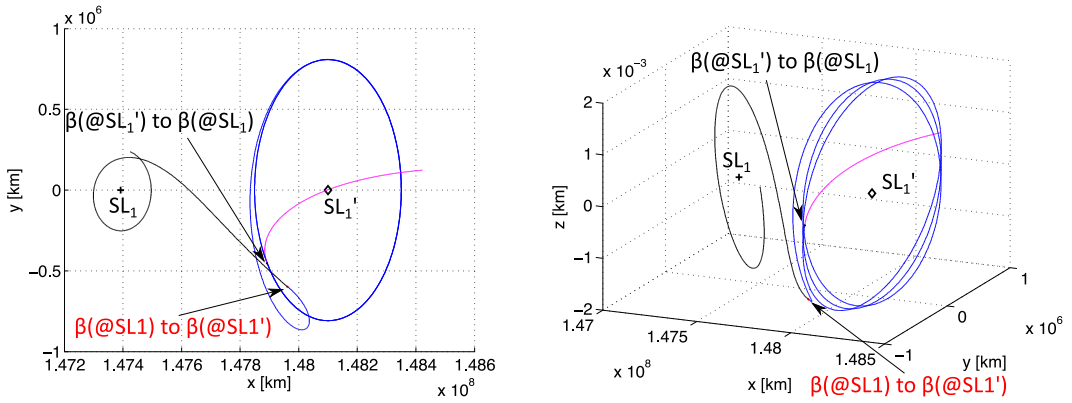

(a) View in the x-y plane of the synodic reference frame centered at the center of mass.

(b) 3D view in the synodic reference frame centered at the center of mass.

Figure 6.10: Evolution of the trajectory when a second SRP manoeuvre is given by changing the lightness parameter, β, to the initial value.

- The effect of a change in β causes a shift along the x-axis in the position of the equilibrium point. Thus, the libration point gets closer to the Sun for high value of β;
- The transfer is allowed when a change in β is given from high to lower values. The spacecraft will always move in the opposite direction with the Sun due to the effect of the SRP acceleration as shown in Figure 6.11 for the black arrow;
- The transfer is possible at the heteroclinic connection when the unstable manifold of the departure Lissajous orbit (red line in Figure 6.11) intersect the stable manifold of the target Lissajous orbit (green line in Figure 6.11);
- A direct transfer from the departure Lissajous orbit is not possible for a geometrical reason. Indeed, the stable manifold of the target Lissajous orbit does not intersect the departure Lissajous orbit but just its unstable manifold as shown in Figure 6.11;
- The values in the initial β_0 and the final β_M depend on the geometrical intersection at the heteroclinic point. Indeed, the heteroclinic point has to be located between the two equilibrium points as shown in Figure 6.11. This condition depends on the location of the equilibrium points, for instance on β_0 and β_M.

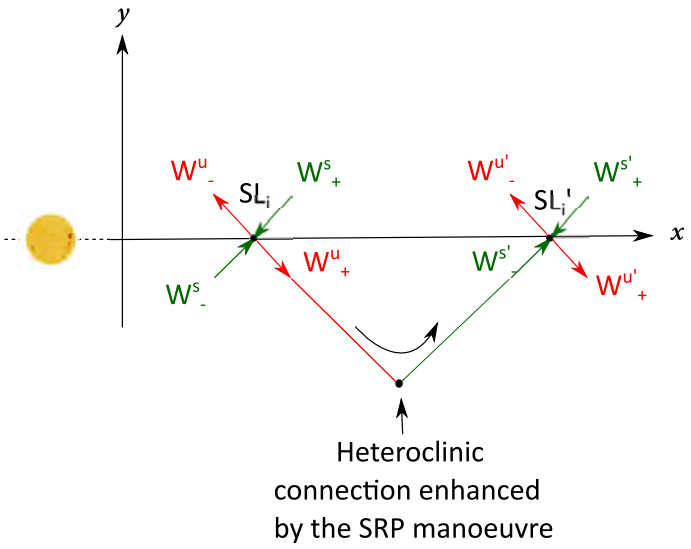

Figure 6.11: Heteroclinic connection between the equlibrium points before (SL_i) and after (SL_i') the SRP manoeuvre.

After analysing the transfer along one unstable trajectory of the departure Lissajous orbit, the transfer was then performed along the entire unstable manifold. The selected arc of the departure Lissajous orbit is the same shown in Figure 6.5 with an initial β_0 equal to 0.04. Due to the SRP manoeuvre, the initial lightness parameter was reduced of 50% such that $\beta_M = 0.02$.

Figure 6.12 shows the amplitudes of the unstable, A_1', in Figure 6.12(a) and stable, A_2', in Figure 6.12(b) manifolds of the target Lissajous orbit as a function of the time along the unstable manifold of the departure orbit (in x) and the time along the departure Lissajous orbit (in y). As one can see, A_1' decrease along the unstable manifold of the departure Lissajous orbit; while, A_2' increases. The time of SRP manoeuvre can be found when A_1' reaches values of the order of 10^{-8}.

As before, Figure 6.13 shows the transfer strategy for a Sun-pointing area. The black tube identifies the unstable manifold of the departure Lissajous orbit; while the blue tube shows the stable manifold of the target Lissajous orbit after the SRP manoeuvre. Different leaving trajectories from the departure Lissajous reaches the same target Lissajous orbit from different phases. Figure 6.13(b) shows in black the selected arc of the departure Lissajous orbit. Conversely, the red curves are associated to the target Lissajous orbit that can be better seen in Figure 6.14.

Figure 6.15 and Figure 6.16 show the phase space for eight leaving trajectories of the departure Lissajous orbit. It is interesting to note that the instantaneous change in the phase space is influenced by the selected trajectory in which the SRP manoeuvre is given. For instance, the trajectories number 21 in Figure 6.15(d), 22 in Figure 6.16(a) and 25 in Figure 6.16(b) show a little instantaneous change in the phase space due to the SRP manoeuvre. On the other end, the trajectories number 1 in Figure 6.15(a), 9

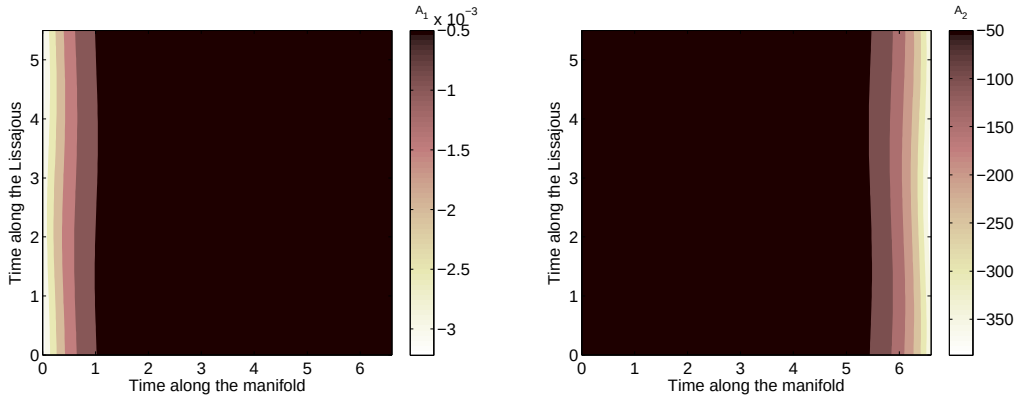

(a) Amplitude A_1' of the unstable manifold of the target Lissajous orbit.

(b) Amplitude A_2' of the stable manifold of the target Lissajous orbit.

Figure 6.12: Amplitude of the unstable, A_1', and stable, A_2', manifolds of the target Lissajous orbit as a function of the leaving point of the departure Lissajous orbit and the points along its unstable manifold.

in Figure 6.15(b), 20 in Figure 6.15(c), 30 in Figure 6.16(c) and 40 in Figure 6.16(d) show big instantaneous changes in the phase space.

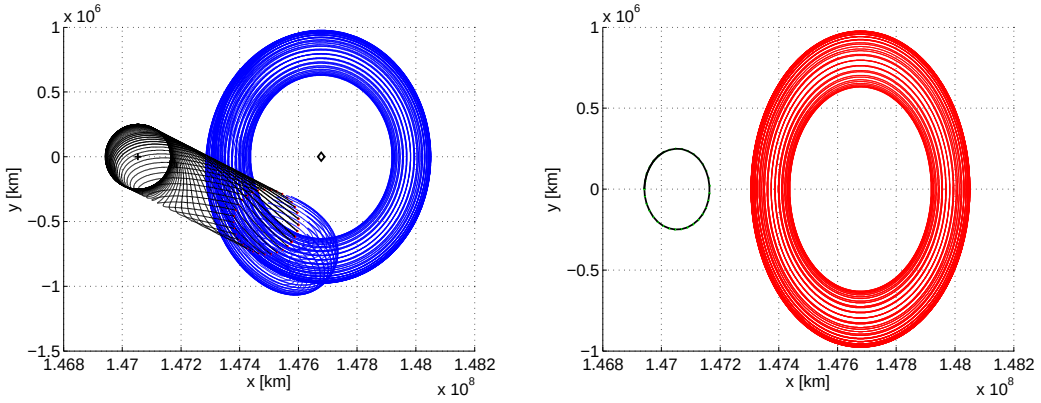

(a) Transfer trajectories.

(b) departure and target Lissajous orbits.

Figure 6.13: Transfer trajectories from the departure (black) and target (red) Lissajous orbits.

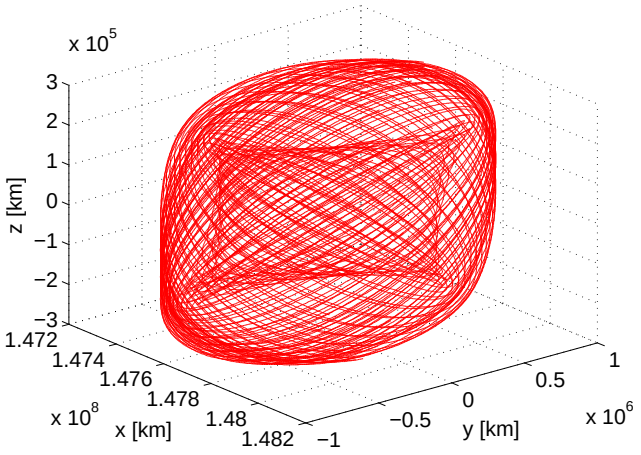

Figure 6.14: Target Lissajous orbit.

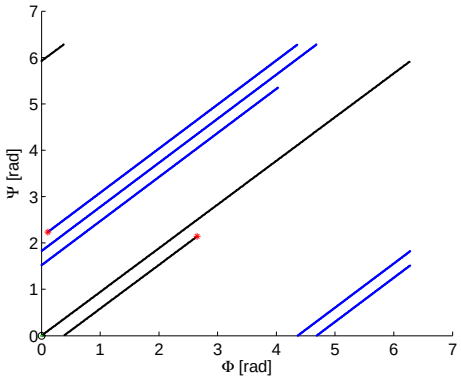

(a) Leaving trajectoy number 1.

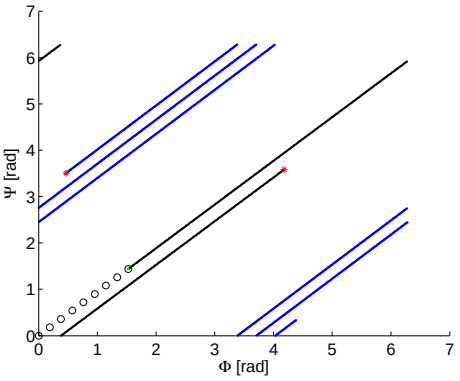

(b) Leaving trajectoy number 9.

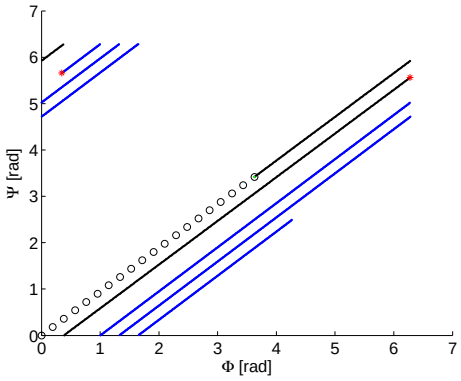

(c) Leaving trajectoy number 20.

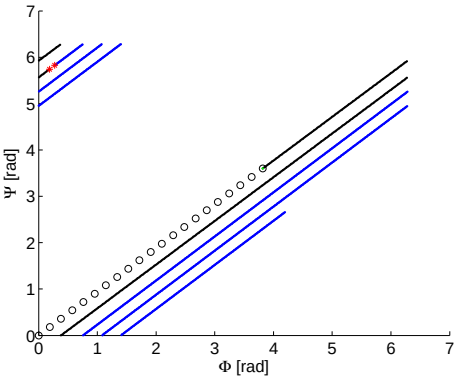

(d) Leaving trajectoy number 21.

Figure 6.15: Phase space of trajectories number 1, 9, 20 and 21 of the unstable manifold of the departure Lissajous orbits.

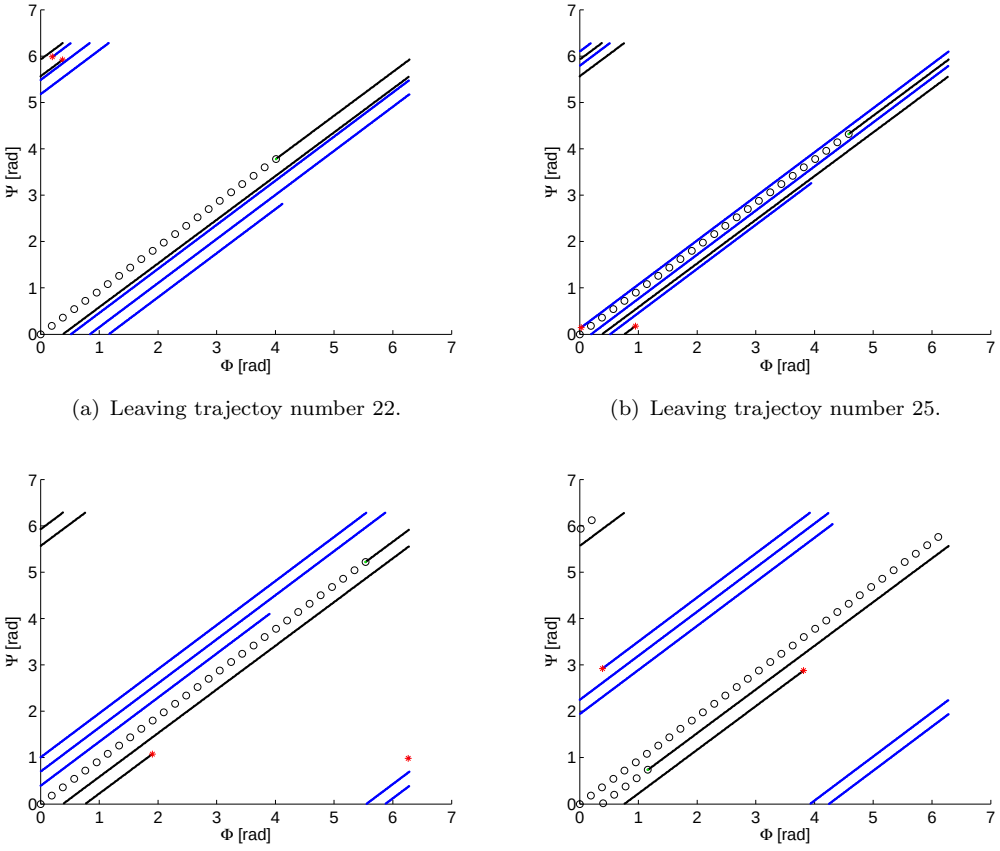

(a) Leaving trajectoy number 22.

(b) Leaving trajectoy number 25.

(c) Leaving trajectoy number 30.

(d) Leaving trajectoy number 40.

Figure 6.16: Phase space of trajectories number 22, 25, 30 and 40 of the unstable manifold of the departure Lissajous orbits.

A sensitivity analysis was carried out by changing the departure square Lissajous orbit amplitude on the order of 25,000 km 250,000 km and 750,000 km and it is possible to make the following considerations:

- If the amplitude of the departure Lissajous orbit is increased, it is necessary to select a higher value in initial lightness parameter, β_0, to guarantee the heteroclinic connection between the two Libration points. For example, for $A_y = A_z = 25{,}000$ km a $\beta_0 = 0.01$ (i.e., SOHO's spacecraft in Table 2.6) and a $\beta_M = 0.001$ guarantees the heteroclinic connection. However, for $A_y = A_z = 250{,}000$ km requires a $\beta_0 = 0.03$ (i.e., Herschel's spacecraft in Table 2.6) and a $\beta_M = 0$ (the manoeuvre decreases of 100% the initial β_0);
- If the amplitude of the departure Lissajous is fixed, the more β_0 is increased a smaller fraction in the reduction of β_0 due to the manoeuvre is required to guarantee a heteroclinic connection. For example for $A_y = A_z = 250{,}000$ km and $\beta_0 = 0.03$, it is necessary to reduce the reflectivity by 100 %; however, for a $\beta_0 = 0.04$ (i.e., JWST's spacecraft in Table 2.6) the reflectivity is reduced by 50%. The choice in the initial β_0 is a design trade-off to be considered based on the spacecraft's mission requirements when the spacecraft reaches the target orbit.

In Appendix F, an example is shown for a non-square Lissajous orbit with departure orbit like Gaia's mission.

When using SRP manoeuvre, it is possible to connect Libration orbits of different energies through the invariant manifold. In this case, the spacecraft moves from two libration points that belong to a different system due to the effect of the SRP acceleration. Conversely, Canalias et al. (2003) connected Libration point orbits of different energies that belong to the same equilibrium point of the CR3BP.

Although the injection manoeuvre (that places the spacecraft onto the unstable manifold of the departure Lissajous orbit) makes use of the natural dynamics of the CR3BP, further options for the design of the first manoeuvre should be investigated to have an optimal solution. Specially when designing a transfer trajectory that takes into account of the parameters of the target orbit rather than the departure one. Moreover, the transfer time could result in being a further parameter to take into account for a optimal transfer.

6.3 Phase space for solar radiation pressure manoeuvres in the x-y plane

In the previous section, it was demonstrated that a direct transfer from the departure Lissajous orbit to the target Lissajous orbit is not possible for SRP manoeuvres that involve a Sun-pointing area. The interest in a direct transfer is justified when the transfer strategy aims to avoid the spacecraft being in eclipse with the Earth as shown by Canalias et al. (2003). Thus, in this section, SRP manoeuvres that involve a re-orientation of the spacecraft with the Sun-line direction are investigated. Manoeuvres in the x-y plane for a fixed β were considered. This condition is reached when the clock angle, δ, is equal to 90° and the cone angle, α, is free to assume values between ±90°.

6.3.1 Analytical solution for a saddle×focus×center equilibrium

When the libration point moves in the x-y plane, the equilibrium of the collinear points changes from saddle×center×center to saddle×focus×center. Thus, the solutions in Eq. (3.100) does not hold for a general cone angle, α, orientation. In order to find the semi-analytical solution for a saddle×focus×center equilibrium, the general solutions of Eq. (3.87) are:

$$\xi = \sum_{i=1}^{4} A_i e^{\lambda_i t} \qquad \eta = \sum_{i=1}^{4} B_i e^{\lambda_i t} \qquad \zeta = \sum_{i=5}^{6} A_i e^{\lambda_i t}. \tag{6.16}$$

In Eq. (6.16), A_i and B_i are constants and can be found by imposing the initial conditions. By substituting Eq. (6.16) to the first equation in Eq. (3.87), it is possible to find the relationship between the constants $A_{1,2,3,4}$ and $B_{1,2,3,4}$:

$$A_i \lambda_i^2 e^{\lambda_i t} - 2B_i \lambda_i e^{\lambda_i t} - \bar{V}^*_{xx} A_i e^{\lambda_i t} - \bar{V}^*_{xy} B_i e^{\lambda_i t} = 0 \qquad (i = 1, \ldots, 6); \tag{6.17}$$

where, B_i is a function of A_i such as:

$$B_i = \frac{\lambda_i^2 - \bar{V}^*_{xx}}{2\lambda_i + \bar{V}^*_{xy}} \cdot A_i = k_i \cdot A_i \qquad (i = 1, \ldots, 6). \tag{6.18}$$

The semi-analytical solution can be found by substituting the solutions in Eq. (6.16) to the linearised equations of motion in Eq. (3.87) as:

$$\begin{cases} \xi &= A_1 e^{\lambda_1 t} + A_2 e^{\lambda_2 t} + A_3 e^{\lambda_3 t} + A_4 e^{\lambda_4 t} \\ \eta &= B_1 e^{\lambda_1 t} + B_2 e^{\lambda_2 t} + B_3 e^{\lambda_3 t} + B_4 e^{\lambda_4 t} \\ \zeta &= A_5 e^{\lambda_5 t} + A_6 e^{\lambda_6 t} \\ \dot{\xi} &= \lambda_1 A_1 e^{\lambda_1 t} + \lambda_2 A_2 e^{\lambda_2 t} + \lambda_3 A_3 e^{\lambda_3 t} + \lambda_4 A_4 e^{\lambda_4 t} \\ \dot{\eta} &= \lambda_1 B_1 e^{\lambda_1 t} + \lambda_2 B_2 e^{\lambda_2 t} + \lambda_3 B_3 e^{\lambda_3 t} + \lambda_4 B_4 e^{\lambda_4 t} \\ \dot{\zeta} &= \lambda_5 A_5 e^{\lambda_5 t} + \lambda_6 A_6 e^{\lambda_6 t}. \end{cases} \tag{6.19}$$

Thus, by substituting the relationship in Eq. (6.18) to Eq. (6.19), the semi-analytical solution turns into:

$$\begin{cases} \xi &= A_1 e^{\lambda_1 t} + A_2 e^{\lambda_2 t} + A_3 e^{\lambda_3 t} + A_4 e^{\lambda_4 t} \\ \eta &= k_1 A_1 e^{\lambda_1 t} + k_2 A_2 e^{\lambda_2 t} + k_3 A_3 e^{\lambda_3 t} + k_4 A_4 e^{\lambda_4 t} \\ \zeta &= A_5 e^{\lambda_5 t} + A_6 e^{\lambda_6 t} \\ \dot{\xi} &= \lambda_1 A_1 e^{\lambda_1 t} + \lambda_2 A_2 e^{\lambda_2 t} + \lambda_3 A_3 e^{\lambda_3 t} + \lambda_4 A_4 e^{\lambda_4 t} \\ \dot{\eta} &= \lambda_1 k_1 A_1 e^{\lambda_1 t} + \lambda_2 k_2 A_2 e^{\lambda_2 t} + \lambda_3 k_3 A_3 e^{\lambda_3 t} + \lambda_4 k_4 A_4 e^{\lambda_4 t} \\ \dot{\zeta} &= \lambda_5 A_5 e^{\lambda_5 t} + \lambda_6 A_6 e^{\lambda_6 t}. \end{cases} . \tag{6.20}$$

The semi-analytical solution in Eq. (6.20) is associated to the eigenvalues of the type saddle×focus×center equilibrium where:

$$\lambda_{1,2} \simeq \pm\lambda \qquad \lambda_{3,4} = \alpha \pm \omega \cdot i \qquad \lambda_{5,6} = \pm\nu \cdot i. \tag{6.21}$$

Figure 6.17 shows the positions and the stability of the pseudo libration point SL_1 when $\beta = 0.005$, the clock angle, δ, is equal to 90° and the cone angle is varied from ±90°. When the libration point is in the positive y-axis, α is negative and the equilibrium point has a stable focus; while it has an unstable focus in the negative y-axis when α has positive values. When α is 0° or 90°, the equilibrium point belongs to the x-axis and it is of the type saddle×center×center. Specifically, for $\alpha = 0°$ the spacecraft is Sun-pointing; while, for $\alpha = 90°$, the effect of the SRP acceleration vanishes and the equilibrium point corresponds to the solution of the CR3BP dynamics.

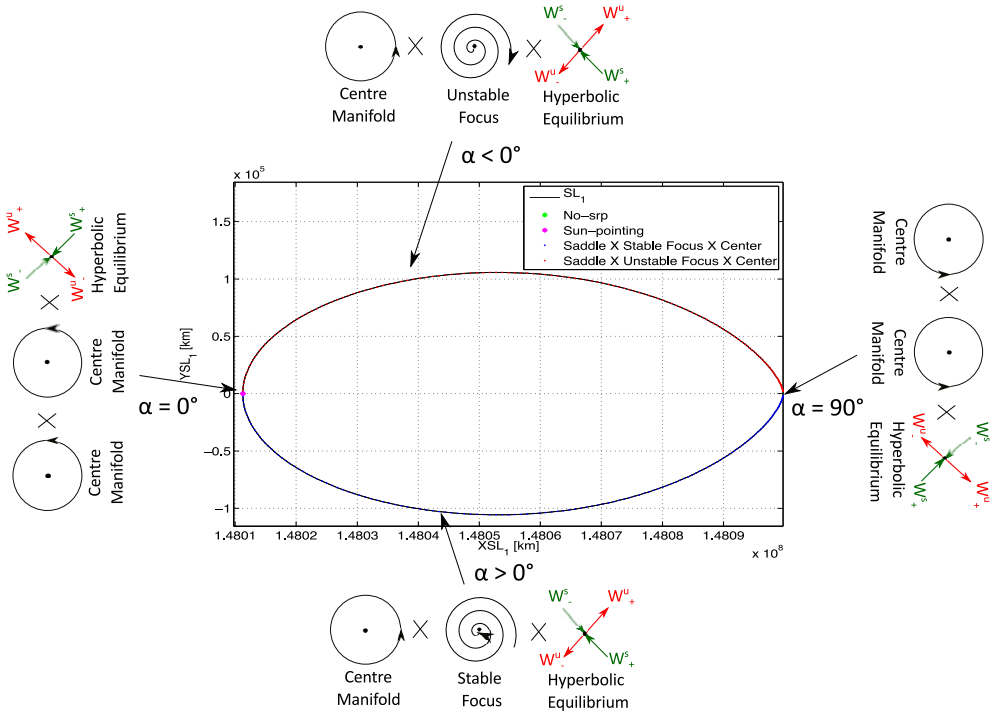

Figure 6.17: Stable and Unstable focus for $\beta = 0.005$, $\delta = 90°$ and α varied between ±90°.

The variable k_i in Eq. (6.20) is defined as follows:

1) For the eigenvalues of the hyperbolic equilibrium, $\lambda_{1,2}$, $k_{1,2}$ is defined as:

$$k_1 = \frac{\lambda^2 - \bar{V}^*_{xx}}{2\lambda + \bar{V}^*_{xy}} \qquad\qquad k_2 = \frac{\lambda^2 - \bar{V}^*_{xx}}{-2\lambda + \bar{V}^*_{xy}}; \tag{6.22}$$

2) For the eigenvalues of the focus equilibrium, $\lambda_{3,4}$, $k_{3,4}$ is defined as:

$$k_3 = \frac{(\alpha + \omega \cdot i)^2 - \bar{V}^*_{xx}}{2(\alpha + \omega \cdot i) + \bar{V}^*_{xy}} \qquad\qquad k_4 = \frac{(\alpha - \omega \cdot i)^2 - \bar{V}^*_{xx}}{2(\alpha - \omega \cdot i) + \bar{V}^*_{xy}}. \tag{6.23}$$

The position vector of the semi-analytical solution in Eq. (6.20) can be written such as:

$$\begin{cases} \xi &= A_1 e^{\lambda_1 t} + A_2 e^{\lambda_2 t} + A_3 e^{\alpha t}\cos(\omega t) + A_4 e^{\alpha t}\sin(\omega t) \\ \eta &= k_1 A_1 e^{\lambda_1 t} + k_2 A_2 e^{\lambda_2 t} + B_3 e^{\alpha t}\cos(\omega t) + B_4 e^{\alpha t}\sin(\omega t) \\ \zeta &= A_5\cos(\nu t) + A_6\sin(\nu t) \end{cases}; \tag{6.24}$$

where B_3 and B_4 are defined respectively:

$$B_3 = A_3\Re(k_4) + A_4\Im(k_4) \qquad\qquad B_4 = A_4\Re(k_3) + A_3\Im(k_3). \tag{6.25}$$

In Eq. (6.25), $\Re(\square)$ and $\Im(\square)$ denote the real and imaginary part of a complex number. The planar solution in ξ and η is now considered since the out-of plane solution ζ is still the one shown in Eq. (3.105). The relationship between the amplitudes and the spacecraft's state vector can be written in a compact way:

$$\begin{Bmatrix} \xi \\ \eta \\ \dot{\xi} \\ \dot{\eta} \end{Bmatrix} = \boldsymbol{M} \cdot \begin{Bmatrix} A_1 \\ A_2 \\ A_3 \\ A_4 \end{Bmatrix}; \tag{6.26}$$

where, $\boldsymbol{M}$ is defined as:

$$\boldsymbol{M} = [\boldsymbol{M}_1|\boldsymbol{M}_2|\boldsymbol{M}_3|\boldsymbol{M}_4]\,. \tag{6.27}$$

In Eq. (6.27), the columns $\boldsymbol{M}_1$ and $\boldsymbol{M}_2$ of matrix $\boldsymbol{M}$ are:

$$\boldsymbol{M}_1 = \begin{Bmatrix} e^{\lambda_1 t} \\ k_1 e^{\lambda_1 t} \\ \lambda_1 e^{\lambda_1 t} \\ k_1\lambda_1 e^{\lambda_1 t} \end{Bmatrix} \qquad\qquad \boldsymbol{M}_2 = \begin{Bmatrix} e^{\lambda_2 t} \\ k_2 e^{\lambda_2 t} \\ \lambda_2 e^{\lambda_2 t} \\ k_2\lambda_2 e^{\lambda_2 t} \end{Bmatrix}; \tag{6.28}$$

while, $\boldsymbol{M}_3$ is:

$$\boldsymbol{M}_3 = \left\{ \begin{array}{l} e^{\alpha t}\cos(\omega t) \\ e^{\alpha t}\left[\Re(k_4)\cos(\omega t) + \Im(k_3)\sin(\omega t)\right] \\ e^{\alpha t}\left[\alpha\cos(\omega t) - \omega\sin(\omega t)\right] \\ e^{\alpha t}\left\{\Re(k_4)\left[\alpha\cos(\omega t) - \omega\sin(\omega t)\right] + \Im(k_3)\left[\alpha\sin(\omega t) + \omega\cos(\omega t)\right]\right\} \end{array} \right\}, \quad (6.29)$$

and $\boldsymbol{M}_4$ is:

$$\boldsymbol{M}_4 = \left\{ \begin{array}{l} e^{\alpha t}\sin(\omega t) \\ e^{\alpha t}\left[\Im(k_4)\cos(\omega t) + \Re(k_3)\sin(\omega t)\right] \\ e^{\alpha t}\left[\alpha\sin(\omega t) + \omega\cos(\omega t)\right] \\ e^{\alpha t}\left\{\Im(k_4)\left[\alpha\cos(\omega t) - \omega\sin(\omega t)\right] + \Re(k_3)\left[\alpha\sin(\omega t) + \omega\cos(\omega t)\right]\right\} \end{array} \right\}. \quad (6.30)$$

The design of the transfer strategy for a general orientation of the spacecraft requires to change the semi-analytical solution presented in Section 6.1.2 for a Sun-pointing area accordingly to the general semi-analytical solution for a saddle×focus×center equilibrium. Note that the general solution also holds also for the Sun-pointing case.

6.3.2 Solar radiation pressure manoeuvre given at the departure Lissajous orbit

Figure 6.18 and 6.19 show the amplitudes of the stable, A_1', and unstable, A_2', manifold of the target Lissajous orbit when a SRP manoeuvre in the cone angle, α, is given. The departure orbit is a square Lissajous orbit with $A_y = A_z = 250{,}000$ km. A lightness parameter, β_0, equal to 0.001 was chosen. The cone angle, α, was varied within $\pm 90°$. In the case of Figure 6.18, the SRP manoeuvre is given for positive values of α; thus, the equilibrium point moves in the negative y-axis. Conversely, Figure 6.19 shows the amplitudes when a negative value of α is selected and the equilibrium point moves in the positive y-axis.

In Figure 6.18, it is possible to observe that for small angles $A_1' \neq A_2'$ with $A_1' < 0$ and $A_2' > 0$; however, they share the same order of magnitude 10^{-7}. Thus, even if A_1' tends to zero, A_2' is not big enough to enhance a direct transfer of the spacecraft. This fact can open up to the design of transfers within transit orbits; however, as previously mentioned, the focus of this study is primarily on transfers within Lissajous orbits. Moreover, the more the cone angle is increased, the more the order of magnitude of A_1' and A_2' increases. This suggests that the effect of large angles makes the solution worse. Indeed, the effect of increasing the angle decreases the reflectivity of the spacecraft by making the value in A_1' and A_2' of the same order and sign.

Figure 6.19 shows the same behaviour in the solutions of Figure 6.18; however, the solution is mirrored. In Figure 6.18, the minimum of A_1' and A_2' is achieved for values in Φ between π and 2π; while, in Figure 6.19, the minimum in $A_{1,2}'$ is given for Φ between 0 and π.

Figure 6.20 shows the amplitudes for a fix value of $\alpha = 1.46°$ for β_0 to 0.01 and 0.02. By increasing the value of the initial β, the value in the amplitudes increases for the same value of α. Thus, it is possible to conclude that also in this case a direct transfer from the departure Lissajous orbit is not possible and an intermediate manoeuvre that aims to inject the spacecraft onto the unstable manifold of the departure orbit should be investigated.

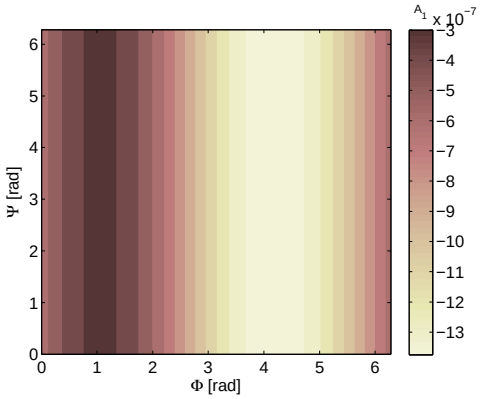

(a) Amplitude of the unstable manifold, A_1', of the target Lissajous orbit: $\alpha = 1.46°$.

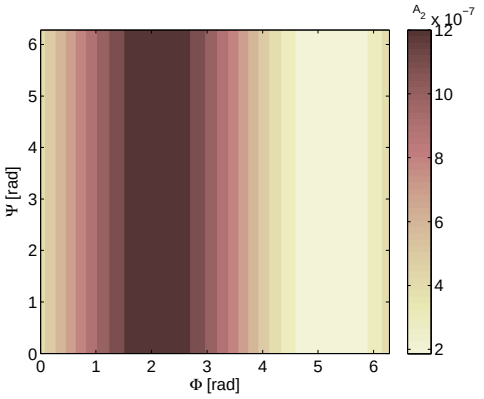

(b) Amplitude of the stable manifold, A_2', of the target Lissajous orbit: $\alpha = 1.46°$.

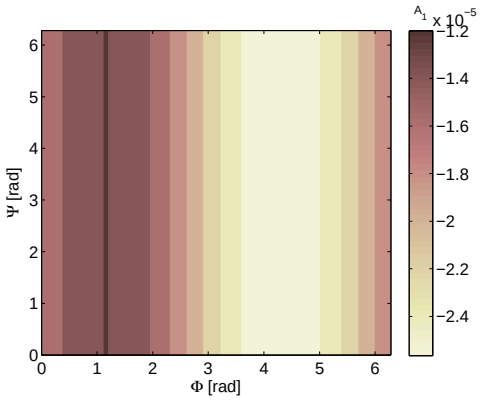

(c) Amplitude of the unstable manifold, A_1', of the target Lissajous orbit: $\alpha = 16.62°$.

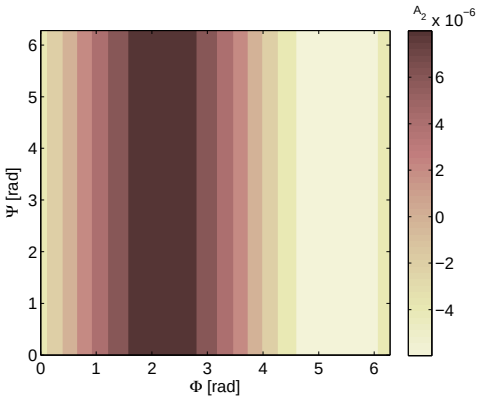

(d) Amplitude of the stable manifold, A_2', of the target Lissajous orbit: $\alpha = 16.62°$.

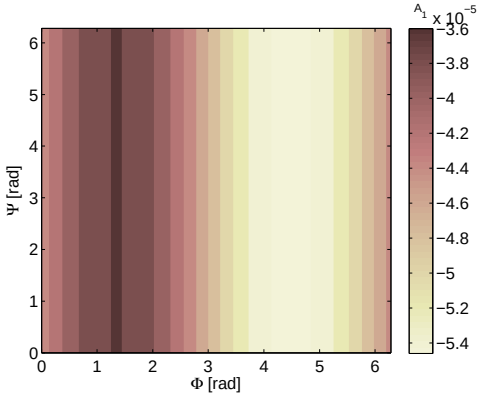

(e) Amplitude of the unstable manifold, A_1', of the target Lissajous orbit: $\alpha = 33.82°$.

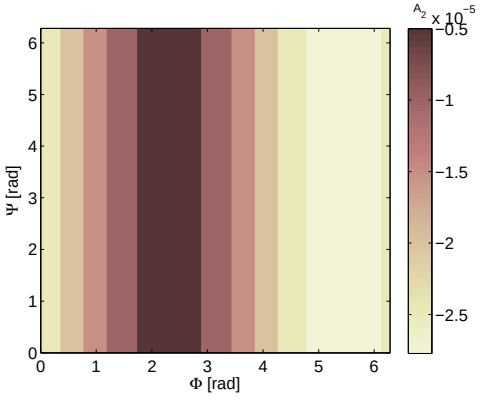

(f) Amplitude of the stable manifold, A_2', of the target Lissajous orbit: $\alpha = 33.82°$.

Figure 6.18: Amplitude of the unstable, A_1', and stable, A_2', manifolds of the target Lissajous orbit with $\beta_0 = 0.001$ when the SRP manoeuvre is given along the departure Lissajous orbit for $\alpha > 0°$.

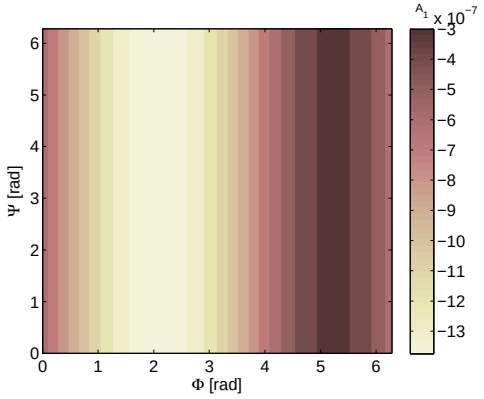

(a) Amplitude of the unstable manifold, A_1', of the target Lissajous orbit: $\alpha = -1.46°$.

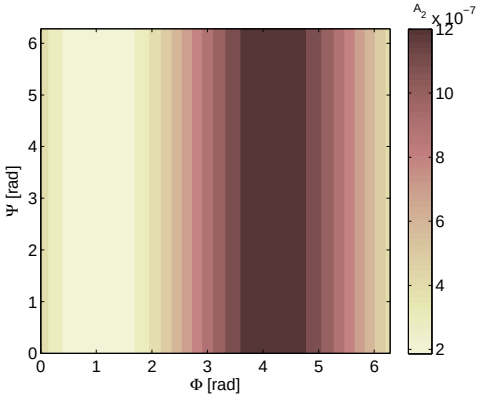

(b) Amplitude of the stable manifold, A_2', of the target Lissajous orbit: $\alpha = -1.46°$.

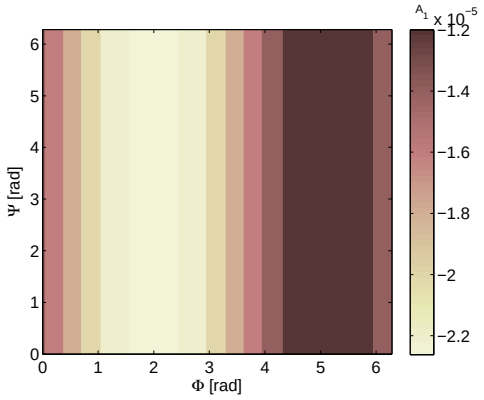

(c) Amplitude of the unstable manifold, A_1', of the target Lissajous orbit: $\alpha = -14.90°$.

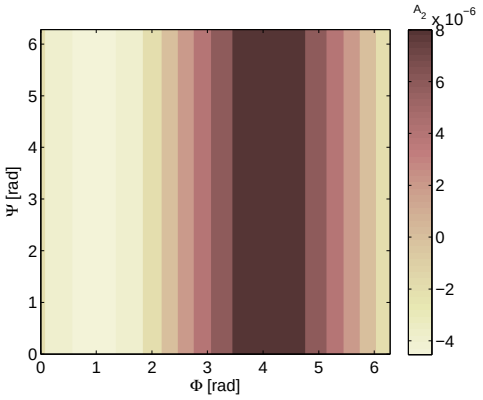

(d) Amplitude of the stable manifold, A_2', of the target Lissajous orbit: $\alpha = -14.90°$.

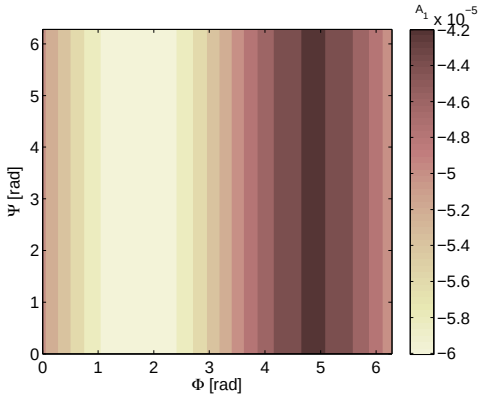

(e) Amplitude of the unstable manifold, A_1', of the target Lissajous orbit: $\alpha = -37.83°$.

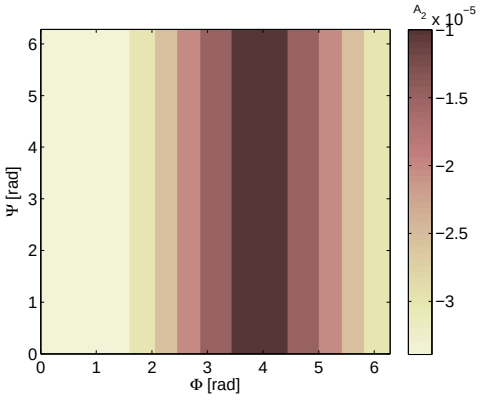

(f) Amplitude of the stable manifold, A_2', of the target Lissajous orbit: $\alpha = -37.83°$.

Figure 6.19: Amplitude of the unstable, A_1', and stable, A_2', manifolds of the target Lissajous orbit with $\beta_0 = 0.001$ when the SRP manoeuvre is given along the departure Lissajous orbit for $\alpha < 0°$.

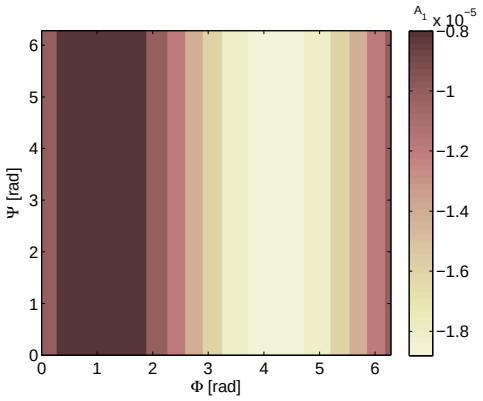

(a) Amplitude of the unstable manifold, A_1', of the target Lissajous orbit: $\beta_0 = 0.01$.

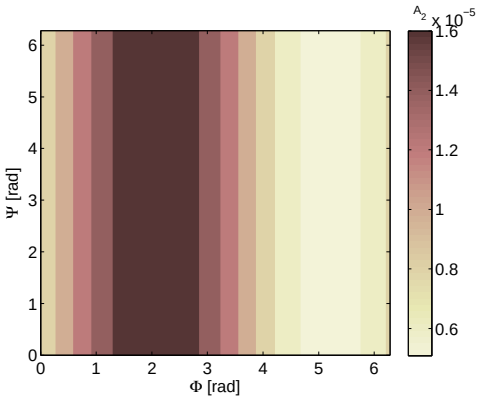

(b) Amplitude of the stable manifold, A_2', of the target Lissajous orbit: $\beta_0 = 0.01$.

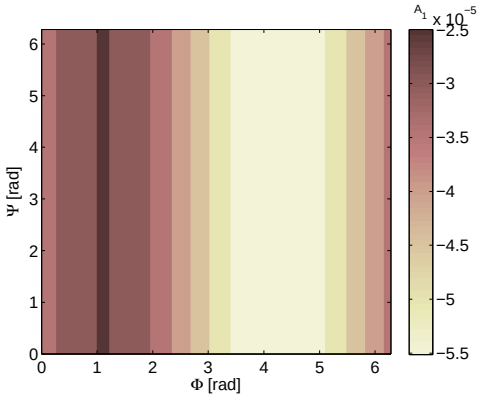

(c) Amplitude of the unstable manifold, A_1', of the target Lissajous orbit: $\beta_0 = 0.02$.

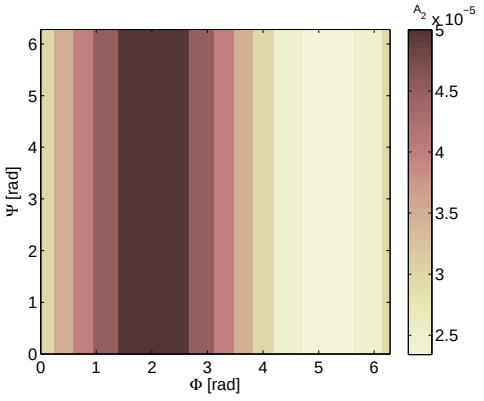

(d) Amplitude of the stable manifold, A_2', of the target Lissajous orbit: $\beta_0 = 0.02$.

Figure 6.20: Amplitude of the unstable, A_1', and stable, A_2', manifolds of the target Lissajous orbit with $\beta_0 = 0.01$ and 0.02 when the SRP manoeuvre is given along the departure Lissajous orbit for $\alpha = 1.46°$.

6.4 Deployable structure solutions

The design of the transfer trajectories enhanced by solar radiation pressure acceleration requires the use of a fixed variable reflective area Sun-pointing or fixed geometry re-orientable reflective area.

In the first case, the reflectivity of an initial Sun-pointing area is reduced to allow transfer between Lissajous orbits. Thus, the use of Reflective Control Devices (RCDs) can be exploited to reduce the reflectivity of a sunshade structure as demonstrated by the Ikaros mission (Tsuda et al., 2013). In Earth's orbit missions, Lücking et al. (2012c) uses the RCDs to travel in the phase space. Figure 6.21 shows that when the RCDs are on, the effective reflective area is white; while, when the RCDs are off (gray areas), the effective reflective area is reduced (white areas). Similar results can be achieved for solar panels through the use of flaps that aim to reduce the reflective area as shown in Figure 6.22.

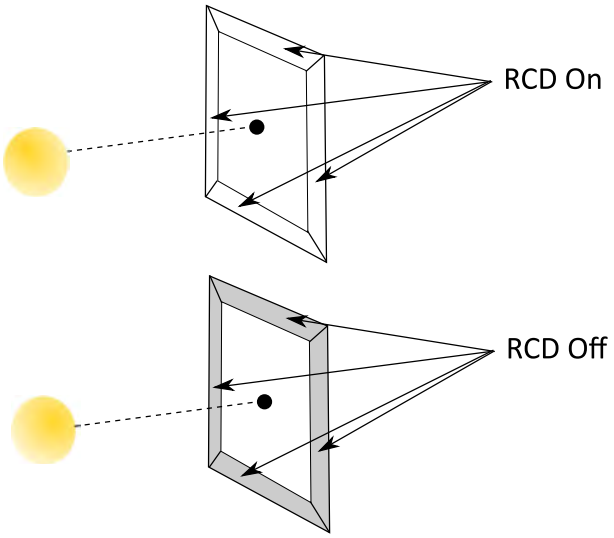

Figure 6.21: Sunshade with reflecive control devices.

For example in Figure 6.13, an initial lightness number of $\beta_0 = 0.04$ and a final lightness number of $\beta_M = 0.002$ were presented. If the sunshade of the satellite is considered as the major reflective surface, a reflectivity coefficient, C_r^s, of 1.92 at the beginning of life was taken into account. Table 6.1 shows the size in the reflective area needed for different class of satellites. Note that the James Webb Space Telescope have a sunshade of 264 m^2 with a spacecraft mass of 6500 kg while in this case a 272.33 m^2 of sunshade can be used for SRP transfer manoeuvre of a 10 kg spacecraft. In this chapter, a preliminary study on using solar radiation pressure to enhance transfer within Lissajous orbits was carried out, thus further studies are required to find optimal solution for example in minimising the reflective deployable area required. It seems quite challenging for a class

Mass [kg]	A_0 [$\mathbf{m}^2$]	A_M [$\mathbf{m}^2$]
1	27.233	13.616
10	272.33	136.165
100	2723.3	1361.65
1000	$2.723 \cdot 10^{-4}$	$1.361 \cdot 10^{-4}$

Table 6.1: Spacecraft area required before and after the manoeuvre for different class of satellites.

of satellites as LPO spacecraft where a mass of the order of 1000 kg is usually required. This technique seems more promising for small class of satellite like nanosatellites (1-10 kg). This is related to problem in packing extended deployable structures for large science missions. The current transfer technique could be possibly used for solar sail mission at LPO. For the example previously shown, a total mass of the spacecraft of 85 kg (included the weight of the sail) with 48.11 m-span for a squared solar sail is required. For a kapton substrate (7.1 g/m^2) and aluminium surface coating (1.35 g/m^2), the solar sail weight is 19.56 kg. For the mast structure (2 $\times$ 68.0413 m) with linear density of 70 g/m an additional mass of 9.5257 kg has to be allocated to support the solar sail. Thus, 29.0857 kg are associated to the solar sail by ensuring 55.91 kg allocated for the payload from the total spacecraft mass that correspond to the bus weight of JAXA Ikaros solar sail (20 m-span). Currently, JAXA is performing a ground test to deploy a 50 m-span solar sail for JAXA future mission to Trojans asteroids. However, a lighter system is needed to ensure sufficient mass allocated for the payload.

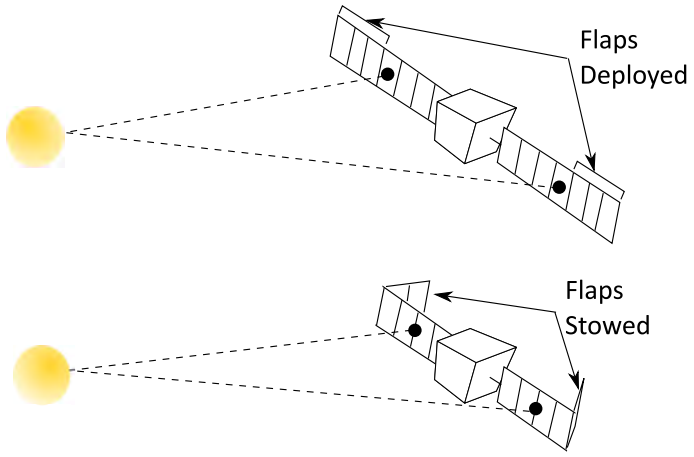

Figure 6.22: Solar panels with flaps.

Finally, in the case of a fixed reflective area, attitude control manoeuvres are investigated to perform the transfer between Lissajous orbits by re-orienting the pre-existing spacecraft's reflective on-board structures such as:

- the solar panels,
- the sunshade, or
- the spacecraft's antennas.

In this case, we can't draw any conclusion about the feasibility of re-orienting transfer manoeuvres onto the spacecraft structural configuration as a satisfactory solution was not found yet. The re-orientation manoeuvre approach has to be studied further for demonstrating wherever it is a feasible technique or not. The analysis shown in this chapter was mainly focused in developing the technique to ensure the transfer within Lissajous orbits for a Sun-pointing spacecraft, however further works should aim in minimising the area required to ensure the fuel-free transfer for LPO class of satellite.

An important remark is that this study do not include the effect in the optical degradation when designing the SRP manoeuvre. As shown by Dachwald et al. (2005), the effect of degradation affects the position of the equilibrium points presented in Section 3.5.2. The effect of the degradation do not affect much equilibrium solutions around L_1, Figure 3.7, while equilibrium solutions about L_2, Figure 3.7, are severely restricted by limiting the regions where transfer within Lissajous orbits can be done with a SRP manoeuvre.

6.5 Summary

In this chapter, the invariant manifold theory is applied for the design of transfer trajectories within the Sun-Earth system enhanced by the solar radiation pressure acceleration. When a solar radiation pressure manoeuvre is given, the libration point's coordinates change position. A semi-analytical approximation is used to design the transfer strategy that makes use of the geometry of two libration points: the one before and after the manoeuvre. The semi-analytical solution depends on the stability of the equilibrium points. Thus, due to the effect of a solar radiation pressure manoeuvre, the equilibrium points to become a saddle×focus×center type; where, the semi-analytical solution is extended here to the case of focus equilibrium. Two types of solar radiation pressure manoeuvres have been investigated: for a Sun-pointing area, where the lightness parameter is changed, and for a fixed reflective area, where the spacecraft is re-oriented with the Sun-line direction.

This chapter has succeeded in demonstrating that transfer trajectories between Lissajous orbits are possible for a Sun-pointing spacecraft while SRP manoeuvres that involve a re-orientation of the spacecraft needs to be further explored. The major research findings of this chapter are:

- the development of a strategy that use the geometry of a moving equilibrium point,
- the change in a Sun-pointing spacecraft reflectivity allows transfers toward higher amplitude orbits (i.e. for a possible extension of the spacecraft's nominal mission),
- the Sun-pointing manoeuvre can be done by exploiting on board deployable structures (i.e. by equipping deployable structures with embedded RCDs devices or by adding additional flaps),
- the semi-analytical solution of the center manifold was derived for a general orientation of the spacecraft's reflective deployable areas.

When an LPO spacecraft reaches the end-of-life, if no action is taken then the uncontrolled spacecraft presents a collision risk for future LPO missions. To prevent the formation of space debris in the Earth-LPO region, an end-of-life disposal strategy to safely dispose the LPO spacecraft needs to be formulated. This problem will be addressed in next chapter.

Chapter 7

End-of-Life Disposal through Solar Radiation Pressure

Many years of unregulated human space activities have created a significant amount of space *pollution*. Pollution is partially caused by spacecraft reaching the end of their operational *life*. This causes an increase in the number of dismissed and uncontrolled man-made objects in space, compromising future space activities. As mentioned in Chapter 1 and Chapter 2, space agencies are currently investing their resources to preserve the space environment. Much effort is made to tackle the problem of space debris for spacecraft in low Earth orbit. However, less concern is given to spacecraft in libration point orbits.

Since new technologies are investigated in this thesis for future LPOs missions, concern is given to include the end-of-life mission phase in this space mission study and to answer the last research question stated in Chapter 1:

Q.5 - *How can we design an end-of-life disposal strategy that makes use of solar radiation pressure enhancing devices to dispose of a spacecraft safely in a graveyard trajectory?*

Thus, this chapter presents an EOL disposal option to prevent the formation of space debris for the disposal of LPO spacecraft. The EOL represents a new topic for this kind of space mission as space agencies do not currently have guidelines for the EOL of LPO spacecraft. This work was initiated within a European project lead by the University of Southampton in collaboration with the University of Strathclyde and SpaceDyS and founded by the European Space Agency. This ESA project investigates EOL disposal concepts for LPO and high elliptical orbit missions (Colombo et al., 2014b, 2015a) where the author was in charge of the design of a fuel-free solution for the LPO end-of-life disposal.

An EOL propellant-free disposal strategy for libration point orbits which uses solar radiation pressure to restrict the evolution of the spacecraft motion is proposed here. The spacecraft is initially disposed of in the unstable manifold leaving the libration point orbit before a reflective Sun-pointing surface is deployed to enhance the effect of the SRP acceleration. Therefore, the consequent increase in energy prevents the spacecraft's return to Earth. Three European Space Agency missions are selected as test case scenarios: Herschel (Appendix B.3.1), SOHO (Appendix B.3.2) and Gaia (Appendix B.3.3). The SRP EOL disposal was initially investigated in the circular restricted three-body problem dynamics with SRP. Then, the effect of the Earth's orbit eccentricity onto the proposed disposal is taken into account. Thus, the SRP EOL disposal is extended to the elliptic restricted three-body problem dynamics with SRP. Finally, guidelines for the EOL disposal of future libration point orbit missions are proposed. Olikara et al. (2015) initially proposed a disposal option through a Δv manoeuvre and a comparison between the two EOL disposal is investigated in this chapter.

The results of this chapter were published in Soldini et al. (2016a) and in an under review publication (Soldini et al., 2015b).

7.1 Disposal strategy concept

In Section 3.6, it was shown that the effect of SRP acceleration has consequences on the shape of the total potential energy and, for instance, on the form of the zero velocity curves. From Figure 3.14, it was clear that the effect of a SRP manoeuvre can cause the closure or the opening of the ZVCs in correspondence of the libration points' bottle neck regions. In Chapter 6, this phenomenon was exploited to enhance transfer trajectories within the Sun-Earth system by opening the ZVCs at the bottle neck regions after the manoeuvre. Conversely, in the design of the end-of-life disposal, the spacecraft must avoid to cross the libration points' bottle neck regions and re-enter on Earth. Thus, an EOL SRP manoeuvre is given to close the ZVCs at the bottle neck regions.

For the EOL disposal enhanced by the SRP acceleration, the main goal is to find the minimum deployable area required to close the zero-velocity curves at the pseudo libration point, SL_2, to confine the motion of the spacecraft outside the Earth-L_2 protected regions. The minimum area is determined through numerical optimisation by satisfying the constraint. This restriction requires that the additional area should increase the energy of the system to reach the energy at the pseudo libration point.

To design a strategy that enables the SRP manoeuvre to close the ZVCs at SL_2, the unstable manifold towards the outer part of the system is followed. The unstable manifold is computed by integrating the trajectory forward in time with a perturbation of $+\epsilon = 10^{-6}$ which corresponds to a displacement error in the spacecraft position of 200

km (Koon et al., 2008; Gómez et al., 2001). Further details in the numerical computation of the unstable manifolds were given in Section 3.11.

Figure 7.1 shows an example of the SRP disposal strategy for a two-dimensional case. The time used for the manifold evolution is about 400 non-dimensional time units; which corresponds to 63.5 years. A number of trajectories (in grey, Figure 7.1(a)) which belong to this unstable tube are selected with their initial condition close to the LPO.

As can be seen from Figure 7.1(a), a spacecraft injected towards the unstable manifolds without closing the ZVCs is unsafe. Indeed, the disposed spacecraft could represent a potential hazard to other operating spacecraft in LPOs or Earth's orbit; hence, this approach is not sustainable. In particular, the highlighted trajectory in Figure 7.1(a) (bold black line) shows that after 29.5 years the spacecraft will encounter the Earth and the L_2 regions since the ZVCs have a trajectory gateway at L_2.

A point P_1 along each natural trajectory legs is selected (Figure 7.1(b)), where a Sun-pointing reflective surface is deployed (Figure 7.1(c)). This allows the closure of the ZVCs at SL_2. The trajectories evolution after the deployment of the SRP enhancing device was verified by computing the new trajectory legs with the added effect of β (Figure 7.1(d)). In this case, β corresponds to a value of 0.00132[1]. It can be verified that, in correspondence of any point of the following evolution, the ZVCs are closed (see dashed line in Figure 7.1(d)). By enhancing the effect of SRP, the energy of the system was changed without any propellant costs. Afterwards, the energy does not change along the resulting trajectory if the deployable area is passively stabilised with the Sun. Finally, even if the L_2-LPO region is not completely protected (Figure 7.1(d)), the probability of crossing region close to L_2 is now lower.

[1]This value of β corresponds to 861 m^2 for a 1000 kg of spacecraft.

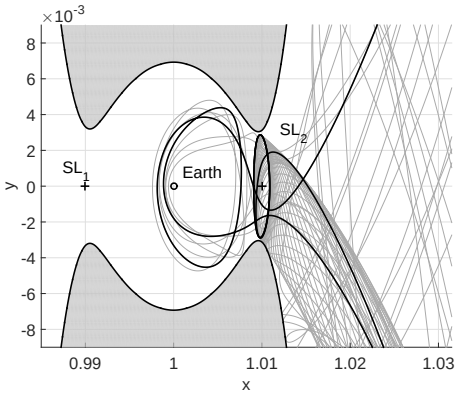

(a) Unstable manifold: the highlighted trajectory encounters the Earth after 29.5 years.

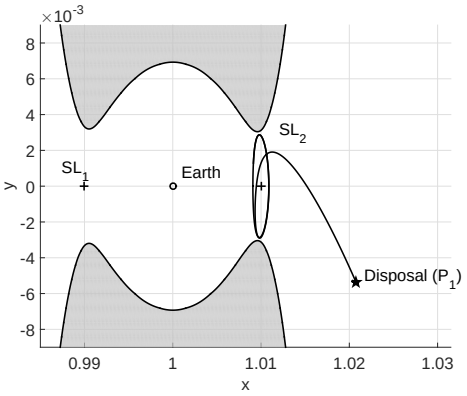

(b) Selected trajectory where the deployment is done after 68.04 days from the leaving LPO.

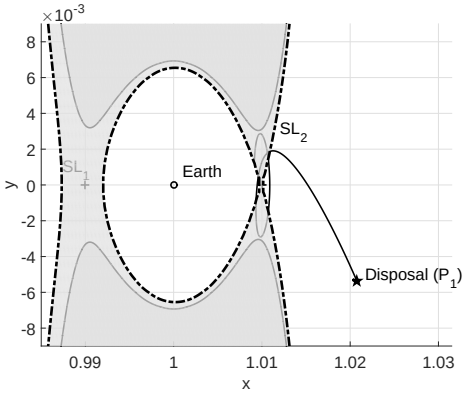

(c) Deployment of a Sun-pointing area in P_1 to close the zero-velocity curves in SL_2.

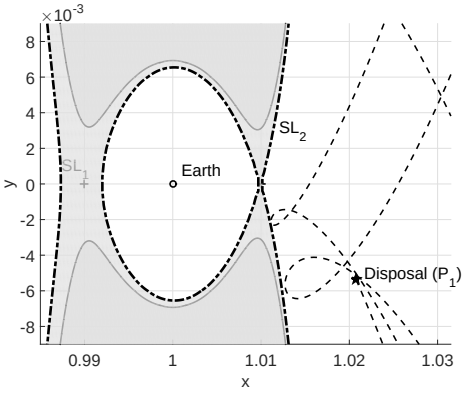

(d) Trajectory evolution after the deployment in P_1, black dashed is integrated for 63.5 years.

Figure 7.1: End-of-life disposal manoeuvre at 68.04 days since the manifold injection, with 63.5 years of trajectory evolution. This is a critical case to make the strategy more clear, i.e. before the deployment the SRP was zero.

7.2 Energy approach in the circular restricted three-body problem with solar radiation pressure

A spacecraft equipped with a deployable EOL device, can close the ZVCs at SL_2. This device is configured to be Sun-pointing ($\hat{\boldsymbol{r}} = \hat{\boldsymbol{N}}$) and auto-stabilised, so the SRP force admits a potential form as shown in Section 3.3 (DRL-101-08, 1996; Ceriotti et al., 2013).

The same formulation was analysed in two different cases:

- the first one when the effect of SRP is taken into account only after the surface deployment, and
- the second one when the effect of SRP is considered since the injection into the manifold. Then the minimum area required is computed as a delta SRP effect due to, for example, the deployment of reflective flaps from the original spacecraft sunshade configuration.

In this thesis, only the second case is discussed because including the SRP from the manifold injection influences the manifold evolution (i.e., small perturbations in the position), while the required reflective area for the disposal is very similar in the two cases. When a near-perfect reflective flap is deployed, the energy equation in Eq. (3.81) increases to:

$$E(x, y, z, \dot{x}, \dot{y}, \dot{z}, \beta_0, \Delta\beta) = \frac{1}{2}(\dot{x}^2 + \dot{y}^2 + \dot{z}^2) - V(x, y, z) + U_s(x, y, z, \beta_0 + \Delta\beta) \quad (7.1)$$

where, β_0 represents the nominal spacecraft configuration and $\Delta\beta$ the effect of the additional area. The full expression of the terms in Eq. (7.1) is rewritten such as:

$$E(\boldsymbol{x}, \beta_0, \Delta\beta) = \frac{1}{2}v^2 - \frac{1}{2}(x^2 + y^2) - (1 - \beta_0)\frac{\mu_{Sun}}{r_{Sun-p}} - \frac{\mu_{Earth}}{r_{Earth-p}} + \Delta\beta\frac{\mu_{Sun}}{r_{Sun-p}} \quad (7.2)$$

where, v is the magnitude of the spacecraft velocity $\{\dot{x}, \dot{y}, \dot{z}\}$ along the manifold (before the deployment $\beta = \beta_0$, in Eq. (C.79)). In order to find the minimum area required to close the ZVCs at SL_1 or SL_2, it is necessary to satisfy the following constraint:

$$E(\boldsymbol{x}_{SL_j}, \beta_0, \Delta\beta_{min}) = E(\boldsymbol{x}_{P_1}, \beta_0, \Delta\beta_{min}) \quad (7.3)$$

where, $\boldsymbol{x}_{SL_j} = \left\{x_{SL_j}, 0, 0, 0, 0, 0\right\}$ is the position of the collinear Lagrange point with SRP. So Eq. (3.81) can be written as:

$$\begin{aligned} \tfrac{1}{2}v_{P_1}^2 = \; & \tfrac{1}{2}(x_{P_1}^2 + y_{P_1}^2 - x_{SL_j}^2) - \mu_{Sun}(1 - \beta_0)\left[\tfrac{1}{r_{Sun-SL_j}} - \tfrac{1}{r_{Sun-P_1}}\right] \\ & -\mu_{Earth}\left[\tfrac{1}{r_{Earth-SL_j}} - \tfrac{1}{r_{Earth-P_1}}\right] + \mu_{Sun}\Delta\beta\left[\tfrac{1}{r_{Sun-SL_j}} - \tfrac{1}{r_{Sun-P_1}}\right] \end{aligned} \quad (7.4)$$

where the index "j" refers to the location (either SL_1 or SL_2) where the closure occurs. From the numerical point of view the boundaries of $\Delta\beta$ required during the optimisation are 0 and 1-β_0. Note that the expression of $\Delta\beta$ cannot be found explicitly from Eq. (7.4) since the position of the pseudo libration point is function of $\Delta\beta$ as well, see Table 3.3, thus a numerical optimisation is required. By comparing this strategy with the strategy by Olikara et al. (2015), where a Δv manoeuvre is used to close the curves, the energy is increased, as shown in Figure 7.2(b) (dashed line), rather than decreased (dashed line in Figure 7.2(a)). As previously shown in Chapter 3, this behaviour is explained by knowing that changes in the shape of the potential energy are a result of the effect of the SRP manoeuvre (light gray line in Figure 7.2(b)). Figure 7.2 is done for a value of $\mu = 0.3$ to aid visualisation, where in both cases the black straight line corresponds to the energy of the spacecraft before the disposal.

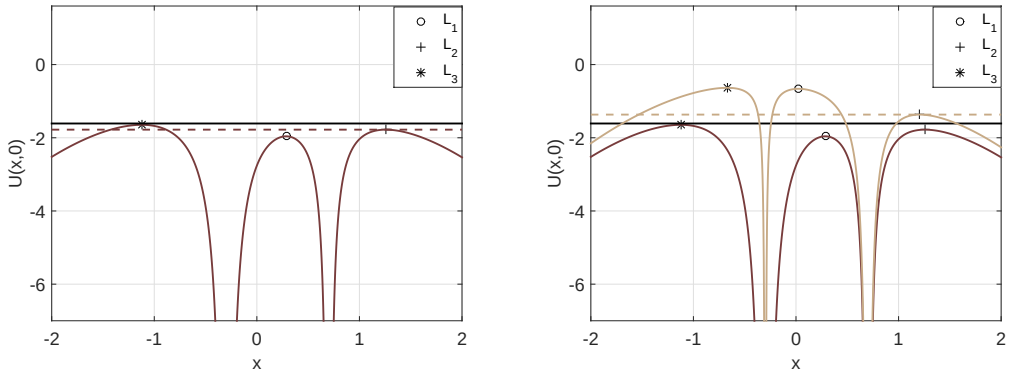

(a) Due to a traditional Δv manoeuvre, the energy of the system decreases to reach the energy of L_2 (dashed line).

(b) Due to the effect of a deployable area, the energy of the system increases to reach the energy of SL_2 (dashed line).

Figure 7.2: Comparison between the traditional Δv and SRP disposal strategies.

The constraints in the SRP strategy with respect to the traditional Δv are investigated. When using SRP, β can assume values between zero and one thus limiting the value assumed by the energy at the pseudo libration point, SL_j. Moreover, the acceleration of SRP is constrained in direction and this will restrict the location of the spacecraft's motion after the deployment.

To demonstrate this, without loss of generality, the problem was simplified to a planar motion with $\beta_0 = 0$, therefore $\beta = \beta_0 + \Delta\beta = \Delta\beta$. For simplicity, a state vector P_1 that has only one non-zero component in the x-direction and a velocity magnitude which respects the conservation of the energy is considered. In this way, it is possible to investigate when the energy intersection, in Eq. (3.81) is feasible for the zero velocity closure in SL_j.

Figure 7.3 and Figure 7.4 displays the right (i.e., coloured gray scale line) and the left (i.e., black line) hand side of Eq. (3.81) evaluated at SL_1 and SL_2, respectively for

different values of β. As it can be seen, a feasible solution that allows the ZVCs curves to be closed does not always exist. This is evident in Figure 7.3 for the solution $x = 0.65$. As already mentioned, β is constrained within 0 and 1, so the value of the increased energy is constrained (see Table 7.1). Finally, it is interesting to note that, by comparing Figure 7.3 and Figure 7.4, a lower β is required to close the ZVCs in SL_2 rather then in SL_1.

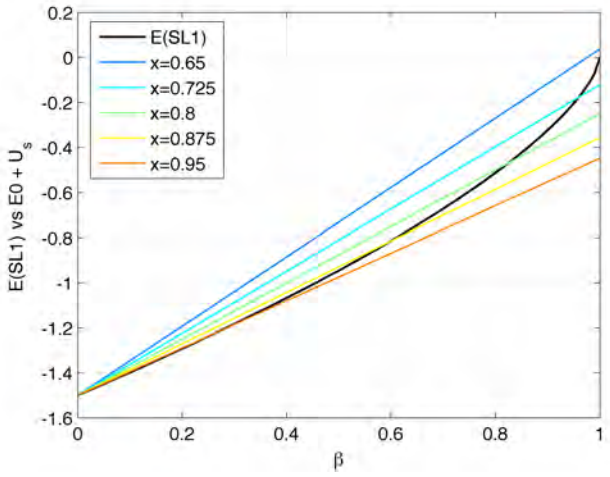

Figure 7.3: Intersection with $E(x_{SL_1}, \beta)$ and right side of Eq. (3.81) in correspondence of SL_1.

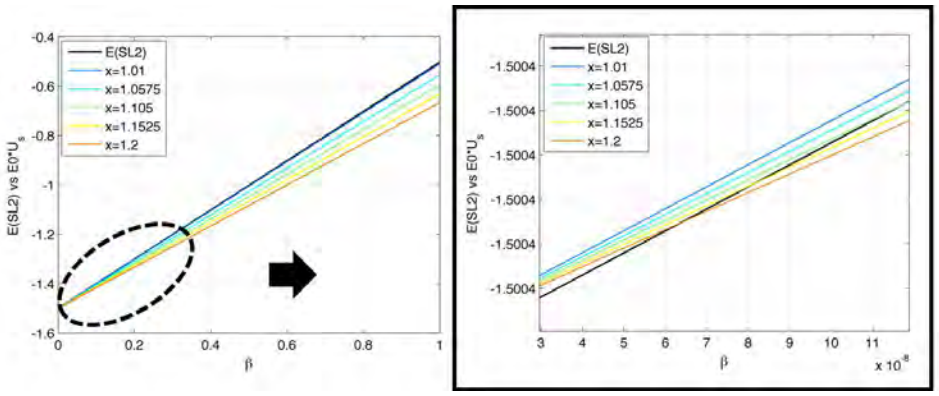

Figure 7.4: Intersection with $E(x_{SL_2}, \beta)$ and right side of Eq. (3.81) in correspondence of SL_2 with zoom in correspondence of region of intersection.

Another main difference with the traditional Δv is that, due to the constraint in the direction of the SRP acceleration, the spacecraft cannot be disposed toward the Sun by closing the curves at SL_1. This evidence was already demonstrated in Chapter 6; where, a transfer trajectory towards the Sun direction was not possible.

In the case of traditional propulsion, the ΔE is defined by Olikara et al. (2015) such as:

$$\Delta E = E_{L_2} - E = \frac{1}{2}(V_{clsr}^2 - V^2) < 0, \tag{7.5}$$

where, V^2_{clsr} is introduced in Eq (G.2) of Appendix G.1. The shape of the ZVC for closure is given by the energy of L_2. V_{clsr} can be computed at any point where the motion is permitted with the only constraint of $V^2_{clsr} > 0$ (no point inside the forbidden region). In case of SRP, there is less freedom in the selection of the point since $U_s > 0$ is the constraint in ΔE such as:

$$\Delta E = E_{SL_2} - E = U_s; \tag{7.6}$$

where, E_{SL_2} is the energy of SL_2, E is the energy of the spacecraft before the deployment as in Eq. (7.3) for $\beta = \beta_0$ and U_s is defined as in Eq. (3.26) by setting $\beta = \Delta\beta$.

Indeed, U_s is the potential of SRP forces which are constrained in direction and it is function of β that assumes values within 0 and 1. Thus, $U_s^{min}(\beta = 0) < U_s(\beta) < U_s^{max}(\beta = 1)$ (where $U_s^{min}(\beta = 0) = 0$), so $0 < U_s(\beta) < U_s^{max}(\beta = 1)$. This constraint obliges the spacecraft to be always at the right-hand side of the maximum coordinate of SL_2 that occurs when $\beta = 1$. The higher is β, the more the region around the Sun and the Earth decreases since SL_1 and SL_3 collapse in the centre of mass (circa the Sun) and SL_2 gets very close to the Earth, as shown in Figure 3.6(b).

In Figure 7.5, a comparison with SRP and Δv manoeuvres for the closure of the ZVCs is shown. A point along the LPO is selected for the EOL manoeuvre (black star) which is on the left-hand side of L_2. As one can see, when SRP is used the Lagrangian point moves such that after the closure the spacecraft is disposed on a graveyard orbit around the Sun, Figure 7.5(a)-7.5(b), while with traditional Δv the disposal is towards the Sun Figure 7.5(c)-7.5(d).

This can be verified also by looking at Eq. (7.4), which, in the case considered, is simplified as:

$$\begin{aligned} \tfrac{1}{2}v^2_{P_1} = \; & \tfrac{1}{2}(x^2_{P_1} + y^2_{P_1} - x^2_{SL_j}) - \mu_{Sun}(1-\beta)\left[\frac{1}{r_{Sun-SL_j}} - \frac{1}{r_{Sun-P_1}}\right] \\ & -\mu_{Earth}\left[\frac{1}{r_{Earth-SL_j}} - \frac{1}{r_{Earth-P_1}}\right], \end{aligned} \tag{7.7}$$

when, $\beta_0 = 0$. In order to achieve the closure at SL_j, it is necessary to satisfy Eq. (7.7). The left side of Eq. (7.7) contains the squared velocity for a generic point P_1, which is a positive term. Therefore, in order to demonstrate that with SRP the closure towards the Sun is not permitted, the sign of Eq. (7.7) is studied to ensure that its left-hand side is positive (that means $v^2_{P_1} > 0$). In this thesis, only the case in which P_1 is between the Earth and SL_2 region is shown (see Figure 7.6); however, it can be easily demonstrated that the same results can be achieved if P_1 is one of the gray points in Figure 7.6.

For the case shown in Figure 7.6, the condition of $V^2_{P_1} > 0$ can be guaranteed only if P_1 stays at the right-hand side of the Lagrangian point at which the curve is closed (for example SL_1). This can be easily demonstrated for $\beta = 1$ when the gravitational

β	x_{L_1}	x_{L_2}
0	0.989985982354727	1.010075200010617
1	$-0.105864912811615 \cdot 10^{-4}$	1.001739126300185

Table 7.1: Positions of L_1 and L_2 as a function of SRP.

effect of the Sun is counteracted by the SRP: the square of the velocity can be positive only if the point is on the right-hand side of the Libration point. This result can be extended for cases where β is less than one by studying the sign of each term in Eq. (7.7) accordingly. In conclusion, to ensure that $V_{P_1}^2 > 0$, the key point is that P_1 should stay at the right side of SL_2. This condition is necessary, but not sufficient to find β that closes the ZVCs since, as already shown, there are some cases where a solution does not exist, for instance when the β required is higher than 1, as shown in Figures 7.3-7.4. Finally, it is interesting to note that, when the velocity in P_1 is zero, P_1 is coincident to SL_j.

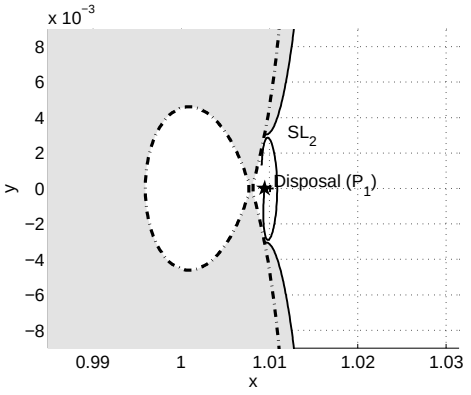

(a) EOL disposal with SRP. The β required is 0.02499.

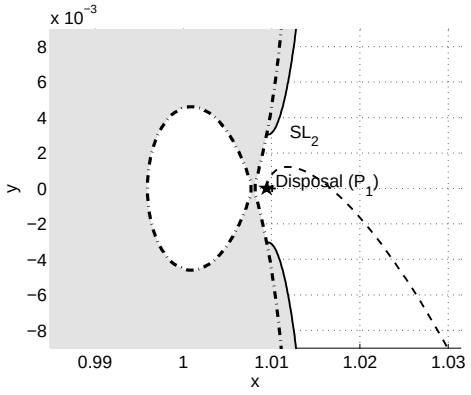

(b) After the closure the spacecraft is at the right-hand side of SL_2.

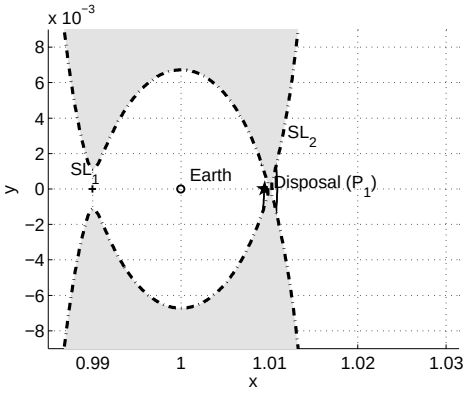

(c) EOL disposal with ΔV manoeuvre.

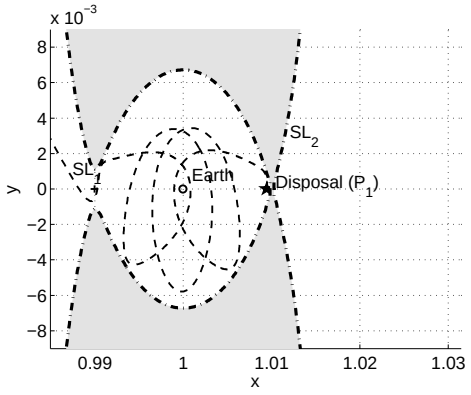

(d) After the closure the spacecraft is at the left-hand side of L_2.

Figure 7.5: Comparison of SRP and ΔV strategies when the point of disposal is at the left-hand side of the Lagrangian point L_2.

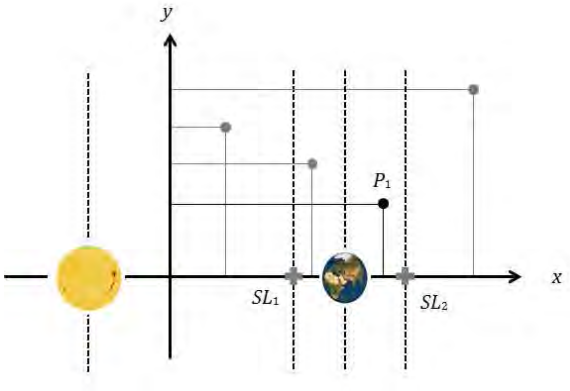

Figure 7.6: Reference system for studying the clousure in SL_j.

7.2.1 Solar radiation pressure equivalent Δv

The SRP equivalent Δv_{eq} quantifies how much theoretical Δv would be needed for a traditional propulsion system to augment the energy of the spacecraft achieved by a reflective SRP manoeuvre. Note that, this Δv_{eq} cannot be effectively achieved by a propulsion system since the effect of SRP also changes the shape of the potential, which is not possible with a traditional propulsion-based approach. $E_0 = E(x_0, y_0, z_0, \dot{x}_0, \dot{y}_0, \dot{z}_0, \beta_0)$ (see Eq. (7.3)) is set as the initial energy of the system before the deployment and E_{SL_2} is set as the energy of the system after the deployment (Eq. (7.2) evaluated at SL_2). Now let's make the hypothesis that E_{SL_2} is achieved with a traditional propulsion system; therefore, the energy is written as in Eq. (7.2) by setting $\Delta\beta = 0$ and find V_{clsr}. V_{clsr} is the velocity on the manifold after a hypothetical manoeuvre is given and the equivalent Δv_{eq} can be derived as:

$$\Delta v_{eq} = V_{clsr} - V = \sqrt{V^2 + 2\Delta\beta \frac{\mu_{Sun}}{r_{Sun-p}}} - V. \tag{7.8}$$

This equation will be applied in the next section in order to compare the proposed strategy with the one of Olikara et al. (2015) in term of Δv budget. The traditional Δv equation with the effect of SRP is reported in Appendix G.1 in Eq. (G.2)-(G.3) derived by Olikara et al. (2015).

7.2.2 Disposal constraints

When disposing a spacecraft into a graveyard orbit around the Sun-(Earth+Moon) system, it is important to identify safe regions to avoid the spacecraft from returning to the vicinity of the Earth, threatening its artificial satellites. This is particularly the case for spacecraft around L_1 (i.e., SOHO spacecraft); where, a departing Δv is given towards L_2 to achieve the condition of the ZVCs closure as SL_2 after an SRP manoeuvre is provided along the LPO's unstable manifold. This is done because it was demonstrated that the

spacecraft cannot be bounded with this strategy in the region on the left of SL_1. For this reason, the deployment is done only beyond L_2 that means:

$$x > x_{L_2}. \tag{7.9}$$

In the case of a spacecraft at L_1, there are two more checks to take into account. One related, to the Earth's safe region, where all trajectories that cross a protected sphere around the Earth are discarded through:

$$d_{Earth-p} \geq \frac{R}{AU}. \tag{7.10}$$

In Eq. (7.10), AU is one astronomical unit, R was set equal to 60,000 km (greater than the GEO distance) and $d_{Earth-p}$ is the distance Earth-Spacecraft defined such as:

$$d_{Earth-p} = ||\boldsymbol{r}_{Earth} - \boldsymbol{r}_p||. \tag{7.11}$$

In Eq. (7.11), $\boldsymbol{r}_{Earth}$ and $\boldsymbol{r}_p$ are the distances of the Earth and the spacecraft from the centre of mass. Secondly, among the trajectories that safely pass close to the Earth, some of them come back after few revolutions to L_1 towards the Sun; also, in this case, the trajectories are discarded for the disposal and the condition in Eq. (7.9) holds.

7.3 Mission like scenarios

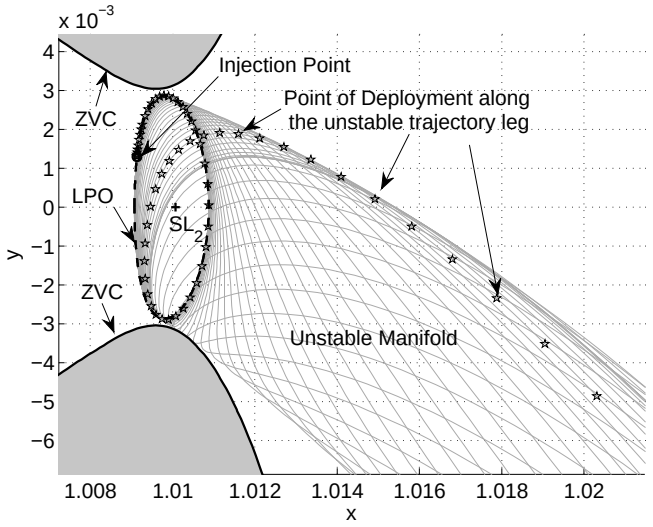

Figure 7.7: The disposal strategy scheme in the CR3BP-SRP: LPO (dashed line), unstable manifold (gray trajectories), injection point (black point), point of deployment (star) and SL_2 (plus symbol).

In this section, three ESA mission like scenarios are investigated: Gaia, Herschel and SOHO. The initial spacecraft parameters in terms of: initial deployable area (A_0), dry mass (m_{dry}), initial area-to-mass ratio (A_0/m_{dry}) and its correspondent lightness parameter (β_0) are shown in Table 7.2.

Figure 7.7 shows a qualitative representation of the disposal strategy designed in the CR3BP-SRP used for the numerical computation. A number of trajectories which belong to the unstable tube are selected (grey trajectories in Figure 7.7) with their initial condition (black point in Figure 7.7) close to the LPO (dashed black line). Then, to assess the deployable area requirements, a series of points along each natural trajectory legs are selected (black stars), where a Sun-pointing reflective surface can be deployed. Deploying a reflective structure in one of these points allows the closure of the ZVCs at SL_2 as shown in Figure 7.1.

Gaia was placed in a Lissajous orbit around L_2 and its mission objective is to provide a 3D map of our galaxy (Hechler and Cobos, 2002). Gaia's mission overview is given in Appendix B.3.3. For the EOL analysis, several trajectories were selected starting along the Lissajous orbit, from 5.59 to 6.1 years since the start of the mission. Each unstable trajectory is obtained by integrating forward in time over six years. Figure 7.8(a) shows the area-to-mass requirement as a function of the curvilinear coordinate on the LPO (y-axis and black point in Figure 7.7) and the time along the trajectory leg (x-axis and black stars in Figure 7.7). The time step selected along the trajectory leg (between two

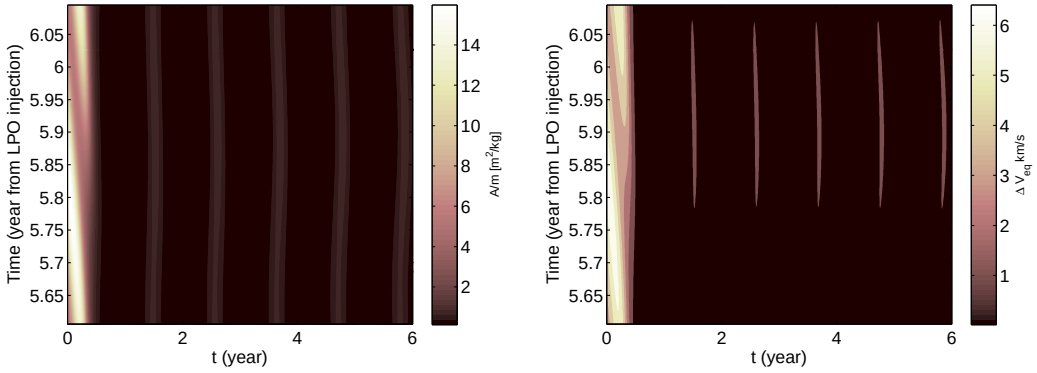

(a) Gaia area-to-mass ratio for disposal within six years.

(b) Gaia Δv_{eq} for the closure in SL_2 within six years.

Figure 7.8: Gaia area-to-mass ratio and equivalent Δv_{eq}.

black stars in Figure 7.7) is 0.05 in non-dimensional units, which, corresponds to 2.89 days.

Figure 7.8(b) shows the magnitude of the Δv_{eq} due to the effect of the increasing energy of the system after the deployment. The spacecraft-Sun distance and the initial solar radiation pressure acceleration of Gaia are represented in Figure 7.9 as a function of the curvilinear coordinate on the Lissajous during six years of disposal. This also shows that the peaks in the area-to-mass ratio required are due to the fact that, along one trajectory, the spacecraft motion oscillates around the ZVCs.

Finally, it is interesting to compare the equivalent Δv_{eq}, Figure 7.8(b) with the traditional Δv (Olikara et al. (2015) and Colombo et al. (2014b)) in Figure 7.10. In the case of using a traditional propulsion system, the energy is decreased rather than increased by giving a Δv to close the curve as said in Section 7.2. For this traditional case it is not always possible to perform the manoeuvre close to the departing epoch from the initial orbit as the white area in Figure 7.10 is representative of the forbidden region; where the manoeuvre can not be performed. This does not happen when exploiting SRP since the shape of the potential is changing and the velocity of the spacecraft does not change at the moment of the deployment.

Herschel was launched in 2009 (Bauske, 2009) and its mission objective was to study the stars and galaxy formations. Herschel was placed in a halo orbit around L_2 with a period of 180 days (see Appendix B.3.1). To study the disposal of Herschel, 40 trajectories equally distributed along the halo were selected in this work. The time step along the halo was set to 4.6 days; where the initial condition considered along the halo is on the side further from the Sun. Each single unstable trajectory is obtained by integrating forward in time for six years. The time step selected along the trajectory leg is 0.05 in non-dimension units, which corresponds to 2.89 days. Figure 7.11(a) represents the required area-to-mass ratio at the EOL. Compared with the Gaia's spacecraft, the

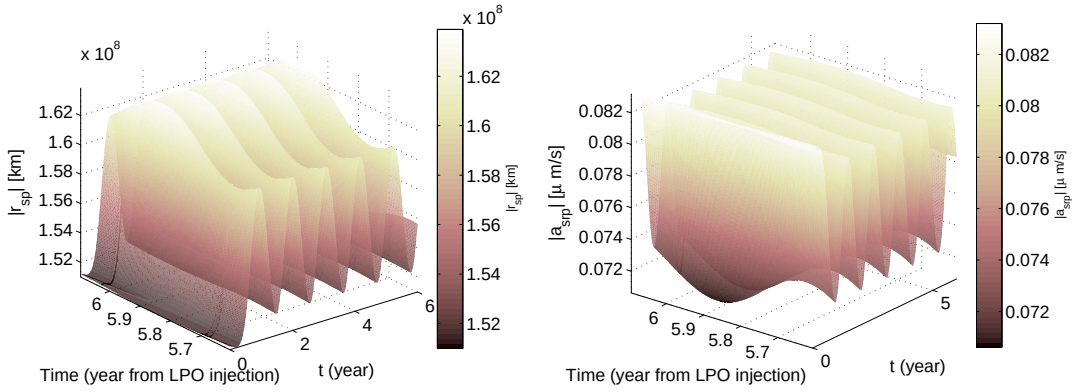

(a) Distance from the Sun.

(b) SRP acceleration.

Figure 7.9: Distance from the Sun and SRP acceleration for Gaia $A/M_{dry} = 0.059$ m^2/kg.

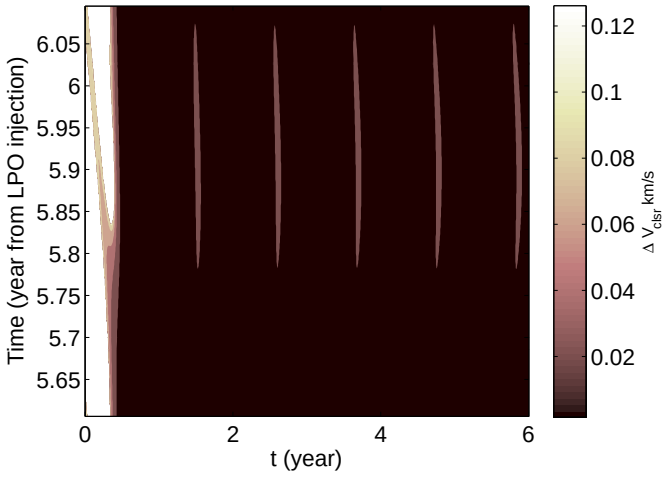

Figure 7.10: Gaia Δv for the closure in L_2 within six years with traditional propulsion, where the initial β_0 of Gaia is included in the dynamics.

maximum area required is higher since Herschel has a higher total mass than Gaia. Consequently, the trend in the equivalent Δv_{eq} is also higher (see Figure 7.11(b)).

SOHO was lunched in 1995 and it was placed in a halo orbit with a period of 178 days around L_1 as shown in Appendix B.3.2; therefore, the disposal in SL_2 should be done more carefully than in the case of Herschel and Gaia as SOHO spacecraft is in a orbit around L_1. After the injection from the halo to the unstable manifold towards the outer system, the disposal was investigated up to 6 years from the moment of injection. In the case of SOHO, it is necessary to select carefully the trajectories crossing the region of the Earth as outlined in Section 7.2.2. Figure 7.13(a) shows, as for Herschel and Gaia, the trend in the area-to-mass ratio required at the EOL.

Regarding the results, SOHO is a satellite with a similar mass magnitude as Gaia. Since SOHO is placed in a halo around L_1, it is interesting to note that the disposal is not

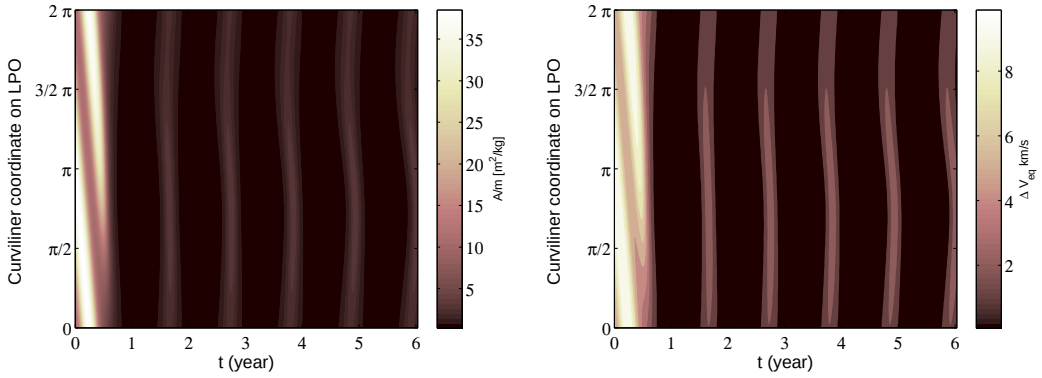

(a) Herschel area-to-mass ratio for disposal within six years.

(b) Herschel Δv_{eq} for the closure in SL_2 within six years.

Figure 7.11: Herschel area-to-mass ratio and equivalent Δv_{eq}.

S/C	$\mathbf{A_o}$	$\mathbf{m_{dry}}$	$\mathbf{A_o/m_{dry}}$	$\boldsymbol{\beta_o}$ **(@** $\mathbf{A_o/m_{dry}}$**)**
Gaia	69	1392	0.059	$8.98 \cdot 10^{-5}$
Herschel	16	3144	0.0051	$7.803 \cdot 10^{-6}$
SOHO	22	1602	0.021	$3.2 \cdot 10^{-5}$

Table 7.2: Initial spacecraft parameters (Colombo et al., 2014b).

always possible when compared with Herschel and Gaia cases. Indeed, it is possible to see that the white strips correspond to two class of trajectories: the one that goes bellow 60,000 km from Earth and the one that never passes by the gateway at L_2[2]. Moreover, the coloured stripes show when the spacecraft crosses the L_2 gateway; therefore, some unstable trajectories can spend several years crossing the Earth region and then reaching L_2. For example, trajectories that cross L_2 after two years are not fast and efficient disposal solution as they increase the costs of missions operations. The range of values in the area-to-mass ratio and the Δv_{eq} for SOHO are an average of the Herschel and Gaia cases (see Figure 7.12).

As already proved, when exploiting SRP it is not possible to dispose of the spacecraft towards the Sun as for the Δv manoeuvre. However, Van Der Weg et al. in Colombo et al. (2014b) presented a comparison in the Δv required for the SOHO mission for a disposal towards the Sun and towards the outer part of the solar system, after L_2. It can be seen that the order of magnitude in the required Δv is similar for both the disposal options. The main difference is in the additional operational cost of transferring from L_1 to L_2 that it is the only option when using SRP.

[2]After several revolutions around the Earth, this trajectory goes back towards the Sun.

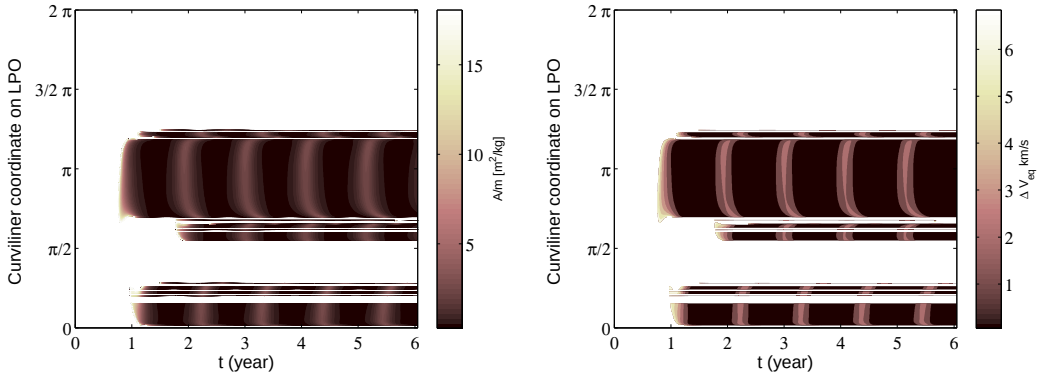

(a) SOHO area-to-mass ratio for disposal within six years.

(b) SOHO Δv_{eq} for the closure in SL_2 within six years.

Figure 7.12: SOHO area-to-mass ratio and equivalent Δv_{eq}.

7.3.1 Deployable structure solutions

The minimum required delta area in the CR3BP-SRP is a deployed square area with a span of around 28 m for Herschel, an equivalent 21 m-span for SOHO and 11 m-span for Gaia as shown in Table 7.3, where the range in the area-to-mass ratio presented in Figures 7.8(a), 7.11(a) and 7.13(a) are also shown in the table. An additional EOL device for Herschel mission cannot be easily achieved with additional flaps since their current sunshade configuration in term of shape does not allow the deployment of flaps. SOHO can potentially support additional solar panel flaps; however, the area provided by the solar panel is too small to support 20-m span area (i.e., solar concentrator), while Gaia spacecraft configuration can potentially enhance EOL devices.

Note that JAXA has recently demonstrated the capability to deploy a 20 m-span sail with the Ikaros mission (Tsuda et al., 2013). Therefore, the disposal of Herschel seems to be the most technologically challenging to achieve with a deployed area due to the required 28 m span. However, spacecraft with the same characteristics in terms of configurations and masses such as Herschel and SOHO, would need an specifically designed EOL stabilising deployable cone sail like the one used for attitude control (i.e., GOES mission (DRL-101-08, 1996)) or the pyramid sail proposed by Ceriotti et al. (2013) in order to achieve passive attitude stabilisation.

In the cases studied, the EOL change in area is on the order of a 20 m-span square sail which will cover the spacecraft bus when deployed. Thus, a different configuration should be investigated to accommodate the area required (for example, in case the spacecraft's sunshade is covered by the EOL device, the EOL area should be bigger enough to include the shaded sunshade area).

Table 7.3 shows the minimum deployable area required for the end-of-life. An example of self-stabilised structure are cone-sail. Cone-sail have a kapton substrate (7.1 g/m^2

of density) and an aluminium surface coating of 1.35 g/m^2 density. The correspondent weight for the cone-sail is 1.5879 kg for Gaia spacecraft, 7.066 kg for Herschel and 3.79 kg for the case of SOHO spacecraft. The final weight of the cone-sail depends on the height of the cone which is a parameter that needs to be determined by considering the torques effect on to the satellite. For example, Gaia spacecraft has a circular sunshade of radius 4.68 m. By choosing a cone-sail with a base of radius 4.68 m, the heigh of the cone is given by:

$$h_c = \frac{1}{r}\sqrt{\frac{A_{min}^2}{\pi^2} - r^4}, \tag{7.12}$$

which correspond to a cone-sail heigh of 11.89 m for Gaia, 56.68 m for Herschel and 30.147 m for SOHO. Gaia spacecraft is the best solution for the LPO class of satellites studied. The heigh determine the weight of the boom to support the cone-sail with density between 20-70 g/m that for Gaia spacecraft correspond to an additional mass of 0.24-0.8 kg. Figure 7.13(a) shows the configuration of the EOL disposal cone-sail for Gaia spacecraft. Note that in this mass budget analysis, it was supposed that the on-board reflective deployable structures of the satellite such as sunshade and solar array do not contribute to the initial area of the end-of-life deployable device. However, the deployment of flaps could potentially reduce the area needed for passively stabilising the spacecraft after the end-of-life manoeuvre.

Importantly, this study shows that, the EOL phase should be taken into account as part of the mission design; in this way, it would be possible to include additional deployable areas which would expand on the existing projected area of the satellite; where the final shape configuration should be such that it guarantees passive attitude stabilisation. An example of alternative design for a class of spacecraft like Gaia would be to consider the circular sunshade of Gaia's spacecraft as the minor base of a truncated cone of a self-stabilised end of life device. Thus, A_0 is the area of the sunshade (minor base) and correspond to 69 m^2 (4.68 m radius r). The major base of the truncated cone is supposed to have a radius $R = 1.5 \cdot r$ that correspond to 7.02 m. The heigh of the truncated cone cane be calculated as:

$$h_{tc} = \sqrt{\frac{\Delta A_{min}^2}{\pi^2 (R+r)^2} - (R-r)^2}, \tag{7.13}$$

which correspond to 2.23 m. In this case, the mass of the cone-sail lateral surface (yellow area in Figure 7.13(b)) is 1.005 kg. The major base of the truncated cone could be potentially kept in shape by a toroidal support ring as for reflectors and antennas. A boom of perimeter 44.107 m is here required with correspondent mass included between 0.88-3.08 kg. This solution is lighter than the previous option as an additional boom (external boom in Figure 7.13(a)) between the cone sail and the spacecraft should be considered for the first configuration. In the second configuration, the heigh of the end-of-life device is just 2.23 m compared with the 11.89 m required for the first configuration. Note that Gaia spacecraft heigh is 2.3 m while the heigh of the EOL device proposed in Figure 7.13(b) is 2.23 m. In conclusion, the design of sunshade and solar array

S/C	A/m [m²/kg]	β(@A/m)	A_{min} [m²]	ΔA_{min} [m²] (m-span[3])
Gaia	0.135-15.98	$2.1 \cdot 10^{-4}$-0.02446	187.92	118.92 (10.9)
Herschel	0.266-38.52	$4.06 \cdot 10^{-4}$-0.059	836.304	820.304 (28.64)
SOHO	0.28-18.08	$4.35 \cdot 10^{-4}$-0.028	448.56	426.56 (20.65)

Table 7.3: Required reflective area and lightness parameter.

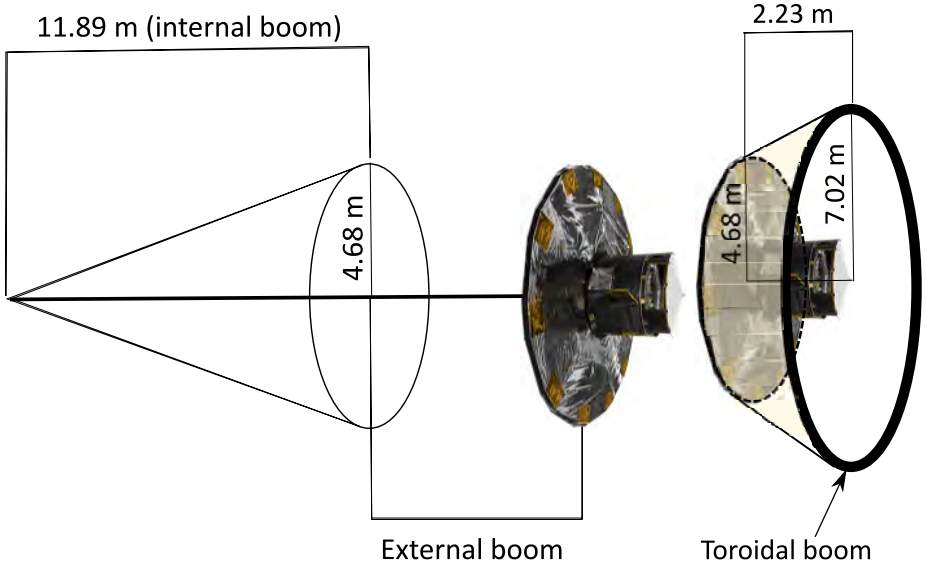

(a) End-of-life cone-sail: first configuration.

(b) End-of-life device: second configuration.

Figure 7.13: End-of-life structural concept for Gaia spacecraft.

for LPO spacecraft should take into account of deployable mechanism and structural configurations to enhance the effect of SRP at the end-of-life.

Olikara et al. (2015) proposed a similar EOL option by using a traditional impulsive manoeuvre to perform the closure of the ZVCs. Figure 7.10 shows the requirement in Δv_{clsr} for Gaia spacecraft. The required range of Δv_{clsr} along the manifold is between 10-120 m/s. As for the case of EOL devices, the total initial mass of the spacecraft is 1000 kg where the finial total mass after the Δv_{clsr} manoeuvre is given through the Tsiolkovsky equation:

$$m_f = m_0 e^{-\frac{\Delta v_{clsr}}{I_{sp} g_0}}. \tag{7.14}$$

In Eq. (7.14), m_0 is the initial wet mass of the spacecraft before the manoeuvre (1000 kg), I_{sp} is the specific impulse of the engine and for Gaia spacecraft correspond to 291 s, g_0 is the gravity acceleration and m_f is the final wet mass of the spacecraft. The mass of propellant consumed to perform the Δv_{clsr} is given by:

$$m_p = m_0 - m_f, \tag{7.15}$$

[3]E.g., squared flap or additional EOL device (not to scale).

that correspond to a mass of propellant between 3.6223-42.612 kg. The second configuration presented in Figure 7.13(b) for the EOL device of Gaia spacecraft requires a mass between 1.885-4.085 kg. This evidence shown that if the EOL device concept make use of pre-existing deployable reflective areas on the spacecraft, such as sunshade and solar array, the mass required for the EOL device is comparable to the mass of propellant required for the traditional propulsion. It is possible to conclude that next generation of LPO satellite that make use of SRP propulsion can take advantage of the EOL technique presented in this chapter, where the additional mass required for the EOL device can be further reduce in the design phase of deployable reflective structures. Compared with traditional propulsion technique, the EOL devices are a new developing technology, while impulsive propulsion represents a highly reliable space system. However, current mission do not allocate a Δv for EOL disposal and space agencies have to select an EOL option based on the left propellant at the end of the operational mission. Thus, also in case of traditional propulsion, the EOL manoeuvre should be taken into account in the mass budget at the design phase of LPO mission.

7.3.2 Discussion

The main features of the disposal strategy by means of solar radiation pressure for the ZVCs closure are:

- The device should be constrained to be Sun-pointing; thus, a self-stabilised deployable structure is required;
- The disposal using SRP can be achieved to close the ZVCs at SL_2; while, the condition of closing the curves at SL_1 and dispose the spacecraft towards the Sun can not be achieved;
- It should be also taken into account that, to inject the spacecraft onto the unstable manifold a small Δv manoeuvre is required for current mission in LPO;
- Since the acceleration of SRP is a function of the inverse square of the Sun-spacecraft distance, the minimum required area for the disposal is lower if the deployment is done far away from the Sun. Thus, SL_2 is much closer to L_2. Therefore, it is possible to better protect the L_2 region. Note that, half of the nominal halo orbit is also protected from spacecraft impact hazards once the curves are closed because it is at the far side of L_2 and SL_2 with the Sun.
- In the case where the energy associated with the initial spacecraft orbit is higher, a higher area is required to perform the closure of the ZVCs at the same distance from the Sun as already proved for traditional propulsion by Olikara et al. (2015).

The effect of the Earth's orbit eccentricity on to EOL disposal strategy is extended for the elliptic restricted three-body problem dynamics with SRP to verify the robustness of the SRP EOL strategy for LPO missions.

7.4 End-of-life disposal through solar radiation pressure: energy approach in the elliptic restricted-three body problem

The proposed disposal strategy exploits the effect of solar radiation pressure to bound the spacecraft's motion in a safely graveyard orbit around the Sun. The design of the deployed area was made without taking into account of the effect of perturbations. The effect of perturbations as the Earth's orbit eccentricity can affect the energy of the spacecraft. Thus, the energy variation from the value used in the manoeuvre design cannot guarantee a safely disposal as the bottleneck region can potentially reopen at L_2.

An energy approach in the ER3BP-SRP is now investigated that builds on the work previously developed for the CR3BP-SRP. Chapter 4 presents the theory in the ER3BP-SRP. In particular, the equations of motion, the energy and the approximation of ZVCs were previously introduced.

When taking into account the effect of the Earth's orbit eccentricity, a similar approach to the CR3BP-SRP is adopted. When a near-perfect reflective surface is deployed, the energy for the elliptic dynamics in Eq. (4.23) increases to:

$$E(f_0, \boldsymbol{x}(f_0), f, \beta_0, \Delta\beta) = \frac{1}{2}v^2 - \Omega(\beta_0, \Delta\beta) + I(\beta_0, \Delta\beta) \tag{7.16}$$

where, v is the magnitude of the spacecraft's velocity $\{x', y', z'\}$ in pulsating coordinates along the manifolds (before the deployment $\beta = \beta_0$, in Eq. (7.16)). In order to find the minimum area required to close the ZVCs at SL_2, it is necessary to satisfy the constraint in Eq. (7.3) for the ER3BP-SRP dynamics.

7.4.1 Disposal constraints for the elliptic restricted-three body problem disposal

As for the CR3BP-SRP dynamics, to identify the possible solution region in the ER3BP-SRP, it is convenient to look at the sign of the squared velocity of the spacecraft after the area has been deployed since an exact representation of the ZVCs is not known,

$$V_{new}^2 = 2\left[E(\boldsymbol{x}_{SL_2}, \beta_0, \Delta\beta_{min}) + 2\Omega - 2I\right]. \tag{7.17}$$

The solution obtained after the optimisation is feasible if the following inequality condition in the spacecraft's velocity is preserved:

$$V_{new}^2 > 0. \tag{7.18}$$

A further condition is added so that, long transfer trajectories are discarded if they are not pass through the L_2 gate within the disposal time of six months. This can be guaranteed by checking that the x component of the spacecraft position (black stars, Figure 7.7) is higher than the minimum distance from the LPO (point along the dashed line in Figure 7.7 with minimum distance from the barycentre) such as:

$$x(for\ any\ time\ within\ 6\ months) > min(x_{LPO}). \tag{7.19}$$

Note that in this work, the passage of the spacecraft in vicinity of L_2 after the insertion into an heliocentric graveyard orbit is defined as the Close Approach (CA).

7.4.2 Numerical implementation

The condition in Eq. (7.3) for the ER3BP-SRP dynamics was further simplified to decrease the time required for the computation of the lightness parameter. Considering a true anomaly where the deployment occurs, f_d, the integral I has a discontinuity due to the effect of the added $\Delta\beta$ when $f \geq f_{d^+}$. Thus, the integral I, across the deployment, corresponds to a step function. The energy of the spacecraft right after the deployment, f_{d^+}, is:

$$E(f_{d^+}) = \frac{1}{2}V(f_{d^+})^2 - \Omega(f_{d^+}) + \int_{f_0}^{f_d} \frac{e\sin f}{(1+e\cos f)^2} W_d df + \int_{f_d}^{f_{d^+}} \frac{e\sin f}{(1+e\cos f)^2} W_{d^+} df; \tag{7.20}$$

where $\Omega(f_{d^+})$ is:

$$\begin{aligned} \Omega(f_{d^+}) = \ & \tfrac{1}{(1+e\cos f_{d^+})} \left[\tfrac{1}{2}\left(x(f_{d^+})^2 + y(f_{d^+})^2 - e\cdot z(f_{d^+})^2\cos f_{d^+}\right) + \right. \\ & \left. [1-(\beta_0+\Delta\beta)]\, \tfrac{\mu_{Sun}}{r_{Sun-P(f_{d^+})}} + \tfrac{\mu_{Earth}}{r_{Earth-P(f_{d^+})}}\right]. \end{aligned} \tag{7.21}$$

while, W_d before and W_{d^+} after the deployment are respectively:

$$W_d = \frac{1}{2}\left[x(\tilde{f})^2 + y(\tilde{f})^2 + z(\tilde{f})^2\right] + (1-\beta_0)\frac{\mu_{Sun}}{r(\tilde{f})_{Sun-P}} + \frac{\mu_{Earth}}{r(\tilde{f})_{Earth-P}}, \tag{7.22}$$

and

$$W_{d^+} = \frac{1}{2}\left[x(\tilde{f})^2 + y(\tilde{f})^2 + z(\tilde{f})^2\right] + [1-(\beta_0+\Delta\beta)]\frac{\mu_{Sun}}{r(\tilde{f})_{Sun-P}} + \frac{\mu_{Earth}}{r(\tilde{f})_{Earth-P}}. \tag{7.23}$$

Note that if the distance between f_d and f_2 (point after the deployment) is infinitesimal, f_2 tends to f_{d^+}, the second integral in Eq. (7.20) turns to zero and the energy in Eq. (7.20) is approximated to:

$$E(f_{d^+}) = \frac{1}{2}V(f_{d^+})^2 - \Omega(f_{d^+}) + \int_{f_0}^{f_d} \frac{e\sin f}{(1+e\cos f)^2} W_d df. \tag{7.24}$$

The important remark here is that the integral does not depend on $\Delta\beta$ so it effectively becomes a constant value for the optimiser. The same consideration can be done for the pseudo libration point energy:

$$\begin{aligned} E(\boldsymbol{x}_{SL_2}(f_{d^+})) \quad &= -\Omega(\boldsymbol{x}_{SL_2}(f_{d^+})) + \textstyle\int_{f_0}^{f_d} \frac{e\sin\tilde{f}}{(1+e\cos\tilde{f})^2} W(\boldsymbol{x}_{L_2}(f_d)) d\tilde{f} + \\ &\textstyle\int_{f_d}^{f_{d^+}} \frac{e\sin\tilde{f}}{(1+e\cos\tilde{f})^2} W(\boldsymbol{x}_{SL_2}(f_{d^+})) d\tilde{f}. \end{aligned} \tag{7.25}$$

where,

$$W(\boldsymbol{x}_{L_2}(f_d)) = \frac{1}{2}x_{L_2}^2 + (1-\beta_0)\frac{\mu_{Sun}}{r_{Sun-L_2}} + \frac{\mu_{Earth}}{r_{Earth-L_2}} \tag{7.26}$$

and

$$W(\boldsymbol{x}_{SL_2}(f_{d^+})) = \frac{1}{2}x_{SL_2}^2 + [1-(\beta_0+\Delta\beta)]\frac{\mu_{Sun}}{r_{Sun-SL_2}} + \frac{\mu_{Earth}}{r_{Earth-SL_2}}. \tag{7.27}$$

Finally, Eq. (7.25) can be further simplified as:

$$E(\boldsymbol{x}_{SL_2}(f_{d^+})) = \frac{1}{1+e\cos f_d}\left[W(\boldsymbol{x}_{L_2}(f_d)) - W(\boldsymbol{x}_{SL_2}(f_{d^+}))\right] - \frac{W(\boldsymbol{x}_{L_2}(f_d))}{1+e\cos f_0}. \tag{7.28}$$

The condition of deployment in Eq. (3.81) is numerically implemented as:

$$E(\boldsymbol{x}_{SL_2}(f_{d^+})) = E(f_{d^+}). \tag{7.29}$$

The main advantage of this formulation with respect to Eq. (7.3) is that the integral, I, does not depend of $\Delta\beta$ therefore this avoid the added computational time required if β was inside the integral.

7.4.3 Robustness of the surface of minimum energy for the end-of-life study: application to the Gaia mission

Due to the non-autonomous nature of the ER3BP-SRP, an approximation of the integral, I, is needed. In Chapter 4, a comparison of different ZVCs approximations was carried out by also showing a lack in the literature; where a good understanding of the ZVCs for the ER3BP-SRP and their relation with the spacecraft's dynamics was missing. Through this comparison, modified version of the surface of minimum energy by Luk'yanov (2005) was chosen to approximate the ZVCs.

The aim of this section is to demonstrate that a closure at L_2 guarantees a safe disposal also under the effect of the Earth's orbit eccentricity. Thus, this section investigates the robustness of the surface of minimum energy and how to link the SME to the behaviour of the spacecraft. Four trajectories leaving the LPO when the Earth+Moon are at f_0 = 0°, 90°, 180° and 270° are selected to verify when the representation of the ZVCs by Luk'yanov (2005) is robust. Note that the leaving points of the LPO are a function of f_0 (black point, Figure 7.7). The goal here is to link the behaviour along the spacecraft trajectories to the approximated ZVCs. The energy along the trajectory is conserved and constant when f_0 is fixed. This is shown in Figure 7.14, where the energies at L_2 (black coloured lines) and of the spacecraft (grey coloured lines) are shown for the ER3BP (straight line) and CR3BP (dashed line) respectively. As it is more evident for $f_0 = 90°$, Figure 7.14(b), and for $f_0 = 270°$, Figure 7.14(d), the energy of the spacecraft is above the energy at the libration point L_2 for both the CR3BP and ER3BP. This suggests that the ZVCs are open at L_2 in both cases. Thus, a manoeuvre is required when disposing the spacecraft into a graveyard orbit around the Sun to close the gateway at L_2.

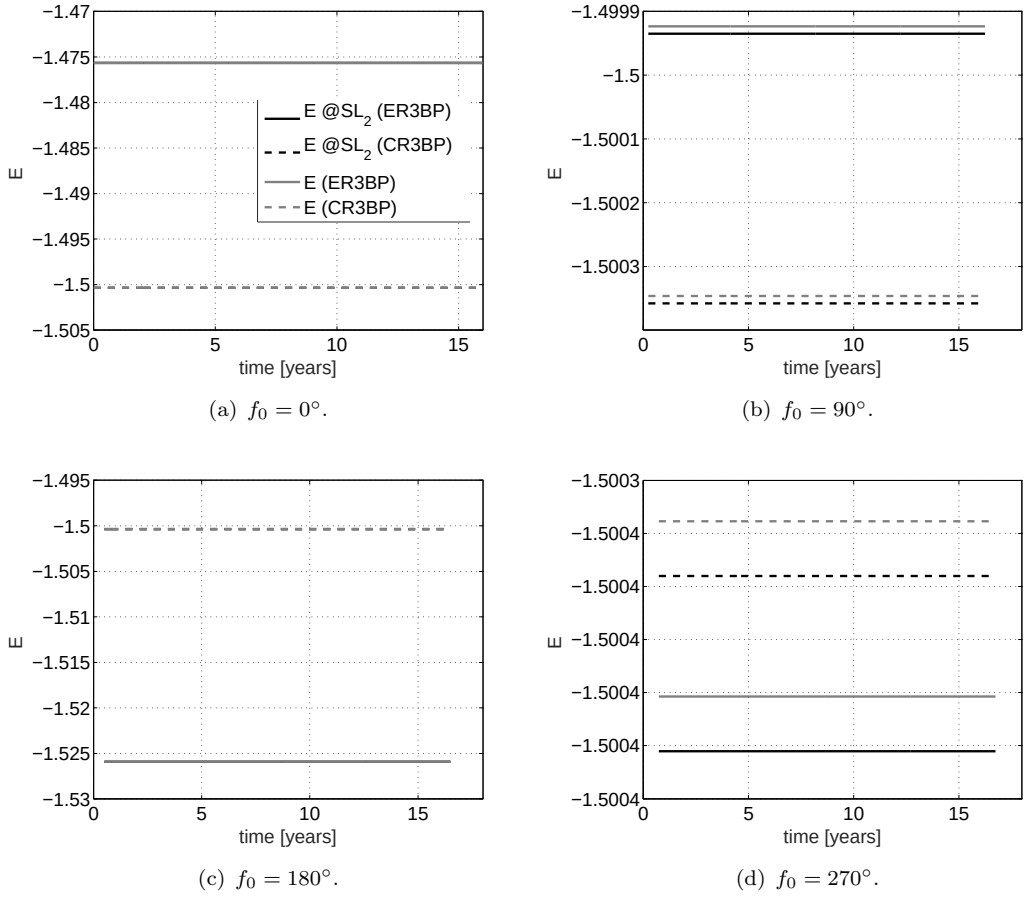

(a) $f_0 = 0°$. (b) $f_0 = 90°$.

(c) $f_0 = 180°$. (d) $f_0 = 270°$.

Figure 7.14: Energy in the ER3BP and CR3BP of the spacecraft and L_2 for trajectories leaving the LPO of Gaia at $f_0 = 0°$, 90°, 180° and 270°.

As already proven in Section 4.4.3, W_{min} does not correspond to a condition of I_{min}; this means that using this approximation can be conservative or can underestimate the integral I. Since an exact representation of the ZVCs is not possible, the analysis of the robustness of this approximation can be performed by looking at the energy of the spacecraft along a selected leaving trajectory from the LPO (grey trajectories, Figure 7.7). In this way, some conclusions can be made. First of all, Campagnola et al. (2008) already showed that Ω can be split into two parts containing the pulsating true anomaly effect and the position of the spacecraft.

Figure 7.15 shows, for the case of $f_0 = 0°$, the comparison of the trend of $2I$ with respect to the pulsating part of Ω, Ω_A (Figure 7.15(a)) and the error between the two terms (Figure 7.15(b)). It is possible to note that the two terms almost cancel out as shown in Figure 7.15(a). From this observation, Campagnola et al. (2008) concluded that the oscillation of the approximated ZVCs is possibly an artificial behaviour due to the approximation.

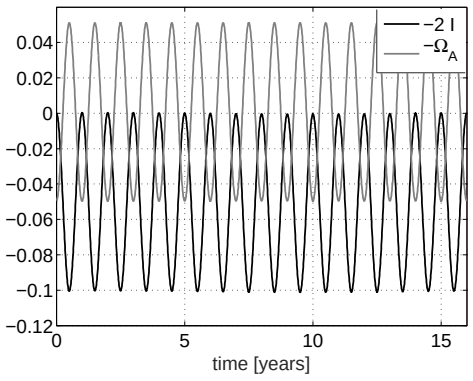

(a) $-2 \cdot I$ and $-\Omega_A$.

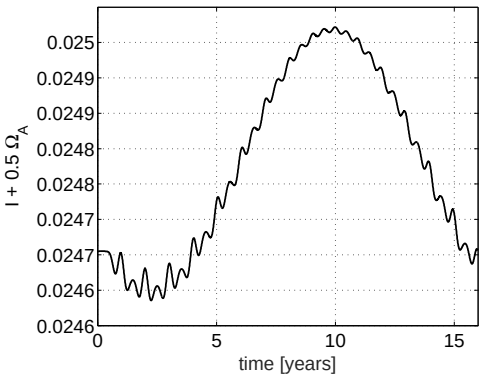

(b) Error between I and $0.5 \cdot \Omega_A$.

Figure 7.15: Comparison with the oscillation of the integral I and the pulsating part of the potential energy Ω_A: the two terms have opposite behaviour; however, they do not completely cancel out, for $f_0 = 0°$.

In Figure 7.15(b), two oscillations can be observed. The low-frequency oscillations correspond to a 16-year cycle and it is due to the spacecraft CA at L_2 while the high-frequency oscillations are related to the inversion of the spacecraft velocity along the trajectory that occurs due to the spacecraft encounter of the ZVCs.

Since the exact ZVCs in Eq. (4.33) cannot be represented, Figure 7.16 shows, for $f_0 = 0°$, the exact energy of the spacecraft computed as in Eq. (7.16) in comparison with the approximated energy as in Eq. (4.43) moreover, the correspondent error. Figure 7.16(a) show that Luk'yanov's approximation can underestimate or overestimate the real energy of the spacecraft (bold black line) while the error between the two energies is $-2 \cdot \tilde{u}$ as expected from Figure 7.16(b). $-2 \cdot \tilde{u}$ is the error made when approximated the energy with the Surface of Minimum Energy (SME). As the spacecraft reaches the CA point,

the approximated energy is a good representation of the energy of the system. The CA is the point of interest when a manoeuvre for closing the ZVCs at L_2 is given.

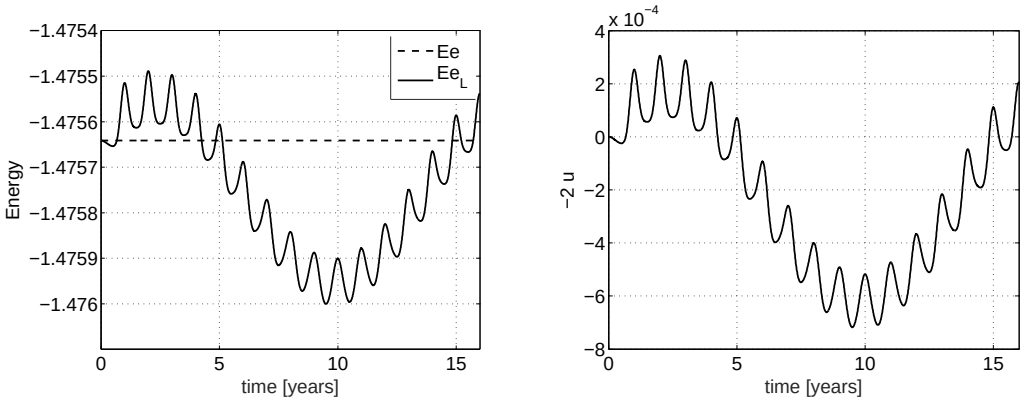

(a) Energy.

(b) Error in the energy.

Figure 7.16: Energy and the error commeted, for $f_0 = 0°$, when computing the approximated energy of the spaceraft. In Figure 7.16(a), the energy of the spacecraft is in black dashed line while the SME approximated energy is in black line.

The dependence of Ω_A from the true anomaly and the spacecraft position vector can be further simplified as shown in Eq. (4.35). The term $e\cos f/(1+e\cos f)$ is a trigonometric function that depends just on the true anomaly which is the independent variable for the integration. Figure 7.17 shows the trend of the term $2(\Omega_c + 0.5z^2)$ that is a function of the spacecraft distance from the centre of mass as shown in Figure 7.17(b). Figure 7.17(c) indicates that this term has a parabolic behaviour with the distance from the centre of mass.

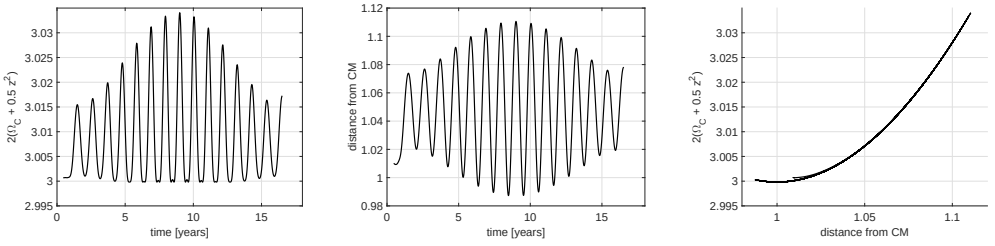

(a) $2\cdot(\Omega_C - 0.5z^2)$ term vs time.

(b) Distance from Centre of Mass (CM) vs time.

(c) $2\cdot(\Omega_C - 0.5z^2)$ term vs distance from CM.

Figure 7.17: Trend of $2\cdot(\Omega_C - 0.5z^2)$ as a function of the integration time and the distance from the centre of mass for $f_0 = 180°$.

The term Ω_A is thus a composition between two functions, one trigonometric and one dependant on the distance of the spacecraft with respect to the centre of mass.

Figure 7.18 shows the correlation of the exact, Eq. (4.33), (dashed black line) and approximated, Eq. (4.43), (black and gray line) potential energy along the trajectory (Figure 7.18(a)-7.18(c)). The grey line represents the approximation with the SME

while the black line is the approximation for $I = 0$. Note that the error produced in the estimation of the potential energy of the spacecraft by neglecting I is very high while the approximation with the SME (grey line) is a good approximation. The error produced in the potential energy is shown in Figure 7.18(d)-7.18(f) where the zero line is the desired value. The grey shadow box represents condition with $\Delta\Omega < 0$, where the approximated potential energy is conservative while the approximation is underestimating the exact solution when it is above the zero line. By looking at the approximated ZVCs at one fixed instant along the simulation time, as shown in Figure 7.18(g)-7.18(h), it is possible to predict (thanks to the sign of $\Delta\Omega$ of the spacecraft) whether the spacecraft is inside ($\Delta\Omega < 0$, overestimation of the ZVCs) or outside ($\Delta\Omega \geq 0$, underestimation of the ZVCs for solution > 0, exact estimation for solution equal 0) the approximated forbidden regions. The oscillations are bigger when the integral is discarded while the error produced by the SME approximation is tiny and the results are very close to the $\Delta\Omega = 0$ line.

A sensitivity analysis between the error produced with the approximated integral and the characteristic of the system in term of μ and second primary's orbit eccentricity e is carried out. In Table 3.2 a combination of μ and e are listed for different systems. Figure 7.19(a) shows the amplitude in the integral approximation error ($\max(-2 \cdot \tilde{u}) - \min(-2 \cdot \tilde{u})$) for μ between $10^{-8} - 0.5$ and e between $0 - 0.9$, while Figure 7.19(b) shows the trend of the error for smaller value in μ and e. Figure 7.19 was obtained by setting the energy of the spacecraft at L_2 and placing the spacecraft at its initial condition for $x_0 = x_{L_2} + 0.005$ and $y_0 = z_0 = 0$. Starting with this set of position data and energy at L_2, the modules of the velocity were found. The orientation of the velocity was set as α =25° in the azimuth and δ =0° in the elevation (Figure 4.12). Each trajectory departs when the second primary is at the pericenter ($f_0 = 0°$ in the true anomaly). The integration time of each trajectory is set to 15 years. For each trajectory, $\tilde{u}$ and its amplitude were computed.

When $e = 0$, the system turns into the CR3BP, thus the error is zero since $I = 0$. In general, the approximation is good for small eccentricities, which is the case for Gaia spacecraft in the Sun-(Earth+Moon) system. However, when the eccentricity (e) is low, the error seems to increase with μ for a fixed value of e, while for high values of e (Figure 7.19(b)) it decreases with μ. This suggests that the SME is not a good approximation of the dynamics for a system like double-stars.

The effect of the eccentricity plays an important role when predicting the probability of a spacecraft's re-entry after the injection into the unstable manifold. For example, if the spacecraft is injected into the unstable manifold when the Earth+Moon true anomaly is 195.2° and the trajectory is integrated in both the CR3BP and the ER3BP dynamical models, it is shown in Figure 7.20 that the ER3BP model predicts the re-entry of the spacecraft after 30 years while the CR3BP model does not. The idea is to investigate if the energy approach prevents the spacecraft's re-entry when analysed in the ER3BP

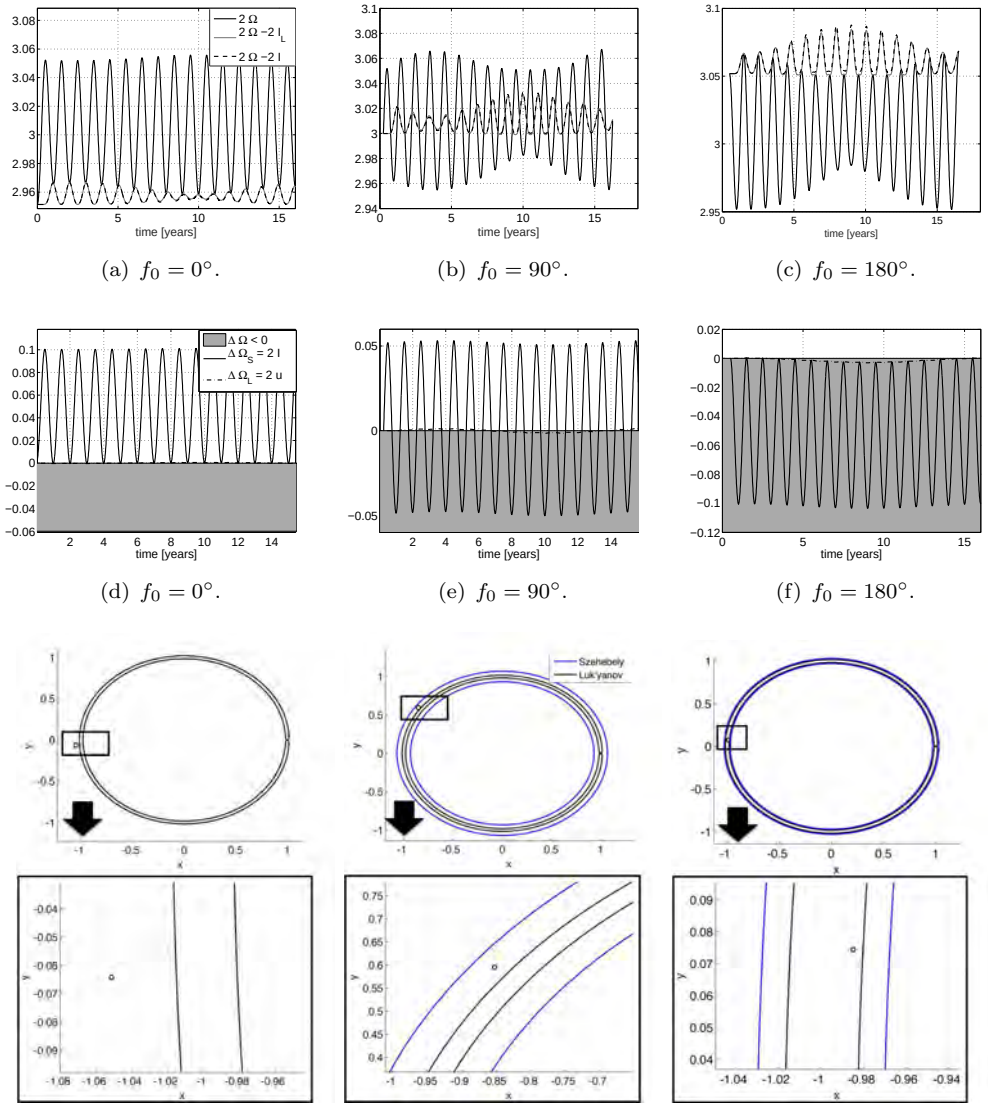

(a) $f_0 = 0°$. (b) $f_0 = 90°$. (c) $f_0 = 180°$.

(d) $f_0 = 0°$. (e) $f_0 = 90°$. (f) $f_0 = 180°$.

(g) $f_0 = 0°$ and $t = 7.9579$ years. (h) $f_0 = 90°$ and $t = 8.2051$ years. (i) $f_0 = 180°$ and $t = 8.4578$ years.

Figure 7.18: Correlation between the exact and approximated potential energy along the spacecraft trajectory and the approximated ZVCs.

after a long simulation time. Using this method, the spacecraft that previously re-entered after 30 years, does not now re-enter over a simulation time of 600 years due to the area deployment. When the spacecraft gets close to SL_2, its velocity is inverted in the rotating frame, suggesting that the effect of SRP has closed the ZVCs in the elliptical case.

Here, the aim is to verify that the ZVCs approximated are closed at the Earth CA. To avoid the re-entry, the ZVCs has to be closed when the spacecraft is in the vicinity of

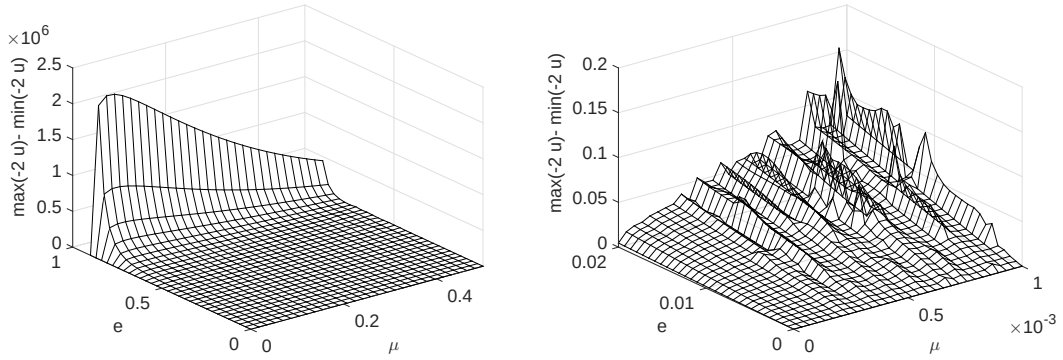

(a) Solutions for all possible μ and e.

(b) Solutions for small μ and e.

Figure 7.19: Amplitude in the approximation error as a function of the mass parameter, μ, and the eccentricity, e.

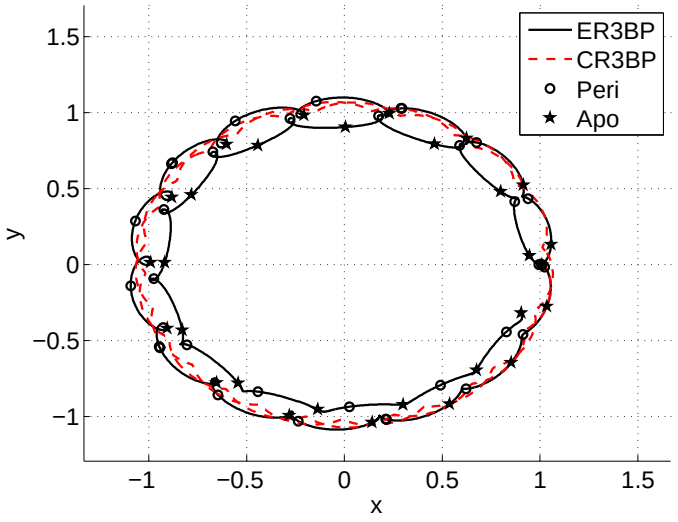

Figure 7.20: Trajectory evolution in the CR3BP (dashed line) and in the ER3BP when leaving the LPO at $f_0 = 195.2$ [deg]. The simulation time is of 30 years.

the gateway in L_2. Note that the curve can be open at L_2 when the spacecraft is at a significant distance from the Earth gateway. Indeed, it was demonstrated that the SME are a good approximation for the Sun-(Earth+Moon) system at the CA. Figure 7.21, shows the evolution of the spacecraft trajectory in the CR3BP (dashed line), in the ER3BP when no deployment is performed (black line) and the evolution of the trajectory in the ER3BP after the deployment (grey line). The deployment occurs 1.7 years after departing from the LPO while the first Earth's encounter happens after 15.3 years.

A good approximation of the ZVCs can be achieved when $\Delta\Omega$ is close to zero as shown in Figure 7.22(a). Two epochs were selected before the deployment (black dashed circles) and at the CA (black circle) in Figure 7.22(a). These two conditions are shown in Figure 7.22(b) where the black dashed rectangle corresponds to an epoch of 1.6802 years after

the departure (epoch before the deploy is performed) and the black rectangle shows the ZVCs at an epoch of 15.2879 (epoch of the first CA). In conclusion, the SME are an exact representation of the ZVCs when $\Delta\Omega$ is close to zero and this condition occurs when the spacecraft is close to the Earth. Consequently, it is possible to conclude that, the SME are a good approximation of the exact ZVCs in the ER3BP when the spacecraft is at the CA. By using the SME approximation, it is possible to check that the ZVCs at the CA are effectively closed in SL_2 as a consequence of the disposal manoeuvre. This confirms the validity of the energy approach: therefore, from now on, this method will be used to compute the area-to-mass ratio required since the closure at SL_2 is guaranteed at the CA.

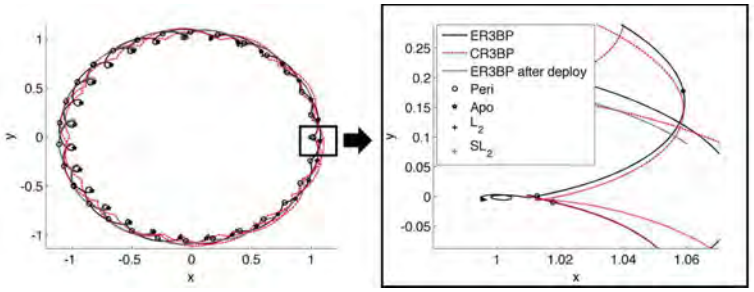

Figure 7.21: Trajectory of the spacecraft in the CR3BP (dashed line), ER3BP without deployment (black line) and evolution of the trajectory in ER3BP after the deployment (gray line).

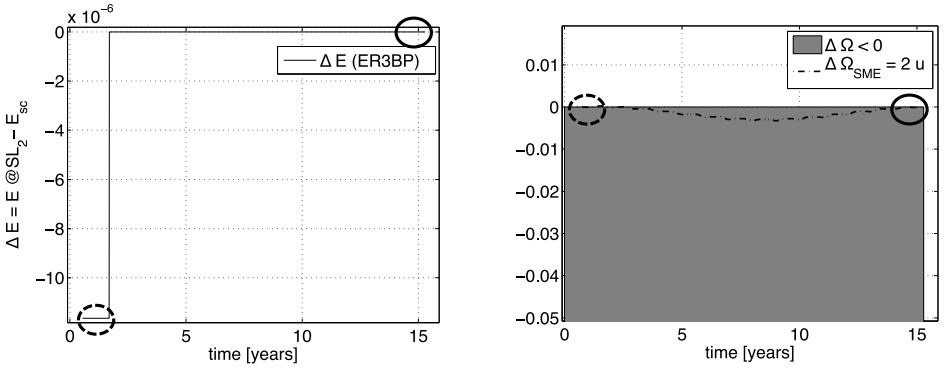

(a) Δ Energy and $\Delta\Omega$ along the spacecraft trajectory.

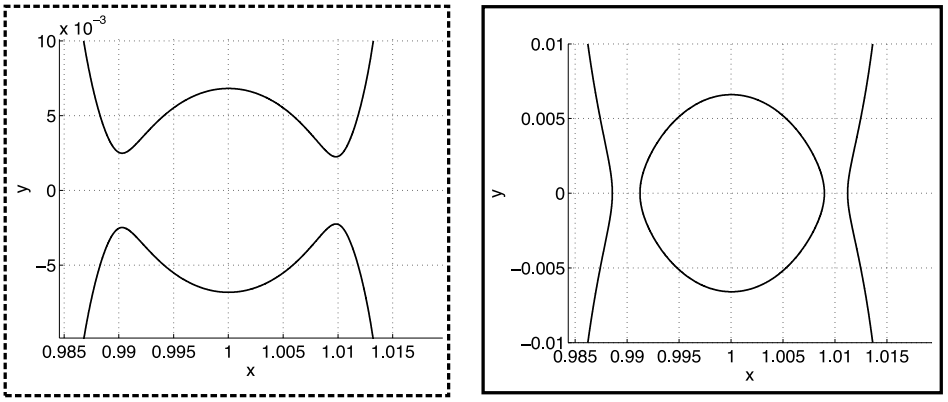

(b) Approximated SME ZVCs before the deployment and at the first Earth close approach.

Figure 7.22: The surfaces of minimum energy are shown, when $\Delta\Omega_{SME}$ is circa zero: before and after the deployment.

7.4.4 Remarks for the disposal in the elliptic restricted three-body problem

The ZVCs cannot be easily computed for the ERTBP-SRP dynamics; thus, approximated solutions have been investigated. The SME were selected since they are a good approximation of the ZVCs for small eccentricity, e. In order to link the ZVCs tool with the dynamics, a different interpretation of the Jacobi constant definition is given by the author. The effect of the approximation adds an artificial oscillating behaviour of the approximated ZVCs as demonstrated by Campagnola et al. (2008).

7.5 End-of-life disposal for Gaia mission with the effect of the Earth's orbit eccentricity

In this section, the effect of the Earth's orbit eccentricity on the disposal of Gaia is investigated. A sensitivity analysis of the area-to-mass ratio required for the disposal

is performed as a function of the LPO initial injection manoeuvre. Thus, uncertainties related to the selected unstable manifold are also considered.

7.5.1 Design of the unstable manifold: sensitivity analysis

A small Δv manoeuvre is required to inject the spacecraft onto the selected unstable manifold. A sensitivity analysis on the required deployable area is done as a function of the orientation angles, α and δ, (as shown in Figure 4.12) and of the Δv magnitude. Note that the LPO injection manoeuvre in this analysis is assumed to be a Δv manoeuvre using attitude control thrusters engine as, in this work, the focus is on the design of the second manoeuvre. After the injection onto the unstable manifold, the area deployed is computed at each point of the unstable trajectories leaving the LPO (grey curves, Figure 7.7). However, future missions in LPOs could use the effect of SRP to perform both the initial injection and disposal (black point, Figure 7.7) manoeuvres through two successive area deployments.

Four leaving points along Gaia's orbit are selected as examples of the initial injection, when the true anomaly (f_0) of the Earth+Moon is equal to 0° (perigee), 90°, 180° (apogee) and 270° and the magnitude in the Δv changes by 0.1, 1, 10 and 100 m/s. The change in the Δv direction results in different trajectory legs departing from the same initial point of the LPO. Eq. (4.19) is integrated for a maximum of 1 year (grey trajectory, Figure 7.7). This mission constraint in the time of disposal is given by ESA to limit the mission operational costs; where it is preferable to perform the deployment within six months after leaving the LPO (Colombo et al., 2014c).

The area required for the deployment is computed using Eq. (3.81) along each point, that lies on the trajectory leg. The analysis produced 464 solutions in δ (29 angles) as a result of the Δv (4 values) and the leaving point from the LPO (f_0, 4 points) as shown in Figure 7.23. Each solution is then computed for different value of α (29 angles).

Figure 7.23 represents the minimum area-to-mass ratio [4] required to reach the energy of SL_2 along each trajectory departing from a single point from the LPO, f_0, with a fixed magnitude in the Δv and a change in the Δv orientations angles. Note that in this analysis, a sensitivity study to check the evolution of the area-to-mass ratio required to reach the energy of SL_2 under the effect of the unstable manifold uncertainties is carried out. This helps to understand how uncertainties in the first manoeuvre affect the area-to-mass ratio required in the ER3BP.

Images in the same row in Figure 7.23 have the same departing point from the LPO while each column in Figure 7.23 have the same fixed Δv. In Figure 7.23, the Δv is

[4]For minimum area-to-mass ratio here we refer to the area-to-mass required to achieve the energy of SL_2 indeed a higher energy above SL_2 should be considered to avoid uncertainties in the pointing requirements and the reflectivity of the area deployed.

increased along each row of figures from left to right. By raising the Δv as you move from Figure 7.23(a) to Figure 7.23(d), it can be seen that the white area increases. This corresponds to regions where α identifies inward trajectories (i.e., towards the Sun) that are discarded since the interest is to dispose of the spacecraft towards the outer solar system. Moreover, the effect of increasing the Δv corresponds to a higher area-to-mass ratio required for the closure within one year. This is due to the increasing spacecraft velocity as the energy of the system is increased; thus, the zero-velocity curves are opened further and a higher area-to-mass ratio is required to close than the curves at SL_2.

When the Δv is too high as in 100 m/s, the optimiser gives the maximum theoretical value of $\beta_{max} = 1$ (i.e., maximum area-to-mass ratio). Thus, in this case, the closure is not achieved for high Δv values of the first manoeuvre. For departing trajectory legs when the Earth+Moon is at a value of f_0 between 0° and 180°, the minimum area-to-mass ratio is achieved for small α and δ. Conversely, for 90° and 270°, small in-plane and out-of-plane angles correspond to high area-to-mass ratio solutions (Figure 7.23).

It should be noted that there is not a unique solution of α and δ that guarantees a minimum area-to-mass ratio for the four departing trajectories analysed when the Δv values are of the order of 0.1 m/s. Indeed, when α and δ are close to zero, the area is minimum for $f_0 = 0°$ and 180°, while it is maximum for $f_0 = 90°$ and 270°. However, for Δv values of the order of 1 m/s and 10 m/s, it is possible to identify a fixed α and δ for the four departing trajectories analysed. An optimum value of α and δ should be picked for any given trajectory as a function of the Δv.

As previously shown, there is some general symmetry in δ; thus, a general analysis can be done by assuming this symmetry in the domain because the changes are minor when δ is varied. Under this approximation, the study will be focused on half of the solutions.

A particular case is when $\delta = -90°$ or 90°, where the solution does not depend on α. In this case, the solution is constant and continuous in α. This case is explored in more depth in Figure 7.24(a), where the figure displays the leaving trajectories when $\delta = -90°$. As one can see for any value of α, there is a unique leaving trajectory and the required area-to-mass ratio is shown in Figure 7.24(b). Thus, this simple scenario allows the evolution of the area-to-mass ratio as a function of Δv and the departure point from the LPO. The possible solution region is pointed along the trajectories, where after the optimisation a feasible area-to-mass ratio can be found and the spacecraft reaches the energy of SL_2.

From Figure 7.24, it should be noted that the solution is coincident for all values of α (a unique trajectory leg can be found when $\delta = \pm 90°$ for any α). The minimum area required corresponds to a large distance along the trajectory from when the spacecraft velocity drifts to zero. In some cases, the minimum corresponds to a perigee solution, but this depends on the initial true anomaly, f_0, of the Earth+Moon when leaving the LPO. The bold line in Figure 7.24(b) shows when the solution has a β value less than

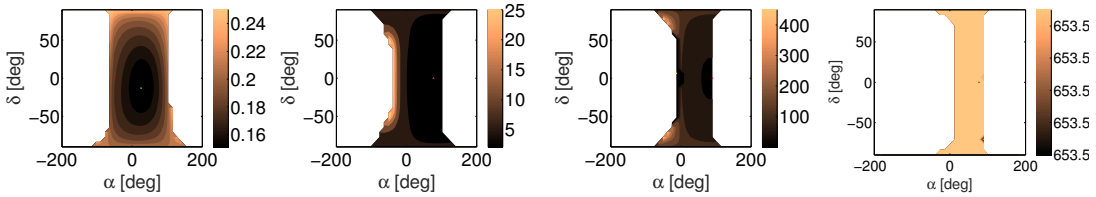

(a) $f_0 = 0°$ and $\Delta v = 0.1$ m/s. (b) $f_0 = 0°$ and $\Delta v = 1$ m/s. (c) $f_0 = 0°$ and $\Delta v = 10$ m/s. (d) $f_0 = 0°$ and $\Delta v = 100$ m/s.

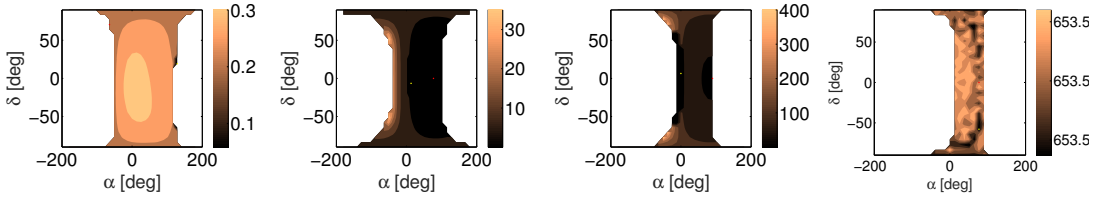

(e) $f_0 = 90°$ and $\Delta v = 0.1$ m/s. (f) $f_0 = 90°$ and $\Delta v = 1$ m/s. (g) $f_0 = 90°$ and $\Delta v = 10$ m/s. (h) $f_0 = 90°$ and $\Delta v = 100$ m/s.

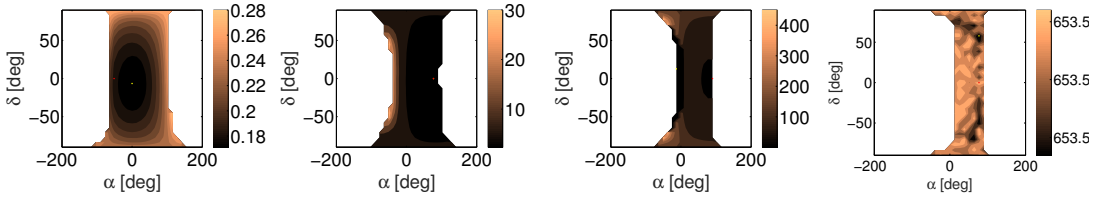

(i) $f_0 = 180°$ and $\Delta v = 0.1$ m/s. (j) $f_0 = 180°$ and $\Delta v = 1$ m/s. (k) $f_0 = 180°$ and $\Delta v = 10$ m/s. (l) $f_0 = 180°$ and $\Delta v = 100$ m/s.

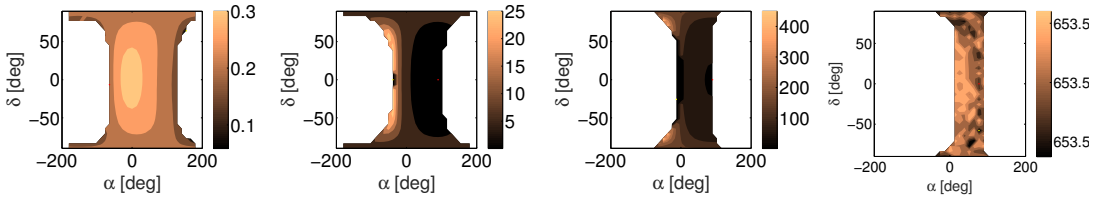

(m) $f_0 = 270°$ and $\Delta v = 0.1$ m/s. (n) $f_0 = 270°$ and $\Delta v = 1$ m/s. (o) $f_0 = 270°$ and $\Delta v = 10$ m/s. (p) $f_0 = 270°$ and $\Delta v = 100$ m/s.

Figure 7.23: Minimum area-to-mass ratio required for the zero-velocity curves closure as a function of the departing point from the LPO when the Earth+Moon is at specific epoch (f_0). At each epoch, the LPO leaving trajectory is function of the magnitude in the Δv and its orientation. The overall simulation time is set to 1 year. The color bar denotes the area-to-mass ration in m^2/kg.

or equal to 0.02446 which is the maximum lightness parameter found for Gaia in the CR3BP-SRP study. In this case, all the solutions in Figure 7.24(b) have an area-to-mass lower than the required one in the CR3BP-SRP.

This is also demonstrated in Figure 7.26 where the sequence of figures shows how the possible solution region evolves (discontinuity in α) by changing the out-of-plane angle, δ. The Δv to leave the LPO is 1 m/s and the departure point from the LPO is when the Earth+Moon has a true anomaly of 270°. Starting with $\delta = -90°$ in Figure 7.26(a),

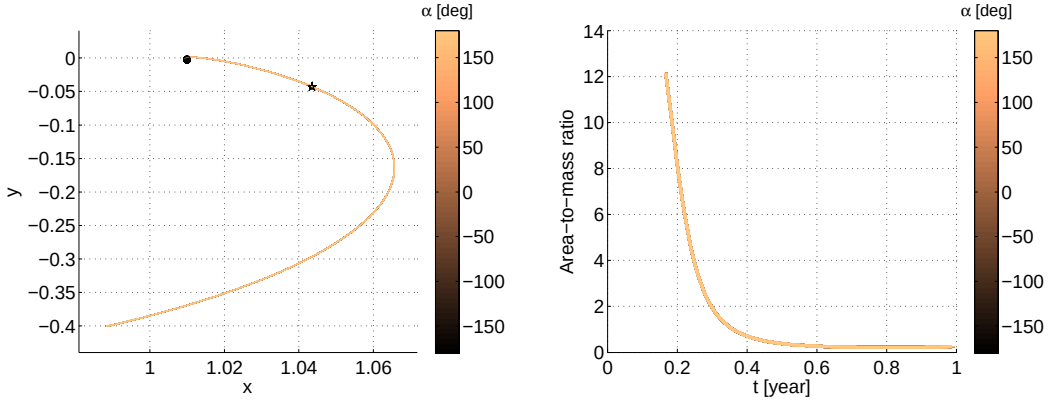

(a) Trajectories evolution as a function of α: (b) Area-to-mass ratio required along the trajectories Earth+Moon at the perigee (cicle) and apogee (star). as a function of α, when $\delta = -90°$.

Figure 7.24: Solution departing when the Earth+Moon is at $f_0 = 0°$ (perigee), $\delta = -90°$ and $\Delta v = 0.1$ m/s.

δ is steadily increased so that in Figure 7.26(f) δ reaches a value of 0° (exploiting the symmetry of δ). In particular, Figure 7.26(a), shows that the solution is independent of α and it is representative of the case previously shown in Figure 7.24, while Figure 7.26(l) shows the evolution of the area-to-mass ratio when δ is less than or equal to zero degrees.

As δ is increased from $-90°$ to 0°, the number of feasible area-to-mass ratio solutions is shown to decrease. This corresponds to the decrease in the possible solution region, as demonstrated by the discontinuity in time for a fixed α (white area). Note that; the possible solution region occurs when β is close to 1. The interpretation of the possible solution region is different from the case of the forbidden region created when using traditional propulsion (Olikara et al., 2015). Indeed, the spacecraft is always on the right-hand side of the pseudo Libration point after the SRP manoeuvre. Thus, the condition in Eq. (7.18) is guaranteed when SRP is exploited. However, the check in Eq. (7.18) is done here to verify the solution from the optimisation. When β is close to 1 but less than the maximum, the solution can be found and the area-to-mass is around 653.59 m^2 kg^{-1}. When the spacecraft is close to the condition of zero velocity, the optimiser returns $\beta = 1$, but in reality the constraint in Eq. (3.81) is not achieved; thus, the check in Eq. (7.18) allows these solutions to be numerically spotted. From Figure 7.26(f) to Figure 7.26(l) the influence of α can begin to be seen; therefore this results in the increase of the overall area-to-mass ratio required.

For small δ, the region of re-entry trajectories increases (white area for all the time for a fixed α) with a consequent reduction in the range of α, where the deployment is possible from -50° to 100°, Figure 7.26.

Figure 7.25 shows the evolution of the area-to-mass ratio as a function of α for $\delta = -64.28°$, $-51.43°$ and $-38.57°$, which correspond to the same solutions shown in Figure

Δv [m/s]	$f_0 = 0°$	$f_0 = 90°$	$f_0 = 180°$	$f_0 = 270°$
0.1	0.152-0.25	0.0587-0.3	0.1712-0.28	0.0587-0.3
1	2.1182-25	0.0587-35	2.2787-30	0.0587-25
10	0.0587-450	0.0587-400	0.0587-450	0.0587-450
100	653.59	653.59	653.59	653.59

Table 7.4: Range of area-to-mass [m^2 kg^{-1}] ratio required in 1 year.

7.26(d)-7.26(f). The peaks in Figure 7.25(c) correspond to solutions where the spacecraft velocity goes close to zero and the corresponding discontinuity in the peak is due to the appearance of the infeasible solution region. Note that in this case, the minimum-area-to-mass ratio required is higher than the case found in the CR3BP-SRP (bold lines in Figure 7.25). This shows the importance of determining the uncertainty in the LPO initial injection manoeuvre.

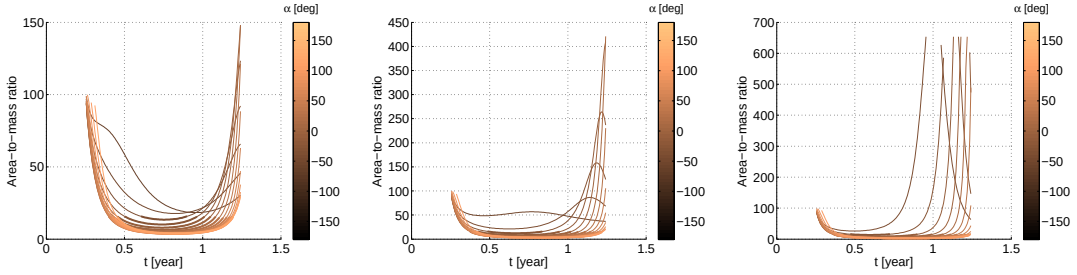

(a) $\delta = -64.28°$. (b) $\delta = -51.43°$. (c) $\delta = -38.57°$.

Figure 7.25: Area-to-mass ratio required to achive the condition in Eq. (3.81) along the trajectories as a function of the in-plane angle, α, for a fixed value in the out-of-plane angle, δ , when the Earth+Moon is at $f_0 = 270°$ on the departing point of the LPO, $\Delta v = 1$ m/s and the integration is over a period of 1 year.

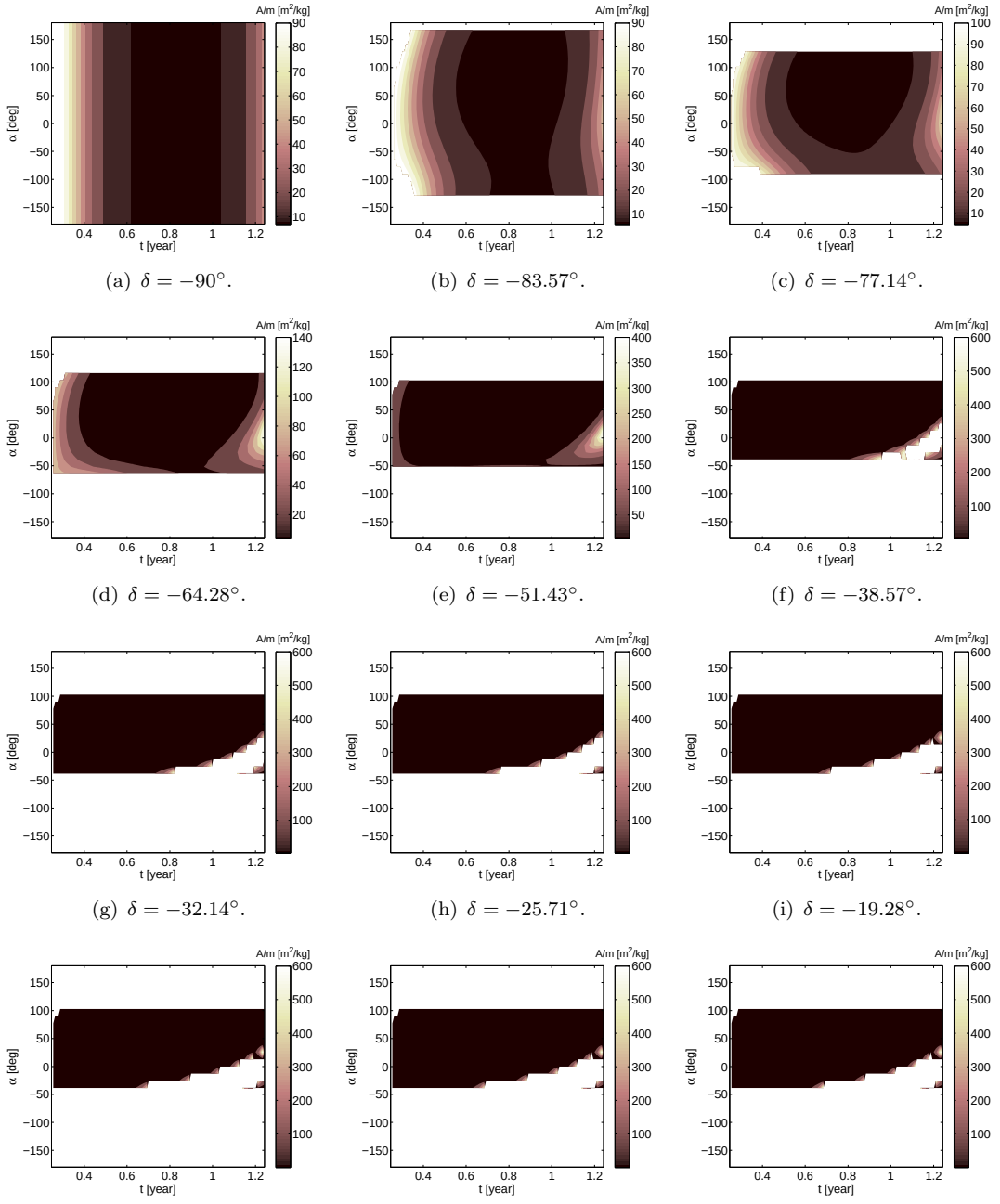

(a) $\delta = -90°$. (b) $\delta = -83.57°$. (c) $\delta = -77.14°$.

(d) $\delta = -64.28°$. (e) $\delta = -51.43°$. (f) $\delta = -38.57°$.

(g) $\delta = -32.14°$. (h) $\delta = -25.71°$. (i) $\delta = -19.28°$.

(j) $\delta = -12.86°$. (k) $\delta = -6.43°$. (l) $\delta = 0°$.

Figure 7.26: Area-to-mass ratio required to achive the condition in Eq. (3.81) along the trajectories as a function of the out-of-plane, δ, and the in-plane angle, α, when the Earth+Moon is at $f_0 = 270°$ on the departing point of the LPO, $\Delta v = 1$ m/s and the integration is over a period of 1 year.

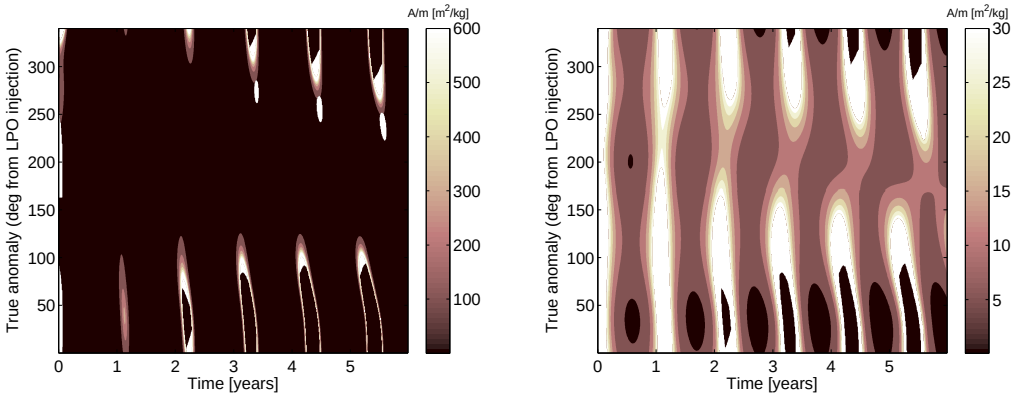

(a) Area-to-mass ratio required.

(b) Area-to-mass ratio below 30 m^2/kg.

Figure 7.27: Evolution of the area-to-mass ratio, the distance from the barycentre, the position angle, θ_z, and the true anomaly of the Earth+Moon along the unstable manifold for 6 years.

7.5.2 Area required along a selected manifold

From the sensitivity analysis on the injection into the unstable manifold, a manifold is selected in which the Δv orientation angles are $\delta = -90°$ and $\alpha = 0°$. As said, the solution is, in this case, simple and independent of α. This clear case helps to identify which parameters influence the minimum area-to-mass ratio required in the ER3BP-SRP. The magnitude in the Δv is 1 m/s.

Figure 7.27 shows the evolution along the unstable manifold of the area-to-mass ratio. The minimum lightness parameter required, β, is $8.98 \cdot 10^{-5}$, which corresponds to a minimum area-to-mass ratio of 0.0587 m^2/kg as shown in Figure 7.27(a). Figure 7.27(a) shows values in the area-to-mass ratio where the white region denotes infeasible solutions for the optimiser, while Figure 7.27(b) shows the area-to-mass ratio for solutions below 30 m^2/kg (feasible area).

Figure 7.28 shows, the integral I, the distance of Gaia spacecraft from the barycentre, the position angle on the barycentre of the synodic system and the position of the Earth+Moon regarding the true anomaly. Figure 7.28(a) shows the evolution of the integral, I, of Eq. (4.25) along the manifold before the deployment ($\beta = \beta_0$) as a function of f_0. It can be seen that the minimum of I is achieved when departing at the apocenter (180°) while the maximum is when departing at the pericenter (0° or 360°) which is consistent with Figure 4.4(b).

The minimum area-to-mass ratio does not always correspond to the maximum distance of the spacecraft from the barycentre since the solution depends on other parameters in the ER3BP-SRP. Thus, the area-to-mass ratio trend along the manifold is compared with three main effects: the spacecraft's distance from the barycentre shown in Figure 7.28(b), the position angle with respect to the barycentre in the synodic frame, $\theta_z =$

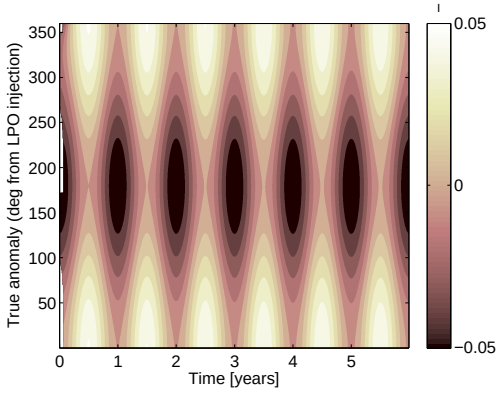

(a) Integral I before the deployment.

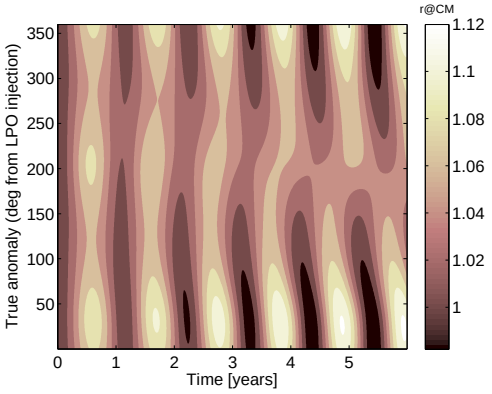

(b) Gaia's distance from the barycentre.

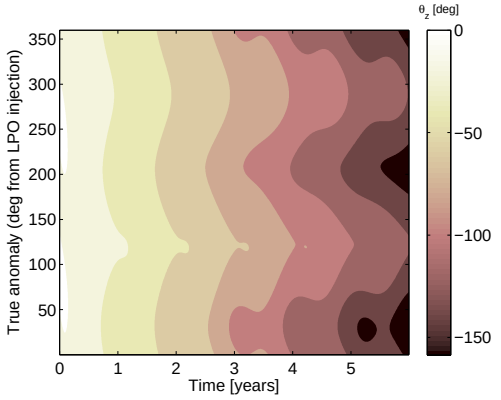

(c) Position angle with respect to the barycentre of the synodic system.

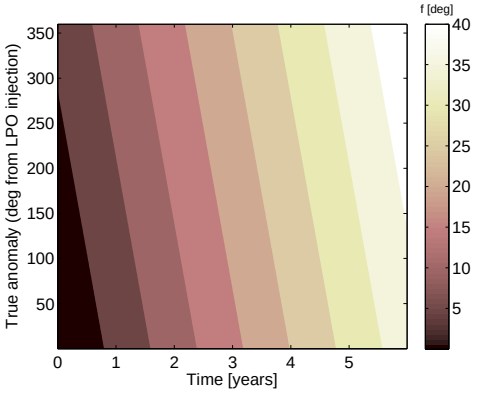

(d) True anomaly of the Earth+Moon evolution.

Figure 7.28: Evolution of the area-to-mass ratio, the distance from the barycentre, the position angle, θ_z, and the true anomaly of the Earth+Moon along the unstable manifold for 6 years.

$\tan^{-1}(y/x)$, Figure 7.28(c), and the true anomaly of the Earth+Moon along Gaia's trajectory in Figure 7.28(d). In Figure 7.27(b), the peaks in the area-to-mass ratio required correspond to the minimum distance of the spacecraft from the centre of mass (Figure 7.28(b)). Over six years in the simulation time (time constraint of disposal), it seems that the spacecraft area-to-mass ratio is primarily influenced by the spacecraft distance from the centre of mass that is circa the distance from the Sun in the Sun-(Earth+Moon) system. However, phenomena of drifting in the distance from the centre of mass can be spotted in Figure 7.28(b) which is due to the effect of the position angle, θ_z and the true anomaly, f of the Earth+Moon (Figures 7.28(c)-7.28(d)). In this case, the exact area required for the ZVCs closure along the manifold was found. Note that this value is the required β to reach the condition in Eq. (7.3) instantaneously.

As already demonstrated in Section 4.4 through the SME approximation of the ZVCs, the condition in Eq. (7.3) guarantees the closure at SL_2; however, the optimum solution should be investigated along the manifold depending on the disposal requirements as the

time within the disposal can be performed due to mission operations constraints (six months) and the time in which the closure after the deployment is guaranteed.

7.6 Perturbing effects

The perturbing effects that can affect the ZVCs closure are interesting aspects to assessing in future work. Among them, it should be mentioned:

- The effects of uncertainties in the lightness parameter due to the shape of the spacecraft or due to the decline in the reflectivity through the time. The decade in the reflectivity property of the deployed area will affect the energy of the spacecraft. It will reduce the effect of the effective reflective area. Thus, we expect that the curves can open again due to the decrease in the spacecraft energy. This justifies the inclusion of an area margin depending on how long the closure after the deployment has to be guaranteed;
- Uncertainties in the pointing direction will cause the ZVCs to open. A conservative approach is to find the maximum area-to-mass ratio required within six months along the selected disposal unstable trajectory to be given at any time within six months and include a margin due to uncertainties in the reflectivity of the spacecraft and the pointing angle requirements;
- As previously stated, a Δv manoeuvre is required to leave the LPO. However, this depends on the type of technology. For example, current missions to LPOs use a traditional propulsion system throughout the regular mission lifetime. Therefore, it is more convenient to use a small Δv manoeuvre to leave the LPO rather than SRP, this Δv can be achieved by using the attitude control engines. Conversely, for future solar sail missions to LPO, it would be interesting to exploit SRP also to leave the LPO. In this way, two consecutive deployments are needed to fall off the LPO and to close the zero-velocity curves in SL_2.

7.7 Summary

This chapter proposes an end-of-life strategy which uses a solar radiation enhancing deployable device to close the zero velocity curves at the pseudo-Lagrangian point SL_2, preventing the spacecraft's Earth return. The simulations have focused on studying the motion of the spacecraft after the deployment of a device at one location along the unstable manifold. Furthermore, an area margin should be included to counteract the effect of perturbations in the full body system. Therefore, an analysis was performed in the ER3BPs to verify the effect of the Earth's eccentricity on the disposal strategy and to quantify the area margin that should be included. From this study, it appears that the effect of the Earth's eccentricity can not be neglected when performing the closure of the zero-velocity curves.

This chapter successfully developed a disposal strategy for solar radiation assisted missions at LPOs. The major research findings for the disposal in the CR3BP are:

- the spacecraft has to be Sun-pointing and the disposal manoeuvre is given with a passively-stabilised deployable structure (i.e. cone sail);
- the disposal using SRP can be achieved to close the ZVCs at SL_2; while, the condition of closing the curves at SL_1 and the disposal of the spacecraft towards the Sun can not be achieved;
- the minimum required area for the disposal is lower if the deployment is done further away from the Sun;
- in the case where the energy associated with the initial spacecraft orbit is higher, a higher area is required to perform the closure of the ZVCs at the same distance from the Sun.

When the effect of the Earth's orbit eccentricity is taken into account, this chapter has demonstrated that:

- the modified surface of minimum energy derived in Chapter 4 is a good approximation of the ZVCs when the spacecraft is at the Earth's close approach;
- the surfaces of minimum energy were used as a tool to demonstrate that the energy approach developed in the CR3BP still holds for the ER3BP;
- the requirements of the area-to-mass ratio were analysed under the effect of uncertainness in the computation of the unstable manifold. It was shown that the injection manoeuvre to leave the LPO influences the area-to-mass ratio required to close the ZVCs. High initial Δv requires higher deployable area;

- along a selected unstable manifold, the area required depends primarily on the spacecraft's distance from the Sun. However, a phenomenon of drifting in the area required is due to the effect of the position angle, θ_z and the true anomaly, f.

Chapter 8

Conclusions and Future Work

This research study was set out to explore the use of Solar Radiation Pressure (SRP) for the design and control of trajectories in the restricted three-body problem of the Sun-Earth system and has identified:

- a control law for the station-keeping of spacecraft in libration point orbits;
- a methodology to transfer between quasi-periodic orbits, and
- an end-of-life strategy to safely dispose of the spacecraft into a graveyard orbit around the Sun.

The study has also sought to determine where it is possible to control a spacecraft in an LPO by using solar radiation pressure manoeuvres from the beginning to the end of the mission and, consequently, to derive the structural drivers in term of:

- reflective area required, and
- spacecraft pointing accuracy.

The state of the art on harnessing SRP for the design and control of space missions in the RTBP is inconclusive on several important questions within the design of reflective deployable devices and the required methodologies for trajectories design and control. The study sought to answer two main research questions:

Q.1 - *Can pre-existing spacecraft's reflective deployable structures enhance the design and control of solar radiation pressure assisted missions in the restricted three-body problem?*

Q.2 - *Which structural requirements are needed for the design of solar radiation pressure missions from the beginning to the end of the spacecraft's lifetime?*

To answer to those *ultimate* questions, *former* questions had to be formulated and answered such as:

Q.3 - *What type of control law can be used for stabilising spacecraft at libration point orbits that make use of solar radiation pressure propulsion?*

Q.4 - *Which methodology can be used to perform transfers between quasi-periodic orbits enhanced by solar radiation pressure manoeuvres?*

Q.5 - *How can we design an end-of-life disposal strategy that makes use of solar radiation pressure enhancing devices to dispose of a spacecraft safely into a graveyard trajectory?*

8.1 Research findings

The main research findings are chapter specific and were summarised within the respective chapters:

Chapter 5 - Hamiltonian Structure-Preserving Control,

Chapter 6 - Design of Transfer Trajectories enhanced by Solar Radiation Pressure, and

Chapter 7 - End-of-Life Disposal through Solar Radiation Pressure.

This section will synthesise the research findings to answer the study five research questions. The approach used to answer question 3 to 5 focuses on the design of spacecraft trajectories through SRP manoeuvres that make use of the invariant manifold theory.

Q.3 - *What type of control law can be used for stabilising spacecraft at libration point orbits that make use of solar radiation pressure propulsion?*

- **Preserving the Hamiltonian structure of the R3BP**: The Hamiltonian structure preserving control has been shown to exploit the natural dynamics of the R3BP by preserving its Hamiltonian nature. The effect of the HSP control is to create an artificial centre equilibrium that makes use of the Lyapunov stability to remove the hyperbolic equilibrium. Compared to other techniques that take advantage of the invariant manifold theory such as the Floquét Modes control, the HSP control is robust to non-linearities and requires a little control acceleration.
- **Control of high amplitude orbits**: The available literature on the HSP control is restricted to low amplitude orbits where the stability along the orbit is of the centre×centre×hyperbolic type. In the case of high amplitude planar LPOs and DPOs, the stability along the orbit change from

centre×centre×hyperbolic to centre×centre×focus; thus, an extended HSP control law was derived from handling the change of stability along the orbit. This opens up the use of HSP controllers independently from the size of the selected orbit.

- **Harnessing solar radiation pressure**: The HSP control requires a low-thrust control acceleration that was shown to be a good candidate for harnessing SRP. It requires an actuator system with variable geometry; while, the spacecraft's pointing accuracy is on the same order of magnitude of the spacecraft's sunshade pointing requirements. The most efficient control parameters are the reflective area and the in-plane angle, α. As high amplitude orbits are highly unstable when compared with low amplitude orbits, a spacecraft in high amplitude orbits requires precise orbit insertion manoeuvre and high reflective surfaces to keep the spacecraft on the nominal orbit.

Q.4 - *Which methodology can be used to perform transfers between quasi-periodic orbits enhanced by solar radiation pressure manoeuvres?*

- **Design of solar radiation pressure manoeuvres that cancel out the unstable invariant manifold**: This transfer approach makes use of the natural dynamics of the linearised equations of motion for the design of SRP manoeuvres. The idea is to cancel out the unstable manifold of the target Lissajous orbit by means of the SRP manoeuvre. This guarantees that, after the given SRP manoeuvre, the spacecraft will follow the stable manifold of the target Lissajous orbit.
- **Use of the phase space and the geometry of the equilibrium points**: The phase space is used to understand how the SRP manoeuvre affects the phases of the Lissajous orbit. It was shown that depending on when the manoeuvre is given, the effect of the SRP results in an instantaneous change in the Φ and Ψ effective phases. This transfer method uses the geometry of two equilibrium points to achieve the desired transfer as the effect of SRP results in changes in the position of the equilibrium points. Thus, before and after the manoeuvre, the spacecraft follows the dynamics of two different equilibrium points. This results in a transfer strategy between orbits with different energies that also belongs to different CR3BP-SRP systems. Moreover, the SRP manoeuvre can be seen as an instantaneous change in the spacecraft's position (with respect to the libration point reference frame); while, for the traditional propulsion, the Δv manoeuvre results in an instantaneous change in the spacecraft's velocity.
- **Change in reflectivity or the in-plane orientation**: The SRP manoeuvre was designed in two different ways. First, it was analysed as a manoeuvre which was controlled by changes in the reflectivity of a Sun-pointing deployable structure. Thus, the SRP manoeuvre is controlled by changes in the

lightness parameter, β. Secondly, a fixed reflective deployable area was considered (i.e., β is fixed); where, the SRP manoeuvre is achieved through changes in orientation of the spacecraft's in-plane angle, α. In both cases, a direct transfer from a departure Lissajous orbit was analysed; where the manoeuvre was given at the departure Lissajous orbit. It was shown that a direct transfer to the target Lissajous orbit is not possible as the SRP manoeuvre does not cancel out the unstable manifold of the target Lissajous orbit. Although a direct transfer among Lissajous orbits is not possible through SRP manoeuvres, it could be that transfers among transit orbits of the R3BP are possible when the manoeuvre is given at the departure Lissajous orbit.

For the case when the SRP manoeuvre is enhanced by changes in reflectivity, a two manoeuvre transfer strategy was also investigated. The first manoeuvre was carried to inject the spacecraft into the unstable manifold of the departure Lissajous orbit; while, the second manoeuvre was enhanced through SRP. Therefore, the SRP manoeuvre aims to cancel out the unstable manifold of the target Lissajous orbit. This manoeuvre is feasible when the spacecraft's reflectivity is reduced (since the SRP acceleration is constrained in direction) and it allows transfers from low to high amplitude Lissajous orbits.

Q.5 - *How can we design an end-of-life disposal strategy that makes use of solar radiation pressure enhancing devices to dispose of a spacecraft safely into a graveyard trajectory?*

- **End of Life disposal strategy**: The end of life disposal strategy enhanced by SRP manoeuvre was first designed in the CR3BP. First, a manoeuvre is given to fall off from the LPO. The spacecraft is thus injected into the unstable manifold of the LPO. Along the unstable manifold, a Sun-pointing reflective deployable device is deployed to confine the spacecraft in a heliocentric graveyard orbit. The effect of increasing the reflectivity of the spacecraft affects the shape of the potential energy. Thus, by deploying a Sun-pointing reflective device, it is possible to close the zero velocity curves at the L_2 bottleneck region, preventing the spacecraft's Earth re-entry at the end of its lifetime.

  The optimal area required for the disposal manoeuvre, designed in the CR3BP, is computed by using an energy approach. Along the unstable manifold, the area required decreases depending on how far the spacecraft is from the Sun. As this is a disposal manoeuvre, the deployed area should passively stabilise the spacecraft. For example a conic sail could be used with the proper spacecraft design to achieve the right positioning of the center of mass with respect to the centre of pressure.

It was also demonstrated that it is not possible to dispose the spacecraft towards the Sun. Thus, spacecraft in orbit around L_1 should be injected towards L_2 before performing the disposal manoeuvre. This is one of the major differences between a disposal manoeuvre with traditional Δv and the SRP.

- **Effect of the Earth's orbit eccentricity**: The effect of the Earth's orbit eccentricity for the SRP EOL disposal was investigated. The validity of the EOL energy approach was verified for the disposal strategy designed in the ER3BP. This required the approximation of the zero velocity curves for the ER3BP as an explicit solution cannot be found in this case. A modified definition of the surface of minimum energy extended to SRP applications was proposed. By applying this definition, it was possible to demonstrate that the energy approach developed for the CR3BP still holds for the ER3BP. Finally, a sensitivity analysis on uncertainty in the injection manoeuvre was carried out for the ER3BP. The area required for the disposal of the spacecraft is a function of the first injection manoeuvre and on the position of the Earth+Moon barycentre with the Sun.

After the design of a control law for LPOs, a transfer methodology between Lissajous orbits and an end-of-life disposal strategy, it was possible to answer to the *ultimate* research questions.

Q.1 - *Can pre-existing spacecraft's reflective deployable structures enhance the design and control of solar radiation pressure assisted missions in the restricted three-body problem?*

- **Deployable harnessing SRP devices**: The study shows that there is no unique answer to this question. Especially when considering the spacecraft mission design from the beginning to the end of the satellite lifetime. In the case of transfers between Lissajous orbits, it is possible to conclude that pre-existing spacecraft's reflective deployable structures can be used to perform the SRP manoeuvre. On the other hand, the end of life disposal strategy proposed requires deployable structures that can passively stabilise the spacecraft. This could be achieved through cone-shape devices; however, further research should be done to investigate that this effect can be accomplished by deploying additional flaps from existing areas. The case of the orbit control actuators requires the design of a new variable geometry deployable structure. This study attempts a preliminary answer to this ultimate research question. However, further research should be done to perform a thorough analysis on the problem.

Q.2 - *Which structural requirements are needed for the design of solar radiation pressure missions from the beginning to the end of the spacecraft's lifetime?*

- **Orbit control actuators**: The HSP control law for SRP applications requires a variable reflective area and a re-orientation of the spacecraft. In this case, it should be investigated how to vary the geometry of the actuators. Although the type of variable area should be further investigated, the pointing accuracy required for the HSP control is on the order of magnitude of the spacecraft's sunshade pointing requirements.
- **Transfer control devices**: The SRP transfer manoeuvre between Lissajous orbits can be achieved by using reflective control devices that aim to reduce the reflective area of a Sun-pointing sunshade or by using solar panel flaps to achieve the same effect. Conversely, if the reflective area is fixed, the manoeuvre can be given by re-orienting the spacecraft on board deployable structures.
- **End of life disposal devices**: The SRP end-of-life strategy requires the deployment of a fixed area that is Sun-pointing. It must passively stabilise the spacecraft thus the use of cone shape devices should be further investigated.

One of the primary research outcomes is the development of a dynamical system tools called 'Controlled Routes by Using Innovative Solar-radiation Equipment'. The CRUISE toolbox merges well known methods for the computation of dynamical objects (i.e., target orbit, invariant manifolds and zero velocity curves) in the restricted three-body problem as well as the newly developed methodologies for the design and control of LPOs mission assisted by SRP manoeuvres. The CRUISE algorithm architecture is presented in Appendix A.

8.2 Research impact

If the influence of solar radiation pressure can be utilised then mission lifetimes will no longer be so restricted by propellant usage. These lifetimes would increase which in turn would consequential reduce the rate of increase in these post mission lifetime debris objects. The reduction of man-made objects will have a positive impact on to the overall mission costs and will contribute to preserving the space environment. This research represents a starting point for the design of new SRP harnessing devices which would be an area of new commercial development and investment. The study attempts to provide the mission applications and the associated methodologies for the design of SRP manoeuvres in the R3BP; where SRP is the main source of propulsion. The impact of this research was already recognised by the European Space Agency as the end-of-life disposal enhanced by solar radiation pressure was selected as one possible disposal option for future missions in LPOs. The research proposed could influence further understanding and applications of SRP propulsion. Possible areas of further understand are identified below:

- The development of advanced technology for the design of future spacecraft where SRP devices are part of the spacecraft's propulsion system.

- Making end-of-life disposal for LPOs part of the mission planning phase.

- The study investigated the design of missions in the Sun-Earth system, where the major scientific space missions are related to monitoring the Sun or observing the Universe. However, it can be potentially extended to all missions; where, a fuel-free solar radiation assisted propulsion is possible. This requires that the solar radiation is a strong environmental effect compared with the planets gravitational effects. An example of a strongly perturbed environment in the solar system can be found in Near Earth Objects (NEOs).

  NEOs are small sized objects (of the order of 1 km) and, consequently, the order of magnitude of solar radiation acceleration is comparable to the asteroids' gravitational effect. Asteroids proximity operations are difficult for several reasons such as the gravitational acceleration of the Sun and other planets, the solar radiation, the irregular asteroids' shape and their spinning motion. This technical challenge has highly demanding requirements in the Guidance, Navigation and Control, and Attitude, Determination and Control subsystems design. As a result of the proposed research, the CRUISE toolbox can be easily extended, for example, to space missions in the Sun-Asteroid system.

- The findings of this study could be exploited for missions to mitigate global warming for example by placing a thin film reflectors in L_1 to reduce the solar radiation reaching the Earth. However, as shown by Bewick et al. (2012) thin film reflectors still present a high manufacturing engineering challenge.

- The methodology developed in this study can be potentially extended to large inflatable structures such as solar power collectors. A space solar power satellite is a concept that has emerged over several decades; the solar power is collected in space and used for terrestrial applications. Current advanced concepts considered by NASA are the integrated symmetrical concentrator and the Abacus/Reflector concept (Wie and Roithmayer, 2001). In the case of a SSPS such as Abacus, the area-to-mass ratio is around 0.4 m^2/kg, which is large when compared to 0.02 m^2/kg for a typical geosynchronous communication satellite. This requires large control torques to counteract SRP. For example, abacus requires 85,000 kg of propellant per year for station-keeping, and attitude control (Wie and Roithmayer, 2001). As a result, this leads to a heavy and consequently expensive system. Thus, the proposed study can potentially inspire methodologies for harnessing SRP in SSPS applications.

8.3 Study limitations

This study has proposed methodologies for the design of space missions in the R3BP assisted by SRP. As a direct consequence of these methods, this study encountered some limitations, which need to be considered:

- As a general comment, the study has shown that a substantial reduction of the spacecraft's onboard propellant can be achieved when SRP is the major method of control. However, in the design of the transfer trajectories and the end-of-life disposal, an intermediate manoeuvre was required to inject the spacecraft onto the unstable manifold. In this case, an impulsive Δv manoeuvre given by the attitude control thrusters was considered. It would be interesting to investigate if an SRP manoeuvre could be used instead. In this way, two consecutive deployments are needed to leave the LPO and to perform the transfer or the end of life manoeuvres.

- The dynamical model used is valid under certain hypotheses; thus, an uncertainty analysis should be carried out to add the gravitational effect of the Moon or other planets (i.e. high fidelity model). Note that the hypotheses made do not compromise the main research findings as they are based on widely used methods for preliminary missions design. Moreover, the R3BP is a good starting dynamical model to develop new trajectories design and control techniques.

- In this study, the spacecraft was modelled as a point mass; thus, the effect of the attitude dynamics are not coupled with the spacecraft's trajectory dynamics. This represents the next step to further the current research study.

- The proposed HSP control law is designed for the CR3BP and it should be verified in the case of more complex dynamics. Moreover, an automatic search of the control's gains should be investigated to determine an optimal solution. Finally, the HSP control law does not include any constraints in time or in the magnitude of the control acceleration. Thus, further work should include the mission operational constraints. For example, the variations in the controlled area required should be limited through a discrete control law.

- The transfer methodology proposed is currently designed for the linearised dynamics of the CR3BP. It should be extended to the non-linear dynamics of the CR3BP and then to a high fidelity model. Moreover, a preliminary result in transfer trajectories through re-orienting the spacecraft are proposed but should be further investigated. For example, an optimised transfer solution should be investigated with the possibility of including the transfer time as an optimum parameter and a discrete control law to limit fluctuations in the area required.

- The proposed end-of-life disposal strategy requires a deployable structure that passively stabilises the spacecraft. Thus, the coupled attitude and orbit dynamics

should be included in further study to determine the EOL device's shape and the inertia needed to achieve this condition.

8.4 Recommendation for future research

From the research gaps shown in Section 8.3, future work is needed to fill the gaps presented by the limitations of this study. Moreover, the ultimate goal of this research is to eventually enable space missions to achieve their mission objectives solely by using SRP. Exploring the following as future research strategies can facilitate the attainment of this goal:

- The design of a multi-body dynamics tool including the spacecraft's attitude dynamics to the current design.
- An investigation into using solar radiation pressure manoeuvres to leave the LPO.
- For the case of the Hamiltonian structure-preserving control, it will be interesting to investigate the design of variable-geometry deployable actuators or to have a discrete control law to facilitate the design of the actuators.
- In the case of transfer trajectories, future works will continue the analysis initiated in this preliminary study. The aim will be to analyse the advantage of using SRP manoeuvres that involve a re-orientation of the spacecraft. Moreover, it would be beneficial to extend the solution to the non-linear dynamics and to investigate an optimal transfer solution. This methodology could be potentially investigated for transfer between transit orbits of the R3BP.
- For the case of the end-of-life disposal, it is critical to examine uncertainties in the pointing requirements. When the deployed structure is not perfectly Sun-pointing, the SRP acceleration cannot be modelled as potential energy. Thus, this would opens up further understanding into how this affects the closure of the zero velocity curves.

  Future work will also aim to couple the attitude dynamics of a Sun-pointing deployable structure with the spacecraft's dynamics in the restricted three-body problem. This will enhance the design of passively stabilised structures with a cone-like shape. The inertia required and the distance of the cone-sail with the spacecraft's centre of mass will depend on the desired torques to keep the spacecraft passively stabilised.

  Finally, when a high fidelity model is used, the zero velocity curves no longer exist; thus, further research should aim to investigate the proposed end-of-life strategy for the generalised dynamical model.

The time required to address the proposed future works depends on the astrodynamics research tool available to researchers that aim to further the current thesis work. For example, researcher with experience in high-fidelity model or coupling attitude dynamics with the spacecraft dynamics will have a great advantage in furthering the current study. The task proposed are an extension of the current research in: orbit control, transfer trajectories and end-of-life for libration point spacecraft and they are intended to be a near future research work.

Solar radiation pressure assisted missions have been shown to be feasible for the design and control of trajectories of LPOs from the beginning to the end of the spacecraft lifetime. SRP is a natural and unlimited source of *propellant*. Due to this unlimited propellant, space missions that use SRP have longer mission lifetimes, potentially decreasing the number of spacecraft launched to LPOs. Reducing the number of launches will reduce the Space Agencies overall cost budget allocated for LPOs missions. A reduced number of spacecraft at LPOs will also make the space market more sustainable by limiting the potential space debris in the vicinity of the libration points. Furthermore, the single space mission cost budget is highly related to the mass of the spacecraft, where the pre-storage of onboard propellant has a significant impact on the overall single mission cost. Thus, a SRP device has the key advantage of reducing the costs relating to the propulsion system. These facts provide evidence that underlines the importance to further research into solar radiation pressure enhancing devices for LPO missions which is needed to make this technology economically accessible.

Appendix A

Controlled Routes by Using Innovative Solar-radiation Equipment (CRUISE) code architecture

CRUISE code is an Astrodynamic toolbox written in Matlab. It merges well known tools in Astrodynamics for the computation of dynamical objects (for example target orbit, stability criterion, equations of the dynamics and others) label as Astrodynamic Tools in Figure A.1 as well as new Astrodynamic Techniques as a result of this thesis work (Figure A.1). Figure A.2, Figure A.3 and Figure A.4 show a schematic representation of the three branches of CRUISE code: Orbit Control (OC), Orbital Transfer (OT) and End-Of-Life (EOL) disposal.

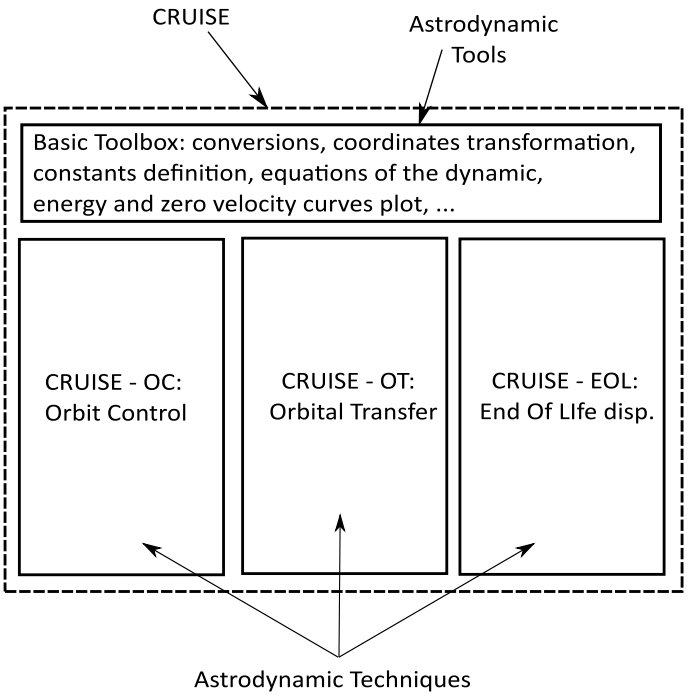

Figure A.1: CRUISE code scheme

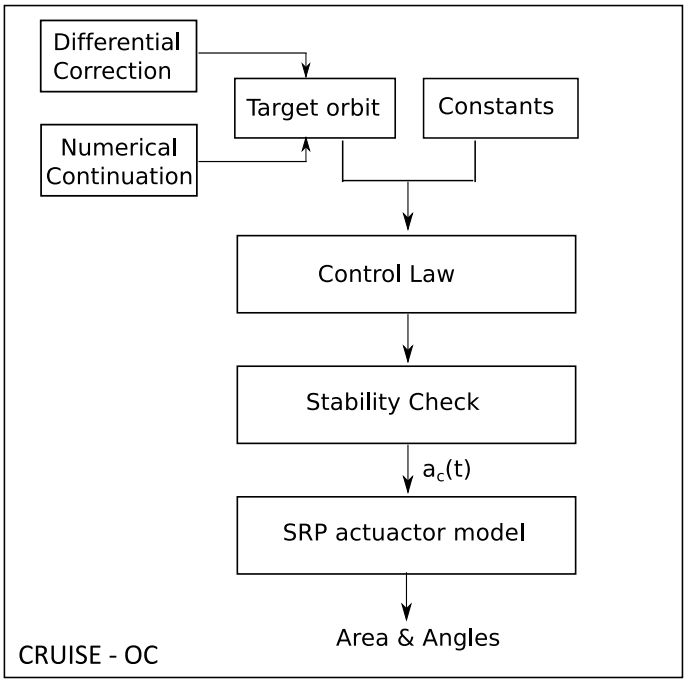

Figure A.2: CRUISE code scheme: Orbit Control (OC).

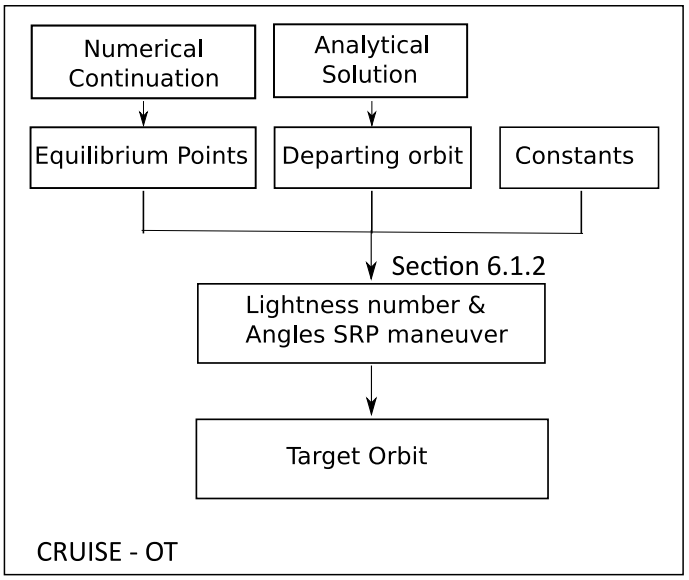

Figure A.3: CRUISE code scheme: Orbital Transfer (OT).

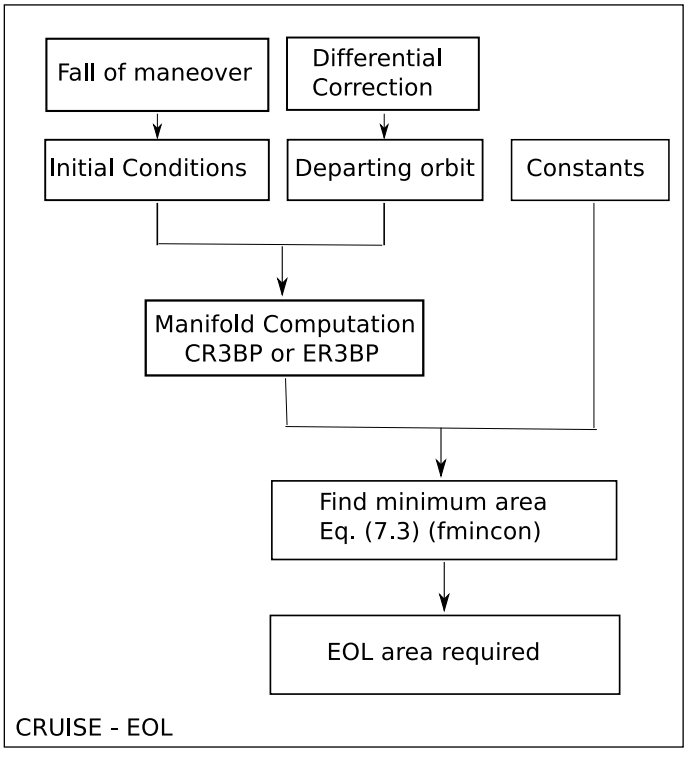

Figure A.4: CRUISE code scheme: End-Of-Life (EOL) disposal.

Appendix B

Restricted Three-Body Problem

B.1 Orbital elements

In space mission design, the Kepler problem describes the motion of a spacecraft or a small celestial body around a massive celestial body that is a solution of Eq. (2.1), Section 2.1. The solutions of the Kepler problem are keplerian orbits or conics as circular and ellipse shape orbits. Thus, the motion of the spacecraft can be determine through six scalar quantities as the three components in position and velocity. Alternatively, there exist other six scalar quantities that can unequivocally determine the shape and the orientation of the spacecraft's orbit. These quantities are known as orbital elements.

Figure B.1 shows the definition of the orbital elements with respect to two reference frames: the inertial and the Perifocal (PQW) reference frames. The inertial reference frame is usually centred at the celestial body of interest with coordinates x_i, y_i and z_i as shown in Figure B.1(a). The x_i and y_i components define the "reference plane" shown in Figure B.1(a). Figure B.1(a) shows the orientation of the spacecraft's orbit with respect to the reference plane. The perifocal reference frame (PQW) has the spacecraft's orbit plane as reference and it is centred in the selected celestial body, Figure B.1(b). The axis p indicate the pericenter (minimum distance from the celestial body) and w is perpendicular to the orbit plane; while, q is oriented such as to define a right-hand system. The intersection of the reference plane of the inertial system and the spacecraft's orbit plane is called ascending node.

The orientation of the orbit with respect to the inertial frame requires the definition of three angles: the right angle of the ascending node, Ω, the argument of perigee, ω, and the inclination, i. The right angle of the ascending node, Ω, is the angle between the x_i and the ascending node, N, the argument of perigee, ω, is the angle between the ascending node and the pericenter, p; while, the inclination, i, is the angle between z_i and w.

The remaining three elements define the shape and the position of the spacecraft with respect to the pericenter. The true anomaly, f, is the angle between the pericenter, p, and the spacecraft distance from the celestial body, r, as shown in Figure B.1(b). The shape of the orbit is determined by the semimajor axis, a, that is half of the pericenter-apocenter distance and the eccentricity, e, that tells how much is the deviation of the orbit from being a circle. The eccentricity, e, is greater or equal to 0 (circle). When $e = 1$, the orbit is open and is a parabola; while, for e strictly between 0 and 1, the orbit is a close loop and is an ellipse. In case of e major then 1, the orbit as a shape of an hyperbole.

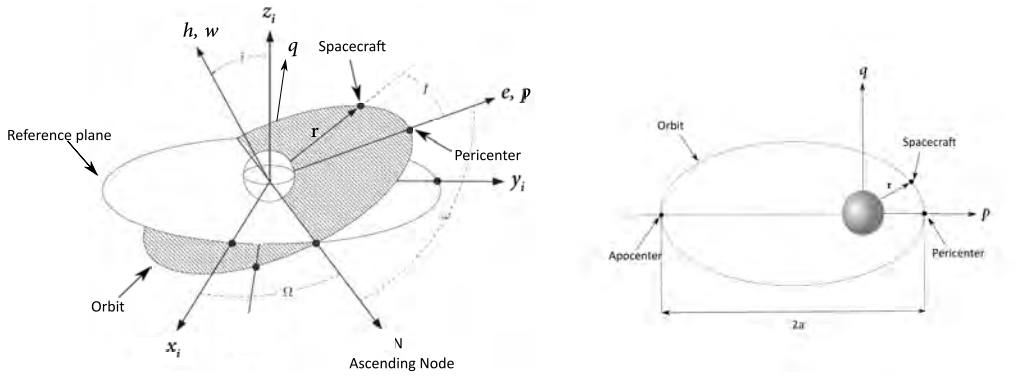

(a) Definition of the orbital elements.

(b) Perifocal reference frame (PQW).

Figure B.1: Definition of the orbital elements and the perifocal reference frame (PQW).

Finally, the trajectory of the spacecraft, r, can be expressed as a function of the orbital elements:

$$r = \frac{a(1-e^2)}{1+e\cos f}. \tag{B.1}$$

B.2 Physical interpretation of the $L_{1,2}$ collinear points

For the 3^{rd} Kepler law, the closer an object is to the Sun, the faster it will move. Thus, any spacecraft placed in a keplerian orbit around the Sun, smaller than Earth's, will soon overtake our planet. However, if the spacecraft is placed directly between the Sun-Earth line, the Earth's gravity pull is in opposite direction and will cancel some of the Sun's pull. The spacecraft will slow done as a weaker pull towards the Sun requires less speed to maintain its orbit. If the distance from the Sun is such that the Earth and the Sun gravity pulls cancel out, the spacecraft will travel slowly to keep the its position between the Sun and the Earth. This is what happen to a spacecraft placed at L_1. L_1 is a good platform to monitor the Sun since the solar wind reaches L_1 an hour before reaching Earth. SOHO is the ESA/NASA current mission at L_1 to study the Sun's outer corona.

Similar to L_1, a spacecraft placed in a orbit beyond the Earth's orbit should travel slower than the Earth. However, the extra pull of our planet added to the Sun's pull allows the spacecraft to move faster. This is the case of a spacecraft at L_2. Spacecraft at L_2 are in a good location to observe the Universe as the Earth is in a smaller orbit around the Sun and cannot interfere with the spacecraft filed of view. Examples of missions at L_2 are: Hershel, Plank and Gaia.

B.3 Mission Scenario

B.3.1 Herschel mission

Herschel spacecraft is a space telescope that was placed in a Lissajous orbit in L_2. Herschel has 3.5 m single mirror telescope used to perform infrared observation of the dark universe. The Herschel spacecraft was 7.5 m high with a cross section of 4×4 m. The launch mass was about 3.4 tonnes. The orbits amplitude are 750,000 km along the y-axis (A_y) and 450,000 km along the z-axis (A_z). Table B.1 summarises the Herschel mission fact sheet. Figure B.2 shows the Herschel spacecraft (Figure B.2(a)) and its nominal orbit (Figure B.2(b)).

Hershel	
Launch	2009
End of mission	2013
Mass [kg]	3400
Size [m]	7,5 m (high) and 4×4 (cross section)
Orbit	Lissajous orbit around L_2 of the Sun-Earth system
Objectives	• Study of the formation of the galxies; • Creation of the stars; • Observe the chemical composition of the atmospheres and surfaces of comets, planets and satellites; • Examine of the molecular chemistry of the universe.

Table B.1: Herschel fact sheet.

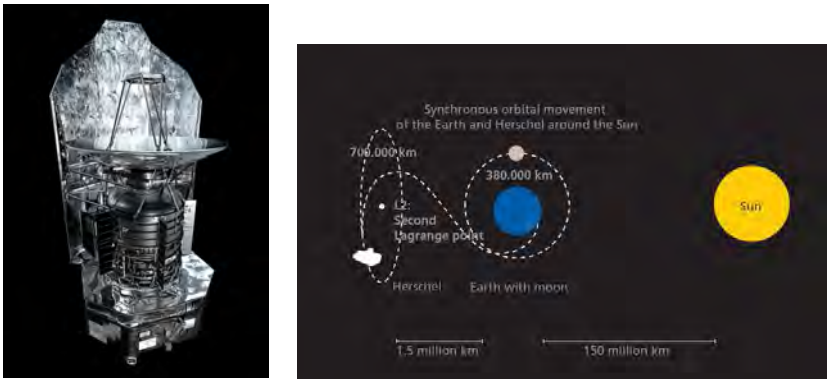

(a) Herschel spacecraft. (b) Herschel trajectory.

Figure B.2: Herschel spacecraft and orbit overview (image credit ESA).

B.3.2 SOHO mission

SOHO mission is designed to study the internal structure of the Sun, its atmosphere and the origin of the solar wind. SOHO spacecraft has a total mass of 1850 kg. The length of the spacecraft along the Sun-pointing axis is of 4.3 m. The solar panels of SOHO has a span of 9.5 m. Table B.2 shows the SOHO mission fact sheet. The SOHO spacecraft and its orbit are shown in Figure B.3. The halo orbit of SOHO has 106,448 km in A_x, 666,672 km in A_y and 120,000 km in A_z.

SOHO	
Launch	1995
End of mission	2018
Mass [kg]	1850
Size [m]	4.3 m (length) with solar panels of 9.5 m (span)
Orbit	Halo orbit around L_1 of the Sun-Earth system
Objectives	• Database of the solar surface; • Discoverer of comets even if not design for this purpose; • Rapid changes of the magnetic field.

Table B.2: SOHO fact sheet.

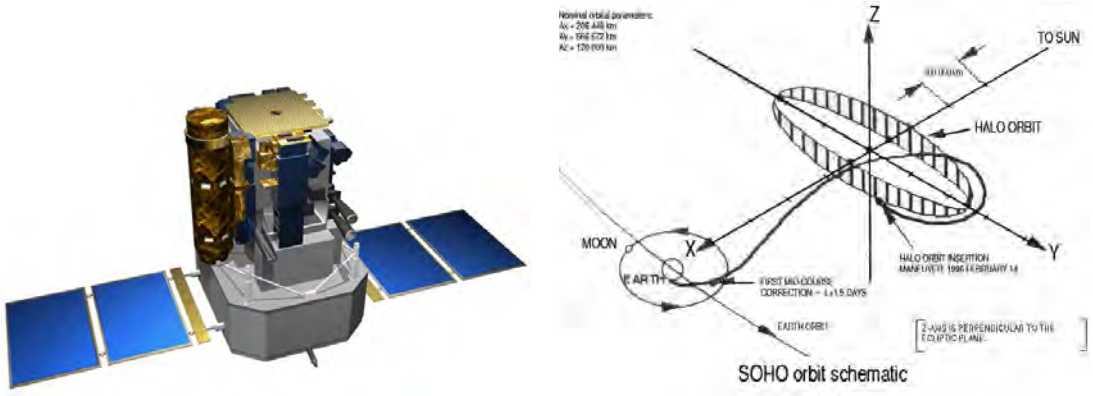

(a) SOHO spacecraft.

(b) SOHO trajectory.

Figure B.3: SOHO spacecraft and orbit overview (image credit ESA).

B.3.3 Gaia mission

Gaia mission spacecraft is in a Lissajous orbit around L_2. Gaia mission objectives are to observe our Galaxy to map the stars and investigate its origin. Gaia has a 12.8 m^2 triple-junction solar array to provide the required power and a sunsheild disk of 10 m in diameter. Gaia's orbit amplitudes are 340,000 km in A_y and 90,000 km in A_z. Table B.3 shows Gaia mission data sheet; while, Figure B.4 shows the spacecraft and its nominal orbit.

Gaia	
Launch	2013
End of mission	nominal mission of 5 years (2018)
Mass [kg]	2030
Size [m]	10 m diameter sunsheild and 12.8 m^2 in the solar array
Orbit	Lissajous type orbit around L_2 of the Sun-Earth system
Objectives	• Survey of the stars of our Galaxy; • Investigate the origin and the evolution of our Galaxy.

Table B.3: Gaia fact sheet.

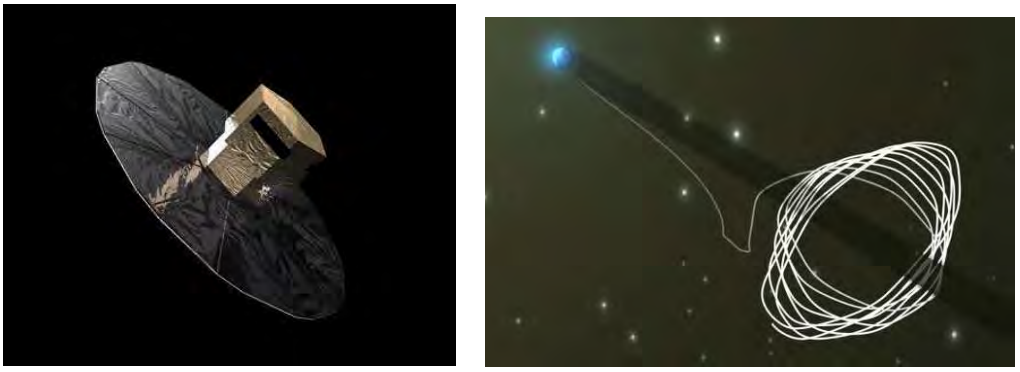

(a) Gaia spacecraft. (b) Gaia trajectory.

Figure B.4: Gaia spacecraft and orbit overview (image credit ESA).

Appendix C

Circular Restricted Three-Body Problem

C.1 Derivative of the direction cosine matrix and velocity composition theorem

$\mathbf{C}_{ri}(t)$ is the direction cosine matrix between the rotating frame, $\mathscr{F}_r$, and the inertial frame, $\mathscr{F}_i$, which are related as:

$$\mathscr{F}_r = \mathbf{C}_{ri}(t)\mathscr{F}_i. \tag{C.1}$$

Eq. (C.1) can be inverted as follow:

$$\mathscr{F}_i^T = \mathscr{F}_r^T\mathbf{C}_{ri}(t). \tag{C.2}$$

By deriving Eq. (C.2) in time, Eq. (C.2) turns into:

$$\mathbf{0} = \dot{\mathscr{F}}_r^T\mathbf{C}_{ri} + \mathscr{F}_r^T\dot{\mathbf{C}}_{ri}. \tag{C.3}$$

By noticing that, in Eq. (C.3), the terms $\dot{\mathscr{F}}_i^T$ vanishes, the term $\dot{\mathscr{F}}_r^T$ becomes a function of:

$$\dot{\mathscr{F}}_r^T = [\boldsymbol{\omega}_{ri}]_\times\mathscr{F}_r^T, \tag{C.4}$$

where, $\boldsymbol{\omega}_{ri}$ is the angular velocity of $\mathscr{F}_r$ with respect to $\mathscr{F}_i$, and it is defined as: $\boldsymbol{\omega}_{ri} = \boldsymbol{\omega}_{ri}^T\mathscr{F}_r$. Finally, it is possible to rewrite Eq. (C.4) such as:

$$\mathbf{0} = \mathscr{F}_r^T([\boldsymbol{\omega}_{ri}]_\times\mathbf{C}_{ri} + \dot{\mathbf{C}}_{ri}), \tag{C.5}$$

and the differential equation of $\mathbf{C}_{ri}(t)$ is:

$$\dot{\mathbf{C}}_{ri} = -[\boldsymbol{\omega}_{ri}]_{\times}\mathbf{C}_{ri}. \tag{C.6}$$

C.1.1 Velocity composition theorem

The change of coordinates from a syderal to a synodic reference frame for the spacecraft position vector is:

$$\boldsymbol{r}_i = \mathbf{C}_{ri}^T\boldsymbol{r}, \tag{C.7}$$

while, the velocity can be derived through the velocity composition theorem such as:

$$\dot{\boldsymbol{r}}_i = \dot{\boldsymbol{r}}_i + \boldsymbol{\omega}_{ri} \times \boldsymbol{r}_i. \tag{C.8}$$

Thus, if we now add Eq. (C.7) in Eq. (C.8), it is possible to obtain the follow relation in the spacecraft velocities:

$$\dot{\boldsymbol{r}}_i = \mathbf{C}_{ri}^T\dot{\boldsymbol{r}} + \boldsymbol{\omega}_{ri} \times \mathbf{C}_{ri}^T\boldsymbol{r}, \tag{C.9}$$

which, turns into its full expression such as:

$$\dot{\boldsymbol{r}}_i = \begin{bmatrix} 0 & -n & 0 \\ n & 0 & 0 \\ 0 & 0 & 0 \end{bmatrix} \begin{bmatrix} \cos nt & -\sin nt & 0 \\ \sin nt & \cos nt & 0 \\ 0 & 0 & 1 \end{bmatrix} \boldsymbol{r} + \begin{bmatrix} \cos nt & -\sin nt & 0 \\ \sin nt & \cos nt & 0 \\ 0 & 0 & 1 \end{bmatrix} \dot{\boldsymbol{r}}. \tag{C.10}$$

A compact way to write the spacecraft inertial velocities is:

$$\dot{\boldsymbol{r}}_i = \begin{Bmatrix} \dot{x}_i - \omega_z y_i \\ \dot{y}_i + \omega_z x_i \\ \dot{z}_i \end{Bmatrix}. \tag{C.11}$$

C.2 Lagrangian approach: rotating dynamics

The equations of motion in the rotating dimensionless dynamics are derived here. The absolute acceleration, $\boldsymbol{a}_a$, is a function of: the relative acceleration, $\boldsymbol{a}_r$, the system acceleration, $\boldsymbol{a}_\tau$, and the Coriolis acceleration, $\boldsymbol{a}_c$, such as:

$$\boldsymbol{a}_a = \boldsymbol{a}_r + \boldsymbol{a}_\tau + \boldsymbol{a}_c. \tag{C.12}$$

The system acceleration, $\boldsymbol{a}_\tau$, is stated such as:

$$\boldsymbol{a}_\tau = \boldsymbol{a}_{CM} + \dot{\boldsymbol{\omega}} \times \boldsymbol{d}_{CM} + \boldsymbol{\omega} \times \boldsymbol{\omega} \times \boldsymbol{d}_{CM}. \tag{C.13}$$

In the CR3BP, $\dot{\boldsymbol{\omega}}$ and $\boldsymbol{a}_{CM}$ are null, so Eq. (C.13) turns into:

$$\boldsymbol{a}_\tau = \boldsymbol{\omega} \times \boldsymbol{\omega} \times \boldsymbol{d}_{CM}. \tag{C.14}$$

For this reason, $\boldsymbol{a}_\tau$ has only the contribution of the centrifugal acceleration. The Coriolis acceleration, $\boldsymbol{a}_c$, is defined as:

$$\boldsymbol{a}_c = 2\boldsymbol{\omega} \times \boldsymbol{v}_r. \tag{C.15}$$

Finally, the equations of motion now turns into:

$$\boldsymbol{a}_a = \boldsymbol{a}_r + \boldsymbol{\omega} \times \boldsymbol{\omega} \times \boldsymbol{r} + 2\boldsymbol{\omega} \times \boldsymbol{v}_r; \tag{C.16}$$

where, the relative acceleration is shown to be such as:

$$\boldsymbol{a}_r = \left\{ \begin{array}{c} \ddot{x} \\ \ddot{y} \\ 0 \end{array} \right\}. \tag{C.17}$$

The distance from the centre of mass is defined such as:

$$\boldsymbol{r} = \left\{ \begin{array}{c} x \\ y \\ 0 \end{array} \right\}, \tag{C.18}$$

while, the centrifugal and Coriolis accelerations are:

$$\boldsymbol{a}_{centr} = \left\{ \begin{array}{c} -n^2 x \\ -n^2 y \\ 0 \end{array} \right\}, \tag{C.19}$$

and

$$\boldsymbol{a}_c = \left\{ \begin{array}{c} -2n\dot{x} \\ 2n\dot{y} \\ 0 \end{array} \right\}, \tag{C.20}$$

respectively. Finally, the equations of motion in the rotating Lagrangian dimensionless coordinate are:

$$\left\{ \begin{array}{l} \ddot{x} - 2n\dot{x} - n^2 x = -\frac{\mu_{Sun}(x - x_{Sun})}{r^3_{Sun-p}} - \frac{\mu_{Earth}(x - x_{Earth})}{r^3_{Earth-p}} \\ \ddot{y} + 2n\dot{y} - n^2 y = -\frac{\mu_{Sun} y}{r^3_{Sun-p}} - \frac{\mu_{Earth} y}{r^3_{Earth-p}} \\ \ddot{z} = -\frac{\mu_{Sun} z}{r^3_{Sun-p}} - \frac{\mu_{Earth} z}{r^3_{Earth-p}} \end{array} \right. , \tag{C.21}$$

where, the mean motion, n is unitary.

C.3 Cannonball solar radiation pressure model

The SF can be expressed as function of the Sun luminosity, L_{Sun}, so that:

$$SF = \frac{L_{Sun}}{4\pi r_{Earth-Sun}^2}. \tag{C.22}$$

For a specular reflective surface[1], the Eq. (3.22) turns into:

$$\boldsymbol{a}^s = 2P_{srp}\frac{A}{m}\left\langle \hat{\boldsymbol{N}}\cdot\hat{\boldsymbol{r}}\right\rangle^2 \hat{\boldsymbol{N}}. \tag{C.23}$$

The mass-to-area ratio, m/A, is renamed as σ, the sail load, and by substituting Eq. (3.24) and Eq. (C.22) to Eq. (3.28), it possible to have:

$$\boldsymbol{a}^s = \frac{2L_{Sun}}{4\pi r_{Earth-Sun}^2 c}\frac{r_{Earth-Sun}^2}{r_{Sun-p}^2}\frac{1}{\sigma}\left\langle \hat{\boldsymbol{N}}\cdot\hat{\boldsymbol{r}}\right\rangle^2 \hat{\boldsymbol{N}}. \tag{C.24}$$

Having multiplied and divided Eq. (C.23) by the Sun gravitational parameter, μ_{Sun}, the equation becomes:

$$\boldsymbol{a}^s = \frac{L_{Sun}}{2\pi c\mu_{Sun}}\frac{1}{\sigma}\frac{\mu_{Sun}}{r^2}\left\langle \hat{\boldsymbol{N}}\cdot\hat{\boldsymbol{r}}\right\rangle^2 \hat{\boldsymbol{N}}. \tag{C.25}$$

Eq. (C.25) can be further simplified as:

$$\boldsymbol{a}^s = \beta\frac{\mu_{Sun}}{r_{Sun-p}^2}\left\langle \hat{\boldsymbol{N}}\cdot\hat{\boldsymbol{r}}\right\rangle^2 \hat{\boldsymbol{N}}, \tag{C.26}$$

where, in Eq. (C.26), $\beta = \sigma^*/\sigma$ is the lightness parameter and $\sigma^* = \frac{L_{Sun}}{2\pi c\mu_{Sun}}$ is the Sun load.

C.4 Solar radiation pressure model: cone and clock angles

The equations of the normal to the reflective surface are given here in more details as:

$$\begin{aligned}\hat{\boldsymbol{N}} = \quad & \frac{\cos\alpha}{|\boldsymbol{r}_{Sun-p}|}\begin{Bmatrix} x-x_{Sun} \\ y \\ z \end{Bmatrix} + \frac{\sin\alpha\cos\delta}{|(\boldsymbol{r}_{Sun-p}\times\hat{z})\times\boldsymbol{r}_{Sun-p}|}\begin{Bmatrix} -(x-x_{Sun})z \\ -yz \\ y^2+(x-x_{Sun})^2 \end{Bmatrix} \\ + \quad & \frac{\sin\alpha\sin\delta}{|\boldsymbol{r}_{Sun-p}\times\hat{z}|}\begin{Bmatrix} y \\ -(x-x_{Sun}) \\ 0 \end{Bmatrix},\end{aligned} \tag{C.27}$$

[1] $\rho_s = 1$ and $\rho_a = \rho_d = 0$

where $|\boldsymbol{r}_{Sun-p}|$ is given by:

$$|\boldsymbol{r}_{Sun-p}| = \sqrt{(x - x_{Sun})^2 + y^2 + z^2}, \tag{C.28}$$

while, $|\boldsymbol{r}_{Sun-p} \times \hat{z}|$ is defined as:

$$|\boldsymbol{r}_{Sun-p} \times \hat{z}| = \sqrt{(x - x_{Sun})^2 + y^2}. \tag{C.29}$$

Finally, $|(\boldsymbol{r}_{Sun-p} \times \hat{z}) \times \boldsymbol{r}_{Sun-p}|$ is obtained as:

$$|(\boldsymbol{r}_{Sun-p} \times \hat{z}) \times \boldsymbol{r}_{Sun-p}| = \sqrt{(x - x_{Sun})^2 z^2 + y^2 z^2 + ((x - x_{Sun})^2 + y^2)^2}. \tag{C.30}$$

C.5 Collinear Lagrangian points computation

In this section, the fifth-order polynomial for the computation of the collinear libration points is derived. The two celestial bodies selected are the Sun and the Earth; however, the solution holds for different values of μ. In case of SL_1, $r_{Sun-p} = x_{SL_1} + \mu$ and $r_{Earth-p} = 1 - \mu - x_{SL_1}$. By substituting the value of r_{Sun-p}, $r_{Earth-p}$, x_{Sun} and x_{Earth}, Eq. (3.58) turns into:

$$x_{SL_1} - \frac{(1-\beta)(1-\mu)(x_{SL_1} + \mu)}{(x_{SL_1} + \mu)^3} - \frac{\mu(x_{SL_1} + \mu - 1)}{(1 - \mu - x_{SL_1})^3} = 0. \tag{C.31}$$

The Eq. (C.31) can be simplified as follow:

$$x_{SL_1} - \frac{(1-\beta)(1-\mu)}{(x_{SL_1} + \mu)^2} + \frac{\mu}{(x_{SL_1} + \mu - 1)^2} = 0, \tag{C.32}$$

and, it is also possible to rewrite Eq. (C.32) as:

$$\frac{x_{SL_1}(x_{SL_1} + \mu)^2(x_{SL_1} + \mu - 1)^2 - (1-\beta)(1-\mu)(x_{SL_1} + \mu - 1)^2 + \mu(x_{SL_1} + \mu)^2}{(x_{SL_1} + \mu)^2(x_{SL_1} + \mu - 1)^2} = 0. \tag{C.33}$$

In order to find the position of SL_1 with respect to the Earth (i.e. smaller celestial body), the expression of $x_{SL_1} = 1 - \mu - \gamma_1$ should be substituted in Eq. (C.33):

$$(1 - \mu - \gamma_1)(1 - \gamma_1)^2(-\gamma_1)^2 - (1-\beta)(1-\mu)(-\gamma_1)^2 + \mu(1 - \gamma_1)^2 = 0. \tag{C.34}$$

The final expression of the fifth-order SL_1 polynomial is:

$$\gamma_1^5 - (3 - \mu)\gamma_1^4 + (3 - 2\mu)\gamma_1^3 - (\mu + (1-\mu)\beta)\gamma_1^2 + 2\mu\gamma_1 - \mu = 0. \tag{C.35}$$

In case of SL_2, $r_1 = x_{SL_2} + \mu$ and $r_2 = -1 + \mu + x_{SL_2}$. By substituting the value of r_{Sun-p}, $r_{Earth-p}$, x_{Sun} and x_{Earth}, the Eq. (3.58) turns into Eq.(C.36):

$$x_{SL_2} - \frac{(1-\beta)(1-\mu)(x_{SL_2}+\mu)}{(x_{SL_2}+\mu)^3} - \frac{\mu(x_{SL_2}+\mu-1)}{(-1+\mu+x_{SL_2})^3} = 0. \tag{C.36}$$

The Eq. (C.36) can be simplified as follow

$$x_{SL_2} - \frac{(1-\beta)(1-\mu)}{(x_{SL_2}+\mu)^2} - \frac{\mu}{(x_{SL_2}+\mu-1)^2} = 0. \tag{C.37}$$

Again, Eq. (C.37) should be written as:

$$\frac{x_{SL_2}(x_{SL_2}+\mu)^2(x_{SL_2}+\mu-1)^2 - (1-\beta)(1-\mu)(x_{SL_2}+\mu-1)^2 - \mu(x_{SL_2}+\mu)^2}{(x_{SL_2}+\mu)^2(x_{SL_2}+\mu-1)^2} = 0. \tag{C.38}$$

The position of SL_2 with respect to the Earth can be found by substituting the expression of $x_{SL_2} = 1 - \mu + \gamma_2$ in the equation Eq. (C.38):

$$(1-\mu+\gamma_2)(1+\gamma_2)^2(\gamma_2)^2 - (1-\beta)(1-\mu)(\gamma_2)^2 - \mu(1+\gamma_2)^2 = 0. \tag{C.39}$$

The final expression of the fifth-order SL_2 polynomial is:

$$\gamma_2^5 + (3-\mu)\gamma_2^4 + (3-2\mu)\gamma_2^3 + (-\mu+\beta(1-\mu))\gamma_2^2 - 2\mu\gamma_2 - \mu = 0. \tag{C.40}$$

In case of SL_3, $r_{Sun-p} = -x_{SL_3} - \mu$ and $r_{Earth-p} = 1 - \mu - x_{SL_3}$. By substituting the value of r_{Sun-p}, $r_{Earth-p}$, x_{Sun} and x_{Earth}, the equation Eq.(3.58) turns into:

$$x_{SL_3} - \frac{(1-\beta)(1-\mu)(x_{SL_3}+\mu)}{(-x_{SL_3}-\mu)^3} - \frac{\mu(x_{SL_3}+\mu-1)}{(1-\mu-x_{SL_3})^3} = 0. \tag{C.41}$$

The Eq. (C.41) can be simplified as follow

$$x_{SL_3} + \frac{(1-\beta)(1-\mu)}{(x_{SL_3}+\mu)^2} + \frac{\mu}{(x_{SL_3}+\mu-1)^2} = 0. \tag{C.42}$$

Finally, the Eq. (C.42) has been written as:

$$\frac{x_{SL_3}(x_{SL_3}+\mu)^2(x_{SL_3}+\mu-1)^2 + (1-\beta)(1-\mu)(x_{SL_3}+\mu-1)^2 + \mu(x_{SL_3}+\mu)^2}{(x_{SL_3}+\mu)^2(x_{SL_3}+\mu-1)^2} = 0. \tag{C.43}$$

In order to find the position of SL_3 with respect to the Sun (i.e. bigger celestial body), the expression of $x_{SL_3} = -\mu - \gamma_3$ can be substituted in Eq. (C.43):

$$(-\mu-\gamma_3)(-\gamma_3)^2(-1-\gamma_3)^2 + (1-\beta)(1-\mu)(-1-\gamma_3)^2 + \mu(-\gamma_3)^2 = 0. \tag{C.44}$$

The final expression of the fifth-order SL_3 polynomial is:

$$\gamma_3^5+(2+\mu)\gamma_3^4+(1+2\mu)\gamma_3^3-(1-\beta)(1-\mu)\gamma_3^2-2(1-\beta)(1-\mu)\gamma_3-(1-\beta)(1-\mu)=0. \quad \text{(C.45)}$$

C.6 Double derivatives of the total potential, V

The second derivatives of the potential V are:

- In the x-axis, V_{xx}:

$$V_{xx}=1-\frac{\mu_{Sun}}{r_{Sun-p}^3}\left[1-\frac{3(x-x_1)^2}{r_{Sun-p}^2}\right]-\frac{\mu_{Earth}}{r_{Earth-p}^3}\left[1-\frac{3(x-x_2)^2}{r_{Earth-p}^2}\right] \quad \text{(C.46)}$$

- In the y-axis, V_{yy}:

$$V_{yy}=1-\frac{\mu_{Sun}}{r_{Sun-p}^3}\left[1-\frac{3y^2}{r_{Sun-p}^2}\right]-\frac{\mu_{Earth}}{r_{Earth-p}^3}\left[1-\frac{3y^2}{r_{Earth-p}^2}\right] \quad \text{(C.47)}$$

- In the z-axis, V_{zz}:

$$V_{zz}=-\frac{\mu_{Sun}}{r_{Sun-p}^3}\left[1-\frac{3z^2}{r_{Sun-p}^2}\right]-\frac{\mu_{Earth}}{r_{Earth-p}^3}\left[1-\frac{3z^2}{r_{Earth-p}^2}\right]. \quad \text{(C.48)}$$

The cross derivative in x and y, V_{xy} is:

$$V_{xy}=\mu_{Sun}\frac{3(x-x_1)y}{r_{Sun-p}^5}+\mu_{Earth}\frac{3(x-x_2)y}{r_{Earth-p}^5}. \quad \text{(C.49)}$$

The cross derivative in x and z, V_{xz} is:

$$V_{xz}=\mu_{Sun}\frac{3(x-x_1)z}{r_{Sun-p}^5}+\mu_{Earth}\frac{3(x-x_2)z}{r_{Earth-p}^5}. \quad \text{(C.50)}$$

The cross derivative in y and z, V_{yz} is:

$$V_{yz}=\mu_{Sun}\frac{3y\cdot z}{r_{Sun-p}^5}+\mu_{Earth}\frac{3y\cdot z}{r_{Earth-p}^5}. \quad \text{(C.51)}$$

C.7 Double derivatives of the solar radiation pressure acceleration, a^s

The double derivatives of the SRP acceleration is defined as:

$$\boldsymbol{a}^{\boldsymbol{s}}_{\boldsymbol{rr}} = K \cdot \boldsymbol{N_{rr}}, \tag{C.52}$$

where K is defined as:

$$K = \beta \frac{\mu_{Sun}}{r^2_{Sun-p}} \cos^2 \alpha, \tag{C.53}$$

and the matrix $\boldsymbol{N_{rr}}$ is defined as:

$$\boldsymbol{N_{rr}} = \begin{bmatrix} \hat{N}_{xx} & \hat{N}_{xy} & \hat{N}_{xz} \\ \hat{N}_{yx} & \hat{N}_{yy} & \hat{N}_{yz} \\ \hat{N}_{zx} & \hat{N}_{zy} & \hat{N}_{zz} \end{bmatrix}. \tag{C.54}$$

The components of matrix $\boldsymbol{N_{rr}}$ are defined as:

- $\hat{N}_{xx}$:

$$\begin{aligned} \hat{N}_{xx} = \; & -\frac{2(x-x_{Sun})\hat{N}_x}{r^2_{Sun-p}} + \frac{\cos\alpha(y^2+z^2)}{r^3_{Sun-p}} - \frac{\sin\alpha\sin\delta y(x-x_{Sun})}{|r_{Sun-p}\times z|^3} \\ & + \frac{\sin\alpha\cos\delta z((x-x_{Sun})^4 - y^2z^2 - y^4)}{|(r_{Sun-p}\times\hat{z})\times r_{Sun-p}|^3}; \end{aligned} \tag{C.55}$$

- $\hat{N}_{xy}$:

$$\begin{aligned} \hat{N}_{xy} = \; & -\frac{2y\hat{N}_x}{r^2_{Sun-p}} - \frac{\cos\delta(x-x_{Sun})y}{r^3_{Sun-p}} + \frac{\sin\alpha\sin\delta(x-x_{Sun})^2}{|r_{Sun-p}\times\hat{z}|^3} \\ & + \frac{\sin\alpha\cos\delta(x-x_{Sun})yz(2(x-x_{Sun})^2+2y^2+z^2)}{|(r_{Sun-p}\times\hat{z})\times r_{Sun-p}|^3}; \end{aligned} \tag{C.56}$$

- $\hat{N}_{xz}$:

$$\hat{N}_{xz} = -\frac{2z\hat{N}_x}{r^2_{Sun-p}} - \frac{\cos\alpha(x-x_{Sun})z}{r^3_{Sun-p}} - \frac{\sin\alpha\cos\delta(x-x_{Sun})((x-x_{Sun})^2+y^2)^2}{|(r_{Sun-p}\times\hat{z})\times r_{Sun-p}|^3}; \tag{C.57}$$

- $\hat{N}_{yx}$:

$$\begin{aligned} \hat{N}_{yx} = \; & -\frac{2(x-x_{Sun})\hat{N}_y}{r^2_{Sun-p}} - \frac{\cos\alpha(x-x_{Sun})y}{r^3_{Sun-p}} - \frac{\sin\alpha\sin\delta y^2}{|r_{Sun-p}\times\hat{z}|^3} \\ & + \frac{\sin\alpha\cos\delta(x-x_{Sun})yz(2(x-x_{Sun})^2+2y^2+z^2)}{|(r_{Sun-p}\times\hat{z})\times r_{Sun-p}|^3}; \end{aligned} \tag{C.58}$$

- $\hat{N}_{yy}$:

$$\begin{aligned} \hat{N}_{yy} = \; & -\frac{2y\hat{N}_y}{r^2_{sun-p}} + \frac{\cos\alpha((x-x_{Sun})^2+z^2)}{r^3_{Sun-p}} + \frac{\sin\alpha\sin\delta y^2}{|r_{Sun-p}\times\hat{z}|^3} \\ & - \frac{\sin\alpha\cos\delta z((x-x_{Sun})^2(z^2+(x-x_{Sun})^2) - y^4)}{|(r_{Sun-p}\times\hat{z})\times r_{Sun-p}|^3}; \end{aligned} \tag{C.59}$$

- $\hat{N}_{yz}$:

$$\hat{N}_{yz} = -\frac{2z\hat{N}_y}{r^2_{Sun-p}} - \frac{\cos\alpha zy}{r^3_{Sun-p}} - \frac{\sin\alpha\cos\delta y((x-x_{Sun})^2+y^2)^2}{|(r_{Sun-p}\times\hat{z})\times r_{Sun-p}|^3}; \tag{C.60}$$

- $\hat{N}_{zx}$:

$$\hat{N}_{zx} = -\frac{2(x-x_{Sun})\hat{N}_z}{r^2_{Sun-p}} - \frac{\cos\alpha(x-x_{Sun})z}{r^3_{Sun-p}} + \frac{\sin\alpha\cos\delta(x-x_{Sun})z^2((x-x_{Sun})^2+y^2)}{|(r_{Sun-p}\times\hat{z})\times r_{Sun-p}|^3}; \tag{C.61}$$

- $\hat{N}_{zy}$:

$$\hat{N}_{zy} = -\frac{2y\hat{N}_z}{r^2_{Sun-p}} - \frac{\cos\alpha yz}{r^3_{Sun-p}} + \frac{\sin\alpha\cos\delta yz^2((x-x_{Sun})^2+y^2)}{|(r_{Sun-p}\times\hat{z})\times r_{Sun-p}|^3}; \tag{C.62}$$

- $\hat{N}_{zz}$:

$$\hat{N}_{zz} = -\frac{2z\hat{N}_z}{r^2_{Sun-p}} + \frac{\cos\alpha((x-x_{Sun})^2+y^2)}{r^3_{Sun-p}} - \frac{\sin\alpha\cos\delta z((x-x_{Sun})^2+y^2)^2}{|(r_{Sun-p}\times\hat{z})\times r_{Sun-p}|^3}. \tag{C.63}$$

C.8 Double derivatives of the total potential at the equilibrium points, $\bar{V}^*$

In this case, the system is still conservative and for a Sun-pointing sail the double derivatives of the potential are:

- L_1: $\bar{V}^*_{xy} = \bar{V}^*_{xz} = \bar{V}^*_{yz} = 0$ and:

$$\bar{V}^*_{xx} = 1 - 2\left[\frac{(\mu-1)(1-\beta)}{|\gamma_1-1|^3} - \frac{\mu}{\gamma_1^3}\right] = 1 + 2c_{2,\beta}, \tag{C.64}$$

$$\bar{V}^*_{yy} = 1 - \frac{(1-\mu)(1-\beta)}{|\gamma_1-1|^3} - \frac{\mu}{\gamma_1^3} = 1 - c_{2,\beta}, \tag{C.65}$$

and

$$\bar{V}^*_{zz} = -\frac{(1-\mu)(1-\beta)}{|\gamma_1-1|^3} - \frac{\mu}{\gamma_1^3} = -c_{2,\beta}; \tag{C.66}$$

where $c_{2,\beta}$ is:

$$c_{2,\beta} = \frac{(1-\mu)(1-\beta)}{|\gamma_1-1|^3} + \frac{\mu}{\gamma_1^3}. \tag{C.67}$$

- L_2: $\bar{V}^*_{xy} = \bar{V}^*_{xz} = \bar{V}^*_{yz} = 0$ and:

$$\bar{V}^*_{xx} = 1 - 2\left[\frac{(\mu-1)(1-\beta)}{|\gamma_2+1|^3} - \frac{\mu}{\gamma_2^3}\right] = 1 + 2c_{2,\beta}, \tag{C.68}$$

$$\bar{V}^*_{yy} = 1 - \frac{(1-\mu)(1-\beta)}{|\gamma_2+1|^3} - \frac{\mu}{\gamma_2^3} = 1 - c_{2,\beta}, \tag{C.69}$$

and

$$\bar{V}^*_{zz} = -\frac{(1-\mu)(1-\beta)}{|\gamma_2+1|^3} - \frac{\mu}{\gamma_2^3} = -c_{2,\beta}; \tag{C.70}$$

where $c_{2,\beta}$ is:

$$c_{2,\beta} = \frac{(1-\mu)(1-\beta)}{|\gamma_2+1|^3} + \frac{\mu}{\gamma_2^3}. \tag{C.71}$$

- L_3: $\bar{V}^*_{xy} = \bar{V}^*_{xz} = \bar{V}^*_{yz} = 0$ and:

$$\bar{V}^*_{xx} = 1 - 2\left[\frac{(\mu-1)(1-\beta)}{\gamma_3^3} - \frac{\mu}{|\gamma_3+1|^3}\right] = 1 + 2c_{2,\beta}, \tag{C.72}$$

$$\bar{V}^*_{yy} = 1 - \frac{(1-\mu)(1-\beta)}{\gamma_3^3} - \frac{\mu}{|\gamma_3+1|^3} = 1 - c_{2,\beta}, \tag{C.73}$$

and

$$\bar{V}^*_{zz} = -\frac{(1-\mu)(1-\beta)}{\gamma_3^3} - \frac{\mu}{|\gamma_3+1|^3} = -c_{2,\beta}; \tag{C.74}$$

where $c_{2,\beta}$ is:

$$c_{2,\beta} = \frac{(1-\mu)(1-\beta)}{\gamma_3^3} + \frac{\mu}{|\gamma_3+1|^3}. \tag{C.75}$$

C.9 State transition matrix

The state transition matrix $\boldsymbol{\Phi}$ gives the linear relationship between a small initial and a final displacement:

$$\delta x(t_1) = \boldsymbol{\Phi}(\boldsymbol{X}_0, t_1)\delta x(t_0), \tag{C.76}$$

where, $\boldsymbol{\Phi}(\boldsymbol{X}_0, t_1)$ is defined as in Eq. (C.77) and $\phi(t_1, x_0)$ is its flow map:

$$\boldsymbol{\Phi}(\boldsymbol{X}_0, t_1) = \frac{\partial \phi(t_1, x_0)}{\partial x_0}. \tag{C.77}$$

The state transition matrix can be computed only numerically by means of the dynamical linearised equations, and it becomes important when using the differential correction, computing the manifolds and design the Hamiltonian structure preserving control:

$$\dot{\boldsymbol{\Phi}}(\boldsymbol{X}_0, t) = \boldsymbol{A}\boldsymbol{\Phi}(\boldsymbol{X}_0, t); \tag{C.78}$$

where, the matrix $\boldsymbol{A}$ is defined as in Eq. (3.88).

When, $t = t_0$ the state transition matrix is an identity so that $\boldsymbol{\Phi}(\boldsymbol{X}_0, t_0) = \boldsymbol{I}$. On the other hand, when $t = T$ the state transition matrix after one period, T is known as the monodromy matrix $\boldsymbol{M} = \boldsymbol{\Phi}(T)$ of the periodic orbit (PO). It determines if initial perturbations decay or grow, so this matrix becomes important when studying the PO stability.

C.10 Differential correction algorithm in x_0 and $\dot{y}_0$

For the condition of a periodic orbit in 3D, the initial guess is located on the $x-z$ plane with a component of velocity along the y-axis. The $x-z$ plane is the plane of symmetry of the orbit, where the position in y, the velocity in x and in y should be zero at $t_0 = 0$.

The state vectors are respectively defines as: $\boldsymbol{X}(t_0 = 0) = \{x(t_0), 0, z(t_0), 0, \dot{y}(t_0), 0\}$ and $\boldsymbol{X}(t_1 = \frac{T}{2}) = \{x(t_1), 0, z(t_1), 0, \dot{y}(t_1), 0\}$. The system of equations is now:

$$\begin{cases} \ddot{x} - 2\omega_0 \dot{y} = V_x + a_x^s \\ \ddot{y} + 2\omega_0 \dot{x} = V_y + a_y^s \\ \ddot{z} = V_z + a_z^s \end{cases} . \tag{C.79}$$

Where, V has been previously defined in Eq. (3.40). The six first-order equations can be rewritten by redefining the state vector as $\boldsymbol{X} = \{x_1, x_2, x_3, x_4, x_5, x_6\} = \{x, y, z, \dot{x}, \dot{y}, \dot{z}\}$ or more simply $\boldsymbol{X} = \{x_1, x_2, x_3, x_4, x_5, x_6\} = \{x, y, z, v_x, v_y, z_z\}$.

$$\begin{cases} \dot{x}_1 = x_4 \\ \dot{x}_2 = x_5 \\ \dot{x}_3 = x_6 \\ \dot{x}_4 = 2x_5 + \frac{\partial V}{\partial x_1} + \frac{\partial a^s}{\partial x_1} \\ \dot{x}_5 = -2x_4 + \frac{\partial V}{\partial x_2} + \frac{\partial a^s}{\partial x_2} \\ \dot{x}_6 = \frac{\partial V}{\partial x_3} + \frac{\partial a^s}{\partial x_3} \end{cases} . \tag{C.80}$$

The equations of motion can be represented in a compact way: $\dot{\boldsymbol{X}} = f(\boldsymbol{X})$. The solution to the differential equation is $\Phi(\boldsymbol{X}, t)$ (state transitional matrix), where $\Phi(\boldsymbol{X}, 0) = \boldsymbol{X}$ and $\partial\Phi(\boldsymbol{X}, t)/\partial t = f(\Phi(\boldsymbol{X}, t))$. The initial guess will be $\boldsymbol{X} = \{x, 0, z, 0, v_y, 0\}$ which is a necessary condition for having a symmetric and periodic orbit. In that way, $\Phi(\boldsymbol{X}, T_{1/2}) = \{x, 0, \tilde{z}, \tilde{v}_x, \tilde{v}_y, \tilde{v}_z\}$. The differential correction aims to have $\tilde{v}_x = 0$ and $\tilde{v}_z = 0$, and it will change the initial guess in v_{y_0} and x_0 by having fixed the initial position in z_0 until it converges after half a period:

$$\Phi(\boldsymbol{X} + \Delta\boldsymbol{X}, T_{1/2} + \Delta T) = \Phi(\boldsymbol{X}, T_{1/2}) + \left[\frac{\partial \boldsymbol{\Phi}(\boldsymbol{X}, T_{1/2})}{\partial \boldsymbol{X}}\right] \Delta\boldsymbol{X} + \frac{\partial\Phi(\boldsymbol{X}, T_{1/2})}{\partial t}\Delta t. \tag{C.81}$$

The choice is restricted to the initial condition so that $\Delta\boldsymbol{X} = \{\Delta x, 0, \Delta z, 0, \Delta v_y, 0\}$ and the system to solve is:

$$\left[\frac{\partial \boldsymbol{\Phi}(\boldsymbol{X}, T_{1/2})}{\partial \boldsymbol{X}}\right] \begin{Bmatrix} \Delta x \\ 0 \\ \Delta z \\ 0 \\ \Delta v_y \\ 0 \end{Bmatrix} + \boldsymbol{f}(\Phi(\boldsymbol{X}, T_{1/2}))\Delta t = \begin{Bmatrix} x^* \\ 0 \\ z^* \\ 0 \\ v_y^* \\ 0 \end{Bmatrix} - \begin{Bmatrix} x \\ 0 \\ \tilde{z} \\ \tilde{v}_x \\ \tilde{v}_y \\ \tilde{v}_z \end{Bmatrix}; \tag{C.82}$$

where,

$$\left[\frac{\partial \boldsymbol{\Phi}(\boldsymbol{X}, T_{1/2})}{\partial \boldsymbol{X}}\right] = \begin{bmatrix} \phi_{11} & \phi_{12} & \phi_{13} & \phi_{14} & \phi_{15} & \phi_{16} \\ \phi_{21} & \phi_{22} & \phi_{23} & \phi_{24} & \phi_{25} & \phi_{26} \\ \phi_{31} & \phi_{32} & \phi_{33} & \phi_{34} & \phi_{35} & \phi_{36} \\ \phi_{41} & \phi_{42} & \phi_{43} & \phi_{44} & \phi_{45} & \phi_{46} \\ \phi_{51} & \phi_{52} & \phi_{53} & \phi_{54} & \phi_{55} & \phi_{56} \\ \phi_{61} & \phi_{62} & \phi_{63} & \phi_{64} & \phi_{65} & \phi_{66} \end{bmatrix}. \tag{C.83}$$

The system to solve is:

$$\begin{cases} \phi_{21}\Delta x + \phi_{23}\Delta z + \phi_{25}\Delta v_y + f_2\Delta t = 0 \\ \phi_{41}\Delta x + \phi_{43}\Delta z + \phi_{45}\Delta v_y + f_4\Delta t = -\tilde{v}_x \\ \phi_{61}\Delta x + \phi_{63}\Delta z + \phi_{65}\Delta v_y + f_6\Delta t = -\tilde{v}_z \end{cases}. \tag{C.84}$$

In Eq. (C.84), Δx, Δz, Δv_y and Δt are the unknown. Having fixed the initial condition in z where $\Delta z = 0$, now the system of Eq. (C.84) are three equations in three unknowns. This will provide the position along the x-axis, the velocity along the y-axis and the half orbit period. Δt is computed by

$$\Delta t = -\frac{\phi_{21}\Delta x + \phi_{25}\Delta v_y}{f_2}. \tag{C.85}$$

By substituting Δt (Eq. (C.85)) in the second and the third equations of Eq. (C.84). The system can be simplified as:

$$\begin{cases} A\Delta x + B\Delta v_y = -\tilde{v}_x \\ C\Delta x + D\Delta v_y = -\tilde{v}_z \end{cases}. \tag{C.86}$$

In Eq. (C.86), A, B, C and D are:

$$\begin{cases} A = (\phi_{41} - \frac{f_4}{f_2}\phi_{21}) \\ B = (\phi_{45} - \frac{f_4}{f_2}\phi_{25}) \\ C = (\phi_{61} - \frac{f_6}{f_2}\phi_{21}) \\ D = (\phi_{65} - \frac{f_6}{f_2}\phi_{25}) \end{cases}. \tag{C.87}$$

Thus, Δv_y and Δx are respectively:

$$\Delta v_y = \frac{(-\tilde{v}_z + \frac{C}{A}\tilde{v}_x)}{(D - \frac{C \cdot B}{A})} \tag{C.88}$$

and,

$$\Delta x = -\frac{(\tilde{v}_x + B)}{A}\Delta v_y. \tag{C.89}$$

Then, at every new iteration the initial guess is modified as follow:

$$\boldsymbol{X}^{i+1} = \boldsymbol{X}^i + \Delta\boldsymbol{X} = \left\{ \begin{array}{c} x^i \\ 0 \\ z^i \\ 0 \\ v_y^i \\ 0 \end{array} \right\} + \left\{ \begin{array}{c} \Delta x \\ 0 \\ 0 \\ 0 \\ \Delta v_y \\ 0 \end{array} \right\}. \tag{C.90}$$

C.11 Differential correction algorithm in E_0

The differential correction algorithm is now modified for having x-axis symmetric periodic orbit with E_0 fixed. The state vector is now augmented with the energy as $\boldsymbol{X}(t) = \{x(t), y(t), \dot{x}(t), \dot{y}(t), E(t)\}$. By looking for x-axis symmetric and periodic solution, the position in y and the velocity in x should be zero at t_0 and $t_1 = T/2$: $\boldsymbol{X}(t_0) = \{x(t_0), 0, 0, \dot{y}(t_0), E(t_0)\}$ and $\boldsymbol{X}(t_1) = \{x(t_1), 0, 0, \dot{y}(t_1), E(t_1)\}$. Then, the equation of the energy derivative Eq. (C.91) should be added to the dynamic equations Eq. (C.79):

$$\dot{E} = \ddot{x}\dot{x} + 2\dot{y}\dot{x} + V_x\dot{x} + a_x^s\dot{x} + \ddot{y}\dot{y} - 2\dot{x}\dot{y} + V_y\dot{y} + a_y^s\dot{y}. \tag{C.91}$$

The four first-order equations can be written by redefining the state vector as $\boldsymbol{X} = \{x_1, x_2, x_3, x_4, x_5\} = \{x, y, \dot{x}, \dot{y}, E\}$ or more simply $\boldsymbol{X} = \{x_1, x_2, x_3, x_4, x_5\} = \{x, y, v_x, v_y, E\}$ and the equations of motion are:

$$\left\{ \begin{array}{l} \dot{x}_1 = x_3 \\ \dot{x}_2 = x_4 \\ \dot{x}_3 = 2x_4 + \frac{\partial V}{\partial x_1} + \frac{\partial a^s}{\partial x_1} \\ \dot{x}_4 = -2x_3 + \frac{\partial V}{\partial x_2} + \frac{\partial a^s}{\partial x_2} \\ \dot{x}_5 = \dot{x}_3 x_3 + V_x x_3 + a_x^s x_3 + \dot{x}_4 x_4 + V_y x_4 + a_y^s x_4 \end{array} \right. . \tag{C.92}$$

As before, the equation of motion can be written in a compact way: $\dot{\boldsymbol{X}} = f(\boldsymbol{X})$. The solution of the differential equation is $\Phi(\boldsymbol{X}, t)$ (state transitional matrix), where $\Phi(\boldsymbol{X}, 0) = \boldsymbol{X}$ and $\partial\Phi(\boldsymbol{X}, t)/\partial t = f(\Phi(\boldsymbol{X}, t))$. The initial guess will be $\boldsymbol{X} = \{x, 0, 0, v_y, E\}$, which is a necessary condition for having a symmetric and periodic orbit. In that way, $\Phi(\boldsymbol{X}, T_{1/2}) = \{\tilde{x}, 0, \tilde{v}_x, \tilde{v}_y, \tilde{E}\}$. The differential correction aims to have $\tilde{v}_x = 0$ and $\tilde{E} = E^*$, and it will change the initial guess in v_{y_0} and in x_0 by having fixed the initial energy E_0 until it converges to a null velocity in x after half a period. The choice of the initial condition is restricted to $\Delta\boldsymbol{X} = \{\Delta x, 0, 0, \Delta v_y, \Delta E\}$ and solve the following

equations:

$$\left[\frac{\partial \boldsymbol{\Phi}(\boldsymbol{X}, T_{1/2})}{\partial \boldsymbol{X}}\right] \begin{Bmatrix} \Delta x \\ 0 \\ 0 \\ \Delta v_y \\ \Delta E \end{Bmatrix} + \boldsymbol{f}(\Phi(\boldsymbol{X}, T_{1/2}))\Delta t = \begin{Bmatrix} x^* \\ 0 \\ 0 \\ v_y^* \\ E^* \end{Bmatrix} - \begin{Bmatrix} \tilde{x} \\ 0 \\ \tilde{v}_x \\ \tilde{v}_y \\ \tilde{E} \end{Bmatrix}, \tag{C.93}$$

where, the derivative in $\boldsymbol{\Phi}$ is:

$$\left[\frac{\partial \boldsymbol{\Phi}(\boldsymbol{X}, T_{1/2})}{\partial \boldsymbol{X}}\right] = \begin{bmatrix} \phi_{11} & \phi_{12} & \phi_{13} & \phi_{14} & \phi_{15} \\ \phi_{21} & \phi_{22} & \phi_{23} & \phi_{24} & \phi_{25} \\ \phi_{31} & \phi_{32} & \phi_{33} & \phi_{34} & \phi_{35} \\ \phi_{41} & \phi_{42} & \phi_{43} & \phi_{44} & \phi_{45} \\ \phi_{51} & \phi_{52} & \phi_{53} & \phi_{54} & \phi_{55} \end{bmatrix}, \tag{C.94}$$

and the system turns into:

$$\begin{cases} \phi_{21}\Delta x + \phi_{24}\Delta v_y + \phi_{25}\Delta E + f_2\Delta t = 0 \\ \phi_{31}\Delta x + \phi_{34}\Delta v_y + \phi_{35}\Delta E + f_3\Delta t = -\tilde{v}_x \\ \phi_{51}\Delta x + \phi_{54}\Delta v_y + \phi_{55}\Delta E + f_5\Delta t = E^* - \tilde{E} \end{cases}. \tag{C.95}$$

In Eq. (C.95), Δx, Δv_y, ΔE and Δt are four unknown. Having fixed the initial conditions in E, $\Delta E = 0$, so now Eq. (C.95) are three equations in three unknowns. This will provide the velocity along y-axis, the position in x and the half orbit period. Δt is defined as:

$$\Delta t = -\frac{\phi_{21}}{f_2}\Delta x - \frac{\phi_{24}}{f_2}\Delta v_y. \tag{C.96}$$

The Eq. (C.95) can be rewrite as Eq. (C.97)

$$\begin{cases} a\Delta x + b\Delta v_y = -\tilde{v}_x \\ a\Delta x + b\Delta v_y = E^* - \tilde{E} \end{cases}. \tag{C.97}$$

Where, $a = \phi_{31} - \frac{f_3}{f_2}\phi_{21}$, $b = \phi_{34} - \frac{f_3}{f_2}\phi_{24}$, $c = \phi_{51} - \frac{f_5}{f_2}\phi_{21}$ and $d = \phi_{54} - \frac{f_5}{f_2}\phi_{24}$.
Finally, Δx can be found as:

$$\Delta x = -\frac{b}{a}\left(d - \frac{cb}{a}\right)^{-1}\left(\frac{c\tilde{v}_x}{a} + E^* - \tilde{E}\right), \tag{C.98}$$

and Δv_y as:

$$\Delta v_y = \left(d - \frac{cb}{a}\right)^{-1}\left(\frac{c\tilde{v}_x}{a} + E^* - \tilde{E}\right) - \frac{\tilde{v}_x}{a}. \tag{C.99}$$

Then, at every new iteration the initial guess is modified as follow:

$$\boldsymbol{X}^{i+1} = \boldsymbol{X}^{i} + \Delta\boldsymbol{X} = \left\{ \begin{array}{c} x^i \\ 0 \\ 0 \\ v_y^i \\ E^i \end{array} \right\} + \left\{ \begin{array}{c} 0 \\ 0 \\ 0 \\ \Delta v_y \\ \Delta E \end{array} \right\}. \tag{C.100}$$

Appendix D

Elliptic Restricted Three-Body Problem

D.1 Description of the primaries motion: Kepler problem

The equation of the ellipses, r, is defined in Eq. (B.1) of Section B.1. A synodic reference frame with angular velocity, $\dot{f} = df/dt^*$, is introduced. The angular motion is given by the third Kepler's Law as follow:

$$h = r^2 \frac{df}{dt^*}. \tag{D.1}$$

By knowing that the momentum of angular motion is defined as:

$$h = \sqrt{\mu a(1-e^2)}, \tag{D.2}$$

the angular velocity is now:

$$\frac{df}{dt^*} = \frac{h}{r^2} = \frac{\mu^{\frac{1}{2}}(1+ecos(f))^{\frac{1}{2}}}{a^{\frac{3}{2}}(1-e^2)^{\frac{3}{2}}}. \tag{D.3}$$

D.2 Coordinate transformation

For a planar motion in the x-y plane, the transformation from synodic to sidereal reference frames is given by:

$$\begin{cases} X = \bar{x}\cos(nt^*) - \bar{y}\sin(nt^*) \\ Y = \bar{x}\sin(nt^*) + \bar{y}\cos(nt^*) \end{cases}; \tag{D.4}$$

where, X and Y are the dimensional coordinates in a fix (sidereal) system. Instead $\bar{x}$ and $\bar{y}$ are the dimensional coordinate in a rotating (synodic) system. Eq. (D.4) is

written in a compact way as:

$$\boldsymbol{R} = \boldsymbol{A}\boldsymbol{r}; \tag{D.5}$$

where, the matrix $\boldsymbol{A}$ is defined as:

$$\boldsymbol{A} = \begin{bmatrix} \cos(nt^*) & -\sin(nt^*) \\ \sin(nt^*) & \cos(nt^*) \end{bmatrix} \tag{D.6}$$

However, it is simpler to introduce the complex vector Ψ by writing:

$$\Psi = \psi e^{if}; \tag{D.7}$$

where, Ψ is:

$$\Psi = X + iY, \tag{D.8}$$

and ψ is:

$$\psi = \bar{x} + i\bar{y} \tag{D.9}$$

D.3 Transformation to a non-uniformly synodic reference frames

By using the complex vector Ψ in Eq. (D.8), the equations of motion in a sidereal reference frame are:

$$\frac{d^2\Psi}{dt^{*2}} = -M_{Sun}G\frac{\Psi - \Psi_{Sun}}{R^3_{Sun}} - m_{Earth+Moon}G\frac{\Psi - \Psi_{Earth}}{R^3_{Earth}}. \tag{D.10}$$

By substituting Eq. (D.7) in Eq. (D.10), the left-hand side of Eq. (D.10) turns into:

$$\frac{d^2\Psi}{dt^{*2}} = \frac{d^2}{dt^{*2}}\left(\psi e^{if}\right) = \frac{d}{dt^*}\left[\frac{d}{dt^*}\left(\psi e^{if}\right)\right], \tag{D.11}$$

$$\frac{d}{dt^*}\left[\frac{d}{dt^*}\left(\psi e^{if}\right)\right] = \frac{d}{dt^*}\left[\frac{d\psi}{dt^*}e^{if} + \psi e^{if} i\frac{df}{dt^*}\right], \tag{D.12}$$

$$\frac{d}{dt^*}\left[\frac{d\psi}{dt^*}e^{if} + \psi e^{if} i\frac{df}{dt^*}\right] = \frac{d^2\psi}{dt^{*2}}e^{if} + \frac{d\psi}{dt^*}e^{if} i\frac{df}{dt^*} + \frac{d\psi}{dt^*}e^{if} i\frac{df}{dt^*} + \psi e^{if} i\frac{df}{dt^*} i\frac{df}{dt^*} + \psi e^{if} i\frac{d^2f}{dt^{*2}}, \tag{D.13}$$

and

$$\frac{d^2\Psi}{dt^{*2}} = \left[\frac{d^2\psi}{dt^{*2}} + 2i\frac{d\psi}{dt^*}\frac{df}{dt^*} + i^2\psi\left(\frac{df}{dt^*}\right)^2 + \psi i\frac{d^2f}{dt^{*2}}\right]e^{if}. \tag{D.14}$$

Instead, the right-hand side of Eq. (D.10) turns into:

$$\left[-GM_{Sun}\frac{(\psi-\psi_{Sun})}{R_{Sun}^3}-Gm_{Earth+Moon}\frac{(\psi-\psi_{Earth})}{R_{Earth}^3}\right]e^{if}. \tag{D.15}$$

By imposing Eq. (D.14) equal to Eq. (D.15), the following equality holds:

$$\begin{bmatrix}\left[\frac{d^2\psi}{dt^{*2}}+2i\frac{d\psi}{dt^*}\frac{df}{dt^*}+i^2\psi\left(\frac{df}{dt^*}\right)^2+\psi i\frac{d^2f}{dt^{*2}}\right]e^{if}= \\ \left[-GM_{Sun}\frac{(\psi-\psi_{Sun})}{R_{Sun}^3}-Gm_{Earth+Moon}\frac{(\psi-\psi_{Earth})}{R_{Earth}^3}\right]e^{if}\end{bmatrix}, \tag{D.16}$$

and

$$\frac{d^2\psi}{dt^{*2}}+2i\frac{d\psi}{dt^*}\frac{df}{dt^*}=-GM_1\frac{(\psi-\psi_{Sun})}{R_{Sun}^3}-Gm_{Earth+Moon}\frac{(\psi-\psi_{Earth})}{R_{Earth}^3}+\psi\left(\frac{df}{dt^*}\right)^2-\psi i\frac{d^2f}{dt^{*2}}\ ; \tag{D.17}$$

where, R_{Sun} and R_{Earth} are:

$$R_{Sun}=|\Psi-\Psi_{Sun}|=|\psi-\psi_{Sun}|=|\psi-\bar{x}_{Sun}|=|\bar{x}-\bar{x}_{Sun}+i\bar{y}| \tag{D.18}$$

and

$$R_{Earth}=|\Psi-\Psi_{Earth}|=|\psi-\psi_{Earth}|=|\psi-\bar{x}_{Earth}|=|\bar{x}-\bar{x}_{Earth}+i\bar{y}|, \tag{D.19}$$

respectively. Finally, Eq. (D.18) and Eq. (D.19) turn into:

$$R_{Sun}=\left[(\bar{x}-\bar{x}_{Sun})^2+\bar{y}\right]^{\frac{1}{2}} \tag{D.20}$$

and

$$R_{Earth}=\left[(\bar{x}-\bar{x}_{Earth})^2+\bar{y}\right]^{\frac{1}{2}}, \tag{D.21}$$

respectively. The complex component of the primaries are always on the real axis, and for the Russian convention (Szebehely and Giacaglia, 1964), it is possible to write:

$$\psi_{Sun}=\bar{x}_{Sun}=\frac{P_{Sun}}{1+e\cos f}, \tag{D.22}$$

and

$$\psi_{Earth}=\bar{x}_{Earth}=-\frac{P_{Earth}}{1+e\cos f}. \tag{D.23}$$

P_{Sun} and P_{Earth} are positives and their relation is [1]

$$\frac{P_{Sun}}{P_{Earth}}=\frac{a_{Sun}}{a_{Earth}}=\frac{m_{Earth+Moon}}{M_{Sun}}; \tag{D.24}$$

[1]For the CRTB, the balance between the gravitational and the centrifugal forces requires: $G\frac{M_{Sun}m_{Earth+Moon}}{l^2}=m_{Earth+Moon}d_{2CM}=M_{Sun}d_{1CM}$

where, a_{Sun} and a_{Earth} are the semimajor axis of the elliptic orbits of M_{Sun} and $m_{Earth+Moon}$. In case of, $f = nt^*$, $e = 0$, $P_{Sun} = a_{Sun} = d_{1CM}$ and $P_{Earth} = a_{Earth} = d_{2CM}$ these equations correspond to the circular restricted three body problem.

D.4 Transformation to dimensionless pulsating coordinates

The pulsating coordinates for the complex vector are:

$$\xi = \frac{\psi}{r} = \frac{\bar{x}}{r} + i\frac{\bar{y}}{r} = x + iy. \tag{D.25}$$

The primaries are fixed in the synodic reference frame and their coordinates are:

$$x_{Sun} = \frac{\bar{x}_{Sun}(1 + e\cos f)}{a(1 - e^2)} \tag{D.26}$$

and

$$x_{Earth} = \frac{\bar{x}_{Earth}(1 + e\cos f)}{a(1 - e^2)}. \tag{D.27}$$

By substituting Eq. (D.22-D.23) to Eq. (D.26-D.27), we have:

$$x_{Sun} = \frac{P_{Sun}}{a(1 - e^2)} = \frac{a_{Sun}(1 - e^2)}{a(1 - e^2)} = \frac{a_{Sun}}{a}, \tag{D.28}$$

and

$$x_{Earth} = -\frac{P_{Earth}}{a(1 - e^2)} = -\frac{a_{Earth}(1 - e^2)}{a(1 - e^2)} = -\frac{a_{Earth}}{a}. \tag{D.29}$$

For the American and European formulations, the primaries coordinates are:

$$x_{Sun} = -\frac{P_{Sun}}{a(1 - e^2)} = -\frac{a_{Sun}(1 - e^2)}{a(1 - e^2)} = -\frac{a_{Sun}}{a}, \tag{D.30}$$

and

$$x_{Earth} = \frac{P_{Earth}}{a(1 - e^2)} = \frac{a_{Earth}(1 - e^2)}{a(1 - e^2)} = \frac{a_{Earth}}{a}. \tag{D.31}$$

D.5 From var ψ and t^* to var x, y and f

By knowing that $\psi = \xi r$, it is possible to define:

$$\dot{\psi} = \dot{\xi}r + \xi\dot{r}, \tag{D.32}$$

and

$$\ddot{\psi} = \ddot{\xi}r + \dot{\xi}\dot{r} + \dot{\xi}\dot{r} + \xi\ddot{r}; \tag{D.33}$$

which, it is the first term of the left side of the Eq. (D.17) and $\dot{\xi} = d\xi/dt^*$. The true anomaly angle, f, was chosen as the independent variable as:

$$\frac{d}{dt^*} = \frac{df}{dt^*}\frac{d}{df}. \tag{D.34}$$

Thus,

$$\frac{d^2\psi}{dt^{*2}} = \frac{d^2\xi}{dt^{*2}}r + 2\frac{d\xi}{dt^*}\frac{dr}{dt^*} + \xi\frac{d^2r}{dt^{*2}}; \tag{D.35}$$

where ,

$$\frac{d^2\xi}{dt^{*2}}r = \frac{d}{dt^*}\left[\frac{df}{dt^*}\frac{d\xi}{df}\right]r = \left[\frac{d^2f}{dt^{*2}}\frac{d\xi}{df} + \left(\frac{df}{dt^*}\right)^2\frac{d^2\xi}{df^2}\right]r \tag{D.36}$$

and

$$2\frac{d\xi}{dt^*}\frac{dr}{dt^*} = 2\frac{df}{dt^*}\frac{d\xi}{df}\frac{dr}{dt^*} \tag{D.37}$$

therefore

$$\frac{d^2\psi}{dt^{*2}} = \left[\frac{d^2f}{dt^{*2}}\frac{d\xi}{df} + \left(\frac{df}{dt^*}\right)^2\frac{d^2\xi}{df^2}\right]r + 2\frac{df}{dt^*}\frac{d\xi}{df}\frac{dr}{dt^*} + \xi\frac{d^2r}{dt^{*2}}. \tag{D.38}$$

The second term on the left-hand side of Eq. (D.17) is:

$$2i\frac{df}{dt^*}\frac{d\psi}{dt^*} = 2i\frac{df}{dt^*}\left[\xi\frac{dr}{dt^*} + r\frac{d\xi}{df}\frac{df}{dt^*}\right]; \tag{D.39}$$

while, the right-hand side of Eq. (D.17) is:

$$-GM_{Sun}\frac{\xi - \xi_{Sun}}{r^2 r_{Sun}^3} - Gm_{Earth+Moon}\frac{\xi - \xi_{Earth}}{r^2 r_{Earth}^3}, \tag{D.40}$$

so

$$r_{Sun}^2 = |\xi - \xi_{Sun}|^2 = (x - x_{Sun})^2 + y^2 \tag{D.41}$$

and

$$r_{Earth}^2 = |\xi - \xi_{Earth}|^2 = (x - x_{Earth})^2 + y^2. \tag{D.42}$$

For the Russian formulation, the dimensionless primaries' coordinates are:

$$x_{Sun} = \frac{a_{Sun}}{a} = \frac{\mu a}{a} = \mu \tag{D.43}$$

and

$$x_{Earth} = -\frac{a_{Earth}}{a} = -\frac{(1-\mu)a}{a} = \mu - 1. \tag{D.44}$$

For the American and European formulation, the dimensionless primaries' coordinates are:

$$x_{Sun} = -\frac{a_{Sun}}{a} = -\frac{\mu a}{a} = -\mu, \tag{D.45}$$

and

$$x_{Earth} = \frac{a_{Earth}}{a} = \frac{(1-\mu)a}{a} = 1 - \mu. \tag{D.46}$$

Eq. (D.17) is written as:

$$\left[\frac{d^2f}{dt^{*2}}\frac{d\xi}{df}+\left(\frac{df}{dt^*}\right)^2\frac{d^2\xi}{df^2}\right]r+2\frac{df}{dt^*}\frac{d\xi}{df}\frac{dr}{dt^*}+\xi\frac{d^2r}{dt^{*2}}+2i\frac{df}{dt^*}\left[\xi\frac{dr}{dt^*}+r\frac{d\xi}{df}\frac{df}{dt^*}\right]= -GM_{Sun}\frac{\xi-\xi_{Sun}}{r^2r_{Sun}^3}-Gm_{Earth+Moon}\frac{\xi-\xi_{Earth}}{r^2r_{Earth}^3}+\xi r\left(\frac{df}{dt^*}\right)^2-i\xi r\frac{d^2f}{dt^{*2}} \quad (D.47)$$

so

$$r\left(\frac{df}{dt^*}\right)^2\left[\frac{d^2\xi}{df^2}+2i\frac{d\xi}{df}\right]+\xi\left[\frac{d^2r}{dt^{*2}}-r\left(\frac{df}{dt^*}\right)^2\right]+\left(\frac{d\xi}{df}\right)\left(r\frac{d^2f}{dt^{*2}}+2\frac{dr}{dt^*}\frac{df}{dt^*}\right) = -GM_{Sun}\frac{\xi-\xi_{Sun}}{r^2r_{Sun}^3}-Gm_{Earth+Moon}\frac{\xi-\xi_{Earth}}{r^2r_{Earth}^3}; \quad (D.48)$$

where, $r=\frac{a(1-e^2)}{1+e\cos f}$ which is the solution of the Kepler problem involving the two primaries. The angular momentum integral is defined as:

$$\left(r^2\frac{df}{dt^*}\right)^2=a(1-e^2)G(M_{Sun}+m_{Earth+Moon}); \quad (D.49)$$

while, the derivative of the angular momentum is:

$$r\frac{d^2f}{dt^{*2}}+2\frac{dr}{dt^*}\frac{df}{dt^*}=0. \quad (D.50)$$

The equations of motion are derived as:

$$\frac{d^2r}{dt^{*2}}-r\left(\frac{df}{dt^*}\right)^2=-\frac{G(M_{Sun}+m_{Earth+Moon})}{r^2}. \quad (D.51)$$

By substituting the integral of the angular momentum to Eq. (D.51), Eq. (D.51) turns into:

$$\frac{d^2r}{dt^{*2}}-r\left(\frac{df}{dt^*}\right)^2=-\frac{r^2}{a(1-e^2)}\left(\frac{df}{dt^*}\right)^2. \quad (D.52)$$

Now Eq. (D.48) over $r\left(\frac{df}{dt^*}\right)^2$ gives:

$$r\left(\frac{df}{dt^*}\right)^2=\frac{G(M_{Sun}+m_{Earth+Moon})a(1-e^2)}{r^3}; \quad (D.53)$$

where, Eq. (D.48) is written in a compact way as:

$$r\dot{f}^2\xi''+\xi(\ddot{r}-r\dot{f}^2)+\xi'(r\ddot{f}+2\dot{r}\dot{f})=-GM_{Sun}\frac{\xi-\xi_{Sun}}{r^2r_{Sun}^3}-Gm_{Earth+Moon}\frac{\xi-\xi_{Earth}}{r^2r_{Earth}^3}. \quad (D.54)$$

By combining Eq. (D.50) and Eq. (D.51), Eq. (D.54) turns into:

$$r\dot{f}^2\xi^{''}+r\dot{f}^2 2i\xi^{'}-\xi\frac{G(M_{Sun}+m_{Earth+Moon})}{r^2}=-GM_{Sun}\frac{\xi-\xi_{Sun}}{r^2r_{Sun}^3}-Gm_{Earth+Moon}\frac{\xi-\xi_{Earth}}{r^2r_{Earth}^3}. \tag{D.55}$$

Eq. (D.55) over $r\dot{f}^2$ gives:

$$\xi^{''}+2i\xi^{'}-\xi\frac{G(M_{Sun}+m_{Earth+Moon})}{r^2r\dot{f}^2}=-\frac{GM_{Sun}}{r\dot{f}^2}\frac{\xi-\xi_{Sun}}{r^2r_{Sun}^3}-\frac{Gm_{Earth+Moon}}{r\dot{f}^2}\frac{\xi-\xi_{Earth}}{r^2r_{Earth}^3}, \tag{D.56}$$

and by substituting the expression of $r\dot{f}^2$ in Eq. (D.56), Eq. (D.56) becomes:

$$\begin{array}{l}\xi^{''}+2i\xi^{'}-\xi\frac{r}{a(1-e^2)}=-\frac{M_{Sun}}{M_{Sun}+m_{Earth+Moon}}\frac{r}{a(1-e^2)}\frac{\xi-\xi_{Sun}}{r_{Sun}^3}\\ -\frac{m_{Earth+Moon}}{M_{Sun}+m_{Earth+Moon}}\frac{r}{a(1-e^2)}\frac{\xi-\xi_{Earth}}{r_{Earth}^3}\end{array}. \tag{D.57}$$

By knowing that $r=a(1-e^2)/(1+e\cos f)$, it is possible to write:

$$\begin{array}{rl}\xi^{''}+2i\xi^{'}-\frac{\xi}{1+e\cos f}= & -\frac{M_{Sun}}{M_{Sun}+m_{Earth+Moon}}\frac{1}{1+e\cos f}\frac{\xi-\xi_{Sun}}{r_{Sun}^3}\\ & -\frac{m_{Earth}}{M_{Sun}+m_{Earth+Moon}}\frac{1}{1+e\cos f}\frac{\xi-\xi_{Earth}}{r_{Earth}^3}\end{array}, \tag{D.58}$$

so

$$\xi^{''}+2i\xi^{'}=\frac{1}{1+e\cos f}\left[\xi-\mu_{Sun}\frac{\xi-\xi_{Sun}}{r_{Sun}^3}-\mu_{Earth}\frac{\xi-\xi_{Earth}}{r_{Earth}^3}\right]. \tag{D.59}$$

By recalling that ξ is the complex dimensionless coordinate $\xi=x+yi$, the equations of motion in dimensionless pulsating coordinate are:

$$\left\{\begin{array}{l}x^{''}-2y^{'}=\frac{1}{1+e\cos f}\left[x-\mu_{Sun}\frac{x-x_{Sun}}{r_{Sun}^3}-\mu_{Earth}\frac{x-x_{Earth}}{r_{Earth}^3}\right]\\ y^{''}+2x^{'}=\frac{1}{1+e\cos f}\left[y-\mu_{Sun}\frac{y}{r_{Sun}^3}-\mu_{Earth}\frac{y}{r_{Earth}^3}\right].\end{array}\right. \tag{D.60}$$

For the Russian formulation, r_{Sun} and r_{Earth} are:

$$r_{Sun}=\sqrt{(x-\mu)^2+y^2}, \tag{D.61}$$

and

$$r_{Earth}=\sqrt{(x+1-\mu)^2+y^2}, \tag{D.62}$$

respectively; while, for the American and European formulation, they correspond to:

$$r_{Sun}=\sqrt{(x+\mu)^2+y^2}, \tag{D.63}$$

and

$$r_{Earth}=\sqrt{(x+\mu-1)^2+y^2}, \tag{D.64}$$

respectively.

D.6 Spatial elliptical restricted three-body problem

In this section, the equations of motions are extended to the third dimension. This can be done as the third coordinate, z, does not take place in the transformation (since the rotation is along the z-axis). By knowing that:

$$z = \frac{\zeta}{r}, \tag{D.65}$$

the equations of motion along the z-axis in dimensional coordinates are:

$$\ddot{\zeta} = -\frac{GM_{Sun}(\zeta - \zeta_{Sun})}{R_{Sun}^3} - \frac{Gm_{Earth+Moon}(\zeta - \zeta_{Earth})}{R_{Earth}^3}. \tag{D.66}$$

Eq (D.65) is rewritten as:

$$\zeta = zr(f); \tag{D.67}$$

where, $r(f)$ is defined as:

$$r(f) = \frac{a(1-e^2)}{1 + e\cos(f)} = (1 + e\cos(f))^{-1}a(1-e^2). \tag{D.68}$$

By deriving Eq (D.67) two times in time, Eq. (D.67) becomes,

$$\dot{\zeta} = \dot{r}z + r\dot{z}, \tag{D.69}$$

for the first derivative and,

$$\ddot{\zeta} = \ddot{r}z + \dot{r}\dot{z} + \dot{r}\dot{z} + r\ddot{z}, \tag{D.70}$$

for the second derivative.

Given a vector, $\square$, the derivative of $\square$ in t^* is:

$$\dot{\square} = \frac{d\square}{dt^*} = \frac{df}{dt^*}\frac{d\square}{df} = \dot{f}\square'. \tag{D.71}$$

From Eq. (D.71), Eq (D.70) in dimensionless coordinates is:

$$\ddot{\zeta} = \ddot{r}z + 2\dot{r}\dot{f}z' + r\frac{d}{dt^*}\left[\dot{f}z'\right], \tag{D.72}$$

and

$$\ddot{\zeta} = \ddot{r}z + 2\dot{r}\dot{f}z' + r\left[\ddot{f}z' + \dot{f}^2z''\right]. \tag{D.73}$$

Eq. (D.73) is the left-hand side of the equations of motion along z and Eq. (D.73) over $r\dot{f}^2$ gives:

$$\frac{\ddot{r}z}{r\dot{f}^2} + \frac{2\dot{r}\dot{f}z'}{r\dot{f}^2} + \frac{r\ddot{f}z'}{r\dot{f}^2} + z'' = ... \tag{D.74}$$

and

$$z^{''} + \frac{\ddot{r}z}{r\dot{f}^2} + \frac{z^{'}}{\dot{f}^2 r}\left[2\dot{r}\dot{f} + r\ddot{f}\right] = ... \tag{D.75}$$

In Eq (D.75), the derivative of the angular momentum, $(r^2\dot{f})^2$, is zero $(2\dot{r}\dot{f} + r\ddot{f} = 0)$, thus Eq. (D.75) simplifies as:

$$z^{''} + \frac{\ddot{r}z}{r\dot{f}^2} = ... \tag{D.76}$$

The first derivative of Eq (D.68) is:

$$\dot{r} = \frac{ae(1-e^2)\sin f}{(1+e\cos f)^2}\dot{f}, \tag{D.77}$$

while, the second derivative over $r\dot{f}^2$ is:

$$\frac{\ddot{r}}{r\dot{f}^2} = \frac{ae(1-e^2)\sin f}{(1-e\cos f)^2}\frac{\ddot{f}}{r\dot{f}^2} + \frac{ae(1-e^2)\cos f}{(1+e\cos f)^2}\frac{1}{r} + \frac{2ae^2(1-e^2)(\sin f)^2}{(1+e\cos f)^3}\frac{1}{r}. \tag{D.78}$$

The first term on the right-hand side of Eq. (D.78) is simplified by the definition of $r = a(1-e^2)/(1+e\cos f)$ as:

$$\frac{ae(1-e^2)\sin f}{(1-e\cos f)^2}\frac{\ddot{f}}{r\dot{f}^2} = \frac{e\sin f}{(1-e\cos f)}\frac{\ddot{f}}{\dot{f}^2}. \tag{D.79}$$

$\dot{f}$ and $\ddot{f}$ over $\dot{f}^2$ are:

$$\dot{f} = \frac{G^{1/2}(M_{Sun} + m_{Earth+Moon})^{1/2}}{a^{3/2}(1-e^2)^{3/2}}(1+e\cos f)^2, \tag{D.80}$$

and

$$\frac{\ddot{f}}{\dot{f}^2} = -\frac{2e\sin f}{(1+e\cos f)}, \tag{D.81}$$

respectively. Finally, the first term on the right-hand side of Eq. (D.78) is:

$$\frac{ae(1-e^2)\sin f}{(1-e\cos f)^2}\frac{\ddot{f}}{r\dot{f}^2} = -\frac{2e\sin f}{1+e\cos f}. \tag{D.82}$$

The second term on the right-hand side of Eq. (D.78) is:

$$\frac{ae(1-e^2)\cos f}{(1+e\cos f)^2}\frac{1}{r} = \frac{e\cos f}{1+e\cos f}. \tag{D.83}$$

The third term on the right-hand side of Eq. (D.78) is:

$$\frac{2ae^2(1-e^2)(\sin f)^2}{(1+e\cos f)^3}\frac{1}{r} = \frac{2e^2(\sin f)^2}{(1+e\cos f)^2}. \tag{D.84}$$

Finally, Eq. (D.78) turns into:

$$\frac{\ddot{r}}{r\dot{f}^2} = \frac{e\cos f}{1+e\cos f} = 1 - \frac{1}{1+e\cos f}. \tag{D.85}$$

The equations of motion along z-axis are:

$$z'' + \left[1 - \frac{1}{1+e\cos f}\right] z = \left[-\frac{GM_{Sun}z}{r^2 r_{Sun}^3} - \frac{Gm_{Earth+Moon}z}{r^2 r_{Earth}^3}\right] \frac{1}{r\dot{f}^2}. \tag{D.86}$$

The first term on the right-hand side of Eq. (D.86) is:

$$-\frac{Gm_{Earth+Moon}z}{r^2 r_{Earth}^3}\frac{1}{r\dot{f}^2} = -\frac{\mu_{Earth}z}{(1+e\cos f)r_{Earth}^3}. \tag{D.87}$$

Finally, the equations of motion along z-axis are:

$$z'' + z = \frac{1}{1+e\cos f}\left[z - \frac{\mu_{Sun}}{r_{Sun}^3}z - \frac{\mu_{Earth}}{r_{Earth}^3}z\right]. \tag{D.88}$$

The system of equations of motion are in dimensionless, non-uniformly rotating and pulsating coordinates are:

$$\begin{cases} x'' - 2y' = \frac{1}{1+e\cos f}\left[x - \mu_{Sun}\frac{x-x_{Sun}}{r_{Sun}^3} - \mu_{Earth}\frac{x-x_{Earth}}{r_{Earth}^3}\right] \\ y'' + 2x' = \frac{1}{1+e\cos f}\left[y - \mu_{Sun}\frac{y}{r_{Sun}^3} - \mu_{Earth}\frac{y}{r_{Earth}^3}\right] \\ z'' + z = \frac{1}{1+e\cos f}\left[z - \frac{\mu_{Sun}}{r_{Sun}^3}z - \frac{\mu_{Earth}}{r_{Earth}^3}z\right] \end{cases}. \tag{D.89}$$

For the Russian formulation, r_{Sun} and r_{Earth} are:

$$r_{Sun} = \sqrt{(x-\mu)^2 + y^2 + z^2}, \tag{D.90}$$

and

$$r_{Earth} = \sqrt{(x+1-\mu)^2 + y^2 + z^2}, \tag{D.91}$$

respectively; while, for the American and European formulation, they are:

$$r_{Sun} = \sqrt{(x+\mu)^2 + y^2 + z^2}, \tag{D.92}$$

and

$$r_{Earth} = \sqrt{(x+\mu-1)^2 + y^2 + z^2}, \tag{D.93}$$

respectively.

Appendix E

Hamiltonian Structure Preserving and Floquét Mode Controllers

E.1 Hamiltonian structure preserving control law extended to the third dimension

The eigenvalues of the linearised dynamics are the solutions of the characteristic equations $D(\lambda) = |\boldsymbol{A} - \lambda \boldsymbol{I}| = 0$, where the characteristic polynomial is:

$$\Lambda^3 + b\ \Lambda^2 + c\ \Lambda + d = 0. \tag{E.1}$$

In Eq. (E.1), b, c and d are defined as:

$$\begin{cases} b = 4 - V_{xx} - V_{yy} - V_{zz} \\ c = -V_{xy}^2 - V_{xz}^2 + V_{xx}V_{yy} - V_{yz}^2 - 4V_{zz} + V_{xx}V_{zz} + V_{yy}V_{zz} \\ d = -|\boldsymbol{V_{rr}}| \end{cases} . \tag{E.2}$$

The aim of the controller is to place the poles on the imaginary axis, so an artificial centre manifold stabilises the periodic orbit by removing the stable and unstable manifolds (i.e. hyperbolic equilibrium). The discriminant of the equation must be > 0 in order to have three real and distinct roots:

$$\Delta = b^2\ c^2 - 4\ c^3 - 4\ b^3\ d - 27\ d^2 + 18\ b\ c\ d. \tag{E.3}$$

In order to have an instantaneous map of real eigenvalues and two pairs of imaginary eigenvalues, the polynomial in Eq. (E.1) must have one positive and two negative roots. If $\Delta > 0$ there are three real and distinct solutions. For a cubic polynomial, it is

possible to guarantee only one positive root by following the Descartes' rule of signs. Thus, $b > 0$, $c < 0$, $d < 0$ (or $|\boldsymbol{V_{rr}}| > 0$) and $\Delta > 0$. When, $\Delta < 0$ there are two couples of complex and conjugate roots and one real root. However, the extension to this case is not included yet in our analysis.

E.1.1 Eigenvalues of the characteristic polynomial

The solutions of Eq. (E.1) are (Spigel et al., 2013):

$$Q = \frac{3c - b^2}{9}, \quad R = \frac{9bc - 27d - 2b^3}{54}, \quad S = (R + \sqrt{Q^3 + R^2})^{1/3}, \quad T = (R - \sqrt{Q^3 + R^2})^{1/3}, \tag{E.4}$$

and

$$\begin{cases} \Lambda_1 & = S + T - \frac{b}{3} \\ \Lambda_2 & = -\frac{(S+T)}{2} - \frac{b}{3} + \frac{(S-T)\cdot i}{2} \\ \Lambda_3 & = -\frac{(S+T)}{2} - \frac{b}{3} - \frac{(S-T)\cdot i}{2} \end{cases}. \tag{E.5}$$

So now the six eigenvalues can be found as: $\lambda_1 = \sqrt{\Lambda_1}$, $\lambda_2 = -\sqrt{\Lambda_1}$, $\lambda_3 = \sqrt{\Lambda_2}$, $\lambda_4 = -\sqrt{\Lambda_2}$, $\lambda_5 = \sqrt{\Lambda_3}$ and $\lambda_6 = -\sqrt{\Lambda_3}$.

E.1.1.1 Eigenvectors of the characteristic polynomial

The eigenvectors can now be found by solving the system: $(\boldsymbol{A} - \lambda_i \boldsymbol{I}) \cdot \widehat{\boldsymbol{x}} = 0$, so:

$$\begin{cases} \dot{\widehat{x}} = \lambda_i \widehat{x} \\ \dot{\widehat{y}} = \lambda_i \widehat{y} \\ \dot{\widehat{z}} = \lambda_i \widehat{z} \\ (V_{xx} - \lambda_i^2)\widehat{x} + (V_{xy} + 2\omega_0 \lambda_i)\widehat{y} + V_{xz}\widehat{z} = 0 \\ (V_{xy} - 2\omega_0 \lambda_i)\widehat{x} + (V_{yy} - \lambda_i^2)\widehat{y} + V_{yz}\widehat{z} = 0 \\ V_{xz}\widehat{x} + V_{yz}\widehat{y} + (V_{zz} - \lambda_i^2)\widehat{z} = 0 \end{cases}. \tag{E.6}$$

Setting an arbitrary parameter for $\widehat{x} = 1$, one of the infinitive eigenvectors for λ_i can be determined. The interest here is in solving the following system:

$$\begin{cases} (V_{xx} - \lambda_i^2) + (V_{xy} + 2\omega_0 \lambda_i)\widehat{y} + V_{xz}\widehat{z} = 0 \\ (V_{xy} - 2\omega_0 \lambda_i) + (V_{yy} - \lambda_i^2)\widehat{y} + V_{yz}\widehat{z} = 0 \\ V_{xz} + V_{yz}\widehat{y} + (V_{zz} - \lambda_i^2)\widehat{z} = 0 \end{cases} \tag{E.7}$$

which has three equations and two unknowns. Thus, there are three different options to find the solution. The general eigenvector is defined as:

$$\begin{Bmatrix} \widehat{x} \\ \widehat{y} \\ \widehat{z} \\ \dot{\widehat{x}} \\ \dot{\widehat{y}} \\ \dot{\widehat{z}} \end{Bmatrix} = \begin{Bmatrix} 1 \\ u_i \\ u_{2_i} \\ \lambda_i \\ \lambda_i \cdot u_i \\ \lambda_i \cdot u_{2_i} \end{Bmatrix}. \tag{E.8}$$

In the case of solving the first two equations of Eq. (E.7), the solution is:

$$\widehat{y} = \frac{V_{xz}(V_{xy} - 2\omega_0\lambda_i) + V_{yz}(\lambda_i^2 - V_{xx})}{V_{yz}(V_{xy} + 2\omega_0\lambda_i) - V_{xz}(V_{yy} - \lambda_i^2)} = u_i, \tag{E.9}$$

and

$$\widehat{z} = \frac{(-V_{xy}^2 + 4\omega_0^2\lambda_i^2 - V_{yy}\lambda_i^2 + V_{yy}V_{xx} + \lambda_i^4 - \lambda_i^2 V_{xx})}{V_{yz}(V_{xy} + 2\omega_0\lambda_i) - V_{xz}(V_{yy} - \lambda_i^2)} = u_{2_i}. \tag{E.10}$$

If now the first and the third equations of Eq. (E.7) are solved together, the solution becomes:

$$\widehat{y} = \frac{(V_{xx} - \lambda_i^2)(V_{zz} - \lambda_i^2) - V_{xz}^2}{V_{xz}V_{yz} - (V_{xy} + 2\omega_0\lambda_i)(V_{zz} - \lambda_i^2)} = u_i \quad \widehat{z} = \frac{(V_{xy} + 2\omega_0\lambda_i)V_{xz} - (V_{xx} - \lambda_i^2)V_{yz}}{V_{xz}V_{yz} - (V_{xy} + 2\omega_0\lambda_i)(V_{zz} - \lambda_i^2)} = u_{2_i}. \tag{E.11}$$

Finally by solving the second and the third equations of Eq. (E.7), the solution turns into:

$$\widehat{y} = \frac{(V_{xy} - 2\omega_0\lambda_i)(V_{zz} - \lambda_i^2) - V_{yz}V_{xz}}{V_{yz}^2 - (V_{yy} - \lambda_i^2)(V_{zz} - \lambda_i^2)} = u_i \quad \widehat{z} = \frac{(V_{yy} - \lambda_i^2)V_{xz} - (V_{xy} - 2\omega_0\lambda_i)V_{yz}}{V_{yz}^2 - (V_{yy} - \lambda_i^2)(V_{zz} - \lambda_i^2)} = u_{2_i}. \tag{E.12}$$

E.2 Floquét mode control: x-axis control (single axis)

In this case, a single axis control in the x direction is selected (Keeter, 1994), which is the one with higher contributions of the gravity source ($\Delta v_x \neq 0$ and $\Delta v_y = \Delta v_z = 0$). Thanks to this simple case, there are now only five unknowns:

$$\begin{Bmatrix} \delta_{1x} \\ \delta_{1y} \\ \delta_{1z} \\ \delta_{1\dot{y}} \\ \delta_{1\dot{z}} \end{Bmatrix} = \begin{bmatrix} \delta_{2x} & \delta_{3x} & \dots & \delta_{6x} \\ \delta_{2y} & \delta_{3y} & \dots & \delta_{6y} \\ \delta_{2z} & \delta_{3z} & \dots & \delta_{6z} \\ \delta_{2\dot{y}} & \delta_{3\dot{y}} & \dots & \delta_{6\dot{y}} \\ \delta_{2\dot{z}} & \delta_{3\dot{z}} & \dots & \delta_{6\dot{z}} \end{bmatrix} \cdot \begin{Bmatrix} \alpha_2 \\ \alpha_3 \\ \alpha_4 \\ \alpha_5 \\ \alpha_6 \end{Bmatrix} \qquad \delta\boldsymbol{x}_{1\boldsymbol{x}} = \tilde{E}_{\boldsymbol{x}} \cdot \bar{\alpha} \tag{E.13}$$

therefore $\bar{\alpha}$ and Δv_x are:

$$\bar{\alpha} = \tilde{E}_{\boldsymbol{x}}^{-1} \cdot \delta\boldsymbol{x}_{1\boldsymbol{x}} \qquad \Delta v_x = \sum_{i=2}^{n} \alpha_i \cdot \delta_{i\dot{x}} - \delta_{1\dot{x}}. \tag{E.14}$$

E.3 Derivatives of the solar radiation pressure acceleration

In Section 5.6, the control acceleration is given by the solar radiation pressure actuators, where knowledge of the Jacobian matrix in Eq. (5.75) is required. In this section, the derivatives of the SRP accelerations with respect to α (in-plane angle), δ (out-of-plane angle) and β (lightness parameter, function of the area-to-mass ratio) is shown. The spacecraft-Sun vector is defined with respect to the rotating system by two angles: Φ (in-plane) and Ψ (out-of-plane). These two angles are function of the spacecraft-Sun vector components and are defined as:

$$\Phi = \arctan\left(\frac{y}{(x - x_{Sun})}\right), \quad \text{and} \quad \Psi = \arctan\left(\frac{z}{(x - x_{Sun})^2 + y^2}\right), \tag{E.15}$$

respectively. The projection of the spacecraft-Sun vector on the x-y plane is defined as:

$$\boldsymbol{r}_{xy,Sun-p} = \sqrt{(x - x_{Sun})^2 + y^2}. \tag{E.16}$$

The partial derivatives of the SRP acceleration with respect to α are defined as:

$$\frac{\partial \boldsymbol{a}}{\partial \alpha} = \begin{Bmatrix} a_{x\alpha} \\ a_{y\alpha} \\ a_{z\alpha} \end{Bmatrix}, \tag{E.17}$$

where the components in x, y and z are:

$$a_{x\alpha} = \begin{array}{l} \frac{\beta\cdot(\mu-1)\cos(\delta+\Psi)\cdot\left[-2z\cdot\boldsymbol{r}_{xy,Sun-p}\cos(\frac{3\alpha}{2}+\Phi)\sin(\frac{\alpha}{2})\sin(\delta)\right.}{[(x+\mu)^2+y^2+z^2]^{\frac{3}{2}}} \\ \left.\frac{+\cos(\delta)(z^2\sin(\alpha+\Phi)\cdot\boldsymbol{r}_{xy,Sun-p}^2\sin(2\alpha+\Phi))\right]}{[(x+\mu)^2+y^2+z^2]^{\frac{3}{2}}}, \end{array} \tag{E.18}$$

$$a_{y\alpha} = \begin{array}{l} \frac{-\left[\beta(\mu-1)\cos(\delta+\Phi)\left(\cos(\delta)\left(z^2\cos(\alpha+\Psi)+\boldsymbol{r}^2_{xy,Sun-p}\cos(2\alpha+\Phi)\right)\right.\right.}{[(x+\mu)^2+y^2+z^2]^{\frac{3}{2}}} \\ \frac{\left.\left.+2z\boldsymbol{r}_{xy,Sun-p}\sin(\frac{\alpha}{2})\sin(\frac{3\alpha}{2}+\Psi)\right)\right]}{[(x+\mu)^2+y^2+z^2]^{\frac{3}{2}}}, \end{array} \tag{E.19}$$

and

$$a_{z\alpha} = \frac{\beta(\mu-1)\sin(\alpha)\left[\boldsymbol{r}^2_{xy,Sun-p}\cos(\delta) - z\boldsymbol{r}_{xy,Sun-p}\sin(\delta)\sin(\delta+\Psi)\right]}{[(x+\mu)^2+y^2+z^2]^{\frac{3}{2}}}. \tag{E.20}$$

As for the partial derivatives in α, the definition for the derivatives in δ is:

$$\frac{\partial \boldsymbol{a}}{\partial \delta} = \left\{ \begin{array}{c} a_{x\delta} \\ a_{y\delta} \\ a_{z\delta} \end{array} \right\}, \tag{E.21}$$

where the partial derivative in x is:

$$a_{x\delta} = \begin{array}{l} \frac{\beta(1-\mu)\cos(\alpha+\Psi)\left[\cos(\delta+\Phi)\left(-z\boldsymbol{r}_{xy,Sun-p}(-1\cos(\alpha))\cos(\delta)-(z^2+\boldsymbol{r}^2_{xy,Sun-p}\cos(\alpha))\sin(\delta)\right)\right.}{[(x+\mu)^2+y^2+z^2]^{\frac{3}{2}}} \\ \left.-\frac{\left((z^2+\boldsymbol{r}^2_{xy,Sun-p}\cos(\alpha))\cos(\delta)-z\boldsymbol{r}_{xy,Sun-p}(-1\cos(\alpha))\sin(\delta)\right)\sin(\delta+\Phi)\right]}{[(x+\mu)^2+y^2+z^2]^{\frac{3}{2}}}, \end{array} \tag{E.22}$$

the derivative in y is:

$$a_{y\delta} = \begin{array}{l} \frac{\beta(1-\mu)\sin(\alpha+\Phi)\left[\cos(\delta+\Psi)\left(-z\boldsymbol{r}_{xy,Sun-p}(-1\cos(\alpha))\cos(\delta)-(z^2+\boldsymbol{r}^2_{xy,Sun-p}\cos(\alpha))\sin(\delta)\right)\right.}{[(x+\mu)^2+y^2+z^2]^{\frac{3}{2}}} \\ \left.-\frac{\left((z^2+\boldsymbol{r}^2_{xy,Sun-p}\cos(\alpha))\cos(\delta)-z\boldsymbol{r}_{xy,Sun-p}(-1+\cos(\alpha))\sin(\delta)\right)\sin(\delta+\Psi)\right]}{[(x+\mu)^2+y^2+z^2]^{\frac{3}{2}}}, \end{array} \tag{E.23}$$

while the derivative in z is:

$$a_{z\delta} = \begin{array}{l} \frac{\beta(1-\mu)\left[\cos(\delta+\Psi)\left((z^2+\boldsymbol{r}^2_{xy,Sun-p}\cos(\alpha))\cos(\delta)-z\boldsymbol{r}_{xy,Sun-p}(-1\cos(\alpha))\sin(\delta)\right)\right.}{[(x+\mu)^2+y^2+z^2]^{\frac{3}{2}}} \\ \left.\frac{\left(-z\boldsymbol{r}_{xy,Sun-p}(-1\cos(\alpha))\cos(\delta)-(z^2\boldsymbol{r}^2_{xy,Sun-p}\cos(\alpha))\sin(\delta)\right)\sin(\delta+\Psi)\right]}{[(x+\mu)^2+y^2+z^2]^{\frac{3}{2}}}. \end{array} \tag{E.24}$$

For the case of the derivatives in β, the solution is written in a compact way as:

$$\frac{\partial \boldsymbol{a}}{\partial \beta} = (1-\mu)\left\langle \frac{\boldsymbol{r}_{Sun-p}}{|\boldsymbol{r}_{Sun-p}|},\ \hat{\boldsymbol{N}} \right\rangle^2 \cdot \hat{\boldsymbol{N}}. \tag{E.25}$$

In Eq. (E.25), the scalar product between the spacecraft-Sun vector and the normal vector to the reflective surface is defined as:

$$\left\langle \frac{\boldsymbol{r}_{Sun-p}}{|\boldsymbol{r}_{Sun-p}|},\ \hat{\boldsymbol{N}} \right\rangle = \frac{(z^2+(y^2+(x+\mu)^2)\cos(\alpha))\cos(\delta) - z\cdot\boldsymbol{r}_{xy,Sun-p}(\cos(\alpha)-1)\sin(\alpha)}{(x+\mu)^2+y^2+z^2}, \tag{E.26}$$

where, the normalised spacecraft-Sun vector is a function, by definition, of the angles Φ and Ψ :

$$\frac{\boldsymbol{r}_{Sun-p}}{|\boldsymbol{r}_{Sun-p}|} = \left\{ \begin{array}{c} \cos(\Phi) \cdot \cos(\Psi) \\ \sin(\Phi) \cdot \cos(\Psi) \\ \sin(\Psi) \end{array} \right\}. \tag{E.27}$$

Appendix F

Transfer Trajectory for a Sun-pointing manoeuvre for Gaia's Lissajous Orbit

Figure F.1 shows the selected arc of the departure Lissajous orbit to perform the transfer. The departure Lissajous orbit has the same amplitudes A_y and A_z of Gaia's mission presented in Appendix B.3.3. In this case an initial β_0 equal to 0.04 is selected and β_M turns to 0.02 due to the SRP manoeuvre.

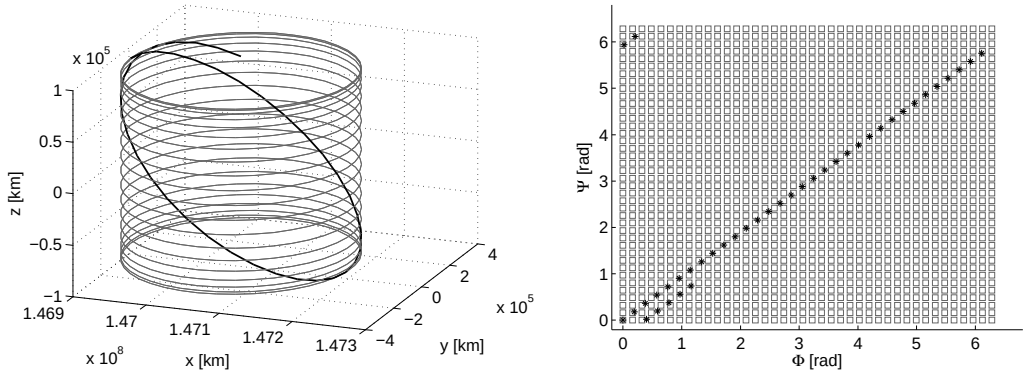

(a) Lissajous orbit in the synodic refernce frame centred at the centre of mass.

(b) Liassajous orbit in the phase space centred at the centre of mass.

Figure F.1: Departure Lissajous orbit in the synodic reference frame and in the phase space.

Figure F.2 shows the amplitudes of the unstable, A_1, and stable, A_2, manifolds of the target Lissajous orbit along the unstable manifold of the departure Lissajous orbit.

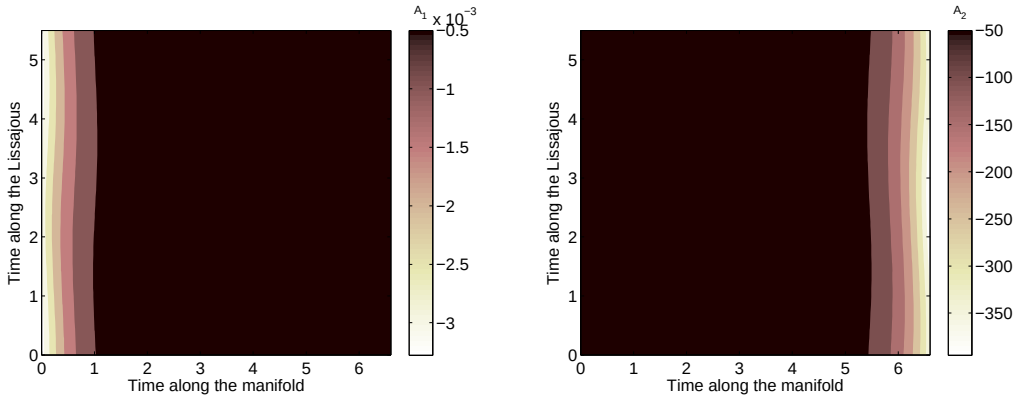

(a) Amplitude A_1 of the unstable manifold of the traget Lissajous orbit.

(b) Amplitude A_2 of the stable manifold of the traget Lissajous orbit.

Figure F.2: Amplitude of the unstable, A_1, and stable, A_2, manifolds of the target Lissajous orbit as a function of the leaving point of the departure Lissajous orbit and the points along its unstable manifold.

Figure F.3, shows the unstable manifold of the departure Lissajous orbit, in black, and the stable manifold of the target Lissajous orbit, in blue. The departure and the target Lissajous orbits are shown in Figure F.3(b) in black and red respectively.

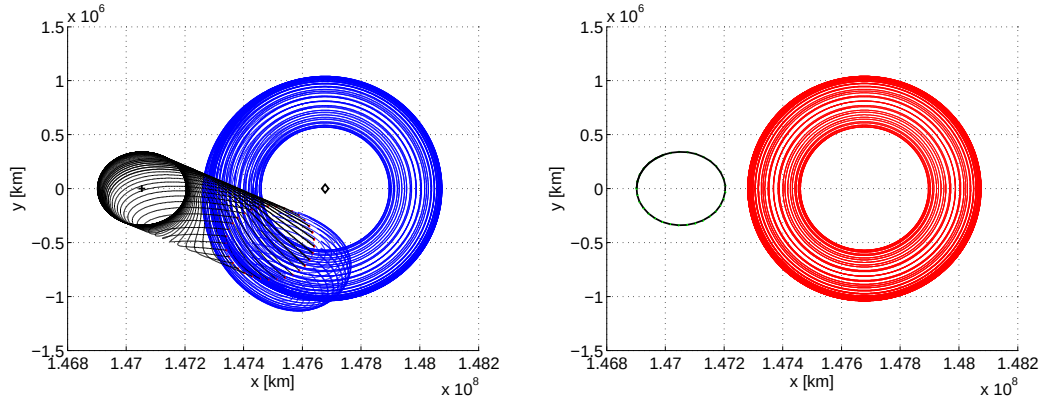

(a) Transfer trajectories.

(b) Departure and target Lissajous orbits.

Figure F.3: Transfer trajectories from the departure (black) and target (red) Lissajous orbits.

Figure F.4 shows the transfer strategy in the phase space of four unstable trajectory leaving the departure Lissajous orbit. The trajectory number 21 in Figure F.4(b) shows a tiny jump in the phase space. Conversely, the trajectories number 20, 28 and 48 show instantaneous variations in the phases due to the SRP manoeuvre.

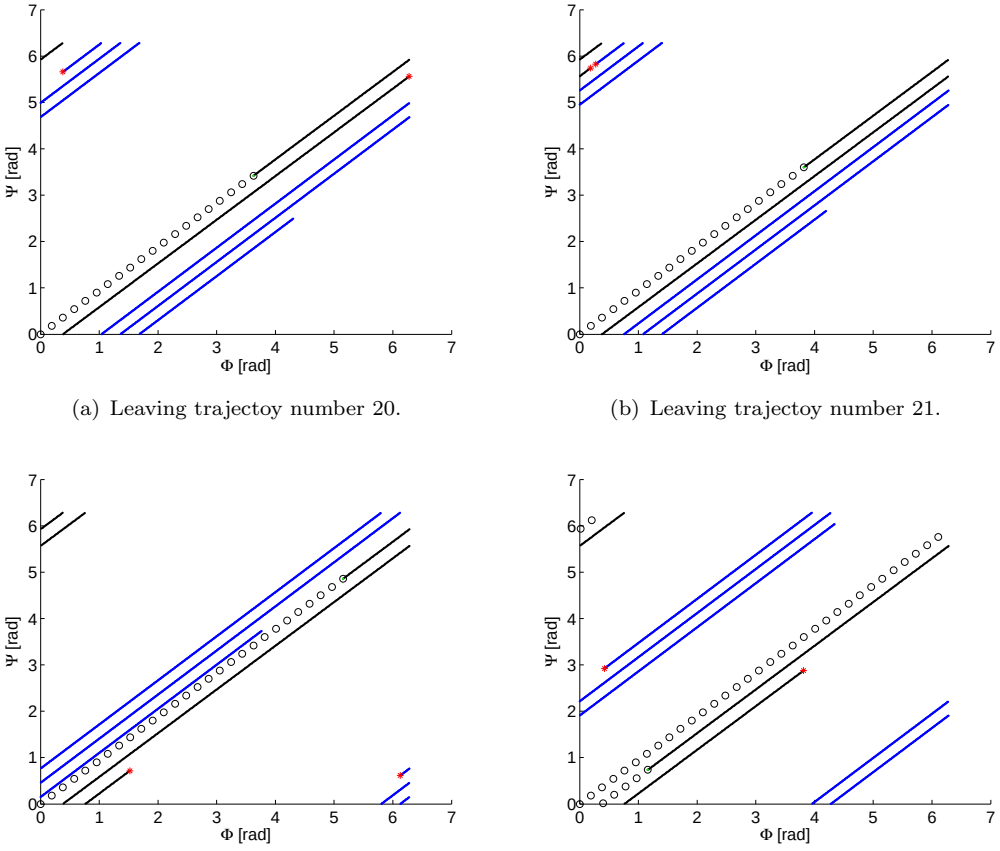

(a) Leaving trajectoy number 20.

(b) Leaving trajectoy number 21.

(c) Leaving trajectoy number 28.

(d) Leaving trajectoy number 40.

Figure F.4: Phase space of trajectories number 20, 21, 28 and 40 of the unstable manifold of the departure Lissajous orbit.

Appendix G

End-of-Life Disposal

G.1 Traditional Δv with the effect of solar radiation pressure

In this section, the strategy with the Δv disposal by Olikara et al. (2013) is presented here with the additional effect of the SRP perturbation. In case that Olikara et al. (2013) would have taken into account the effect of SRP for a Sun-pointing spacecraft, the condition of closure would be:

$$E_{SL_2} = \frac{1}{2}V_{clsr}^2 - \frac{1}{2}(x^2+y^2) - (1-\beta_0)\frac{\mu_{Sun}}{r_{Sun-p}} - \frac{\mu_{Earth}}{r_{Earth-p}} \tag{G.1}$$

and V_{clsr} is now defined as:

$$V_{clsr} = \sqrt{2E_{SL_2} + (x^2+y^2) + 2\left[(1-\beta_0)\frac{\mu_{Sun}}{r_{Sun-p}} + \frac{\mu_{Earth}}{r_{Earth-p}}\right]}. \tag{G.2}$$

The Δv for closing the zero-velocity curves when an initial effect of SRP (β_0) is included is:

$$\Delta v_s = V_{clsr} - V, \tag{G.3}$$

as shown in Figure 7.10.

Now, if Eq. (G.2-G.3) is compared with the one presented by Olikara et al. (2013) it is possible to verify that the effect of SRP implies a higher Δv. Indeed, with the same initial state vector V, the Δv_s required (when SRP is considered) would be higher than the Δv required without considering SRP. In conclusion, also when using traditional Δv to close the curves, it can be useful to include a margin in the Δv due to the uncertainty in the reflectivity of the spacecraft since SRP is one of the major perturbations after the gravitational effect. The solution presented in Figure 7.10 makes use of Eq. (G.3).

Thus, it is slightly different when compared with the results of Olikara et al. (2013), for instance, the location of the forbidden region is shifted.

References

Alessi, E. M., Colombo, C., and Landgraf, M. (2014). Re-entry Disposal analysis for Libration Point Orbit missions. *In Proceedings of the 24th International Symposium on Space Flight Dynamics, ISSFD*, Laurel, Maryland, May 5-9 2014.

Alessi, E. M., Gómez, G., and Masdemont, J. J. (2010). Two-manoeuvres transfers between LEOs and Lissajous orbits in the Earth-Moon system. *Advances in Space Research*, 45:1276–1291. Doi: 10.1016/j.asr.2009.12.010.

Anderson, R. L. and Lo, M. W. (2004). The role of the invariant manifolds in low thrust trajectory design (Part II). *In Proceeding of the AIAA/AAS Astrodynamics Specialist Conference*, AIAA-2004-5305, Providence, Rhode Island, 16-19 August, 2004.

Astrom, K. J. and Wittenmark, B. (1996). *Computer-Controlled Systems: Theory and Design (3rd Ed.)*. Prentice-Hall, Inc. Upper Saddle River, NJ, USA.

Baoyin, H. and McInnes, C. R. (2006). Solar sail Equilibria in the Elliptical Restricted Three-Body Problem. *Journal of Guidance, Control and Dynamics*, 29(3):538–543. Doi: 10.2514/1.15596.

Battin, R. H. (1978). *An Introduction to the Mathematics and Methods of Astrodynamics*. New York, N.Y: American Institute of Aeronautics and Astronautics.

Bauske, R. (2009). Operational manoeuvre optimization for the ESA missions Herschel and Planck. *In Proceedings of the 21st International Symposium on Space Flight Dynamics (ISSFD)*, Toulouse, France, September 28 - October 2, 2009.

Bernelli-Zazzera, F., Topputo, F., and Massari, M. (2004). Assessment of mission design including utilization of libration points and weak stability boundaries. *Ariadna id: 03/4103*.

Bewick, R., Sanchez, J., and McInnes, C. (2012). The feasibility of using an L_1 positioned dust cloud as a method of space-based geoengineering. *Advances in Space Research*, 49:212–1228. Doi: 10.1016/j.asr.2012.01.010.

Biggs, J., McInnes, C., and Waters, T. (2008). New Periodic Orbits in the Solar Sail Restricted Three-Body Problem. *In Proceedings of the 2nd Conference on Nonlinear Science and Complexity*, Porto, Portugal, 2008.

Biscari, P., Ruggeri, T., Saccomandi, G., and Vianello, M. (2005). *Meccanica Razionale per l'Ingegneria*. Monduzzi Ed.

Bookless, J. and McInnes, C. (2008). Control of Lagrange point orbits using solar sail propulsion. *Acta Astronautica*, 62:159–176. Doi: 10.1016/j.actaastro.2006.12.051.

Borggräfe, A., Heiligers, J., Ceriotti, M., and McInnes, C. R. (2013). Distributed reflectivity solar sail for extended mission applications. *In Proceedings of the 3rd International Simposyum on Solar Sailing*, Glasgow, Scotland, 2013.

Broucke, R. A. (1968). Periodic orbit in the restricted three-body problem with earth-moon masses. Technical report, Jet Propulsion Laboratory (JPL).

Bruno, A. D. and Varin, V. P. (2007). Periodic solutions of the restricted three-body problem for a small mass ratio. *Journal of Applied Mathematics and Mechanics*, 71(6):933–960. Doi: 10.1016/j.jappmathmech.2007.12.012.

Campagnola, S., Martin, L., and Newton, P. (2008). Subregions of motion and elliptic halo orbits in the elliptic restricted three-body problem. *In Proceedings of the AAS/AIAA Space Flight Mechanics Meeting*, Galveston, TX, United States, January, 2008.

Canalias, E., Cobos, J., and Masdemont, J. J. (2003). Impulsive transfers between Lissajous libration point orbits. *Journal of the Astronautical Sciences*, 51:361–390.

Canalias, E., Gómez, G., Marcote, M., and Masdemont, J. (2004). Assessment of mission design including utilization of libration points and weak stability boundaries. *Ariadna id: 03/4103*.

Celletti, A. and Lhotka, C. (2011). A dynamical system approach to Astrodynamics. *Acta Futura*, (4):53–68. Doi: 10.2420/AF04.2011.53.

Ceriotti, M. and Farrés, A. (2012). Solar sail station keeping of high-amplitude vertical Lyapunov orbits in the Sun-Earth system. *In Proceedings of the 63rd International Astronautical Congress*, Naples, Italy, 1-5 October 2012.

Ceriotti, M., Harkness, P., and McRobb, M. (2013). Variable-geometry solar sailing: the possibility of the quasi-rhombic pyramid. *In Proceedings of the 3rd International Simposyum on Solar Sailing*, Glasgow, Scotland, 2013.

Chobotov, V. A. (2002). *Orbital Mechanichs Third Edition*. AIAA Education Series, Ohio.

Clark, A. C. (1972). *The Wind from the Sun*. HJM, ISBN 0-15-196810-1.

Colombo, C., Alessi, E. A., van der Weg, W., Soldini, S., Letizia, F., Vetrisano, M., Vasile, M., Rossi, A., and Landgraf, M. (2015a). End-of-life disposal concepts for Libration Point Orbit and Highly Elliptical Orbit Missions. *Acta Astronautica*, 110:298–312. Doi: 10.1016/j.actaastro.2014.11.002.

Colombo, C., Letizia, F., Alessi, E. M., and Landgraf, M. (2014a). End-of-life re-entry for highly elliptical orbits: the integral mission. *In Proceedings of the 24th AAS/AIAA Space Flight Mechanics Meeting*, Santa Fe, New Mexico, January 26-30, 2014.

Colombo, C., Letizia, F., Soldini, S., Alessi, E. A., Rossi, A., Vasile, M., Vetrisano, M., van der Weg, W., and Landgraf, M. (2014b). End-of-life disposal concepts for Libration Point and Highly Elliptical Orbit Missions. *Final Report, ESA/ESOC contract No. 4000107624/13/F/MOS*, 10 Feb. 2014.

Colombo, C., Letizia, F., Soldini, S., Alessi, E. A., Vasile, M., Vetrisano, M., van der Weg, W., and Landgraf, M. (2014c). Gaia and LISA Pathfinder heliocentric disposal, Gaia re-entry. *Final Report, ESA/ESOC contract No. 4000107624/13/F/MOS*.

Colombo, C., Letizia, F., Soldini, S., Lewis, H., Alessi, E. M., Rossi, A., Vasile, M., Vetrisano, M., Van der Weg, W., and Landgraf, M. (2014d). End-of-life disposal concepts for libration point and highly elliptical orbit missions. *In Proceedings of the 2nd International Academy of Astronautics Conference on Dynamics and Control of Space Systems (DyCoSS)*, Rome, Italy, 24-26 March, 2014.

Colombo, C., Letizia, F., Soldini, S., and Renk, F. (2015b). Disposal of libration point orbits on a heliocentric graveyard orbit: the Gaia mission. *In Proceedings of the 25th International Symposium on Space Flight Dynamics, ISSFD*, Munic, Germany, Oct., 2015.

Colombo, C., Lewis, H., Letizia, F., Soldini, S., Gossnitzer, L., Alessi, E. M., Rossi, A., Dimare, L., Vasile, M., Van der Weg, W., McInnes, C., Macdonalds, M., and Landgraf, M. (2013). End-o-f-life disposal trajectories for libration point and highly elliptical orbit missions. *In Proceedings of the 64th International Astronautical Congress*, IAC-13.A6.P.24, Beijing, China, 23-27 September, 2013.

Colombo, C. and McInnes, C. R. (2011). Orbital dynamics of Smart-Dust devices with solar radiation pressure drag. *Journal of Guidance, Control, and Dynamics*, 34(6):1613–1631. Doi: 10.2514/1.52140.

Colombo, C., Xu, M., and McInnes, C. R. (2012). Stabilisation of the hyperbolic equilibrium of high area-to-mass spacecraft. *In Proceedings of the 63rd International Astronautical Congress*, Naples, Italy, 1-5 October, 2012.

Conley, C. (1968). Low energy transit orbits in the Restricted Three-Body Problem. *SIAM J. Appl. Math*, 16(4):732–746. Doi: 10.1137/0116060.

Cook, A. (2012). Inflatable and hybrid space structures with a view for end of life satellite removal. Doctorial transfer thesis, Univerity of Southampton.

Dachwald, B., Seboldt, W., Macdonald, M., Mengali, G., Quarta, A. A., McInnes, C. R., Rios-Reyes, L., Scheeres, D. J., Wie, B., Görlich, M., Lura, F., Diedrich, B., Batukin,

V., Coverstone, V. L., Leipold, M., and Garbe, G. P. (2005). Potential Solar Sail Degradation Effects on Trajectory and attitude Control. *In Proceedings of the AIAA Guidance, Navigation, and Control Conference and Exhibit*, 6172.

Darwin, G. H. (1911). Periodic orbits and miscellaneous papers. *Cambridge: University Press*, 4.

Davis, K. E., Anderson, R. L., Scheeres, D. J., and Born, G. H. (2010). The use of invariant manifolds for transfers between unstable periodic orbits of different energies. *Celest Mech Dyn Astr*, 107:471–485. Doi: 10.1007/s10569-010-9285-3.

Demiryont, H. and Moorehead, D. (2009). Electrochromic emissivity modulator for spacecraft thermal management. *Solar Energy Materials and Solar Cells*, 93(12):2075–2078. Doi: 10.1016/j.solmat.2009.02.025.

Deprit, A. (1969). Canonical transformations depending on a small parameter. *Celestial Mechanics*, 1:12–30. Doi: 10.1007/BF01230629.

Deprit, A. and Henrard, J. (1967). Natural families of periodic orbits. *The Astronomical Journal*, 72(2):158–172. Doi: 10.1086/110212.

DRL-101-08 (1996). *GOES I-M DataBook*. Contract NAS5-29500.

Dunhan, D. W. and Farquhar, R. W. (2003). Libration Point Missions, 1978-2002. In Libration Point Orbits and Applications. *In Proceedings of the Conference Aiguablava - World Scientific*, pages 45–72.

Dutt, P. and Sharma, R. K. (2011). Evolution of periodic orbits near the Lagrangian point L_2. *Advances in Space Research*, 47(11):1894–1904. Doi: 10.1016/j.asr.2011.01.024.

Elipe, A. (1992). On the restricted three-body problem with generalized forces. *Astrophysics and space science*, 188:257–269. Doi: 10.1007/BF00644913.

ESA, S. D. M. W. (2015). Esa space debris mitigation compliance verification guidelines. *ESA unclissified for official use document: ESSB-HB-U-002*. link: http://www.iadc-online.org/References/Docu/ESSB-HB-U-002-Issue1

ESA-website (2013). Space debris. `http://www.esa.int/Our_Activities/Operations/Space_Debris/Mitigating_space_debris_generation`. Online; accessed 24-April-2015.

ESA-website (2015a). Euclid mission. `http://sci.esa.int/euclid/`. Online; accessed 25-February-2016.

ESA-website (2015b). Lisa mission. `http://www.esa.int/Our_Activities/Space_Science/LISA_Pathfinder_overview`. Online; accessed 25-February-2016.

Evans, S. W. (2003). *Natural enviroment near the Sun/Earth-Moon L_2 Libration point.* Marshall Space Flight Center, Alabama.

Farquhar, R. W. (1968). The Control and Use of Libration-Point Satellites NASA CR-95948: 1-214. *NASA, Technical Report.*

Farquhar, R. W. (1991). Halo-orbit and Lunar-swingby missions of the 1990's. *Acta Astronautica*, 24:227–234. Doi: 10.1016/0094-5765(91)90170-A.

Farrés, A. (2009). Contribution to the dynamics of a solar sail in the Earth-Sun system. Doctorial thesis, Universitat de Barcelona.

Farrés, A. and Ceriotti, M. (2012). Solar sail station keeping of high-amplitude vertical Lyapunov orbits in the Sun-Earth system. *In Proceedings of the 63^{th} International Astronautical Congress*, Naples, Italy, 1-5 October.

Farrés, A. and Jorba, A. (2008). A Dynamical System Approach for the Station Keeping of a Solar Sail. *The Journal of the Astronautical Sciences*, 56(2):199–230. Doi: 10.1007/BF03256549.

Farrés, A. and Jorba, A. (2010). Dynamics of a solar sail near a halo orbit. *Acta Astronautica*, 67:979–990. Doi: 10.1016/j.actaastro.2010.05.022.

Farrés, A. and Jorba, A. (2014). Station keeping of a solar sail around a halo orbit. *Acta Astronautica*, 94(1):527–539. Doi: 10.1016/j.actaastro.2012.07.002.

Farrés, A. and Jorba, A. (2015). Solar sailing with invariant manifolds in the Earth-Sun system. *In Proceedings of the 66^{the} International Astronautical Congress*, Jerusalem, Israel, 2015.

Farrés, A., Jorba, A., Mondelo, J. M., and Villac, B. (2013). Periodic motion for an imperfect solar sail near an asteroid. *In Proceedings of the 3^{rd} International Simposyum on Solar Sailing*, Glasgow, Scotland, 2012.

Friedland, B. (2005). *Control system design: an introduction to state-space methods.* Dover publication, inc., Mineola, New York.

Friedman, L., Carroll, W., Goldstein, R., Jacobson, R., Kievit, J., Landel, R., Layman, W., Marsh, E., Ploszaj, R., Rowe, W., Ruff, W., Stevens, J., Stimpson, L., Trubert, M., Varsi, G., and Wright, J. (1978). Solar Sailing - The Concept Made Realistic. *In Proceedings of the 16^{th} AIAA Aerospace Sciences Meeting*, Huntsville, Alabama, 16-18 January 1978.

Garwin, R. L. (1958). Solar Sailing - A Practical Method of Propulsion within the Solar System. *Jet Propulsion*, 28:188–189.

Ginoux, J.-M. (2009). Differential geometry applied to dynamical systems. *Nonlinear Science*, 66.

Gómez, G. and Barrabés, E. (2011). Space Manifold Dynamics. *Scholarpedia*, 6:2.

Gómez, G., Jorba, A., Masdemont, J. J., and Simó, C. (1993). Study of the Transfer from the Earth to a Halo Orbit Around the Equilibrium Point L_1. *Celestial Mechanics*, 56(4):541–562. Doi: 10.1007/BF00696185.

Goméz, G., Jorba, A., Masdemont, J. and, S. C., and Rodriguez-Canabal, J. (1991). Study refinement of semi-analytical halo orbit theory. *Final Report, ESA/ESOC contract No. 8625/89/D/MD(SC)*.

Gómez, G., Jorba, A., Simó, C., and Masdemont, J. J. (1998). Study of the transfer between halo orbits. *Acta Astronautica*, 43(9-10):493–520. Doi: 10.1007/BF00696185.

Gómez, G., Koon, W. S., Marsden, J. E., Masdemont, J. J., and Ross, S. D. (2004). Connecting orbits and invariant manifolds in the spatial restricted three-body problem. *Nonlinearity*, 17:1571–1606. Doi: 10.1088/0951-7715/17/5/002.

Gómez, G., Llibre, J., Matínez, R., and Simó, C. (2001). Dynamics and mission design near libration points - Volume I: Fundamentals: the case of collinear libration points, volume 2 of World Scientific Monograph Series in mathematics . *World Scientific*.

Gordon, S. C. (1993). Orbit determination error analysis and comparison of station-keeping costs for Lissajous and halo-type libration point orbits and sensitivity analysis using experimental design techniques. *NASA*, N93-24721:395–409.

Guttag, M. and Boyce, M. C. (2015). Locally and Dynamically Controllable Surface Topography Through the Use of Particle-Enhanced Soft Composites. *Adv. Funct. Mater.*, 25:3641–3647. Doi: 10.1002/adfm.201501035.

Hamilton, N. H., Folta, D., and Carpenter, R. (2014). Formation flying satellite around the L2 Sun-Earth libration point. *In Proceedings of the AIAA/AAS Astrodynamics Specialist Conference*, AIAA-2002-4528, Monterey, California, 5-8 August, 2002.

Hawkins, J. (1996). *GOES I-M DataBook*. Technical report, NASA Contract No. NASA5-29500, US.

Hechler, M. and Cobos, J. (2002). Herschel, Planck and GAIA Orbit Design. *In Proceedings of the 7^{th} International Conference on Libration Point Orbits and Application*, Parador d'Aiguablava, Girona, Spain, 10-14 June, 2002.

Hénon, M. (1965a). Numerical Exploration of the Restricted Problem. I. *Astron. and Astrophys.*, 28:499.

Hénon, M. (1965b). Numerical Exploration of the Restricted Problem. II. *Astron. and Astrophys.*, 28:992.

Hénon, M. (1966a). Numerical Exploration of the Restricted Problem. III. *Astron. and Astrophys.*, 1:57.

Hénon, M. (1966b). Numerical Exploration of the Restricted Problem. IV. *Astron. and Astrophys.*, 2:49.

Hénon, M. (1968). Numerical Exploration of the Restricted Problem. V. *Astron. and Astrophys.*, 1:223–238.

Hill, G. W. (1886). On the Part of the Motion of Lunar Perigee Which is a Function of the Mean Motions of the Sum and Moon. *Acta Math.*, 8:1–36. Doi: 10.1007/BF02417081.

Hill, J. R., Wang, K. W., Fang, H., and Quijano, U. (2010). Actuator grouping optimization on flexible space reflectors. *In Proceedings of the SPIE - The International Society for Optical Engineering*, 7977. Doi: 10.1117/12.880086.

Howell, K. (2009). Solar sailing. `http://www.insightcruises.com/pdf/sa07_slides/Solar_Sailing.pdf`. Online; accessed 19-June-2013.

Howell, K. C. (2001). Familes of Orbits in the Vicinity of the Collinear Libration Points. *Journal of the Astronautical Sciences*, 49(1):107–125. Doi: 10.2514/6.1998-4465.

Howell, K. C. and Pernicka, H. J. (1993). Stationkeeping method for libration point trajectories. *Journal of Guidance, Control, and Dynamics*, 16(1):115–159. Doi: 10.2514/3.11440.

Jackson, J. (1913). Retrograte satellite orbits. *MNRAS*, 74(2):62–82. Doi: 10.1093/mnras/74.2.62.

Janhunen, P. (2013). Freely guided photonic blade for scalable E-sail, compactly storable heliogyro and deorbiting. *In Proceedings of the 3^{rd} International Simposyum on Solar Sailing*, Glasgow, Scotland, 11-13 June 2013.

Jorba, A. and Masdemont, J. J. (1999). Dynamics in the Center Manifold of the Restricted Three Body Problem. *Physica D*, 132:189–213. Doi: 10.1016/s0167-2789(99)00042-1.

Katherine, Y. and Villac, B. (2010). Periodic orbits families in the Hill's three-body problem with solar radiation pressure. *Advances in the Astronautical Sciences Series*, 136:285–300.

Keeter, M. (1994). Station-keeping strategies for Libration point orbits: target points and Floquét mode approaches. Master thesis, Purdue University.

Kelvin, L. (1892). *Collected papers*, IV:516.

Khalil, H. (2002). *Nonlinear systems*. Upper Saddle River, N.J.: Prentice Hall.

Koon, W. S., Lo, M. W., Marsden, J. E., and Ross, S. D. (2002). Constructing a low energy transfer between jovian moons. *Celestial Mechanics*, 292:129–146.

Koon, W. S., Lo, M. W., Marsden, J. E., and Ross, S. D. (2008). *Dynamical systems, the three-body problem and space mission design*. Marsden Books, ISBN 978-0-615-24095-4.

Koon, W. S., Marsden, J. E., and Ross, S. D. (2000). Heteroclinic connections between periodic orbits and resonance transitions in celestial mechanics. *Chaos*, 10(2):427–469. Doi: 10.1063/1.166509.

Kuchment, P. (1993). *Floquet Theory for Partial Differential Equations*. vol. 60 of Operator Theory: Advances and Appliations, Switzerland.

Kumar, T. P. and Behdinan, K. (2008). Variable structure controle for satellite attitude stabilization in elliptic orbits using radiation pressure. *Acta Astronautica*, 64:359–373. Doi: 10.1016/j.actaastro.2008.08.003 .

Lara, M. and Russell, R. (2006). Concerning the family g of the restricted three-body problem. *In Proceedings of the IX Jornadas de Trabajo en Mecanica Celeste*, Jaca, Hesca, Spain, 2006.

Leach, R. and Neal, K. L. (2002). Discussion of micro-Newton thruster requirements for a drag-free control system. *In Proceedings of the 16^{th} Annual/USU Conference on Small Satellites*, August 12-15, Logan, Utah US.

Lo, M. W., Anderson, R. L., Lam, T., and Whiffen, G. (2006). The role of the invariant manifolds in low thrust trajectory design (part iii). *In Proceedings of the AAS/AIAA Spaceflight Dynamics Conference*, AIAA-06-190, Tampa, Florida, 22-26 January, 2006.

Lücking, C., Colombo, C., and McInnes, C. R. (2012a). A Passive Satellite Deorbiting Strategy for Medium Earth Orbit Using Solar Radiation Pressure and the J2 Effect. *Acta Astronautica*, 77:197–206. Doi: 10.1016/j.actaastro.2012.03.026.

Lücking, C., Colombo, C., and McInnes, C. R. (2012b). Orbital Dynamics of High Area-to-Mass Ratio Spacecraft with J2 and Solar Radiation Pressure for Novel Earth Observation and Communication Services. *Acta Astronautica*, 81(1):137–150. Doi: 10.1016/j.actaastro.2012.07.009.

Lücking, C., Colombo, C., and McInnes, C. R. (2013a). Solar Radiation Pressure-Augmented Deorbiting: Passive End-of-Life Disposal from High-Altitude Orbits. *Journal of Spacecraft and Rockets*, page Doi: 10.2514/1.A32478.

Lücking, C. M., Colombo, C., and McInnes, C. R. (2012c). Electrochromic orbit control for smart-dust devices. *Journal of Guidance, Control, and Dynamics*, 35(5):1548–1558. Doi: 10.2514/1.55488.

Lücking, C. M., Colombo, C., and McInnes, C. R. (2013b). Orbit evolution, maintenance and disposal of spacechip swarms through elecrto-chromic control. *Acta Astronautica*, 82(1):25–37. Doi: 10.2514/1.55488.

Luk'yanov, L. G. (2005). Energy conservation in the restricted elliptical three-body problem. *Astronomy reports*, 49(12):1018–1027. Doi: 10.1134/1.2139818.

Matukuma, T. (1930). On the periodic orbits in Hill's case. *In Proceedings of the Imperial Academy of Japan*, 6(1):6–8. Doi: 10.2183/pjab1912.6.6.

Matukuma, T. (1932). Periodic orbits in Hill's case. *In Proceedings of the Imperial Academy of Japan, Second paper*, 8(5):147–150. Doi: 10.2183/pjab1912.8.147.

Matukuma, T. (1933). Periodic orbits in Hill's case. *In Proceedings of the Imperial Academy of Japan, Third paper*, 9(8):364–366. Doi: 10.2183/pjab1912.9.364.

McInnes, A. I. S. (2000). Strategies for solar sail mission design in the circular restricted three-body problem. Master of science in engineering, Purdue University.

McInnes, C. R. (1999). *Solar sailing: technology, dynamics and mission applications.* Springer-Verlag, New York.

McInnes, C. R. (2003). Solar sailing: orbital mechanics and missions applications. *Advances in Space Research*, 31(8):1971–1980. doi: 10.1016/S0273-1177(03)00172-8 .

McInnes, C. R., McDonald, A. J. C., Simmons, J. F. L., and MacDonald, E. W. (1994). Solar sail parking in restricted three-body systems. *Journal of Guidance, Control and Dynamics*, 17(2):399–406. Doi: 10.2514/3.21211.

McMahon, J. W. (2011). An analytical theory for the perturbative effect of solar radiation pressure on natural and artificial satellites. Doctorial thesis, Univerity of Colorado.

Moulton, F. R. (1920). *Periodic orbits: in collaboration with D. Buchanan, T. Buck, F. L. Griffin, W. R. Longley and W. D. MacMillan.* Carnegie Institution of Washington, Washington.

Murphy, D. and Macy, B. (2004). Demonstration of a 10 m Solar Sail System. *45th AIAA/ASME/ASCE/AHS/ASC Structures, Structural Dynamics and Material Conference*, Palm Springs, CA, 2004:698–708.

Musen, P. (1960). The influence of the solar radiation pressure on the motion of an artificial satellite. *Journal of Geophysical Research*, 65(5):1391–1396. Doi: 10.1029/JZ065i005p01391.

Musielak, Z. E. and Quarles, B. (2015). The three-body problem. *Reports on Progress in Physics, arXiv:1508.02312 [astro-ph.EP]*, 77(6):1–30. Doi: 10.1088/0034-4885/77/6/065901.

NASA-website (1976). LAGEOS mission. `http://science.nasa.gov/missions/lageos-1-2/`. Online; accessed 29-February-2016.

NASA-website (1995). Safety standard 1740.14. `http://orbitaldebris.jsc.nasa.gov/mitigate/safetystandard.html`. Online; accessed 24-January-2016.

NASA-website (2003). Wind mission. `http://wind.nasa.gov/orbit.php`. Online; accessed 29-February-2016.

NASA-website (2016). James Webb Space Telescope mission. `http://jwst.nasa.gov/about.html`. Online; accessed 25-February-2016.

Noam, T., Karen, R., David, F., and Kimberly, T. (1998). Using solar radiation pressure to control L_2 orbits. *In Proceedings of the AAS/GFC International Symposium on Space Flight Dynamics*, 100(1):617–627.

Olikara, Z., Gómez, G., and Masdemont, J. J. (2013). End-of-life disposal of libration point orbit spacecraft. *In Proceedings of the* 64^{th} *International Astronautical Congress*, IAC-13.C1.82., Beijing, China, 23-27 September, 2013.

Olikara, Z. P., Gómez, G., and Masdemont, J. J. (2015). Dynamic Mechanisms for Spacecraft Disposal from Sun-Earth Libration Points. *Journal of Guidance, Control, and Dynamics*, 38(10):1976–1989. Doi: 10.2514/1.G000581.

Olive, J. P., Overbeek, T. V., and Fleck, B. (2013). Soho monthly trending report. *SOHO/PRG/TR/769 Oct 15*.

Patapoff, H. (1967). Site accessibility analysis for advanced lunar missions. *Final Report prepared for Advanced Spaceraft Technology Division NASA Manned Spacecraft Center*, Volume I, Houston, Texas, Contract NAS 9-4810, 30 June 1967.

Perozzi, E. and Ferraz-Mello, S. (2010). Space manifold dynamics. novel spaceways for science and exploration. *Springer*, New York.

Peter, C. H. (2004). *Spacecraft Attitude Dynamics*. Dover Publications, Toronto.

Poynting, J. H. (1904). Radiation in the solar system: its effects on temperature and its pressure on small bodies . *Philos. Trans. R. Soc. London Ser. A*, 202:525–552. `http://www.jstor.org/stable/90892`.

Quarta, M. G. and Janhunen, A. A. P. (2008). Electric sail performance analysis. *Journal of Spacecraft and Rockets*, 45(1):122–129. Doi: 10.2514/1.31769.

Renner, U. (1979). Attitude control by solar sailing - a promising experiment with OTS-2. *European Space Agency*, 3:35–40.

Richardson, D. L. (1980). Analytic Construction of Periodic Orbits About the Collinear Points. *Chelestial Mechanics*, 22:241–253. Doi: 10.1007/BF01229511.

Romero-Gómez, M. (2006). The role of the invariant manifolds in the formation of spiral arms and rings in barred galaxies. Doctorial thesis, Univeritat Politécnica de Catalunya and Universitat Rovira i Virgili.

Sathyanarayan, M. N., Rao, M. N., Nataraju, B. S., Viswanatha, N., Chary, M. L., Balan, K. S., Murthy, V. S., Aller, R., and Kumar, H. N. S. (1994). INSAT-2A and 2B deployment mechanisms. *In Proceedings of the 28th Aerospace Mechanisms Symposium*, NASA Lewis Research Center, May, 1994.

Scheeres, D. J., Hsiao, F.-Y., and Vinh, N. X. (2003a). Stabilizing motion relative to an unstable orbit: Applications to spacecraft formation flight. *Journal of Guidance, Control, and Dynamics*, 26(1):62–73. Doi: 10.2514/2.5015.

Scheeres, D. J., Hsiao, F.-Y., and Vinh, N. X. (2003b). Stabilizing Motion Relative to an Unstable Orbit: Applications to Spacecraft Formation Flight. *Journal of Guidance, Control, and Dynamics*, 26(1):62–73. Doi: 10.2514/2.5015 .

Schuerman, D. W. (1980). The restricted three-body problem including radiation pressure. *The Astrophysical Journal*, 238(1):337–342. Doi: 10.1086/157989.

Serban, R.and Koon, W. S., Lo, M. W., Marsden, J. E., Petzold, L. R., Ross, S. D., and Wilson, R. S. (2002). Halo orbit mission correction manoeuvres using optimal control. *Automatica*, 38:571–583. Doi: 10.1016/S0005-1098(01)00279-5.

Shahid, K. and Kumar, K. D. (2010). Spacecraft Formation Control at the Sun-Earth L_2 libration point using Solar Radiation Pressure. *Journal of Spacecraft and Rockets*, 47(4):614–626. doi: 10.2514/1.47342.

Shapiro, I. I. and Harrison, M. J. (1960). Perturbations of the orbit of the echo balloon. *Science*, 132(3438):1484–1486. Doi: 10.1126/science.132.3438.1484.

Simó, C., Gómez, G., Llibre, J., Martínez, R., and Rodríguez, J. (1987). On the Optimal Station Keeping Control of Halo Orbits. *Acta Astronautica*, 15:391–397. Doi: 10.1016/0094-5765(87)90175-5.

Sohon, R. L. (1995). Attitude stabilization by means of solar radiation pressure. *ARS Journal*, 29(5):371–373. Doi: 10.1016/0038-092X(59)90167-7.

Soldini, S., Colombo, C., and Walker, S. (2013). Adaptive structures for spacecraft orbit control. *In Proceedings of the 64th International Astronautical Congress*, IAC-13.C1.9.10, Beijing, China, 23-27 September, 2013.

Soldini, S., Colombo, C., and Walker, S. (2014a). Comparison of hamiltonian structure-preserving and floquét mode station-keeping for libration-point orbits. *In Proceedings of the AIAA/AAS Astrodynamics Specialist Conference*, AIAA-2014-4118, San Diego, California, 4-7 August 2014.

Soldini, S., Colombo, C., and Walker, S. (2014b). A feasibility study of solar radiation pressure feedback control strategy for unstable periodic orbits in the restricted three-body problem. *In Proceedings of the 65th International Astronautical Congress*, IAC-14.C1.6.13, Toronto, Canada, 29 September-3 October, 2014.

Soldini, S., Colombo, C., and Walker, S. (2015a). Solar radiation pressure end-of-life disposal for libration-point orbits in the elliptic restricted three-body problem. *In Proceedings of the AAS/AIAA Astrodynamics Space Flight Mechanics Meeting*, Williamsburg, VA, 11-15 January, 2015.

Soldini, S., Colombo, C., and Walker, S. (2015b). Solar radiation pressure enhanced disposal in the elliptic restricted three-body problem: applications to the gaia mission. *Celestial Mechanics and Dynamical Astronomy*, December 2015. (Under review).

Soldini, S., Colombo, C., and Walker, S. (2016a). The end-of-life disposal of satellites in libration-point orbits using solar radiation pressure. *Adv. Space Res.*, 57:1664–1679. Doi:10.1016/j.asr.2015.06.033.

Soldini, S., Colombo, C., and Walker, S. (2016b). Solar radiation pressure feedback control strategy for unstable periodic orbits in the restricted three-body problem. *Journal of Guidance, Control, and Dynamics*, January 2016. (Under review).

Soldini, S., Colombo, C., Walker, S., and Landgraf, M. (2014c). Libration-point orbit missions disposal at the end-of-life through solar radiation pressure. *In Proceedings of the* 2^{nd} *International Academy of Astronautics Conference on Dynamics and Control of Space Systems (DyCoSS)*, Rome, Italy, 24-26 March, 2014.

Soldini, S., Gómez, G., Masdemont, J. J., Colombo, C., and Walker, S. (2016c). Design of transfer trajectories: solar radiation pressure assisted mission near libration points. *Journal of Guidance, Control, and Dynamics.* (In preparation).

Spigel, M. R., Lipschutz, S., and Liu, J. (2013). *Schaum's outline of mathematical handbook of formulas and tables.* The McGraw-Hill Companies, US.

Stramacchia, M., Colombo, C., and Bernelli-Zazzera, F. (2016). Distant retrograde orbits for space-based near Earth objects detection. *Adv. Space Res., In Press*, xxx:xxx–xxx.

Strömgren, E. (1922). Forms of periodic motion in the restricted problem and in the general problem of three bodies, according to researches executed at the Observatory of Copenhagen. *Publikationer og mindre Meddeler fra Kobenhavns Observatorium*, 39:3–29.

Szebehely, V. (1967). *Theory of orbits in the restricted problem of three bodies.* Academic Press Inc., New York.

Szebehely, V. and Giacaglia, G. E. O. (1964). On the elliptic restricted three body problem. *The Astronomical Journal*, 69(3):230–235.

Szenkovits, F., Makó, Z., and Csillik, I. (2004). Polynomial representation of the zero velocity surfaces in the spatial elliptic restricted three-body problem. *Pure Mathematics and Application*, 15(2-3):323–322.

Tene, N., Richon, K., Folta, D., and Tene, K. (1998). Using solar radiation pressure to control L_2 orbits. *Advances in the Astronautical Sciences*, 100(2):617–627.

Thurman, R. and Worfolk, P. A. (1996). The geometry of halo orbits in the circular restricted three-body problem. Doctorial thesis, University of Minnesota.

Tsuda, Y., Mori, O., Funase, R., Sawada, H., Yamamoto, T., Saiki, T., Endo, T., Yonekura, K., Hoshino, H., and Kawaguchi, J. (2013). Achievement of ikaros japanese deep space solar sail demonstration mission. *Acta Astronautica*, 82(2):183–188. Doi: 10.1016/j.actaastro.2012.03.032.

Vallado, D. A. (2004). *Foundamentals of Astrodynamics*. Space Technology Library.

Van der Weg, W. J. and Vasile, M. (2014). Sun-Earth L_1 and L_2 to Moon transfers exploiting natural dynamics. *Celest. Mech. Dyn. Astr*, 120:287–308. Doi: 10.1007/s10569-014-9581-4.

Verrier, P. and Waters, T. (2013). Families of periodic orbits for solar sails in the CRTBP. *In Proceedings of the 3^{rd} International Simposyum on Solar Sailing*, Glasgow, Scotland, 2012.

Villac, B., Ribalta, G., Farrés, A., Jorba, A., and Mondelo, J. M. (2012). Using solar arrays for orbital control near small bodies. Trade-offs characterization. *In Proceedings of the AIAA/AAS Astrodynamics Specialist Conference*, Minneapolis, Minnesota, 2012.

Wertz, J. R. (1999). *Spacecraft Attitude Determination and Control*. Kluwer Academic Publishers, Torrance, CA.

Wie, B. (2004). *Space Vehicle Dynamics and Control*. AIAA Education Series, Toronto.

Wie, B. and Roithmayer, C. M. (2001). Integrated orbit attitude and structural control system design for space solar power satellites. *NASA/TM-2001-210854*.

Wiesel, W. E. and Pohlen, D. J. (1994). Canonical Floquét theory. *Celestial Mechanics and Dynamical astronomy*, 58(1):81–96. Doi: 10.1007/BF00692119.

Wiley, C. [pseudonym Saunders, R. . (1951). Clipper Ships of Space. *Astounding Science-Fiction*, May 1951.

Willis, P. and Hsieh, C. H. (1999). Space Applications of Polymeric Materials. *Scociety of Polymer Science*, Kobunshi, Japan, 1999. Doi: hdl:2014/18396.

Xin, M., B. S. N. and Pernicka, H. J. (2008). Libration Point Stationkeeping Using the θ-D Technique. *Journal of the Astronautical Sciences*, 56(2):231–250. Doi: 10.1007/BF03256550.

Xu, M. and Xu, S. (2009). Structure-preserving stabilization for hamiltonian system and its applications in solar sail. *Journal of Guidance, Control, and Dynamics*, 32(3):997–1004. Doi: 10.2514/1.34757 .

Yárnoz, G. D., Sánchez, J. P., and McInnes, C. R. (2013). Easly Retrievable Objects among the NEO Population. *Celest Mech Dyn Astr*, 116(4):367–388. Doi: 10.1007/s10569-013-9495-6.

Yárnoz, G. D., Scheeres, D. J., and McInnes, C. R. (2014). On the a and g families of symmetric periodic orbits in the Photo-gravitational Hill problem and their application to asteroids. *In Proceedings of AIAA/AAS Astrodynamics Specialist Conference*, San Diego, CA, 4-7 August 2014.